FEATURED ARTICLE | Absolute Lymphocyte Count After COVID-19 Vaccination Is Associated with Vaccine-Induced Hypermetabolic Lymph Nodes on ^{18}F-FDG PET/CT: A Focus in Breast Cancer Care. Romain-David Seban et al. See page 1231.

Immune response upon COVID-19 vaccination on ^{18}F-FDG PET/CT

1. COVID-19 vaccination
2. Blood analysis: lymphocyte count
3. ^{18}F-FDG PET/CT scan
4. Prediction of v-HLN with lymphocyte count

Vaccine-induced hypermetabolic lymph nodes (v-HLN)
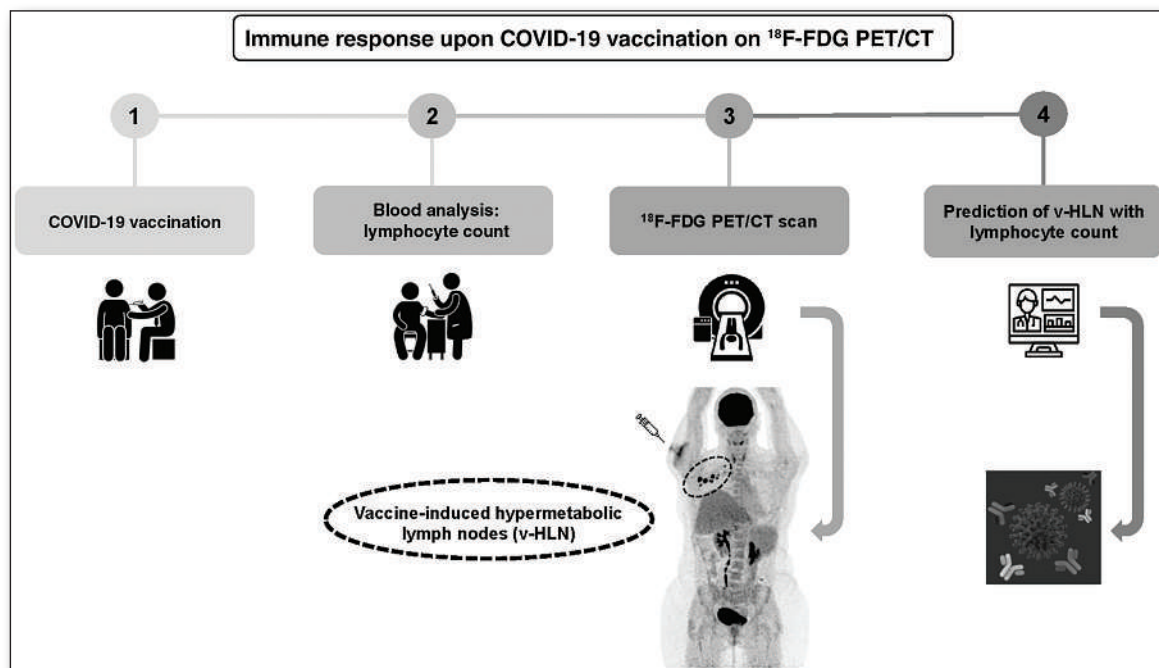
Enhanced ^{225}Ac therapy in solid tumors: combining carriers with complementary intratumoral microdistributions to deliver α-particles more efficiently and effectively. Alaina Howe et al. See page 1223.

TechneLite®
Technetium Tc 99m Generator

Tc 99m: The **core** of nuclear medicine imaging[1,2]

EFFICIENT AND RELIABLE[3]

- **Greater than 50 years of TechneLite® generator manufacturing expertise[3]**

- **Our 5th generation of dry-column technetium-99m generator advances[3]**

- **100% Assay and Mo-99 breakthrough testing[3]**

- **100% terminal sterilization following filling and in-process test elutions[3]**

INDICATIONS AND USAGE:

The TechneLite® generator is a source of sodium pertechnetate Tc 99m for use in the preparation of FDA-approved diagnostic radiopharmaceuticals, as described in the labeling of these diagnostic radiopharmaceutical kits.

Sodium Pertechnetate Tc 99m Injection is used IN ADULTS as an agent for:
- Thyroid Imaging
- Salivary Gland Imaging
- Urinary Bladder Imaging (direct isotopic cystography) for the detection of vesico-ureteral reflux
- Nasolacrimal Drainage System Imaging

Sodium Pertechnetate Tc 99m Injection is used IN CHILDREN as an agent for:
- Thyroid Imaging
- Urinary Bladder Imaging (direct isotopic cystography) for the detection of vesico-ureteral reflux

CONTRAINDICATIONS: None known.

Important Safety Information:

Allergic reactions including anaphylaxis have been reported infrequently following the administration of Sodium Pertechnetate Tc 99m Injection.

WARNINGS:

Radiation risks associated with the use of Sodium Pertechnetate Tc 99m Injection are greater in children than in adults and, in general, the younger the child, the greater the risk owing to greater absorbed radiation doses and longer life expectancy. These greater risks should be taken firmly into account in all benefit-risk assessments involving children. Long-term cumulative radiation exposure may be associated with an increased risk of cancer.

PRECAUTIONS:

Since the eluate does not contain an antimicrobial agent, it should not be used after 12 hours from the time of TechneLite®, Technetium Tc 99m Generator, elution. After the termination of the nasolacrimal imaging procedure, blowing the nose and washing the eyes with sterile distilled water or an isotonic sodium chloride solution will further minimize the radiation dose. As in the use of any radioactive material, care should be taken to minimize radiation exposure to patients and occupational workers. Radiopharmaceuticals should be used only by physicians who are qualified by training and experience and who are licensed in the safe handling of radionuclides.

Please see following page(s) for brief Prescribing Information. Full Prescribing Information may be accessed at https://www.lantheus.com//assets/TechneLite-PI-_513160-0719mktg.pdf

LANTHEUS™

References:
1. World Nuclear Association, http://www.world-nuclear.org/information-library/non-power-nuclear-applications/radioisotopes-research/radioisotopes-in-medicine.aspx Accessed April 1, 2019 2. FDA News Release, February 8, 2018, https://www.fda.gov/NewsEvents/Newsroom/PressAnnouncements/ucm595990.htm Accessed April 1, 2019 3. Quality data on file, Lantheus Medical Imaging, Inc.

TechneLite®
Technetium Tc 99m Generator

FOR DIAGNOSTIC USE

BRIEF SUMMARY

Please see Full Prescribing Information available at https://www.lantheus.com//assets/TechneLite-PI-_513160-0719mktg.pdf for complete Information.

INDICATIONS AND USAGE:

The Technelite generator is a source of sodium pertechnetate Tc 99m for use in the preparation of FDA-approved diagnostic radiopharmaceuticals, as described in the labeling of these diagnostic radiopharmaceutical kits.

Sodium Pertechnetate Tc 99m Injection is used IN ADULTS as an agent for:

> Thyroid Imaging
> Salivary Gland Imaging
> Urinary Bladder Imaging (direct isotopic cystography) for the detection of vesico-ureteral reflux.
> Nasolacrimal Drainage System Imaging

Sodium Pertechnetate Tc 99m Injection is used IN CHILDREN as an agent for:

> Thyroid Imaging
> Urinary Bladder Imaging (direct isotopic cystography) for the detection of vesico-ureteral reflux.

CONTRAINDICATIONS: None known.

WARNINGS: Radiation risks associated with the use of Sodium Pertechnetate Tc 99m Injection are greater in children than in adults and, in general, the younger the child, the greater the risk owing to greater absorbed radiation doses and longer life-expectancy. These greater risks should be taken firmly into account in all benefit-risk assessments involving children.

Long-term cumulative radiation exposure may be associated with an increased risk of cancer.

PRECAUTIONS:

General

As in the use of any radioactive material, care should be taken to minimize radiation exposure to the patient consistent with proper patient management and to ensure minimum radiation exposure to occupational workers.

Since the eluate does not contain an antimicrobial agent, it should not be used after 12 hours from the time of TECHNELITE®, Technetium Tc 99m Generator elution.

After the termination of the nasolacrimal imaging procedure, blowing the nose and washing the eyes with sterile distilled water or an isotonic sodium chloride solution will further minimize the radiation dose.

Radiopharmaceuticals should be used only by physicians who are qualified by training and experience in the safe handling of radionuclides and whose experience and training have been approved by the appropriate government agency authorized to license the use of radionuclides.

Carcinogenesis, Mutagenesis, Impairment of Fertility

No animal studies have been performed to evaluate carcinogenic potential or whether Sodium Pertechnetate Tc 99m affects fertility in males or females.

Pregnancy

Animal reproductive studies have not been conducted with Sodium Pertechnetate Tc 99m. It is also not known whether Sodium Pertechnetate Tc 99m can cause fetal harm when administered to a pregnant woman or can affect reproduction capacity. Sodium Pertechnetate Tc 99m Injection should be given to a pregnant woman only if clearly needed.

Ideally examinations using radiopharmaceuticals, especially those elective in nature, of a woman of childbearing capability should be performed during the first few (approximately 10) days following the onset of menses.

Nursing Mothers

Sodium Pertechnetate Tc 99m is excreted in human milk during lactation; therefore formula feedings should be substituted for breast feeding.

This radiopharmaceutical preparation should not be administered to pregnant or lactating women unless expected benefits to be gained outweigh the potential risks.

Pediatric Use

See INDICATIONS and DOSAGE AND ADMINISTRATION sections. Also see the description of additional risks under WARNINGS.

Geriatric Use

Clinical studies of TechneLite® did not include sufficient numbers of subjects aged 65 and over to determine whether they respond differently from younger subjects. Other reported clinical experience has not identified differences in responses between the elderly and younger patients. In general, dose selection for an elderly patient should be cautious, usually starting at the low end of the dosing range, reflecting the greater frequency of decreased hepatic, renal, or cardiac function, and of concomitant disease or other drug therapy.

ADVERSE REACTIONS: Allergic reactions including anaphylaxis have been reported infrequently following the administration of Sodium Pertechnetate Tc 99m Injection.

Lantheus Medical Imaging

331 Treble Cove Road

N. Billerica, MA 01862 USA

For Ordering Call Toll-Free: 800-299-3431
All other business: 800-362-2668

(In Massachusetts and International, call 978-667-9531)

Patent: http://www.lantheus.com/patents/index.html

LANTHEUS

JNM
The Journal of NUCLEAR MEDICINE

The Official Publication of **SNMMI**

JNM The Journal of NUCLEAR MEDICINE

2022 SNMMI Henry N. Wagner, Jr., MD, Best Abstract of the Year

A presentation on longer-term outcomes of [225]Ac-DOTATATE–targeted α therapy in patients with advanced-stage somatostatin receptor–expressing metastatic gastroenteropancreatic neuroendocrine tumors (GEP-NETs) was named as the Henry N. Wagner, Jr., MD, Abstract of the Year on June 13 at the SNMMI Annual Meeting in Vancouver, Canada. The study, titled "A phase II clinical study on [225]Ac-DOTATATE therapy in advanced-stage GEP-NET patients," was presented by Bal et al. from the All India Institute of Medical Sciences (New Delhi). This is the second year that research from this group was recognized with the Best Abstract Award, this time reporting on an expanded cohort with longer follow-up. Each year, SNMMI chooses an abstract that best exemplifies the most promising advances in the field of nuclear medicine and molecular imaging. This year, the awardee was chosen from more than 1,000 abstracts submitted for the meeting and voted on by reviewers and society leadership.

The study included 83 GEP-NET patients (34 women, 49 men; mean age, 54 ± 11.6 y; range, 25–74 y), of whom 56 had prior ^{177}Lu-DOTATATE treatment (24 stable disease, 32 progressive disease) and 27 had prior peptide-receptor radionuclide therapy. Participants were treated with a median of 4 (range, 1–10) [225]Ac-DOTATATE targeted α therapy cycles (100–120 kBq/kg body weight) and a renal protection protocol. Over a median follow-up of 18 months, 24 patients died, with 12- and 24-month overall survival (OS) of 85.3% and 67.6%, respectively. At a median follow-up of 27 months, estimated median OS was <50%. For the 74 patients who had undergone radiographic progression-free survival (rPFS) assessment, the median rPFS was not reached at the 18-month median follow-up, with 2 patients (2.7%) showing a complete response, 32 (43.2%) a partial response, 25 (34%) presenting with stable disease, and 15 (20%) with progressive disease. A higher percentage of patients who had failed previous ^{177}Lu-DOTATATE
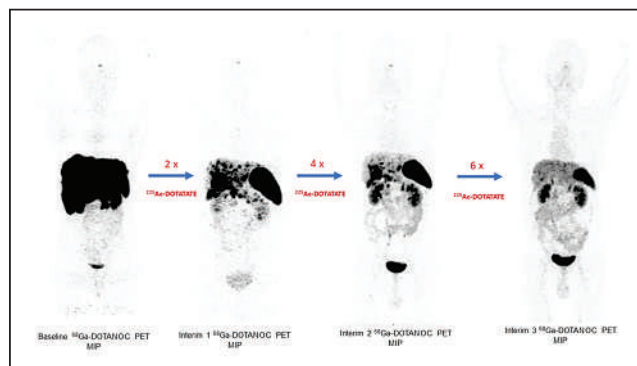
2022 SNMMI Abstract of the Year Excellent sustained response in a 34-year-old male with pancreatic neuroendocrine tumor. Baseline ^{68}Ga-DOTANOC PET maximum-intensity projection image (MIP) (left) shows intense somatostatin receptor expression in the pancreas, multiple abdominopelvic lymph nodes, and extensive liver metastases. The patient underwent 6 cycles of [225]Ac-DOTATATE (100–120 kBq/kg body weight; shown left to right in increments of 2 cycles) and remained under follow-up at 48 months.

treatment showed progressive disease (34%) than those who had not (11%). Only 1 grade 3/4 toxicity was noted.

"[225]Ac-DOTATATE is a promising therapy option that adds a new dimension to the treatment of end-stage GEP-NETs, especially for patients who have tried all other standard therapy options," said Chandrasekhar S. Bal, MD, DNB, DSc (HC), professor and head of the Department of Nuclear Medicine and PET at the All India Institute of Medical Science. "These results warrant a phase III randomized control trial to assess the true efficacy of [225]Ac-DOTATATE versus ^{177}Lu-DOTATATE."

"The results from this study not only emphasize the promise and success of targeted α therapies but also reflect growing global interest in these life-extending treatments," said Heather Jacene, MD, SNMMI Scientific Program Committee chair. "We look forward to further research on this topic in the future."

Cherry Receives 2022 Benedict Cassen Prize

Simon R. Cherry, PhD, known for his pioneering work in the development of PET technology and codevelopment of the EXPLORER total-body PET scanner, was awarded the Benedict Cassen Prize during the June SNMMI 2022 Annual Meeting in Vancouver, Canada. This honor is awarded every 2 years by the Education and Research Foundation (ERF) for Nuclear Medicine and Molecular Imaging in recognition of outstanding achievement and work leading to a major advance in nuclear medicine science.

"Dr. Cherry has dedicated his whole career to advancing molecular imaging," said ERF President Munir Ghesani, MD. "This award is a wonderful recognition of his seminal contributions to nuclear medicine instrumentation and molecular imaging generally, including his pioneering advancement of small-animal PET, PET/MR hybrid imaging, and total-body PET."

During a special plenary session at SNMMI's Annual Meeting, Cherry delivered the Cassen Lecture, titled "A Matter of Time." He discussed historical developments contributing to today's molecular imaging technologies.

Cherry received his undergraduate degree in physics and astronomy from University College London (UK) in 1986 and his doctorate in medical physics from the Institute of Cancer Research at the University of London in 1989. After a postdoctoral fellowship at the University of California, Los Angeles (UCLA), he joined the faculty in the UCLA Department of Molecular and Medical Pharmacology in 1993. In 2001, he went to the University of California, Davis (UC Davis) as a professor in the Department of Biomedical Engineering and established the Center for Molecular and Genomic Imaging, which he directed from 2004 to 2016. Cherry served as chair of the Department of Biomedical Engineering from 2007 to 2009 and is currently a Distinguished Professor at UC Davis. He is a coleader of the EXPLORER project with Ramsey Badawi, PhD.

Cherry is a founding member of the Society for Molecular Imaging (now the World Molecular Imaging Society) and an elected fellow of 6 professional societies, including the Institute of Electrical and Electronics Engineers (IEEE) and the Biomedical Engineering Society. He received the Academy of Molecular Imaging Distinguished Basic Scientist Award (2007), the Society for Molecular Imaging Achievement Award (2011), and the IEEE Marie Sklodowska-Curie Award

Simon R. Cherry, PhD, with Ramsey Badawi, PhD (left), and Munir Ghesani, MD (right).

(2016) for "contributions to the development and application of in vivo molecular imaging systems." In 2016, he was elected to the National Academy of Engineering and in 2017 to the National Academy of Inventors. Cherry has authored more than 300 peer-reviewed journal articles, review articles, and book chapters in the field of biomedical imaging. He is also lead author of the widely used textbook *Physics in Nuclear Medicine*, now in its 4th edition.

The Cassen Prize honors Benedict Cassen (1902–1972), whose invention of the rectilinear radioisotope scanner—the first instrument capable of making an image of radiotracer distribution in body organs of living patients—was seminal to the development of clinical nuclear medicine. Cherry is the 16th individual since 1994 to receive this prestigious $25,000 award from the ERF.

"It is a tremendous honor to receive the Benedict Cassen Prize," Cherry said. "In our quest to develop much more sensitive PET systems, we hope to improve our understanding of the human body in both health and disease and open up future applications for the field of molecular imaging, while at the same time improving diagnosis and disease management for patients today. These new systems that are being developed by us and others are the logical and ultimate manifestation of Benedict Cassen's pioneering work on organ and body imaging, and it is therefore particularly meaningful to receive an award named after him."

SPECTRUM
DYNAMICS MEDICAL

VERITON-CT®
DIGITAL SPECT/CT

Optimization of Every Step

Spectrum Dynamics has integrated its ground-breaking BroadView Technology design into the VERITON-CT system, providing a digital platform enabling routine 3D imaging in Nuclear Medicine. The result is optimization of every step, from image acquisition to interpretation.

VERITON-CT digital SPECT/CT combines the best-in-class CZT detectors, novel system design, high resolution CT, and advanced software technology to elevate the performance of 360˚ digital SPECT/CT.

BroadView Technology
Proprietary swiveling detector design provides increased sensitivity for faster scans
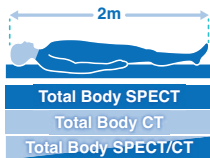
Total Body 3D Imaging
2m
Total Body SPECT
Total Body CT
Total Body SPECT/CT
200cm continuous coverage vertex to feet
SPECT | CT | SPECT/CT

80cm NM and CT bore
ALL SIZES
Wide Bore SPECT/CT
80cm NM and CT bore

Choice of 16/64 slice
16/64
Choice of high-resolution CT for diagnostic applications and low dose total body CTAC

TruView Console
One platform, one location for clinical care decision-making:
1. Acquisition
2. Advanced quantitative reconstruction
3. Both 3D and 4D data analysis and review

VERITON-CT Feature Application: 3D Dynamic Imaging

TruFlow for VERITON-CT offers real-time 3D in-vivo fast dynamic imaging to capture the radiopharmaceutical distribution, uptake, or clearance over time in 3D SPECT/CT parametric imaging.

TruFlow

spectrum-dynamics.com
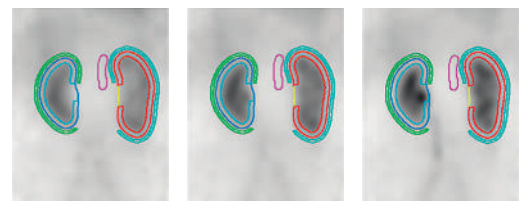
Schwaiger Recognized with de Hevesy Nuclear Pioneer Award

Markus Schwaiger, MD, a scientist known for his contributions to cardiac PET imaging, was named on June 12 as the 2022 recipient of the Georg Charles de Hevesy Nuclear Pioneer Award, presented by SNMMI at its 2022 Annual Meeting in Vancouver, Canada. Schwaiger was recognized for his significant work in multimodal imaging to visualize and quantify biologic processes. He played a key role in the advancement of nuclear cardiology, focusing on molecular mechanisms to develop novel quantitative methods and radiotracers. His translational approach included both preclinical and clinical trials, resulting in the creation of novel diagnostic and image-guided therapeutic paradigms. Schwaiger's research interests also included oncologic PET, as well as the diagnosis and treatment of thyroid endocrine and neuroendocrine diseases.

"Dr. Schwaiger has proven himself a scientific, clinical, educational, and administrative leader throughout his entire career," said 2021–2022 SNMMI President Richard L. Wahl, MD. "From his work in establishing PET as the standard for myocardial viability to his pioneering role in PET/MR imaging, his training of new generations of nuclear medicine leaders, and his establishment of centers of excellence at the Technical University of Munich, his dedication to the field has profoundly changed the way we practice nuclear medicine and molecular imaging."

Schwaiger completed his medical studies at the University of Freiburg and the Freie Universität Berlin (both in Germany). He completed a postdoctoral fellowship at the University of Cincinnati (OH) and returned to Germany as a resident at the Deutsches Herzzentrum München. From there, his career took him to the University of California, Los Angeles, where, as a fellow and assistant professor, he utilized PET to contribute novel insights to the field of cardiology. In 1986, Schwaiger moved to the University of Michigan (Ann Arbor), where he led the nuclear cardiology and cardiac PET program. He returned to Germany in 1993, serving as the director of the Department of Nuclear Medicine at the Klinikum Rechts der Isar of the Technische Universität München. He became the medical director and CEO there in 2016 and retired in 2021.

Each year since 1960, SNMMI has presented the de Hevesy Award to an individual for outstanding contributions to the field of nuclear medicine. De Hevesy received the 1943 Nobel Prize in chemistry for his work in determining the absorption, distribution, metabolism, and elimination of radioactive compounds in the human body. His work led to the foundation of nuclear medicine as a tool for diagnosis and therapy. The list of previous recipients of this award includes numerous Nobel laureates—such as Ernest Lawrence, PhD, who built the world's first cyclotron for production of radionuclides, and Glenn Seaborg, PhD, who discovered more than half a dozen new elements.

"I am honored to receive SNMMI's Georg Charles de Hevesy Nuclear Medicine Pioneer Award," said Schwaiger. "At every stage throughout my career I have had the pleasure of working with very talented colleagues who inspired and supported me. Together we have advanced the field of nuclear medicine and molecular imaging. Now, I am excited to observe and to applaud what the next generation of researchers in nuclear medicine will discover."
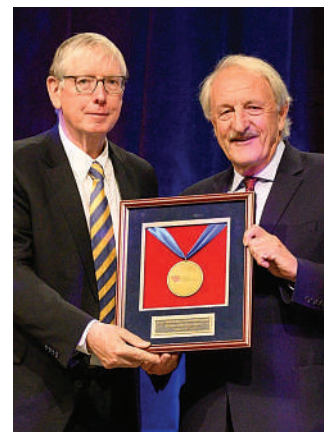
Markus Schwaiger, MD (right), receives de Hevesy Award from Richard L. Wahl, MD.

Mach Honored with SNMMI 2022 Paul C. Aebersold Award

Robert H. Mach, PhD, was named as the 2022 recipient of the prestigious Paul C. Aebersold Award during the June SNMMI Annual Meeting in Vancouver, Canada. Mach is the Britton Chance Professor of Radiology and director of the PET Radiochemistry Program at the University of Pennsylvania (Philadelphia). Mach has spent the majority of his career developing PET radiotracers to study the molecular basis of disease, and his research has spanned the fields of substance abuse, neurology, oncology, and cardiovascular disease. His major contributions to the field include the use of PET to identify the effects of socially derived stress on dopamine receptor function; identification of the role of a ternary complex among the sigma-2 receptor/TMEM97, LDL receptor, and progesterone receptor membrane component 1 in providing the high levels of cholesterol needed to support tumor cell proliferation; and the use of computational chemistry methods to study small molecule–protein interactions in the design of PET radiotracers. Several ongoing clinical trials focus on radiotracers developed in his lab.

Vasken Dilsizian, MD, chair of the SNMMI Committee on Awards, congratulated Mach on this achievement: "Robert is a truly deserving recipient of this esteemed award. His work with radiotracers has been the basis of many important research studies that have advanced the field of nuclear medicine and molecular imaging over the years."

Mach received his undergraduate degree in chemistry from the State University of New York (SUNY; Potsdam) in 1978 and a doctorate in medicinal chemistry from the SUNY School of Pharmacy (Buffalo) in 1985. He later served as a professor, director of the cyclotron facility, and head of the Radiological Chemistry Lab at the Mallinckrodt Institute of Radiology at the Washington University School of Medicine in St. Louis (MO).

An active member of the nuclear medicine and molecular imaging community, Mach is a past president of the SNMMI Radiopharmaceutical Sciences Council and a former board member of the Society of Radiopharmaceutical

Robert H. Mach, PhD, receives Aebersold Award. From left: Richard Wahl, MD; Carolyn Anderson, PhD; Mach; and Heather Jacene, MD.

Sciences. He received the SNMMI Michael J. Welch Award in 2018 and a Distinguished Investigator Award from the American Academy for Radiology and Biomedical Imaging Research in 2019. He has published more than 300 peer-reviewed articles and book chapters and holds 28 patents on radiotracer development. Mach is currently the principal investigator for 2 research centers funded by the National Institutes of Health (NIH) and has served on numerous review panels for NIH and the Department of Energy.

The Aebersold Award is named for Paul C. Aebersold, PhD, a pioneer in the biologic and medical application of radioactive materials and the first director of the Atomic Energy Commission's Division of Isotope Development. The award recognizes outstanding achievement in basic science applied to nuclear medicine and was first presented in 1973. The SNMMI Committee on Awards selects the recipient.

"It truly is an honor to be recognized by my colleagues and SNMMI for the Aebersold Award," said Mach. "This would not have been possible without the contributions of a very talented group of graduate students, postdocs, and research collaborators over the course of my career."

John G. Morris, AO, MBBS (1934–2022)

John Morris, MBBS, who made pioneering and influential contributions in Australia by taking radionuclide techniques from the research laboratory into clinical practice and by training the first generation of Australian nuclear medicine specialists, died in May. He was instrumental in bringing cyclotrons and PET to Australia, culminating in the official opening of the National Medical Cyclotron and the Royal Prince Alfred Hospital (RPAH) Sydney PET program in March 1992.

After graduating in medicine from the University of Sydney and completing residency in 1963, Morris became a clinical tutor in the Medical School at Sydney University. It was there that he met James McRae, MBBS, PhD, a physician and senior lecturer in medi-

John Morris, MBBS, at the National Medical Cyclotron, Sydney, Australia, 1992.

cine who had obtained his doctorate in medical physics in the 1950s at the Donner Lab (Berkeley, CA), where E.O. Lawrence, PhD, had developed the first cyclotron and won the 1939 Nobel Prize in Physics. McRae wanted to create a radiation medicine unit within the Medical School in Sydney, and Morris was attracted to this interesting new development. Their group carried out tracer (nonimaging) studies to investigate physiologic pathways in disease, unlike most other radioisotope units in Australia at the time that focused mainly on thyroid disease.

Morris oversaw, along with McRae, the movement of this service into clinical practice at RPAH in 1967. McRae was appointed as director of Diagnostic Isotope Services at RPAH, and Morris was appointed as the first nuclear medicine physician and eventually department head when McRae returned to the Donner Lab in 1971. Morris remained director of nuclear medicine at RPAH until 1999. His long career spanned the early days of radioisotope tracer studies, the first imaging studies using the rectilinear scanner and then the gamma camera, to tomographic imaging with SPECT and the introduction of PET.

McRae and Morris lobbied in the 1960s for the Australian Atomic Energy Commission (AAEC; forerunner of the Australian Nuclear Science and Technology Organisation), which operated Australia's only nuclear reactor, the 10-MW High Flux Australian Reactor, to become involved in radionuclide production for nuclear medicine and to add a cyclotron in Australia. They succeeded in their first goal around 1970, establishing a daily delivery of radiopharmaceuticals from the AAEC site in Sydney to all Australian capital cities, but it would be more than 20 years before the first cyclotron for medical radionuclide production came online in Australia.

Morris's continued advocacy for a medical cyclotron was instrumental in the decision of the Australian government in the 1980s to fund a National Medical Cyclotron, the first in Australia, and to support a proposed PET facility at RPAH. In preparation for the introduction of PET, Morris was responsible for creating a program that sent early career scientists, physicians, and technologists to train in internationally renowned PET centers, providing the opportunity to spend time overseas and return with knowledge and enthusiasm to implement this technology.

Perhaps more than anyone, Morris was instrumental in establishing nuclear medicine in Australia as a specialty of internal medicine staffed by physicians and strongly resistant to integration into radiology. His colleagues were not always in agreement, although his success in attracting and training a generation of nuclear medicine physicians who eventually led a large number of nuclear medicine departments around the country is a defining legacy of his vision and commitment to the field.

Morris also made an impact on the international nuclear medicine stage. He had a long association with the International Atomic Energy Agency (IAEA) and in 1967 accepted a 4-month assignment from the IAEA to establish a nuclear medicine department at Panduri Hospital (Bucharest, Romania). This led to an ongoing association between the IAEA and Morris's department at RPAH, which became the host site in Australia for IAEA regional training courses in physics, instrumentation, and computing, plus serving as the main site for development of the Distance-Assisted Training program for technologists. This program was extraordinarily successful and was rolled out throughout the region, translated into many languages, and eventually used in Latin America, producing more than 1,200 nuclear medicine technologist graduates in developing and emerging countries.

Morris had numerous interests outside his professional life. He owned a racehorse agistment and stud property near Sydney, and horse racing was a great interest. He helped introduce nuclear medicine bone scanning in performance horses in Sydney, later extending to small animal veterinary practice at the university in dogs and cats. He was widely read, with an extensive library, especially of Australian literature, and collected paintings by well-known Vietnamese artist Bui Xuan Phai.

After retiring from RPAH Morris remained active in lobbying for wider recognition of nuclear medicine procedures and expansion of the range of studies that could be undertaken. He received numerous awards, including the Australian Nuclear Association Award (the first medical graduate to receive this) and Honorary Life Membership in the Australian and New Zealand Society of Nuclear Medicine. He was made an Officer of the Order of Australia, one of Australia's highest honors, in 1999 "for service to the development of nuclear medicine through the establishment of the national medical cyclotron and the nuclear medicine PET centre." Morris will remain for many, quite literally, the father of Australian nuclear medicine.

Dale Bailey, PhD
Sydney, Australia
Andrew Scott, MBBS, MD
Melbourne, Australia

SNMMI 2022 Annual Meeting—In Person at Last

Virginia Pappas, CAE, SNMMI CEO

SNMMI hosted more than 6,700 physicians, scientists, technologists, pharmacists, laboratory professionals, and others from more than 131 countries at its hybrid 2022 Annual Meeting, June 11–14. Close to 60% of registrants attended in-person in Vancouver, Canada, and 40% took advantage of the meeting's virtual platform. For many, this was the first in-person professional meeting since the COVID pandemic began in 2020. SNMMI followed the recommendations of the SNMMI COVID Task Force to promote a safe environment for attendees, who were required to show proof of vaccination, and masking was mandatory in all convention center meeting rooms.

The meeting provided in-person attendees the opportunity to hear first-hand about the latest innovations in the field and to interact with colleagues from around the world. For those who could not attend in person, the virtual meeting was a convenient and effective way to participate.

More than 130 continuing education (CE) and scientific sessions were offered, covering the latest research in nuclear medicine–related cardiology, neurology, oncology, therapy, radiopharmaceutical science, basic science, and more. Five concurrent tracks provided attendees with up to 270 CE credits. The Annual Meeting exhibit hall featured 175 exhibitors, and the poster hall (in-person and virtual) included more than 800 posters.

Saturday's opening plenary session featured a special welcome and traditional music and dance from First Nation performers, as well as a greeting from the counsel general of France, the 2022 Highlight Country, and a talk by the president of the French Society of Nuclear Medicine. Sunday's Henry N. Wagner, Jr., MD, Lecture was presented by E.G. Elisabeth de Vries, MD, PhD, discussing opportunities to improve patient care in "Seeing the light with molecular imaging for systemic cancer treatment decisions." In Monday's Cassen Lecture, Simon Cherry, PhD, spoke on "A matter of time," reflecting on the evolution of nuclear medicine, the revolution in associated therapy, and new and upcoming developments in physics and equipment. In Tuesday's SNMMI-TS plenary session, best-selling author Paul Krismer addressed "Whole-person happiness." The meeting concluded with the Henry N. Wagner, Jr., MD, Highlights Symposium, with expert speakers covering new developments in nuclear medicine oncology, neuroscience, cardiology, and general nuclear medicine. SNMMI TV daily coverage of the meeting, along with featured interviews, is available at http://ow.ly/mEh130smUs1.

Interactive events kicked off with Saturday's opening reception in the exhibit hall. Sunday's events began at 6:30 AM with a well-attended Women in Nuclear Medicine breakfast featuring Meredith Walker, cofounder and executive director of Amy Poehler's Smart Girls. Later, "molecular hubs" drew first-time attendees, early-career professionals, and others together to meet colleagues and friends. The annual Knowledge Bowl was followed by a Diversity, Equity, and Inclusion Ice Cream Social; a Sunday poster mixer and reception; a new Monday Meet-the-Author poster hall reception; a variety of young professionals' events; and many other networking events and receptions, supplemented by an array of invited and peer-coordinated gatherings surrounding the meeting.

SNMMI and the Education and Research Foundation for Nuclear Medicine and Molecular Imaging presented a number of major awards at the meeting (see articles in this issue). A full list of awards will be published in SNMMI's 2022 Awards Guide.

At the Henry N. Wagner, Jr., Highlights Symposium, the scientific highlights of the Annual Meeting were presented in the context of modern molecular medicine. The SNMMI Henry N. Wagner, Jr., MD, Image of the Year—a depiction of ^{68}Ga-FAPI-46 PET signal after acute anterior myocardial infarction—was announced. The image was created by Johanna Diekmann, MD, and colleagues for their abstract "Predicting remodeling and outcome from molecular imaging of fibroblast activation in patients after acute myocardial infarction." The Henry N. Wagner, Jr., MD, Best Paper of the Year was awarded to Chandrasekhar S. Bal, MD, DNB, DSc (HC), and colleagues for their study "A phase II clinical study on ^{225}Ac-DOTATATE therapy in advanced stage gastroenteropancreatic neuroendocrine tumor patients."

For those who purchased the virtual meeting add-on, all scientific and CE sessions are available within the education portal on the SNMMI website. All abstracts are available on *The Journal of Nuclear Medicine* website.

Thanks to all attendees, exhibitors, speakers, SNMMI leaders and volunteers, and SNMMI staff for making this year's Annual Meeting an educational, enriching, and fun experience! I look forward to seeing everyone again at our 2023 Annual Meeting, June 24–27, at McCormick Place in Chicago, IL.

Aetna Reverses Cardiac PET/CT Noncoverage Policy

On June 16, SNMMI announced that Aetna, Inc. (Hartford, CT) had reversed a recent noncoverage policy on cardiac PET, in part as a result of responses from SNMMI and the American Society of Nuclear Cardiology (ASNC). SNMMI had received word earlier in the spring that Aetna would refuse coverage for hybrid PET/CT (CPT codes 78429–78431, 78433) on the basis that it was "experimental/investigational" and "not identified as widely used and generally accepted for the proposed uses as reported in nationally recognized peer-reviewed medical literature." The policy stated, "The fusion of PET and CT imaging into a single system (PET/CT fusion) is considered experimental and investigational for cardiac indications; a PET scan without CT is adequate to evaluate the myocardium (NIA, 2005)."

SNMMI and ASNC then sent a letter to Aetna requesting that the noncoverage policy be reversed, noting, "this decision is inconsistent with standards and practice for cardiac PET imaging across the United States." The groups added "not covering hybrid PET/CT denies patient access to standard-of-care testing that is required to make life-saving clinical decisions." The letter referred to the 2016 joint ASNC imaging guidelines and SNMMI procedure standards and position statement for the role of PET/CT in evaluation of coronary artery disease (*J Nucl Cardiol.* 2016;23:1227–1231), which have been accepted by the American Medical Association RVS Update Committee and multiple payers, including the Centers for Medicare and Medicaid Services.

Within a few days of receiving the letter, Aetna announced the reversal of the noncoverage policy. SNMMI leadership praised this outcome and Aetna's swift response.

SNMMI

SNMMI Launches Mars Shot Fund for Nuclear Medicine Research

SNMMI announced on June 13 the creation of the Mars Shot Fund, an initiative to raise $100 million for research in nuclear medicine, molecular imaging, and therapy. At the time of the announcement, the fund had received $600,000 in grants and pledges. The fund's organizers also hope to work to increase federal spending in the target areas. The SNMMI Mars Shot initiative stemmed from an article published in *The Journal of Nuclear Medicine* (2021;62[1]:6–14) that focused on the potential of innovations in the field. Richard Wahl, MD, 2021–2022 SNMMI president, and coauthors detailed 5 areas for needed growth, including oncologic imaging, cardiac imaging, neurologic imaging, physics and data science, and radiopharmaceutical therapy. "Research and development are critical to advancing these 5 areas of growth; however, current funding is lacking," said Wahl. "The National Institutes of Health [NIH] funding line is at about 10% right now. The Mars Shot Fund is a way to help fund highly innovative, high-impact research that might not be funded by NIH or other agencies."

The Mars Shot Fund is led by a board of scientists and funders, as well as a scientific advisory board. As additional funding is obtained, research support will be available through a grant application process. Applications will be reviewed by SNMMI study sections. Individuals and organizations have already made generous donations to the fund. SNMMI is advising the U.S. Congress to include a line item for the Mars Shot Fund in the Department of Energy or Department of Defense budgets in the coming session. Individuals are also being asked to contribute to the fund.

"We are in a revolutionary period for nuclear medicine, molecular imaging, and therapy," said Wahl. "It's essential that we capitalize on the momentum of this unparalleled innovation now so that we can continue to transform the nature of disease prevention, diagnosis, and treatment in the near future." Contributions to the Mars Shot Fund to support nuclear medicine and molecular imaging research can be made through www.snmmi.org/marsshot.

SNMMI

CDC Awards Funding for Cancer Prevention and Control

The Centers for Disease Control and Prevention (CDC) announced on June 8 first-year funding awards of $215 million in a 5-y, $1.1 billion investment into 3 national programs to prevent and control cancer. Eighty-six unique recipients from state, local, tribal, and territorial public health organizations and academic institutions received funding. Funded programs will demonstrate ways in which proven strategies advance health equity and build capacity in cancer prevention and control. Targeted outcomes include improving provision of clinical preventive services, facilitating planning among partners to promote evidence-based strategies in communities, and improving cancer surveillance.

"Today we know cancer as a disease that we often diagnose too late, but thankfully we have a few ways to prevent it and tackle stark inequities across races, regions, and resources," said Health and Human Services Secretary Xavier Becerra. "This funding is a critical investment in support of President Biden's Cancer Moonshot initiative and our efforts to help ensure that everyone in the United States equitably benefits from the tools we have to detect and diagnose cancer."

This new round of funding supports progress toward the CDC cancer prevention and control goals to reduce preventable cancers, ensure the right screening at the right time for the best outcomes, and improve health and wellness for cancer survivors leading to longer, healthier lives. The awardees will work within the framework of 3 national

cancer programs: the National Breast and Cervical Cancer Early Detection program, the National Comprehensive Cancer Control Program, and the National Program of Cancer Registries.

"This funding helps organizations work together to take action, address preventable health disparities, and close gaps in cancer care access, quality, and outcomes," said Becerra.

U.S. Centers for Disease Control and Prevention

Cancer Grand Challenge Awardees Announced

The National Cancer Institute (NCI) and Cancer Research UK, the world's leading funders of cancer research, announced on June 16 the awardees of $100 million in the Cancer Grand Challenges Program. The program aims to provide multiple rounds of funding for multidisciplinary research teams from around the world with novel ideas that have the greatest potential to advance cancer research and improve outcomes for people affected by cancer. The awards were announced at the Cancer Grand Challenges Summit in Washington, DC.

A total of 169 research teams from more than 60 countries submitted preliminary proposals addressing 1 of the 9 challenges posed by the Cancer Grand Challenges program. From those submissions, 11 teams were chosen by an expert group, including patient perspectives, to receive seed funding to develop their ideas into full proposals. Each of the 4 funded teams will receive up to $25 million. The winning multidisciplinary teams will: (1) explore cancer cachexia as a tumor-driven syndrome; (2) elucidate the action and targeting of extrachromosomal DNA in tumor evolution and treatment resistance; (3) develop engineered T-cell therapies for childhood cancer, with a focus on the tumor microenvironment; and (4) investigate the mechanisms that trigger normal cells to become cancerous. The awarded teams represent multidisciplinary international collaborations.

"The partnership with Cancer Research UK to develop the projects funded for the Cancer Grand Challenges program will enable a global collaboration on a disease that has touched everyone around the world," said Douglas R. Lowy, MD, acting director of NCI. "We're confident these multidisciplinary teams of scientists—with the flexibility and scale to innovate and carry out cutting-edge research—will be able to address several critical cancer research problems that can advance the understanding of cancer and benefit patients."

"Through this unique partnership, Cancer Grand Challenges fosters scientific creativity of the highest order, giving priority to innovative ideas that are beyond what can be supported through more traditional mechanisms," said Dinah S. Singer, PhD, NCI deputy director for scientific strategy and development. The next funding rounds of the NCI–Cancer Research UK partnership are planned for 2023 and 2025. For more information about the Cancer Grand Challenges program, visit https://www.cancer.gov/cancer-grand-challenges.

National Cancer Institute

International Conference on Radioactive Source Safety and Security

The International Conference on the Safety and Security of Radioactive Sources: Accomplishments and Future Endeavors was held by the International Atomic Energy Agency (IAEA) June 20–24 in Vienna, Austria, with more than 600 senior government officials and representatives from interested organizations. "As more people gain access to the huge benefits of radioactive sources, the work you and we are doing becomes even more important," IAEA Director General Rafael Mariano Grossi said to conference participants. He reported that more than 140 countries had so far expressed political commitment to the IAEA's Code of Conduct, making it the primary international instrument defining principles for safety and security of radioactive sources.

The conference included presentations in 6 main topic areas: safety and security of radioactive sources throughout their lifecycle, collaboration among national stakeholders, regulatory control of radioactive sources, sustainability and effectiveness of national infrastructures (including lessons learned from the COVID-19 pandemic), international cooperation, and preparation and response to radiologic incidents and emergencies involving radioactive sources.

International Atomic Energy Agency

NorthStar and Curie Announce ^{225}Ac Supply Agreement

NorthStar Medical Radioisotopes (Beloit, WI) and Curie Therapeutics, Inc. (Cambridge, MA), announced on June 7 the signing of a long-term priority access supply agreement for the therapeutic medical radioisotope ^{225}Ac. Under the terms of the agreement, NorthStar will provide Curie Therapeutics with priority access to its electron accelerator–produced no-carrier-added (nca) ^{225}Ac, which is free of long-lived radioactive contaminants and byproducts that pose regulatory and waste management challenges for hospitals and health systems.

"NorthStar is defining the supply chain for commercial-scale, reliable, and environmentally preferred therapeutic radioisotope production. We are very excited to be partnering with Curie Therapeutics, an emerging leader in the development of precision radiopharmaceuticals," said Stephen Merrick, president and CEO of NorthStar. "Clinical research and commercial use of ^{225}Ac are severely constrained by chronic short supply due to limitations of current production technologies. Our company is positioned to be the first commercial-scale producer of ^{225}Ac, utilizing our nca ^{225}Ac production technology which utilizes state-of-the-art electron-beam accelerator production that provides increased capacity and scheduling flexibility." Merrick reported that construction of the dedicated NorthStar ^{225}Ac production facility has begun, with initial production of radiochemical-grade ^{225}Ac slated for late 2023. The company expects to submit a Drug Master File to the U.S. Food and Drug Administration in 2024, which, on acceptance, will allow NorthStar to

JNM Impact Factor Rises Again

SNMMI and editors of *The Journal of Nuclear Medicine* (*JNM*) announced on June 28 that the publication had achieved the highest impact factor in its history, ranking fourth among all medical imaging journals, according to new data released in the *2021 Journal Citation Reports*. "This continued rise in visibility emphasizes not only the high quality of the journal but also the rise in importance of nuclear medicine as a whole," said *JNM* editor-in-chief Johannes Czernin, MD. "Revolutionary advances in nuclear medicine research are resulting in revolutionary care for patients."

JNM's impact factor increased more than 10% over last year, from 10.057 (2020) to 11.082 (2021). With 35,215 total citations, the journal was fourth in impact factor and third in Journal Citation Indicator among 200 journals in the medical imaging category. *JNM*'s total citations increased by 7%, and its 5-year impact factor increased almost 15%. Among nuclear medicine journals, *JNM* continues to have the highest impact factor, total citations, 5-year impact factor, Eigenfactor and normalized Eigenfactor scores, and article influence score.

"This is a tribute to the contributions of diverse scientists from all areas of the field, from advances in imaging instrumentation to important aspects of theranostic and therapeutic approaches," said Czernin. *JNM* has highlighted some of those advances in recent supplements focused on personalized dosimetry for cancer therapy, nuclear endocrinology, and molecular imaging of neurodegeneration.

The impact factor is a quantitative measure of the frequency with which an article in a journal is cited. It is used as a measure of the overall influence of a journal within scientific, professional, and academic communities. "I am grateful for the support of SNMMI and its Publications Committee, the valuable contributions of our staff, the vital input from our editorial board and reviewers, and the dedication and expertise of the team of associate editors whose work made this success possible," said Czernin.

SNMMI

(*Continued from page 17N*)

provide Current Good Manufacturing Practice–grade ^{225}Ac.

NorthStar Medical Radioisotopes
Curie Therapeutics, Inc.

Thomas J. Maloney, 1929–2022

Thomas J. Maloney, of Friendswood, TX, whose involvement with nuclear medicine and the radiopharmaceutical industry spanned more than half a century, died on March 29 at the age of 92. He was well known in nuclear medicine as the founder and owner of Iso-Tex Diagnostics, Inc., a radiopharmaceutical manufacturing firm, and Tel-Test, Inc., a provider of molecular reagents. Both companies were in Friendswood.

Maloney's long career began with completion of a 4-y apprentice program at General Electric (GE) as a tool and die maker, from which he transferred into the GE top-secret atomic submarine and Microgun research programs. He also trained in mechanical engineering at Union College (Schenectady, NY). He enlisted as a Graduate Officer candidate in the U.S. Army, where he served as an Expert Infantry Officer, Paratrooper 101st Airborne Division, Company Commander, Regimental Law Officer, and a commissioned First Lieutenant, Infantry. He later worked at Union Carbide as a mechanical engineer supervisor and a senior licensed atomic energy reactor operator in Tuxedo Park, NY, producing radiochemicals. He went on to become president of Cambridge Nuclear and later of Bio Nuclear (Houston, TX), before founding Iso-Tex and Tel-Test in 1975. His long career in the radiopharmaceutical industry included multiple patents, New Drug Applications, and Investigational New Drug applications.

Houston Chronicle

Scientific studies reported at the 2022 SNMMI Annual Meeting in Vancouver, Canada, June 11–14, covered a broad range of topics in molecular imaging, therapy, instrumentation, research, and clinical practice. A number of these studies were reported in national and international media. Following is a selection and brief overview of some of these presentations.

Self-Collimating Cardiac SPECT

Researchers from Tsinghua University (Beijing, China) and the University of Buffalo (East Amherst, NY) reported on a "Feasibility study of a self-collimating SPECT for fast dynamic cardiac imaging." The authors described development and validation of a system in which active detectors in a multilayer architecture carry out the dual functionality of detection and collimation, improving on documented limitations of mechanical collimators. The results hold promise for "expanding clinical applications of dynamic cardiac SPECT imaging by eliminating the impact of respiratory motion, increasing patient throughput, enabling ultra-low-dose imaging, and precisely quantifying myocardial blood flow and coronary flow reserve."

"SPECT is an important noninvasive imaging tool for the diagnosis and risk stratification of patients with coronary heart disease," said Debin Zhang, a doctoral student at Tsinghua University. "However, conventional SPECT suffers from long scan time and poor image quality as a result of relying on a mechanical collimator. The new SPECT system is capable of performing fast-framed dynamic scans with high quality."

"The technology proposed in this work may drive a paradigm shift in all single-photon-emission–based molecular imaging and nuclear medicine technologies," said Tianyu Ma, PhD, associate professor at Tsinghua University and senior author of the study. "The new detector design opens up a broad range of possibilities for development of new imaging systems with better image quality, higher speed, and better diagnostic accuracy in molecular imaging."

PSMA PET Mapping and Salvage Radiation Therapy

Multiple presentations at this year's SNMMI meeting covered studies on prostate-specific membrane antigen (PSMA) targeting. "PSMA PET mapping of postoperative local recurrence and impact on prostate fossa contouring guidelines for salvage radiation therapy [SRT]," was the focus of a report from researchers at the University of California, Los Angeles (UCLA), the University of Miami Miller School of Medicine (FL), and the VA Greater Los Angeles Healthcare System (CA). The authors used ^{68}Ga-PSMA-11 PET/CT data to analyze typical patterns of disease in patients experiencing biochemical recurrence of prostate cancer in the prostate fossa after radical prostatectomy. They evaluated correlations between clinical target volumes (CTVs) delineated using the Radiation Therapy Oncology Group (RTOG) contouring guidelines and patterns of PSMA PET–identified recurrence in the prostate fossa. A total of 230 patients with such recurrence on PSMA PET were included in the analysis (127 patients with PSMA-detected recurrence limited to the prostate fossa, 30 with PSMA-detected disease spread to pelvic nodes only, 34 to distant organs and/or extrapelvic nodes only, and 39 to both pelvic nodes and distant organs/extrapelvic nodes).

The authors found that in patients experiencing biochemical recurrence with disease limited to the posterior fossa, the RTOG contouring guidelines for salvage radiation therapy covered the full extent of the disease in 41% of patients. In 46%, the recurrence was only partly covered, and in 13% recurrence was located fully outside the CTV. They concluded that this study suggested that PSMA PET should be incorporated into updated radiation treatment contouring guidelines. "This study has the potential to redefine prostate bed contouring guidelines to improve the therapeutic ratio for patients receiving postoperative radiotherapy," said Ida Sonni, MD, lead author from UCLA. "Nuclear medicine and molecular imaging advances, such as PSMA PET, have the ability to guide individualized, tailored treatments that will ultimately benefit all our patients."

Melanoma-Targeting Radiopharmaceutical Pair

Researchers from the National Institute of Radiological Sciences/National Institutes for Quantum and Radiological Science and Technology (Chiba, Japan) reported on "Theranostics of melanoma-targeting metabotropic glutamate receptor 1 [GRM1] with a novel small-molecular radiopharmaceutical pair." They described the design, synthesis, and development of a novel small-molecular radiopharmaceutical theranostic duo, 1 intended for PET imaging and labeled with ^{11}C (^{11}C-1) and the other intended for therapy and labeled with ^{211}At (^{211}At-1). The theranostic potentials of the radiolabeled pair were explored in GRM1-positive B16F10 melanoma-bearing mice. ^{11}C-1 PET imaging was performed to visualize the melanoma, and mice were treated with ^{211}At-1 and monitored for tumor growth and adverse effects. Serial ex vivo biodistribution studies were conducted after imaging in subgroups of mice.

PET clearly visualized targeted melanomas with good tumor-to-background contrast. Ex vivo biodistribution studies verified the consistent increase of ^{11}C-1, which reached 12.29 ± 2.44 %ID/g tissue in the targeted melanomas at 90 min after injection and rapidly cleared from nontarget organs. Treatment with ^{211}At-1 showed "unequivocal and durable" antitumor efficacy with only a single treatment (2.96 MBq). No decreases in body weight and no liver or kidney damage were observed during the study period in the mice injected with ^{211}At-1.

"The results of this study highlight the strong potential of using ^{11}C-1 and ^{211}At-1 as theranostic agents for the management of GRM1-positive tumors," said Lin Xie, MD, PhD, first author of the presentation and a senior researcher at the National Institutes for Quantum and Radiological Science and Technology. "This radiopharmaceutical pair may have broad application and help to bring us 1

step closer to winning the fight against solid cancers."

AI-Generated Virtual CT for PSMA PET

Investigators from the National Cancer Institute (NCI; Bethesda and College Park, MD) reported on "Artificial intelligence [AI]–generated PET images for prostate-specific membrane antigen [PSMA] PET/CT studies: Quantitative and qualitative assessment." The group's novel method used AI techniques to reduce or eliminate the need for CT-based attenuation correction, creating a virtual attenuation correction model for PET.

Data for AI model development were generated from >300 clinical ^{18}F-DCFPyL PSMA PET/CT studies, each including a non-attenuation-corrected PET, attenuation-corrected PET, and low-dose CT. Studies were then assigned to 3 sets for training ($n = 185$), validation ($n = 60$), and testing ($n = 60$). A 2D Pix2Pix generator was then used to create synthetic attenuation-corrected PET scans from the original non-attenuation-corrected PET. For qualitative evaluation, 2 nuclear medicine physicians reviewed 20 of the 60 testing PET/CT studies in a randomized order, blinded to whether images were attenuation corrected by CT or with the virtual process. Readers were able to successfully detect lesions on the AI-generated PET images with reasonable sensitivity values, although they reported poor image quality, a result of downscaling and loss of uptake values during pre- and post-processing of AI-generated images.

"High-quality artificial intelligence-generated images preserve vital information from raw PET images without the additional radiation exposure from CT scans," said Kevin Ma, PhD, first author of the study and a postdoctoral researcher at NCI. "This opens opportunities for increasing the frequency and number of PET scans per patient per year, which could provide more accurate assessment for lesion detection, treatment efficacy, radiotracer effectivity, and other measures in research and patient care."

Novel PET Agent for Meningioma Imaging

Authors from University Hospital/ Ludwig Maximilians Universität (LMU) Munich (Germany), the Technische Universität Dortmund (Germany), Heidelberg University (Mannheim, Germany), and the University of Alberta (Edmonton, Canada) reported on "Next-generation PET/CT imaging in meningioma: First clinical experiences using the novel somatostatin-receptor [SSTR]–targeting peptide ^{18}F-SiTATE." ^{18}F-SiTATE has previously shown superior imaging properties in neuroendocrine tumors. This study included 86 patients with known or suspected meningiomas who underwent ^{18}F-SiTATE PET/CT. Among factors assessed were SUV_{mean} and SUV_{max} in tumors, healthy organs, and nonmeningioma lesions. Transosseous extension of meningiomas was assessed on PET and compared to morphologic imaging on CT or MR. A total of 177 lesions were classified by ^{18}F-SiTATE PET as meningioma and 41 as nonmeningioma lesions (including post-therapeutic changes, schwannomas, etc.). Ninety-one (51.1%) meningiomas showed partial transosseous extension, and 24 (13.6%) showed predominantly intraosseous extension. Forty-eight (27.1%) of the meningioma lesions were not clinically suspected and/or not detected on previous conventional imaging. SUV_{mean} was lowest in healthy brain tissue, followed by bone marrow, parotid gland, and pituitary gland. SUV_{max} was significantly higher in meningiomas than in nonmeningioma lesions; however, high uptake was found in some nonmeningioma lesions (malignant pituitary adenoma, schwannoma, sinusitis). No adverse events were associated with the study.

Researchers noted that the ^{18}F-SiTATE agent's longer half-life than ^{68}Ga-DOTATATE and ^{68}Ga-DOTATOC and independence from ^{68}Ge/^{68}Ga generators confer significant logistic advantages that could enable widespread use of SSTR-targeted imaging in neurooncology. "This study shows that ^{18}F-SiTATE PET/CT has a high feasibility for the detection of meningiomas, including bone involvement. This is especially important since bone involvement has major impact on surgery and radiotherapy planning for meningioma patients yet cannot be properly assessed using standard morphological imaging," said Marcus Unterrainer, MD, PhD, MSc, first author and a radiologist and nuclear medicine physician at LMU.

PET Links Obstructive Sleep Apnea Cardiovascular Disease

Investigators from the Yale University School of Medicine (New Haven, CT) and Ocean University Medical Center/ Hackensack Meridian Health (Brick, NJ) reported that "Obstructive sleep apnea [OSA] severity is associated with abnormal ^{82}Rb myocardial PET blood flow reserve [MFR]." They assessed correlations between markers of OSA severity (frequency of upper airway obstruction, hypoxia severity, and clinical symptoms of sleepiness) with coronary microvascular disease.

The cross-sectional analysis included 346 patients who underwent diagnostic overnight polysomnography and ^{82}Rb cardiac PET perfusion imaging. Obstructive features were categorized using the apnea–hypopnea index (AHI) as mild or no, moderate, or severe OSA. Abnormal MFR was defined as a ratio of stress to rest myocardial blood flow <1.5 after rate-pressure product correction. Odds ratios of abnormal MFR for each of the OSA severity categories were calculated, with resulting models adjusted for multiple comorbidities, demographics, and lifestyle factors. Although patients with abnormal MFR were generally older on average than those with normal MFR (62 and 59 y, respectively), no associations were noted between abnormal MFR and sex, race, body mass index, hypertension, or hyperlipidemia. The frequency of abnormal MFR increased with worsening AHI. Individuals with severe OSA were more than twice as likely to have abnormal MFR than those with mild or no OSA or those with nonsevere OSA.

"Interestingly, the significant relationship between OSA severity and MFR persisted among those with normal heart PET perfusion scans and no prior history of coronary artery disease," said Ehimen Aneni, MD, MPH, first author and an instructor at the Yale University School of Medicine. "The findings of this study may begin to explain why people with obstructive sleep apnea develop heart disease, including heart failure. Future studies should focus on the role of MFR in risk stratification and prognosis of OSA, as well as on the impact of OSA-specific therapy on MFR."

Practicing Medicine in Wartime Ukraine
A Conversation Between Yaroslav Kmetyuk, Johannes Czernin, and Ken Herrmann

Yaroslav Kmetyuk[1], Johannes Czernin[2], and Ken Herrmann[3]

[1]All-Ukrainian Radiosurgery Center, Clinical Hospital "Feofaniya," Kyiv, Ukraine; [2]David Geffen School of Medicine at UCLA, Los Angeles, California; and [3]Department of Nuclear Medicine, Universitätsklinikum Essen, Essen, Germany

Johannes Czernin, editor in chief of *The Journal of Nuclear Medicine*, and Ken Herrmann, a professor of nuclear medicine at the Universitätsklinikum Essen (Germany), talked with Yaroslav Kmetyuk, head of the All-Ukrainian Radiosurgery Center at the "Feofaniya" Hospital in Kyiv, Ukraine, about challenges in medical practice during the ongoing war. Dr. Kmetyuk received his medical education at Ivano-Frankivsk State Medical Academy (Ivano-Frankivsk, Ukraine), where he subsequently interned in radiology. At the P.L. Shupnik National Medical Academy of Postgraduate Education (Kyiv, Ukraine), he specialized in nuclear medicine. He completed additional nuclear medicine training at University Hospital Freiburg (Germany). Since 2008 he has been at the Clinical Hospital "Feofaniya," where he created the first PET/CT center in Ukraine, including staffing, quality assurance programs, and radiopharmacy production. His current oversight includes both radiation oncology and nuclear medicine. The following conversation took place on May 24, 2022.

Dr. Czernin: *The Russian invasion of the independent Ukraine began on February 24, 2022, in the middle of your regular work schedule. What was this like as a practicing physician? How did you adapt to the constant shelling and bombing and continue to support your patients?*

Dr. Kmetyuk: On February 24 I woke up to the sound of missiles and helicopters. It took half an hour to get my family and belongings together, and we went to the hospital, where I would spend the next 1.5 months.

Dr. Herrmann: *With your family?*

Dr. Kmetyuk: No. My family stayed for 2 very long nights in the hospital, and then I managed to send them to western Ukraine.

Dr. Herrmann: W*here did you send them? It must have been difficult to find a place.*

Dr. Kmetyuk: Actually, I grew up in the western part of Ukraine, close to Lviv, and I graduated from medical school there. My parents still live there, so when I had the opportunity to put my family on a special emigration bus, I sent them. They spent a few weeks with my parents and then went on to Poland. In May, however, they came back from Poland—back to Ukraine.

Dr. Czernin: *Are they still in western Ukraine?*

Dr. Kmetyuk: Yes, in the western part of Ukraine it feels much safer, and there are fewer air and bomb alerts.

Dr. Czernin: *How were you able to continue to work while all of this was going on? I understand that you were living in the hospital basement and maintaining a regular clinic schedule for as many patients as possible. You never stopped patient care, did you?*

Dr. Kmetyuk: We never stopped radiation therapy, because it's not good to stop at half of the planned dose. Many patients were still in Kyiv without the ability to evacuate to a safer place. I had a minimal staff for providing radiation therapy. During most of March we had to discontinue nuclear medicine services, but by the end of March we resumed work, including both radiopharmacy production and clinical service.

Yaroslav Kmetyuk, MD, PhD

Dr. Herrmann: *In previous communications you noted that you and your radiation oncology and nuclear medicine staff moved into the hospital. How many people joined you living in the hospital?*

Dr. Kmetyuk: For approximately 1.5 months 15–20 people lived with me in the basement. It was just enough staff to provide full-time radiation therapy. And we were able to bring back the diagnostics within a month.

Dr. Herrmann: *Can you tell us a little more about life in the basement with your team? Did you have enough food? You were (and continue to be) facing an extremely serious and changing situation every day.*

Dr. Kmetyuk: I work in a public clinic. "Feofaniya" is a multidisciplinary hospital, with many departments. Most of the staff from other departments lived and worked here as well, providing care for patients and for injured civilians and soldiers. The nuclear medicine department was also involved, because the CT scanners in the radiology department could not meet the needs of all those injured people. We used the PET/CT scanners for CT trauma imaging. Most of the surgeons and physicians lived here in the hospital so as not to waste time in dangerous commuting. It was impossible to move around old Kyiv, especially in the first weeks, when the street fighting took place. You probably saw on TV the blown-up tanks and military equipment on the streets. Some of our workers came under fire in the street. They are all alive, and no one was seriously injured. It was much smarter to live in the hospital, which has good shelters in the basement. And we were needed here: we not only participated in medical care but also provided social and humanitarian aid. Personnel brought food to the hospital, and we had enough to survive.

Dr. Czernin: *How many medical and technical staff in all were living in the hospital at the peak of this crisis period?*

Dr. Kmetyuk: I think around 350 people lived in the hospital.

Dr. Czernin: *Did in-patient service also continue? Was the hospital fully occupied with patients?*

Dr. Kmetyuk: All patients who could be safely checked out of the hospital were discharged during the first days. Patients who needed continuing care stayed in the hospital. The biggest challenge was that air raid alerts were sounding all the time, and we could hear the constant shelling and bombing. It was difficult, because when this happened, all patients had to be moved to the basement. This was especially challenging for the resuscitation team, who had to transport all patients on artificial ventilation and oxygen.

Dr. Herrmann: *You were extremely busy. Did you even have time to worry? How do you function under these conditions? How do you handle this kind of stress and pressure?*

Dr. Kmetyuk: It's much easier not to go crazy when you are very busy. Even when we are not with patients, we try to do something useful, even if it's only to move furniture to protect the windows or unload a truck with humanitarian aid—types of work that doctors do not do in everyday life.

Dr. Czernin: *In April, the Russians withdrew from Kyiv. Is the bombing largely over, or are the attacks continuing?*

Dr. Kmetyuk: The first month and a half was very dangerous because of the artillery. The Russians were so close that ground shelling came without air alerts. Ballistic missiles are still coming to Kyiv, hitting buildings and killing people. The last hit was last week. But the air alerts now sound off only 3–5 times per day. These alerts last for about an hour. You can imagine that it's not easy to work in this situation. We have to decide whether to continue with ongoing treatments. For radiation treatment, the patient usually stays in the treatment area with 2 team members who stay to finish the procedure. We do the same with PET scanning—we finish the acquisition and then take the patient to the shelter. Family members and accompanying persons are moved to the basement immediately when air alerts sound off.

FIGURE 1. Patients waiting in basement at Clinical Hospital "Feofaniya" in Kyiv.

˝For approximately 1.5 months 15–20 people lived with me in the basement. It was just enough staff to provide full-time radiation therapy.˝

Dr. Herrmann: *I would like to know, how we can help? Is there anything we can do apart from saying that we feel with you? Or is there anything where you say, "I wish you guys would do this for us?"*

Dr. Kmetyuk: Actually, you have helped a lot with your support. We see every day that European countries unite with the United States to provide increased support. Now, as the threat of tactical nuclear strikes and the threat of enemy-occupied nuclear power plants persists, we need portable radiation detectors. Other equipment, especially if not included in the list of critical wartime purchases, is needed. One example is that before the war in my department I found an error of up to 10% in standard dose calibrator measurements for ^{18}F (leakage of inert gas from the chamber). Because this equipment is not included in the critical list, we will not be able to upgrade in the near future. I am also encouraged by your personal support. The knowledge that you are ready to help in case of, for example, my family being somewhere in Europe and unable to find assistance is very important for me, Ken. Since the beginning of the war, I have received numerous letters of support from colleagues in Europe, in particular my friend and guide to the world of PET/CT, Philipp T. Mayer, from University Hospital Freiburg, Germany, and a longtime fellow hematologist, Andrea Galamini, from the Lacassagne Cancer Center in Nice, France.

Dr. Czernin: *After the withdrawal of the troops from Kyiv, the Russian army moved to the eastern part of Ukraine. Are you in contact with the hospitals in this region, and how are they handling the current massive attacks and destruction?*

Dr. Kmetyuk: We have 46 nuclear medicine departments in our country of 40 million people, with only 4 PET/CT scanners. Nine of these departments have radiation treatment units. Kharkiv, a large city to the north and close to the Russian border, cannot currently provide diagnostic or therapeutic services because of the lack of medical staff. Many people left Kharkiv.

Dr. Czernin: *In a totally different context, the U.S. health care system lost many nurses and hospital employees at all levels during COVID. On a much larger relative scale you also have millions of refugees and displaced people. Do you have enough nursing, physician, and technologist capacity?*

Dr. Kmetyuk: Some of the medical personnel went to the west or to Europe, and some of them are still there. But many health personnel in eastern Ukraine, close to the fight, came to Kyiv. We
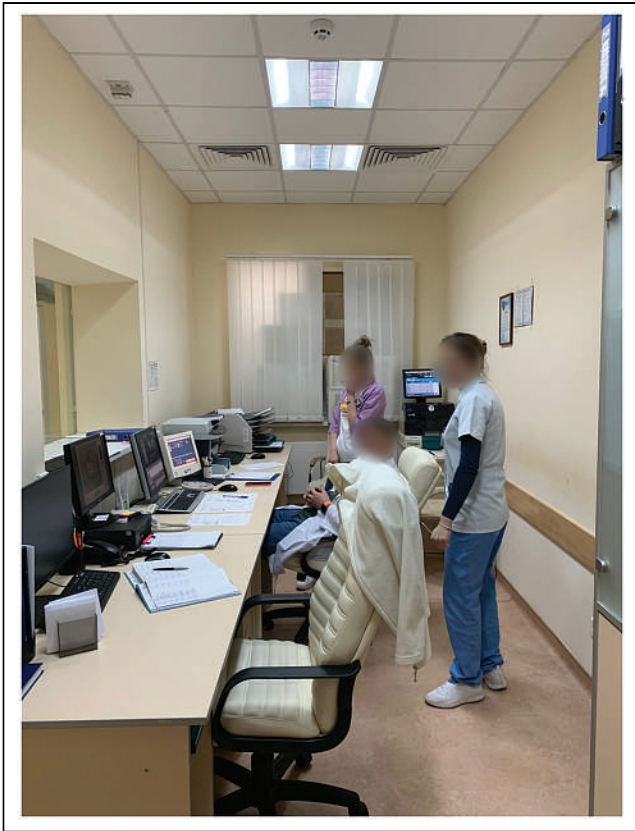
FIGURE 2. Author's nuclear medicine staff in the scanning room. Note boxes stacked against window to block flying glass from bombardment.

FIGURE 3. Soldiers from the trauma department.

"I am proud of the colleagues with whom I work, and I admire their courage. I hope we will win soon and rebuild Ukraine to become an even better country than before."

can now include these people in our workforce. We have 60 new doctors, nurses, and other medical staff.

Dr. Czernin: *When they come, is there a spirit of patriotism— that they have to do their part in the hospital to help the country?*

Dr. Kmetyuk: More than that: some of our colleagues from my hospital are now in various positions in the Ukrainian army.

Dr. Herrmann: *How do you cover for them when they go to the army?*

Dr. Kmetyuk: We have the time that until recently we spent with our families, on our hobbies, in our sports, and so on. It's not so hard to cover for your friend who fights if you live in the hospital. We get patients from the battlefield on trains, buses, helicopters, and every other means of transport, because the military hospitals in the west are totally full. Some doctors from my hospital went to Dnipro, to perform surgery at the largest military hospital there. But after a week they decided that it is easier to move patients here for treatment. We remain very busy here.

Dr. Herrmann: *You showed us several photographs illustrating the situation in the hospital. Can you explain what they show?*

Dr. Kmetyuk: Yes, you can see patients waiting in the basement (Fig. 1) and our staff in the scanning room (Fig. 2). The

windows are blocked with boxes to prevent glass from breaking in a close bombardment. Figure 3 shows soldiers from the trauma department, and Figure 4 shows my colleague, who came for a few days to perform some CT-guided biopsies and went back to Kharkiv to fight.

Dr. Herrmann: *What do you wish for, and what do you think is going to happen?*

Dr. Kmetyuk: People are better adapted to the situation now. In Kyiv it's much easier than it was 3 months ago, but you never know what to expect from Russia. They can try to attack Kyiv again at any time from the Belarus border. Our people who came back to Kyiv are nervous and traumatized. We don't know what will happen tomorrow. We try to live, to work, and to help people. I hope that it will end 1 day, hopefully soon, and all our families will be together.

Dr. Herrmann: *I am very impressed with the Ukrainian leadership. The president is a hero.*

Dr. Kmetyuk: He is. Yes, he inspires all of us, of course. President Zelensky could have left the country, but he did not. The same with the head of our hospital, Igor Semeniv, who stayed in the hospital throughout. It inspired our personnel. So, everybody stayed.

FIGURE 4. Author's medical colleague, who is also a fighter in Ukrainian army and was treated at Clinical Hospital "Feofaniya."

Dr. Czernin: Yaroslav, we're coming to the end of this very emotional, moving, and sometimes sad discussion, buoyed by your optimism and heroism. Do you have a message to convey to our international readership?

Dr. Kmetyuk: I did not prepare a formal message, but I can share with you my thoughts. I work in a rather narrow medical field. But now I see all these severe trauma cases—injuries that are just horrible—and I know that every one of us, every doctor, every nurse, especially in this time must do their best to work because this help is crucially important. I am proud of the colleagues with whom I work, and I admire their courage. I hope we will win soon and rebuild Ukraine to become an even better country than before.

Dr. Herrmann: *I hope that if I am ever in a similar position that I can be half as brave as you.*

Dr. Kmetyuk: Thank you.

Dr. Czernin: *Thank you very much, Yaroslav. We look forward to seeing you when this is all over.*

SIR-Spheres Activity Measurements Reveal Systematic Miscalibration

Stephen A. Graves[1–3], Molly Martin[1], Ashok Tiwari[1,4], Michael Merrick[1,2], and John Sunderland[1,4]

[1]Department of Radiology, University of Iowa, Iowa City, Iowa; [2]Department of Biomedical Engineering, University of Iowa, Iowa City, Iowa; [3]Department of Radiation Oncology, University of Iowa, Iowa City, Iowa; and [4]Department of Physics, University of Iowa, Iowa City, Iowa

The purpose of this work was to perform an independent and National Institute of Standards and Technology–traceable activity measurement of ^{90}Y SIR-Spheres (Sirtex). γ-spectroscopic measurements of the ^{90}Y internal pair production decay mode were made using a high-purity germanium detector. **Methods:** Measured annihilation radiation detection rates were corrected for radioactive decay during acquisition, dead time, source attenuation, and source geometry effects. Detection efficiency was determined by 2 independent and National Institute of Standards and Technology–traceable methods. **Results:** Measured SIR-Spheres vials ($n = 5$) contained more activity than specified by the manufacturer calibration; on average, the ratio of measured activity to calibrated was 1.233 ± 0.030. Activity measurements made using 2 distinct efficiency calibration methods agreed within 1%. **Conclusion:** The primary SIR-Spheres activity calibration appears to be a significant underestimate of true activity.

Key Words: TARE; radioembolization; radiopharmaceutical therapy

Dosimetry-guided radiopharmaceutical therapy is gaining traction in nuclear medicine and adjacent fields. Several agents have been approved with a requirement of dosimetry (^{131}I-metaiodobenzylguanidine, ^{90}Y TheraSphere [Boston Scientific]), but even agents that do not currently carry a dosimetry mandate (e.g., ^{177}Lu-DOTA-TATE and ^{90}Y SIR-Spheres [Sirtex]) are increasingly being used under dosimetry-guided treatment paradigms. This increase is evidenced by a recent survey indicating that a majority (64%) were clinically administering SIR-Spheres according to absorbed dose rather than body surface area–derived activity, which is the current U.S. Food and Drug Administration–approved label method (1). Additionally, combination-therapy approaches have been gaining popularity, particularly in combining radiopharmaceutical therapy with external-beam radiotherapy, immunotherapy, or both (2–5). As this trend continues, it is critical that our field develop standard practices for measurement, delivery, and verification of absorbed radiation dose. Perhaps the most fundamental consideration is whether we are administering a quantity of radioactive material that is consistent with what is prescribed by the authorized user.

In this work, we describe a series of 2 independent high-purity germanium (HPGe) spectrographic measurements—grounded to National Institute of Standards and Technology (NIST)–traceable sources and measurement—to determine the activity contained within SIR-Spheres vials before patient treatment in relation to the manufacturer-provided activity calibration.

MATERIALS AND METHODS

SIR-Spheres and Manufacturer Calibration

^{90}Y SIR-Spheres are received from the manufacturer in a glass vial within a lead pig. With agitation, the spheres are uniformly suspended in about 5 mL of sterile water; however, within about 2 min of nonagitation the microspheres settle to the bottom of the vial, with approximately 4 mL of water supernatant. Vials can be received from the manufacturer with varying activity levels, by way of delivery on various days before the date and time of reference calibration; however, the same number of spheres (±5%) is present within a vial regardless of the activity provided. Each vial is specified by the manufacturer to contain 3 GBq (81 mCi) ± 10% at the date and time of calibration (often on the day of treatment at 6:00 PM Eastern Standard Time). Vials expire 24 h after the calibration date and time, regardless of the precalibration date of receipt.

Although the nominal activity of any individual vial is specified as 3 GBq ± 10%, on request the manufacturer will provide a certificate of measurement of the vial at the production facility. This certificate contains an exact activity measurement of a particular vial within the manufacturer's own ion chamber, decay-corrected to the date and time of calibration. Activity within this report is provided with 4 significant figures (e.g., 3.004 GBq) and without any associated measurement-uncertainty specification. This certificate, and the associated activity vial, are the primary mechanisms by which a user site or radiopharmacy establishes dose calibrator dial settings before initiation of a clinical program. This procedure was performed at the University of Iowa in 2012 for initial dose calibrator configuration. An additional certificate was obtained for one of the samples measured in this work (received April 26, 2021) to confirm that the University of Iowa dose calibrator remained traceable to the manufacturer's ion chamber. A single dose calibrator (Capintec CRC-15R) was used for all measurements described here.

HPGe Spectrometry

^{90}Y activity measurements were performed by HPGe spectroscopic measurements (Ortec GEM20P4-70) via counting of the 511-keV annihilation emission produced following the 32-parts-per-million internal pair production decay mode of ^{90}Y (6). Energy and peak-shape calibration was performed using NIST-traceable sources (^{241}Am, ^{57}Co, ^{137}Cs, ^{60}Co, and ^{152}Eu; SD, 1.16%; Eckert and Ziegler). A custom high-density-polyethylene source holder (1 cm thick, density = 0.966 ± 0.009 g/cm^3) was manufactured and used to ensure local positron annihilation during

spectral acquisition. This source holder and an example patient vial are shown in Figure 1.

All patient vials were measured at a distance of 210 cm from the detector (surface-to-surface distance), with acquisition durations of 3–6 h. All samples were measured 1 d before the calibration date and thus were expected to be in the range of 4–5 GBq. Despite the lack of abundant γ-emissions, the high levels of activity and associated Bremsstrahlung emissions induced relatively high dead times during data collection—ranging between 22.5% and 25.6% depending on the sample, as estimated by Ortec HPGe electronics. Because of the importance of dead-time correction in these measurements, a separate experiment was performed to validate the accuracy of dead-time estimation provided by Ortec. Details on this measurement are included in the supplemental section (available at http://jnm.snmjournals.org). Spectral peak areas were determined using the SAMPO algorithm, which uses a well-established peak-fitting method ([7]).

Efficiency Calibration

Detector efficiency was calibrated via 2 distinct methods.

In method 1, NIST-traceable sources (^{241}Am, ^{57}Co, ^{137}Cs, ^{60}Co, and ^{152}Eu; Eckert and Ziegler) were used to establish absolute detection efficiency as a function of energy, with the sources in the same position as the patient vial during counting. Because this efficiency estimate does not account for self-attenuation of 511-keV emissions within the source vial and holder, Monte Carlo simulations were performed to determine the appropriate self-absorption correction factor. Simulations were performed in Monte Carlo N-particle code, version 6.2, and verified using the Geant4 Application for Tomographic Emission. Details on these simulations are provided in the supplemental materials.

In method 2, a NIST-traceable calibrated quantity of ^{18}F (∼37 MBq in 3 mL) was placed within an empty SIR-Spheres vial, and spectral acquisition was performed under conditions identical to those for ^{90}Y measurements, including geometry and dead time. Under these conditions, a 511-keV efficiency calibration was obtained by comparing the observed 511-keV count rate with the known emission rate within the ^{18}F sample. ^{18}F samples were calibrated using a ^{68}Ge/^{68}Ga standard tied to a NIST ^{18}F measurement for dose calibrator configuration ([8]). The ^{18}F sample was assayed under calibrated conditions (3 mL in a 5-mL syringe) with quantitative transfer and decay correction before spectrometry.

FIGURE 1. Photograph of custom high-density-polyethylene source holder and example SIR-Spheres patient vial.

Activity Determination and Measurement Uncertainty

^{90}Y activity was determined from the measured peak area, detector live time, detection efficiency, and literature value of the internal pair production branching ratio ([6]). The branching ratio measured by Selwyn et al. ([6])—$(31.86 \pm 0.47) \times 10^{-6}$—was used for this work; this ratio generally agrees with other measurements ([9]), as well as being the value recommended by the Decay Data Evaluation Project, last updated in 2015 ([10]). Second-order corrections were applied for radioactive decay during spectral acquisitions, background 511-keV count rate, and geometry effects (^{18}F vs. ^{90}Y). These corrections are detailed in the supplemental materials.

Determination of measurement uncertainty in this work followed NIST guidelines ([11]) and the International Organization for Standardization expression of uncertainty ([12]). Type A uncertainty in this experiment consisted of statistical uncertainty in the measured 511-keV peak area for each sample. Several sources of type B uncertainty were characterized, including Monte Carlo statistical uncertainty, glass vial thickness (inter- and intravial variability), source holder thickness, positron range effects, dead-time correction precision, positron branching ratio uncertainty, and several additional factors relating to detection efficiency determination. All uncertainties are specified in terms of SE (1 SD), and propagation followed the standard root-sum-of-squares method ([13]).

RESULTS

The local dose calibrator at the University of Iowa agreed with the manufacturer's certificate of calibration within 0.5%, suggesting that historic dose calibrator readings (Capintec CRC-15R; dial setting, 56 × 10) have been a reasonable surrogate for the manufacturer's activity calibration. A review of the last 100 patient vials received by the University of Iowa revealed that the manufacturer has been consistent with its product label of 3.00 GBq (±10%) at the date and time of calibration, according to activity measurements using a dose calibrator. These data are presented in Figure 2. Of 100 patient vials, only one was outside the manufacturer-specified range.

Activities measured by HPGe assay were substantially higher than manufacturer-specified values (Table 1). The estimated ratio of absolute activity to what has been specified by the manufacturer was 1.233 ± 0.030. This final value represents the average of results for all samples and for both method 1 and method 2 within each sample.
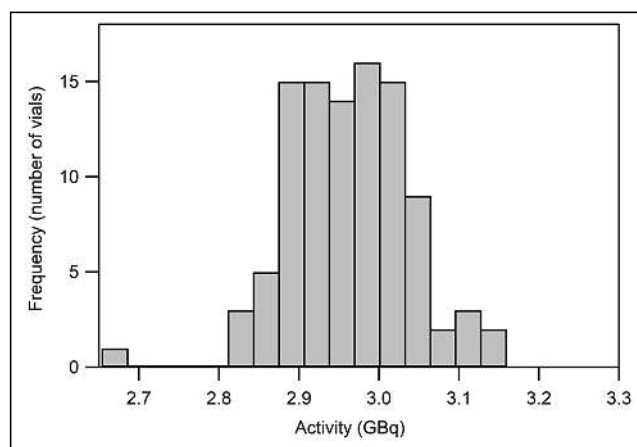
FIGURE 2. Distribution of activities received from manufacturer at time of calibration, as measured by manufacturer-traceable dose calibrator (n = 100, received between February 2019 and April 2021).

TABLE 1
Summary of Measured Patient Vial Activities, Decay-Corrected to Date and Time of Calibration

Sample	Manufacturer (GBq)	HPGe method 1 (GBq)	HPGe method 2 (GBq)	HPGe/manufacturer ratio
1	2.65	3.25 (±3.8%)	3.28 (±3.4%)	1.232
2	2.84	3.43 (±4.2%)	3.46 (±3.8%)	1.212
3	2.99	3.73 (±4.0%)	3.77 (±3.6%)	1.254
4	3.00	3.67 (±4.0%)	3.71 (±3.6%)	1.229
5	3.08	3.80 (±4.2%)	3.83 (±3.8%)	1.240
Average				1.233 ± 0.030

Activity quantitation by methods 1 and 2 provided virtually identical results, with method 2 yielding values about 1.0% higher than method 1. Agreement between these methods suggests that the experimentally determined 511-keV detection efficiency (number measured/number emitted) is robust to experimental approach. Background 511-keV count rate (0.090 ± 0.006 cps) was small in comparison with experimental samples (~2.2 cps). Despite estimated detector dead times of 22.5%–25.6%, correction for these effects was accurate when explicitly accounting for a slight bias above approximately 10% dead time (the supplemental materials provide details).

Variation in the ratio of HPGe-determined activity to dose calibrator–determined activity across samples was consistent with statistical uncertainty within individual measurements. Measurement durations of 3–6 h per patient vial provided statistical uncertainty of 2.5%–3.1% in measured 511-keV peak areas. Components of overall measurement uncertainty are listed in Table 2, with uncertainty being largely dominated by counting statistical uncertainty (~2.5%), uncertainty in the internal pair production branching ratio of ^{90}Y (1.48%) (6), efficiency calibration (method 1, 1.9%), and ^{18}F calibration (method 2, 1.2%). When the measurement was performed multiple times, statistical uncertainty was reduced to an acceptable level in the final calibration specification. Uncertainty in the final ratio (±2.47%) includes uncertainty in measurements and systematic effects, correction having been applied for all known systematic effects.

DISCUSSION

We have identified a miscalibration associated with the SIR-Spheres product. The ratio of our measured activity levels to those provided by the manufacturer calibration is 1.233 ± 0.030. This indicates that about 23% more activity has been administered to patients than anticipated and prescribed. Although this result is potentially a regulatory concern (per Nuclear Regulatory Commission criteria for reportable medical events, ±20% from prescribed), this finding is not immediately concerning from a medical or ethical standpoint.

TABLE 2
Components of Measurement Uncertainty from Representative Patient Vial (Sample 1)

Uncertainty	Type A (methods 1 and 2)	Type B (method 1)	Type B (methods 1 and 2)	Type B (method 2)
Net peak area	2.50%			
Glass density and thickness (intervial variation)			0.40%	
Monte Carlo statistical uncertainty		0.05%		
Glass density and thickness (intravial variation)		0.70%		
High-density polyethylene density and thickness		0.12%		
Volume and activity-distribution effects		0.50%		0.91%
Efficiency calibration (energy interpolation)		1.50%		
Efficiency calibration (traceable source activities)		1.16%		
Positron range effects (simulated vs. ^{90}Y)		1.28%		
Dead-time correction			0.10%	
^{90}Y positron branching ratio			1.48%	
Positron range effects (^{18}F vs. ^{90}Y)				0.75%
^{18}F activity calibration				1.00%
^{18}F decay correction and residual				0.63%
Total	2.50%	2.45%	1.54%	1.67%
Average of methods 1 and 2				3.29%

TABLE 3
Dose Calibrator Settings and Prior Data

Reference	Dose calibrator dial setting	Implied calibration error
Current SIR-Spheres calibration*	56 × 10 (model, CRC-15R)	—
Selwyn, 2008 (15)	—	~23%–31%
Moore, 2007 (16)	24 × 10 (model, CRC-15R)	29%
Ferreira, 2016 (17)	32 × 10 (model, CRC-25R)	~20%[†]
This work	29 × 10 (model, CRC-15R)	23%

*Current SIR-Spheres calibration dial setting may differ by institution and instrument; however, 56 × 10 is setting used on University of Iowa CRC-15R to match manufacturer activity specification.
[†]Estimated using CRC-15R; true discrepancy may differ slightly when using correct model (CRC-25R).

From discussion with the manufacturer, this discrepant activity standard has been consistent throughout the availability of this product, including early trials and associated data reviewed by the U.S. Food and Drug Administration for approval (14). This statement is corroborated by a report in 2008 by Selwyn et al. (15) indicating that a SIR-Spheres vial was found to have 26% ± 1.8% more activity than the nominal manufacturer value (3.00 GBq ± 10%) (15). In his measurement, Selwyn et al. did not compare directly against the manufacturer activity calibration; however, on the basis of our data presented in Figure 2, there is a good chance that the calibrated quantity of activity was between 2.9 and 3.1 GBq, thus implying a miscalibration on the order of 23%–31%. Additional evidence was presented in a 2007 abstract by Moore et al. (16), wherein a calibrated quantity of ^{90}Y-chloride was used to determine appropriate dose calibrator settings for SIR-Spheres. Their reported dose calibrator setting (24 × 10, Capintec CRC-15R) was evaluated on the University of Iowa CRC-15R, and this dial setting displayed about 29% more activity than the manufacturer calibration (56 × 10 on our particular device). Work by Ferreira et al. (17) established accurate SIR-Spheres calibration factors for the Vinten 671 (0.0678 pA/MBq) and the Capintec CRC-25R (dial setting 32 × 10). Although a CRC-25R was not available for comparison at our institution, use of 32 × 10 on the University of Iowa CRC-15R displays about 20% more activity than the manufacturer calibration. These reports (15–17), summarized in Table 3, are consistent with our findings and support the theory that a systematic calibration error has been present for SIR-Spheres over approximately the last 14 y.

According to the manufacturer, more than 100,000 patients have been treated with SIR-Spheres worldwide, with more than 1,000 health-care providers currently offering this treatment. This treatment is generally regarded as an excellent option for patients with hepatic tumors. A systematic miscalibration of administered activity has little to no bearing on the accepted safety and efficacy of this agent; however, this finding will have significant scientific implications moving forward. Additional efforts by the manufacturer are needed to precisely establish an absolute activity standard for SIR-Spheres. These changes should come about in collaboration with at least one institution capable of making absolute activity measurements, such as NIST or another group that has already made significant progress toward establishing a SIR-Sphere measurement standard (18,19).

Existing publications addressing liver dose–toxicity relationships with glass and resin microspheres have consistently demonstrated a lower dose toxicity threshold from resin spheres. Work by Chiesa et al. showed that mean liver doses in excess of 70 Gy from glass microspheres were associated with more than a 50% probability of normal-tissue complications (20). By comparison, data from resin microspheres indicate that a 50% probability of normal-tissue complications is associated with a mean liver dose of 52 Gy (95% CI, 44–61 Gy) (21). With the assumption that prior studies were conducted using manufacturer-recommended activity calibration techniques, the miscalibration identified in our work indicates a somewhat narrower toxicity discrepancy—approximately 64 Gy (resin) versus 70 Gy (glass) when correcting for this effect. This finding necessitates reevaluation of published dosimetry data and interpretations thereof.

The discovery of this miscalibration points to a broader issue in the field of radiopharmaceutical therapy: there is a lack of generalizable methods for independent verification of activity calibration by end users, such as what is done in radiation oncology for linear accelerator and sealed source assay. Efforts should be made to extend the capabilities of currently accredited dosimetry calibration laboratories to include unsealed sources, or a new mechanism for independent calibration verification should be established.

CONCLUSION

The primary SIR-Spheres activity calibration appears to be an underestimate of true activity. HPGe spectroscopic measurements of annihilation radiation emissions have provided an estimate of 1.233 ± 0.030 for the ratio of true activity to activity specified by the manufacturer calibration. This finding should be independently verified, and the manufacturer should take steps to establish an accurate and traceable activity standard.

DISCLOSURE

ACKNOWLEDGMENTS

KEY POINTS

QUESTION: How do measured SIR-Spheres activities compare with the nominal manufacturer calibration?

PERTINENT FINDINGS: The nominal SIR-Spheres activity calibration appears to be an underestimate of true activity. HPGe spectroscopic measurements of annihilation radiation emissions have provided an estimate of 1.233 ± 0.030 for the ratio of true activity to activity specified by the manufacturer calibration.

IMPLICATIONS FOR PATIENT CARE: A revised activity calibration is needed, which will result in changes to clinical activity prescribing patterns.

REFERENCES

1. Sjögreen Gleisner K, Spezi E, Solny P, et al. Variations in the practice of molecular radiotherapy and implementation of dosimetry: results from a European survey. *EJNMMI Phys.* 2017;4:28.
2. Mikell J, Cuneo K, Dewaraja Y. Boosting ^{90}Y SIRT with SBRT: a planning study with ^{90}Y PET and TCP/NTCP models [abstract]. *Eur J Nucl Med Mol Imaging.* 2020;47(suppl 1):S61.
3. Kasi P, Toskich B, Chandrasekharan C, et al. Immunotherapy with Y90-radioembolization for metastatic colorectal cancer (iRE-C) [abstract]. *J Clin Oncol.* 2020; 38(suppl):TPS276.
4. Hobbs RF, McNutt T, Baechler S, et al. A treatment planning method for sequentially combining radiopharmaceutical therapy and external radiation therapy. *Int J Radiat Oncol Biol Phys.* 2011;80:1256–1262.
5. Dietrich A, Koi L, Zöphel K, et al. Improving external beam radiotherapy by combination with internal irradiation. *Br J Radiol.* 2015;88:20150042.
6. Selwyn RG, Nickles R, Thomadsen B, DeWerd L, Micka J. A new internal pair production branching ratio of ^{90}Y: the development of a non-destructive assay for ^{90}Y and ^{90}Sr. *Appl Radiat Isot.* 2007;65:318–327.
7. Aarnio P, Nikkinen M, Routti J. SAMPO 90 high resolution interactive gamma-spectrum analysis including automation with macros. *J Radioanal Nucl Chem.* 1992;160:289–295.
8. Zimmerman BE, Cessna JT. Development of a traceable calibration methodology for solid ^{68}Ge/^{68}Ga sources used as a calibration surrogate for ^{18}F in radionuclide activity calibrators. *J Nucl Med.* 2010;51:448–453.
9. Dryák P, Šolc J. Measurement of the branching ratio related to the internal pair production of Y-90. *Appl Radiat Isot.* 2020;156:108942.
10. Chisté V. ^{90}Y-comments on evaluation of decay data. In: *Table of Radionuclides (Comments on Evaluation).* Bureau International des Poids et Mesures; 2008:181–184.
11. Taylor BN, Kuyatt CE. *Guidelines for Evaluating and Expressing the Uncertainty of NIST Measurement Results.* National Institute of Standards and Technology; 1994:1–20.
12. *Guide to the Expression of Uncertainty in Measurement.* International Organization for Standardization; 1995:122.
13. Bevington PR, Robinson DK. *Data Reduction and Error Analysis for the Physical Sciences.* 2nd Ed. McGraw-Hill. 1992;7:415–416.
14. Dezarn WA, Cessna JT, DeWerd LA, et al. Recommendations of the American Association of Physicists in Medicine on dosimetry, imaging, and quality assurance procedures for ^{90}Y microsphere brachytherapy in the treatment of hepatic malignancies. *Med Phys.* 2011;38:4824–4845.
15. Selwyn R, Micka J, DeWerd L, Nickles R, Thomadsen B. The calibration of-labeled SIR-Spheres using a nondestructive spectroscopic assay. *Med Phys.* 2008; 35:1278–1279.
16. Moore S, Park M-A, Limpa-Amara N, Gallagher P, Mahmood A. Measurement of Y-90 resin microsphere activity using dose calibrators [abstract]. *J Nucl Med.* 2007;46(suppl 2):74P.
17. Ferreira KM, Fenwick AJ, Arinc A, Johansson LC. Standardisation of ^{90}Y and determination of calibration factors for ^{90}Y microspheres (resin) for the NPL secondary ionisation chamber and a Capintec CRC-25R. *Appl Radiat Isot.* 2016;109: 226–230.
18. Mo L, Avci B, James D, et al. Development of activity standard for ^{90}Y microspheres. *Appl Radiat Isot.* 2005;63:193–199.
19. Lourenço V, Bobin C, Chisté V, et al. Primary standardization of SIR-Spheres based on the dissolution of the ^{90}Y-labeled resin microspheres. *Appl Radiat Isot.* 2015;97:170–176.
20. Chiesa C, Mira M, Maccauro M, et al. A dosimetric treatment planning strategy in radioembolization of hepatocarcinoma with ^{90}Y glass microspheres. *Q J Nucl Med Mol Imaging.* 2012;56:503–508.
21. Strigari L, Sciuto R, Rea S, et al. Efficacy and toxicity related to treatment of hepatocellular carcinoma with ^{90}Y-SIR spheres: radiobiologic considerations. *J Nucl Med.* 2010;51:1377–1385.

FAPI PET Opens a New Window to Understanding Immune-Mediated Inflammatory Diseases

Torsten Kuwert[1], Christian Schmidkonz[1], Olaf Prante[1], Georg Schett[2], and Andreas Ramming[2]

[1]Department of Nuclear Medicine, Friedrich-Alexander-University Erlangen-Nürnberg and University Hospital Erlangen, Erlangen, Germany; and [2]Department of Internal Medicine 3, Rheumatology and Immunology, Friedrich-Alexander-University Erlangen-Nürnberg and University Hospital Erlangen, Erlangen, Germany

In vivo visualization of inflammatory lesions has been revolutionized by PET with ^{18}F-FDG as a tracer and by MRI with gadolinium-labeled contrast media. Apart from other indications, ^{18}F-FDG PET and MRI have substantially improved the diagnosis and monitoring of immune-mediated inflammatory diseases such as arthritis and connective tissue diseases. Although the visualization of active inflammation is well established, the detection of tissue response and tissue remodeling processes, which accompany immune-mediated inflammatory diseases and lead to organ damage, has until recently not been possible. Tissue remodeling processes during inflammation are based on mesenchymal stroma cell activation and expansion in parenchymatous organs or the synovial membrane of inflamed joints. These cells express specific markers, such as fibroblast activation protein (FAP), that can be visualized by radiolabeled compounds (e.g., FAP inhibitors [FAPIs]) using PET. First evidence shows that focal accumulation of FAPI tracers, indicating active tissue remodeling, is observed in patients with immune-mediated inflammatory diseases that are characterized by a combination of chronic inflammation and tissue responses, such as systemic sclerosis, IgG4 syndrome, or spondyloarthritis. Such FAPI-positive remodeling lesions are not always ^{18}F-FDG–positive, indicating that inflammation and tissue responses can be disentangled by such methods. These data suggest that tracers such as FAPI allow visualization of the dynamics of tissue responses in immune-mediated inflammatory diseases in vivo. This development opens new options for recognition of tissue remodeling in the context of chronic inflammation, as expanded herein.

Activated fibroblasts express FAP, a type II transmembrane protease with dipeptidyl peptidase and endopeptidase activity. Resting fibroblasts and most other cell types have only minor or no FAP expression. Recently, radiolabeled quinoline-based tracers suitable for PET that act as FAPIs have been developed (1). The initial goal of this development was to image stromal reactions in tumors and metastases (2). Considerable evidence is emerging on the clinical utility of FAPI PET in oncology (3,4).

Tissue remodeling is also a consequence of chronic inflammation. Activation of fibroblasts is therefore not only confined to tumors but also occurs in immune-mediated inflammatory diseases such as systemic sclerosis and IgG4-related disease and inflammatory arthritis.

In these diseases, fibroblast activation may eventually lead to severe organ dysfunction, causing disability or—when parenchymatous organs are involved—even death. Tissue remodeling is the critical step for eliciting damage in immune-mediated inflammatory diseases (5). To date, imaging methods used in immune-mediated inflammatory diseases are mostly confined to detection of inflammation. PET with ^{18}F-FDG or MRI with gadolinium-labeled contrast media has been used to detect and quantify inflammation. However, these methods do not visualize the process of mesenchymal stromal activation and therefore do not allow detection of the process of tissue destruction. Furthermore, techniques such as CT allow quantification of accumulated damage rather than measurement of the dynamic process of tissue change.

Application of FAPI PET in immune-mediated inflammatory diseases has revealed localized tracer accumulation reflecting mesenchymal tissue responses in various diseases such as fibrotic lung and liver diseases, as well as arthritis and colitis (4). A striking example of how mesenchymal stroma activation affects organ function is pulmonary fibrosis, which can arise as an idiopathic disorder or in the context of autoimmune diseases such as systemic sclerosis. Pulmonary fibrosis is often a severe and progressive condition leading to respiratory failure. Diagnosis is established using clinical criteria and high-resolution CT. Two recent publications have shown that FAPIs accumulate in pulmonary fibrosis: Röhrich et al. reported elevated FAPI uptake in 15 patients with different subtypes of fibrotic interstitial lung disease without further specification of their subtypes (6). There was a significant but moderate correlation between CT indices of fibrosis and FAPI uptake measured in the fibrotic areas. The authors hypothesized that FAPI PET/CT might have a role in evaluating the course of pulmonary fibrosis and, in particular, in monitoring the effect of treatment. Bergmann et al. studied a group of 21 patients with systemic sclerosis-associated pulmonary fibrosis using ^{68}Ga-FAPI-04 PET/CT (7). Systemic sclerosis patients also showed an increased FAPI accumulation in the fibrotic areas of the lungs. FAPI uptake was related to parameters of more active disease as measured by higher clinical activity scores. Furthermore, Bergmann et al. could demonstrate that the magnitude of FAPI uptake correlated with progression of disease independently of the extent of involvement on CT scans and lung function at baseline. In 5 patients treated with the tyrosine kinase inhibitor and antifibrotic agent nintedanib, changes in FAPI uptake paralleled the response to treatment as determined by changes in lung function. These latter findings are in contrast to those published for ^{18}F-FDG PET/CT, which were not predictive for treatment
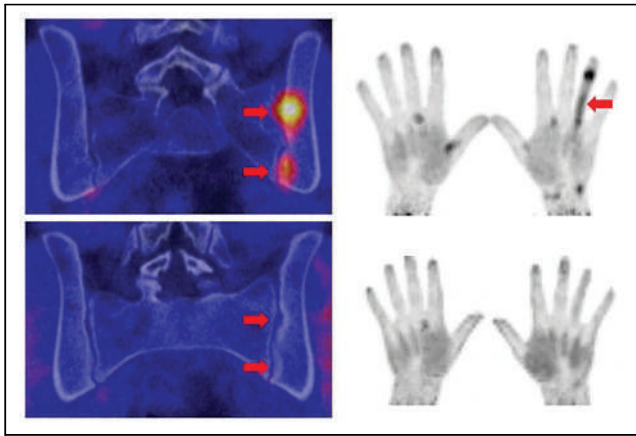
FIGURE 1. ^{68}Ga-FAPI PET images before treatment (top row) and after treatment (bottom row) in patient with spondyloarthritis manifesting with sacroiliitis (upper left panel) and dactylitis of fourth finger. Left upper and lower images are coronal PET/CT fusion images of the sacroiliac joints, and right upper and lower images 3D–volume-rendered PET datasets of the hands. Arrows indicate tracer accumulation and erosions, respectively.

response in an article published by Bondue et al. (*8*), indicating that FAPI PET–based detection of fibrotic tissue responses is more closely related to the pathologic process of systemic sclerosis than the detection of an inflammatory ^{18}F-FDG signal by PET. In any case, larger studies are required to clarify and establish a role for FAPI PET in monitoring the treatment response of interstitial lung disease.

Because ^{18}F-FDG PET detects inflammatory processes, one may ask whether FAPI radioligands provide additional insight into chronic inflammation processes beyond that given by ^{18}F-FDG. In this context, interesting data have been published for IgG4-related disease, a rare prototypical disorder that combines autoimmune inflammation with tumefactive tissue fibrosis affecting the pancreas and biliary tree, the salivary glands, the kidneys, the aorta, and other organs. Immune-targeted therapies effectively inhibit inflammation but may not be suited to tackle fibrotic tissue changes, requiring detection of whether IgG4-related disease is based primarily on inflammatory or fibrotic lesions in an individual patient. Evidence from histopathology indicates that IgG4-related disease can progress from an inflammatory-proliferative to a fibrotic phase, each of which requires different therapeutic approaches. Most patients with IgG4-related disease show ^{18}F-FDG–positive inflammatory lesions; however, FAPI-positive lesions have also been described (*9*). Schmidkonz et al. used both ^{18}F-FDG and FAPI PET to study a group of 27 patients with IgG4-related disease (*10*). They demonstrated that ^{18}F-FDG–positive lesions showed dense lymphoplasmacytic infiltrations of IgG4-positive plasma cells in histology, whereas FAPI-positive lesions harbored abundant activated fibroblasts. Moreover, they could also show that FAPI uptake did not correlate with ^{18}F-FDG uptake, suggesting that the two tracers

visualize two different aspects of IgG4-related disease. In their patient cohort, the responsiveness of fibrotic lesions to immunotherapy was far less pronounced than that of inflammatory ones, suggesting that FAPI PET might find a role in guiding more specific therapy in this disorder.

In summary, this paradigmatic evidence is just the start for a wider use of FAPI PET imaging in immune-mediated inflammatory diseases. Other potential indications for FAPI PET are spondyloarthritis, in which tissue responses lead to ankylosis (Fig. 1); rheumatoid arthritis, which is associated with resident tissue responses that manifest in synovial hyperplasia; and colitis, in which tissue responses trigger strictures in the gut. These examples may further extend the clinical role of FAPI PET as it offers a completely new view on tissue remodeling, fibrosis, and damage in chronic inflammatory diseases. These findings also offer new possibilities for early recognition of the tissue remodeling process, prediction of damage, and response to antifibrotic therapies. Hence, nuclear medicine of the future will likely step out of what has been called the "hegemony of ^{18}F-FDG" (*11*) also in rheumatology.

DISCLOSURE

No potential conflict of interest relevant to this article was reported.

REFERENCES

1. Lindner T, Loktev A, Altmann A, et al. Development of quinoline-based theranostic ligands for the targeting of fibroblast activation protein. *J Nucl Med.* 2018;59: 1415–1422.
2. Loktev A, Lindner T, Mier W, et al. A tumor-imaging method targeting cancer-associated fibroblasts. *J Nucl Med.* 2018;59:1423–1429.
3. Sollini M, Kirienko M, Gelardi F, Fiz F, Gozzi N, Chiti A. State-of-the-art of FAPI-PET imaging: a systematic review and meta-analysis. *Eur J Nucl Med Mol Imaging.* 2021;48:4396–4414.
4. Dendl K, Koerber SA, Kratochwil C, et al. FAP and FAPI-PET/CT in malignant and non-malignant diseases: a perfect symbiosis? *Cancers (Basel).* 2021;13:4946.
5. Croft AP, Campos J, Jansen K, et al. Distinct fibroblast subsets drive inflammation and damage in arthritis. *Nature.* 2019;570:246–251.
6. Röhrich M, Leitz D, Glatting FM, et al. Fibroblast activation protein-specific PET/CT imaging in fibrotic interstitial lung diseases and lung cancer: a translational exploratory study. *J Nucl Med.* 2022;63:127–133.
7. Bergmann C, Distler JHW, Treutlein C, et al. ^{68}Ga-FAPI-04 PET-CT for molecular assessment of fibroblast activation and risk evaluation in systemic sclerosis-associated interstitial lung disease: a single-centre, pilot study. *Lancet Rheumatol.* 2021;3:e185–e194.
8. Bondue B, Castiaux A, Van Simaeys G, et al. Absence of early metabolic response assessed by ^{18}F-FDG PET/CT after initiation of antifibrotic drugs in IPF patients. *Respir Res.* 2019;20:10.
9. Luo Y, Pan Q, Yang H, Peng L, Zhang W, Li F. Fibroblast activation protein-targeted PET/CT with ^{68}Ga-FAPI for imaging IgG4-related disease: comparison to ^{18}F-FDG PET/CT. *J Nucl Med.* 2021;62:266–271.
10. Schmidkonz C, Rauber S, Atzinger A, et al. Disentangling inflammatory from fibrotic disease activity by fibroblast activation protein imaging. *Ann Rheum Dis.* 2020;79:1485–1491.
11. Hicks RJ, Roselt PJ, Kallur KG, Tothill RW, Mileshkin L. FAPI PET/CT: will it end the hegemony of ^{18}F-FDG in oncology? *J Nucl Med.* 2021;62:296–302.

Advances in Detector Instrumentation for PET

Andrea Gonzalez-Montoro[1], Muhammad Nasir Ullah[1], and Craig S. Levin[1–4]

[1]*Department of Radiology, Molecular Imaging Program at Stanford University, Stanford, California;* [2]*Department of Physics, Stanford University, Stanford, California;* [3]*Department of Electrical Engineering, Stanford University, Stanford, California; and* [4]*Department of Bioengineering, Stanford University, Stanford, California*

During the last 3 decades, PET has become a standard-of-care imaging technique used in the management of cancer and in the characterization of neurologic disorders and cardiovascular disease. It has also emerged as a prominent molecular imaging method to study the basic biologic pathways of disease in rodent models. This review describes the basics of PET detectors, including a detailed description of indirect and direct 511-keV photon detection methods. We will also cover key detector performance parameters and describe detector instrumentation advances during the last decade.

Key Words: PET; scintillation detectors; semiconductor detectors; spatial and energy resolution; coincidence time resolution; CTR

P ET imaging uses radioactive contrast agents for diagnosis and therapy monitoring of various medical conditions. PET imaging provides unique information on the cellular and molecular pathways of disease within the human body, complementary to that provided by γ-cameras and SPECT. PET is also quite often used for small-animal molecular imaging studies (*1*).

A PET study begins with the administration of a radioactive tracer. PET data acquisition is based on the coincident detection of millions of pairs of oppositely directed 511-keV photons, each of which results from the annihilation of a positron (a decay product of the tracer's radionuclide label) with its antiparticle (the electron present in all atoms of the molecules comprising patient tissues).

The resulting annihilation photons are detected using high-atomic-number, high-density, and thick radiation detectors typically arranged in a cylindric geometry (e.g., Fig. 1).

BASICS OF PET DETECTORS

The detection method for characterizing the incoming annihilation photons can be generally divided into 2 different categories: indirect and direct. In indirect (scintillation) detection, each incoming annihilation photon interacts within the scintillation crystal through photoelectric or Compton scatter interactions. The deposited energy is first converted into a cascade of visible (lower-energy) light photons and then into an electrical current using one or more photodetectors. This is the detection method used in all current commercially available PET systems (*2*). In direct detection, each incoming photon interaction is directly converted into electrical signals using semiconductor crystals. To date, this approach has been explored only in research (*3,4*). Each of these methods has its own advantages and limitations.

Indirect Detection Method (Scintillation Detection)

Scintillation detectors for PET use an inorganic crystal, which each incoming 511-keV annihilation photon interacts with (via Compton scatter or the photoelectric effect), producing a quickly ejected recoil electron. Each ejected electron travels through the material and ionizes it through coulombic interactions, creating a track of secondary electrons (*5*) that are liberated from the crystal's intrinsic electronic valence band into the conduction band. Through a subsequent deexcitation process in which those excited electrons drop into available energy states of the host crystal, or those of an impurity introduced into the crystal, the resulting ionization charge is converted to a flash of isotropically emitted visible light (*6*). The crystal is coupled to a photodetector element that collects the light and converts it into an electrical signal, followed by readout electronics (*7*).

Inorganic Scintillation Crystals Used in PET. Ideal inorganic scintillation materials should have a high effective atomic number (Z_{eff}) and density, and the resulting signals should have a fast rise and decay time, which are crucial for good coincidence timing resolution. To promote the generation of visible-light photons (i.e., optical photons), except for a few intrinsic scintillators such as bismuth germanium oxide (BGO), a small concentration of an impurity, called an activator, is introduced into the inorganic scintillation crystal (*8*).

A scintillator suitable for PET should have the following properties: high light yield, which is the number of optical photons
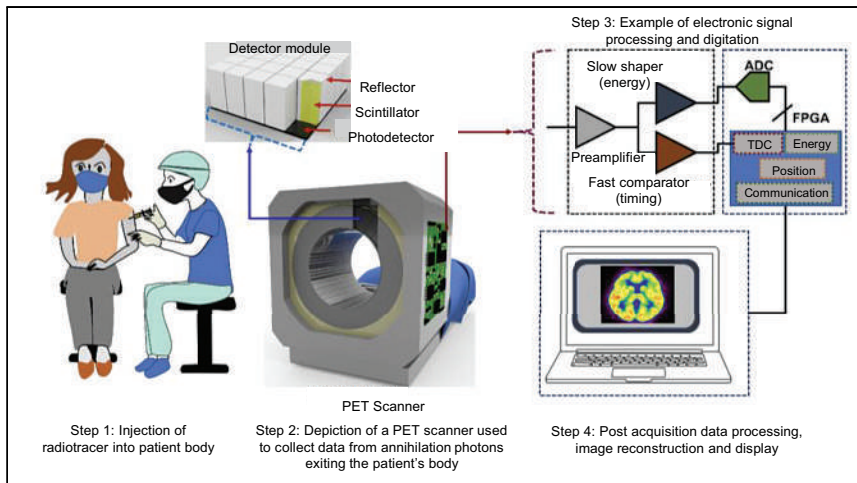
FIGURE 1. Illustration of PET imaging process: from left to right, radiolabeled tracer is injected into patient body, then PET scan is performed, and finally acquired annihilation photon data are processed to reconstruct images. ADC = analog-to-digital converter; FPGA = field programmable gate array; TDC = time-to-digital converter.

generated per unit of deposited energy from the interaction; good linearity, to ensure that the number of generated optical photons is proportional to the energy deposited by the incident radiation; transparency to the wavelength of its own emission spectra, to facilitate the transport of generated scintillation light to the photodetector; a high Z_{eff}, a high density and a relatively wide thickness (e.g., 2 cm), for favorable 511-keV interaction probability; a fast rise time and short decay time for the induced luminescence, to facilitate excellent temporal resolution and count rate performance; and a high refraction index, to promote total internal reflection off the crystal element sides and to increase the efficiency of light collection into the photodetector. Different inorganic scintillator materials have been used in PET detectors; Supplemental Table 1 (supplemental materials are available at http://jnm.snmjournals.org) summarizes the most commonly used inorganic scintillators and their properties for the purpose of indirect radiation detection. To promote good spatial resolution, energy resolution, and coincidence time resolution (CTR) performance, important aspects to consider in addition to high light yield, Z_{eff}, and density, and short rise and decay times, are the reflector applied to the scintillator crystal surfaces (to constrain the generated light photons within the crystal), the crystal surface condition (e.g., polished or rough), and the scintillator–photodetector coupling medium (9).

Although most modern PET systems are built using lutetium-based scintillation crystals (e.g., lutetium–yttrium oxyorthosilicate [LYSO]) because of their high light yield and excellent timing properties, there has been a recent resurgence of studies that explore BGO, especially its achievable timing properties using prompt luminescence emissions (10). As the field is moving toward scanners with a long axial field of view, BGO is especially attractive because of its significantly decreased production cost and increased Z_{eff} compared with lutetium-based crystals.

Regarding crystal configuration, there are 2 main geometries used in PET detectors, namely discrete array and monolithic, as depicted in Supplemental Figures 1A and

1B, respectively. Discrete crystal arrays are most commonly used in commercial PET scanners and comprise a matrix (i.e., array) of individual small rod-shaped scintillation elements, whereas the monolithic scintillator design (currently in only one commercial scanner design) consists of a large single piece of scintillation material, and therefore, there are no interelement gaps. Advantages and disadvantages of each configuration can be found in a previous publication (11).

Photodetectors Used in PET Scintillation Detectors. For the detection and conversion of the generated scintillation photons into measurable electrical signals, the scintillator is coupled to one or more photodetector elements. Generally, the photodetectors used in PET can be divided into 2 groups: photomultiplier tubes (PMTs) and silicon photomultipliers (SiPMs). PMTs are economically advantageous, have high gain and low noise, and are sensitive for light in the visible region of the electromagnetic spectra. However, they are relatively large, bulky, and affected by magnetic fields, making it impossible to use them in PET/MRI hybrid systems. Figure 2A shows the operation principle of PMTs (6). SiPMs are semiconductor (solid-state) light detectors with a very high gain, a low-temperature drift, a low operating voltage, an excellent temporal response, and an insensitivity to magnetic fields (6). They are much more compact than PMTs, with a pixel size on the order of the size of typical discrete crystal elements used in PET and with minimal dead area. Figure 2B depicts an SiPM array, zoomed in on the pixel internal circuit structure. The SiPM pixel comprises a 2-dimensional array of thousands of single-photon avalanche photodiodes operating in Geiger mode, known as microcells. When a single scintillation photon strikes a single microcell, a charge carrier (electron or hole, depending on the configuration) is generated with a certain probability and then accelerated through a strong electric field, triggering an avalanche in the gain region. The charge carriers from all microcells in each SiPM pixel are collected and summed in parallel, producing an output signal proportional to the number of impinging scintillation photons hitting that SiPM pixel that can be measured in real time. Depending on whether readout electronics are external to the devices or integrated within the sensor technology, SiPMs can be classified as either analog or digital, respectively (12).

Most newer-generation PET systems use SiPMs instead of PMTs (13). To provide accurate information on the incoming photon interaction location, energy, and arrival time, the factors
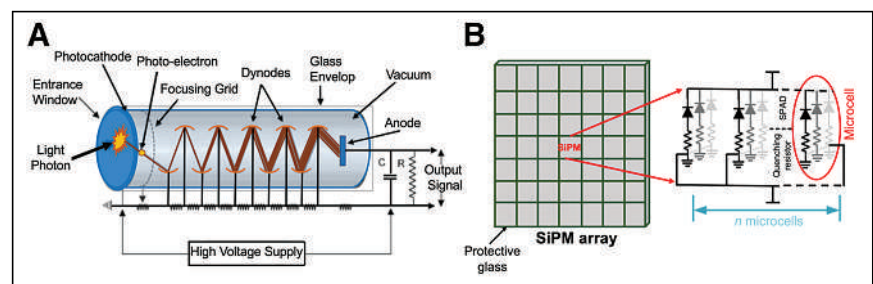
FIGURE 2. Schematic of PMT (A) and SiPM array (B), zooming on circuitry of one SiPM comprising 2-dimensional array of thousands of microcells. SPAD = single photon avalanche diode.

contributing to the SiPM noise and timing jitter, such as dark count rates, optical crosstalk, afterpulsing, and dead time, must be considered when designing SiPM-based systems (*14*).

For the crystal–photodetector coupling, it is better to use coupling media with refractive indices between those of the photodetector and the scintillator crystal to reduce light transmission losses. Regarding crystal–photodetector arrangement, for the discrete crystal design, photodetectors are commonly coupled to the small end of the crystal (end readout, Figs. 3A–3C). Nevertheless, designs attaching the photodetector to the entrance surface (Fig. 3D) (*9*), at the side surfaces (Fig. 3E) (*9*), or to both top and bottom surfaces (for 511-keV photon depth of interaction [DOI] positioning) (Fig. 3F) (*14*), or even covering the 4 lateral edges of a monolithic crystal (Fig. 3G) (the more common arrangement was depicted in Supplemental Fig. 1B, with the photodetector coupled to a large face of the crystal (*11*)), have also been studied, reporting good overall performance but, for some of the designs, at the cost of increasing the number of photodetectors or gaps between adjacent crystal elements (*14*).

There are 2 basic configurations to couple discrete scintillation crystals to photodetectors, namely light sharing and one-to-one coupling. In the light-sharing configuration, optical photons generated in one crystal element are collected in more than one photodetector, or a single photodetector collects the optical photons from more than one crystal element. The monolithic design (e.g., Supplemental Figs. 1B and 3F) involves substantial light sharing: for an interaction occurring in the center of the crystal, almost all SiPMs in the matrix receive signal. In the one-to-one crystal–photodetector coupling approach, each crystal element is optically isolated from its neighbors and coupled to its own photodetector pixel. In this configuration, the spatial resolution of such a detector is limited mainly by the width of the discrete crystal elements (*5*). The photodetector output signals may be read independently or multiplexed for fewer readout channels (*15*), as described in the following section. In the case of the monolithic crystal, the spread of scintillation light within the crystal leads to significant detector dead time at high count rates and spatial resolution degradation near the edges (*16*), which have a negative effect on timing performance throughout the crystal since there is an increased variance in the photon arrival time determination (*17*).

Front-End Readout Electronics for PET Scintillation Detectors. The front-end readout and data acquisition electronics are responsible for processing and digitizing the photodetector output signals and transmitting those digitized signals to a workstation (personal computer) for further processing and image reconstruction. Analog SiPMs provide analog electrical signals. High-speed analog-to-digital converters are used to accurately digitize these analog signals (e.g., Fig. 1C), from which one can extract the crystal location, energy, and arrival time of the photon interaction. Because of their flexibility, reliability, and cost effectiveness, field-programmable gate arrays (e.g., Fig. 1C) are the digital signal hardware units most often applied to control, receive, and process the digitized data from the analog-to-digital converters before transmitting to the personal computer for further software analysis and image reconstruction.

In terms of signal-to-noise ratio (SNR), the best approach to extracting 511-keV photon interaction position and temporal resolution is to read every single element in the photodetector matrix individually. However, this typically implies digitizing a huge number of signals, which is challenging, costly, and requires complex readout and data acquisition schemes. To address this challenge, multiplexing schemes that merge two or more photodetector output signals have been implemented (*18*). Multiplexing reduces the overall readout channel count but at the cost of signal integrity and postprocessing computational burden. For a readout design that combines several output channels, the exact interaction position of the 511-keV photon within the detector element that generated the electronic signal is unknown at the output of a multiplexed readout chain and therefore requires the application of algorithms or techniques (*19*) at the postprocessing stage to extract information such as photon interaction position, energy, and timing.

The most popular multiplexing methodology is Anger logic (the widely used in NaI-based γ-cameras), in which all photodetector signals are combined, such as through a resistive network (*20*). However, such multiplexing of output signals may require significant light sharing between the photodetectors, requiring a high light-output scintillator to obtain good spatial resolution. Thus, there is a tradeoff between the degree of multiplexing and the overall detector performance (*20*). Nevertheless, this multiplexing scheme provides the advantage of reducing the number of output channels and the overall complexity of a system but typically affects key performance parameters such as spatial, timing, and energy resolutions and count-rate performance. An alternative approach is to use capacitive multiplexing schemes or a hybrid multiplexing scheme in which resistive and capacitive networks are used in parallel (*21*). These different types of multiplexing schemes have a goal of improving one or more key parameters and can be adopted accordingly depending on the application.

Although some examples have been given, photodetector signal multiplexing in PET system design is generally an open area in which continued research is required to come up with optimized solutions for given detector configurations. For the readout schemes described, system designers often use application-specific integrated circuit (ASIC) chips—the so-called system on a chip (*22*)—which are customized for a particular use. ASIC readouts possess a small footprint and can be used to read, preprocess, and digitize each SiPM photodetector element independently or the resulting channels after multiplexing. Because of the customized design of ASICs for a specific type of detector and requirement, they often can yield performance parameters superior to those from readout circuits built using discrete components (*23*).

More recently, approaches based on artificial intelligence have been proposed for
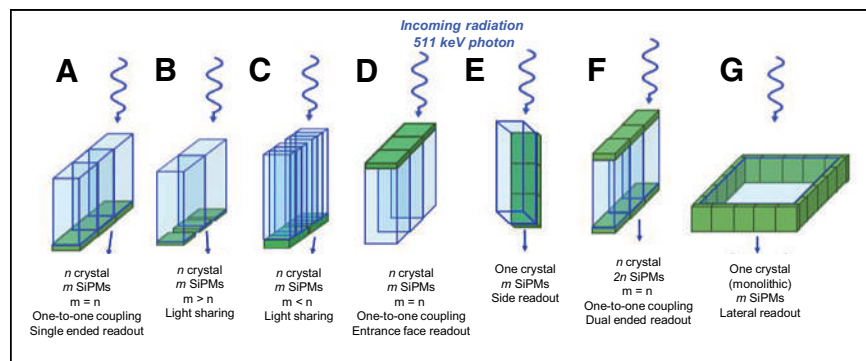
FIGURE 3. Schematic of different scintillation crystal–photodetector coupling approaches. End readout configurations with one-to-one coupling (A), light sharing (B and C), one-to-one coupling but with SiPMs on entrance face (D), side readout (E), dual-ended readout (F), and lateral readout (G) (a more common configuration is depicted in Supplemental Fig. 1B).

3-dimensional photon interaction positioning and time stamp estimation in PET for highly multiplexed readout schemes (24). Preliminary experiments have shown promising results (25).

Direct Detection Method

Semiconductor detectors are commonly used in the field of radiation detection for direct conversion of the incoming radiation into electrical signals (without the intermediate process of creation, transport, and collection of light) and are currently under research for use in PET (3,4,26). In semiconductor photon detectors, the 511-keV photon interaction physics are exactly the same as in the indirect detection (scintillation) case, in which the ionizing interactions create a track of electron–hole pairs. However, what differs is the signal formation and collection process. In a semiconductor detector, under the influence of an applied bias voltage on electrodes deposited on opposing sides of the crystal, the mobile charge carriers drift toward and induce a current on either electrode (electrons drift toward the anode whereas holes drift toward the cathode) as depicted in Supplemental Figure 2 (4). The integral of induced current over time provides the total induced charge on each electrode, which, aside from charge-attenuating effects, is directly proportional to the energy of the 511-keV photon interaction. The resulting current signal is read through highly sensitive and low-noise electronic circuitry. Typically, the first component of the front-end readout circuitry chain is a charge-sensitive amplifier. The basic function of the charge-sensitive amplifier is to integrate the current signal and convert it into a voltage signal, as well as to match electrical impedance between the detector and subsequent electronics (4). The charge-sensitive amplifier is typically followed by a shaping amplifier, which amplifies the signal and filters out the noise contents from the output signal of the charge-sensitive amplifier to improve SNR. The shaping amplifier also plays the important role of quickly decaying the signal down to baseline to avoid pile-up issues and make the data acquisition system ready for processing of subsequent signals without compromising the precision of extraction of time and energy information from the signal. The output of the shaping amplifier can be fed to an analog-to-digital converter for signal digitization and postprocessing.

Because of a single-step 511-keV photon-induced ionization-to-current conversion, semiconductor detectors exhibit a greatly decreased (compared with scintillation-based radiation detectors) statistical variation in signal amplitude as a function of the photon energy, thus yielding more precise energy measurements (i.e., higher energy resolution), which are highly desirable in imaging applications. However, one of the major limitations of semiconductor photon detectors is poor CTR, which limits the use of semiconductor detectors in the design of time-of-flight (TOF) PET scanners (27). The poorer temporal precision of semiconductor radiation detectors than of scintillation detectors results from the fact that the output signal is produced by the drift of charge, which is much slower and has larger temporal variation than the propagation and collection of light. Despite these drawbacks, there is still the possibility of using semiconductor radiation detectors for the design of high-resolution PET scanners (3,28) or in other applications in which timing performance is not of the utmost importance. So far, there are no clinical PET systems using semiconductor-based detectors.

To be used as an effective radiation detector for PET, a semiconductor material must have high Z_{eff} and density and be at least a few centimeters thick for highly efficient detection of 511-keV photons; it also should have high resistivity and low leakage current and should yield a high number of electron–hole pairs per interaction for the best detector SNR. The semiconductor radiation crystals that have been most often studied for PET detectors are cadmium zinc telluride (4,29) and cadmium telluride. Additionally, thallium bromide has also been recently studied (30). The basic properties of these 3 semiconductor detectors are summarized in Supplemental Table 2.

PET DETECTOR PERFORMANCE PARAMETERS

Intrinsic Spatial Resolution

The intrinsic spatial resolution of a PET detector is defined by the spatial spread of detected annihilation photon counts measured by stepping a positron point source across the surface of PET detectors that are operated in electronic coincidence (to collect the resulting oppositely directed annihilation photons), also known as the coincidence point-spread function (CPSF). The resolution is defined as the full width at half maximum (FWHM) of a gaussian fit to the CPSF and is usually characterized in 3 dimensions: 2 planar coordinates (x,y) in combination with the DOI coordinate (z) within the crystal.

At the system level, the intrinsic spatial resolution of the PET detector is an important parameter affecting PET image quality and, in the discrete crystal design, is affected mainly by the crystal element dimensions and the positioning algorithm used to retrieve the coordinates. Positron range and annihilation photon acollinearity variations also contribute to the measured (x,y) CPSF (5). In detector designs without signal multiplexing, the contribution from the detector is roughly half the width of the crystal element; in light-sharing and signal-multiplexing designs, an additional decoding term should be applied (7). For the overall (x,y) PET system spatial resolution, one would multiply intrinsic spatial resolution by an additional blurring factor because of the imperfect image reconstruction process, as shown in Equation 1. The reconstructed image voxel size is usually chosen to be roughly one third to one half the intrinsic resolution (31). Annihilation photon acollinearity depends on scanner diameter. Positron range depends on the positron-emitting radionuclide and the tissue traversed by the positron. The contribution from the detector depends on the detector element width.

$$R_{int} = \sqrt{\left(\frac{R_{det}}{2}\right)^2 + R_{pos}^2 + b^2 + 0.0044 \cdot R_{acol}^2}, \qquad \text{Eq. 1}$$

where R_{int} is intrinsic spatial resolution, R_{det} is the contribution from the detector, R_{pos} is the positron range, b is the blurring factor, and R_{acol} is annihilation photon acollinearity. Submillimeter (x,y) intrinsic resolution has been achieved for both indirect and direct detection methods. Supplemental Figure 3 shows examples of PET systems with intrinsic resolution of less than 1 mm (3,32). Supplemental Figure 3A depicts an example of indirect detection of the measured PSF across 2 opposing detector modules, each consisting of 8 × 8 arrays of 0.9 × 0.9 × 1 mm³ LYSO scintillation crystals coupled to a position-sensitive avalanche photodiode. An average CPSF of 0.84 ± 0.02 mm was measured; the figure was extracted from a previous publication (33). Supplemental Figure 3C shows an example of the direct detection method using a monolithic CZT crystal arranged edge-on with respect to incoming photons, with intrinsic resolution determined by the 1-mm pitch of the anode electrode, which was segmented into strips; the reported CPSF averaged over 3 anode strips was 0.78 ± 0.1 mm FWHM, including the 250-μm diameter of the point source. This figure was extracted from a previous publication (34).

Regarding the monolithic crystal-based detector design, an additional challenge is the truncation of scintillation light at the edges, which degrades the spatial, timing, and energy resolutions in these regions (7). Several approaches to mitigating this effect have been tested, such as different crystal surface treatments (e.g., covering the edges with an optical absorber) or novel photodetector arrangements (9,11). Moreover, monolithic detectors require 2-dimensional calibration procedures to estimate the 511-keV photon interaction position within the scintillator. These calibration procedures are usually based on hardware collimation methods in which a physically collimated beam source is moved across the front face of the scintillator to generate look-up tables that are used to decode the measured positions into metric units (5). Supplemental Figure 3B shows an example of a calibration pattern acquired using a 15-mm-thick LYSO monolithic crystal and a collimated array of ^{22}Na sources with 1.5-mm pitch. The collimator had 30-mm thickness and drilled holes 1.2 mm in diameter. The bottom panel of Supplemental Figure 3B shows the count histogram along the columns in the image of the data inside the red band, achieving an average (x,y) spatial resolution of 0.82 ± 0.02 mm after taking into account the hole diameter, with significant degradations observed within a few millimeters from all 4 edges (33).

A high-sensitivity PET system design is desirable for realizing both high spatial resolution and reconstructed image SNR. This can be achieved by using scintillation crystals at least 2 cm long (thick) for high-efficiency detection of 511-keV photons. However, nearly all commercially available PET detectors do not measure the DOI of the photon interaction. This lack of DOI information can produce significant limitations in positioning annihilation photon interactions due to a parallax error that occurs when incoming annihilation photons enter the detectors at oblique angles and interact at varying depths within the crystals. This leads to increased spatial-resolution blurring as the source moves outward from the center, radially.

However, retrieving DOI information is not straightforward and usually requires additional scintillator layers (e.g., phoswich approaches (35,36)) or photodetector elements (dual-end readout methods)—or special crystal surface treatments and reflectors (9,36)—and additional readout channels, thus increasing manufacturing cost and system complexity (8). The drawbacks of most of these DOI methods is that they can determine only one DOI, representing a problem when the photon interacts more than once in the detector crystals (intercrystal scatter) before depositing all its energy (i.e., a Compton scatter followed by a photoelectric absorption), which is roughly 2- to 3-fold more likely to occur than a single photoelectric interaction for small (<4 mm in width) crystals. To address this problem, some advanced detector designs enable determination of x, y, and z coordinates when there is more than one 511-keV photon interaction (3,32), enabling an accurate estimate of the first interaction for improved reconstructed image quality and accuracy (37).

Energy Resolution

The energy resolution is a measure of the detector's ability to distinguish between photon interactions at different energies and represents the precision with which a PET detector can measure the deposited energy of the photon interaction. It is quantified by the FWHM of a gaussian fit to the photopeak observed in the measured spectrum of detected photon energies. Good energy resolution helps to filter out 511-keV photons that have undergone Compton scatter in the patient tissues before being detected, since it allows the application of a narrow energy window for rejection of these scattered coincidences, thus improving image contrast and

accuracy while still being able to collect high count statistics in the measured photopeak. Semiconductor detectors provide better energy resolution because of low statistical variation in signal amplitude as a function of photon energy. For the sake of comparison of direct and indirect detection, the energy spectrum of a ^{22}Na radiation source acquired using a 3 × 3 × 10 mm^3 lutetium–gadolinium orthosilicate scintillator crystal element coupled to an SiPM (9), and a 39 × 39 × 5 mm^3 cadmium zinc telluride semiconductor detector crystal arranged edge-on with respect to incoming photons (38), are shown in Supplemental Figures 4A and 4B, respectively. In discrete and monolithic crystal array–based detectors, the energy resolution depends on the scintillator light yield, light collection efficiency variations as a function of annihilation photon DOI, the dimensions of the crystal element and its optical coupling to the photodetector, properties of the latter such as photon detection efficiency, and the noise level of the electronic readout.

CTR

The CTR of a PET system defines the uncertainty in measuring the arrival time difference between photons for each annihilation photon pair of a coincidence event, over many events. The CTR is determined by several factors, including the intrinsic properties of the scintillation crystal (light yield, rise and decay times), reflective materials applied to the crystal, the geometry of the crystal, the number of scintillation photons collected by the photodetector, crystal-to-photodetector coupling configurations, photodetector detection efficiency and noise properties, and the readout electronics chain (39). Achieving precise CTR allows one to constrain the location of each annihilation event along the system lines of response using the technique known as TOF (2). Using TOF information, each event is placed closer to its true origin along the line of response connecting 2 coincidence detector elements in a PET system during the image reconstruction process, thus improving the reconstructed image SNR (Eq. 2) (9).

$$SNR = \left(\frac{D}{\Delta X}\right)^{1/2} = \left(\frac{2 \cdot D}{c \cdot \Delta T}\right)^{1/2}, \qquad \text{Eq. 2}$$

where $\Delta X = (c \cdot \Delta T / 2)$ is the annihilation coordinate uncertainty along each line of response, c is the speed of the light, ΔT is CTR, and D is the imaging subject diameter, assuming it is circular. As an example, if the CTR improves from 400 to 100 ps, then from Equation 1, a gain in reconstructed image SNR of a factor of $\sqrt{4}$ (=2) is expected.

The image SNR boost using TOF can be exploited to improve lesion visualization and the accuracy of uptake measurements or reduce the required dose or the scan time. The design of TOF PET scanners requires careful consideration of the scanner photon sensitivity and the CTR performance (39,40). Supplemental Figure 4C shows an example of the measured time difference (i.e., coincidence time) spectrum, which is again typically quantified by the FWHM, using a detector design based on a 3 × 3 × 10 mm^3 lutetium–gadolinium orthosilicate scintillator crystal element side-coupled to a 3 × 3 mm^3 SiPM (9).

Count-Rate Performance

Count rate is defined as the number of events recorded by a detector per unit of time. The count-rate capability of PET systems is constrained because a large number of incoming photon events has to be detected and processed by a finite number of detector channels, each channel requiring a certain processing time

depending on the detector and readout electronics design. Thus, the total number of counts that can be collected within a reasonable time frame is limited (*40*). In an ideal PET system, the net count rate would increase linearly with increasing activity in the field of view. However, real systems experience count losses due primarily to dead time caused by event pile-up effects. These effects must be estimated accurately and corrected in order for quantitative PET studies to be performed; in this regard, several methods have been proposed to alleviate count-rate losses (*41*). With the introduction of SiPM-based detectors, the pile-up and resulting dead time and loss in quantitative accuracy observed at high count rates is reduced when compared with previous PMT-based scanners (*42*).

Count-rate measurements do not directly indicate image SNR in the presence of random and Compton scatter coincidence backgrounds. Instead, the noise-equivalent count rate figure of merit is used, providing a standard measure of the SNR of a PET system (*40*).

DISCUSSION

Currently, PET imaging is a valuable molecular imaging technique and is used clinically to yield tailored diagnostic and prognostic information. Advances in PET detector design and instrumentation in the last decade have led to significant improvements in PET image quality and accuracy. Supplemental Table 3 summarizes the main performance parameters of commercial TOF PET scanners (*2*). However, there are potentially a few directions for improvement: commercially available clinical PET scanners are still not efficient in detecting 511-keV photon pair coincidences (i.e., photon sensitivity) relative to theoretic scanner designs (*43*) and offer limited spatial resolution ($\sim$4 mm at the system center, which degrades away from the center).

One direct (but costly) approach to improving PET system sensitivity is that of the Explorer collaboration (*44*)—as well as other designs (*45*)—to improve the system geometric efficiency by greatly increasing its axial length. The axial length of most commercially available PET systems ranges between 15 and 26 cm, exhibiting sensitivities of 0.6%–2% for the 70-cm-long National Electrical Manufacturers Association line source measurement. For reducing the cost of PET systems with a long axis, there has been recent significant interest in BGO (*10*).

Another indirect option to enhance PET system sensitivity is to improve CTR and, thus, the precision of photon TOF information during the reconstruction process, which provides an effective sensitivity boost by enhancing reconstructed image SNR. The best state-of-the-art scanner achieves an approximately 214-ps CTR (*46*). However, with progress in the development of SiPMs (*12,13*), high-end PMTs, and scintillators, a CTR at or below a 100-ps FWHM may be achievable in future-generation TOF PET systems (*4,9*).

PET system spatial resolution and sensitivity improvements have been proven useful to better characterize and quantify lesions or to reduce the radiation dose or scanning time. To improve the spatial resolution of PET scanners, one may use smaller crystal elements along with sensitivity improvements to realize the desired higher resolution with good image SNR. Recently, artificial-intelligence algorithms are being explored for use with PET instrumentation (*24*). For example, they have been used to achieve homogeneous submillimetric resolution in the entire field of view using a monolithic-crystal–based design (*11*).

CONCLUSION

PET constitutes the molecular imaging technique of excellence in nuclear medicine. However, to further extend the use of PET, some instrumentation improvements need to be accomplished. These advancements include reaching high 3D spatial resolution (in the range of $\sim$1$-$2 mm); achieving CTR values below 100 ps to enable the inclusion of precise TOF information during the reconstruction process; and maximizing photon detection sensitivity. The present review covers these points by describing the basics of PET detector technology, the most relevant instrumentation milestones completed during the last decade, and the future of PET detector technology.

REFERENCES

1. Phelps ME. Positron emission tomography provides molecular imaging of biological processes. *Proc Natl Acad Sci USA.* 2000;97:9226–9233.
2. Surti S, Karp JS. Update on latest advances in time-of-flight PET. *Phys Med.* 2020; 80:251–258.
3. Abbaszadeh S, Levin CS. New-generation small animal positron emission tomography system for molecular imaging. *J Med Imaging (Bellingham).* 2017;4:011008.
4. Gu Y. *High-Resolution Small Animal Positron Emission Tomography System Based on 3-D Position-Sensitive Cadmium Zinc Telluride Photon Detectors.* Stanford University; 2014:26–40.
5. Levin CS, Hoffman EJ. Calculation of positron range and its effect on the fundamental limit of positron emission tomography system spatial resolution. *Phys Med Biol.* 1999;44:781–799.
6. Bizarri G. Scintillation mechanisms of inorganic materials: from crystal characteristics to scintillation properties. *J Cryst Growth.* 2010;312:1213–1215.
7. Bailey DL, Karp JS, Surti S. Physics and instrumentation in PET. In: Bailey DL, Townsend DW, Valk PE, Maisey MN, eds. *Positron Emission Tomography.* Springer; 2005:13–39.
8. Melcher CL. Scintillation crystals for PET. *J Nucl Med.* 2000;41:1051–1055.
9. Gonzalez-Montoro A, Pourashraf S, Lee MS, Cates JW, Levin CS. Study of optical reflectors for a 100ps coincidence time resolution TOF-PET detector design. *Biomed Phys Eng Express.* 2021;7:65008.
10. Gonzalez-Montoro A, Pourashraf S, Cates JW, Levin CS. Cherenkov radiation-based coincidence time resolution measurements in BGO scintillators. *Front Phys (Lausanne).* 2022;10:816384.
11. Gonzalez-Montoro A, Gonzalez AJ, Pourashraf S, et al. Evolution of PET detectors and event positioning algorithms using monolithic scintillation crystals. *IEEE Trans Radiat Plasma Med Sci.* 2021;5:282–305.
12. Schaart DR, Charbon E, Frach T, Schulz V. Advances in digital SiPMs and their application in biomedical imaging. *Nucl Instrum Methods Phys Res A.* 2016;809: 31–52.
13. Acerbi F, Gundacker S. Understanding and simulating SiPMs. *Nucl Instrum Methods Phys Res A.* 2019;926:16–35.
14. Berg E, Cherry SR. Innovations in instrumentation for positron emission tomography. *Semin Nucl Med.* 2018;48:311–331.
15. Cherry SR, Jones T, Karp JS, Qi J, Moses WW, Badawi RD. Total-body PET: maximizing sensitivity to create new opportunities for clinical research and patient care. *J Nucl Med.* 2018;59:3–12.
16. Downie E, Yang X, Peng H. Investigation of analog charge multiplexing schemes for SiPM based PET block detectors. *Phys Med Biol.* 2013;58:3943–3964.
17. Kim H, Kao C-M, Hua Y, Xie Q, Chen C-T. Multiplexing readout for time-of-flight (TOF) PET detectors using striplines. *IEEE Trans Radiat Plasma Med Sci.* 2021;5:662–670.
18. LaBella A, Petersen E, Cao X, Zeng X, Zhao W, Goldan A. 36-to-1 multiplexing with Prism-PET for high resolution TOF-DOI PET [abstract]. *J Nucl Med.* 2021; 62(suppl 1):38.
19. Chinn G, Olcott PD, Levin CS. Sparse signal recovery methods for multiplexing PET detector readout. *IEEE Trans Med Imaging.* 2013;32:932–942.
20. Hobson PR. Measurement Instrumentation and Sensors Handbook: Electromagnetic, Optical, Radiation, Chemical, and Biomedical Measurement, by J.G. Webster and H. Eren. *Contemp Phys.* 2015;56:505–506.
21. Park H, Ko GB, Lee JS. Hybrid charge division multiplexing method for SiPM-based high-resolution PET detectors. *Phys Med Biol.* 2017;62:4390–4405
22. Gao W, Gao D, Wei T, Hu Y. Survey of front-end readout ASICs for positron emission tomography imaging. *Guti Dianzixue Yanjiu Yu Jinzhan/Res Progress Solid State Electronics.* 2012;32:590–599.

23. Nadig V, Schug D, Weissler B, Schulz V. Evaluation of the PETsys TOF-PET2 ASIC in multi-channel coincidence experiments. *EJNMMI Phys.* 2021; 8:30.

24. Ullah MN, Levin CS. Application of artificial intelligence in PET instrumentation. *PET Clin.* 2022;17:175–182.

25. Sitek A, Ahn S, Asma E, et al. Artificial intelligence in PET: an industry perspective. *PET Clin.* 2021;16:483–492.

26. Takei T, Shiga T, Morimoto Y, et al. A novel PET scanner with semiconductor detectors may improve diagnostic accuracy in the metastatic survey of head and neck cancer patients. *Ann Nucl Med.* 2013;27:17–24.

27. Ullah MN, Pratiwi E, Cheon J, Choi H, Yeom JY. Instrumentation for time-of-flight positron emission tomography. *Nucl Med Mol Imaging.* 2016;50:112–122.

28. Abbaszadeh S, Gu Y, Reynolds PD, Levin CS. Characterization of a sub-assembly of 3D position sensitive cadmium zinc telluride detectors and electronics from a sub-millimeter resolution PET system. *Phys Med Biol.* 2016;61:6733–6753.

29. Abbaspour S, Mahmoudian B, Islamian JP. Cadmium telluride semiconductor detector for improved spatial and energy resolution radioisotopic imaging. *World J Nucl Med.* 2017;16:101–107.

30. Ariño-Estrada G, Mitchell GS, Kwon SI, et al. Towards time-of-flight PET with a semiconductor detector. *Phys Med Biol.* 2018;63:04LT01.

31. Groll AN. *Hybrid Pixel-Waveform Semiconductor Detectors: Novel Detector Readout for Semiconductor PET Imaging of Small Animal Neurodegenerative Models.* Dissertation. University of Illinois at Urbana-Champaign; 2017.

32. Shakirin G, Crespo P, Fiedler F, Wagner A, Enghardt W. Optimum voxel size for reconstruction of in-beam PET data. In: *2008 IEEE Nuclear Science Symposium Conference Record.* IEEE; 2008:5066–5069.

33. Hsu DFC, Freese DL, Reynolds PD, Innes DR, Levin CS. Design and performance of a 1 mm³ resolution clinical PET system comprising 3-D position sensitive scintillation detectors. *IEEE Trans Med Imaging.* 2018;37:1058–1066.

34. Gu Y, Matteson JL, Skelton RT, et al. Study of a high-resolution, 3D positioning cadmium zinc telluride detector for PET. *Phys Med Biol.* 2011;56:1563–1584.

35. González-Montoro A, Sánchez F, Bruyndonckx P, Cañizares G, Benlloch JM, González AJ. Novel method to measure the intrinsic spatial resolution in PET detectors based on monolithic crystals. *Nucl Instrum Methods Phys Res A.* 2019; 920:58–67.

36. Ullah MN, Pratiwi E, Park JH, Lee K, Choi H, Yeom J-Y. Wavelength discrimination (WLD) TOF-PET detector with DOI information. *Phys Med Biol.* 2020;65: 055003.

37. Ullah MN, Park JH, Pratiwi E, Kim GB, Yeom J-Y. Wavelength discrimination (WLD) detector optimization for time-of-flight positron emission tomography with depth of interaction information. *Nucl Instrum Meth A.* 2020;982:164498.

38. Ullah MN, Pratiwi E, Park JH, et al. Studies on sub-millimeter LYSO:Ce, Ce:GAGG, and a new Ce:GFAG block detector for PET using digital silicon photomultiplier. *Nucl Instrum Methods Phys Res A.* 2018;911:115–122.

39. Pratx G, Levin CS. Bayesian reconstruction of photon interaction sequences for high-resolution PET detectors. *Phys Med Biol.* 2009;54:5073–5094.

40. Pourashraf S, Gonzalez-Montoro A, Won JY, et al. Scalable electronic readout design for a 100 ps coincidence time resolution TOF-PET system. *Phys Med Biol.* 2021;66:85005.

41. Cherry SR, Dahlbom M. PET: Physics, instrumentation, and scanners. *PET Springer*, 2004;1–124.

42. Wagatsuma K, Miwa K, Sakata M, et al. Comparison between new-generation SiPM-based and conventional PMT-based TOF-PET/CT. *Phys Med.* 2017;42: 203–210.

43. Vandenberghe S, Moskal P, Karp JS. State of the art in total body PET. *EJNMMI Phys.* 2020;7:35.

44. Usman S, Patil A. Radiation detector deadtime and pile up: a review of the status of science. *Nucl Eng Technol.* 2018;50:1006–1016.

45. Badawi RD, Shi H, Hu P, et al. First human imaging studies with the EXPLORER total-body PET scanner. *J Nucl Med.* 2019;60:299–303.

46. Ullah MN, Levin CS. Application of artificial intelligence in PET instrumentation. *PET Clin.* 2022;17:175–182.

Use of ^{64}Cu-DOTA-Trastuzumab PET to Predict Response and Outcome of Patients Receiving Trastuzumab Emtansine for Metastatic Breast Cancer: A Pilot Study

Joanne E. Mortimer[1], James R. Bading[1], Paul H. Frankel[2], Mary I. Carroll[1], Yuan Yuan[1], Jinha M. Park[3], Lusine Tumyan[3], Nikita Gidwaney[3], Erasmus K. Poku[4], John E. Shively[4], and David M. Colcher[4]

[1]Department of Medical Oncology and Experimental Therapeutics, City of Hope, Duarte, California; [2]Department of Information Sciences, City of Hope, Duarte, California; [3]Department of Radiology, City of Hope, Duarte, California; and [4]Department of Cancer Molecular Imaging and Therapy, Beckman Research Institute of the City of Hope, Duarte, California

We hypothesized that functional imaging with ^{64}Cu-DOTA-trastuzumab PET/CT would predict the response to the antibody–drug conjugate trastuzumab–emtansine (T-DM1). **Methods:** Ten women with metastatic human epidermal growth factor receptor 2–positive breast cancer underwent ^{18}F-FDG PET/CT and ^{64}Cu-DOTA-trastuzumab PET/CT on days 1 and 2 before treatment with T-DM1. **Results:** T-DM1–responsive patients had higher uptake than nonresponsive patients. Day 1 minimum SUV_{max} (5.6 vs. 2.8, $P < 0.02$), day 2 minimum SUV_{max} (8.1 vs. 3.2, $P < 0.01$), and day 2 average SUV_{max} (8.5 vs. 5.4, $P < 0.05$) for ^{64}Cu-DOTA-trastuzumab all favored responding patients. Tumor-level response suggested threshold dependence on SUV_{max}. Patients with a day 2 minimum SUV_{max} above versus below the threshold had a median time to treatment failure of 28 mo versus 2 mo ($P < 0.02$). **Conclusion:** Measurement of trastuzumab uptake in tumors via PET/CT is promising for identifying patients with metastatic breast cancer who will benefit from T-DM1.

Key Words: breast; oncology; PET; breast cancer; breast PET

Overexpression of human epidermal growth factor receptor 2 (HER2) occurs in 15%–20% of breast cancers and determines candidacy for trastuzumab, which improves disease outcome for all stages of HER2-positive breast cancer (1–3).

We have used ^{64}Cu-DOTA-trastuzumab PET/CT to study women with recurrent or metastatic breast cancer (4) and reported a positive correlation between tumor uptake of ^{64}Cu-DOTA-trastuzumab and HER2 status as measured by immunohistochemistry (4,5). Trastuzumab–emtansine (T-DM1) is an antibody–drug conjugate that uses trastuzumab to target HER2-positive breast cancer and deliver its cytotoxic payload, emtansine (6). T-DM1's mechanism of action and use as a single agent are advantageous for correlating trastuzumab imaging with treatment response. We report the results of a pilot study testing whether pretreatment ^{64}Cu-DOTA-trastuzumab PET/CT can predict benefit from T-DM1 for HER2-positive metastatic breast cancer.

MATERIALS AND METHODS

Patient Selection

Eligibility requirements included metastatic or recurrent HER2-positive breast cancer in patients who were to receive T-DM1, were 18 y old or older, had an Eastern Cooperative Oncology Group performance status of 0–2, had a normal cardiac ejection fraction, and had at least 1 metastasis with a diameter of at least 2.0 cm. Patients could not have received trastuzumab for 4 or more weeks. Eligibility was confirmed by tumor biopsy for HER2 assessment and ^{18}F-FDG PET/CT. The City of Hope Institutional Review Board approved the study, and all patients provided written informed consent (NCT02226276).

Treatment

The patients underwent a clinical examination and toxicity assessment before each cycle of T-DM1. Follow-up ^{18}F-FDG PET/CT was performed after every 2 cycles of T-DM1 for up to 18 mo and at the discretion of the treating oncologist thereafter. Treatment response was evaluated by PERCIST (7).

[64]Cu-DOTA-Trastuzumab-PET/CT

[64]Cu was provided by the Mallinckrodt Institute of Radiology, Washington University School of Medicine. Radiolabeled trastuzumab was prepared and administered according to IND 109971 as previously described (4).

Scans were acquired with a Discovery STe 16 PET/CT device (GE Healthcare) operated in 3-dimensional mode. The PET axial field of view and slice thickness were 15.4 cm and 3.3 mm, respectively. PET images were iteratively reconstructed as previously described (5) and had a measured resolution of 9 mm in full width at half maximum. ^{64}Cu-DOTA-trastuzumab PET/CT was performed during the first day (day 1) and second day (day 2) after injection. Quantitative imaging with ^{64}Cu-DOTA-trastuzumab was supported by direct measurement of activity concentrations in peripheral venous blood samples drawn before imaging on days 1 and 2. Measurement of ^{64}Cu-DOTA trastuzumab uptake is described in Supplemental Figure 1 (supplemental materials are available at http://jnm.snmjournals.org).

Antibody scans were interpreted in relation to baseline ^{18}F-FDG scans by a radiologist different from those who evaluated the ^{18}F-FDG PET/CT scans. Quantitative analysis was performed using XD (version
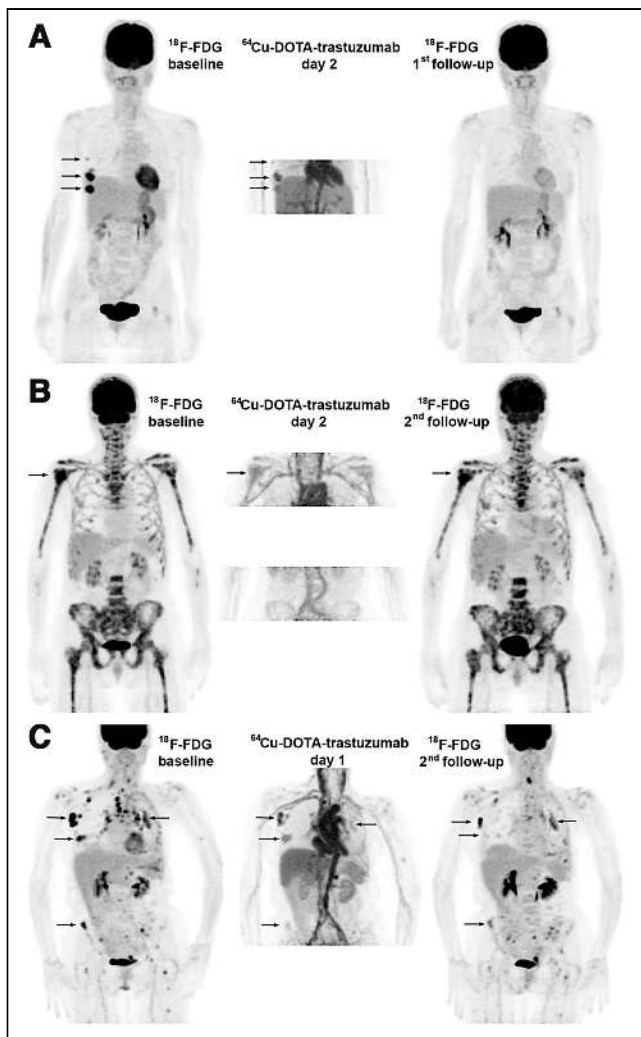
FIGURE 1. Treatment effects. Images are maximum-intensity projections with upper intensity thresholds (black color) corresponding to SUV of 7 and 10 g/mL for ^{18}F-FDG and ^{64}Cu-DOTA-trastuzumab, respectively. (A) Response with baseline ^{18}F-FDG–positive disease limited to right breast and axilla (arrows). All lesions were well visualized with ^{64}Cu-DOTA-trastuzumab, and follow-up ^{18}F-FDG showed complete response. (B) Nonresponse with extensive ^{18}F-FDG–positive bone metastasis. (Arrow indicates PERCIST target tumor.) Tumor uptake of ^{64}Cu-trastuzumab was low (day 2 target tumor SUV$_{max}$, 5.5 g/mL). Disease progression occurred after 4 cycles of T-DM1. (C) Nonresponse with widely disseminated ^{18}F-FDG–positive disease. Tumor uptake of ^{64}Cu-DOTA-trastuzumab was variable, and tumor response at second ^{18}F-FDG follow-up (after 4 cycles of T-DM1) was correspondingly mixed.

3.6; Mirada Medical). Correction for altered ^{18}F-FDG biodistribution in follow-up examinations is shown in Supplemental Figure 2.

Tumor uptake was measured in terms of voxel SUV$_{max}$ (*4,5*). Measurements were limited to tumors measurable for baseline ^{18}F-FDG uptake. Tumor images strongly overlapped by positively imaged adjacent features (e.g., a vessel or organ) were rejected for uptake measurement. Those that were strongly positive and well separated from adjacent features were segmented via a maximum voxel-based thresholding technique (*8*). The methods used for tumor assessment and numbers of tumors assessed are in Supplemental Tables 1 and 2.

Statistical Plan and Analysis

The study was designed to accrue 10 patients to explore the relationship between tumor uptake of ^{64}Cu-DOTA-trastuzumab and tumor response. For individual tumors, a hierarchic (tumor-within-patient) linear mixed-effects model was used to evaluate the association between day 1 or day 2 SUV$_{max}$ and response. The best SUV$_{max}$ cut points for individual tumors were used in patient-level response (Fisher exact test), and planned comparisons of average (or minimum) uptake in responsive versus nonresponsive patients used the *t* test. All *P* values are 2-sided. Cox regression was used for time to treatment failure (TTF) (the supplemental materials provide additional details).

RESULTS

Ten patients were enrolled, and their characteristics are in Supplemental Table 3. Five experienced a response, and 5 were nonresponders; TTF ranged from 1.3 mo (early death) to 46 mo. Two patients continued in long-term follow-up at 62 and 78 mo from the initiation of chemotherapy. Figure 1 compares ^{64}Cu-DOTA-trastuzumab and ^{18}F-FDG PET scans for 3 patients with varying responses to T-DM1.

Fifty-nine ^{18}F-FDG baseline-measurable tumors met the criteria for measurability of ^{64}Cu-DOTA-trastuzumab uptake, and 31 (day 1) and 25 (day 2) were also measured for response. Over half the data for individual tumors came from 2 patients (Figs. 1B and 1C).

Individual tumor response appeared to have a distinct threshold dependence on uptake of ^{64}Cu-DOTA-trastuzumab, especially on day 2 (Fig. 2). Although the optimal uptake threshold settings accurately separated responsive from nonresponsive tumors, those results are not statistically significant in a hierarchical model of tumors within patient for this 10-patient cohort.

Patient-level response was positively related to tumor uptake of ^{64}Cu-DOTA-trastuzumab, and the thresholds that optimally related uptake to best response for individual tumors also accurately separated patients by response to T-DM1 (Fig. 3). Responsive patients had a significantly higher day 2 average, day 1 minimum, and day 2 minimum SUV$_{max}$ than nonresponsive patients. In the categoric analysis (intrapatient average or minimum tumor SUV$_{max}$ > response threshold, yes/no, vs. responsive, yes/no), day 1 results were significant for minimum SUV$_{max}$, whereas day 2 results were significant for both metrics. For day 2, all patients with the lowest tumor uptake above the threshold responded, whereas no patients with the lowest tumor uptake below the threshold responded.

TTF was positively related to measured tumor uptake of ^{64}Cu-DOTA-trastuzumab (Table 1). For day 2, the relationship was statistically significant for both patient-level uptake metrics. Depending on the metric, the day 2 tumor response threshold discriminated patients with a median TTF of 2 versus 23 or 28 mo.

The supplemental materials include additional details about patients, treatment, response assessment, and ^{64}Cu-DOTA-trastuzumab image analysis.

DISCUSSION

We demonstrated a significant association between tumor uptake of ^{64}Cu-DOTA-trastuzumab and patient benefit (response and TTF) from treatment with T-DM1. The ZEPHIR trial found pretreatment tumor imaging with ^{89}Zr-trastuzumab PET/CT to be predictive of patient response and TTF in T-DM1 therapy for HER2-positive metastatic breast cancer (*9,10*). The pretreatment work-up included ^{18}F-FDG PET/CT. ^{89}Zr-trastuzumab PET/CT scans acquired 4 d after injection were assessed by radiologists' qualitative inspection.
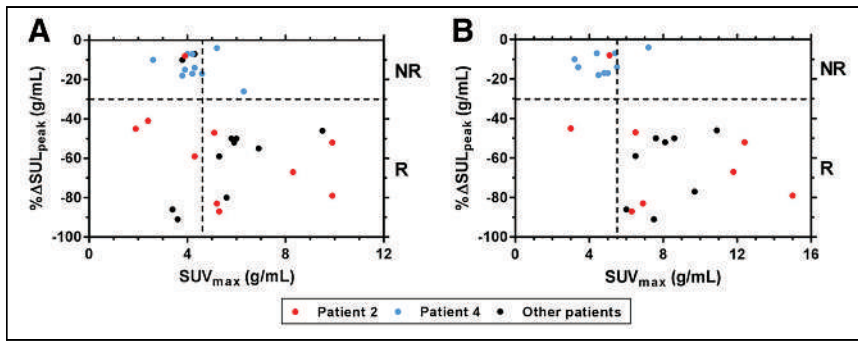
FIGURE 2. Percentage change in ^{18}F-FDG uptake (%ΔSUL$_{peak}$) is plotted vs. ^{64}Cu-DOTA-trastuzumab SUV$_{max}$ measured on days 1 (A) and 2 (B). Horizontal and vertical dashed lines show, respectively, PERCIST threshold for positive response (-30%) and thresholds (day 1, 4.6 g/mL; day 2, 5.5 g/mL) that maximized accuracy of ^{64}Cu-DOTA-trastuzumab uptake in separating responsive from nonresponsive tumors. NR = nonresponsive; R = responsive.

Our quantitative study corroborates the ZEPHIR trial's finding that tumor uptake of trastuzumab on PET/CT correlates with patient response and outcome with T-DM1. Using SUV$_{max}$ measurement, moreover, we found an apparent threshold relationship between tumor response and tumor uptake 1 and 2 d after injection of ^{64}Cu-DOTA-trastuzumab. The response thresholds for individual tumors also accurately separated patients by response and TTF. Based on published data for ^{89}Zr-trastuzumab (*11,12*), we estimate that the ^{64}Cu-DOTA-trastuzumab SUV$_{max}$ T-DM1 response threshold is modestly greater than blood pool SUV at 4 d postinjection (Supplemental Fig. 3 and associated text). This is consistent with the criterion for "relevant" tumor uptake of ^{89}Zr-trastuzumab vis-à-vis response to T-DM1 in the ZEPHIR trial.
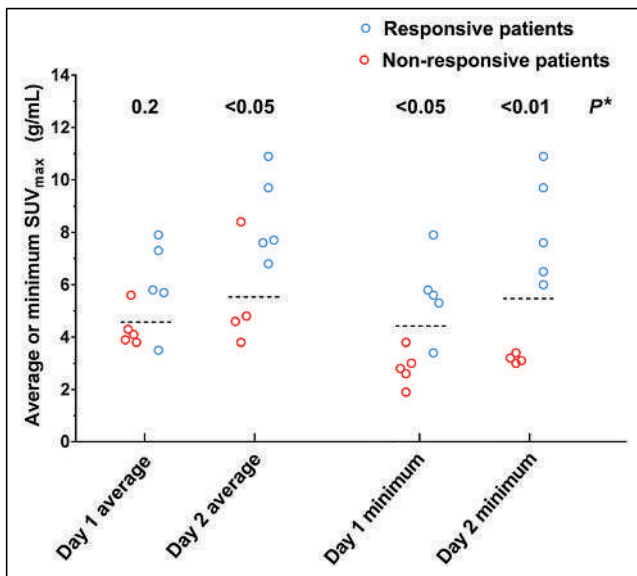
FIGURE 3. Relationship between patient best response to T-DM1 and measured tumor uptake of ^{64}Cu-DOTA-trastuzumab. Dashed lines show optimal thresholds relating response to uptake for individual tumors (day 1, 4.6 g/mL; day 2, 5.5 g/mL). Group mean SUV$_{max}$ (responsive vs. nonresponsive patients) was significantly different (*t* test) for day 2 average (8.5 vs. 5.4, $P < 0.05$), day 1 minimum (5.6 vs. 2.8, $P < 0.02$), and day 2 minimum (8.1 vs. 3.2, $P < 0.01$). ($P = 0.08$ for day 1 average). *Fisher exact test for response vs. threshold.

The current study demonstrated some disadvantages of ^{64}Cu (half-life, 12.8 h) relative to ^{89}Zr (half-life, 3.3 d). ^{64}Cu does not provide whole-body coverage with an acceptable scan duration and adequate count density for accurate and precise measurement of tumor uptake. In the current study, the low count rate limited coverage of disease burden on day 2. Overlap with images of adjacent blood vessels reduced the number of tumor images measurable for ^{64}Cu-DOTA-trastuzumab SUV$_{max}$. Variations in time between injection and scan ($t_{scan} - t_{inj}$) imposed by difficulty in scheduling research scans amid clinical operations added noise to measurements of tumor SUV$_{max}$. The resulting error is inversely related to $t_{scan} - t_{inj}$ and thus inherently much worse for scans on days 1 and 2 than scans on day 4 or later. The problem is well illustrated by the patient (Fig. 1A) with the shortest day 1 time to scan (16 h). Although the patient had a complete response to T-DM1, SUV$_{max}$ was below the empiric response threshold for both of her measurable tumors on day 1, whereas on day 2, SUV$_{max}$ was above the threshold.

Despite limitations imposed by the relatively short half-life of ^{64}Cu, we have demonstrated that measurement of tumor uptake of trastuzumab at 1–2 d after injection can be effective in identifying patients unlikely to benefit from T-DM1 therapy. Further work is required to develop measurement of trastuzumab uptake as a predictor of clinical benefit from T-DM1. Trastuzumab imaging may identify patients who could benefit from T-DM1 and thus avoid the toxicity of chemotherapy. Trastuzumab imaging may also identify women who might not otherwise be considered for HER2-directed treatment (*13*).

We previously reported on the patient depicted in Figure 1C, whose disease demonstrated heterogeneous uptake of ^{64}Cu-DOTA-trastuzumab and a correspondingly mixed response to T-DM1 (*14*). This case suggests that trastuzumab imaging may identify patients who could benefit from combining T-DM1 with chemotherapy or other treatments.

CONCLUSION

Tumor uptake of ^{64}Cu-DOTA-trastuzumab, measured in terms of SUV$_{max}$ at 1–2 d after injection, was positively associated with patient response and TTF in T-DM1 therapy of HER2-positive metastatic breast cancer. The relationship between SUV$_{max}$ and tumor response appeared to have a sharp threshold, and the threshold for individual tumor response was also effective in separating patients who did and did not benefit from T-DM1. Thus, measurement of trastuzumab uptake in tumors via PET/CT is highly promising for patient selection in treatment of metastatic breast cancer with T-DM1.

DISCLOSURE

TABLE 1
^{64}Cu-DOTA-Trastuzumab Uptake and TTF

Tumor uptake		Patients > threshold		Patients ≤ threshold			
Metric	Cut point (g/mL)*	n	Median TTF (mo)	n	Median TTF (mo)	Hazard ratio	P†
Day 1 average SUV$_{max}$	4.6	5	18	5	3	0.3 (0.1−1.3)	0.10
Day 2 average SUV$_{max}$	5.5	6	23	3	2	0.1 (0.0−0.9)	0.01
Day 1 minimum SUV$_{max}$	4.6	4	26	6	3	0.3 (0.1−1.3)	0.09
Day 2 minimum SUV$_{max}$	5.5	5	28	4	2	0.1 (0.0−1.0)	0.02

*Optimal threshold relating uptake to response for individual tumors.
†Log rank test.
Hazard ratios are >cut point relative to ≤cut point. Data in parentheses are 95% CIs.

KEY POINTS

QUESTION: Is tumor uptake of ^{64}Cu-DOTA-trastuzumab as measured by PET/CT predictive of treatment benefit from T-DM1 in metastatic HER2-positive breast cancer?

PERTINENT FINDINGS: Response to T-DM1 was positively associated with tumor uptake of ^{64}Cu-DOTA-trastuzumab, measured as SUV$_{max}$. Tumor response appeared to have a distinct threshold dependence on SUV$_{max}$, and the response threshold for individual tumors accurately separated patients with respect to response and TTF.

IMPLICATIONS FOR PATIENT CARE: Pretreatment functional imaging of trastuzumab may help in selecting patients likely to benefit from T-DM1.

REFERENCES

1. Rimawi MF, Schiff R, Osborne CK. Targeting HER2 for the treatment of breast cancer. *Annu Rev Med.* 2015;66:111–128.
2. Giordano SH, Temin S, Chandarlapaty S, et al. Systemic therapy for patients with advanced human epidermal growth factor receptor 2–positive breast cancer: ASCO clinical practice guideline update. *J Clin Oncol.* 2018;36:2736–2740.
3. Wolff AC, Hammond MEH, Allison KH, et al. Human epidermal growth factor receptor 2 testing in breast cancer: American Society of Clinical Oncology/College of American Pathologists clinical practice guideline focused update. *J Clin Oncol.* 2018;36:2105–2122.
4. Mortimer JE, Bading JR, Colcher DM, et al. Functional imaging of human epidermal growth factor receptor 2–positive metastatic breast cancer using ^{64}Cu-DOTA-trastuzumab PET. *J Nucl Med.* 2014;55:23–29.
5. Mortimer JE, Bading JR, Park JM, et al. Tumor uptake of ^{64}Cu-DOTA-trastuzumab in patients with metastatic breast cancer. *J Nucl Med.* 2018;59:38–43.
6. Burris HA III, Rugo HS, Vukelja SJ, et al. Phase II study of the antibody drug conjugate trastuzumab-DM1 for the treatment of human epidermal growth factor receptor 2 (HER2)–positive breast cancer after prior HER2-directed therapy. *J Clin Oncol.* 2011;29:398–405.
7. Wahl RL, Jacene H, Kasamon Y, Lodge MA. From RECIST to PERCIST: evolving considerations for PET response criteria in solid tumors. *J Nucl Med,* 2009; 50(suppl 1):122S–150S.
8. Boellaard R, Krak NC, Hoekstra OS, Lammertsma AA. Effects of noise, image resolution, and ROI definition on the accuracy of standard uptake values: a simulation study. *J Nucl Med.* 2004;45:1519–1527.
9. Clark AS, DeMichele A, Mankoff D. HER2 imaging in the ZEPHIR study. *Ann Oncol.* 2016;27:555–557.
10. Gebhart G, Lamberts LE, Wimana Z, et al. Molecular imaging as a tool to investigate heterogeneity of advanced HER2-positive breast cancer and to predict patient outcome under trastuzumab emtansine (T-DM1): the ZEPHIR trial. *Ann Oncol.* 2016;27:619–624.
11. Laforest R, Lapi SE, Oyama R, et al. [^{89}Zr]trastuzumab: evaluation of radiation dosimetry, safety, and optimal imaging parameters in women with HER2-positive breast cancer. *Mol Imaging Biol.* 2016;18:952–959.
12. O'Donoghue JA, Lewis JS, Pandit-Taskar N, et al. Pharmacokinetics, biodistribution, and radiation dosimetry for ^{89}Zr-trastuzumab in patients with esophagogastric cancer. *J Nucl Med.* 2018;59:161–166.
13. Ulaner GA, Hyman DM, Ross DS, et al. Detection of HER2-positive metastases in patients with HER2-negative primary breast cancer using ^{89}Zr-trastuzumab PET/CT. *J Nucl Med.* 2016;57:1523–1528.
14. Mortimer JE, Shively JE. Functional imaging of human epidermal growth factor receptor 2–positive breast cancers and a note about NOTA. *J Nucl Med.* 2019;60: 23–25.

Follicular Lymphoma Treated with First-Line Immunochemotherapy: A Review of PET/CT in Patients Who Did Not Achieve a Complete Metabolic Response in the GALLIUM Study

Sally F. Barrington[1], Farheen Mir[2], Tarec Christoffer El-Galaly[3], Andrea Knapp[4], Tina G. Nielsen[4], Denis Sahin[4], Michael Wenger[5], Lale Kostakoglu[6], Judith Trotman[7], and Michel Meignan[8]

[1]School of Biomedical Engineering and Imaging Sciences, King's College London and Guy's and St. Thomas' PET Centre, King's College London, King's Health Partners, London, United Kingdom; [2]Department of Haematology, Royal Marsden NHS Foundation Trust, London, United Kingdom; [3]Department of Hematology, Aalborg University Hospital, Aalborg, Denmark; [4]Product Development Oncology, F. Hoffmann-La Roche Ltd., Basel, Switzerland; [5]Pharma Development Oncology, Genentech Inc., South San Francisco, California; [6]Department of Radiology and Medical Imaging, University of Virginia, Charlottesville, Virginia; [7]Hematology Department, Concord Repatriation General Hospital, University of Sydney, Concord, New South Wales, Australia; and [8]LYSA Imaging, Hôpitaux Universitaires Henri Mondor and Université Paris–Est Créteil, Créteil, France

Complete metabolic response (CMR) on PET/CT was the sole independent predictor of overall survival in the PET substudy of the phase III GALLIUM trial (NCT01332968) in first-line treatment of high-tumor-burden follicular lymphoma. The aim of this analysis was to further investigate the outcome of patients not achieving CMR. **Methods:** Two international experts rereviewed PET/CT scans from patients failing to achieve CMR assessed by the Independent Review Committee masked otherwise to committee results. Metabolic response category and Deauville score were assigned. Progression-free survival (PFS) was investigator-assessed with contrast-enhanced CT. Kaplan–Meier methodology was used to estimate landmark PFS and time to next treatment from end of induction by Deauville score. Patients who experienced CT-based progressive disease at the end of induction were excluded. **Results:** Fifty-four patients were reviewed. Six had CMR, 37 had a partial metabolic response, 2 had no metabolic response, and 9 had progressive metabolic disease. Patients were reassigned to CMR because ^{18}F-FDG uptake was considered inflammatory ($n = 2$), was considered incidental neoplasia ($n = 2$), or was visually close to liver uptake but quantitatively lower ($n = 2$). There was a trend for shorter PFS and time to next treatment for patients with a Deauville score of 5 than a score of 4. High-grade mesenteric uptake at the end of induction was common, occurring in 20 patients with non-CMR, 14 of whom achieved CMR at all other sites. Only 3 of 14 (21%) patients with mesenteric uptake as the only site of disease experienced progression or death within 24 mo, whereas 4 of 6 patients (67%) with mesenteric and additional sites of ^{18}F-FDG–avid disease experienced progression or death within 24 mo. All patients with early progression had measurable disease on contrast-enhanced CT at ^{18}F-FDG–avid sites at the end of induction. **Conclusion:** After induction immunochemotherapy, CMR was assigned after reassessment in some patients, in whom increased ^{18}F-FDG uptake was considered due to inflammation or incidental neoplasia rather than to lymphoma. Quantitative assessment to confirm the visual impression of residual uptake in lesions is suggested. Isolated mesenteric ^{18}F-FDG uptake is likely a common false-positive finding at the end of induction and does not warrant changes in clinical management or disease surveillance unless there is measurable disease on contrast-enhanced CT or clinical suspicion of active disease.

Key Words: follicular lymphoma; PET; response assessment

Patients with follicular lymphoma treated with first-line immunochemotherapy with complete metabolic response (CMR) on PET using the 5-point Deauville score have a better prognosis than patients who do not achieve CMR (1). In a landmark analysis of 508 patients with baseline and end-of-induction PET/CT scans in the prospective phase III GALLIUM study (NCT01332968), the progression-free survival (PFS) 2.5 y from randomization for patients achieving CMR (Deauville score of 1, 2, or 3) was 87.4% (95% CI, 83.7–90.2), compared with 54.9% (95% CI, 40.5–67.3) for patients failing to do so, with a Deauville score of 4 or 5 assigned as non-CMR (2). PET/CT was superior to contrast-enhanced CT for predicting PFS and overall survival. The 2014 Lugano response criteria (3,4) incorporating the Deauville score were superior to the previous standard, the 2007 International Harmonization Project criteria (5). The Lugano criteria also proposed combining the Deauville score with interval changes in ^{18}F-FDG uptake to assign metabolic response categories (3,4), analogous to the anatomic response categories used for CT reporting.

The Lugano criteria have been suggested as a suitable platform for response-adapted therapy in follicular lymphoma (2), with different management strategies already being tested for patients with advanced follicular lymphoma with CMR versus non-CMR after first-line immunochemotherapy using the Deauville score as a binary measure of response (6,7). This suggested suitability may be partly because there are no published data to our knowledge about ordinal Deauville scores or metabolic response categories, nor is there information about patterns of ^{18}F-FDG uptake that

might be associated with early progression or death in patients with follicular lymphoma and non-CMR at the end of induction. Patients with lymphoma usually have high response rates, which make analysis of the small numbers of patients with non-CMR challenging. It is becoming clear, however, that a positive PET finding may not carry uniform prognostic weight, with clinical trials on aggressive lymphomas reporting that patients with a PET score of 5 have inferior outcomes to patients with a PET score of 4 and treating this group differently (8–11). The aims of this ancillary analysis from the GALLIUM PET study were, therefore, to report PFS according to Deauville score and metabolic response category and to evaluate any PET/CT findings, such as disease distribution, on end-of-induction scans that might be associated with early progression or death in patients with non-CMR.

MATERIALS AND METHODS

The details of the GALLIUM trial (12) and the PET analysis (2) have been reported previously. In brief, previously untreated patients with advanced-stage grades 1–3a follicular lymphoma requiring immunochemotherapy were eligible. Patients were randomized 1:1 to receive either obinutuzumab or rituximab followed by the same maintenance antibody for up to 2 y. The chemotherapy was cyclophosphamide, vincristine, and prednisone; cyclophosphamide, doxorubicin, vincristine, and prednisone; or bendamustine, decided by the treating site. PFS was assessed by investigators using contrast-enhanced CT scans. PFS24 was defined as progression or death within 24 mo from the end of induction.

PET/CT response was a secondary endpoint, with scans mandated for the first 170 patients and optional thereafter. All PET/CT scans were performed according to a standardized study protocol with pre-specified time windows. The GALLIUM study was approved by local Institutional Review Boards and conducted in accordance with the Declaration of Helsinki and good clinical practice. All patients gave written informed consent.

Baseline and end-of-induction PET/CT and contrast-enhanced CT scans were read prospectively by an independent review committee using the International Harmonization Project criteria, which were the international standard at the time. The PET/CT scans were retrospectively reviewed by the independent review committee using the 2014 Lugano criteria (3,4). Patients with progressive metabolic disease in GALLIUM had an unexpectedly longer PFS than patients with a partial metabolic response on independent review committee evaluation, though this difference did not reach statistical significance. Two international experts were invited to rereview baseline and end-of-induction PET/CT scans that had been assessed as non-CMR by the independent review committee. Deauville score and metabolic response category were assigned without knowledge of the independent review committee results or any clinical information at the time of scan review, with differences between the 2 reviewers resolved by consensus. A Deauville score of 5 was assigned when uptake in lesions that were present at baseline was at least 3 times higher than the SUV$_{max}$ in the liver at response or in the presence of new lesions considered to be lymphoma-related. Lymphomatous lesions were considered measurable if 2 dimensions were recorded on contrast-enhanced CT, with the longest diameter being at least 15 mm for nodal sites and at least 10 mm for extranodal sites (4).

Kaplan–Meier methodology was used to estimate landmark PFS distributions and time to next antilymphoma treatment from the end of induction therapy for each response category. Patients who experienced progressive disease (CT-based assessment) at the end of induction were excluded from the landmark analyses.

RESULTS

By independent review committee assessment, there were 55 patients with non-CMR without CT-defined progressive disease at the end of induction. One patient was excluded from further analysis, as not all ^{18}F-FDG–avid sites present on the baseline scan were included on the end-of-induction PET/CT scan. Median follow-up for these 54 patients was 75.1 mo (range, 5.9–92.3 mo) from the end of induction.

Six of the remaining 54 patients in the current analysis were reassigned to CMR. Thirty-seven patients had a partial metabolic response, 2 patients had no metabolic response, and 9 patients had progressive metabolic disease.

Two of the 6 patients reassigned to CMR by both reviewers, compared with the independent review committee, had new uptake at sites not involved at baseline. These areas of new uptake were considered to be more in keeping with a sarcoidlike reaction and inflammatory uptake in degenerative disease at a facet joint than with new sites of follicular lymphoma, with CMR at all other sites. Two patients had abnormal uptake determined by the reviewers to be due to a neoplasm different from follicular lymphoma, also in the context of CMR elsewhere. One of these patients had unchanged uptake in an incidental thyroid nodule, in keeping with a probable thyroid neoplasm. Follow-up information was not available. The second patient had increasing ^{18}F-FDG uptake in a focus in the cecum and in a probable liver metastasis. The cecal uptake was later confirmed to be colonic adenocarcinoma on biopsy (Fig. 1). Two patients had low-grade residual uptake in the mesentery and the subpectoral region, respectively, which were close to the intensity of maximum uptake in the liver visually but less than the liver on quantitative measurement and hence reassigned as CMR. Five of the 6 patients reassigned to CMR did not experience PFS24. The remaining patient, with inflammatory arthropathy, experienced progression, presenting with a new parotid node 11 mo after the end of induction, a site of initial disease on the baseline scan that had responded at the end of induction on both PET/CT and contrast-enhanced CT.

Forty-eight patients were assigned as non-CMR by the current reviewers, 26 with a Deauville score of 4 and 22 with a Deauville score of 5. The PFS and time to next antilymphoma treatment for patients with a Deauville score of 5 was shorter than for patients with a Deauville score of 4, but the differences did not reach statistical significance. The hazard ratios were 1.33 (95% CI, 0.69–2.59; $P = 0.39$) and 1.37 (95% CI, 0.64–2.92; $P = 0.41$) for PFS and time to next antilymphoma treatment, respectively (Fig. 2). Fourteen of 37 (37.8%) patients with a partial metabolic response, 2 of 2 patients with no metabolic response, and 2 of 9 (22.2%) patients with progressive metabolic disease experienced PFS24 (Fig. 3), prompting a careful review of appearances that might not represent lymphoma and could represent false-positive uptake. Six of the 9 patients with progressive metabolic disease had increased or new uptake in the mesentery, 2 with measurable disease on CT. In 5 of these patients, the mesentery was the only site of disease, and only 1 of the 9 patients with the largest residual mesenteric node (42 × 24 mm) experienced progression from follicular lymphoma within the residual mesenteric site 5.5 mo after end-of-induction PET scans, at which time the patient commenced antilymphoma treatment (Fig. 4). The remaining 5 patients did not experience early progression (Fig. 5). One patient died without progression. Median follow-up for nonprogressing patients was 74.5 mo (range, 16.5–0.9 mo).
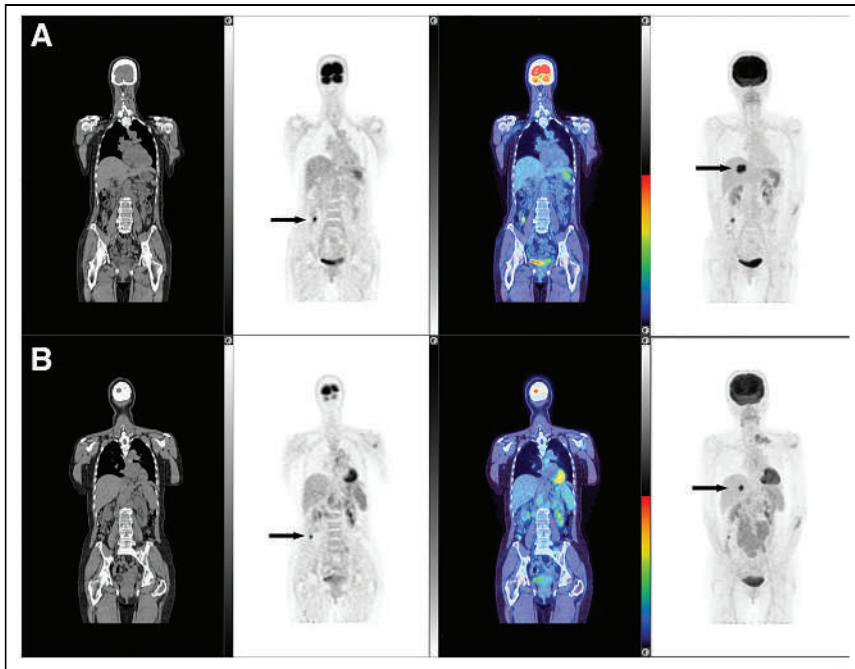
FIGURE 1. Patient scan with CT, PET, fused, and maximum-intensity-projection coronal images, from left to right. Scans at end of induction and at baseline are shown in A and B, respectively. ^{18}F-FDG uptake is seen in focus in cecum (arrowed in A on PET image) and in liver (arrowed in A on maximum-intensity-projection image) at end of induction, which was increased compared with baseline scan (arrowed in B on PET and maximum-intensity-projection images). There was CMR at other sites, including left supraclavicular and upper abdominal nodes. Patient did not experience progression from follicular lymphoma, but biopsy of cecum confirmed adenocarcinoma. Images are scaled to a maximum SUV of 7 for display.

In the current analysis of a subgroup of patients assigned as non-CMR, high residual or new mesenteric uptake associated with lymph nodes or mesenteric stranding was a common finding. Twenty of 48 (41.7%) patients had abnormal ^{18}F-FDG uptake in the mesentery at the end of induction (Fig. 6). All 20 patients had mesenteric involvement at baseline. The location of mesenteric uptake was not always identical at baseline and response but, allowing for bowel or mesenteric movement and reduction in other nodal responding masses, was concerning for the presence of residual lymphoma. Fourteen of 20 (70.0%) patients had mesenteric uptake in the context of CMR at all other baseline ^{18}F-FDG–avid sites, with a median mesenteric SUV$_{max}$ of 10.6 (range, 3.1–18.7), only 3 of whom (21.0%) progressed; all had measurable mesenteric disease on CT and commenced antilymphoma treatment within 3 mo of progression. Six of 20 patients had mesenteric uptake and additional sites of abnormal ^{18}F-FDG uptake, 4 of whom progressed within 24 mo (66.7%); the progression in 2 of these 4 patients was at mesenteric sites, and one of these 2 patients also had progression of renal disease. All had measurable mesenteric disease on CT. Three of the patients with PFS24 commenced antilymphoma treatment within 3 mo of progressive disease, and 1 commenced treatment 26 mo after progression on contrast-enhanced CT. The presence of measurable

disease in the mesentery was difficult to assess on the low-dose CT scan acquired as part of the PET/CT examination, and the size of lesions measured during this post hoc review was not reliable when compared with the measurements obtained on dedicated contrast-enhanced CT scans of the abdomen and pelvis.

The change in SUV$_{max}$ with treatment has been suggested as a marker of inadequate response in aggressive non-Hodgkin lymphoma (*13,14*). The mean reduction in SUV$_{max}$ was 35.5% among patients who had a PFS24 event (range, −91.4 to +12.1%) and was 34.3% (range, −91.1 to +121.3%) among patients who remained alive without progression.

DISCUSSION

Few patients treated with immunochemotherapy for high-tumor-burden follicular lymphoma fail to achieve a CMR at the end of induction. In this ancillary analysis of the 12% (55) of patients with non-CMR from the GALLIUM PET study, as assessed by the independent review committee, the current reviewers reassigned 6 patients to CMR. Four were reassigned by virtue of new or persistent sites of ^{18}F-FDG uptake not considered to be follicular lymphoma (new uptake was considered to be due to a sarcoidlike reaction and an inflammatory arthropathy in 2 patients, and persistent uptake was considered to be due to an incidental thyroid nodule and colonic cancer in another 2 patients). New areas of uptake unlikely to be related to lymphoma, especially in the context of response elsewhere, are not considered to represent progressive metabolic disease in the Lugano criteria and are designated by the suffix X after the PET score given to residual lymphomatous lesions (e.g., score 3X or 4X) (*3*) and by implication to sites of persistent or increased uptake attributable to other etiologies. Two patients with residual uptake close in intensity to the liver visually but measured as quantitatively lower than maximum liver uptake
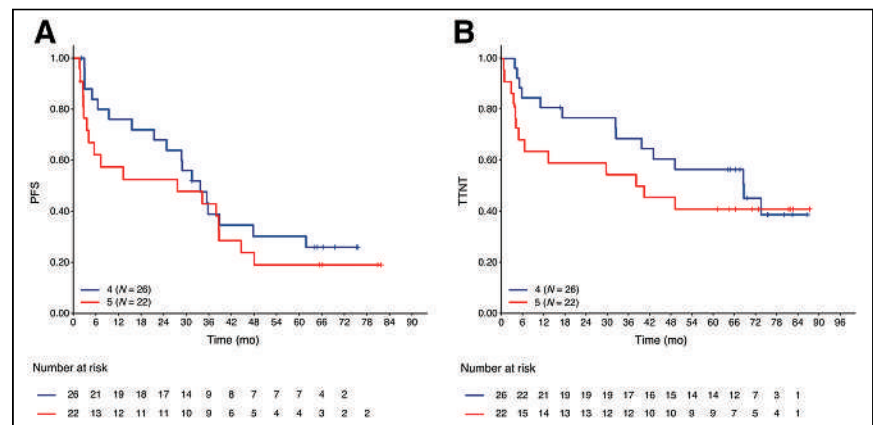
FIGURE 2. Landmark Kaplan–Meier plots of PFS (A) and time to next antilymphoma treatment (B) by Deauville scores 4 and 5 at end of induction. TTNT = time to next antilymphoma treatment.
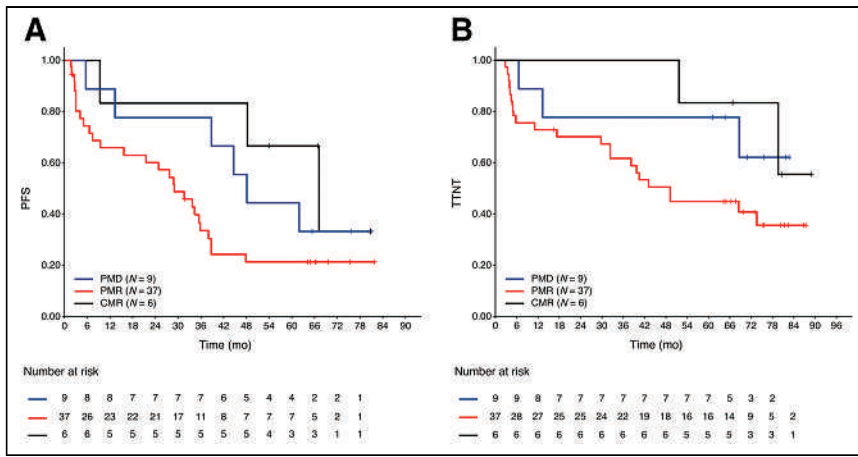
FIGURE 3. Landmark Kaplan–Meier plots of PFS (A) and time to next antilymphoma treatment (B) at end of induction by metabolic response category in patients classified as non-CMR by independent review committee. PMD = progressive metabolic disease; PMR = partial metabolic response; TTNT = time to next antilymphoma treatment.

were also reassigned to CMR. It is recommended that visual assessment be confirmed using quantitative assessment to avoid misinterpretation, which can be influenced by the adjacent background (15,16). Only the patient with inflammatory arthropathy experienced progression, at a different nodal site.

Nine patients in this analysis using Lugano criteria were assigned as having progressive metabolic disease by expert reviewers, and the observation that 7 of these patients did not experience early progression was surprising and prompted scrutiny of all scans of patients with non-CMR. Persistent or new focal uptake in the mesentery was relatively common (20/48; 42%) in this non-CMR population; only 1 of these patients did not have baseline abnormal mesenteric uptake. An important finding was that just 3 of the 14 patients (21%) with mesenteric uptake who had CMR at all other sites developed early progression, and among patients who progressed in mesenteric sites, all had measurable disease on CT at the time of the first non-CMR assignment. Mesenteric uptake with CMR elsewhere was observed in 3 patients who received obinutuzumab and 11 with rituximab, suggesting it was not related to mesenteric reactivity to the administration of a more potent antibody. This observation suggests that mesenteric uptake has a high likelihood of being false-positive, perhaps inflammatory or representing a delayed metabolic response, especially in the context of CMR elsewhere. In our series, disease progression never occurred in mesenteric sites in the absence of measurable disease on CT at the end of induction. Regression of mesenteric lesions, however, also occurred in 4 patients who had measurable mesenteric disease on the contrast-enhanced CT at the end of induction with CMR at other sites, only 1 of whom progressed at another site 4 mo after the end of induction. By comparison, 15 of 34 patients with nonmesenteric ^{18}F-FDG uptake had a

PFS24 event (44%), which was similar to the rate of progression or death of 45% previously reported in the non-CMR population at 2.5 y.

Mesenteric panniculitis on CT has been reported in around 2% of patients with non-Hodgkin lymphoma (17), most commonly follicular lymphoma (18), and is also associated with solid cancers, autoimmune disease, infection, and abdominal trauma. It is more commonly found in male patients (18–20). On biopsy, these appearances are associated with inflammation and fat necrosis (19). Radiologic features that help to distinguish lymphomatous involvement from inflammatory uptake at diagnosis are reported to be nodules at least 1 cm in size, increased attenuation giving the appearance of a misty mesentery, sometimes calcification and the absence of a fat ring or halo around the mesenteric vessels, or a pseudocapsule (17,19). ^{18}F-FDG uptake was reported in only 2 of 44 patients who underwent PET scanning in a retrospective review of all patients with the appearance of mesenteric panniculitis on abdominal CT scans over a 5-y period in a single U.S. radiology network and has been used as a feature to differentiate lymphoma from other causes of panniculitis (18,20). After treatment for lymphoma, distinguishing CT features may disappear, and calcification may occur within nodal masses. Case reports have suggested that follow-up CT imaging may be helpful to determine whether CT changes suggestive of panniculitis resolve, remain stable, or progress along with the underlying lymphoma (17,18,20). Stable changes were reported in 80%—and improvement in appearances in 9%—of cases using CT in 1 series (18). Ishiyama et al. recently reported 3 patients with lymphoma, where new mesenteric uptake on PET/CT with CMR elsewhere,
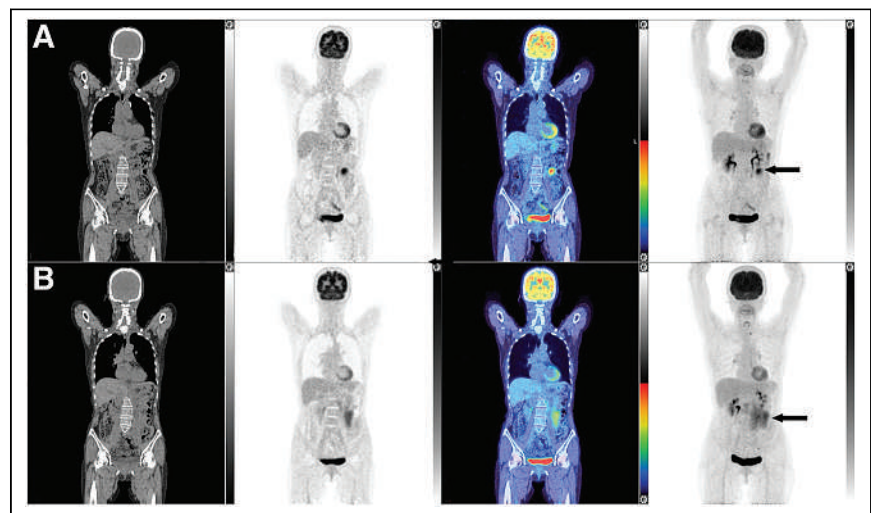
FIGURE 4. Patient scan with CT, PET, fused, and maximum-intensity-projection coronal images, from left to right. Increased ^{18}F-FDG uptake is seen in mesentery on end-of-induction PET/CT scan (A) (SUV$_{max}$, 11.4; arrowed in A and B), with CMR at all other sites demonstrated on baseline scan (B). Lesion measured 42 × 24 mm on contrast-enhanced CT, and patient experienced progression of mesenteric node at 5.5 mo on contrast-enhanced CT. Images are scaled to a maximum SUV of 7 for display.
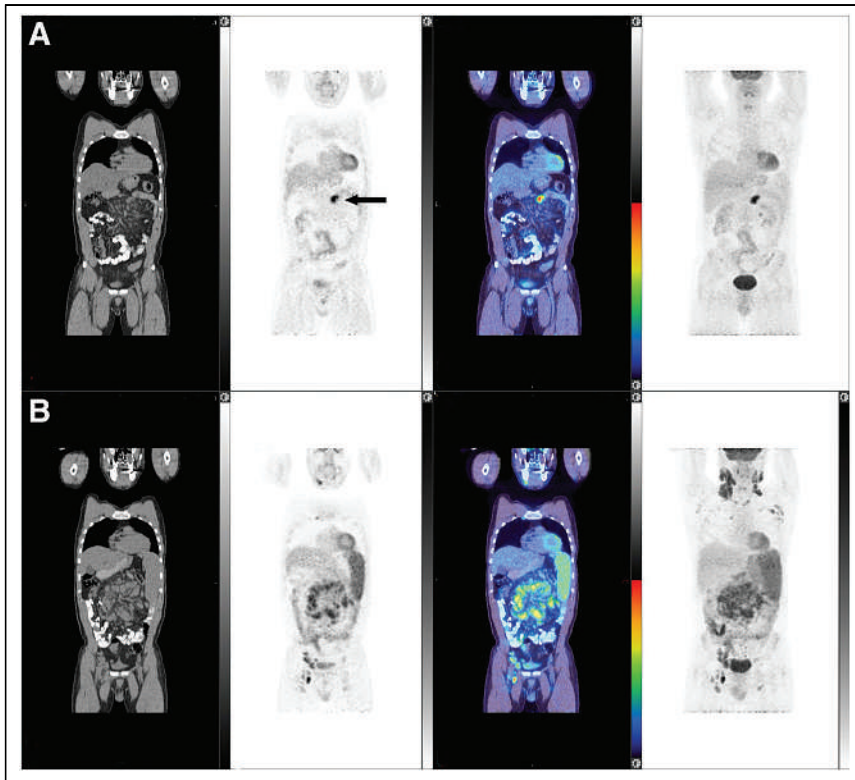
FIGURE 5. Patient scan with CT, PET, fused, and maximum-intensity-projection coronal images, from left to right. Residual ^{18}F-FDG uptake is seen in mesentery on end-of-induction PET/CT scan (A) (SUV$_{max}$, 11.6; arrowed in A), with CMR at all other sites demonstrated on baseline scan (B). Patient did not experience progression. Images are scaled to a maximum SUV of 7 for display.

similar to our findings, showed reduced ^{18}F-FDG uptake over time, with an excisional biopsy in 1 patient with follicular lymphoma demonstrating fat necrosis and histiocyte infiltration (21). Four patients in our series with abnormal ^{18}F-FDG uptake in the mesentery in isolation and measurable disease on CT who did not experience disease progression showed regression of lesions on contrast-enhanced CT suggesting an inflammatory component that may be treatment-related. Delayed response in the bone marrow and large nodal masses, also likely inflammatory, are recognized in aggressive lymphomas with focal ^{18}F-FDG uptake at diagnosis (16,22). The Lugano classification considered that "in the case of persistent focal changes in the bone marrow in the context of nodal response consideration should be given to further evaluation with MRI, biopsy or an interval scan" (4). Our findings suggest that similar caution should be exercised in the case of persistent or new sites of mesenteric uptake in patients with follicular lymphoma, especially in the context of response at other disease sites. The use of change in SUV did not appear to be helpful for response discrimination or determining whether mesenteric uptake was a false-positive.

This review was limited by the small number of patients who fail to achieve CMR with effective treatment of follicular lymphoma. The reviewers in the current analysis were masked to independent review committee results but were aware that patients had been categorized as non-CMR. The review was not powered to determine the association of Deauville score or metabolic response category with patient outcomes, although there was a trend for shorter PFS and time to next antilymphoma treatment in patients with a Deauville score of 5 as previously reported in aggressive lymphomas (8–11).

CONCLUSION

In some patients initially considered as non-CMR, CMR was assigned on rereview because alternative pathology, rather than lymphoma, was considered to be the cause of new or increased ^{18}F-FDG uptake, and use of the suffix X in this circumstance is recommended as per international guidelines (3). Quantitative assessment to confirm the visual impression of residual uptake in lesions is also suggested to avoid erroneous classification of non-CMR (14,16). Mesenteric ^{18}F-FDG uptake is a common false-positive finding at the end of induction in patients with follicular lymphoma who fail to achieve CMR, most likely because of inflammatory uptake rather than residual lymphoma, especially in the context of CMR at all other disease sites. On the basis of our results, contrast-enhanced CT is recommended to determine whether mesenteric uptake is accompanied by measurable disease on CT, as early progression did not occur in patients without corresponding CT abnormalities. Furthermore, no changes in clinical management or disease surveillance strategy are recommended when isolated mesenteric ^{18}F-FDG uptake is present at the end of induction without measurable disease on CT or a clinical suspicion of active disease. These patients and their families can be reassured and managed as other patients with CMR.
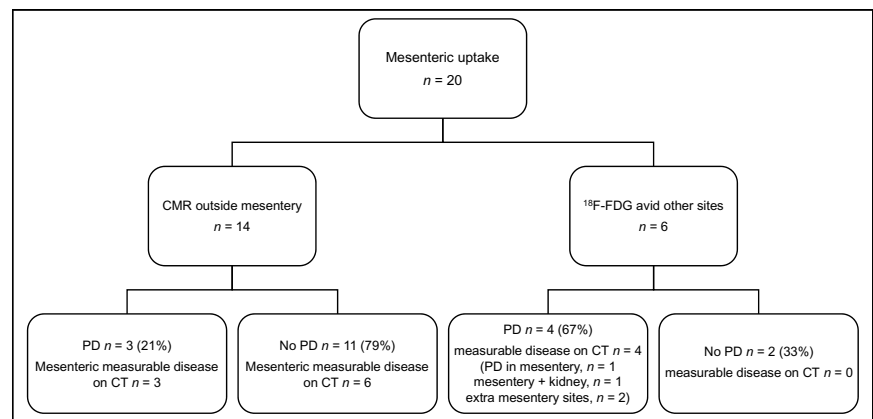
FIGURE 6. PFS24 events on follow-up CT in patients with abnormal ^{18}F-FDG uptake in mesentery at end of induction. PD = progressive disease.

KEY POINTS

QUESTION: What is the outcome of patients from the GALLIUM trial with follicular lymphoma treated with first-line immunochemotherapy who did not achieve CMR?

PERTINENT FINDINGS: In the PET substudy of the GALLIUM trial, CMR on PET/CT was the sole independent predictor of overall survival in patients with follicular lymphoma; here, we investigated the outcome of patients who did not achieve a CMR. We found that isolated mesenteric ^{18}F-FDG uptake is likely a false-positive finding at the end of induction and does not warrant changes in clinical management or disease surveillance unless there is measurable disease on contrast-enhanced CT or clinical suspicion of active disease.

IMPLICATIONS FOR PATIENT CARE: Our results highlight that isolated mesenteric ^{18}F-FDG uptake is a false-positive finding at the end of induction in follicular lymphoma. We suggest contrast-enhanced CT for assessment, if appropriate, as early progression never occurred in the absence of measurable disease; this is important for clinical practice as these patients and their families can be reassured and managed as other patients with CMR.

REFERENCES

1. Trotman J, Luminari S, Boussetta S, et al. Prognostic value of PET-CT after first-line therapy in patients with follicular lymphoma: a pooled analysis of central scan review in three multicentre studies. *Lancet Haematol.* 2014;1:e17–e27.
2. Trotman J, Barrington SF, Belada D, et al. Prognostic value of end-of-induction PET response after first-line immunochemotherapy for follicular lymphoma (GALLIUM): secondary analysis of a randomised, phase 3 trial. *Lancet Oncol.* 2018;19:1530–1542.
3. Barrington SF, Mikhaeel NG, Kostakoglu L, et al. Role of imaging in the staging and response assessment of lymphoma: consensus of the international conference on malignant lymphomas imaging working group. *J Clin Oncol.* 2014;32:3048–3058.
4. Cheson BD, Fisher RI, Barrington SF, et al. Recommendations for initial evaluation, staging, and response assessment of Hodgkin and non-Hodgkin lymphoma: the Lugano classification. *J Clin Oncol.* 2014;32:3059–3068.
5. Cheson BD, Pfistner B, Juweid ME, et al. Revised response criteria for malignant lymphoma. *J Clin Oncol.* 2007;25:579–586.
6. Federico M, Mannina D, Versari A, et al. Response oriented maintenance therapy in advanced follicular lymphoma: results of the interim analysis of the FOLL 12 trial conducted by the Fondazione Italiana Linfomi. *Hematol Oncol.* 2019;37:153–154.
7. Pettitt AR, Barrington S, Kalakonda N, et al. NCRI PETReA trial: a phase 3 evaluation of PET-guided, response-adapted therapy in patients with previously untreated, advanced-stage, high-tumour-burden follicular lymphoma. *Hematol Oncol.* 2019;37:67–68.
8. Barrington SF, Phillips EH, Counsell N, et al. Positron emission tomography score has greater prognostic significance than pretreatment risk stratification in early-stage Hodgkin lymphoma in the UK RAPID study. *J Clin Oncol.* 2019;37:1732–1741.
9. Ceriani L, Martelli M, Gospodarowicz MK, et al. Positron emission tomography/computed tomography assessment after immunochemotherapy and irradiation using the Lugano classification criteria in the IELSG-26 study of primary mediastinal B-cell lymphoma. *Int J Radiat Oncol Biol Phys.* 2017;97:42–49.
10. Johnson P, Federico M, Kirkwood A, et al. Adapted treatment guided by interim PET-CT scan in advanced Hodgkin's lymphoma. *N Engl J Med.* 2016;374:2419–2429.
11. Hertzberg M, Gandhi M, Butcher B, et al. Early treatment intensification with R-ICE chemotherapy followed by autologous stem cell transplantation (ASCT) using Zevalin-BEAM for patients with poor risk diffuse large B-cell lymphoma (DLBCL) as identified by interim PET/CT scan performed after four cycles of R-CHOP-14: a multicenter phase II study of the Australasian Leukaemia Lymphoma Study Group (ALLG) [abstract]. *Blood.* 2015;126:815.
12. Marcus R, Davies A, Ando K, et al. Obinutuzumab for the first-line treatment of follicular lymphoma. *N Engl J Med.* 2017;377:1331–1344.
13. Lin C, Itti E, Haioun C, et al. Early ^{18}F-FDG PET for prediction of prognosis in patients with diffuse large B-cell lymphoma: SUV-based assessment versus visual analysis. *J Nucl Med.* 2007;48:1626–1632.
14. Itti E, Lin C, Dupuis J, et al. Prognostic value of interim ^{18}F-FDG PET in patients with diffuse large B-cell lymphoma: SUV-based assessment at 4 cycles of chemotherapy. *J Nucl Med.* 2009;50:527–533.
15. Itti E, Juweid ME, Haioun C, et al. Improvement of early ^{18}F-FDG PET interpretation in diffuse large B-cell lymphoma: importance of the reference background. *J Nucl Med.* 2010;51:1857–1862.
16. Barrington SF, Kluge R. FDG PET for therapy monitoring in Hodgkin and non-Hodgkin lymphomas. *Eur J Nucl Med Mol Imaging.* 2017;44:97–110.
17. Khasminsky V, Ram E, Atar E, Steinminz A, Issa N, Bachar GN. Is there an association between mesenteric panniculitis and lymphoma? A case control analysis. *Clin Radiol.* 2017;72:844–849.
18. Ehrenpreis ED, Roginsky G, Gore RM. Clinical significance of mesenteric panniculitis-like abnormalities on abdominal computerized tomography in patients with malignant neoplasms. *World J Gastroenterol.* 2016;22:10601–10608.
19. Horton KM, Lawler LP, Fishman EK. CT findings in sclerosing mesenteritis (panniculitis): spectrum of disease. *Radiographics.* 2003;23:1561–1567.
20. Zissin R, Metser U, Hain D, Even-Sapir E. Mesenteric panniculitis in oncologic patients: PET-CT findings. *Br J Radiol.* 2006;79:37–43.
21. Ishiyama M, Matesan M. Mesenteric panniculitis mimicking early recurrence at end-of-treatment evaluation in malignant lymphoma: differentiation by active surveillance with F-18 FDG PET/CT imaging. *Radiol Case Rep.* 2020;15:1006–1010.
22. Schöder H, Polley MC, Knopp MV, et al. Prognostic value of interim FDG-PET in diffuse large cell lymphoma: results from the CALGB 50303 clinical trial. *Blood.* 2020;135:2224–2234.

Head-to-Head Comparison of ^{68}Ga-FAPI-46 and ^{18}F-FDG PET/CT for Evaluation of Head and Neck Squamous Cell Carcinoma: A Single-Center Exploratory Study

Chetsadaporn Promteangtrong, Dheeratama Siripongsatian, Attapon Jantarato, Anchisa Kunawudhi, Peerapon Kiatkittikul, Sukanya Yaset, Natphimol Boonkawin, and Chanisa Chotipanich

National Cyclotron and PET Centre, Chulabhorn Hospital, Chulabhorn Royal Academy, Bangkok, Thailand

^{68}Ga-conjugated fibroblast activation protein inhibitor (^{68}Ga-FAPI) has become an attractive agent for PET. This study aimed to compare ^{68}Ga-FAPI-46 PET/CT with ^{18}F-FDG PET/CT for detecting primary cancer and metastatic lesions in patients with head and neck squamous cell carcinoma (HNSCC). **Methods:** Twelve patients and 28 patients with HNSCC underwent ^{68}Ga-FAPI-46 and ^{18}F-FDG PET/CT for initial staging and recurrence detection, respectively. The concordance and diagnostic accuracy of both tracers were analyzed. Semiquantitative parameters, including SUV_{max}, SUV_{mean}, and tumor-to-background ratio, were compared. Fibroblast activation protein (FAP) expression tumor volume and total lesion FAP expression of ^{68}Ga-FAPI-46 were compared with metabolic tumor volume and total lesion glycolysis of ^{18}F-FDG, respectively. Differences between semiquantitative parameters were analyzed using paired t testing. **Results:** ^{68}Ga-FAPI-46 PET/CT was 83.3% and 96.4% concordant with ^{18}F-FDG PET/CT for initial staging and recurrence detection, respectively. Eighteen lesions had histopathologic validation, and both tracers displayed 100% sensitivity, 50% specificity, and 94.4% accuracy for lesion-based analysis. FAP expression tumor volume was greater than metabolic tumor volume ($P < 0.05$), but no significant differences were observed for the other parameters. **Conclusion:** ^{68}Ga-FAPI-46 PET/CT showed good concordance with, and comparable diagnostic performance to, ^{18}F-FDG PET/CT for initial staging and recurrence detection in HNSCC patients.

Key Words: FAPI; FDG; PET/CT

Head and neck squamous cell carcinoma (HNSCC) is the sixth most common carcinoma worldwide, with 890,000 new cases and 450,000 deaths reported in 2018 (*1*). The treatment of HNSCC depends on the anatomic site, tumor stage, and functional outcome. Early-stage cancers are treated with a single modality, such as surgery or radiotherapy alone, whereas locally advanced cancers require multimodal treatment, which is often a combination of surgery, radiotherapy, and chemotherapy. Therefore, accurate tumor staging is crucial for planning treatment strategies. ^{18}F-FDG PET/CT is a widely accepted tool for imaging various cancers. However, ^{18}F-FDG PET/CT has some limitations when used for HNSCC. High glucose uptake is observed in several normal tissues, such as salivary glands, lymphoid tissues, and lymph nodes. Furthermore, false-positive uptake may occur in areas of peritumoral inflammation or after surgery and radiotherapy (*2*).

The tumor microenvironment in HNSCC is a mix of tumor and stromal cells, including endothelial cells, immune cells, and cancer-associated fibroblasts. Cancer-associated fibroblasts secrete a broad range of growth factors, cytokines, and chemokines that promote tumor growth, angiogenesis, and recruitment of immunosuppressive immune cells and thus have a role in HNSCC invasion and progression (*3*). Fibroblast activation protein (FAP) is overexpressed by cancer-associated fibroblasts in several types of cancer, including HNSCC, with relatively low expression in normal tissue. ^{68}Ga-conjugated FAP inhibitor (FAPI), has been developed for targeting FAP and tumor stromal visualization (*4*). In previous studies, ^{68}Ga-FAPI-04 PET/CT showed a higher sensitivity than ^{18}F-FDG PET/CT in various types of cancers (*5*), and FAPI PET precisely delineated HNSCC for radiotherapy planning (*6*). The aim of this study was to conduct a head-to-head comparison of ^{68}Ga-FAPI-46 PET/CT and standard ^{18}F-FDG PET/CT imaging for detecting primary cancer and metastatic lesions in patients with HNSCC.

MATERIALS AND METHODS

Study Design

This was a single-center exploratory comparative-imaging study. The study was approved by the Human Research Ethics Committee of
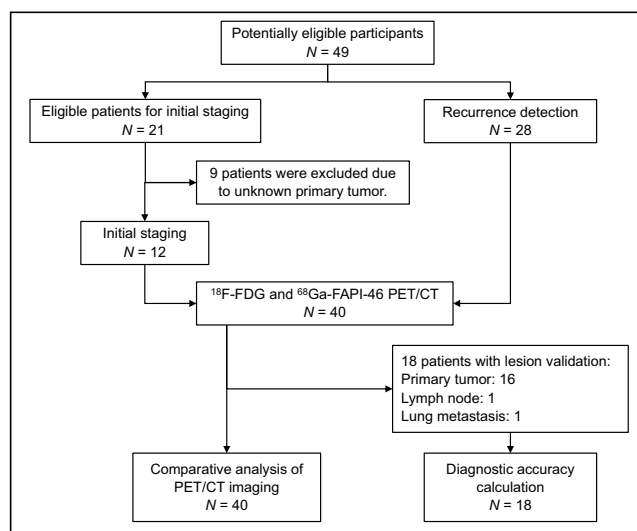
FIGURE 1. Flowchart of study design.

TABLE 1
Characteristics of Study Patients

Patient no.	Age (y)	Sex	Primary tumor	Indication
1	48	M	Tongue	Recurrence detection
2	65	F	Lip	Recurrence detection
3	65	M	Pyriform fossa	Recurrence detection
4	57	M	Tongue	Recurrence detection
5	65	M	Base of tongue	Initial staging
6	57	F	Nasopharynx	Recurrence detection
7	49	F	External ear canal	Recurrence detection
8	35	F	Nasal cavity	Recurrence detection
9	54	F	Nasopharynx	Recurrence detection
10	62	M	Nasopharynx	Recurrence detection
11	69	F	Oropharynx	Initial staging
12	62	F	Tongue	Initial staging
13	58	M	Pyriform fossa	Initial staging
14	79	M	Tongue	Recurrence detection
15	67	M	Pyriform fossa	Recurrence detection
16	77	M	Retromolar trigone	Recurrence detection
17	45	F	Oral mucosa	Initial staging
18	51	M	Nasopharynx	Initial staging
19	59	M	Nasopharynx	Initial staging
20	55	M	Base of tongue	Recurrence detection
21	50	M	Tongue	Initial staging
22	32	F	Nasopharynx	Recurrence detection
23	60	M	Base of tongue	Recurrence detection
24	60	M	Glottis	Recurrence detection
25	61	M	Pyriform fossa	Recurrence detection
26	69	M	Nasopharynx	Recurrence detection
27	63	M	Floor of mouth	Recurrence detection
28	62	M	Pyriform fossa	Initial staging
29	74	M	Nasopharynx	Recurrence detection
30	86	M	Nasopharynx	Recurrence detection
31	55	M	Nasopharynx	Initial staging
32	49	F	Nasopharynx	Recurrence detection
33	53	M	Nasopharynx	Recurrence detection
34	47	M	Nasopharynx	Recurrence detection
35	23	M	Nasopharynx	Recurrence detection
36	42	F	Tongue	Recurrence detection
37	46	M	Nasopharynx	Recurrence detection
38	32	F	Nasopharynx	Recurrence detection
39	51	M	Nasopharynx	Initial staging
40	72	F	Tongue	Initial staging

Study Population

Potentially eligible HNSCC patients were recruited for enrollment in this study from August 2020 through May 2021. The inclusion criteria were pathologically confirmed HNSCC, an age of more than 18 y, and scheduled PET/CT for initial staging or suspected recurrence. Exclusion criteria included a fasting blood sugar of more than 150 mg/dL,
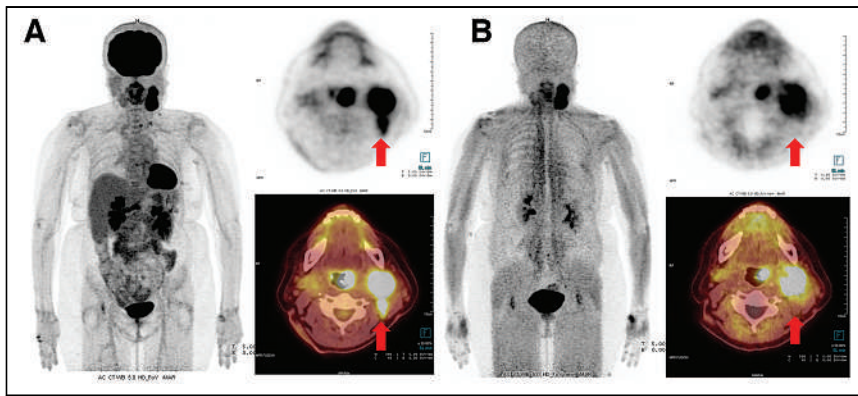
FIGURE 2. ^{18}F-FDG PET/CT (A) and ^{68}Ga-FAPI-46 PET/CT (B) images of 69-y-old woman with left oropharyngeal cancer, stage IVA, who underwent PET/CT for initial staging. ^{18}F-FDG PET/CT detected involved lymph nodes on left side at levels IIA and IIB, whereas ^{68}Ga-FAPI-46 PET/CT did not detect level IIB node (arrows). Left IIB node was confirmed as nodal metastasis by anatomic abnormality criteria.

pregnancy or breast feeding, and unwillingness to participate. The flowchart of the study design is presented in Figure 1.

Preparation of ^{68}Ga-FAPI-46

^{68}Ga-FAPI-46 was synthesized using an iTG ^{68}Ge/^{68}Ga generator and automated module (iQS-TS; ITM Medical Isotopes) and a good-manufacturing-practice–compliant process, as previously described (7,8) with some modifications.

PET/CT Imaging

^{18}F-FDG and ^{68}Ga-FAPI-46 PET/CT were performed on separate days within a 2-wk period. The patients fasted for 6 h before undergoing ^{18}F-FDG PET/CT, whereas no specific preparation was required for ^{68}Ga-FAPI-46 PET/CT. Before the ^{18}F-FDG PET/CT scan, the plasma glucose level was determined to ensure it was no more than 150 mg/dL. The tracer dose was calculated according to the patient's weight in kilograms (2.59 MBq/kg for ^{18}F-FDG; 2.0 MBq/kg for ^{68}Ga-FAPI-46). Sixty minutes after intravenous administration, scanning was performed from the vertex to the proximal thigh using a

64-slice Biograph Vision PET/CT scanner (Siemens Healthcare GmbH) in 3-dimensional mode with continuous bed motion, at a speed of 1.6–1.8 mm/s. The matrix was 440×440, and the reconstruction methods were True X (Siemens) and time of flight. The CT parameters were a tube voltage of 120 kV, a current of 25 mAs, and a slice thickness of 3.0 mm. ^{68}Ga-FAPI-46 PET/CT was performed for comparative purposes without impacting the final patient management.

PET/CT Imaging Analysis

^{18}F-FDG PET/CT scans were interpreted separately from ^{68}Ga-FAPI-46 PET/CT scans within 2 wk of each other by board-certified nuclear medicine physicians working in consensus. One team interpreted the ^{18}F-FDG PET/CT scans, and a second team interpreted the ^{68}Ga-FAPI-46 PET/CT scans; one of the interpreters was on both teams (5 interpreters total). The interpreters were unaware of the clinical data at the time of review. PET, CT, and PET/CT images were viewed using a Syngo.via workstation (Siemens Healthcare GmbH).

An area of focal uptake visually higher than that of the surrounding background was considered positive. The lesion was categorized as a primary tumor, nodal metastasis, or distant metastasis. Nodal metastasis was classified according to location: neck, supraclavicular, mediastinal, axillary, or intraabdominal. Involvement of the brain, visceral organs in the chest and abdomen, bone, and soft tissues was classified as individual sites. Synchronous and second primary tumors were also analyzed. For initial staging, the clinical TNM stage of HNSCC was based on the eighth edition of the American Joint Committee on Cancer staging system (9).

The 3 designated physicians of each team drew 3-dimensional voxels of interest around the lesions and performed semiquantitative analysis, making adjustments to avoid false-positive results in regions of normal physiologic uptake. The tumor region was delineated automatically using an SUV that was 40% of the SUV$_{max}$. The SUV$_{max}$, SUV$_{mean}$, and tumor-to-background ratio (T/B) of the primary tumor and distant

TABLE 2
Comparative ^{18}F-FDG and ^{68}Ga-FAPI-46 PET/CT Results for Initial Staging

Patient no.	Primary tumor	TNM		Stage	
		^{18}F-FDG	^{68}Ga-FAPI-46	^{18}F-FDG	^{68}Ga-FAPI-46
5	Base of tongue	T2N2cM0	T2N2cM0	IVA	IVA
11	Oropharynx	T1N2bM0	T1N2bM0	IVA	IVA
12	Tongue	T3N2cM0	T3N2cM0	IVA	IVA
13	Pyriform fossa	T1N3bM0	T1N3bM0	IVB	IVB
17	Oral mucosa	T3N1M0	T3N1M0	III	III
18	Nasopharynx	T3N2M0	T3N2M0	III	III
19	Nasopharynx	T3N1M0	T3N1M0	III	III
21	Tongue	T3N0M0	T3N0M0	III	III
28	Pyriform fossa	T3N2bM0	T3N2bM1	IVA	IVC
31	Nasopharynx	T2N2M1	T2N1M1	IVB	IVB
39	Nasopharynx	T2N0M0	T2N0M0	II	II
40	Tongue	T2N0M0	T2N0M0	II	II
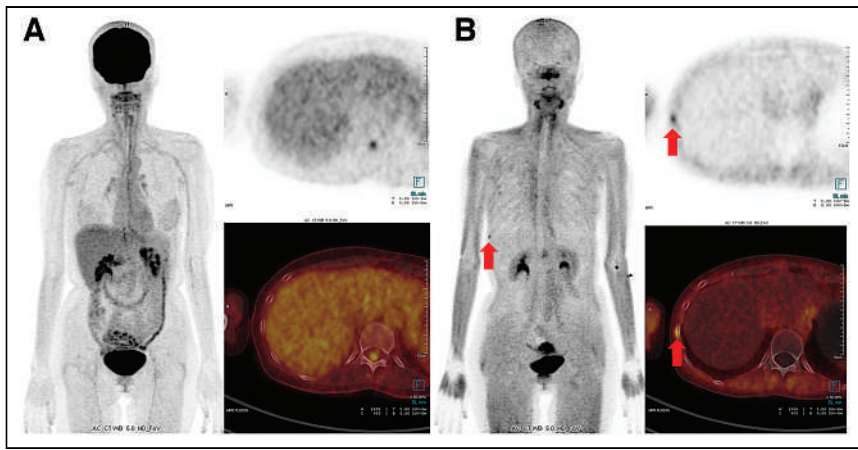
FIGURE 3. ^{18}F-FDG PET/CT (A) and ^{68}Ga-FAPI-46 PET/CT (B) images of 49-y-old woman with nasopharyngeal cancer after concurrent chemoradiation who underwent PET/CT for recurrence detection. ^{68}Ga-FAPI-46 PET/CT showed focal uptake, without corresponding ^{18}F-FDG uptake, in small sclerotic lesion at ninth right lateral rib, which was suspected of being bone metastasis (arrows).

metastases were recorded. T/B was determined by dividing SUV$_{max}$ by the SUV$_{mean}$ of contralateral normal tissue. Metabolic tumor volume (MTV) and total lesion glycolysis assessed by ^{18}F-FDG were compared with the equivalent values assessed by ^{68}Ga-FAPI-46 (FAP expression tumor volume [FTV] and total lesion FAP expression, respectively). The T/B was determined by dividing tumor SUV$_{max}$ by the SUV$_{mean}$ of contralateral normal tissue. MTV and FTV were calculated by multiplying the number of voxels in the tumor region by voxel size. Total lesion glycolysis and total lesion FAP expression were calculated by multiplying MTV or FTV, respectively, by the corresponding SUV$_{mean}$ for each tumor volume. If multiple positive lesions occurred at a single metastatic site, the lesion with the highest activity was analyzed. For nodal metastasis, the SUV$_{max}$ was calculated for each site.

TABLE 3
Comparative ^{18}F-FDG and ^{68}Ga-FAPI-46 PET/CT Results for Recurrence Detection

Patient no.	Primary tumor	Recurrence site	^{18}F-FDG avidity	^{68}Ga-FAPI-46 avidity	PET/CT result
1	Tongue	None	Y	Y	FP
2	Lip	Primary, LN	Y	Y	TP
3	Pyriform fossa	Primary, LN	Y	Y	TP
4	Tongue	Primary, LN	Y	Y	TP
6	Nasopharynx	None	N	N	TN
7	External ear canal	Primary, LN	Y	Y	TP
8	Nasal cavity	None	N	N	TN
9	Nasopharynx	Primary	Y	Y	TP
10	Nasopharynx	Lung	Y	Y	TP
14	Tongue	None	Y	Y	FP
15	Pyriform fossa	Primary	Y	Y	TP
16	Retromolar trigone	Primary, LN	Y	Y	TP
20	Base of tongue	Primary, LN, lung, thyroid	Y	Y	TP
22	Nasopharynx	LN, bone	Y	Y	TP
23	Base of tongue	None	N	N	TN
24	Glottis	Primary, LN	Y	Y	TP
25	Pyriform fossa	LN, liver, adrenal gland	Y	Y	TP
26	Nasopharynx	Primary, LN, lung	Y	Y	TP
27	Floor of mouth	Primary, LN, bone, muscle	Y	Y	TP
29	Nasopharynx	None	N	N	TN
30	Nasopharynx	LN, lung	Y	Y	TP
32	Nasopharynx	Bone	N	Y	FN for ^{18}F-FDG; TP for ^{68}Ga-FAPI
33	Nasopharynx	None	N	N	TN
34	Nasopharynx	LN, nasal turbinate	Y	Y	TP
35	Nasopharynx	None	N	N	TN
36	Tongue	None	N	N	TN
37	Nasopharynx	None	N	N	TN
38	Nasopharynx	LN, lung, pleura	Y	Y	TP

FP = false positive; LN = lymph node; TP = true positive; TN = true negative; FN = false negative.

TABLE 4
Comparative Diagnostic Accuracy of ^{18}F-FDG and ^{68}Ga-FAPI-46 PET/CT

Diagnostic accuracy (%)	^{18}F-FDG	^{68}Ga-FAPI-46
Sensitivity	100	100
Specificity	50	50
Positive predictive value	94.1	94.1
Negative predictive value	100	100
Accuracy	94.4	94.4

Reference Standard

Histopathology served as the gold standard for analysis of diagnostic accuracy. The reference standard for nonbiopsied lesions was the anatomic abnormality observed on CT or MRI. An anatomic criterion for nodal metastasis was either a cluster of at least 3 size-independent nodes at 1 site or fewer than 3 lymph nodes, at least 1 of which measured at least 1 cm along the short axis or had a spheric form or central necrosis. The anatomic criteria for lung metastasis included solid pulmonary nodules, a reticulonodular pattern, cavitating nodules, or lymphangitis carcinomatosis. The anatomic criteria for bone metastasis were lytic or sclerotic lesions with cortical breakthrough, a periosteal reaction, an expansile appearance, pathologic fracture on CT, or an abnormal marrow signal intensity on MRI. The anatomic criterion for distant metastasis was a nodule or mass lesion at another site. Lesions showing focally increased uptake above the background level and with corresponding anatomic criteria were defined as true-positives. Patients with negative PET/CT findings were followed up clinically for at least 3 mo to confirm a true-negative result.

Statistical Analysis

The primary outcome was concordance of ^{8}F-FDG and ^{68}Ga-FAPI-46 PET/CT results for initial staging and recurrence detection. The secondary outcome was the diagnostic accuracy of both tracers. Comparison of semiquantitative parameters was the tertiary outcome.

The visually interpreted PET/CT images were compared with the reference standards. Concordance rates between the 2 tracers for initial staging and recurrence detection were calculated. The diagnostic accuracy of both tracers defined by sensitivity, specificity, positive predictive value, negative predictive value, and accuracy was calculated for lesions with histopathologic validation. Differences in semiquantitative parameters

between ^{18}F-FDG and ^{68}Ga-FAPI-46 PET/CT were analyzed using paired t tests. Data are presented as number or as mean $\pm$ SD. A P value of less than 0.05 was considered statistically significant. STATA software, version 11 (StataCorp LLC), was applied for all analyses.

RESULTS

The characteristics of each patient are shown in Table 1.

Twenty-five primary tumors were detected in 25 patients using both tracers. The mean size of the primary tumors was 3.5 ± 1.4 cm, with a minimum and maximum of 1.5 and 7.4 cm, respectively.

^{18}F-FDG and ^{68}Ga-FAPI-46 identified 128 and 94 lymph nodes, respectively. Overall, there were 33 sites (17 neck, 5 supraclavicular, 1 axillary, 7 mediastinal, and 3 intraabdominal) of nodal involvement in 24 patients detected by both tracers. ^{18}F-FDG PET/CT detected more lymph nodes than did ^{68}Ga-FAPI-46 PET/CT; however, the numbers of sites involved did not differ between the 2 tracers. The sizes of detected nodes ranged from 0.4 to 4.2 cm. Patient with lower nodal detection by ^{68}Ga-FAPI-46 are shown in Figure 2.

Ten of 40 patients presented with distant metastases involving 15 sites (5 pulmonary, 5 bone, 1 pleural, 1 thyroidal, 1 adrenal, 1 hepatic, and 1 muscle). Synchronous tumors were noted in 4 patients (supraglottis in 1 and esophagus in 3). Two patients had a second primary thyroid cancer with histopathologic confirmation. The lesions at each site were detected with both tracers, except for 2 bone lesions in 2 patients that were observed only on ^{68}Ga-FAPI-46 PET/CT. Both bone lesions were confirmed by anatomic criteria for bone metastasis.

Concordance of ^{18}F-FDG and ^{68}Ga-FAPI-46 PET/CT

There was no difference in the assessment of TNM staging between the 2 tracers in 10 of 12 patients, with 83.3% concordance. ^{68}Ga-FAPI-46 PET/CT upstaged 1 patient (patient 28). The upstaged lesion was confirmed by MRI after a marrow change at the right scapula and suspected bone metastasis. In patient 31, ^{68}Ga-FAPI-46 PET/CT detected a lower number of nodal metastases than did ^{18}F-FDG; the multiple nodal metastases were confirmed by anatomic criteria (the size of the 1 discordant node was 1.0 cm in the short axis and 1.2 cm in the long axis). The PET/CT results for initial staging are detailed in Table 2.

A difference in recurrence detection between the 2 tracers was observed in only 1 of 28 patients, with 96.4% concordance. In this patient, ^{68}Ga-FAPI-46 PET/CT showed focal uptake without corresponding ^{18}F-FDG uptake in a sclerotic lesion at the ninth right rib, which was a suspected bone metastasis according to our criteria. Images of the discordant cases are presented in Figure 3. The false-positive results in patient 1 may be explained by postoperative inflammation due to primary-tumor excision about 1 mo before the PET studies. False-positive results with biopsy validation in patient 14 may be explained by postradiation fibrotic changes at 5 mo after radiation. The PET/CT results for recurrence detection are detailed in Table 3.

Diagnostic Accuracy of ^{18}F-FDG and ^{68}Ga-FAPI-46 PET/CT

Eighteen lesions had histopathologic results. Both tracers detected 16 true-positive, 1 true-negative, and 1 false-positive lesions.
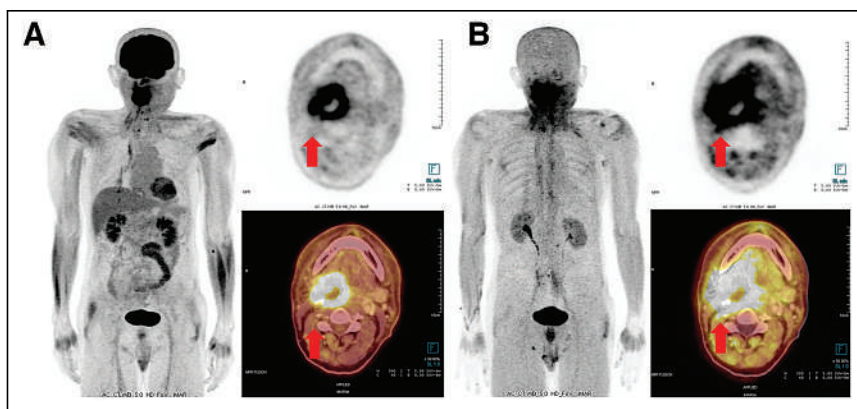
FIGURE 4. ^{18}F-FDG PET/CT (A) and ^{68}Ga-FAPI-46 PET/CT (B) images of 60-y-old man with glottic cancer who underwent PET/CT for recurrence detection. Recurrent tumor avid for ^{18}F-FDG and ^{68}Ga-FAPI-46 was seen at right side of oropharynx (arrows). MTV was 19.37 cm^3. FTV was 33.75 cm^3.

TABLE 5
Comparisons of Semiquantitative Parameters Between ^{18}F-FDG and ^{68}Ga-FAPI-46 PET/CT of Primary Tumor and Distant Metastasis

Parameter	^{18}F-FDG	^{68}Ga-FAPI-46	P
Primary tumor			
SUV$_{max}$	18.59 ± 9.61 (7.15–43.11)	19.28 ± 7.45 (6.40–42.39)	0.65
SUV$_{mean}$	10.82 ± 6.10 (2.54–24.64)	11.10 ± 4.83 (4.17–28.07)	0.78
T/B	10.21 ± 5.89 (1.54–26.37)	11.04 ± 5.03 (2.21–23.51)	0.45
MTV vs. FTV	7.36 ± 5.07 (1.34–21.66)	10.33 ± 9.44 (0.86–35.37)	0.03
TLG vs. TLF	94.91 ± 117.20 (7.14–517.65)	122.58 ± 132.85 (8.88–500.50)	0.06
Distant metastasis			
SUV$_{max}$	13.59 ± 7.64 (3.86–31.69)	16.89 ± 9.96 (3.09–34.22)	0.09
SUV$_{mean}$	7.82 ± 4.45 (2.23–18.42)	9.74 ± 5.67 (1.80–18.18)	0.09
T/B	30.39 ± 55.85 (1.53–254.4)	20.54 ± 13.57 (1.69–52.63)	0.44
MTV vs. FTV	10.52 ± 19.41 (0.18–81.23)	9.02 ± 15.27 (0.25–54.42)	0.33
TLG vs. TLF	109.87 ± 255.52 (1.43–1151.59)	135.92 ± 260.12 (0.78–976.03)	0.36

TLF = total lesion FAP expression (^{68}Ga-FAPI); TLG = total lesion glycolysis (^{18}F-FDG).
Data are mean ± SD followed by range.

No false-negative results were found. The diagnostic accuracy of ^{68}Ga-FAPI-46 and ^{18}F-FDG PET/CT is shown in Table 4.

Comparison of Semiquantitative Parameters

There were no significant differences in semiquantitative parameters, except for the FTV of the primary tumor, which was significantly higher than MTV ($P = 0.03$). An example of a patient with a higher FTV than MTV is shown in Figure 4. The semiquantitative comparisons of primary tumor and distant metastasis are shown in Table 5. The semiquantitative parameters for nodal metastasis are compared in Table 6.

DISCUSSION

To our knowledge, this study was the first head-to-head comparison of diagnostic performance and semiquantitative parameters—such as uptake, image contrast, and tumor volume—between ^{68}Ga-FAPI-46 and ^{18}F-FDG PET/CT in HNSCC patients. ^{68}Ga-FAPI-46 PET/CT had an 83.3% and 96.4% concordance with ^{18}F-FDG PET/CT for initial staging and recurrence detection, respectively. Lesion-based analysis showed comparable diagnostic accuracy. All primary tumors were detected by both tracers. The number of avid nodes detected by ^{68}Ga-FAPI-46 was less than that detected by ^{18}F-FDG. Our findings corresponded with those of Serfling et al. (10), who reported that ^{18}F-FDG PET/CT had a higher detection rate for cervical nodal metastases than did ^{68}Ga-FAPI PET/CT, if the metastatic nodes were smaller than 0.7 cm; smaller nodes resulted in weaker FAP expression and delayed conversion of normal fibroblasts to cancer-associated fibroblasts. However, ^{68}Ga-FAPI-46 may have higher tumor specificity than ^{18}F-FDG, potentially resulting in fewer instances of false-positive uptake in inflamed or otherwise reactive lymph nodes. Differences in detection of avid nodes will require further verification. Our findings were discordant with those of Chen et al. (5), who observed higher sensitivity and lower specificity for nodal metastatic detection by ^{68}Ga-FAPI-04 than by ^{18}F-FDG PET/CT. However, Chen et al. compared ^{68}Ga-FAPI with ^{18}F-FDG PET/CT in various types of cancer, with only 6 HNSCC patients. In our study, ^{68}Ga-FAPI-46 and ^{18}F-FDG PET/CT showed consistency for detection of distant metastases in most cases. However, we

TABLE 6
Semiquantitative Comparisons Between ^{18}F-FDG and ^{68}Ga-FAPI-46 PET/CT for Nodal Metastasis

Site	Median size (cm)	No. of detected nodes		SUV$_{max}$		P
		^{18}F-FDG	^{68}Ga-FAPI-46	^{18}F-FDG	^{68}Ga-FAPI-46	
Neck	1.3	85	56	13.67 ± 7.38	16.91 ± 9.35	0.08
Supraclavicular	0.8	5	4	9.97 ± 3.47	7.16 ± 2.01	
Mediastinal	0.8	30	22	9.21 ± 4.22	8.64 ± 4.54	
Axillary	1.1	3	3	18.64*	10.98*	
Intraabdominal	0.9	5	9	15.83 ± 7.02	31.84 ± 9.00	
All	1.1	128	94	12.55 ± 6.68	15.04 ± 10.25	

*No SD because the SUV$_{max}$ was derived from 1 patient's data.
P value is for SUV$_{max}$. SUV$_{max}$ is mean ± SD.

observed detection differences in 2 bone lesions that showed ^{68}Ga-FAPI-46 avidity but no ^{18}F-FDG uptake. Chen et al. reported a false-positive ^{68}Ga-FAPI–avid bone lesion because of myelofibrosis, which was not observed with ^{18}F-FDG. When histopathologic confirmation is not practical, multimodal imaging is required to obtain morphologic details on metastasis.

Compared with ^{18}F-FDG PET/CT, ^{68}Ga-FAPI-46 PET/CT showed higher contrast images with lower physiologic background in the brain, salivary glands, and Waldeyer ring. However, we found no significant differences between the 2 tracers for SUV_{max}, SUV_{mean}, T/B, or total lesion glycolysis versus total lesion FAP expression in the primary tumors. No significant differences in these semiquantitative parameters were observed between the tracers for nodal and distant metastases. Although there may be some variation in methods of SUV measurement, our results were consistent with those of Ballal et al. (*11*), who demonstrated that patients with head and neck cancer had comparably high uptake of ^{68}Ga-DOTA.squaramide-FAPI and ^{18}F-FDG. Our findings did not agree with those of Pang et al. (*12*), who observed higher uptake of ^{68}Ga-FAPI than of ^{18}F-FDG in primary and metastatic lesions of patients with gastric, duodenal, and colorectal cancers. This difference may be explained by differences in glucose metabolism among various tumor cell types. Pang et al. studied patients with adenocarcinoma or signet-ring cell carcinoma. More than 50% of their subjects were gastric cancer patients who showed low-to-moderate ^{18}F-FDG avidity, whereas our study recruited HNSCC patients, who usually demonstrate high ^{18}F-FDG uptake.

Interestingly, we observed a significantly higher FTV than MTV for the primary HNSCC tumor. Syed et al. (*6*) used ^{68}Ga-FAPI PET/CT to contour head and neck cancer and found that ^{68}Ga-FAPI–based gross tumor volume was significantly different from CT-based gross tumor volume. When ^{68}Ga-FAPI– and CT-based gross tumor volumes were merged using SUV_{max} thresholds of 3-fold (20%–25% SUV_{max}) and 5-fold (40%–50% SUV_{max}), the derived tumor volumes were significantly larger than CT-based volumes. We suggest that ^{68}Ga-FAPI-46–derived FTV may be an important semiquantitative parameter for HNSCC, but this possibility will require further standardization and validation.

The sensitivity, specificity, positive predictive value, negative predictive value, and accuracy of both tracers were 100%, 50%, 94.1%, 100%, and 94.4%, respectively. The 8 patients with negative ^{68}Ga-FAPI-46 and ^{18}F-FDG PET/CT findings had no histopathologic confirmation, resulting in low true-negative results and poor specificity in our study.

Our study was limited by the lack of histopathologic confirmation. Use of a fixed 40% threshold of SUV_{max} was dependent on the signal-to-noise ratio, T/B, and tumor size. An adaptive threshold–based method or taking the background into consideration may be more suitable for tumor delineation. A precise definition of FTV is needed for further study. Although there were some limitations in our study, the diagnostic performance of ^{68}Ga-FAPI-46 PET/CT agreed well with that of standard ^{18}F-FDG PET/CT molecular imaging.

CONCLUSION

^{68}Ga-FAPI-46 PET/CT has good concordance with, and comparable diagnostic performance to, ^{18}F-FDG PET/CT for initial staging and recurrence detection in HNSCC patients. Most semiquantitative parameters were comparable between the 2 tracers. However, the ^{68}Ga-FAPI-46–derived FTV was higher than the MTV of ^{18}F-FDG.

Therefore, FTV may be a potential semiquantitative parameter for tumor volume of primary HNSCC, but further standardization and validation are required.

KEY POINTS

QUESTION: Does ^{68}Ga-FAPI-46 PET/CT compare favorably with ^{18}F-FDG PET/CT in HNSCC patients?

PERTINENT FINDINGS: ^{68}Ga-FAPI-46 PET/CT was 83.3% and 96.4% concordant with ^{18}F-FDG PET/CT for initial staging and recurrence detection, respectively. The diagnostic accuracy of ^{68}Ga-FAPI-46 PET/CT was equivalent to that of ^{18}F-FDG PET/CT. ^{68}Ga-FAPI-46–derived FTV was higher than MTV assessed by ^{18}F-FDG, but the other semiquantitative parameters were comparable.

IMPLICATIONS FOR PATIENT CARE: ^{68}Ga-FAPI-46 PET/CT shows comparable diagnostic performance to ^{18}F-FDG PET/CT in detecting primary and metastatic HNSCC.

REFERENCES

1. Ferlay J, Colombet M, Soerjomataram I, et al. Estimating the global cancer incidence and mortality in 2018: GLOBOCAN sources and methods. *Int J Cancer.* 2019;144:1941–1953.
2. Hentschel M, Appold S, Schreiber A, et al. Serial FDG-PET on patients with head and neck cancer: implications for radiation therapy. *Int J Radiat Biol.* 2009;85:796–804.
3. Johnson DE, Burtness B, Leemans CR, Lui VWY, Bauman JE, Grandis JR. Head and neck squamous cell carcinoma. *Nat Rev Dis Primers.* 2020;6:92.
4. Kratochwil C, Flechsig P, Lindner T, et al. ^{68}Ga-FAPI PET/CT: tracer uptake in 28 different kinds of cancer. *J Nucl Med.* 2019;60:801–805.
5. Chen H, Pang Y, Wu J, et al. Comparison of [^{68}Ga]Ga-DOTA-FAPI-04 and [^{18}F]FDG PET/CT for the diagnosis of primary and metastatic lesions in patients with various types of cancer. *Eur J Nucl Med Mol Imaging.* 2020;47:1820–1832.
6. Syed M, Flechsig P, Liermann J, et al. Fibroblast activation protein inhibitor (FAPI) PET for diagnostics and advanced targeted radiotherapy in head and neck cancers. *Eur J Nucl Med Mol Imaging.* 2020;47:2836–2845.
7. Lindner T, Loktev A, Altmann A, et al. Development of quinoline-based theranostic ligands for the targeting of fibroblast activation protein. *J Nucl Med.* 2018;59:1415–1422.
8. Loktev A, Lindner T, Mier W, et al. A tumor-imaging method targeting cancer-associated fibroblasts. *J Nucl Med.* 2018;59:1423–1429.
9. Lydiatt WM, Patel SG, O'Sullivan B, et al. Head and neck cancers: major changes in the American Joint Committee on Cancer eighth edition cancer staging manual. *CA Cancer J Clin.* 2017;67:122–137.
10. Serfling S, Zhi Y, Schirbel A, et al. Improved cancer detection in Waldeyer's tonsillar ring by ^{68}Ga-FAPI PET/CT imaging. *Eur J Nucl Med Mol Imaging.* 2021;48:1178–1187.
11. Ballal S, Yadav MP, Moon ES, et al. Biodistribution, pharmacokinetics, dosimetry of [^{68}Ga]Ga-DOTA.SA.FAPi, and the head-to-head comparison with [^{18}F]F-FDG PET/CT in patients with various cancers. *Eur J Nucl Med Mol Imaging.* 2021;48:1915–1931.
12. Pang Y, Zhao L, Luo Z, et al. Comparison of ^{68}Ga-FAPI and ^{18}F-FDG uptake in gastric, duodenal, and colorectal cancers. *Radiology.* 2021;298:393–402.

Fluorescent Molecular Imaging Can Improve Intraoperative Sentinel Margin Detection in Oral Squamous Cell Carcinoma

Giri Krishnan[1,2], Nynke S. van den Berg[1], Naoki Nishio[1,3], Shrey Kapoor[1], Jaqueline Pei[1], Laura Freeman[1], Yu-Jin Lee[1], Quan Zhou[1], Stan van Keulen[1], Shayan Farkurnejad[1], James Condon[4], Fred M. Baik[1], Brock A. Martin[5], and Eben L. Rosenthal[1]

[1]Department of Otolaryngology–Head and Neck Surgery, Stanford University School of Medicine, Stanford, California; [2]Department of Otolaryngology, Head and Neck Surgery, The University of Adelaide, Adelaide, SA, Australia; [3]Department of Otorhinolaryngology, Nagoya University Graduate School of Medicine, Nagoya, Aichi, Japan; [4]Department of Public Health, School of Medicine, The University of Adelaide, Adelaide, SA, Australia; and [5]Department of Pathology, Stanford University School of Medicine, Stanford, California

In head and neck cancer, a major limitation of current intraoperative margin analysis is the ability to detect areas most likely to be positive based on specimen palpation, especially for larger specimens where sampling error limits detection of positive margins. This study aims to prospectively examine the clinical value of fluorescent molecular imaging to accurately identify "the sentinel margin," the point on a specimen at which the tumor lies closest to the resected edge in real-time during frozen section analysis. **Methods:** Eighteen patients with oral squamous cell carcinoma were enrolled into a prospective clinical trial and infused intravenously with 50 mg of panitumumab-IRDye 800CW 1–5 d before surgery. Resected specimens were imaged in a closed-field near-infrared optical imaging system in near real-time, and custom-designed software was used to identify locations of highest fluorescence on deep and peripheral margins. The surgeon identified the sentinel margin masked to optical specimen mapping, and then the regions of highest fluorescence were identified and marked for frozen analysis. Final pathology based on specimen reconstruction was used as reference standard. **Results:** Resected specimens were imaged in the operating room, and fluorescence had a higher interobserver agreement with pathology (Cohen κ value 0.96) than the surgeon (Cohen κ value of 0.82) for the location of the closest margin. Plotting margin distance at the predicted sentinel margin location of each observer versus the actual closest margin distance at pathology demonstrated best correlation between fluorescence and pathology ($R^2 = 0.98$) with surgeon ($R^2 = 0.75$). **Conclusion:** Fluorescence imaging can improve identification of the sentinel margin in head and neck cancer resections, holding promise for rapid identification of positive margins and improved oncologic outcomes.

Key Words: head and neck cancer; oral squamous cell carcinoma; tumor margins; fluorescent image-guided surgery; surgical oncology

In head and neck squamous cell carcinoma (HNSCC), surgery requires balancing complete tumor clearance with conservation of uninvolved tissue to preserve airway, voice, and swallowing. Achieving adequate margins can be challenging (*1*) and it is established that positive margins are associated with local recurrence and decreased overall survival. Even with advances in operative techniques and technology, positive margin rates have remained unchanged over the past 30 y (*2,3*).

Assessment of tumor specimens to identify positive margins after removal allows surgeons to resect further tissue from the wound bed is required to achieve adequate tumor clearance. This involves visual inspection and palpation of the specimen, with sampling of areas of concern from the specimen or wound bed for intraoperative frozen section analysis (FSA) (*4*). This process is inconsistent, surgeon-dependent, and complicated by sampling error in larger specimens.

Our group has previously demonstrated that ex vivo fluorescent imaging can identify the point on a specimen surface at which the tumor comes closest to the resection edge—the sentinel margin (*5,6*). The aim of the present study was to evaluate the accuracy and clinical value of fluorescent sentinel margin identification when compared prospectively to current clinical practice. We hypothesized that an objective, focused assessment of a specimen using optical imaging might reduce false-negatives during intraoperative margin assessment, maintain orientation of sampled areas on the specimen to the wound bed, and streamline the margin assessment process.

MATERIALS AND METHODS

Clinical Trial Design

Between June 2018 and December 2019, patients with biopsy-proven primary or recurrent oral squamous cell carcinoma scheduled for curative surgery were enrolled into a prospective single-center, nonrandomized, clinical trial evaluating a fluorescence molecular imaging agent called panitumumab-IRDye800CW. The institutional review board of Stanford University approved this study, and all subjects signed a written informed consent form. The trial was approved by the Food and Drug Administration (FDA) and registered with ClinicalTrials.gov (NCT03733210; NCT02415881; NCT03405142). This study was performed in accordance with the Helsinki Declaration of 1975 and its amendments, FDA's International Conference on Harmonistaion-Good Clinical Practice (ICH-GCP) guidelines and the laws and regulations of the United States.

Study Workflow

Enrolled patients were infused intravenously with 50 mg of panitumumab-IRDye800CW 1–5 d before surgery (*7*). Dosing, timing, and

safety information on panitumumab-IRDye800CW is provided in the supplemental materials (supplemental materials are available at http://jnm.snmjournals.org) (8–17).

The study workflow is outlined in Figure 1. In the operating room, primary tumor specimens, as well as sampled margins for FSA, were imaged ex vivo on the back table immediately after removal from the patient in a closed-field near-infrared optical imaging system (IGP-ELVIS, LICOR Biosciences, Inc.) (18). All tumor resections were 3-dimensional and were therefore repositioned within the IGP-ELVIS to capture each surface in a 2-dimensional plane. Imaged surfaces were denoted mucosal if they primarily captured the mucosal aspect of the resection (Fig. 1A). All other surfaces were denoted deep (Fig. 1B). Only imaged surfaces that required pathologic evaluation by the surgical team were included in the study analysis.

Acquired images were exported as TIFF files from the optical imaging system to a laptop for near-real-time fluorescent analysis of the sentinel margin using ImageJ software (version 1.50i; National Institutes of Health) as previously described (5,6).

To compare our fluorescent analysis against current clinical practice, the board-certified surgeon, masked to fluorescence, was asked to identify the point at which the tumor came closest to the specimen edge ex vivo. This was often done at pathology in collaboration with the pathologist. Their specimen orientation and sentinel margin demarcation was photo- and video-documented. This photo was then used to compare the point of highest fluorescent signal on that surface by registering the 2 images against each other. A margin of error equivalent

to 1 bread loaf at pathology was used when comparing each prediction against final pathology as gold standard. Individual bread loafs are approximately 5 mm thick (19); therefore, if the surgeon or fluorescence is within 5 mm of the true sentinel margin, this would fall within the realm of "close enough" to ink, activating the pathologist select radial margins in the area of concern. Where there was clinical concern that the specimen had close or positive margins, FSA was performed on the presumptive sentinel margins demarcated by the surgeon. These frozen sections were processed and analyzed as standard of care, and the results were reported to the operating team for intraoperative action as appropriate. Margins were defined in this study as clear if ≥5 mm from invasive tumor, close if <5 mm from invasive tumor, and positive if invasive carcinoma or carcinoma in situ was present at the specimen edge (20,21).

Primary tumor specimens underwent routine pathologic processing and assessment, and all tissue cassettes were reimaged in the IGP-ELVIS before paraffin-embedding. A standard synoptic report was generated by a board-certified pathologist, including identification of the final closest margin location and distance on mucosal and deep surfaces as seen on hematoxylin and eosin slides, serving as gold standard to compare the sentinel margin predictions of the surgeon and fluorescence. Epithelial growth factor receptor (EGFR) immunohistochemistry and expression quantification of selected slides were performed as previously described (22).

To map all predicted sentinel margin locations against final pathology, locations were recorded categorically according to which pathology
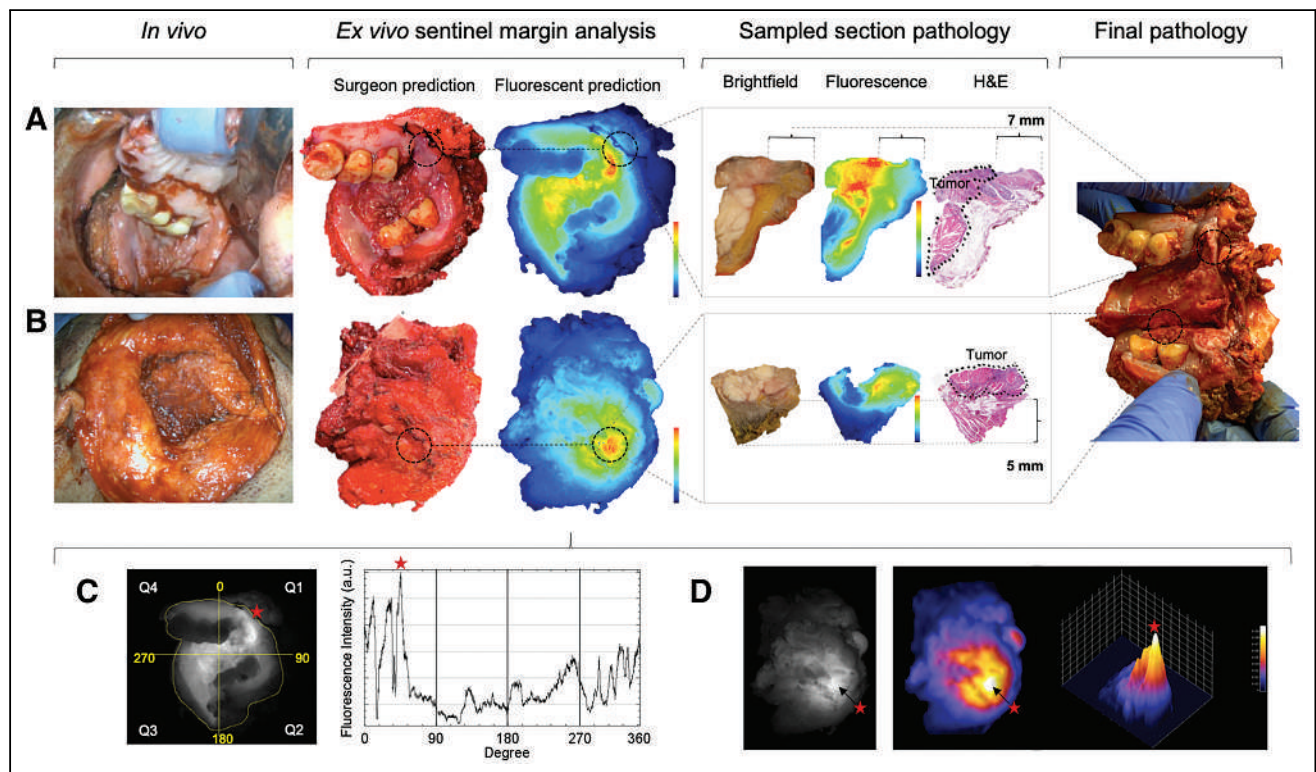
FIGURE 1. Study workflow is demonstrated in representative patient 18 with right-sided retromolar trigone squamous cell carcinoma. Patient was infused intravenously with 50 mg of panitumumab-IRDye800CW 3 d before surgery. From left to right, workflow shows lesion in vivo and then ex vivo, examining mucosal (A) and deep surfaces of resection (B). On both surfaces, surgeon and fluorescence were in agreement as to location of sentinel margin. Sampled tissue from these locations underwent closed-field fluorescent imaging and then hematoxylin and eosin (H&E) staining to evaluate margin distance. (C) Mucosal surface fluorescent sentinel margin analysis in this patient as demonstrated by a mask manually fitted around periphery of specimen within 1 mm of resection edge followed by graph showing the raw fluorescence data of each point along mask in 8-bit gray scale format enabling isolation of area of highest fluorescence on periphery (represented by red star). (D) Deep surface fluorescent sentinel margin analysis as demonstrated using 3-dimensional signal-mapping tool to scale and isolate area of highest fluorescence intensity (represented by red star and arrow).

TABLE 1
Summary of Interobserver Prediction of Sentinel Margin Location and Corresponding Margin Distance Versus Actual Closest Margin Location and Distance at Pathology

Specimen #	Tumor site	pT	Resection	Surface	Predicted sentinel margin location (pathology cassette)			Distance at predicted sentinel margin (mm)		
					Surgeon	Flu	Pathology	Surgeon	Flu	Pathology
1	Lateral tongue	T3	Partial glossectomy	Deep	C11	C11	C11	0	0	0
				Mucosal	C4	C11	C11	10	2	2
2	Lateral tongue	T3	Partial glossectomy	Deep	C8	C14	C14	2	1	1
3	Lateral tongue	T4a	Partial glossectomy	Deep	A1	A1	A1	3	3	3
4	Lateral tongue	T4a	Hemi glossectomy	Deep	FSD 1	FSD 1	FSD 1	2	2	2
				Mucosal	D6	D6	D6	11	11	11
5	Hard palate	T4a	Maxillectomy	Deep	FSB	FSB	FSB	1	1	1
				Mucosal	FSD	FSD	FSD	7	7	7
6	Retromolar trigone	T4	Maxillectomy	Deep	FSA	FSA	FSA	0	0	0
				Mucosal	FSD	FSD	FSD	5	5	5
7	Retromolar trigone	T3	RMT composite resection	Mucosal	FSC	FSC	FSC	0	0	0
				Mucosal	C2	C2	C2	4	4	4
8	Lateral tongue	T2	Partial glossectomy	Mucosal	A5	A5	A8	3	3	1
9	Lateral tongue	T2	Partial glossectomy	Mucosal	A6	A6	A6	5	5	5
10	Retromolar trigone	T4a	RMT composite resection	Deep	C4	C4	C4	6	6	6
				Mucosal	FSB3	FSB3	FSB3	1	1	1
11	Lateral tongue	T2	Partial glossectomy	Mucosal	FSB2	FSB2	FSB2	1	1	1
				Deep	FSB1	FSB1	FSB1	0	0	0
12	Lateral tongue	T4a	Hemi glossectomy	Deep	B1	B1	B1	1	1	1
				Mucosal	FSC1	FSC1	FSC1	0	0	0
13	Retromolar trigone	T4a	Mandibulectomy	Mucosal	FSC2	FSC2	FSC2	5	5	5
14	Retromolar trigone	T4a	RMT composite resection	Mucosal	O9	O20	O20	8	4	4
				Mucosal	FSI	FSI	FSI	10	10	10
15	Buccal	T2	WLE	Deep	FSB	B10	B10	1	1	1
16	Alveolar ridge	T2	Mandibulectomy	Mucosal	D8	D8	D8	4	4	4
17	Buccal	T2	WLE	Mucosal	FSA	FSA	FSA	2	2	2
18	Retromolar trigone	T3	RMT composite resection	Mucosal	B11	B11	B11	7	7	7
				Deep	B16	B16	B16	5	5	5

pT = pathologic T stage; Flu = fluorescence; RMT = retromolar trigone; WLE = wide local excision.

TABLE 2
Accuracy of Observer at Identifying Final Closest Margin Location

	Interobserver agreement with final pathology (Cohen κ)	Accuracy (%)	95% CI	Error rate (%)	P
Surgeon	0.82	0.64	(0.45, 0.83)	17.9	<0.001
Fluorescence	0.96	0.86	(0.72, 1.00)	3.6	<0.001

cassette they belonged to. Where 2 sentinel margin predictions were located on separate areas of a same cassette, they were differentiated with reference to their orientation on the cassette. A ruler was used to measure distance in millimeters from tumor edge (marked by the pathologist) to the specimen edge at each predicted sentinel margin on hematoxylin and eosin slides. Mean fluorescence intensity, defined as total counts per pixel area, divided by pixel area, was calculated for each acquired image of tissue taken intraoperatively for FSA using ImageStudio software (LI-COR Biosciences). Mean fluorescence intensity data were correlated to final tumor status (positive or negative).

Statistical Analysis

SciPy (version 1.4.1; open source), Scikit-learn (version 0.22.2; open source), and GraphPad Prism (version 8.0c; GraphPad Software) were used for statistical analysis. A Cohen κ statistic was used to assess the strength of agreement of sentinel margin location of the 2 observers (surgeon and fluorescence) independently against the gold standard (final pathology). The accuracy and error rate of sentinel margin location of each observer were calculated using standard statistics. The 95% CI of each observer's accuracy was calculated using a t distribution. Accuracy P values were calculated based on the number of cassettes for each specimen, with respect to random choices. Pearson and Spearman correlation coefficients were calculated for margin distances at predicted sentinel margin locations of each observer against the actual closest margin distance at final pathology. A 2-sided P value of 0.05 or less was considered statistically significant.

RESULTS

Observer Agreement and Accuracy in Sentinel Margin Prediction

Primary tumor specimens from 18 patients were included in this study, with 28 specimen surfaces imaged and analyzed. The predicted sentinel margin location and corresponding measured margin distances at these locations per observer compared with final pathology are summarized in Table 1. Overall, areas of highest fluorescence strongly correlated final pathology (Cohen κ, 0.96).
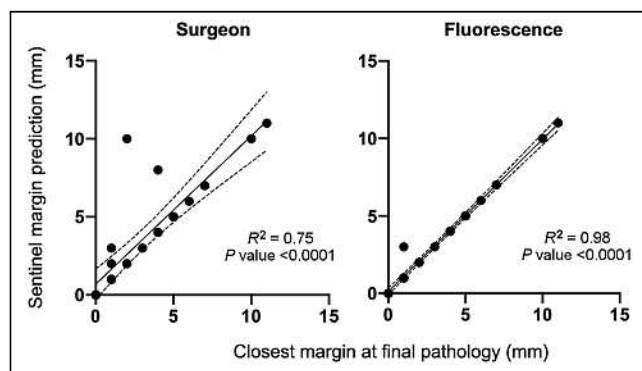
FIGURE 2. Correlation between distance at predicted sentinel margin by observer with distance of closest margin on final pathology.

The surgeon had a relatively lower correlation with final pathology (Cohen κ, 0.81).

The accuracy of fluorescence intensity to identify the true sentinel margin was 96.4% (95% CI, 89.1–100; $P < 0.001$) compared with the surgeon at 82.1% (95% CI, 67.0–97.3; $P < 0.001$) as summarized in Table 2. Plotting margin distance at the predicted sentinel margin of each observer versus the actual closest margin distance at final pathology demonstrates better correlation between fluorescence and final pathology ($R^2 = 0.98$; 95% CI, 0.93–1.00; $P < 0.001$) compared with the surgeon and final pathology ($R^2 = 0.75$; 95% CI, 0.73–1.17; $P < 0.001$) (Fig. 2).

Clinical Value of Fluorescence in Sentinel Margin Analysis

The surgeon's prediction of the sentinel margin disagreed with final pathology in 4 of 28 cases compared with 1 of 28 cases with fluorescence. In the 1 instance in which fluorescence disagreed with final pathology, the fluorescent-predicted sentinel margin location was in concordance with the surgeon's prediction. This agreement equates to a clinically significant improvement in intraoperative frozen section sampling in 3 of 28 (10.7%) surfaces analyzed with fluorescence over current standard of care.

Closer examination of the 1 case in which there was tumor close to the mucosal surface that was not identified by fluorescence as being the area of highest signal revealed that this tumor was in fact a small secondary focus (Fig. 3). Immunohistochemistry staining and EGFR quantification of regions in which each focus of tumor came closest to the peripheral margin demonstrated EGFR expression at both points, but with higher EGFR expression (81.2%) where there was macroscopically visible disease on the main tumor focus versus (43.2%) on the smaller secondary focus (Fig. 4).

In 3 cases in which the fluorescent sentinel margin prediction outperformed conventional palpation by the surgeon, the final margin was close (<5 mm) in all cases, as summarized in Figure 5.

DISCUSSION

This prospective study compares fluorescence with current intraoperative margin assessment, evaluated against final pathology as the gold standard. It builds on previous retrospective studies in which we developed the concept of sentinel margin detection using relative fluorescence intensities and showed that margin distance inversely correlates with areas of highest fluorescent intensity on the deep and mucosal surfaces (5,6). These studies laid the foundation for the current prospective trial but were limited by their retrospective nature, which meant that only specimens for which measurable bread loafs coincided with the intensity peaks on the deep surface, or areas of highest fluorescence intensity on the peripheral surface, could be included for analysis. Tissue is relatively homogeneous, thereby disrupting optical properties and enabling this technique to work consistently across specimens. Furthermore, although EGFR is heterogeneous across the different patient cancer specimens, it is high enough to allow fluorescence to penetrate
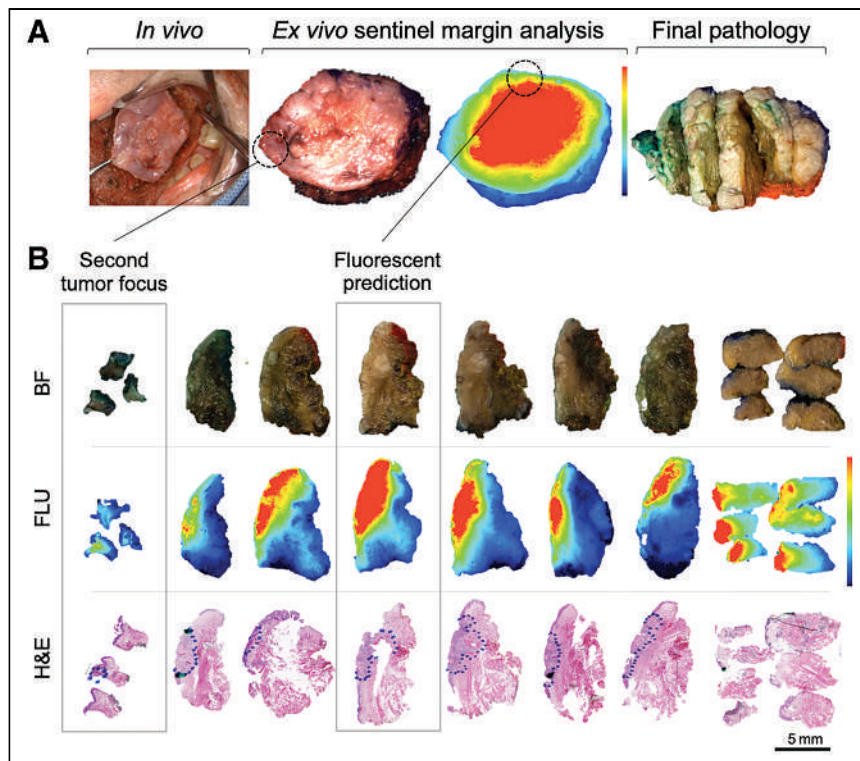
FIGURE 3. (A) Specimen evaluation workflow demonstrating partial glossectomy resection in situ, ex vivo specimen imaged in brightfield and closed-field fluorescence, followed by a depiction of specimen bread-loafed at final pathology. (B) Main centrally located tumor came closest to specimen edge superiorly, at a point accurately identified by both fluorescence and surgeon to be closest margin for this tumor (3 mm). Smaller separate focus of tumor was not macroscopically visible and registered as third highest region of fluorescent signal on peripheral margin. Blue dots outline tumor boundaries on mucosal surface. BF = brightfield; FLU = fluorescence; H&E = hematoxylin and eosin.

through the tissue margin. This study, unlike previous research in this technique, is a prospective comparison to the surgeon.

This study demonstrates that ex vivo fluorescent molecular imaging of head and neck resections can improve objective detection of tumor that comes closest to the specimen edge when compared with standard of care, which was exemplified in 11% of cases in which

fluorescence-based sentinel margin assessment outperformed standard-of-care pathologic assessment by the surgeon, suggesting this approach has potential to improve positive margin rate outcomes. Accurate isolation of the sentinel margin in the operating room within minutes has several benefits. Of highest clinical priority, it holds promise to minimize false-negative intraoperative margin assessment (23). From a resource-use standpoint, reduced tissue sampling and reduced FSA streamline operative workflow and decrease pathology demand (24,25). By identifying the sentinel margin in the operating room immediately after resection, there is promise for improved in vivo and ex vivo orientation of the specimen to the wound bed, which could increase precision during wound bed reresection, although this was not assessed here and requires focused evaluation in future studies (26,27). Anecdotally in this study, fluorescence imaging followed by sentinel margin analysis took approximately 5–10 min to complete (depending on the complexity of the specimen and how many surfaces were being imaged) whereas frozen sectioning typically takes 20–30 min per FSA. Hence, additional benefit can be found in providing directional information to the pathologist for areas to be assessed by FSA.

All 18 HNSCC specimens in this study originated from the oral cavity, but resection units varied, including glossectomies, maxillectomies, mandibulectomies, and composite resections. Our findings demonstrate that fluorescence molecular imaging of complex 3-dimensional resections involving soft tissue and bone is feasible and this is a significant strength of this study, as current ex vivo margin analysis in these complex specimens is particularly difficult (28). It is in these resections that there is a short window of opportunity for surgeon orientation of specimen to wound bed and where communication of margin locations between surgeon and pathologist are prone to error (29).

Before undertaking this study, we hypothesized that specimen positioning and intratumoral heterogeneity of EGFR could impact accuracy of fluorescent sentinel margin identification. In this study, we identified a case in which a smaller tumor satellite with both an associated lower EGFR expression and a lower fluorescence intensity resulted in a false-negative outcome because it lay closer to the resection edge than the main tumor focus. On the basis of this finding, and in line with the results of our previous studies, we would advise that at least 2–3 regions of highest fluorescent signal on a specimen surface be sampled (6). Sampling the 3 areas of highest fluorescence on the peripheral margin would have picked up this separate focus

FIGURE 4. (A) Magnified view of 2 bread loafs demonstrating margin distance of 3 mm, where surgeon and fluorescence predicted sentinel margin on main tumor, compared with margin distance of 1 mm where a sperate secondary focus of tumor came close to anterior specimen edge. (B) Slides confirming presence of squamous cell carcinoma and EGFR expression at point on each tumor focus closest to margin edge. In main tumor, EGFR expression was quantified at 81.2% compared with 43.2% at secondary focus. +ve = positive; H&E = hematoxylin and eosin.

FIGURE 5. Cases in which fluorescence sentinel margin identification demonstrated improved identification of true closest margin when compared with conventional analysis technique by surgeon. (A) Patient 1 with a pT3 right lateral tongue squamous cell carcinoma infused 2 d before surgery. (B) Patient 2 with pT4a right lateral tongue squamous cell carcinoma infused 1 d before surgery. (C) Patient 13 with a pT4a right retromolar squamous cell carcinoma infused 2 d before surgery. BF = brightfield; Flu = fluorescence; H&E = hematoxylin and eosin.

of microscopic disease that was not visually detectable or palpable, consistent with our previous studies (7).

In 1 of the 3 cases in which fluorescence was superior to surgeon sentinel margin prediction, the standard approach still identified a close margin of 2 mm. This highlights an important clinically relevant point, that there may be more than 1 location on a specimen surface, and multiple surfaces on 1 specimen, in which the tumor comes close to the resection edge. It is precisely in these cases where fluorescence can be of significant added value, as reresection from the wound bed at multiple locations may be necessary and without fluorescence guidance may be missed. The specimen imaging techniques are agnostic to the fluorescent agent used and may thus also apply beyond paniatumumab-IRDye800CW (30–32). It is worth mentioning that nonfluorescent optical dyes have been investigated for margin analysis with promising results (33–35).

There are study limitations worth highlighting. First, for a specimen surface whereby the surgeon or pathologist was not concerned about having close margins, fluorescence analysis and FSA were not performed in order to reduce time and allow focus on clinically relevant margin assessment, consistent with the philosophy that the margin assessment strategy should be used for clinical guidance only. Moreover, we did not examine margin distances at high fluorescent areas on specimen surfaces in which there was no clinical suspicion for close margins. As such, we cannot comment on the accuracy of fluorescent imaging at identifying the sentinel margin on all surfaces of all specimens resected in this study. Future trials could circumnavigate the issue of intraoperative delay, by prospectively collecting tissue samples at pathology of the identified sentinel margin location on all surfaces of all specimens (based on both fluorescent analysis and surgeon prediction) and then retrospectively analyze the margin distances on these

tissue samples later. Second, fluorescence margin analysis in this study was performed by 1 person. Although this kept variability in fluorescent margin analysis and interpretation constant, a learning curve for performing the analysis and discrepancies in analysis between users was not examined. With increasing adoption of artificial intelligence technology in surgery, it is foreseeable that future use of this strategy may move toward computer-automated techniques.

CONCLUSION

Image-guided analysis of specimens can improve identification of the true closest margin in 3-dimensional resections with the potential to reduce positive margin rates. Results of the current study determined a clinically significant value of fluorescence-based margin assessment in 11% of patients. A study examining the value of this technique in improving communication of margin location between surgeon and pathologist as well as evaluating the efficacy of surgery-guided reresection should follow.

DISCLOSURE

KEY POINTS

QUESTION: How does ex vivo fluorescent molecular imaging of head and neck cancer resections compare with current standard of care in identifying the true closest margin?

PERTINENT FINDINGS: In this prospective observational clinical trial including 18 consecutive patients who underwent head and neck cancer surgical resections, fluorescence-based sentinel margin assessment outperformed the surgeon at identifying the true closest margin at final pathology in 11% of cases. Fluorescence had a higher interobserver agreement with final pathology (Cohen κ, 0.96) than the surgeon (Cohen κ, 0.82), and plotting the margin distance at the predicted sentinel margin location of each observer versus the actual closest margin distance at final pathology demonstrated best correlation between fluorescence and final pathology ($R^2 = 0.98$).

IMPLICATIONS FOR PATIENT CARE: Broad translation of an ex vivo fluorescent molecular image–based approach to sentinel margin identification could improve accuracy of intraoperative margin sampling, with overall potential to reduce positive margin rates in surgery.

REFERENCES

1. Luryi AL, Chen MM, Mehra S, Roman SA, Sosa JA, Judson BL. Positive surgical margins in early stage oral cavity cancer: an analysis of 20,602 cases. *Otolaryngol Head Neck Surg.* 2014;151:984–990.
2. Smits RW, Koljenović S, Hardillo JA, et al. Resection margins in oral cancer surgery: Room for improvement. *Head Neck.* 2016;38(suppl 1):E2197–E2203.
3. Orosco RK, Tapia VJ, Califano JA, et al. Positive surgical margins in the 10 most common solid cancers. *Sci Rep.* 2018;8:5686.
4. Kain JJ, Birkeland AC, Udayakumar N, et al. Surgical margins in oral cavity squamous cell carcinoma: current practices and future directions. *Laryngoscope.* 2020;130:128–138.
5. van Keulen S, Nishio N, Birkeland A, et al. The sentinel margin: intraoperative ex vivo specimen mapping using relative fluorescence intensity. *Clin Cancer Res.* 2019;25:4656–4662.
6. Fakurnejad S, Krishnan G, van Keulen S, et al. Intraoperative molecular imaging for ex vivo assessment of peripheral margins in oral squamous cell carcinoma. *Front Oncol.* 2020;9:1476.
7. Nishio N, van den Berg NS, van Keulen S, et al. Optimal dosing strategy for fluorescence-guided surgery with panitumumab-irdye800cw in head and neck cancer. *Mol Imaging Biol.* 2020;22:156–164.
8. Giusti RM, Shastri KA, Cohen MH, Keegan P, Pazdur R. FDA drug approval summary: panitumumab (Vectibix). *Oncologist.* 2007;12:577–583.
9. Adams KE, Ke S, Kwon S, et al. Comparison of visible and near-infrared wavelength-excitable fluorescent dyes for molecular imaging of cancer. *J Biomed Opt.* 2007;12:024017.
10. Bhattacharyya S, Patel N, Wei L, et al. Synthesis and biological evaluation of panitumumab-IRDye800 conjugate as a fluorescence imaging probe for EGFR-expressing cancers. *Medchemcomm.* 2014;5:1337–1346.
11. Kalyankrishna S, Grandis JR. Epidermal growth factor receptor biology in head and neck cancer. *J Clin Oncol.* 2006;24:2666–2672.
12. Marshall MV, Draney D, Sevick-Muraca EM, Olive DM. Single-dose intravenous toxicity study of IRDye 800CW in Sprague-Dawley rats. *Mol Imaging Biol.* 2010;12:583–594.
13. Ter Weele EJ, Terwisscha van Scheltinga AG, Linssen MD, et al. Development, preclinical safety, formulation, and stability of clinical grade bevacizumab-800CW, a new near infrared fluorescent imaging agent for first in human use. *Eur J Pharm Biopharm.* 2016;104:226–234.
14. Zinn KR, Korb M, Samuel S, et al. IND-directed safety and biodistribution study of intravenously injected cetuximab-IRDye800 in cynomolgus macaques. *Mol Imaging Biol.* 2015;17:49–57.
15. Day KE, Sweeny L, Kulbersh B, Zinn KR, Rosenthal EL. Preclinical comparison of near-infrared-labeled cetuximab and panitumumab for optical imaging of head and neck squamous cell carcinoma. *Mol Imaging Biol.* 2013;15:722–729.
16. Gao RW, Teraphongphom N, de Boer E, et al. Safety of panitumumab-IRDye800CW and cetuximab-IRDye800CW for fluorescence-guided surgical navigation in head and neck cancers. *Theranostics.* 2018;8:2488–2495.
17. Pei J, Juniper G, van den Berg NS, et al. Safety and Stability of Antibody-Dye Conjugate in Optical Molecular Imaging. *Mol Imaging Biol.* 2021;23:109–116.
18. van Keulen S, van den Berg NS, Nishio N, et al. Rapid, non-invasive fluorescence margin assessment: optical specimen mapping in oral squamous cell carcinoma. *Oral Oncol.* 2019;88:58–65.
19. Williams MD. Determining adequate margins in head and neck cancers: practice and continued challenges. *Curr Oncol Rep.* 2016;18:54.
20. Alicandri-Ciufelli M, Bonali M, Piccinini A, et al. Surgical margins in head and neck squamous cell carcinoma: what is 'close'? *Eur Arch Otorhinolaryngol.* 2013;270:2603–2609.
21. Colevas AD, Sue SY, David GP, et al. NCCN guidelines insights: Head and neck cancers, Version 1.2018. *J Natl Compr Canc Netw.* 2018;16:479–490.
22. Zhou Q, van den Berg NS, Rosenthal EL, et al. EGFR-targeted intraoperative fluorescence imaging detects high-grade glioma with panitumumab-IRDye800 in a phase 1 clinical trial. *Theranostics.* 2021;11:7130–7143.
23. Maxwell JH, Thompson LD, Brandwein-Gensler MS, et al. Early oral tongue squamous cell carcinoma: sampling of margins from tumor bed and worse local control. *JAMA Otolaryngol Head Neck Surg.* 2015;141:1104–1110.
24. Kubik MW, Sridharan S, Varvares MA, et al. Intraoperative margin assessment in head and neck cancer: a case of misuse and abuse? *Head Neck Pathol.* 2020;14:291–302.
25. DiNardo LJ, Lin J, Karageorge LS, Powers CN. Accuracy, utility, and cost of frozen section margins in head and neck cancer surgery. *Laryngoscope.* 2000;110:1773–1776.
26. Kerawala CJ, Ong TK. Relocating the site of frozen sections: is there room for improvement? *Head Neck.* 2001;23:230–232.
27. van Lanschot CGF, Mast H, Hardillo JA, et al. Relocation of inadequate resection margins in the wound bed during oral cavity oncological surgery: a feasibility study. *Head Neck.* 2019;41:2159–2166.
28. Lubek JE, Magliocca KR. Evaluation of the bone margin in oral squamous cell carcinoma. *Oral Maxillofac Surg Clin North Am.* 2017;29:281–292.
29. Weinstock YE, Alava I, 3rd, Dierks EJ. Pitfalls in determining head and neck surgical margins. *Oral Maxillofac Surg Clin North Am.* 2014;26:151–162.
30. Mizushima T, Ohnishi S, Shimizu Y, et al. Fluorescent imaging of superficial head and neck squamous cell carcinoma using a γ-glutamyltranspeptidase-activated targeting agent: a pilot study. *BMC Cancer.* 2016;16:411.
31. Pan J, Deng H, Hu S, et al. Real-time surveillance of surgical margins via ICG-based near-infrared fluorescence imaging in patients with OSCC. *World J Surg Oncol.* 2020;18:96.
32. Christensen A, Juhl K, Persson M, et al. uPAR-targeted optical near-infrared (NIR) fluorescence imaging and PET for image-guided surgery in head and neck cancer: proof-of-concept in orthotopic xenograft model. *Oncotarget.* 2017;8:15407–15419.
33. McCaul JA, Cymerman JA, Hislop S, et al. LIHNCS - Lugol's iodine in head and neck cancer surgery: a multicentre, randomised controlled trial assessing the effectiveness of Lugol's iodine to assist excision of moderate dysplasia, severe dysplasia and carcinoma in situ at mucosal resection margins of oral and oropharyngeal squamous cell carcinoma: study protocol for a randomised controlled trial. *Trials.* 2013;14:310.
34. Petruzzi M, Lucchese A, Baldoni E, Grassi FR, Serpico R. Use of Lugol's iodine in oral cancer diagnosis: an overview. *Oral Oncol.* 2010;46:811–813.
35. Algadi HH, Abou-Bakr AA, Jamali OM, Fathy LM. Toluidine blue versus frozen section for assessment of mucosal tumor margins in oral squamous cell carcinoma. *BMC Cancer.* 2020;20:1147.

Prognostic Value of Urokinase-Type Plasminogen Activator Receptor PET/CT in Head and Neck Squamous Cell Carcinomas and Comparison with ^{18}F-FDG PET/CT: A Single-Center Prospective Study

Louise M. Risør[1], Malene M. Clausen[2], Zaza Ujmajuridze[3], Mohammed Farhadi[3], Kim F. Andersen[1], Annika Loft[1], Jeppe Friborg[2], and Andreas Kjaer[1]

[1]Department of Clinical Physiology, Nuclear Medicine, and PET and Cluster for Molecular Imaging, Copenhagen University Hospital–Rigshospitalet, and Department of Biomedical Sciences, University of Copenhagen, Copenhagen, Denmark; [2]Department of Clinical Oncology, Copenhagen University Hospital, Rigshospitalet, Copenhagen, Denmark; and [3]Department of Clinical Oncology, Næstved Hospital, Denmark

The aim of this phase II clinical trial (NCT02965001) was to evaluate the prognostic value of urokinase-type plasminogen activator receptor (uPAR) PET/CT with the novel ligand ^{68}Ga-NOTA-AE105 in head and neck cancer and compare it with ^{18}F-FDG. **Methods:** Patients with head and neck squamous cell carcinoma referred for curatively intended radiotherapy were eligible and prospectively included in this study. ^{68}Ga-uPAR and ^{18}F-FDG PET/CT were performed before initiation of curatively intended radiotherapy, and the SUV_{max} of the primary tumor was measured on both PET/CT studies by 2 independent readers. Relapse-free survival (RFS) and overall survival (OS) were calculated, and optimal cutoffs were established for ^{68}Ga-uPAR and ^{18}F-FDG PET independently and compared using log rank and Kaplan–Meier statistics, as well as univariate and multivariate analysis in a Cox proportional-hazards model. **Results:** In total, 57 patients were included and followed for a median of 33.8 mo (range, 2.30–47.2, mo). The median SUV_{max} of the primary tumors was 2.98 (range, 1.94–5.24) for ^{68}Ga-uPAR and 15.7 (range, 4.24–45.5) for ^{18}F-FDG. The optimal cutoffs for ^{68}Ga-NOTA-AE105 SUV_{max} in the primary tumor were 2.63 for RFS and 2.66 for OS. A high uptake of ^{68}Ga-NOTA-AE105 (SUV_{max} above cutoff) was significantly associated with poor RFS and OS (log-rank $P = 0.012$ and $P = 0.022$). ^{68}Ga-NOTA-AE105 uptake in the primary tumor was significantly associated with poor RFS in univariate analysis (hazard ratio [HR], 8.53 [95% CI, 1.12–64.7]; $P = 0.038$), and borderline-associated with OS (HR, 7.44 [95% CI, 0.98–56.4]; $P = 0.052$). For ^{18}F-FDG PET, the optimal cutoffs were 22.7 for RFS and 22.9 for OS. An ^{18}F-FDG SUV_{max} above the cutoff was significantly associated with reduced RFS (log-rank $P = 0.012$) and OS (log-rank $P = 0.000$). ^{18}F-FDG uptake was significantly associated with reduced RFS (HR, 3.27 [95% CI, 1.237–8.66]; $P = 0.017$) and OS (HR, 7.10 [95% CI, 2.60–19.4]; $P < 0.001$) in univariate analysis. In a multivariate analysis including ^{68}Ga-uPAR SUV_{max}, ^{18}F-FDG SUV_{max}, TNM stage, and p16 status, only ^{68}Ga-uPAR SUV_{max} remained significant (HR, 8.51 [95% CI, 1.08–66.9]; $P = 0.042$) for RFS. For OS, only TNM stage and ^{18}F-FDG remained significant. **Conclusion:** The current trial showed promising results for the use of ^{68}Ga-uPAR PET SUV_{max} in the primary tumor to predict RFS in head and neck squamous cell carcinoma patients referred for curatively intended radiotherapy when compared with ^{18}F-FDG PET, TNM stage, and p16 status. ^{68}Ga-uPAR PET could potentially become valuable for identification of patients suited for deescalation of treatment and risk-stratified follow-up schemes.

Key Words: urokinase-type plasminogen activator receptor; ^{68}Ga-NOTA-AE105; PET/CT; head and neck cancer; prognostication; risk stratification

Traditionally, head and neck squamous cell carcinoma (HNSCC) has been caused by alcohol and tobacco, but in recent years a rising incidence of oropharyngeal cancers has been associated with human papillomavirus (HPV) (1). HPV-positive tumors currently account for 63% of the oropharyngeal cancer in Western Europe and have a significantly favorable prognosis (2,3). HPV-positive and HPV-negative oropharyngeal cancers represent distinct molecular and clinical entities, and new staging guidelines reduce the stage allocation of HPV-positive tumors based on p16 immunohistochemistry as a surrogate marker of HPV-driven carcinogenesis (3,4). However, recent clinical trials investigating deescalating treatment regimens in low-risk HPV-positive oropharyngeal cancer resulted in inferior survival of the deescalating arms (5–8). To date, no reliable method of identifying candidates for deescalating treatment exists, and HPV-positive and -negative oropharyngeal cancers are treated alike (3,9).

TNM stage and HPV are the most important prognostic factors in HNSCC, but besides HPV no prognostic biomarkers are available in clinical practice. Regarding the prognostic value of ^{18}F-FDG, inconsistent results have been published (9–11).

The urokinase-type plasminogen activator receptor (uPAR) promotes cancer cell invasion by degrading the extracellular matrix and facilitates several carcinogenic processes, such as proliferation and migration (12–14). High uPAR expression has been reported in many cancer types, including HNSCC, and has been associated with aggressive disease, distant metastasis, and poor survival (14). uPAR is located on the cell surface and has limited expression in the surrounding tissue (13). Phase I studies using ^{68}Ga- and ^{64}Cu-labeled AE105 radioligands for uPAR PET in patients with different cancer types have supported the theory that uPAR is target-specific and

encouraged research exploring the potential of uPAR PET as a non-invasive theragnostic agent (*15–17*).

The aim of the current phase II clinical prospective study was to investigate the prognostic value of ^{68}Ga-NOTA-AE105 uPAR PET in HNSCC patients and to compare it with ^{18}F-FDG PET.

MATERIALS AND METHODS

Patient Population

Inclusion criteria were patients with a diagnosis of biopsy-verified cancer of the pharynx, larynx, or oral cavity, referred for curatively intended radiotherapy, who understood the given information, were able to give informed consent, and were at least 18 y old.

Exclusion criteria were pregnancy, lactation or breast feeding, an age above 85 y, obesity (body weight above 140 kg), small cancers of the larynx (stage 1A or 1B), an allergy to ^{68}Ga-NOTA-AE105, metastasis on ^{18}F-FDG PET/CT, other previously known cancers, and claustrophobia. Eligible patients were included after giving written informed consent. The diagnosis of HNSCC and p16 status was verified histologically before inclusion. Information on smoking, alcohol, clinical examination, treatment plan, laboratory and histologic results, medical history, and follow-up examinations was collected from patient records. Disease stage was coded according to the eight edition of the Union for International Cancer Control classification.

The study protocol was approved by the Danish Health and Medicine Authority (EudraCT no. 2016-002082-65) and the Ethical Committee of the Capital Region of Denmark (protocol H-16039798). The study was registered at ClinicalTrials.gov (NCT02965001) and was performed in accordance with the recommendations for good clinical practice, including independent monitoring by the good-clinical-practice unit of the capital region of Denmark.

^{68}Ga-uPAR PET/CT Acquisition

According to national guidelines on treatment of HNSCC, radiotherapy is to be initiated within 11 d of the treatment decision, and ^{18}F-FDG PET/CT and ^{68}Ga-uPAR PET/CT were performed within this period, both as a part of the study. Since radiotherapy increases the risk of osteonecrosis following potential tooth extractions, teeth in risk of subsequent extraction are extracted prophylactically. Patients underwent a dental examination and, in the case of tooth extraction, initiation of radiotherapy was postponed until 2 wk after the procedure. In this case, ^{18}F-FDG PET/CT and ^{68}Ga-uPAR PET/CT were scheduled before or at least 4 d after the procedure.

All patients were injected intravenously with approximately 200 MBq (median, 191 MBq; range, 158–209 MBq) of ^{68}Ga-NOTA-AE105 followed by sequential whole-body PET/CT scanning 20 min after injection. Whole-body ^{68}Ga-NOTA-AE105 PET and diagnostic CT with contrast medium (skull base to proximal thigh) were performed simultaneously using an integrated whole-body PET/CT scanner (Biograph mCT, 64-slice; Siemens). The ligand was synthesized as previously described (*15*).

Patients were immobilized in the supine position on a flat scanner couch, with the arms placed in the standard anatomic position, and no fixating facial mask was applied. The CT scan was performed with 120 kV, 170 mAs, and a pitch of 0.8. The PET data were reconstructed with an iterative method using time of flight, point-spread function, and attenuation correction, with 2 iterations, 21 subsets, and a 2-mm gaussian filter.

Image Analysis

Image data from the ^{68}Ga-uPAR PET/CT and ^{18}F-FDG PET/CT studies were analyzed by 2 certified specialists in nuclear medicine. The readers were blinded to the volumes of interest, the results of the other reader, and the patient information. Volumes of interest were visually contoured on the ^{68}Ga-uPAR PET/CT images corresponding to the localization of the primary tumor on the ^{18}F-FDG PET/CT images. Uptake of the ^{68}Ga-uPAR ligand and ^{18}F-FDG in the volumes of interest was parameterized as SUV_{max} on the ^{68}Ga-uPAR PET/CT and ^{18}F-FDG PET/CT images and documented for both tracers before obtaining information on recurrence and survival.

If a patient had 2 synchronous primary HNSCCs, the tumor with the highest SUV_{max} was included in the statistical analysis. The mean SUV_{max} obtained by the 2 independent readers was included in the statistical analysis.

Treatment and Follow-up

All patients received intensity-modulated radiotherapy with or without concomitant chemotherapy according to national guidelines (*18*). All patients received a prescribed dose of 66–68 Gy in 33 or 34 fractions, 6 fractions per week, and 1 patient received proton radiation. Patients with advanced disease, if assessed fit, received concomitant cisplatin weekly (40 mg/m^2); all patients with normal liver and renal function test results and no neurologic symptoms received a hypoxic radiosensitizer (nimorazole) daily (1,200 mg/m^2). According to national guidelines, all HNSCC patients attended a 5-y follow-up program throughout the study period, and concurrent diseases, visits to other departments, and decease of individuals were followed through the Danish personal identity number.

Statistical Analysis

A sample size of 104 patients was calculated as needed for the study on the basis of the ability to detect an HR of 2.5 with a power of 70% (β, 30%), a significance level (α) of 5%, and a follow-up of 2 y. However, because of the slowdown in performing clinical studies caused by the coronavirus disease 2019 pandemic, the study was delayed, but with a longer follow-up the needed number of events was reached.

Clinical endpoints were relapse-free survival (RFS), disease-free survival (DFS), locoregional control (LRC), and overall survival (OS). RFS was defined as the time from diagnosis to any relapse of the disease at the locoregional (TN) site or distant metastasis (M) site, with deaths from other causes recorded as censoring. DFS was defined as RFS but included death of any reason as an event. Locoregional control was defined as the time from diagnosis to relapse at the locoregional site, with deaths and distant metastasis recorded as censoring. Overall survival (OS) was defined as the time from diagnosis to death of any cause. Follow-up time was calculated from the time of referral for radiotherapy until first relapse, death, or the end of follow-up (January 1, 2021).

The optimal cutoff in discrimination between favorable and poor prognosis was determined with Cutoff Finder, an R-package developed by Budczies et al. (*19*). Associations between biomarker expression beneath or above the cutoff and survival outcomes were visualized in Kaplan–Meier plots using the log-rank test to assess significance of differences. Hazard ratios (HRs) were estimated in univariable and multivariable Cox proportional-hazards models in which the PET parameters were included as binarized parameters according to the defined cutoffs for RFS and OS.

The number of events included in the survival analysis were 17 in RFS analysis and 16 in OS analysis. On the basis of the number of events, 4 predictors were the maximal number of explanatory variables that could reasonably be included in the final multivariable Cox model. In addition to the aim of testing the prognostic value of ^{68}Ga-uPAR SUV_{max} and comparing it with ^{18}F-FDG SUV_{max}, the multivariable analysis also included TNM stage and p16 status (p16-positive oropharyngeal cancer vs. all other tumors), since they are the most important nonimaging prognostic factors in HNSCC (*9*). Model performance was estimated using the Harrell concordance index (C-index).

The interrater reliability of SUV measurement was estimated using the intraclass correlation coefficient.

A *P* value of less than 0.05 was considered statistically significant. Statistical analyses were performed using IBM SPSS Statistics, version 22 (IBM Corp.), and R (http://www.Rproject.org).

RESULTS

Patients

In total, 57 patients recently diagnosed with HNSCC in the pharynx, larynx, or oral cavity and referred for curatively intended radiotherapy at Rigshospitalet and Næstved Hospital, Denmark, were consecutively included in the current study from December 2016 to November 2019 (Fig. 1). None of the patients experienced reactions or adverse events related to the administration of ^{68}Ga-NOTA-AE105. One patient terminated the ^{68}Ga-NOTA-AE105 (uPAR) PET/CT scan because of claustrophobia, and 2 patients were diagnosed with an unknown primary tumor of the head and neck after a lymph node biopsy and were excluded from the statistical analysis. Patient characteristics are shown in Table 1. More than half the patients (59.2%) presented with early-stage disease (stage 1 or 2), and 38.9% had no primary regional nodal disease. Moreover, 61.1% were located in the oropharynx, of which 78.7% were p16 positive. The median follow-up was 33.8 mo (range, 2.30–47.2 mo).

Clinical Follow-up

Locoregional recurrences were histologically verified in 15 of 16 patients, serving as a reference for the study outcome. One patient did not have histologic verification of the locoregional recurrence but had active tumor at the primary site on ^{18}F-FDG
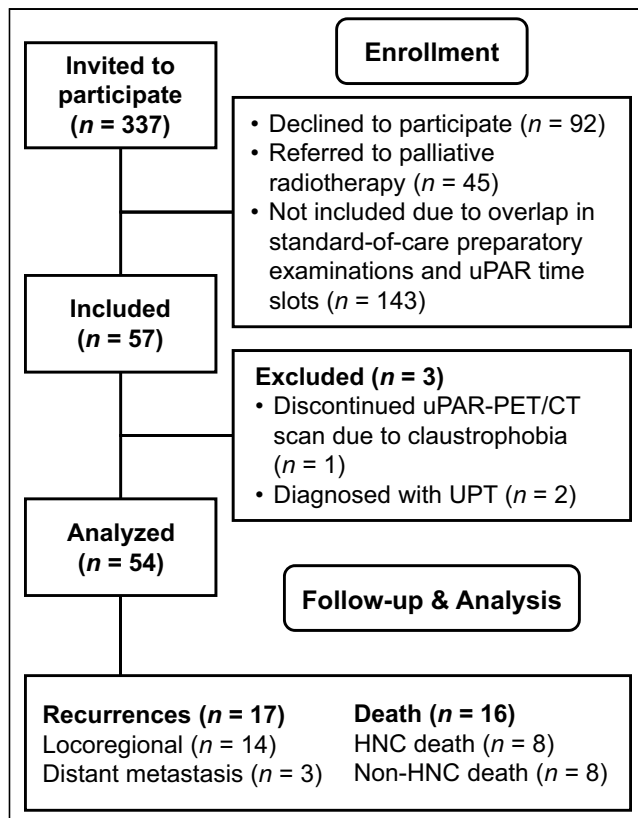
FIGURE 1. CONSORT (Consolidated Standards of Reporting Trials) flow diagram of inclusion process. HNC = head and neck cancer; UPT = unknown primary tumor.

TABLE 1
Patient Characteristics

Characteristic	Variable	Data	%
Total patients		54	100
Sex	Male	45	83.3
	Female	9	16.7
Age			
Mean		67.1	
Range		48–84	
PS	0	51	94.4
	1	3	5.6
Smoking	Never smokers	8	14.8
	Former smokers	24	44.4
	Current smokers	22	40.7
	Pack years		
	Mean	36.7	
	Range	0–150	
Primary site	Oral cavity	3	5.6
	Rhinopharynx	2	3.7
	Oropharynx	33	61.1
	Hypopharynx	8	14.8
	Larynx	8	14.8
P16 (oropharynx)	p16-positive	26	78.7
	p16-negative	7	21.2
EBV-positive		1	1.9
Stage*	I	12	22.2
	II	20	37.0
	III	9	16.7
	IV	13	24.1
T classification	T1	4	7.4
	T2	26	48.1
	T3	13	24.1
	T4	11	20.4
N classification	N0	21	38.9
	N1	14	25.9
	N2	19	35.2
Chemotherapy	No cisplatin	25	46.3
	Cisplatin	29	53.7
Nimorazole	No	5	9.3
	Yes	49	90.7

*According to Union for International Cancer Control classification, eighth edition.

PS = performance status; EBV = Epstein–Barr virus.

Qualitative data are number and percentage; continuous data are mean and range.

PET/CT and histologically verified lung metastases. Biologic material from biopsy or surgery was available from all three patients with suspected distant metastasis. Consequently, we did not experience missing data regarding recurrences, and the two patients with unknown primary tumors were excluded because of missing

data from the primary tumor. No patients were lost to follow-up, and clinicopathologic information was collected before inclusion.

Seventeen patients (31.5%) were diagnosed with recurrence, 7 (13.0%) at the primary site (T site), 5 (9.3%) at the primary site and in the lymph nodes (TN site), and 2 (3.7%) in the lymph nodes (N site); 3 (5.6%) were diagnosed with distant metastases in the lungs (M site). Two of the patients were classified as having residual tumor at the 2-mo follow-up. Ten of the 17 recurrences (58.8%) were p16-negative, whereas 7 (41.2%) were p16-positive. Thirty percent (3/10) of the locoregional recurrences were p16-positive, and all cases (3/3) of distant metastasis were confirmed to be p16-positive. All 17 patients who experienced a relapse completed all fractions of the primary radiotherapy.

During follow-up, 16 patients (29.6%) died: the death was due to HNSCC in 8 (14.8%) and due to non-HNSCC causes in the other 8 (1 [1.9%] from sepsis 1 mo after treatment, 1 from exacerbation of chronic obstructive pulmonary disease, 1 from lung embolism [diagnosed and successfully operated for a recurrence before his death], 1 from discontinuation of his routine treatment of HIV followed by infection, 1 from rectal cancer, 2 from lung cancer, and 1 from unknown causes but without any sign of recurrence at the follow-up 2 mo before his death). None of the noncancer deaths had signs of recurrence at the previous follow-up. The patient who died of sepsis 1 mo after treatment before the first routine follow-up was included in the statistical analyses as not having an event. Imaging performed in the acute phase in the case of sepsis and exacerbation of chronic obstructive pulmonary disease had no sign of recurrence. Four of 6 patients whose death was due to HNSCC were p16-negative (66.7%), whereas 2 (33.3%) were p16-positive.

^{68}Ga-uPAR and ^{18}F-FDG Uptake

The median SUV$_{max}$ of the primary tumors was 2.98 (range, 1.94–5.24) for ^{68}Ga-uPAR uptake and 15.7 (range, 4.24–45.5) for ^{18}F-FDG uptake (Fig. 2). The median interval between the ^{68}Ga-uPAR and ^{18}F-FDG PET/CT was 2.4 d (range, 1–4 d).

Cutoffs and Kaplan–Meier Curves

The optimal cutoffs were determined as the point with the most significant split in the Kaplan–Meier plot (log-rank test), and the corresponding HRs, including 95% CIs, were calculated (19). For ^{68}Ga-uPAR, the cut-points were 2.63 for RFS and 2.66 for OS, separating the patients into a group of 41 (75.6%) above the cutoff and 13 (24.1%) below the cutoff in RFS analysis and a group of 40 (74.1%) above and 14 (25.9%) below in OS analysis. For ^{18}F-FDG PET, the optimized cut-points were 22.7 for RFS and 22.9 for OS, separating the patients into a group of 42 (77.8%) below the cutoff and 12 (22.2%) above the cutoff in RFS analysis and a group of 43 (79.6%) below and 11 (20.4%) above in OS analysis.

Kaplan–Meier curves combined with log-rank analysis for differences showed a significant association between poor RFS (log-rank $P = 0.012$) and OS (log-rank $P = 0.02$) and high ^{68}Ga-uPAR SUV$_{max}$ above the cutoff. Similarly, ^{18}F-FDG SUV$_{max}$ above the cutoff was significantly associated with reduced RFS ($P = 0.012$) and OS ($P < 0.001$) (Fig. 3).

Survival Analysis

Univariate and multivariate analysis using Cox proportional-hazards model is summarized in Table 2. In univariate analysis, high uptake of ^{68}Ga-uPAR (above the cutoff) in the primary tumor was significantly associated with reduced RFS (HR, 8.53 [95% CI, 1.12–64.7]; $P = 0.038$) and was borderline-significantly associated with OS (HR, 7.44 [95% CI, 0.981–56.44]; $P = 0.052$). High
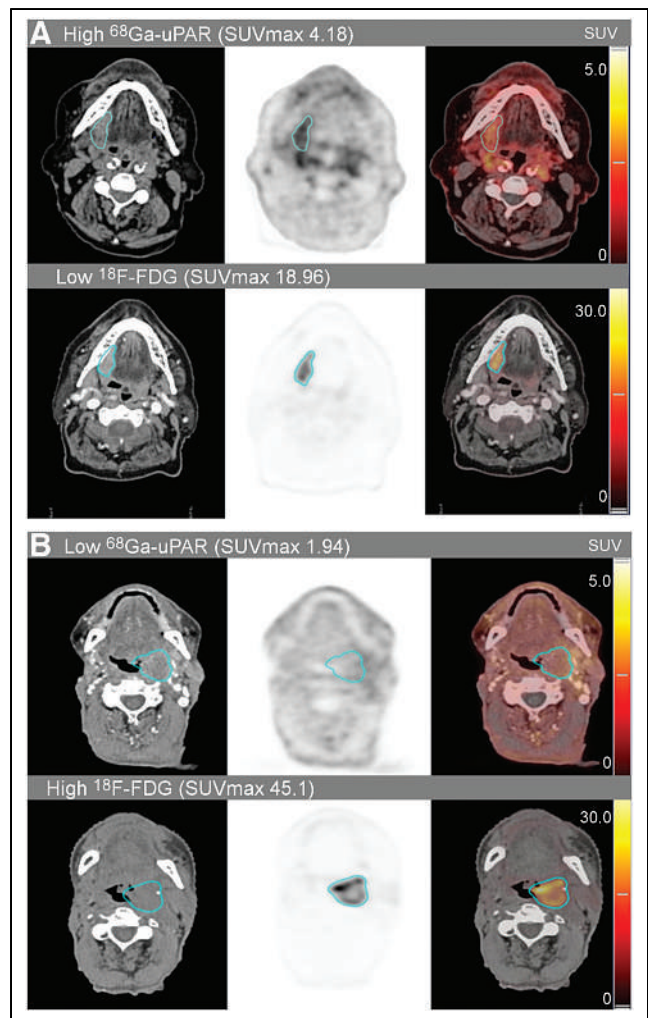
FIGURE 2. Delineated tumor volumes of interest in uPAR PET/CT with ^{68}Ga-NOTA-AE105 and ^{18}F-FDG-PET/CT in two cases with discordant tracer uptake. High ^{68}Ga-uPAR/low ^{18}F-FDG uptake (A) and low ^{68}Ga-uPAR/high ^{18}F-FDG uptake (B). Both cases present with stage 3 oropharyngeal cancer (T3N0M0). High and low refers to above or below the established cutoffs.

uptake of ^{18}F-FDG was significantly associated with reduced RFS (HR, 3.27 [95% CI, 1.237–8.66]; $P = 0.017$) and OS (HR, 7.10 [95% CI, 2.60–19.4]; $P < 0.001$). High TNM stage (S3 or S4) was significantly associated with both RFS (HR, 3.46 (95% CI, 1.216–9.88); $P = 0.020$) and OS (HR, 6.72 [95% CI, 2.12–21.4]; $P = 0.001$). In multivariable analysis, including ^{68}Ga-uPAR SUV$_{max}$, ^{18}F-FDG SUV$_{max}$, TNM stage, and p16, only ^{68}Ga-uPAR SUV$_{max}$ remained significantly associated with RFS (HR, 8.50 [95% CI, 1.11–65.3]; $P = 0.040$), but it was not significantly associated with OS (HR, 4.58 [95% CI, 0.583–36.0]; $P = 0.148$). For OS, a high ^{18}F-FDG SUV$_{max}$ (HR, 4.986 [95% CI, 1.658–14.990]; $P = 0.004$) and TNM stage (HR, 3.856 [95% CI, 1.114–13.343]; $P = 0.033$) remained significantly associated. In disease-free survival analysis, the results reflected the fact that disease-free survival is a combination of RFS and OS events (Supplemental Table 1; supplemental materials are available at http://jnm.snmjournals.org). Because there were too few events, we did not have the statistical power to make conclusions on locoregional control, but the results showed the same trend as RFS.
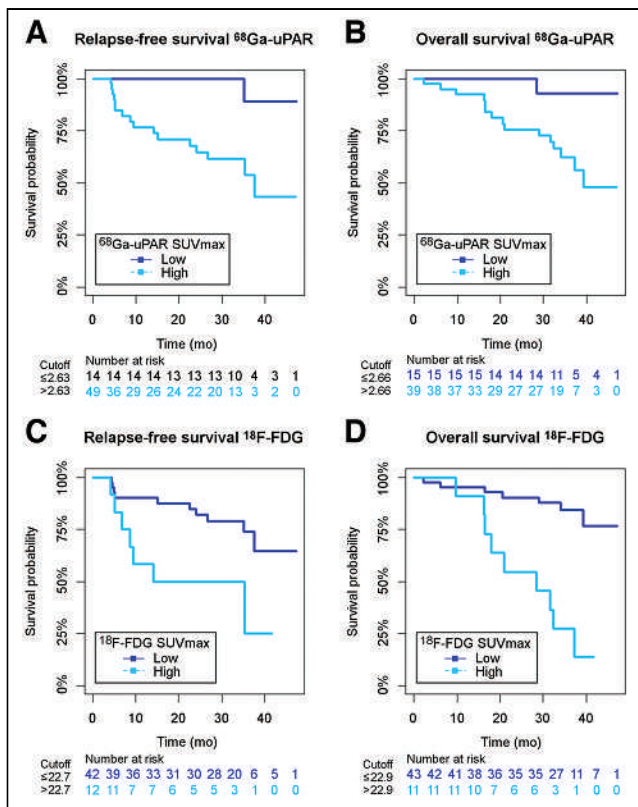
FIGURE 3. Kaplan–Meier plots of RFS for ^{68}Ga-uPAR (A), OS for ^{68}Ga-uPAR (B), RFS for ^{18}F-FDG (C), and OS for ^{18}F-FDG (D) stratified by corresponding ^{68}Ga-uPAR and ^{18}F-FDG SUV$_{max}$ cutoffs.

In post hoc analysis, inclusion of ^{68}Ga-uPAR SUV$_{max}$ in the multivariate Cox model improved the predictive performance in RFS analysis (C-index, 0.74–0.78) and for ^{18}F-FDG (C-index, 0.76–0.78). In OS analysis, inclusion of ^{68}Ga-uPAR SUV$_{max}$ improved the predictive performance (C-index, 0.81–0.84) and for ^{18}F-FDG (C-index, 0.80–0.84). The C-index for a model including only TNM stage and p16 was 0.70 for RFS and 0.77 for OS.

^{68}Ga-uPAR and ^{18}F-FDG Concordance

In post hoc analysis, combining ^{68}Ga-uPAR PET and ^{18}F-FDG into three groups (both scans low, 1 scan high/1 scan low, and both scans high) according to the established cutoffs demonstrated a concordance rate near 40% for RFS and OS and a discordance rate near 60% for RFS and OS. The distribution of the groups is shown in Table 3, and the Kaplan–Meier curves are shown in Figure 4. Overall, there was a significant difference between the groups in RFS and OS analysis (log-rank $P = 0.001$). For RFS and OS, the concordantly high groups had a significantly poorer RFS than the concordantly low groups ($P < 0.0001$). The group with discordant uptake (1 low/1 high) had an intermediate prognosis, with a prognosis significantly more favorable than for the concordantly high groups for both RFS and OS ($P = 0.006$ and $P < 0.0001$) but inferior to the concordantly low groups, although not reaching significance ($P = 0.110$ and $P = 0.069$).

Interrater Reliability

Interrater reliability in measurement of tumor SUV$_{max}$ was good, with an intraclass correlation coefficient of 0.835 (95% CI, 0.713–0.905).

DISCUSSION

The main finding of the current study was the ability of ^{68}Ga-uPAR PET/CT with ^{68}Ga-NOTA-AE105 to predict RFS in HNSCC patients referred for curatively intended radiotherapy. In univariate analysis, ^{18}F-FDG-SUV$_{max}$ also predicted RFS; however, in a multivariate analysis including ^{68}Ga-uPAR SUV$_{max}$, ^{18}F-FDG-SUV$_{max}$, TNM stage, and p16 immunohistochemistry, only ^{68}Ga-uPAR SUV$_{max}$ remained significant.

Accordingly, we demonstrated that a primary tumor ^{68}Ga-uPAR PET SUV$_{max}$ cutoff could be established for identification of high- and low-risk groups of HNSCC patients referred for curatively intended radiotherapy. The PET parameter SUV$_{max}$ is simple to obtain and is the most frequently reported and most reproducible PET uptake metric in the literature (*20*).

The large proportion (8/16, 50%) of non–HNC-related deaths found in our study may explain why ^{68}Ga-uPAR PET was not able to predict OS. The poor general health status of many HNSCC patients is known to result in a high number of non-HNSCC deaths due to competing risks after tobacco and alcohol consumption (*21*). However, our study was not powered to evaluate ^{68}Ga-uPAR PET in predicting HNSCC-related deaths.

Since uPAR expression takes part in the tumor invasion and metastasis process (*12,14*), it is not surprising that high levels of uPAR PET are related to relapse. Previous phase I clinical trials of ^{68}Ga-uPAR PET (*16,17,22*), as well as an array of preclinical studies (*13,23–26*), have demonstrated that ^{68}Ga-uPAR PET indeed visualizes uPAR expression.

^{18}F-FDG PET SUV$_{max}$ is the most common and best-characterized PET uptake metric and is a proposed prognostic marker in various cancers. Therefore, in our study we predefined ^{18}F-FDG PET SUV$_{max}$ for comparison. For HNSCC, several studies have concluded that ^{18}F-FDG PET SUV$_{max}$ does hold prognostic information, but results have been inconsistent. Most of the studies have been retrospective cohort studies, and there has been concern that ^{18}F-FDG is simply a surrogate marker of known clinical risk factors, especially tumor size (*10,11*). However, our results support the evidence that SUV$_{max}$ is a significant predictor of patient outcome for both ^{68}Ga-uPAR and ^{18}F-FDG in univariate analysis.

^{18}F-FDG is not tumor-specific, and various image interpretation pitfalls exist due to physiologic uptake and the complex anatomy of the head and neck (*27*). We found that ^{18}F-FDG PET SUV$_{max}$ could predict OS but not RFS in the multivariate model. ^{68}Ga-uPAR PET remained significant regarding RFS in the multivariate model, but not ^{18}F-FDG PET, demonstrating that the prognostic information obtained with ^{68}Ga-uPAR is different from that obtained with ^{18}F-FDG PET. The two tracers may be used for different purposes and complement each other in providing a detailed noninvasive whole-tumor characterization (*28–30*). ^{68}Ga-uPAR and ^{18}F-FDG concordance could supply additional information to a future risk stratification of low (both low), intermediate (1 low/1 high), and high-risk patients (both high) for personalized treatment and follow-up strategies.

More recent ^{18}F-FDG PET uptake metrics—metabolic tumor volume and total lesion glycolysis—have shown promising prognostic results, and inclusion of such parameters in future and higher-phase studies could be of interest (*31*). Nonetheless, these parameters have several limitations, and no consensus regarding volume segmentation and threshold has been established (*31*). In ^{68}Ga-uPAR PET prognostication, we believe that SUV$_{max}$ is the relevant metric for characterization of the most aggressive phenotype

TABLE 2
Cox Proportional Hazards Model for RFS and OS in Relation to Clinicopathologic Parameters and ^{68}Ga-uPAR and ^{18}F-FDG Uptake

Parameter	Variable	n	RFS Univariate analysis			RFS Multivariate analysis			OS Univariate analysis			OS Multivariate analysis		
			HR	95% CI	P	HR	95% CI	P	HR	95% CI	P	HR	95% CI	P
Sex	Women	9												
	Men	45	3.666	0.486–27.657	0.208				3.109	0.410–23.578	0.273			
Age*			0.993	0.943–1.046	0.802				1.035	0.984–1.090	0.184			
Smoking	<30 pack years	29												
	>30 pack years	25	1.129	0.433–2.947	0.804				3.072	1.060–8.906	0.039			
TNM stage	S1–2	32												
	S3–4	22	3.458	1.211–9.875	0.020	2.702	0.827–8.832	0.100	6.724	2.117–21.355	0.001	4.309	1.239–14.984	0.022
p16	Positive	26												
	Negative	28	2.361	0.864–6.456	0.094	1.006	0.331–3.064	0.991	4.615	1.314–16.212	0.017	1.712	0.438–6.691	0.440
^{68}Ga-uPAR	<Cutoff	13												
	>Cutoff	41	8.530	1.124–64.743	0.038	8.511	1.082–66.949	0.042	7.439	0.981–56.415	0.052	4.584	0.583–36.044	0.148
^{18}F-FDG	<Cutoff	42												
	>Cutoff	12	3.266	1.231–8.662	0.017	2.240	0.724–6.933	0.162	7.098	2.602–19.360	0.000	4.285	1.362–13.479	0.013

*Age was included as continuous covariate.

TABLE 3
Distribution of Patients According to Cutoffs for ^{68}Ga-uPAR PET and ^{18}F-FDG PET SUV$_{max}$ for RFS and OS

Parameter	uPAR low	uPAR high	Total
RFS concordance			
^{18}F-FDG low	12 (22.2%)	30 (55.6%)	42 (77.8%)
^{18}F-FDG high	2 (3.7%)	10 (18.5%)	12 (22.2%)
Total	14 (25.9%)	40 (74.1%)	54 (100%)
OS concordance			
^{18}F-FDG low	12 (22.2%)	31 (57.4%)	43 (79.6%)
^{18}F-FDG high	2 (3.7%)	9 (16.7%)	12 (20.4%)
Total	14 (25.9%)	40 (74.1%)	54 (100%)

within the tumor and as a predictor of prognosis rather than a measure of volume.

The current study represents a first proof of concept in a moderately sized population. Larger future prospective (phase III) studies are needed to establish the exact cutoffs, which may also depend on the exact composition of the population. Nevertheless, with the current SUV$_{max}$ cutoff at 2.63, we identified the 25% of patients with a low risk of recurrence. Because of the considerable toxicity associated with chemoradiotherapy, initiatives to deescalate the treatment for selected patients are being explored, and ^{68}Ga-uPAR may assist with a reliable identification of such low-risk patients (7).

Moreover, there is considerable variation in surveillance strategies after treatment of head and neck cancer (32). Routine imaging is not standardized, and patients often request fewer follow-up visits (33). If results are validated, ^{68}Ga-uPAR PET may contribute to the development of risk-stratified follow-up schedules.

In past decades, research in optimizing treatment for HNSCC patients has focused on the geometric precision of radiotherapy, but a shift toward biologic precision has begun. The prognostic strength of ^{68}Ga-uPAR PET is the quantitative readout from tumor lesions and not a visual delineation, as some tumors may have low or almost no uptake. Accordingly, ^{68}Ga-uPAR PET will not replace ^{18}F-FDG PET as a diagnostic tool. In addition, ^{68}Ga-uPAR PET/CT may become an important companion diagnostic for selection of patients eligible for uPAR-targeted optically guided surgery using a uPAR-targeted optical probe or uPAR-targeted radionuclide therapy, as well as for planning of external-radiation therapy with customization of uPAR-targeted dose delivery of intensity-modulated radiotherapy in patients with high tumor uptake (23,34–37).

CONCLUSION

The current trial evaluating the prognostic impact of ^{68}Ga-uPAR PET/CT using ^{68}Ga-NOTA-AE105 showed that ^{68}Ga-uPAR PET SUV$_{max}$ can predict RFS in HNSCC patients referred for curatively intended radiotherapy. In a multivariate analysis including ^{68}Ga-uPAR SUV$_{max}$, ^{18}F-FDG SUV$_{max}$, TNM stage, and p16 status, only ^{68}Ga-uPAR SUV$_{max}$ remained significant for RFS. For OS, TNM stage and ^{18}F-FDG SUV$_{max}$ were significant.

DISCLOSURE

KEY POINTS

QUESTION: What is the prognostic value of the novel ligand ^{68}Ga-NOTA-AE105 for uPAR PET/CT in HNSCC?

PERTINENT FINDINGS: High primary-tumor uptake of the uPAR PET tracer was associated with poor RFS in HNSCC patients, whereas high primary-tumor uptake of the ^{18}F-FDG PET tracer was associated with poor OS.

IMPLICATIONS FOR PATIENT CARE: uPAR PET/CT offers a potential tool for clinicians to select low-risk HNSCC patients for deescalated treatment regimens to avoid unnecessary toxicity and for a risk-stratified follow-up schedule.
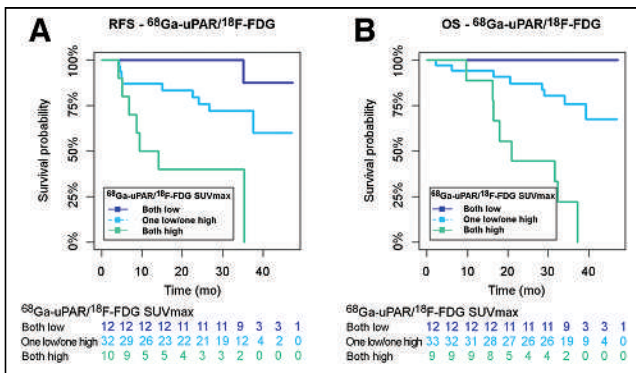
FIGURE 4. Kaplan–Meier plots of RFS (A) and OS (B) for concordant and discordant groups: ^{68}Ga-uPAR and ^{18}F-FDG both low (dark blue); 1 low/1 high (turquoise); and both high (green).

REFERENCES

1. Chaturvedi AK, Engels EA, Pfeiffer RM, et al. Human papillomavirus and rising oropharyngeal cancer incidence in the United States. *J Clin Oncol.* 2011;29:4294–4301.
2. Mehanna H, Franklin N, Compton N, et al. Geographic variation in human papillomavirus-related oropharyngeal cancer: data from 4 multinational randomized trials. *Head Neck.* 2016;38(suppl 1):E1863–E1869.
3. Albers AE, Qian X, Kaufmann AM, Coordes A. Meta analysis: HPV and p16 pattern determines survival in patients with HNSCC and identifies potential new biologic subtype. *Sci Rep.* 2017;7:16715.
4. O'Sullivan B, Huang SH, Su J, et al. Development and validation of a staging system for HPV-related oropharyngeal cancer by the International Collaboration on Oropharyngeal cancer Network for Staging (ICON-S): a multicentre cohort study. *Lancet Oncol.* 2016;17:440–451.
5. Jakobsen KK, Gronhoj C, Jensen DH, et al. Increasing incidence and survival of head and neck cancers in Denmark: a nation-wide study from 1980 to 2014. *Acta Oncol.* 2018;57:1143–1151.

6. Craig SG, Anderson LA, Schache AG, et al. Recommendations for determining HPV status in patients with oropharyngeal cancers under TNM8 guidelines: a two-tier approach. *Br J Cancer.* 2019;120:827–833.

7. Gillison ML, Trotti AM, Harris J, et al. Radiotherapy plus cetuximab or cisplatin in human papillomavirus-positive oropharyngeal cancer (NRG Oncology RTOG 1016): a randomised, multicentre, non-inferiority trial. *Lancet.* 2019;393:40–50.

8. Mehanna H, Robinson M, Hartley A, et al. Radiotherapy plus cisplatin or cetuximab in low-risk human papillomavirus-positive oropharyngeal cancer (De-ESCA-LaTE HPV): an open-label randomised controlled phase 3 trial. *Lancet.* 2019;393: 51–60.

9. Burd EM. Human papillomavirus laboratory testing: the changing paradigm. *Clin Microbiol Rev.* 2016;29:291–319.

10. Clausen MM, Vogelius IR, Kjaer A, Bentzen SM. Multiple testing, cut-point optimization, and signs of publication bias in prognostic FDG-PET imaging studies of head and neck and lung cancer: a review and meta-analysis. *Diagnostics (Basel).* 2020;10:1030.

11. Rasmussen JH, Vogelius IR, Fischer BM, et al. Prognostic value of ^{18}F-fludeoxyglucose uptake in 287 patients with head and neck squamous cell carcinoma. *Head Neck.* 2015;37:1274–1281.

12. Dass K, Ahmad A, Azmi AS, Sarkar SH, Sarkar FH. Evolving role of uPA/uPAR system in human cancers. *Cancer Treat Rev.* 2008;34:122–136.

13. Persson M, Kjaer A. Urokinase-type plasminogen activator receptor (uPAR) as a promising new imaging target: potential clinical applications. *Clin Physiol Funct Imaging.* 2013;33:329–337.

14. Mekkawy AH, Pourgholami MH, Morris DL. Involvement of urokinase-type plasminogen activator system in cancer: an overview. *Med Res Rev.* 2014;34:918–956.

15. Skovgaard D, Persson M, Brandt-Larsen M, et al. Safety, dosimetry, and tumor detection ability of ^{68}Ga-NOTA-AE105: first-in-human study of a novel radioligand for uPAR PET imaging. *J Nucl Med.* 2017;58:379–386.

16. Skovgaard D, Persson M, Kjaer A. Urokinase plasminogen activator receptor-PET with ^{68}Ga-NOTA-AE105: first clinical experience with a novel PET ligand. *PET Clin.* 2017;12:311–319.

17. Persson M, Skovgaard D, Brandt-Larsen M, et al. First-in-human uPAR PET: imaging of cancer aggressiveness. *Theranostics.* 2015;5:1303–1316.

18. *Radiotherapy Guidelines 2020.* DAHANCA; 2020:1–57.

19. Budczies J, Klauschen F, Sinn BV, et al. Cutoff Finder: a comprehensive and straightforward web application enabling rapid biomarker cutoff optimization. *PLoS One.* 2012;7:e51862.

20. Wahl RL, Jacene H, Kasamon Y, Lodge MA. From RECIST to PERCIST: evolving considerations for PET response criteria in solid tumors. *J Nucl Med.* 2009; 50(suppl 1):122S–150S.

21. Gillison ML, Zhang Q, Jordan R, et al. Tobacco smoking and increased risk of death and progression for patients with p16-positive and p16-negative oropharyngeal cancer. *J Clin Oncol.* 2012;30:2102–2111.

22. Skovgaard D, Persson M, Kjaer A. Imaging of prostate cancer using rokinase-type plasminogen activator receptor PET. *PET Clin.* 2017;12:243–255.

23. Persson M, Madsen J, Ostergaard S, et al. Quantitative PET of human urokinase-type plasminogen activator receptor with ^{64}Cu-DOTA-AE105: implications for visualizing cancer invasion. *J Nucl Med.* 2012;53:138–145.

24. Persson M, Hosseini M, Madsen J, et al. Improved PET imaging of uPAR expression using new ^{64}Cu-labeled cross-bridged peptide ligands: comparative in vitro and in vivo studies. *Theranostics.* 2013;3:618–632.

25. Persson M, Liu H, Madsen J, Cheng Z, Kjaer A. First ^{18}F-labeled ligand for PET imaging of uPAR: in vivo studies in human prostate cancer xenografts. *Nucl Med Biol.* 2013;40:618–624.

26. Persson M, El Ali HH, Binderup T, et al. Dosimetry of ^{64}Cu-DOTA-AE105, a PET tracer for uPAR imaging. *Nucl Med Biol.* 2014;41:290–295.

27. Purohit BS, Ailianou A, Dulguerov N, Becker CD, Ratib O, Becker M. FDG-PET/CT pitfalls in oncological head and neck imaging. *Insights Imaging.* 2014;5:585–602.

28. Marcu LG, Reid P, Bezak E. The promise of novel biomarkers for head and neck cancer from an imaging perspective. *Int J Mol Sci.* 2018;19:2511.

29. Song IH, Noh Y, Kwon J, et al. Immuno-PET imaging based radioimmunotherapy in head and neck squamous cell carcinoma model. *Oncotarget.* 2017;8:92090–92105.

30. Christensen A, Kiss K, Lelkaitis G, et al. Urokinase-type plasminogen activator receptor (uPAR), tissue factor (TF) and epidermal growth factor receptor (EGFR): tumor expression patterns and prognostic value in oral cancer. *BMC Cancer.* 2017; 17:572.

31. Rijo-Cedeño J, Mucientes J, Seijas Marcos S, et al. Adding value to tumor staging in head and neck cancer: the role of metabolic parameters as prognostic factors. *Head Neck.* 2021;43:2477–2487.

32. Wong WL. PET-CT for staging and detection of recurrence of head and neck cancer. *Semin Nucl Med.* 2021;51:13–25.

33. Trinidade A, Kothari P, Andreou Z, Hewitt RJ, O'Flynn P. Follow-up in head and neck cancer: patients' perspective. *Int J Health Care Qual Assur.* 2012;25:145–149.

34. Christensen A, Juhl K, Persson M, et al. uPAR-targeted optical near-infrared (NIR) fluorescence imaging and PET for image-guided surgery in head and neck cancer: proof-of-concept in orthotopic xenograft model. *Oncotarget.* 2017;8:15407–15419.

35. Ling CC, Humm J, Larson S, et al. Towards multidimensional radiotherapy (MD-CRT): biological imaging and biological conformality. *Int J Radiat Oncol Biol Phys.* 2000;47:551–560.

36. Atallah I, Milet C, Henry M, et al. Near-infrared fluorescence imaging-guided surgery improves recurrence-free survival rate in novel orthotopic animal model of head and neck squamous cell carcinoma. *Head Neck.* 2016;38(suppl 1):E246–E255.

37. Persson M, Madsen J, Ostergaard S, Ploug M, Kjaer A. ^{68}Ga-labeling and in vivo evaluation of a uPAR binding DOTA- and NODAGA-conjugated peptide for PET imaging of invasive cancers. *Nucl Med Biol.* 2012;39:560–569.

Antiandrogen Therapy Radiosensitizes Androgen Receptor–Positive Cancers to ^{18}F-FDG

Indulekha Singaravelu[1], Henry Spitz[2], Mary Mahoney[3], Zhongyun Dong[4], and Nalinikanth Kotagiri[1]

[1]*Division of Pharmaceutical Sciences, James L. Winkle College of Pharmacy, University of Cincinnati, Cincinnati, Ohio;* [2]*Department of Nuclear and Mechanical Engineering, University of Cincinnati, Cincinnati, Ohio;* [3]*Department of Radiology, University of Cincinnati College of Medicine, Cincinnati, Ohio;* and [4]*Division of Hematology and Oncology, University of Cincinnati College of Medicine, Cincinnati, Ohio*

A subset (35%) of triple-negative breast cancers (TNBCs) expresses androgen receptor (AR) activity. However, clinical trials with antiandrogen drugs have shown limited efficacy, with about a 19% clinical benefit rate. We investigated the therapeutic enhancement of antiandrogens as radiosensitizers in combination with ^{18}F-FDG in TNBC. **Methods:** We screened 5 candidate drugs to evaluate shared toxicity when combined with either ^{18}F-FDG, x-rays, or ultraviolet radiation, at doses below their respective half-maximal inhibitory concentrations. Cytotoxic enhancement of antiandrogen in combination with ^{18}F-FDG was evaluated using cell proliferation and DNA damage assays. Finally, the therapeutic efficacy of the combination treatment was evaluated in mouse tumor models of TNBC and prostate cancer. **Results:** Bicalutamide, an antiandrogen drug, was found to share similar toxicity in combination with either ^{18}F-FDG or x-rays, indicating its sensitivity as a radiosensitizer to ^{18}F-FDG. Cell proliferation assays demonstrated selective toxicity of combination bicalutamide-^{18}F-FDG in AR-positive 22RV1 and MDA-MB-231 cells in comparison to AR-negative PC3 cells. Quantitative DNA damage and cell cycle arrest assays further confirmed radiation-induced damage to cells, suggesting the role of bicalutamide as a radiosensitizer to ^{18}F-FDG–mediated radiation damage. Animal studies in MDA-MB-231, 22RV1, and PC3 mouse tumor models demonstrated significant attenuation of tumor growth through combination of bicalutamide and ^{18}F-FDG in the AR-positive model in comparison to the AR-negative model. Histopathologic examination corroborated the in vitro and in vivo data and confirmed the absence of off-target toxicity to vital organs. **Conclusion:** These data provide evidence that ^{18}F-FDG in conjunction with antiandrogens serving as radiosensitizers has utility as a radiotherapeutic agent in the ablation of AR-positive cancers.

Key Words: antiandrogen therapy; bicalutamide; radiosensitization; ^{18}F-FDG

Concomitant chemotherapy and radiation therapy are an established treatment regimen for many neoplasms (*1–3*). For example, paclitaxel (Taxol; Bristol-Myers Squibb), besides having antiangiogenic properties, is also known to enhance the therapeutic effects of ionizing radiation as revealed in clinical trials (*4*).

Thus, the risks associated with use of both radiotherapy and drugs are considerably high because of unintentional radiation–drug interactions (*5*). Therefore, there is a need for systematic examination of radiation–drug interactions and, more fundamentally, photochemical and biologic interactions between different classes of drugs and radiation in order to enhance therapeutic outcomes.

Recent studies have shown that radionuclides, in contrast to external-beam radiation, can provide the flexibility and extended reach in vivo to trigger therapeutic events in niches where metastatic cancer cells tend to localize, such as bone marrow and lungs (*6,7*). Typically, emissions from radionuclides include ionizing radiation, comprising electron (β^-) particles, positron (β^+) particles, α-particles, Auger electrons, x-rays, and γ-photons, as well as nonionizing radiation, comprising luminescence and ultraviolet–blue light emitted by β-particles, known as Cherenkov radiation. The various types of emissions from a single radionuclide can drive new opportunities in determining beneficial effects in combination with drugs. Because of the associated complexity in dosimetry, these combinations can also be challenging, as they can lead to unintended consequences if the treatment strategy is not optimized. For example, a recent phase III trial of vaginal cuff brachytherapy in combination with paclitaxel/carboplatin chemotherapy in patients with high-risk, early-stage endometrial cancer resulted in acute toxicities to the patients (*8*). Therefore, in our study we sought to identify and characterize compounds that are capable of efficiently harvesting the different energy emissions from diagnostic radionuclides to trigger therapeutic outcomes through synergistic action, without causing radiation or drug toxicity.

Since ^{18}F-FDG PET scans are routinely used in the evaluation of breast cancer patients, we postulated that by leveraging this technique for activating light-sensitive Food and Drug Administration–approved drugs, we could potentially transform toxic chemotherapeutics to nontoxic targeted therapy of untargetable cancers, such as triple-negative breast cancer (TNBC). In this study, we screened various anticancer drugs and explored synergy with different types of radiation sources to identify drugs that exhibit significantly higher toxicity against cancer cells when used in combination with ^{18}F-FDG. Previous studies have explored how nonionizing radiation from radionuclides can be harnessed by drugs and nanoparticles for photoactivated therapy (*6,9*). In this study, we explored how ionizing radiation from diagnostic radionuclides can be used in combination with certain drugs for enhanced cancer therapy while minimizing off-target effects.

MATERIALS AND METHODS

Drug Screening in Combination with ^{18}F-FDG

All drugs (bicalutamide, flutamide, dacarbazine, 5-fluorouracil, and titanocene) were purchased from Apexbio Inc. The drugs were resuspended in dimethylsulfoxide, and aliquots were prepared. The in vitro efficacy of the drugs was investigated in the MDAMB231 cell line (ATCC). The cells were treated with drugs at a subtoxic dose, which was followed by the addition of 3 different activities (7.4, 14.8, and 29.6 MBq) of the radiopharmaceutical, ^{18}F-FDG, procured in phosphate-buffered saline. Medium was replaced after 1 half-life of ^{18}F, approximately 110 min of incubation, to remove excess ^{18}F-FDG that did not internalize in cells. Cell viability was evaluated after 72 h by measuring the mitochondrial activity in live cells using an MTS (3-(4,5-dimethylthiazol-2-yl)-5-(3-carboxymethoxyphenyl)-2-(4-sulfophenyl)-2H-tetrazolium) cell proliferation agent (Promega) and absorbance measurement at 490 nm by Cytation I (BioTek Instruments) in triplicate. Similarly, cell viability was also measured for the cells pretreated with drugs with ultraviolet light (portable mini ultraviolet lamp, 4 W, 365 and 254 nm) for 1 h and ionizing radiation (50–220 kV x-rays, XenX irradiator; Xstrahl). An exposure of 2 Gy was used, which is a clinically used exposure limit for therapeutic purposes. The assays were repeated 3 times.

Androgen Receptor (AR) Expression on Cancer Cells and Cytotoxicity Assessment

AR expression of 22RV1, PC3, MDAMB231, and MCF10A cells (ATCC) was measured by flow cytometry. The cells were stained using standard procedures as outlined in the supplemental materials (available at http://jnm.snmjournals.org). The stained cells were analyzed for AR expression in flow cytometry (LSRII; BD Biosciences). The assays were repeated 3 times for each cell line. The toxicity of bicalutamide combined with ^{18}F-FDG treatment was evaluated using MTS assays in the cell lines following the manufacturer's instructions.

DNA Damage Assessment

DNA damage caused by bicalutamide-^{18}F-FDG in MDAMB231 was determined by cell death detection assays and γH2AX phosphorylation assays. A dose of 7.4 MBq of ^{18}F-FDG was henceforth used for all in vitro and in vivo experiments. Additional details on the cell death detection assay are outlined in the supplemental materials.

To measure γH2AX phosphorylation of histones, cells were harvested in a 96-well plate with a seeding density of 10^4 per well, treated with bicalutamide-^{18}F-FDG, bicalutamide, or ^{18}F-FDG, or left untreated, in triplicate using an EMD H2A.X phosphorylation assay kit (Millipore). Details are in the supplemental materials.

Evaluation of Cell Death Mechanism

Apoptotic cell death and autophagy were quantified by flow cytometry analysis using annexin V-fluorescein isothiocyanate (FITC)/propidium iodide (PI) staining and an autophagy detection kit (Enzo Life Sciences), respectively. Cell cycle analysis was performed by staining the fixed cells with PI dye. Details are in the supplemental materials.

Efficacy of Combined Bicalutamide-^{18}F-FDG Treatment in Animal Models

MDAMB231, 22RV1, and PC3 cultured cancer cells (2×10^6 cells) admixed with Matrigel (Corning Life Sciences) were injected subcutaneously in the flank regions of 6- to 8-wk-old female and male athymic nude mice (Jackson Laboratory). When the tumors reached 200–250 mm^3, the mice were randomized into different treatment groups (5 animals per group). Bicalutamide was administered orally every week at a dose of 60 mg/kg of body weight, and 7.4 MBq of ^{18}F-FDG were injected intraperitoneally for 4 wk. The mice were monitored every 2 d for 30–60 d for survival, adverse effects, and weight loss. Treatment efficacy was evaluated in comparison with no treatment, treatment with bicalutamide alone, and treatment with ^{18}F-FDG alone as control groups. An additional discussion on small-animal ^{18}F-FDG activity can be found in the supplemental materials (10).

Statistical Analysis

All experiments were performed in triplicate, and statistical analyses were performed using Prism software (version 8; GraphPad). P values were determined by 1-way ANOVA, and a P value of less than 0.01 was considered statistically significant in all experiments whenever applicable. The results of in vitro and in vivo analyses are shown as mean $\pm$ SD or as the SEM of 3 or more independent experiments.

RESULTS

Evaluation of Toxicity of Drugs in Combination with ^{18}F-FDG

We evaluated 5 anticancer drugs—5-fluorouracil, dacarbazine, flutamide, bicalutamide, and titanocene—on the basis of their already-established photosensitive properties. 5-fluorouracil is known to induce protein degradation through superoxide radical and photooxidation mechanisms on ultraviolet irradiation (11). Dacarbazine is a photosensitive drug known to synergize with light to produce increased toxicity through a photodegradation mechanism (12). Flutamide and bicalutamide are known to be photoreactive and to induce photosensitive drug eruptions in patients (13,14). Titanocene is an ultraviolet light–sensitive compound that exhibits enhanced phototoxicity through a photodegradation mechanism (6,7). Although all 5 drugs are known to be light-sensitive, it is unclear to which type of radiation—ionizing or nonionizing—they are sensitive. Since ^{18}F-FDG generates both ultraviolet and ionizing radiation, we sought to identify specifically which radiation, between the two, triggered cell death in combination with drugs. Our first objective was to estimate their dark toxicity by identifying their half-maximal inhibitory concentrations in MDAMB231 cells, a representative TNBC cell line (Supplemental Fig. 1). The drugs were then screened and evaluated for their ability to induce cytotoxicity, at doses below their respective half-maximal inhibitory concentrations, in combination with ^{18}F-FDG, x-rays, or ultraviolet radiation. On the basis of the estimated half-maximal inhibitory concentrations, doses of 3.12, 50, 25, 12.5, and 25 μM were selected for 5-fluorouracil, titanocene, dacarbazine, flutamide, and bicalutamide, respectively.

All 5 drugs showed enhanced toxicity when treated with ^{18}F-FDG. However, the toxicity profile for the drugs was unique with respect to sensitivity to ultraviolet light, radiation, or both (Figs. 1A and 1B). Besides ^{18}F-FDG, 5-fluorouracil and titanocene exhibited cytotoxicity in combination with ultraviolet light. Similarly, besides ^{18}F-FDG, flutamide and bicalutamide exhibited cytotoxicity exclusively in combination with x-rays. Dacarbazine, however, exhibited cytotoxicity in combination with both ultraviolet light and x-rays, as well as ^{18}F-FDG. These results suggest that ionizing radiation (flutamide, bicalutamide, and dacarbazine) or nonionizing radiation (5-fluorouracil, titanocene, and dacarbazine) emitted by the radioactive decay of ^{18}F could be playing a role in triggering these drugs. The lower cytotoxicity of ultraviolet light–treated cultures treated with flutamide and bicalutamide, compared with drug alone, likely suggests drug photoinactivation (15).

Bicalutamide Radiosensitizes Cancer Cells to ^{18}F-FDG and X-Rays

Bicalutamide is a molecularly targeted antiandrogen drug that also has radiosensitizing properties. Therefore, we hypothesized that bicalutamide in combination with ^{18}F-FDG will likely enhance cytotoxicity and provide greater control in spatiotemporal modulation
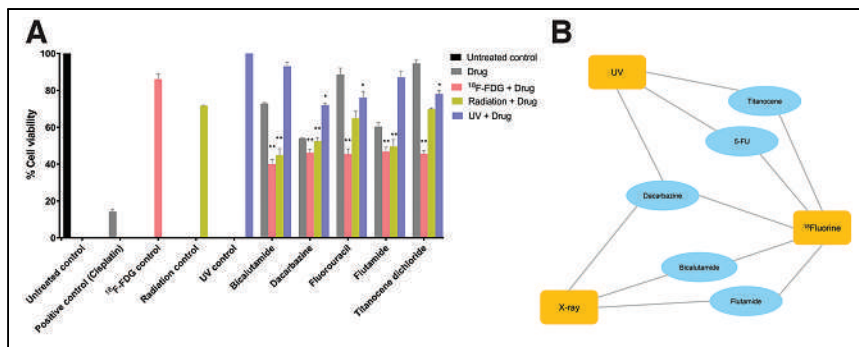
FIGURE 1. (A) Screening of Food and Drug Administration–approved drugs in MDAMB231 cells and evaluation of cell toxicity in combination with ^{18}F-FDG, ultraviolet light, and x-ray exposure. (B) Schematic representation of drugs classified by response to ^{18}F-FDG, ultraviolet light, and x-rays. *$P < 0.01$. **$P < 0.001$. UV = ultraviolet.

of this therapeutic approach. First, we investigated the photophysics behind the reactants, bicalutamide, and ^{18}F-FDG. Photoproducts formed by photoreaction of the drugs with ultraviolet light typically causes type IV hypersensitive (cell-mediated) reactions (*16*). However, we noted earlier that bicalutamide in the presence of ultraviolet light did not induce cytotoxicity. To further confirm whether ultraviolet irradiation of bicalutamide induces the generation of photoproducts, we performed mass spectrometry and Fourier-transform infrared spectroscopy analysis. We observed no change in the structure (Supplemental Fig. 2) or molar mass (Supplemental Fig. 3) of bicalutamide, suggesting that the parent compound was stable even after irradiation with ultraviolet light. These results suggest that irradiating bicalutamide with ^{18}F-FDG likely results in minimal photodegradation. However, to explain the enhanced toxicity observed with bicalutamide-^{18}F-FDG, it is possible that there is biologic cooperation, with bicalutamide blocking the AR and inhibiting DNA damage repair, thereby increasing the susceptibility of cancer cells to radiation damage by ^{18}F-FDG (*17*).

Cytotoxic Enhancement of Bicalutamide-^{18}F-FDG Combination in AR-Positive Cancer Cells

We analyzed 4 human cancer cell lines, 2 prostate and 2 breast cancers, for AR expression by flow cytometry. The prostate cancer cell lines were 22RV1 and PC3, and the breast cancer cell lines were MDAMB231 and MCF10A, the latter being a normal breast epithelial cell line. Although MCF10A and PC3 cells did not display any significant AR expression (Supplemental Figs. 4A and 4B), an estimated 85% of the cultured 22RV1 cells and 81% of the MDAMB231 cells expressed AR (Supplemental Figs. 4C and 4D). We then evaluated the cytotoxicity of the bicalutamide-^{18}F-FDG combination on AR-positive 22RV1 and MDAMB231 cells and AR-negative MCF10A and PC3 cells. We observed that even at a subcytotoxic dose of 25 μM, cytotoxicity (20% inhibitory concentration) of bicalutamide was significantly enhanced after exposure to activity of as low as 7.4 MBq in both MDAMB231 and 22RV1 cells, whereas the 20% inhibitory concentration of bicalutamide alone was 65 μM (Figs. 2A and 2B). We observed an activity-dependent increase in cytotoxicity with 7.4, 14.8, and 29.6 MBq of ^{18}F-FDG. Both MCF10A cells and PC3 cells were unresponsive to either bicalutamide alone or bicalutamide-^{18}F-FDG treatment even at a dose of 50 μM (Figs. 2C and 2D). These results suggest that the combination of bicalutamide-^{18}F-FDG selectively inhibits proliferation of AR-positive cells over non–AR–expressing cells at subcytotoxic monotherapy doses.

Bicalutamide-^{18}F-FDG Treatment Causes DNA Damage

We first investigated whether the cells were experiencing oxidative damage to their DNA, as is typical in radiotherapies. Relative quantification of the DNA fragments obtained in the cell lysate after treatment with bicalutamide and 7.4 MBq of ^{18}F-FDG in MDAMB231 cells was correlated with DNA damage, which is generally considered an early indicator of apoptosis. Using a quantitative enzyme-linked immunosorbent assay–based assay to detect mono- and oligonucleosomes, we observed that bicalutamide-^{18}F-FDG treatment induced increased DNA damage to the cells compared with bicalutamide alone,^{18}F-FDG alone, or no treatment (Fig. 3A). DNA damage was observed to be higher at 5 h after treatment than at 48 h, mainly because nucleosomes are detected before manifestation of the cascade of other apoptotic events and because there are likely to be fewer intact viable cells at 48 h as a consequence of apoptosis.

Phosphorylation of H2AX histone protein typically occurs when DNA double-stranded breaks are induced during exposure of cancer cells to chemotherapeutics or radiation, resulting in DNA rearrangement or apoptosis. Bicalutamide-^{18}F-FDG treatment resulted in a significantly higher chemiluminescence measurement, which correlates with high amounts of γH2AX protein from increased double-stranded breaks in the DNA (Fig. 3B).

Cell cycle and DNA content analysis showed no significant increase in cells occupying the G1/S phase 24 h after treatment. However, 32.8% of the cells were occupying the G_2/M phase when treated with bicalutamide-^{18}F-FDG, compared with 18.3% with bicalutamide alone and 17.3% with ^{18}F-FDG–treated cells and untreated cells (Fig. 3C). This study indicates that the antiproliferative characteristics of bicalutamide-^{18}F-FDG treatment in cancer cells is caused by G_2/M cell cycle arrest after induction of DNA damage, thus preventing the cells with DNA damage from entering the M phase and undergoing mitosis.

Cell Death Mechanism: Apoptosis and Autophagy

Apoptotic cell death is characterized by distinct morphologic changes such as cell shrinkage, DNA condensation, and cell blebbing. These biochemical processes, involving various signaling pathways, are triggered when cells undergo DNA damage and cell cycle arrest. MDAMB231 cells treated with bicalutamide-^{18}F-FDG (7.4 MBq of ^{18}F-FDG, 25 μM of bicalutamide) were evaluated using flow cytometric analysis of annexin V-FITC/PI staining. Figure 4 shows that 32.7% of bicalutamide-^{18}F-FDG–treated cells were found to be in the late apoptotic state, since they stained positively for both annexin V-FITC and PI. In contrast, only 10.6% of untreated and 18.6% of bicalutamide-alone–treated cells stained with both annexin V-FITC and PI. Annexin V-FITC stains cells undergoing apoptosis by staining phosphatidylserine molecules that have translocated to the outside of the cell membrane, whereas PI stains necrotic cells or late apoptotic cells, which are characterized by loss of the integrity of the plasma and nuclear membranes. The high degree of DNA fragmentation and double staining of cells with annexin V and PI suggests apoptosis, rather than necrosis, to be the dominant cell death mechanism as a result of bicalutamide-^{18}F-FDG treatment.
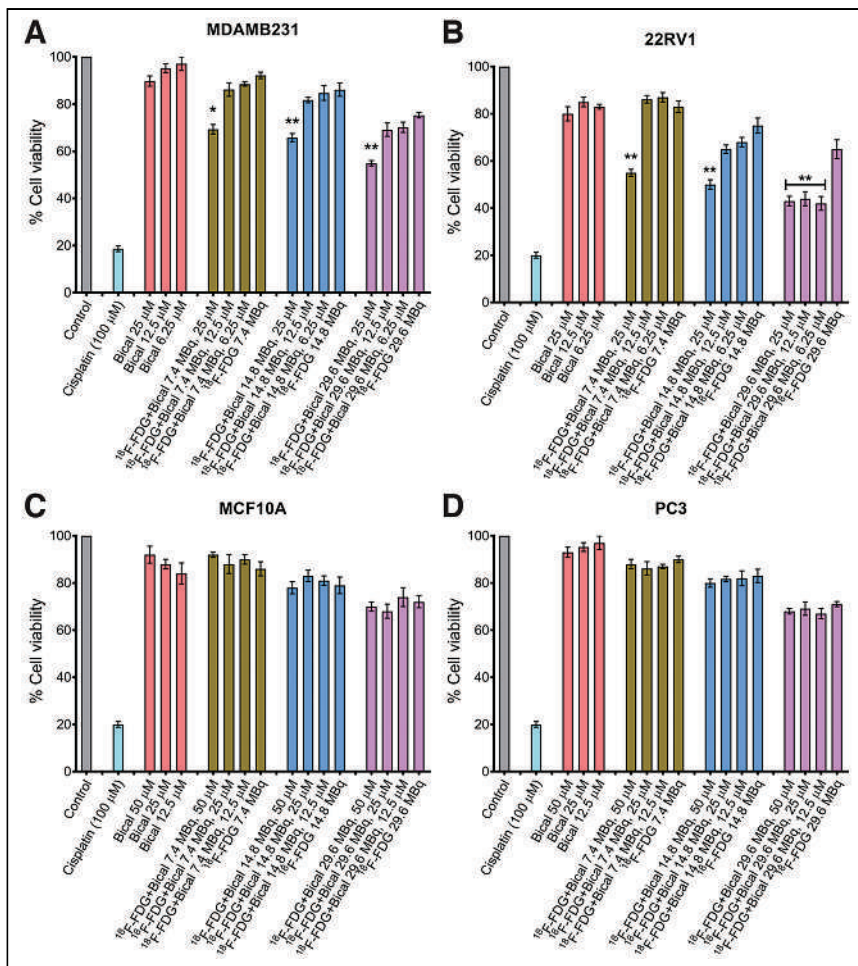
FIGURE 2. Cytotoxicity of bicalutamide-^{18}F-FDG treatment for 72 h in MDAMB231 (A), 22RV1 (B), MCF10A (C), and PC3 (D) cells. *$P < 0.01$. **$P < 0.001$. Bical = bicalutamide.

We next examined whether cells were undergoing autophagy, since ionizing radiation has been shown to induce autophagy in cancer cells (18). The autophagic process is a regulated mechanism involving swelling of the cell membrane and formation of autophagosomes to degrade and recycle the intracellular contents. Cell death by the autophagic process was quantified by analyzing cells stained with Cyto-ID green dye (Enzo Life Sciences) using a flow cytometer. Cyto-ID stains acidic vesicular organelles green at different stages in the process of autophagy before it fuses with lysosomes and is internalized. Figure 5 and Supplemental Figure 5 clearly show a higher fluorescence intensity and upregulation of autophagic activity in cells treated with combined bicalutamide-^{18}F-FDG than in cells treated with bicalutamide alone or ^{18}F-FDG alone or in cells left untreated. Rapamycin- and chloroquine-treated cells were used as positive controls.

Efficacy of Combination Bicalutamide-^{18}F-FDG Treatment in Mouse Xenograft Models

After initiation of treatment, we started observing significant separation between the tumor volume curve of the bicalutamide-^{18}F-FDG and the others, as shown in Figures 6A and 6B. Overall, combination treatment with bicalutamide and ^{18}F-FDG exhibited significant attenuation in tumor growth, compared with bicalutamide alone or ^{18}F-FDG alone, which did not significantly differ from the untreated group.
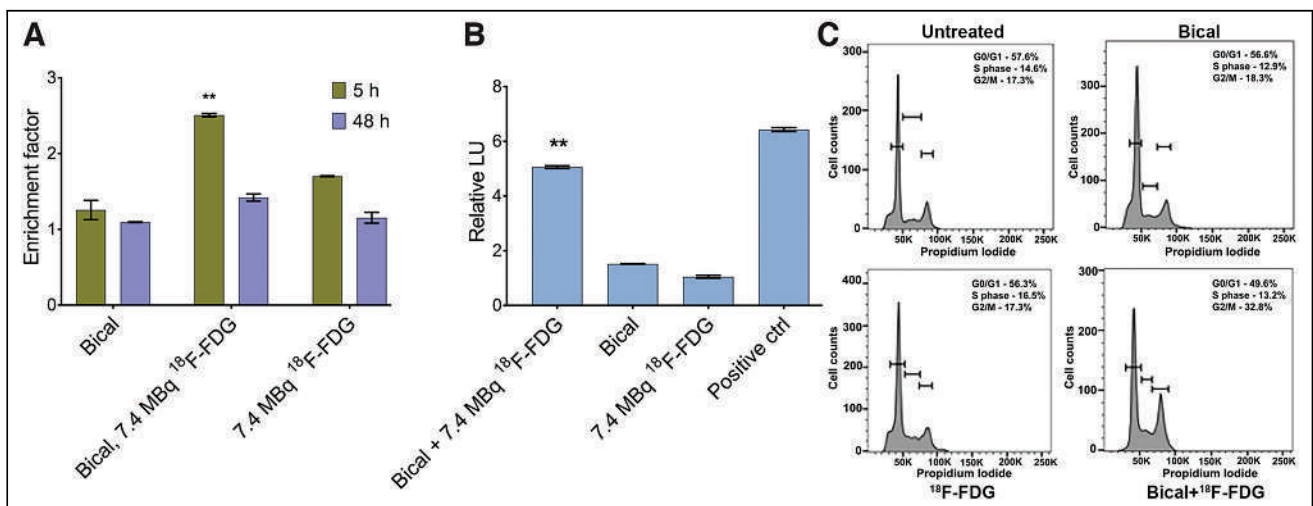
FIGURE 3. (A) Evaluation of DNA damage in bicalutamide-^{18}F-FDG–treated MDAMB231 cells by enzyme-linked immunosorbent assay–based detection of mono- and oligonucleosomes (DNA fragments) as result of DNA fragmentation. (B) Luminescent measurement of phosphorylated γH2AX protein that occurred as result of DNA damage within cells. (C) Determination of cell cycle arrest in various phases due to DNA damage in bicalutamide-^{18}F-FDG–treated cells. **$P < 0.001$. Bical = bicalutamide; ctrl = control; LU = luminescence.
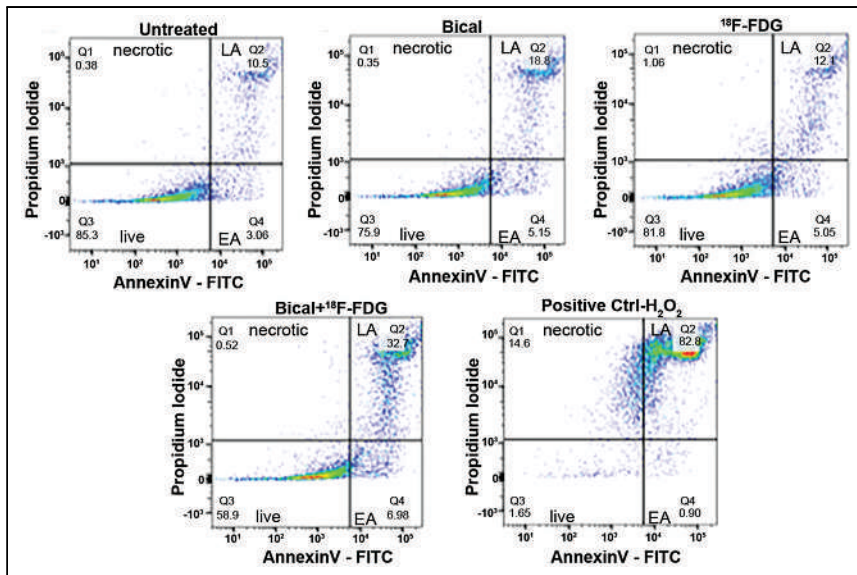
FIGURE 4. Flow cytometric quantification of bicalutamide-^{18}F-FDG–treated MDAMB231 cells undergoing apoptosis in various apoptotic stages. EA = early apoptosis; LA = late apoptosis.

Histopathologic analysis of immunostained MDAMB231 tumor tissues (Supplemental Fig. 6A) revealed that tumor tissues treated with bicalutamide-^{18}F-FDG stained strongly positive for cleaved caspase-3, which is an expression marker for apoptosis and DNA damage. Similarly, with Ki-67 staining, which is a marker for highly proliferating cells, there was a significant reduction in Ki-67 staining in tumors treated with bicalutamide-^{18}F-FDG. We also observed a decreased number of cells staining positively for CD68, suggesting lower degrees of macrophage infiltration within the tumor. Typically, increased tumor growth is also characterized by the presence of CD68-expressing tumor-infiltrating macrophages, playing a key role in promoting tumor initiation and malignant progression. In addition, hematoxylin and eosin staining of brain, heart, liver, and kidney confirmed no evidence of metastatic spread to these organs or of any treatment-related off-target toxicity (Supplemental Fig. 6B).
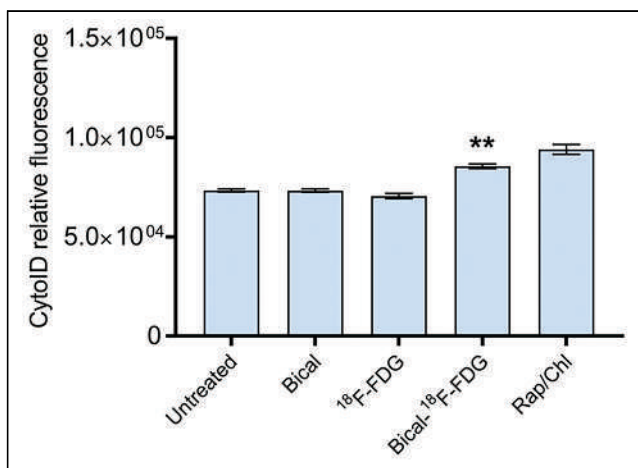
FIGURE 5. Flow cytometric quantification of bicalutamide-^{18}F-FDG–treated MDAMB231 cells undergoing autophagy. Rapamycin/chloroquine-treated cells were used as positive control. **$P < 0.001$. Bical = bicalutamide; Rap/Chl = rapamycin/chloroquine.

To elucidate the role that AR-targeted bicalutamide plays in this dual-specificity strategy, a similar experiment was performed with an AR-negative prostate cancer xenograft model in male nude mice using PC3 cells. Unlike the AR-positive cancer models, the bicalutamide-^{18}F-FDG treated group did not significantly differ from the ^{18}F-FDG or bicalutamide control arms (Fig. 6C). Interestingly, there was a significant increase in PC3 tumor attenuation in mice treated with ^{18}F-FDG, compared with untreated mice or mice treated with bicalutamide alone, further confirming the critical role that AR plays in sensitizing cells to ^{18}F-FDG in TNBC. Histopathologic analyses using staining with terminal deoxynucleotidyl transferase 2′-deoxyuridine, 5′-triphosphate nick-end labeling (DNA damage causing cell death) and CD68 staining for tumor-infiltrating macrophages did not indicate any degree of tumor ablation at the tissue level, as shown in Supplemental Figures 6C and 6D. Because of the nontumorigenic nature of MCF10A cells, tumor induction was not possible for this model.

DISCUSSION

TNBC is an aggressive cancer that lacks estrogen, progesterone, and human epidermal growth factor receptor 2 receptors and therefore cannot be treated with targeted hormone therapies or anti–human epidermal growth factor receptor 2 agents (*19*). As a result, conventional always-on chemotherapy remains the only effective systemic treatment available for these patients. Recent studies have reported that approximately 35% of TNBC patients have shown expression of membrane AR (*20*). Although the role of AR in TNBC is an area of active research, there is evidence that this cancer subset may respond to therapeutic targeting of AR (*21*). Bicalutamide functions by blocking and inhibiting AR and is widely used in the treatment of prostate cancer subtypes that overexpress AR (*22*). However, clinical trials with bicalutamide and other antiandrogen drugs in TNBC have shown limited efficacy, with about a 19% clinical benefit rate (*21*). Therefore, we hypothesized that bicalutamide-activated cytotoxic enhancement of ^{18}F-FDG would improve the outcomes of the combination treatment in TNBC and provide spatiotemporal modulation of therapy as well. This hypothesis is supported by the influence that AR activity has on cell cycle checkpoint inhibition and the DNA damage repair pathway (*23,24*). Prior research has also demonstrated that antiandrogen drugs that block AR activity confer radiosensitivity to traditionally radioresistant AR-positive TNBC cell lines by significantly impairing resolution of double-stranded DNA breaks (*17*). Although TNBCs are chemosensitive, they metastasize rapidly and are characterized by poor prognosis and few therapeutic options. Therefore, use of radionuclides, in contrast to external-beam radiation, extends the in vivo reach to trigger therapeutic events in niches where metastatic cancer cells tend to localize, such as bone marrow and lungs.

Although both targeted hormonal therapy and radiosensitizing roles for bicalutamide would be highly desired in a clinical setting, for our proof-of-concept studies we sought the effective separation of both these properties in order to evaluate the singular role of
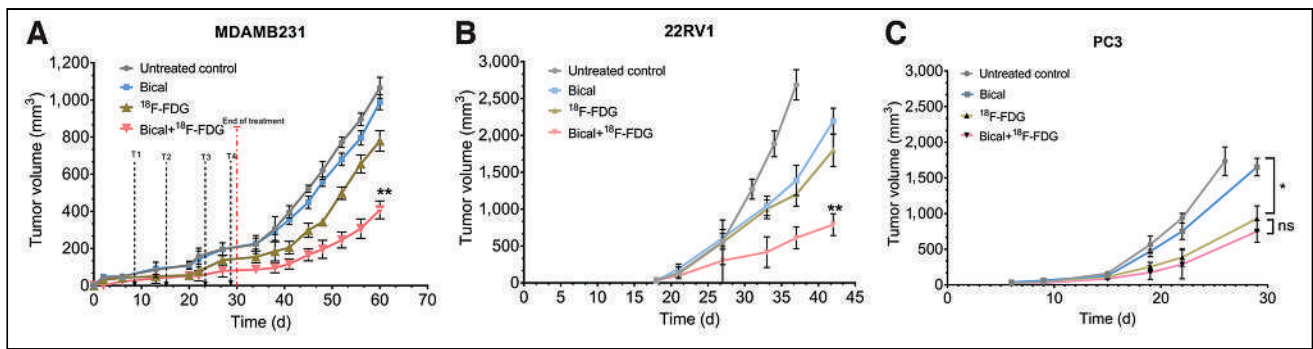
FIGURE 6. Tumor growth demonstrating therapeutic efficacy of combined treatment of bicalutamide-^{18}F-FDG in athymic nude xenograft tumor model induced with subcutaneous MDAMB231 cancer cells (A), 22RV1 cancer cells (B), or PC3 cancer cells (C). $n = 5$/group. *$P < 0.01$. **$P < 0.001$. Bical = bicalutamide.

bicalutamide as a radiosensitizer. In vitro studies revealed that a subcytotoxic dose of bicalutamide in combination with ^{18}F-FDG inhibited cell proliferation, induced double-stranded DNA breaks, and caused cell cycle arrest at the G_2/M phase, leading to apoptotic cell death. Therefore, we can infer that bicalutamide is a potent radiosensitizer because it selectively inhibits DNA damage repair of AR-positive cells caused by ^{18}F-FDG.

Previous reports have shown that apoptosis accounts for approximately only 20% of radiation-induced cell death (25). Therefore, we explored other cell death pathways, such as autophagy, to determine whether multiple pathways are involved in inducing cell death. We observed significant cell death through autophagy, implicating the role of endoplasmic reticulum stress and aberrant protein in the formation of autophagosomes. Although there is still no consensus on attributing specific mechanisms that link radiation and autophagy, there is some evidence that double-stranded DNA breaks may induce endoplasmic reticulum stress (26). The enhanced therapeutic efficacy of the combination treatment in TNBC cells appears to contribute significantly to both the autophagy and the apoptosis cell death pathways.

In vivo therapy studies on AR-positive TNBC and 22RV1 mouse models showed significant attenuation of tumor growth and enhanced therapeutic efficacy in mice treated with bicalutamide-^{18}F-FDG compared with control groups. The therapeutic effect of bicalutamide alone was minimal, as can be attributed to the subtherapeutic concentration used for these studies. However, in an AR-negative PC3 mouse model, we observed no significant attenuation of tumor growth, supporting the critical role bicalutamide plays in radiosensitizing AR-positive tumors to radiation-induced damage from ^{18}F-FDG. Further studies are needed to elucidate the mechanism of enhanced therapeutic efficacy—synergistic versus additive—before translation of this strategy can potentially be realized.

With ^{18}F-FDG, we avoided using an excessively high or nondiagnostic imaging activity, not only to demonstrate the efficiency of bicalutamide as a radiosensitizer in reducing the threshold for radiation damage but also to allay any concerns about potential toxicity during scale-up for translational studies, in which higher activities of ^{18}F-FDG might be deemed unrealistic for use in humans (10). However, additional studies are needed to understand the dosage expectancy of ^{18}F-FDG for potential clinical translation. Gross morphologic analysis, as well as hematoxylin and eosin analysis of major organs, did not reveal any off-target toxicity from treatment. Indeed, further studies are required to estimate absorbed dose in normal organs and collect additional evidence to confirm the absence of off-target toxicity in various vital organs such as brain and bone marrow.

CONCLUSION

We have demonstrated the sensitivity of AR-positive cancer to radiation damage using the diagnostic radiopharmaceutical ^{18}F-FDG in conjunction with bicalutamide, an antiandrogen that serves as a targeted radiosensitizer. These findings open opportunities to investigate other antiandrogens and radionuclides, as synergistic pairs, to enhance therapeutic outcomes. Given the wide range of radionuclides available, studies exploring the mixed radiation emissions and interaction with drugs to identify synergistic enhancement of cell killing would be intriguing.

DISCLOSURE

ACKNOWLEDGMENTS

KEY POINTS

QUESTION: Can antiandrogen hormonal therapy radiosensitize AR-positive cancers to ^{18}F-FDG?

PERTINENT FINDINGS: We observed a significant attenuation, 2-fold, of tumor growth in AR-positive compared with AR-negative cancers.

IMPLICATIONS FOR PATIENT CARE: We envisage that this strategy will benefit AR-positive cancer patients with metastasis by providing an effective image-guided targeted therapy with minimal side effects.

REFERENCES

1. Apisarnthanarax S, Dhruva N, Ardeshirpour F, et al. Concomitant radiotherapy and chemotherapy for high-risk nonmelanoma skin carcinomas of the head and neck. *Int J Surg Oncol.* 2011;2011:464829.

2. Glatzer M, Elicin O, Ramella S, Nestle U, Putora PM. Radio(chemo)therapy in locally advanced nonsmall cell lung cancer. *Eur Respir Rev.* 2016;25:65–70.

3. Calais G, Alfonsi M, Bardet E, et al. Randomized trial of radiation therapy versus concomitant chemotherapy and radiation therapy for advanced-stage oropharynx carcinoma. *J Natl Cancer Inst.* 1999;91:2081–2086.

4. Dicker AP, Williams TL, Iliakis G, Grant DS. Targeting angiogenic processes by combination low-dose paclitaxel and radiation therapy. *Am J Clin Oncol.* 2003;26: e45–e53.

5. Niyazi M, Maihoefer C, Krause M, Rodel C, Budach W, Belka C. Radiotherapy and "new" drugs: new side effects? *Radiat Oncol.* 2011;6:177.

6. Kotagiri N, Sudlow GP, Akers WJ, Achilefu S. Breaking the depth dependency of phototherapy with Cerenkov radiation and low-radiance-responsive nanophotosensitizers. *Nat Nanotechnol.* 2015;10:370–379.

7. Kotagiri N, Cooper ML, Rettig M, et al. Radionuclides transform chemotherapeutics into phototherapeutics for precise treatment of disseminated cancer. *Nat Commun.* 2018;9:275.

8. Randall ME, Filiaci V, McMeekin DS, et al. Phase III trial: adjuvant pelvic radiation therapy versus vaginal brachytherapy plus paclitaxel/carboplatin in high-intermediate and high-risk early stage endometrial cancer. *J Clin Oncol.* 2019;37:1810–1818.

9. Pratt EC, Shaffer TM, Zhang Q, Drain CM, Grimm J. Nanoparticles as multimodal photon transducers of ionizing radiation. *Nat Nanotechnol.* 2018;13:418–426.

10. Taylor K, Lemon JA, Boreham DR. Radiation-induced DNA damage and the relative biological effectiveness of ^{18}F-FDG in wild-type mice. *Mutagenesis.* 2014;29: 279–287.

11. Miolo G, Marzano C, Gandin V, et al. Photoreactivity of 5-fluorouracil under UVB light: photolysis and cytotoxicity studies. *Chem Res Toxicol.* 2011;24:1319–1326.

12. Dorr RT, Alberts DS, Einspahr J, Mason-Liddil N, Soble M. Experimental dacarbazine antitumor activity and skin toxicity in relation to light exposure and pharmacologic antidotes. *Cancer Treat Rep.* 1987;71:267–272.

13. Yokote R, Tokura Y, Igarashi N, Ishikawa O, Miyachi Y. Photosensitive drug eruption induced by flutamide. *Eur J Dermatol.* 1998;8:427–429.

14. Lee K, Oda Y, Sakaguchi M, Yamamoto A, Nishigori C. Drug-induced photosensitivity to bicalutamide: case report and review of the literature. *Photodermatol Photoimmunol Photomed.* 2016;32:161–164.

15. Sortino S, Giuffrida S, De Guidi G, et al. The photochemistry of flutamide and its inclusion complex with beta-cyclodextrin: dramatic effect of the microenvironment on the nature and on the efficiency of the photodegradation pathways. *Photochem Photobiol.* 2001;73:6–13.

16. Sasada K, Sakabe J, Tamura A, et al. Photosensitive drug eruption induced by bicalutamide within the UVB action spectrum. *Eur J Dermatol.* 2012;22:402–403.

17. Speers C, Zhao SG, Chandler B, et al. Androgen receptor as a mediator and biomarker of radioresistance in triple-negative breast cancer. *NPJ Breast Cancer.* 2017;3:29.

18. Zois CE, Koukourakis MI. Radiation-induced autophagy in normal and cancer cells: towards novel cytoprotection and radio-sensitization policies? *Autophagy.* 2009;5:442–450.

19. Schneider BP, Winer EP, Foulkes WD, et al. Triple-negative breast cancer: risk factors to potential targets. *Clin Cancer Res.* 2008;14:8010–8018.

20. Park S, Koo J, Park HS, et al. Expression of androgen receptors in primary breast cancer. *Ann Oncol.* 2010;21:488–492.

21. Gucalp A, Tolaney S, Isakoff SJ, et al. Phase II trial of bicalutamide in patients with androgen receptor-positive, estrogen receptor-negative metastatic breast cancer. *Clin Cancer Res.* 2013;19:5505–5512.

22. Labrie F, Bélanger A, Luu-The V, et al. Gonadotropin-releasing hormone agonists in the treatment of prostate cancer. *Endocr Rev.* 2005;26:361–379.

23. Goodwin JF, Schiewer MJ, Dean JL, et al. A hormone-DNA repair circuit governs the response to genotoxic insult. *Cancer Discov.* 2013;3:1254–1271.

24. Polkinghorn WR, Parker JS, Lee MX, et al. Androgen receptor signaling regulates DNA repair in prostate cancers. *Cancer Discov.* 2013;3:1245–1253.

25. Verheij M, Bartelink H. Radiation-induced apoptosis. *Cell Tissue Res.* 2000;301: 133–142.

26. He L, Kim SO, Kwon O, et al. ATM blocks tunicamycin-induced endoplasmic reticulum stress. *FEBS Lett.* 2009;583:903–908.

Predictors of ^{18}F-DCFPyL PET/CT Positivity in Patients with Biochemical Recurrence of Prostate Cancer After Local Therapy

Esther Mena[1], Steven P. Rowe[2], Joanna H. Shih[3], Liza Lindenberg[1], Baris Turkbey[1], Aloyse Fourquet[1], Frank I. Lin[1], Stephen Adler[4], Philip Eclarinal[1], Yolanda L. McKinney[1], Deborah E. Citrin[5], William Dahut[6], Bradford J. Wood[7], Richard Chang[7], Elliot Levy[7], Maria Merino[8], Michael A. Gorin[9], Martin G. Pomper[2], Peter A. Pinto[10], Janet F. Eary[11], Peter L. Choyke[1], and Kenneth J. Pienta[9]

[1]Molecular Imaging Branch, National Cancer Institute, National Institutes of Health, Bethesda, Maryland; [2]Russell H. Morgan Department of Radiology and Radiological Science, Johns Hopkins University School of Medicine, Baltimore, Maryland; [3]Division of Cancer Treatment and Diagnosis: Biometric Research Program, National Cancer Institute, National Institutes of Health, Bethesda, Maryland; [4]Clinical Research Directorate, Frederick National Laboratory for Cancer Research, Frederick, Maryland; [5]Radiation Oncology Branch, National Cancer Institute, National Institutes of Health, Bethesda, Maryland; [6]Genitourinary Malignancies Branch, National Cancer Institute, National Institutes of Health, Bethesda, Maryland; [7]Center of Interventional Oncology, National Cancer Institute, National Institutes of Health, Bethesda, Maryland; [8]Laboratory of Pathology, National Cancer Institute, National Institutes of Health, Bethesda, Maryland; [9]James Buchanan Brady Urological Institute and Department of Urology, Johns Hopkins University School of Medicine, Baltimore, Maryland; [10]Urologic Oncology Branch, National Cancer Institute, National Institutes of Health, Bethesda, Maryland; and [11]Cancer Imaging Program, National Cancer Institute, National Institutes of Health, Bethesda, Maryland

Our objective was to investigate the factors predicting scan positivity and disease location in patients with biochemical recurrence (BCR) of prostate cancer (PCa) after primary local therapy using prostate-specific membrane antigen–targeted ^{18}F-DCFPyL PET/CT. **Methods:** This was a 2-institution study including 245 BCR PCa patients after primary local therapy and negative results on conventional imaging. The patients underwent ^{18}F-DCFPyL PET/CT. We tested for correlations of lesion detection rate and disease location with tumor characteristics, time from initial therapy, prostate-specific antigen (PSA) level, and PSA doubling time (PSAdt). Multivariate logistic regression analyses were used to determine predictors of a positive scan. Regression-based coefficients were used to develop nomograms predicting scan positivity and extrapelvic disease. **Results:** Overall, 79.2% (194/245) of patients had a positive ^{18}F-DCFPyL PET/CT result, with detection rates of 48.2% (27/56), 74.3% (26/35), 84% (37/44), 96.7% (59/61), and 91.8% (45/49) for PSAs of <0.5, 0.5 to <1.0, 1.0 to <2.0, 2.0 to <5.0, and ≥5.0 ng/mL, respectively. Patients with lesions confined to the pelvis had lower PSAs than those with distant sites (1.6 ± 3.5 vs. 3.0 ± 6.3 ng/mL, $P < 0.001$). In patients treated with prostatectomy ($n = 195$), 24.1% (47/195) had a negative scan result, 46.1% (90/195) showed intrapelvic disease, and 29.7% (58/195) showed extrapelvic disease. In the postradiation subgroup ($n = 50$), ^{18}F-DCFPyL PET/CT was always negative at a PSA lower than 1.0 ng/mL and extrapelvic disease was seen only when PSA was greater than 2.0 ng/mL. At multivariate analysis, PSA and PSAdt were independent predictive factors of scan positivity and the presence of extrapelvic disease in postsurgical patients, with area under the curve of 78% and 76%, respectively. PSA and PSAdt were independent predictors of the presence of extrapelvic disease in the postradiation cohort, with area under the curve of 85%. Time from treatment to scan was significantly longer for prostatectomy-bed–only recurrences than for those with bone or visceral disease (6.2 ± 6.4 vs. 2.4 ± 1.3 y, $P < 0.001$). **Conclusion:** ^{18}F-DCFPyL PET/CT offers high detection rates in BCR PCa patients. PSA and PSAdt are able to predict scan positivity and disease location. Furthermore, the presence of bone or visceral lesions is associated with shorter intervals from treatment than are prostate-bed–only recurrences. These tools might guide clinicians to select the most suitable candidates for ^{18}F-DCFPyL PET/CT imaging.

Key Words: prostate cancer; biochemical recurrence; PSMA; ^{18}F-DCFPyL; PET

Patients with localized prostate cancer (PCa) are usually treated with either radical prostatectomy, some variation of external-beam radiation, brachytherapy, or active surveillance (*1,2*). Despite definitive therapy with either surgery or radiation, approximately 20%–40% of cases will recur within 10 y of the initial treatment (*3*). Biochemical recurrence (BCR) occurs when prostate-specific antigen (PSA) increases during posttreatment monitoring, often without positive findings on conventional imaging, and can be seen months or years after the initial local therapy (*4*).

In the setting of BCR, understanding the specific sites of relapse and the patterns of recurrence improves understanding of the disease process. Local recurrence alone is usually associated with a better prognosis and slower disease kinetics, whereas nodal, bone, or visceral metastases imply a more aggressive phenotype that carries a worse prognosis. Defining the extent of disease spread with imaging can be crucial for therapeutic decision making and mapping potential treatment fields in PCa patients. The lack of sensitivity of conventional imaging (*5*) has limited the understanding of disease spread in BCR. With the advent of positron-emitting (PET) probes targeting prostate-specific membrane antigen (PSMA), molecular

imaging has yielded new insights into PCa recurrence (6), with improved sensitivity and specificity that far exceed conventional imaging and earlier types of PET agents (7). ^{18}F-DCFPyL is a recent U.S. Food and Drug Administration–approved PSMA PET agent with high affinity for PCa (8,9).

Men with recurrent disease are a highly heterogeneous population, carrying different profiles of disease aggressiveness; therefore, selecting the most suitable candidates for imaging with ^{18}F-DCFPyL PET/CT might be critical to optimize its use and to spare lower-risk patients from potentially unnecessary staging procedures. We report the results of ^{18}F-DCFPyL PET/CT in a cohort of 245 BCR PCa patients from 2 institutions. We hypothesized that patients' clinical features, including time from initial treatment, PSA level, and PSA doubling time (PSAdt), might predict the location and extent of disease. We also sought to develop clinical nomograms to assess the likelihood of each patient to have a positive scan and extrapelvic disease, using Gleason score, PSA, and PSAdt as predictive variables, in different settings based on primary initial therapy.

MATERIALS AND METHODS

Patient Population and Study Design

This study included 2 institutional trials compliant with the Health Insurance Portability and Accountability Act. Institutional review boards approved the studies, and all subjects gave written informed consent. We included 245 patients who met the eligibility criteria for protocols NCT03181867 and NCT02825875 (ClinicalTrials.gov): 147 from the National Cancer Institute and 98 from Johns Hopkins Hospital. A cohort of 90 of these patients was previously published (10). Patients had BCR, defined as a PSA of more than 0.2 ng/mL for those who underwent radical prostatectomy or at least 2 ng/mL greater than nadir after radiation (American Society for Radiation Oncology–Phoenix criteria) or considered clinical failure (11). Patients had negative conventional-imaging results (CT and bone scans). Exclusion criteria included current androgen deprivation therapy at enrollment; inability to tolerate PET/CT, and a creatinine level at least 2 times the normal upper limit. Patients were classified by prior initial treatment (prostatectomy vs. radiation). Time from treatment to scan, Gleason score, PSA level, and PSAdt were recorded.

^{18}F-DCFPyL PET/CT Protocol

^{18}F-DCFPyL PET/CT was performed at 2 h after injection using a GE Healthcare Discovery MI DR time-of-flight camera (National Cancer Institute) and at 1 h using a GE Healthcare Discovery RX or a Siemens Biograph mCT time-of-flight camera (Johns Hopkins Hospital). Scanners used low-dose CT (120 kV, 60 mAs). Images were reconstructed with manufacturer-supplied maximum-likelihood or ordered-subsets expectation maximization algorithms.

^{18}F-DCFPyL was synthesized under good-manufacturing-practice conditions, as previously described (8). Patients received an intravenous injection of ^{18}F-DCFPyL (mean injected activity, 296 ± 33.3 MBq [8.0 ± 0.9 mCi]; range, 207.2–325.6 MBq [5.6–8.8 mCi]), followed by whole-body PET/CT at 1–2 h after injection (3 min/bed). Furosemide was not given. Patients were monitored for adverse events during injection, after scanning, and the next day via telephone query.

Imaging Interpretation

Two board-certified nuclear medicine physicians in each institution independently reviewed the images, resolving disagreements by consensus. ^{18}F-DCFPyL PET/CT images were reviewed using MIM (version 6.9.2, MIM Software Inc.) or SyngoVia-20 (Siemens Healthineers). Maximum-intensity-projection, axial, coronal, and sagittal PET/CT images were reviewed. Only clear foci of abnormal uptake above the surrounding background (12), not associated with physiologic uptake or known pitfalls (13), were considered positive. Foci with subtle or very mild uptake not definitive for disease were called indeterminate and considered negative to avoid confusing results. PET-positive lesions in the prostatectomy region/prostate, pelvic/extrapelvic nodes, or organ/bone were classified as recurrence.

Statistical Methods

^{18}F-DCFPyL PET lesion detection rates were analyzed as a function of PSA. Scan positivity was evaluated by stratifying PSA at ranges of <0.5, 0.5 to <1.0, 1.0 to <2.0, 2.0 to <5.0, and ≥5.0 ng/mL. Sites of recurrence by ^{18}F-DCFPyL PET were tested for correlation with PSA, PSAdt, and time from local treatment, using Wilcoxon rank tests. Subgroup analysis was conducted by treatment type (prostatectomy vs. radiation). Patients were categorized as having a Gleason of less than 7 versus 7 or more and as having oligometastases (1–5 lesions) versus multiple metastases (>5 lesions). Descriptive values were expressed as mean ± SD.

The proportional-odds model was used to associate clinical factors with scan results, classifying scans as negative, positive with intrapelvic disease, or positive with extrapelvic disease. Clinical factors included Gleason score, PSA, PSAdt, years since treatment, and treatment type (surgery vs. radiation). Analyses were exploratory; thus, adjustment for multiple comparisons were not implemented. A variable-selection procedure based on the Akaike information criterion was used to determine the best fitted model. Model fit was examined by a calibration plot of the predicted versus observed probability of a positive scan and the presence of extrapelvic disease, calculating observations in each decile of predicted probability. The diagnostic accuracy of the predicted model was measured by area under the curve. Nomograms were generated using the R-package rms (14). All tests were 2-sided, and P values of less than 0.01 were considered significant. Statistical analyses were performed using R, version 3.5.0.

RESULTS

Patient Population

In total, 245 patients (mean age, 66 y; range, 48–85 y) underwent ^{18}F-DCFPyL PET/CT. Median PSA was 1.6 ng/mL (range, 0.2–35.5 ng/mL). Prior primary local therapy consisted of radical prostatectomy (n = 195) or radiation with or without androgen deprivation therapy (n = 50). Patients were not actively receiving androgen deprivation therapy at imaging. The mean time from prostatectomy to scan was 6.1 ± 5.1 y (range, 1.5 mo–23.8 y), and the mean time from radiation was 4.9 ± 3.6 y (range, 9 mo–14.9 y). No adverse events were seen after ^{18}F-DCFPyL injection. Table 1 shows the patient characteristics.

^{18}F-DCFPyL PET/CT Versus PSA

Overall, the patient-based lesion detection rate for ^{18}F-DCFPyL PET/CT was 79.2% (194/245), which increased as PSA increased: 48.2% (27/56), 74.3% (26/35), 84% (37/44), 96.7% (59/61), and 91.8% (45/49) at PSA < 0.5, 0.5 to <1.0, 1.0 to <2.0, 2.0 to <5.0, and ≥5.0 ng/mL, respectively (Fig. 1). Detailed analysis by cohort and institution is reported at Supplemental Tables 1–3 (supplemental materials are available at http://jnm.snmjournals.org). No differences were seen in lesion detection between institutions. Of 51 cases with negative scan results, 13 showed indeterminate findings, with 17 indeterminate foci.

Patients with positive pelvic findings had a significantly lower PSA than those with positive extrapelvic lesions (i.e., retroperitoneal, distant nodes, or bone or visceral sites) (2.8 ± 3.5 vs. 5.0 ± 6.3 ng/mL, P < 0.001), suggesting that pelvic nodes may precede extrapelvic adenopathy. At a PSA of less than 2.0 ng/mL,

TABLE 1
Patient Characteristics

Characteristic	Data
No. of patients	245
Primary local therapy	
Radical prostatectomy $\pm$ radiation therapy $\pm$ androgen deprivation therapy	195
Radiation therapy $\pm$ androgen deprivation therapy	50
Mean age (y)	66 (48–85)
Primary Gleason score	
≤ 6	39
7	120
≥ 8	86
Median PSA (ng/mL)	1.6 (0.2–35.5)
Median PSAdt (mo)	6.8 (0.9–75.2)

Qualitative data are number; continuous data are mean or median and range.

FIGURE 2. ^{18}F-DCFPyL–positive sites by location and PSA. RP = radical prostatectomy.

^{18}F-DCFPyL PET/CT detected a higher proportion of patients with localized pelvic disease, whereas the proportion of patients with extrapelvic lesions was higher than that with intrapelvic lesions for a PSA of more than 5 ng/mL (Fig. 2).

Impact of Time from Local Treatment

The time from prior therapy (prostatectomy vs. radiation) and disease location were evaluated. In the prostatectomy cohort ($n = 195$), time from treatment to scan was longer for men with findings at the prostatectomy bed only than for those with only bone or visceral lesions or for those with nodal lesions (7.4 $\pm$ 6.3 vs. 2.3 $\pm$ 1.3 vs. 3.1 $\pm$ 4.1 y, $P < 0.001$). When findings were confined to the prostatectomy bed, 53.8% of patients were treated less than 8 y before the

FIGURE 1. ^{18}F-DCFPyL PET overall, intrapelvic, and extrapelvic detection rates by PSA.

scan, and 46.1% had prostatectomies performed more than 8 y before the scan. For patients with extraprostatic extension, 75.5% were treated less than 8 y before the scan, and 24.5% were treated more than 8 y before the scan. Thus, ^{18}F-DCFPyL PET/CT–positive nodal findings, bone-plus-nodal disease, bone-only disease, or visceral lesions were seen mostly when initial treatment was less than 8 y beforehand in 79.7%, 88.9%, 100.0%, and 100.0% of cases, respectively (Fig. 3A). The same patterns of disease distribution versus time from initial therapy were seen in a separate analysis by institution. Figure 4 and Supplemental Figure 1 show disease patterns versus time from prostatectomy by PSA and PSAdt. There were no differences in the distribution of times from prostatectomy between patients with oligometastases and those with multiple disease (4.8 $\pm$ 3.8 vs. 5.3 $\pm$ 5.7 y, $P = 0.054$).

In the postradiation cohort ($n = 50$), men with prostate involvement showed significantly longer times from radiation than subjects with bone or visceral lesions (6.7 $\pm$ 4.1 vs. 2.6 $\pm$ 2.8 y) (Fig. 3B). Significantly longer times from radiation were seen in men with pelvic findings only than in men with extrapelvic lesions, with median times of 6.4 $\pm$ 3.7 versus 2.9 $\pm$ 2.8 y. When recurrence was exclusively within the prostate, 38.9% of patients were initially treated more than 8 y before the scan, and 61.1% had radiation less than 8 y before the scan. For positive extraprostatic extension, most patients (93.3%) were treated less than 8 y beforehand. No differences were seen in times from radiation between patients with oligometastases and patients with multiple lesions (3.6 $\pm$ 3.1 vs. 2.9 $\pm$ 2.6 y, $P = 0.66$).

Impact of Clinical Features on Scan Positivity

In the cohort treated with radical prostatectomy ($n = 195$), 75.9% (148/195) showed at least 1 positive lesion (Fig. 5). Lesions confined to the pelvis were seen in 46.2% (90/195) of patients, especially driven by local recurrence at the prostatectomy bed in 44.5% and pelvic nodes in 55.5%, whereas extrapelvic lesions
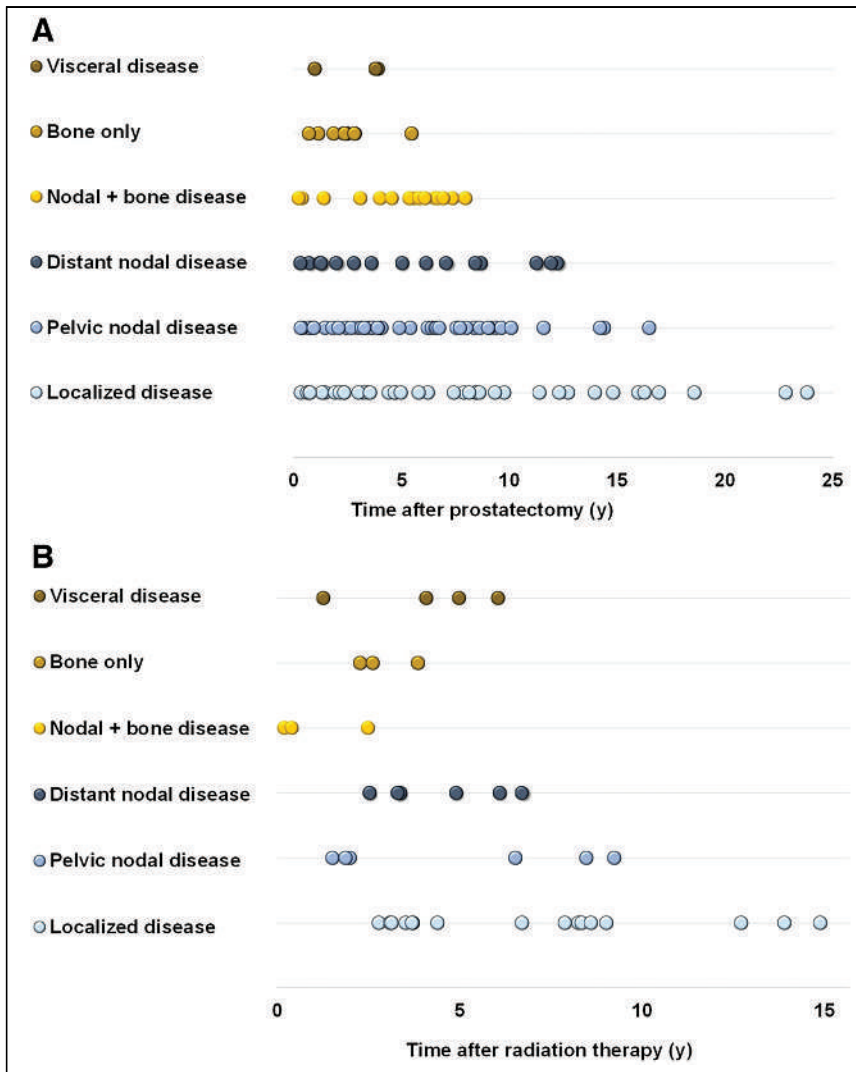
FIGURE 3. Disease location vs. time from prostatectomy (A) and radiation (B).
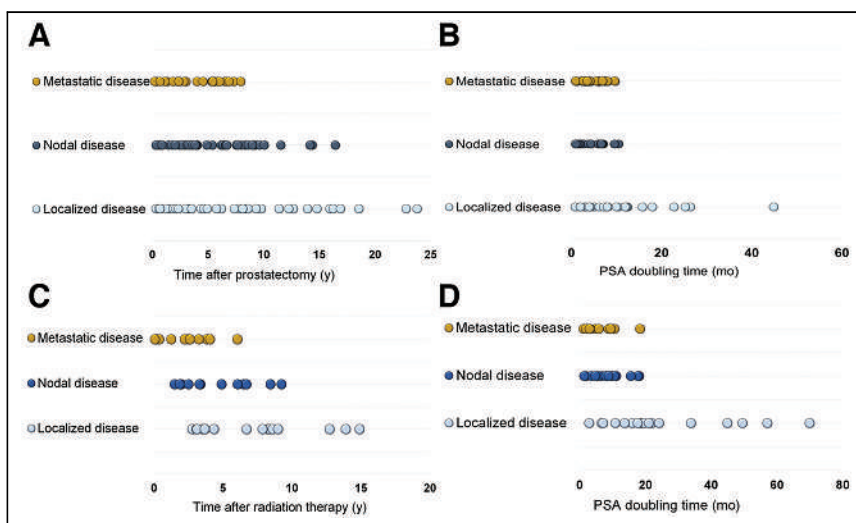
FIGURE 4. Patterns of recurrence vs. time from therapy and PSAdt in postprostatectomy (A and B) and postradiation patients (C and D).

were seen in 29.7% (58/195) of cases, often at a PSA of more than 5.0 ng/mL. PSAdt was significantly longer for patients with disease confined to the pelvis than for those with distant extrapelvic lesions (7.1 ± 8.6 vs. 5.7 ± 2.7 mo, $P < 0.001$).

In patients who received radiation ($n = 50$), only 8% (4/50) had a negative scan result, 48% showed intrapelvic disease (75% within the prostate and 25% in pelvic nodes), and 44% had extrapelvic findings (Fig. 6), and only when PSA was more than 2.0 ng/mL. Similarly, PSAdt was greater for patients with pelvic recurrences than for patients with extrapelvic lesions (17.2 ± 17.1 vs. 6.2 ± 5.7 mo, $P < 0.001$).

The multivariable regression analysis revealed that PSA, PSAdt, and Gleason score (≥ 7) were independent predictive factors of scan positivity and the presence of extrapelvic disease in postsurgical patients. In the postradiation cohort, PSA and PSAdt were independent predictors for the presence of extrapelvic disease. Multivariable derived coefficients were used to develop nomograms to predict the probability of having a positive scan result and extrapelvic disease. The nomogram based on prior therapy were built using Gleason score, PSA, and PSAdt as predictors (Fig. 7). In postsurgical patients, the area under the curve was 78% (95% CI, 68%–89%) for predicting scan positivity and 76% (95% CI, 67%–85%) for predicting extrapelvic disease. In the postradiation cohort, the area under the curve was 85% (95% CI, 71%–98%) for predicting extrapelvic disease. The number of patients having a negative scan was only 4; therefore, the prediction model for scan positivity was not considered for this cohort.

DISCUSSION

This study demonstrated that ^{18}F-DCFPyL PET/CT detects lesions in most BCR patients. Prostatectomy-bed–only recurrence is associated with the longest duration (mean, 7.4 y) from treatment, indicating the least aggressive disease trajectory. Pelvic nodal involvement is associated with a shorter duration (3.1 y) from treatment, implying a more aggressive trajectory, whereas bone and visceral involvement manifests even earlier (2.3 y) after prostatectomy. The postradiation cohort showed a similar pattern, where bone or visceral involvement was seen after a decreased duration from therapy, compared with prostate recurrences (2.6 vs. 6.7 y). We observed no differences in time from treatment between patients with oligometastases and patients with multiple lesions in
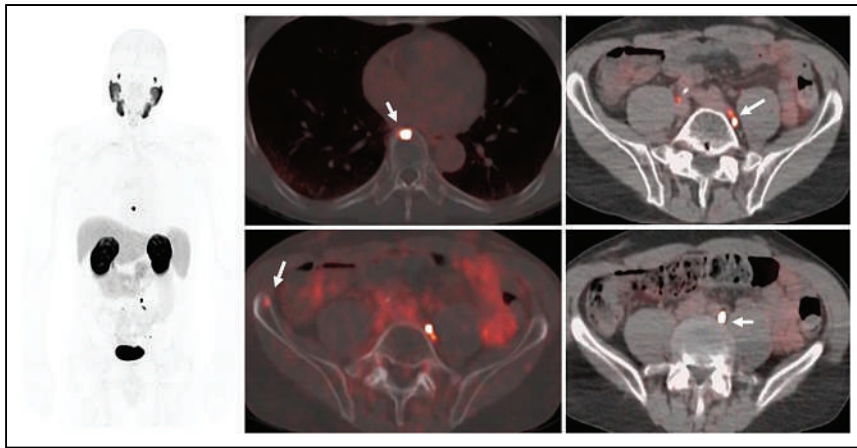
FIGURE 5. A 70-y-old patient with BCR PCa after radiation and 2 y of androgen deprivation therapy (primary tumor, T4N1; Gleason 4 + 5; time from treatment, 2.5 y; prescan PSA, 2.41 ng/mL; PSAdt, 4.7 mo). ^{18}F-DCFPyL PET/CT images including a maximal-intensity projection and axial fused PET/CT images show subcentimeter pelvic nodes (arrow in left iliac nodes) as well as foci at T9 (arrow) and anterior iliac bone (arrow). Follow-up biopsy confirmed bone metastasis at iliac bone.

different clinical settings, suggesting that oligometastatic disease may be an early form of an aggressive phenotype.

The likelihood of having a scan with extrapelvic lesions was determined in surgical and postradiation patients using nomograms. The most relevant predictors for scan positivity were PSA and PSAdt, in line with other studies. For instance, Rauscher et al. (15) proposed a nomogram to predict positive ^{68}Ga-PSMA-11 PET/CT results in BCR patients after prostatectomy with a PSA of no more than 1 ng/mL. In their analysis, PSA and concurrent androgen deprivation therapy were associated with scan positivity. Ceci et al. reported a nomogram with 82% accuracy, based on International
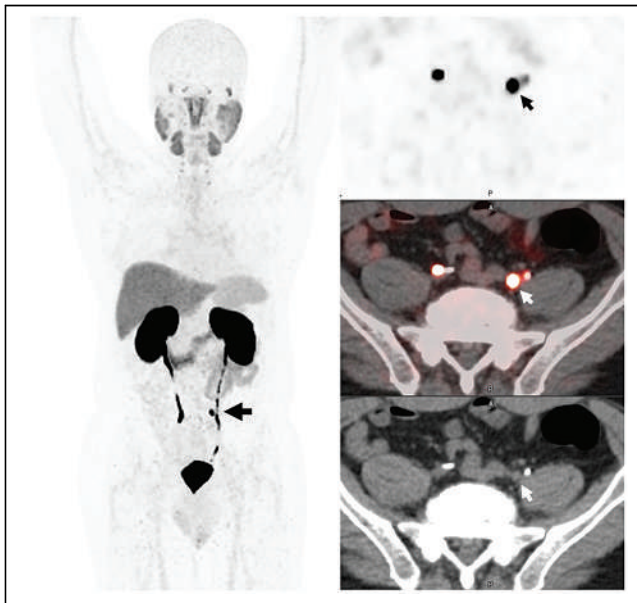
FIGURE 6. A 63-y-old patient with BCR PCa (primary tumor T3bN1, Gleason 4+5) who reached undetectable PSA after prostatectomy and 2 y of androgen deprivation therapy. PSA started to rise 5 y after initial treatment (PSA, 0.3 ng/mL; PSAdt, 3 mo). ^{18}F-DCFPyL PET/CT images including a maximal-intensity projection and axial views of PET, CT, and fused PET/CT demonstrate focal uptake in a 0.5 cm left common iliac node (arrows). This lesion was not biopsied.

Society of Urological Pathology grade, PSA, and PSAdt as predictors of scan positivity (16). Ma et al. explored predictors of overall upstaging (nodal and metastatic) by PSMA PET/CT, constructing a nomogram using PSA, percentage positive core biopsy, Gleason stage, and cT stage; the predictive model missed only 10% of patients who would have benefited from PSMA PET/CT (17).

PSA in the posttreatment setting is a reliable indicator of disease volume, and PSMA PET/CT demonstrates a relationship between PSA and extent of disease, with ascending percentages of positive scans with higher PSAs. PSAs of less than 1.0 ng/mL are associated with local recurrences and pelvic adenopathy, whereas the proportion of patients with extrapelvic nodal involvement rises with a PSA above 1.0 ng/mL. Bone and visceral metastases become a larger proportion of cases above 2.0 ng/mL. There is, however, considerable overlap in individual cases, as the rate of PSA production within tumors varies greatly. Thus, these data fit a general model of recurrent PCa that suggests several trajectories for disease. Slowly evolving recurrences tend to be confined to the prostate bed, whereas more aggressive tumors propagate to first the pelvic nodes and then the retroperitoneal nodes. More aggressive disease tends to rapidly involve bone and visceral organs. Although there is little doubt that tumors evolve over time, the rate at which this happens depends on the nature of the original tumor. This insight is uniquely provided by PSMA PET, as previously, disease could not be detected at this stage with conventional imaging.

The overall ^{18}F-DCFPyL PET/CT positivity rate was 79.2%, with a detection rate of 48.2% at a PSA of less than 0.5 ng/mL, in line with previous reports (10). The results are equivalent to those of Wondergem et al. (18) using ^{18}F-DCFPyL in 248 patients, identifying lesions in 59% of patients at a PSA of less than 0.5 ng/mL and in 96% at a PSA of more than 2.0 ng/mL. ^{18}F-PSMA-1007 PET/CT exhibited a higher detection rate of 62% in patients with low PSAs (0.2–0.5 ng/mL) but similar results to our series for a PSA of more than 0.5 ng/mL (19). One persistent finding across multiple studies using PSMA PET is that approximately one quarter of scans are negative, suggesting that these patients either do not express sufficient PSMA to be detected or lesions are simply too small to be identified; these cases are associated with low PSAs and likely represent the threshold for PET detection. Using PET/MRI may help to overcome this potential limited sensitivity for detection within the prostate fossa (20). On the other hand, high PSAs (>5.0 ng/mL) are also associated with negative scans; such tumors may represent less differentiated PCa variants or may express other surface markers that might be amenable to different targeted imaging agents. Moreover, disease within the prostate bed may be obscured by radiotracer excretion into the bladder. Other ^{18}F-PSMA ligands with low urinary excretion, ^{18}F-PSMA-1007 (21) and ^{18}F-rhPSMA (22), have shown higher local detection rates at low PSAs because the interpretation of lesions near the urinary bladder may be somewhat easier. Several groups proved that the use of diuretics increases detectability of local recurrence, with improved diagnostic certainty for lesions near the bladder and ureters (23,24), although forcing diuresis could be an issue for patients with urinary urgency and might require a longer waiting time for patients or additional scans.
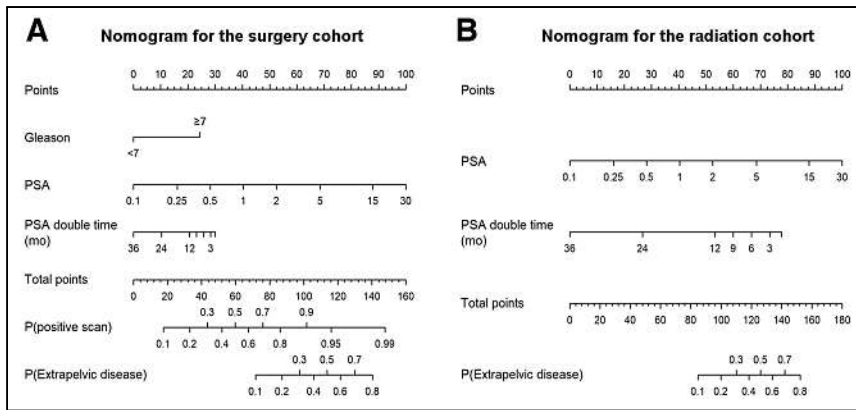
FIGURE 7. Nomogram predicting likelihood of ^{18}F-DCFPyL PET/CT positivity for different settings of BCR patients after prostatectomy (A) or radiation (B). Instructions were to locate patient's PSA value and draw straight line to points axis to determinate number of points toward probability of positive scan, to repeat this process for each variable and sum points for each predictor, and to locate final sum of points on total-point axis and draw line straight down to find probability (P) of having positive scan or having scan with extrapelvic lesions.

^{18}F-DCFPyL–positive pelvic lesions were present in 48% of subjects, whereas extrapelvic disease was found in 30%, almost exclusively when PSA was more than 1.0 ng/mL. This finding is consistent with the clinical experience that control rates with pelvic radiation therapy start to decline when PSA is more than 1 ng/m (25). This agrees with previous data (26,27) assessing the impact of PSMA PET on treatment decisions; patients with a low PSA and disease confined to the pelvis on PSMA PET might benefit from modifications to the plan for radiation treatment, whereas patients with extrapelvic lesions may require systemic therapy. In our cohort, at a PSA of more than 2.0 ng/mL, PSMA PET was almost always positive for recurrence, with distant disease seen in about 30% of prostatectomy patients and 45% of patients after radiation therapy. Furthermore, the presence of distant extrapelvic disease was significantly higher for patients with a rapid PSAdt in both postsurgical and postradiation cohorts, consistent with other prognostic indicators associated with PSAdt (28).

Interesting differences were seen between postsurgical and postradiation recurrences. Negative scan results in patients with a PSA of less than 0.5 ng/mL after surgery were seen in 24% of patients, whereas only 8% of postradiation scans were negative. Postradiation patients tended to show more local recurrences than did postsurgical patients. At a PSA of more than 2.0 ng/mL, recurrences after radiation tended to be extrapelvic, whereas this trend was less evident in postsurgical patients. The distribution of recurrences was somewhat different for postsurgical and postradiation patients. PSA thresholds for positive PSMA PET results were substantially higher in the postradiation cohort. When subjects were treated primarily with radiation, 36% showed positive prostate findings, whereas recurrences outside the prostate were seen in 56% of patients, similar to prior reports using ^{68}Ga-PSMA PET/CT (29).

There were limitations to this study. Perhaps most notably, despite use of ^{18}F-DCFPyL PET/CT at both institutions, the PET acquisition parameters (e.g., time from injection to imaging) varied between institutions. Although detection rates by PSA were overall similar between institutions scanning at 1 versus 2 h after injection, differences in detection rates regarding scan time cannot be addressed since individual patients were scanned at only 1 time point. Further, data harmonization relied on daily quality control

procedures using the standard operating procedure provided by the manufacture for each scanner. Such heterogeneity may have affected the results, although reflecting a real-world scenario that make the findings more broadly applicable, as ^{18}F-DCFPyL is recently Food and Drug Administration–approved. Further, findings were determined at each institution individually, followed by a combined analysis, which might lead to heterogeneity in the results but would recapitulate the use of the PSMA agent across centers. Another limitation is that no interreader variability (κ) is available for this study. Also, analyses were exploratory, and adjustments for multiple comparisons were not implemented. Lastly, at 1 institution, patients were accrued into a broader study of the utility of PSMA PET instead of a dedicated BCR study. As such, this study was not prospectively designed to meet a specific endpoint. Furthermore, the detection rate may differ from the true detection rate since histologic validation was not available for all positive sites. Unfortunately, this is a common problem in studies involving BCR patients, for whom findings are often subcentimeter, deep within the pelvis, often in unsafe locations, or otherwise not feasible to biopsy.

CONCLUSION

^{18}F-DCFPyL PET/CT successfully identifies sites of recurrence proportional to PSA levels when conventional imaging results are negative. ^{18}F-DCFPyL PET/CT demonstrates a high tumor detection rate even at a low PSA (<0.5 ng/mL). Disease recurrence tends to be confined to the pelvis in patients with lower PSAs, but at higher values there is visualization of disease outside the pelvis, particularly when PSA is more than 2.0 ng/mL and PSAdt is less than 6 mo. The presence of bone and visceral lesions was associated with a shorter time after initial treatment and higher PSAs than is the case with prostate-bed–only recurrences. Clinical nomograms proved that PSA and PSAdt were able to predict scan positivity and disease location in BCR patients. These tools might guide clinicians to select the most suitable candidates for PSMA PET.

As with other studies, PSMA PET is not positive in all BCR patients, and approximately 15%–20% have negative scans at low or high PSAs, likely for different reasons. Low-PSA false-negatives are likely due to subthreshold volumes of disease for detection, or overlapping with the urinary bladder within the pelvis, whereas high-PSA false-negatives are likely due to dedifferentiated tumors with low PSMA expression. ^{18}F-DCFPyL PET/CT detection efficacy is comparable to previously published results with ^{68}Ga-PSMA compounds and has logistic advantages because of its longer half-life. The general class of PSMA ligands is destined to significantly change management of BCR patients.

DISCLOSURE

KEY POINTS

QUESTION: Are there factors predicting PSMA PET disease location in BCR PCa patients?

PERTINENT FINDINGS: PSA and PSAdt are able to predict PSMA PET scan positivity and disease location. The presence of bone/visceral lesions is associated with shorter intervals from initial treatment than are prostate-bed–only recurrences.

IMPLICATIONS FOR PATIENT CARE: These tools might guide clinicians to select suitable candidates for ^{18}F-DCFPyL PET/CT.

REFERENCES

1. Mottet N, Bellmunt J, Bolla M, et al. EAU guidelines on prostate cancer. Part II: treatment of advanced, relapsing, and castration-resistant prostate cancer. *Eur Urol.* 2011;59:572–583.
2. Pfister D, Bolla M, Briganti A, et al. Early salvage radiotherapy following radical prostatectomy. *Eur Urol.* 2014;65:1034–1043.
3. Briganti A, Karnes RJ, Gandaglia G, et al. Natural history of surgically treated high-risk prostate cancer. *Urol Oncol.* 2015;33:163.e7–113.
4. Cookson MS, Aus G, Burnett AL, et al. Variation in the definition of biochemical recurrence in patients treated for localized prostate cancer: the American Urological Association Prostate Guidelines for Localized Prostate Cancer Update Panel report and recommendations for a standard in the reporting of surgical outcomes. *J Urol.* 2007;177:540–545.
5. Beer AJ, Eiber M, Souvatzoglou M, Schwaiger M, Krause BJ. Radionuclide and hybrid imaging of recurrent prostate cancer. *Lancet Oncol.* 2011;12:181–191.
6. Ghosh A, Heston WD. Tumor target prostate specific membrane antigen (PSMA) and its regulation in prostate cancer. *J Cell Biochem.* 2004;91:528–539.
7. Rowe SP, Macura KJ, Ciarallo A, et al. Comparison of prostate-specific membrane antigen-based ^{18}F-DCFBC-PET/CT to conventional imaging modalities for detection of hormone-naive and castration-resistant metastatic prostate cancer. *J Nucl Med.* 2016;57:46–53.
8. Szabo Z, Mena E, Rowe SP, et al. Initial evaluation of [^{18}F]DCFPyL for prostate-specific-membrane-antigen (PSMA)-targeted PET imaging of prostate cancer. *Mol Imaging Biol.* 2015;17:565–574.
9. Gorin MA, Rowe SP, Patel HD, et al. Prostate-specific-membrane-antigen targeted ^{18}F-DCFPyL-positron emission tomography/computerized tomography for the preoperative staging of high-risk prostate cancer: results of a prospective, phase II, single center study. *J Urol.* 2018;199:126–132.
10. Mena E, Lindenberg ML, Turkbey IB, et al. ^{18}F-DCFPyL-PET/CT imaging in patients with biochemically recurrent prostate cancer after primary local therapy. *J Nucl Med.* 2020;61:881–889.
11. Roach M III, Hanks G, Thames H Jr, et al. Defining biochemical failure following radiotherapy with or without hormonal therapy in men with clinically localized prostate cancer: recommendations of the RTOG-ASTRO Phoenix consensus conference. *Int J Radiat Oncol Biol Phys.* 2006;65:965–974.
12. Ceci F, Oprea-Lager DE, Emmett L, et al. E-PSMA: the EANM standardized reporting guidelines v1.0 for PSMA-PET. *Eur J Nucl Med Mol Imaging.* 2021;48: 1626–1638.
13. Sheikhbahaei S, Werner RA, Solnes LB, et al. Prostate-specific-membrane-antigen (PSMA)-targeted-PET imaging of prostate cancer: an update on important pitfalls. *Semin Nucl Med.* 2019;49:255–270.
14. Zhang Z, Kattan MW. Drawing nomograms with R: applications to categorical outcome and survival data. *Ann Transl Med.* 2017;5:211.
15. Rauscher I, Duwel C, Haller B, et al. Efficacy, predictive factors, and prediction nomograms for Ga-68-labeled prostate-specific-membrane-antigen-ligand positron-emission tomography/computed tomography in early biochemical recurrent prostate cancer after radical prostatectomy. *Eur Urol.* 2018;73:656–661.
16. Ceci F, Bianchi L, Borghesi M, et al. Prediction nomogram for ^{68}Ga-PSMA-11-PET/CT in different clinical settings of PSA failure after radical treatment for prostate cancer. *Eur J Nucl Med Mol Imaging.* 2020;47:136–146.
17. Ma TM, Gafita A, Shabsovich D, et al. Identifying the best candidates for prostate-specific membrane antigen positron emission tomography/computed tomography as the primary staging approach among men with high-risk prostate cancer and negative conventional imaging. *Eur Urol Oncol.* 2022;5:100–103.
18. Wondergem M, Jansen BHE, van der Zant FM, et al. Early lesion detection with ^{18}F-DCFPyL-PET/CT in 248 patients with biochemically recurrent prostate cancer. *Eur J Nucl Med Imaging.* 2019;46:1911–1918.
19. Giesel FL, Knorr K, Spohn F, et al. Detection efficacy of ^{18}F-PSMA-1007-PET/CT in 251 patients with biochemical recurrence of prostate cancer after radical prostatectomy. *J Nucl Med.* 2019;60:362–368.
20. Metser U, Chua S, Ho B, et al. The contribution of multiparametric pelvic and whole-body MRI to interpretation of ^{18}F-fluoromethylcholine or ^{68}Ga-HBED-CC-PSMA-11-PET/CT in patients with biochemical failure after radical prostatectomy. *J Nucl Med.* 2019;60:1253–1258.
21. Watabe T, Uemura M, Soeda F, et al. High detection rate in [^{18}F]PSMA-1007-PET: interim results focusing on biochemical recurrence in prostate cancer patients. *Ann Nucl Med.* 2021;35:523–528.
22. Rauscher I, Karimzadeh A, Schiller K, et al. Detection efficacy of ^{18}F-rhPSMA-7.3 PET/CT and impact on patient management in patients with biochemical recurrence of prostate cancer after radical prostatectomy and prior to potential salvage treatment. *J Nucl Med.* 2021;62:1719–1726.
23. Alberts I, Huenermund JN, Sachpekidis C, et al. Combination of forced diuresis with additional late imaging in ^{68}Ga-PSMA-11-PET/CT effects on lesion visibility and radiotracer uptake. *J Nucl Med.* 2021;62:1252–1257.
24. Uprimny C, Bayerschmidt S, Kroiss AS, et al. Early injection of furosemide increases detection rate of local recurrence in prostate cancer patients with biochemical recurrence referred for ^{68}Ga-PSMA-11-PET/CT. *J Nucl Med.* 2021;62: 1550–1557.
25. Valicenti RK, Thompson I Jr, Albertsen P, et al. Adjuvant and salvage radiation therapy after prostatectomy: American Society for Radiation Oncology/American Urological Association guidelines. *Int J Radiat Oncol Biol Phys.* 2013;86:822–828.
26. Calais J, Czernin J, Cao M, et al. ^{68}Ga-PSMA-11-PET/CT mapping of prostate cancer biochemical recurrence after radical prostatectomy in 270 patients with a PSA level of less than 1.0 ng/mL: impact on salvage radiotherapy planning. *J Nucl Med.* 2018;59:230–237.
27. Rousseau E, Wilson D, Lacroix-Poisson F, et al. A prospective study on ^{18}F-DCFPyL-PSMA PET imaging in biochemical recurrence prostate cancer. *J Nucl Med.* 2019;60:1587–1593.
28. Antonarakis ES, Chen Y, Elsamanoudi SI, et al. Long-term overall survival and metastasis-free survival for men with prostate-specific antigen-recurrent prostate cancer after prostatectomy: analysis of the center for prostate disease research national database. *BJU Int.* 2011;108:378–385.
29. Einspieler I, Rauscher I, Duwel C, et al. Detection efficacy of hybrid ^{68}Ga-PSMA-PET/CT in prostate cancer patients with biochemical recurrence after primary radiation therapy defined by Phoenix criteria. *J Nucl Med.* 2017;58:1081–1087.

68Ga-PSMA PET/CT for Response Assessment and Outcome Prediction in Metastatic Prostate Cancer Patients Treated with Taxane-Based Chemotherapy

Qaid Ahmed Shagera*[1], Carlos Artigas*[1], Ioannis Karfis[1], Gabriela Critchi[1], Nieves Martinez Chanza[2], Spyridon Sideris[2], Alexandre Peltier[3], Marianne Paesmans[4], Thierry Gil[2], and Patrick Flamen[1]

[1]Department of Nuclear Medicine, Institut Jules Bordet, Université Libre de Bruxelles, Brussels, Belgium; [2]Department of Oncology, Institut Jules Bordet, Université Libre de Bruxelles, Brussels, Belgium; [3]Department of Urology, Institut Jules Bordet, Université Libre de Bruxelles, Brussels, Belgium; and [4]Biostatistics Unit Data Centre, Institut Jules Bordet, Université Libre de Bruxelles, Brussels, Belgium

We aimed to evaluate the role of PET targeting the prostate-specific membrane antigen (PSMA) for response assessment in metastatic prostate cancer (PCa) patients treated with taxane-based chemotherapy (docetaxel or cabazitaxel) and its predictive value on patient outcome. **Methods:** We retrospectively evaluated 37 patients with metastatic hormone-sensitive PCa or metastatic castration-resistant PCa (mCRPC) who underwent 68Ga-PSMA-11 PET/CT at baseline and after the last cycle of taxane-based chemotherapy (docetaxel or cabazitaxel) without treatment modification between scans. Biochemical response (BR) was defined as an undetectable or at least 50% decreased level of prostate-specific antigen, compared with baseline. Associations between BR and different PET parameters were tested. A cutoff of at least a 30% decrease in PSMA total tumor volume (PSMA-TV) was used to define a PSMA response (PSMA-R) versus a PSMA nonresponse (PSMA-NR). Correlations between PSMA PET/CT response and BR were evaluated using the φ-coefficient. Associations between PET response and overall survival (OS) was tested using Cox regression and the Kaplan–Meier method. **Results:** Our cohort comprised 8 (22%) metastatic hormone-sensitive PCa and 29 (78%) mCRPC patients. Twenty-one patients received docetaxel treatment, and 16 received cabazitaxel (median, 6 cycles; interquartile range, 5–8 cycles). BR was found in 18 of 37 patients. Using PSMA total tumor volume, PSMA PET/CT response was concordant with BR in 35 of 37 patients (φ = 0.89, $P < 0.0001$). Eighteen of 37 patients had PSMA-R (6, complete response; 12, partial response), and 19 had PSMA-NR (17, progressive disease; 2, stable disease). After a median follow-up of 23 mo, there was a statistically significant longer OS for PSMA-R than for PSMA-NR (median OS not reached vs. 12 mo, respectively; hazard ratio, 0.10; 95% CI, 0.03–0.39; $P = 0.001$) for the entire population. Among the mCRPC subgroup, differences in OS were also observed (median, 22 vs. 12 mo, respectively; hazard ratio, 0.22; 95% CI, 0.06–0.82; $P = 0.023$), with a 12-mo OS rate of 100% for PSMA-R and 52% for PSMA-NR ($P = 0.011$). **Conclusion:** This retrospective analysis suggests that 68Ga-PSMA-11 PET/CT is a promising imaging modality for assessing response to taxane-based chemotherapy in metastatic PCa. Changes in PSMA expression might be used as a predictive biomarker for OS to help tailor individual therapy and select eligible patients for clinical trials.

Key Words: PSMA; PET/CT; prostate cancer; response; chemotherapy

Prostate cancer (PCa) is the most frequently diagnosed cancer in men in Europe and the United States and the second most common cancer globally (1). Multiple systemic therapies are available for the treatment of metastatic PCa (mPCa). Of them, taxane-based chemotherapies are among the most effective treatments that prolong overall survival (OS). Docetaxel is recommended in metastatic castration-resistant PCa (mCRPC) and metastatic hormone-sensitive PCa (mHSPC) (2,3) because it has shown survival benefit (4,5). However, most patients who receive docetaxel therapy will ultimately develop resistance. In this context, cabazitaxel has been recommended in most guidelines after showing survival benefits in mCRPC patients resistant to docetaxel (2,3,6).

In mPCa, the assessment of response to systemic therapies, including taxane-based chemotherapy, remains challenging and complex. In routine practice, the response assessment is based on clinical evaluation, serum prostate-specific antigen (PSA), and conventional imaging techniques such as bone scintigraphy and computed tomography (CT). All of them are retained in the Prostate Cancer Working Group (PCWG) criteria for response assessment in clinical trials (7). However, they present intrinsic limitations in evaluating response accurately: clinical evaluation remains under clinicians' and patients' subjectivity, serum PSA level does not provide data about the heterogeneity of response and is a nonuseful biomarker in non-PSA–secreting disease, and CT and bone scintigraphy cannot assess the response in bone lesions because of frequent sclerotic or osteoblastic reactions in responding patients (8). Bone scintigraphy can assess only disease progression using the so-called 2 + 2 criteria to avoid the flare phenomenon (7). The last criterion hampers identifying progression in early stages (7). Notably, continuation of a potentially toxic treatment in progressive disease (PD) may further deteriorate the clinical condition of the patient or prevent switching into a new, effective treatment such as prostate-specific membrane antigen (PSMA)–targeted radioligand therapy (9,10). Therefore, there is an unmet need to find a tool to evaluate, in a more timely and accurate manner, the response to chemotherapy in advanced mPCa.

The recent development of PCa imaging using a specific radiotracer targeting PSMA has improved the diagnostic accuracy in
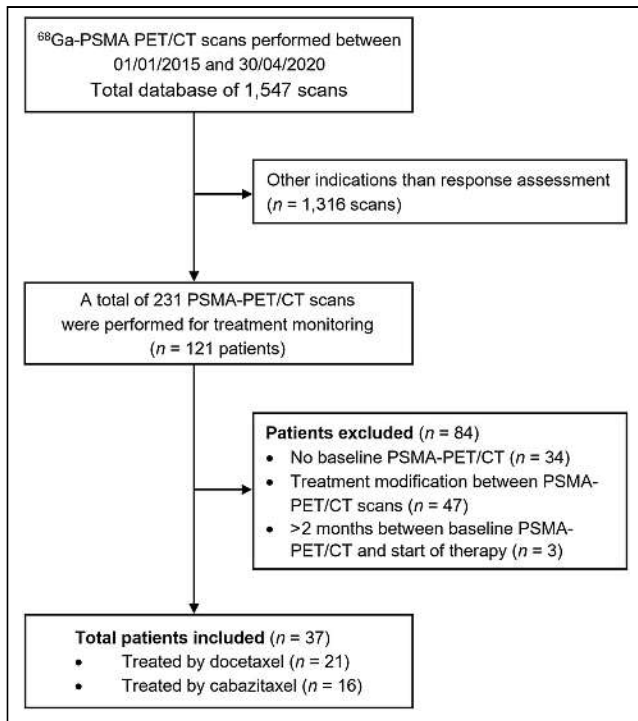
FIGURE 1. Flowchart of patient selection process.

MATERIALS AND METHODS

Patient Population

We retrospectively analyzed a database of all PSMA PET/CT scans obtained at our institution between January 2015 and May 2020 and selected all patients fulfilling the following criteria: histopathology-proven prostate adenocarcinoma, PSMA PET/CT performed within 2 mo before the start of taxane-based chemotherapy (docetaxel or cabazitaxel), and a second PSMA PET/CT scan up to 3 mo after the last cycle, without modification of treatment between scans (Fig. 1). In total, 37 patients were included in the final analysis. Baseline clinical characteristics, including hemoglobin level, alkaline phosphatase level, International Society of Urological Pathology grade group, and primary treatment, were recorded. All PSMA PET/CT scans were requested at the oncologist's discretion. Patients were classified as mHSPC or mCRPC on the basis of the testosterone level at the time of treatment (2). The study was designed in concordance with the Declaration of Helsinki and good clinical practice. The institutional review board and ethical committee approved the study (approval CE3212), and the requirement to obtain informed consent was waived because of its retrospective and descriptive design.

Imaging Protocol

All PSMA PET scanning was performed following our institution's standard operating procedure. Images were acquired 60 $\pm$ 3 min after injection of a 1.9 $\pm$ 0.3 MBq/kg dose of ^{68}Ga-PSMA-11 using a dedicated scanner (Discovery 690 time-of-flight; GE Healthcare). Images were acquired in 3-dimensional mode (2 min per bed

initial staging and in detection of recurrence. PSMA PET coupled to CT provides high-quality images thanks to its high tumor-to-background ratio, improving disease detection rates and significantly impacting patients' clinical management while being more cost-effective and causing less radiation exposure than conventional imaging techniques (11–13). Even if factors influencing PSMA expression levels are not well defined yet, it has been shown that a decrease in PSMA expression after exposure of PCa cells to taxane cytotoxic agents is due to a decrease in the number of viable cells and not to downregulation of PSMA receptor expression (14). Therefore, PSMA PET/CT might be used as an imaging tool to assess taxane chemotherapy cytotoxic effects. A role for PSMA PET/CT in response assessment has been found in previous studies showing promising results (15–21). However, these preliminary findings are still inconclusive because of the heterogeneous treatment modalities considered and the lack of outcome data. Also, there are limited literature data on the role of PSMA PET/CT in assessing response to taxane-based chemotherapy in mPCa, demanding further investigation. In this context, we aimed to investigate the role of ^{68}Ga-PSMA-11 PET/CT for response assessment in mPCa patients treated with taxane-based chemotherapy and its predictive value on patient outcome.
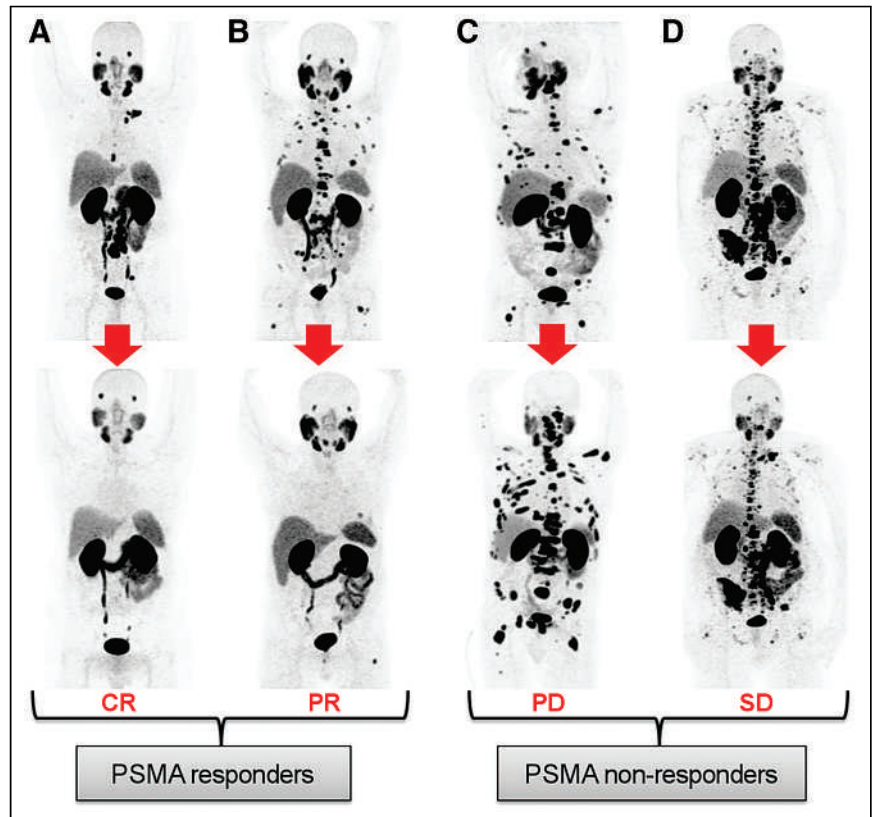
FIGURE 2. Maximum-intensity-projection images of different response scenarios on PSMA PET/CT. PSMA-R: including patients A and B with, respectively, disappearance of all PSMA-positive lesions (CR) or decrease of PSMA-TV > 30% (PR). PSMA-NR: including patients C and D with, respectively, appearance of new lesions and increased PSMA-TV > 30% (PD) or neither new PSMA-positive lesions nor PSMA-TV 30% changes. SD = stable disease.

position) from the middle of the thigh to the vertex. Ordered-subset expectation maximization (2 iterations and 24 subsets, gaussian filter of 6.8 mm in full width at half maximum) was used for image reconstruction. A low-dose CT scan (120 kVp) with no contrast iodine injection was used for attenuation correction and anatomic localization of lesions.

Image Analysis and Quantification

Pre- and posttreatment PSMA PET images were anonymized and stored on our institutional research server. Maximum-intensity projections and axial, sagittal, and coronal PET/CT images were evaluated on a dedicated workstation (AW Server, version 3.2; GE Healthcare). Two independent nuclear medicine physicians performed visual assessments without knowing any patient clinical data or outcomes. Any suggestive lesion with PSMA uptake higher than the background and not related to physiologic uptake was considered pathologic. Volumes of interest were drawn around the total tumor burden on baseline PSMA PET/CT and propagated automatically into the follow-up scan. Automatic segmentation was generated using a fixed SUV threshold of 3 as previously described (22), with manual modification to exclude sites of physiologic uptake (e.g., salivary glands and urinary tract).

SUV was normalized for the patient's lean body mass, and the volumetric parameters were calculated. Semiquantitative parameters were measured, including SUV_{max}, SUV_{mean}, whole-body PSMA total tumor volume (PSMA-TV, the summation of all body lesions), and total lesion PSMA uptake (TL-PSMA, defined as PSMA-TV $\times$ SUV_{mean}).

PSMA PET/CT Response Assessment

The PSMA PET–based response was assessed on a per-patient basis. Given that no specific response criteria have been previously validated for PSMA PET/CT, the cutoff we used was a 30% change in PSMA expression as recommended by the consensus statements on PSMA PET/CT response assessment criteria (23). This cutoff was applied to all analyzed PSMA PET quantification parameters. Four different categories were used: complete response (CR), defined as disappearance of uptake in all pathologic PET-positive lesions; partial response (PR), defined as a decrease of at least 30% of PSMA uptake; stable disease, defined as a change in PSMA expression of between +29% and −29%; and PD, defined as the appearance of at least 2 new lesions or an increase in PSMA uptake by at least 30% from baseline (Fig. 2). A patient with PSMA response (PSMA-R) was a patient presenting CR and PR, and a patient with PSMA nonresponse (PSMA-NR) was a patient presenting PD and stable disease.

Biochemical Response (BR) Assessment

The PSA level measured at the time of PSMA PET/CT, before and after therapy, was recorded (time window, ±1 wk). On the basis of PSA percentage changes, patients were classified as having BR if they had either an undetectable PSA level or a decrease by at least 50%, and patients were classified as having a biochemical nonresponse (BNR) if they had an increase in PSA or a decrease by less than 50%.

Statistical Analysis

Descriptive statistics were computed for the baseline patient characteristics, and distributions were reported with median and interquartile

TABLE 1
Patient Characteristics ($n = 37$)

Characteristic	Data
Age (y)	70 (IQR, 61–74)
ISUP grade	
1–3	10 (27%)
4–5	25 (68%)
Unknown	2 (5%)
Primary treatment	
Surgery	28 (75%)
Radiotherapy	1 (3%)
Systemic therapy	8 (22%)
Baseline PSA (ng/mL)	27 (IQR, 13–85)
Number of cycles	
Docetaxel	6 (range, 4–10)
Cabazitaxel	6 (range, 3–10)
Disease state	
mHSPC	8 (22%)
mCRPC	29 (78%)
Patients with metastasis sites	
Bone	27 (73%)
Lymph nodes	
Pelvic	16 (43%)
Extrapelvic	28 (75%)
Prostatic bed	7 (19%)
Viscera	6 (16%)
Follow-up time (mo)	23 (IQR, 15–30)
First PSMA PET/CT to first cycle (d)	16 (IQR, 9–30)
Last cycle to second PSMA PET/CT (d)	27 (IQR, 18–44)

ISUP = International Society of Urological Pathology.
Qualitative data are number and percentage; continuous data are median and range or IQR.

TABLE 2
Distribution of PSMA PET/CT Responses According to Different PET Parameters and Their Concordance with PSA Response

Parameter	PSA response		φ-coefficient
	Responders	Nonresponders	
SUV_{max}			
Responders	12	0	0.71, $P < 0.0001$
Nonresponders	6	19	
SUV_{mean}			
Responders	9	0	0.58, $P = 0.001$
Nonresponders	9	19	
PSMA-TV			
Responders	17	1	0.89, $P < 0.0001$
Nonresponders	1	18	
TL-PSMA			
Responders	17	1	0.89, $P < 0.0001$
Nonresponders	1	18	

range (IQR) for continuous variables and relative frequencies for categoric variables. The Fisher exact test (for categoric variables) and the Mann–Whitney U test (for continuous variables) were used to explore associations between baseline patient characteristics and PSMA PET response status. The distribution of continuous variables was dichotomized on the basis of the median. The ϕ-coefficient test was performed to analyze the correlation between PSMA PET and PSA-based responses. The Cox regression hazard model was used to evaluate associations between the clinical variables, including hemoglobin, alkaline phosphatase, baseline PSA levels, PSMA PET response, and OS. Univariate significant factors for OS ($P < 0.05$) were included in multivariable analyses. Kaplan–Meier curves were used to plot patient survival and to estimate survival probabilities, and the log-rank test was used to compare the survival curves. A subgroup survival analysis of mCRPC patients was performed. OS was estimated from the second PSMA PET scan to the date of death or last follow-up. A 2-sided P value of less than 0.05 was considered statistically significant. Statistical analyses were performed using SPSS Statistics, version 23.0 (IBM).

RESULTS

Patient Population

Thirty-seven patients were included in the analysis. At the time of baseline PSMA PET, the median age was 70 y (IQR, 61–74 y). At PCa diagnosis, the median International Society of Urological Pathology grade group was 4 (range, 1–5). The median baseline PSA level was 27 ng/dL (IQR, 13–85 ng/dL). The study cohort comprised 8 (22%) mHSPC and 29 (78%) mCRPC patients. Twenty-one (57%) patients received docetaxel, and 16 (43%) received cabazitaxel (median, 6 cycles; IQR, 5–8 cycles). Baseline PSMA PET was performed within a median of 16 d (IQR, 9–30 d) before the first cycle of taxane-based chemotherapy, and the posttreatment scan was done within a median of 27 d (IQR, 18–44 d) after the last cycle. Patient characteristics are summarized in Table 1.

Quantitative PET Parameters

The medians of the quantitative baseline PET parameters PSMA-TV, TL-PSMA, SUV_{max}, and SUV_{mean} were 136 cm^3 (IQR, 24.5–471 cm^3), 1,182 cm^3 (IQR, 146.5–4,086 cm^3), 22.9 (IQR, 10.2–39.6), and 5.7 (IQR, 4.2–9.3), respectively. Posttherapy median percentage changes were −36% (IQR, −86% to +55%) for PSMA-MTV, −43% (IQR, −87% to +93%) for TL-PSMA, −22.4% (IQR, −52% to +8%) for SUV_{max}, and −11% (IQR, −30% to +2%) for SUV_{mean}. The PSMA-response criteria were applied to each PET parameter, and the concordance with PSA response is presented in Table 2. PSMA-TV and TL-PSMA performed equally well and showed the highest concordance, with a ϕ-coefficient of 0.89 ($P < 0.0001$, for both). PSMA-TV was then used as the PET

parameter to define PSMA-R versus PSMA-NR and to evaluate associations with clinical variables and OS.

Response Assessment Based on PSMA PET/CT

Among all patients, 18 patients were classified as PSMA-R (6 CR and 12 PR), and 19 patients were classified as PSMA-NR (17 PD and 2 stable disease). In patients with PR, the median PSMA-TV decrease was −72% (range, −98% to −40%). Among PD patients, 5 patients had an increased PSMA-TV (median, +57%; range, +30% to +84%) and 12 patients had at least 2 new lesions. Finally, 2 patients had stable disease, with a PSMA-TV percentage change of −19% and +18% without new lesions. The percentage changes for each patient are presented in Figure 3A.

Association Between Baseline Clinical Variables and PSMA PET/CT Response

There was a statistically significant difference between PSMA-R and PSMA-NR in terms of disease status (mHSPC vs. mCRPC, $P = 0.001$), baseline hemoglobin level ($P = 0.023$), alkaline phosphatase level ($P = 0.048$), and number of cycles ($P = 0.002$). Regarding the number of cycles, patients with PSMA-R received a median of 6 cycles (IQR, 6–10 cycles), compared with a median
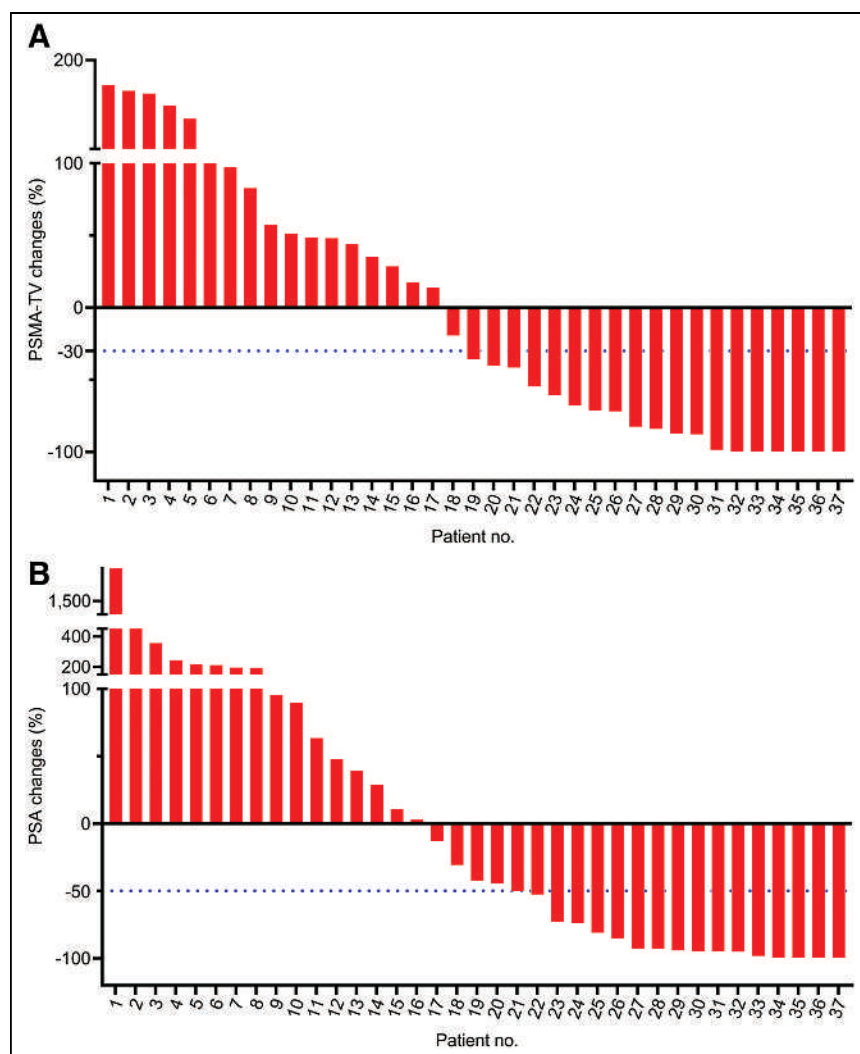
FIGURE 3. Waterfall plot representing individual percentage changes in PSMA-TV (A) and PSA (B) after taxane-based chemotherapy.

of 5 cycles (IQR, 5–6 cycles) for PSMA-NR. On the other hand, there was no significant correlation between the PSMA PET/CT response status and patient age, type of therapy (docetaxel vs. cabazitaxel), International Society of Urological Pathology grade group, primary treatment (local vs. systemic), or baseline PSA (Table 3).

Association Between BR and PSMA PET/CT Response

The median PSA change after therapy was −43% (IQR, −94% to +93%) (Fig. 3B). Eighteen patients had BR with a median PSA decrease of −93% (IQR, −98% to −74%). Of patients with BR, PSMA PET/CT showed CR in 6 patients and PR in 11. Interestingly, of all patients with PR on PSMA PET/CT, 3 patients (27%) had less than 3 residual PSMA lesions after taxane-based chemotherapy and thus could be considered oligoresistant. Nineteen patients had BNR with a median PSA change of +90% (IQR, +11% to +219%); of them, 16 patients had PD on PSMA PET/CT (12 patients with new lesions and 4 with increased PSMA-TV), and 2 patients had no significant PSMA uptake changes (stable disease) on posttherapy PSMA PET (Table 4).

TABLE 3
Differences Between PSMA-R and PSMA-NR Regarding Different Clinical Factors

Parameter	PSMA-R*	PSMA-NR*	P
Age (y)			
≤70	11	8	0.248
>70	7	11	
ISUP grade			
1–3	3	7	0.146
4–5	15	10	
Primary therapy			
Radical therapy	15	14	0.379
Systemic therapy	3	5	
Type of therapy			
Docetaxel	13	8	0.065
Cabazitaxel	5	11	
Disease stage			
mHSPC	8	0	0.001
mCRPC	10	19	
Baseline PSA (ng/mL)			
≤27	10	8	0.413
>27	8	11	
Hemoglobin (g/dL)			
≥13	13	7	0.023
<13	5	12	
Alkaline phosphatase (IU/L)			
≤129	17	12	0.048
>129	1	7	

*Number of patients (n).

ISUP = International Society of Urological Pathology.

Alkaline phosphatase and hemoglobin were dichotomized according to standard reference value in our laboratory. Age and serum PSA were dichotomized according to median.

The PSMA PET/CT response was concordant with PSA response in 95% of patients (100% in mHSPC and 85% in mCRPC), with 17 patients having PSMA-R/BR and 18 having PSMA-NR/BNR ($\phi = 0.89$, $P = 0.0001$). However, 2 mCRPC patients had discordant responses: one had PSMA-R/BNR with a PSMA-TV of −42% but a PSA of +96%; the other had PSMA-NR/BR with PSMA PET/CT showing more than 2 new lesions but a PSA decrease of 52%.

Patient Survival Outcomes According to PSMA PET/CT Response Criteria

At a median follow-up of 23 mo (IQR, 15–30 mo), 16 deaths had occurred. Among the whole population, PSMA-R had longer OS than PSMA-NR (median OS not reached vs. 12 mo, respectively; hazard ratio, 0.10; 95% CI, 0.03–0.39; $P = 0.001$). In the subgroup analysis of mCRPC, a statistically significant difference in OS was also present, with PSMA-R showing longer OS than PSMA-NR (median OS, 22 vs. 12 mo, respectively; hazard ratio, 0.22; 95% CI, 0.06–0.82; $P = 0.023$). In addition, PSMA-R had an increased 12-mo OS of 100%, compared with 52% for PSMA-NR ($P = 0.011$) (Fig. 4). Among the mHSPC subgroup, only 1 death was registered at 27 mo of follow-up. Regarding the 2 patients with a discordant PSMA/PSA response, the patient with PSMA-R/BNR was still alive at 20 mo, whereas the patient with PSMA-NR/BR died 15 mo after the second scan.

PSA-based response criteria were significantly associated with OS in the overall population: OS was longer for BR than for BNR (median OS not reached vs. 12 mo; hazard ratio, 0.16; 95% CI, 0.05–0.56; $P = 0.004$). However, the association of PSA-based response criteria with OS in the mCRPC subgroup was not statistically significant (hazard ratio, 0.35; $P = 0.083$). Other factors associated with OS are presented in Table 5. Because of the small number of events, multivariable analysis was performed on 2 models; PSMA PET/CT response was significant for predicting OS in both model 1 ($P = 0.003$) and model 2 ($P = 0.025$) (Table 5).

DISCUSSION

In this study, the role of PSMA PET/CT for response assessment in mPCa patients undergoing taxane-based chemotherapy was retrospectively evaluated. We selected patients who received only taxane-based chemotherapy, without treatment modification between the baseline and posttherapeutic scans. The results showed a strong correlation between PSMA PET/CT–based response and PSA-based response. Moreover, the PSMA PET response was independently predictive of survival, with a statistically significant difference in OS between PSMA-R and PSMA-NR.

The strong correlation between PSMA PET/CT–based response and PSA-based response was superior to what was previously reported by Seitz et al. (21). They analyzed 23 patients undergoing

TABLE 4
Distribution of Response as Defined According to PSA and PSMA PET/CT

Parameter	PSMA-R		PSMA-NR	
	CR	PR	Stable disease	PD
PSA-R	6	11	0	1
PSA-NR	0	1	2	16

FIGURE 4. (A and B) Kaplan–Meier plots for OS in whole population (A) and in mCRPC subgroup (B). (C and D) Kaplan–Meier plots for OS for PSMA-R vs. PSMA-NR in whole population (C) and in mCRPC subgroup (D). *P* values were obtained from log-rank test.

(SUV_{max}, SUV_{mean}, PSMA-TV, and TL-PSMA), all of them showing a significant correlation with PSA response. Of them, PSMA-TV and PSMA-TL performed equally well and showed the highest concordance, with a ϕ-coefficient of 0.89 ($P < 0.0001$, for both). We selected PSMA-TV for the subsequent analysis of the study. PSMA-TV represents the whole-body PSMA-expressing tumor burden; therefore, PSMA-TV changes may reflect taxane-induced cytotoxic effects. Preclinical data have previously shown that decreased PSMA expression after taxane-based chemotherapy resulted from a decline in the number of viable cells and not from a decrease in PSMA expression on the cell membrane (*14*). Other studies have reported potential value for PSMA-TV in assessing response to different systemic therapies in PCa but none in assessing a homogeneous population under taxane-based chemotherapy (*15,24,25*). We defined the response on PSMA PET/CT using PSMA-TV and a cutoff of a 30% decrease to differentiate PSMA-R from PSMA-NR, as well as the appearance of new lesions, based on the "Consensus Statements on PSMA PET/CT Response Assessment Criteria in Prostate Cancer" (*23*). In our cohort, the 30% cutoff is also close to the median PSMA-TV percentage change (-36%). Interestingly, the posttherapy PSMA PET/CT scan could identify 3 patients presenting PSA and PSMA PR but showing oligoresistant disease, meaning that all metastatic lesions showed a CR except for 1–3 lesions. This is a unique ability of molecular imaging with PSMA PET/CT that cannot be reproduced if one is following up the patient only by using tumor markers such as PSA. PSA changes will give patient-based information but never lesion-based information. This finding will probably open a new area of research to determine whether oligoresistant patients might benefit from additional targeted treatments such as stereotactic body radiation therapy, in a strategy similar to the one proposed for oligometastatic

docetaxel chemotherapy and showed a correlation between PSMA PET/CT response and PSA-based response of 86% for mHSPC and 56% for mCRPC. Our study found a perfect correlation (100%) in the mHSPC subgroup and substantial concordance (85%) in the mCRPC group. Many factors might explain these differences, including the low number of patients or the methodology used to assess response. In fact, the PSMA PET/CT response criteria are not standardized yet. Some investigators have proposed extrapolating PERCIST applied for ^{18}F-FDG PET/CT to the PSMA PET/CT scan (*15,19,21*). Nevertheless, these criteria analyze response in only selected target lesions and not in the whole tumor volume. In patients with diffuse skeletal metastases, selecting individual lesions is practically unfeasible because of the added difficulty in assessing response (*19*). To assess response to treatment on PSMA PET/CT, the treatment-induced percentage changes in different PET quantitative parameters were tested

TABLE 5
Univariate and Multivariate Cox Regression Analyses Presenting Association of Clinical Factors and PSMA PET/CT Response with OS

	Univariate analysis		Multivariate analysis	
Parameter	Hazard ratio	*P*	Hazard ratio	*P*
Model 1				
PSMA response (yes vs. no)	0.10 (0.03–0.39)	0.001	0.10 (0.02–0.44)	0.003
Log PSA (baseline)	1.78 (1.17–2.72)	0.007	1.46 (0.91–2.34)	0.110
Hemoglobin (baseline)	0.64 (0.50–0.81)	0.001	0.53 (0.36–0.77)	0.001
Model 2				
PSMA response (yes vs. no)	0.10 (0.03–0.39)	0.001	0.21 (0.05–0.82)	0.025
Disease state (mHSPC vs. mCRPC)	0.08 (0.01–0.65)	0.019	0.17 (0.02–2.02)	0.162
Log alkaline phosphatase (baseline)	2.63 (1.29–5.36)	0.007	2.07 (0.92–4.67)	0.080

Data in parentheses are 95% CI.

disease at biochemical recurrence—today treated with metastasis-directed therapy (26).

Since PSA can be considered a contested biomarker of response in mCRPC, we evaluated the association of PSMA PET/CT response with OS. In our cohort, the PSMA PET/CT response was significantly associated with OS, showing a statistically significant difference between PSMA-R and PSMA-NR (median OS not reached vs. 12 mo) and a 75% lower hazard rate of death in responding patients. OS in the 2 patients with discordant PSMA/PSA responses was more in line with the PSMA response than with the PSA response. The patient with decreased PSMA expression but increased PSA was alive at 20 mo, whereas the patient presenting new lesions on PSMA PET/CT but decreased PSA (>50%) died at 15 mo of follow-up. Moreover, our results suggest a potential superiority of PSMA PET/CT response over PSA response, as PSMA PET/CT responses could significantly predict OS in mCRPC patients whereas PSA-based responses could not. To the best of our knowledge, this was the first study analyzing the role of PSMA PET/CT response as a predictive biomarker for OS in patients undergoing taxane-based chemotherapy. Future prospective studies must follow to validate this imaging technique as a response assessment tool before its introduction into clinical practice and clinical trials. Other known clinical risk factors, such as disease state, hemoglobin level, and alkaline phosphatase level, were also tested and showed a statistically significant association with OS and with the PSMA PET/CT response. When we tested for possible confounding factors in a multivariable analysis, PSMA PET/CT response remained an independent predictive factor for OS. However, this observation needs to be validated on a larger population.

Assessing response to systemic treatment in mPCa patients using conventional imaging techniques is a difficult task. According to the PCWG criteria, radiographic response with CT or MRI can be measured with RECIST, version 1.1, only in the presence of measurable lesions (excluding sclerotic bone lesions and subcentimetric lymph nodes). With PCa metastatic disease being located predominantly in bone and lymph nodes, RECIST 1.1 is applicable in only a minority of cases. The ability of PSMA PET/CT to accurately detect metastatic disease, and the potential role of PSMA PET/CT in response assessment, may have an important impact on clinical management. Following the PCWG criteria, systemic treatments should not be stopped on the basis of PSA values during the first 12 wk after treatment initiation (7); patients should receive at least 5 cycles of chemotherapy, even if they are finally not responding. That recommendation increases the risk of treatment-related toxicity in patients not benefiting from it, deteriorating the patient's clinical condition, which may, in turn, have a negative impact on the choice of subsequent treatment. In this context, early response assessment with PSMA PET/CT could allow for rapid switching to another effective systemic therapy, such as ^{177}Lu-PSMA-617, which has recently demonstrated a benefit in OS in mCRPC after taxane-based chemotherapy (9,10). Prospective trials are needed to test the negative predictive value of PSMA PET/CT response assessed early during chemotherapy (e.g., after 4–8 wk) instead of at the end of treatment.

Our study had some limitations that emerge from its retrospective design and the limited number of patients. The outcome might have been influenced by the inclusion of a heterogeneous population with mCRPC and mHSPC patients. However, the predictive value of PSMA PET/CT response was confirmed in the subgroup analysis performed on mCRPC patients. Because the study was retrospective, PSMA PET/CT time points were not standardized between patients, but a maximum time window was applied. The study did not compare PSMA PET/CT response to RECIST 1.1 because only a minority of patients had RECIST-measurable disease and because the CT part of the PET/CT was low-dose without contrast injection, making it suboptimal for RECIST 1.1 measurements (27). It is well known that RECIST 1.1 has an inherent limitation in monitoring the response of sclerotic bone metastases, which constitute most of the metastatic presentation in mCRPC patients. Moreover, small lymph nodes are easily depicted with PSMA PET/CT but are not measurable by RECIST 1.1. On the other hand, the recent improvements in semiautomatic segmentation methods and quantification analysis on PSMA PET/CT scans will facilitate its implementation as a response assessment tool in routine clinical practice.

CONCLUSION

This retrospective analysis suggests that ^{68}Ga-PSMA-11 PET/CT is a promising imaging tool to assess response to taxane-based chemotherapy (docetaxel and cabazitaxel) in mPCa patients. Posttherapeutic changes in PSMA expression correlate strongly with PSA and may be used as an independent predictive biomarker for OS, with PSMA-R presenting significantly longer OS than PSMA-NR. This tool might help in tailoring individual treatment and selecting eligible patients for clinical trials. Further prospective studies are needed to confirm these findings.

DISCLOSURE

No potential conflict of interest relevant to this article was reported.

KEY POINTS

QUESTION: Can PSMA PET/CT be used to assess response to taxane-based chemotherapy in mPCa patients?

PERTINENT FINDINGS: Changes in PSMA expression on PET/CT were associated with response to therapy and could independently predict OS. PSMA-R presented a significantly longer OS than PSMA-NR.

IMPLICATIONS FOR PATIENT CARE: PSMA PET/CT is a promising imaging technique that can be used to assess the response to taxane-based chemotherapy and to predict a patient's prognosis.

REFERENCES

1. Bray F, Ferlay J, Soerjomataram I, Siegel RL, Torre LA, Jemal A. Global cancer statistics 2018: GLOBOCAN estimates of incidence and mortality worldwide for 36 cancers in 185 countries. *CA Cancer J Clin.* 2018;68:394–424.
2. Cornford P, Bellmunt J, Bolla M, et al. EAU-ESTRO-SIOG guidelines on prostate cancer. Part II: treatment of relapsing, metastatic, and castration-resistant prostate cancer. *Eur Urol.* 2017;71:630–642.
3. Mohler JL, Antonarakis ES, Armstrong AJ, et al. Prostate cancer, version 2.2019, NCCN clinical practice guidelines in oncology. *J Natl Compr Canc Netw.* 2019; 17:479–505.
4. Tannock IF, de Wit R, Berry WR, et al. Docetaxel plus prednisone or mitoxantrone plus prednisone for advanced prostate cancer. *N Engl J Med.* 2004;351:1502–1512.
5. Sweeney CJ, Chen YH, Carducci M, et al. Chemohormonal therapy in metastatic hormone-sensitive prostate cancer. *N Engl J Med.* 2015;373:737–746.

6. de Bono JS, Oudard S, Ozguroglu M, et al. Prednisone plus cabazitaxel or mitox-antrone for metastatic castration-resistant prostate cancer progressing after doce-taxel treatment: a randomised open-label trial. *Lancet.* 2010;376:1147–1154.

7. Scher HI, Morris MJ, Stadler WM, et al. Trial design and objectives for castration-resistant prostate cancer: updated recommendations from the prostate cancer clini-cal trials working group 3. *J Clin Oncol.* 2016;34:1402–1418.

8. Eisenhauer EA, Therasse P, Bogaerts J, et al. New response evaluation criteria in solid tumours: revised RECIST guideline (version 1.1). *Eur J Cancer.* 2009;45:228–247.

9. Hofman MS, Emmett L, Sandhu S, et al. [177Lu]Lu-PSMA-617 versus cabazitaxel in patients with metastatic castration-resistant prostate cancer (TheraP): a rando-mised, open-label, phase 2 trial. *Lancet.* 2021;397:797–804.

10. Sartor O, de Bono J, Chi KN, et al. Lutetium-177-PSMA-617 for metastatic castration-resistant prostate cancer. *N Engl J Med.* 2021;385:1091–1103.

11. Hofman MS, Lawrentschuk N, Francis RJ, et al. Prostate-specific membrane anti-gen PET-CT in patients with high-risk prostate cancer before curative-intent sur-gery or radiotherapy (proPSMA): a prospective, randomised, multicentre study. *Lancet.* 2020;395:1208–1216.

12. Albisinni S, Artigas C, Aoun F, et al. Clinical impact of 68Ga-prostate-specific membrane antigen (PSMA) positron emission tomography/computed tomography (PET/CT) in patients with prostate cancer with rising prostate-specific antigen after treatment with curative intent: preliminary analysis of a multidisciplinary approach. *BJU Int.* 2017;120:197–203.

13. Fendler WP, Calais J, Eiber M, et al. Assessment of 68Ga-PSMA-11 PET accuracy in localizing recurrent prostate cancer: a prospective single-arm clinical trial. *JAMA Oncol.* 2019;5:856–863.

14. Hillier SM, Kern AM, Maresca KP, et al. 123I-MIP-1072, a small-molecule inhibi-tor of prostate-specific membrane antigen, is effective at monitoring tumor response to taxane therapy. *J Nucl Med.* 2011;52:1087–1093.

15. Grubmüller B, Senn D, Kramer G, et al. Response assessment using 68Ga-PSMA ligand PET in patients undergoing 177Lu-PSMA radioligand therapy for metastatic castration-resistant prostate cancer. *Eur J Nucl Med Mol Imaging.* 2019;46:1063–1072.

16. Plouznikoff N, Artigas C, Sideris S, et al. Evaluation of PSMA expression changes on PET/CT before and after initiation of novel antiandrogen drugs (enzalutamide or abiraterone) in metastatic castration-resistant prostate cancer patients. *Ann Nucl Med.* 2019;33:945–954.

17. Grubmüller B, Rasul S, Baltzer P, et al. Response assessment using [68Ga]Ga-PSMA ligand PET in patients undergoing systemic therapy for metastatic castra-tion-resistant prostate cancer. *Prostate.* 2020;80:74–82.

18. Gupta M, Choudhury PS, Rawal S, Goel HC, Rao SA. Evaluation of RECIST, PERCIST, EORTC, and MDA criteria for assessing treatment response with Ga68-PSMA PET-CT in metastatic prostate cancer patient with biochemical progression: a comparative study. *Nucl Med Mol Imaging.* 2018;52:420–429.

19. Heinzel A, Boghos D, Mottaghy FM, et al. 68Ga-PSMA PET/CT for monitor-ing response to 177Lu-PSMA-617 radioligand therapy in patients with meta-static castration-resistant prostate cancer. *Eur J Nucl Med Mol Imaging.* 2019;46:1054–1062.

20. Kuten J, Sarid D, Yossepowitch O, Mabjeesh NJ, Even-Sapir E. [68Ga]Ga-PSMA-11 PET/CT for monitoring response to treatment in metastatic prostate cancer: is there any added value over standard follow-up? *EJNMMI Res.* 2019;9:84.

21. Seitz AK, Rauscher I, Haller B, et al. Preliminary results on response assessment using 68Ga-HBED-CC-PSMA PET/CT in patients with metastatic prostate cancer undergoing docetaxel chemotherapy. *Eur J Nucl Med Mol Imaging.* 2018;45:602–612.

22. Anton A, Kamel Hasan O, Ballok Z, et al. Use of prostate-specific membrane antigen positron-emission tomography/CT in response assessment following upfront chemohormonal therapy in metastatic prostate cancer. *BJU Int.* 2020;126:433–435.

23. Fanti S, Goffin K, Hadaschik BA, et al. Consensus statements on PSMA PET/CT response assessment criteria in prostate cancer. *Eur J Nucl Med Mol Imaging.* 2021;48:469–476.

24. Santos A, Mattiolli A, Carvalheira JB, et al. PSMA whole-body tumor burden in primary staging and biochemical recurrence of prostate cancer. *Eur J Nucl Med Mol Imaging.* 2021;48:493–500.

25. Jansen BHE, Cysouw MCF, Vis AN, et al. Repeatability of quantitative 18F-DCFPyL PET/CT measurements in metastatic prostate cancer. *J Nucl Med.* 2020;61:1320–1325.

26. Artigas C, Flamen P, Charlier F, et al. 68Ga-PSMA PET/CT-based metastasis-directed radiotherapy for oligometastatic prostate cancer recurrence after radical prostatectomy. *World J Urol.* 2019;37:1535–1542.

27. Schwartz LH, Litiere S, de Vries E, et al. RECIST 1.1: update and clarification—from the RECIST committee. *Eur J Cancer.* 2016;62:132–137.

Prostate-Specific Membrane Antigen Radioligand Therapy Using ^{177}Lu-PSMA I&T and ^{177}Lu-PSMA-617 in Patients with Metastatic Castration-Resistant Prostate Cancer: Comparison of Safety, Biodistribution, and Dosimetry

Christiane Schuchardt*[1], Jingjing Zhang*[2,3], Harshad R. Kulkarni[1], Xiaoyuan Chen[2–4], Dirk Müller[5], and Richard P. Baum[6]

[1]Theranostics Center for Molecular Radiotherapy and Molecular Imaging, Zentralklinik Bad Berka, Bad Berka, Germany; [2]Department of Diagnostic Radiology, Yong Loo Lin School of Medicine, National University of Singapore, Singapore, Singapore; [3]Clinical Imaging Research Centre, Centre for Translational Medicine, Yong Loo Lin School of Medicine, National University of Singapore, Singapore, Singapore; [4]Departments of Surgery, Chemical and Biomolecular Engineering, and Biomedical Engineering, Yong Loo Lin School of Medicine and Faculty of Engineering, National University of Singapore, Singapore, Singapore; [5]University Hospital Ulm, Clinic for Nuclear Medicine, Ulm, Germany; and [6]Curanosticum Wiesbaden-Frankfurt, Center for Advanced Radiomolecular Precision Oncology, Wiesbaden, Germany

The objective of this study was to determine the safety, kinetics, and dosimetry of the ^{177}Lu-labeled prostate-specific membrane antigen (PSMA) small molecules ^{177}Lu-PSMA I&T and ^{177}Lu-PSMA-617 in a large cohort of patients with metastatic castration-resistant prostate cancer (mCRPC) undergoing PSMA radioligand therapy (PRLT). **Methods:** In total, 138 patients (mean age, 70 ± 9 y; age range, 46–90 y) with progressive mCRPC and PSMA expression verified by ^{68}Ga-PSMA-11 PET/CT underwent PRLT. Fifty-one patients received 6.1 ± 1.0 GBq (range, 3.4–7.6 GBq) of ^{177}Lu-PSMA I&T, and 87 patients received 6.5 ± 1.1 GBq (range, 3.5–9.0 GBq) of ^{177}Lu-PSMA-617. Dosimetry was performed on all patients using an identical protocol. The mean absorbed doses were estimated with OLINDA software (MIRD Scheme). Treatment-related adverse events were graded according to the Common Terminology Criteria for Adverse Events, version 5.0, of the National Cancer Institute. **Results:** The whole-body half-lives were shorter for ^{177}Lu-PSMA I&T (35 h) than for ^{177}Lu-PSMA-617 (42 h). The mean whole-body dose of ^{177}Lu-PSMA-617 was higher than that of ^{177}Lu-PSMA I&T (0.04 vs. 0.03 Gy/GBq, $P < 0.00001$). Despite the longer half-life of ^{177}Lu-PSMA-617, the renal dose was lower for ^{177}Lu-PSMA-617 than for ^{177}Lu-PSMA I&T (0.77 vs. 0.92 Gy/GBq, $P = 0.0015$). Both PSMA small molecules demonstrated a comparable dose to the parotid glands (0.5 Gy/GBq, $P = 0.27$). Among all normal organs, the lacrimal glands exhibited the highest mean absorbed doses, 5.1 and 3.7 Gy/GBq, for ^{177}Lu-PSMA-617 and ^{177}Lu-PSMA I&T, respectively. All tumor metastases exhibited a higher initial uptake when using ^{177}Lu-PSMA I&T than when using ^{177}Lu-PSMA-617, as well as a shorter tumor half-life ($P < 0.00001$). The mean absorbed tumor doses were comparable for both ^{177}Lu-PSMA I&T and ^{177}Lu-PSMA-617 (5.8 vs. 5.9 Gy/GBq, $P = 0.96$). All patients tolerated the therapy without any acute adverse effects. After ^{177}Lu-PSMA-617 and ^{177}Lu-PSMA I&T, there was a small, statistically significant reduction in hemoglobin, leukocyte counts, and platelet counts that did not need any clinical intervention. No nephrotoxicity was observed after either ^{177}Lu-PSMA I&T or ^{177}Lu-PSMA-617 PRLT. **Conclusion:** Both ^{177}Lu-PSMA I&T and ^{177}Lu-PSMA-617 PRLT demonstrated favorable safety in mCRPC patients. The highest absorbed doses among healthy organs were in the lacrimal and parotid glands—not, however, resulting in any significant clinical sequel. ^{177}Lu-PSMA-617 demonstrated a higher absorbed dose to the whole-body and lacrimal glands but a lower renal dose than did ^{177}Lu-PSMA I&T. The mean absorbed tumor doses were comparable for both ^{177}Lu-PSMA I&T and ^{177}Lu-PSMA-617. There was a large interpatient variability in the dosimetry parameters. Therefore, individual patient-based dosimetry seems favorable for personalized PRLT.

Key Words: prostate-specific membrane antigen; dosimetry; ^{177}Lu; PSMA radioligand therapy; ^{177}Lu-PSMA I&T; ^{177}Lu-PSMA-617; theranostics

Prostate cancer is the second most frequent cancer and the fifth leading cause of cancer death in men; in 2020, there were almost 1.4 million new cases and 375,000 deaths worldwide (*1*). It carries a poor prognosis when it metastasizes aggressively after initial treatment and becomes castration-resistant (*2*).

A promising treatment modality in the management of metastatic castration-resistant prostate cancer (mCRPC) can be provided when prostate-specific membrane antigen (PSMA) small molecules are radiolabeled; such PSMA-targeted radioligand therapy (PRLT) may use the β-emitting radionuclide ^{177}Lu or the α-emitter ^{225}Ac, as per multiple retrospective studies. ^{177}Lu-PSMA therapy decreased prostate-specific antigen by at least 50% in 32 of 50 men with mCRPC who had progressed after conventional treatment, and the toxicity profile was favorable (*3,4*). In a randomized, open-label phase 2 trial, TheraP, ^{177}Lu-PSMA therapy produced a higher prostate-specific antigen response and fewer adverse events than did cabazitaxel chemotherapy in mCRPC (*5*). Furthermore, targeted α-therapy with ^{225}Ac-PSMA has provided durable disease control after failure of ^{177}Lu-PSMA treatment, when all other therapeutic options have been exhausted (*6–10*).

Currently, the most frequently used PSMA-targeting small-molecule inhibitors are DOTA-PSMA-617 (PSMA-617) and DOTAGA-PSMA I&T (PSMA I&T); "DOTA" and "DOTAGA" denote the cages enclosing the radionuclides, and "I&T" denotes the radionuclide that yields both imaging and therapy. [177]Lu (half-life, 6.7 d) is the radionuclide for theranostics, as it emits a cytotoxic β-particle for effective therapy and also has the ability to quantify γ-emissions, enabling diagnostic evaluation and biodistribution using scintigraphy for dosimetry.

Pilot dosimetric studies of either ^{177}Lu-PSMA-617 or ^{177}Lu-PSMA I&T were performed to estimate the absorbed doses for normal organs and tumor lesions. An initial study that included 7 patients for whom the pretreatment radiation doses were estimated using a tracer amount of ^{177}Lu-PSMA-617 indicated that the dose-limiting organ seemed to be the parotid glands rather than the kidneys and that the radiation dose to the bone marrow was significantly lower than those to the kidneys and the parotid glands (11). These dosimetric studies were obtained in a small number of patients, however, and were given in tracer amounts or a low therapeutic activity; indeed, few publications have addressed the absorbed doses delivered to tumors after ^{177}Lu-PSMA radionuclide therapy, and dosimetric approaches for calculation of the absorbed doses have varied among studies (11–19).

Therefore, for the first time, to our knowledge, we compared ^{177}Lu-PSMA-617 and ^{177}Lu-PSMA I&T using an identical dosimetry protocol. The Bad Berka dose protocol, used in our daily clinical routine, has been established during more than 15 y in the treatment of more than 1,000 neuroendocrine neoplasm patients undergoing peptide receptor radionuclide therapy (20,21). Dosimetric parameters, such as uptake and estimated mean absorbed dose to organs and tumor lesions, were obtained from these dosimetric calculations to evaluate therapeutic response and possible adverse effects.

For this reason, the aim of this study was to determine the safety, kinetics, and dosimetry of the ^{177}Lu-labeled PSMA small molecules ^{177}Lu-PSMA I&T and ^{177}Lu-PSMA-617 in a large cohort of patients with mCRPC undergoing PRLT under an identical dosimetry protocol.

MATERIALS AND METHODS

Patients

In total, 138 patients (mean age, 70 ± 9 y; age range, 46–90 y) with progressive mCRPC who received ^{177}Lu-PSMA I&T or ^{177}Lu-PSMA-617 PRLT at Zentralklinik Bad Berka were enrolled in this retrospective study. Significant PSMA expression of the metastases was confirmed by ^{68}Ga-PSMA-11 PET/CT (Biograph mCT Flow 64; Siemens). The demographics of the patients and the location of metastases are shown in Table 1.

^{177}Lu-PSMA I&T and ^{177}Lu-PSMA-617 were administered in compliance with the German Medicinal Products Act, AMG §13 2b, and in accordance with the responsible regulatory body (Thüringer Landesamt; that is, the government of Thuringia). All patients underwent PRLT under the compassionate-use clause of the German Medicinal Product Act (22). All procedures performed in studies involving human participants complied with the ethical standards of the institutional or national research committee and with the 1964 Helsinki Declaration and its later amendments or comparable ethical standards. The decision to perform PRLT was based on exhaustion of all conventional therapy options; took into account age, renal function, and the adverse effects of possible other therapies; and was made by the referring

TABLE 1
Demographic and Baseline Characteristics of Patients with mCRPC ($n = 138$)

Characteristic	All patients	^{177}Lu-PSMA I&T group	^{177}Lu-PSMA-617 group
Number of patients	138	51	87
Age (y)	70 ± 9 (46–90)	71 ± 9 (46–87)	69 ± 9 (50–90)
ISUP grading			
Group 1	7 (5.1%)	2 (3.9%)	5 (5.7%)
Group 2	20 (14.5%)	3 (5.9%)	17 (19.5%)
Group 3	21 (15.2%)	10 (19.6%)	11 (12.6%)
Group 4	26 (18.8%)	6 (11.8%)	20 (23.0%)
Group 5	39 (28.3%)	18 (35.3%)	21 (24.1%)
NA	25 (18.1%)	12 (23.5%)	13 (14.9%)
PSA level (ng/mL)	216.5 ± 538.7	90.6 ± 158.7	283.3 ± 648.2
Metastases			
Lymph nodes	109 (79.0%)	38 (74.5%)	71 (81.6%)
Bone	108 (78.2%)	39 (76.5%)	69 (79.3%)
Bone marrow	11 (8.0%)	2 (3.9%)	9 (10.3%)
Lung	15 (10.9%)	6 (11.8%)	9 (10.3%)
Liver	12 (8.7%)	4 (7.8%)	8 (9.2%)
Other	36 (26.1%)	10 (19.6%)	26 (29.9%)
Injected activity (GBq)	6.4 ± 1.0 (3.4–9.0)	6.1 ± 1.0 (3.4–7.6)	6.5 ± 1.1 (3.5–9.0)

ISUP = International Society of Urological Pathology; NA = not available; PSA = prostate-specific antigen.
Qualitative data are number and percentage; continuous data are mean and range.

physicians (urologists and oncologists). The study protocol was approved by the local ethics committee (approval 34333/2017/96, Bad Berka). All patients signed a detailed informed consent form before undergoing the treatment, as well as consenting to the use of their anonymized clinical data for scientific purposes. The administered activities are shown in Table 1.

Radiopharmaceuticals and Infusion

[177]Lu labeling of the DOTAGA-based PSMA ligand PSMA I&T (DOTAGA-(I-y)fk(Sub-KuE)) and the PSMA-617 ligand was performed in our good-manufacturing-practice–certified radiopharmacy using previously published methods (23,24). In brief, the PSMA ligand was incubated with the required radioactivity of ^{177}Lu-Cl$_3$ at 90°C for 30 min in sodium acetate buffer (0.4 M, pH 5.5). To this buffer, 5–10 mg of gentisic acid were added to prevent radiolysis. The reaction solutions were diluted with saline to achieve a suitable volume. After sterile filtration, a sample was taken for quality control (radio–high-performance liquid chromatography, radio–thin-layer chromatography, pH, limulus amebocyte lysate testing, sterility testing, retention sample). Radiochemical purity was more than 95% in all cases (in most labeling procedures, >99%). The radiopharmaceutical was administered intravenously over 10–15 min using a dedicated infusion pump system for radionuclide therapy.

Imaging and Dosimetry

Dose estimation requires an accurate determination of the time-dependent activity of the organs and tumors. Thus, most important is the correct evaluation of the distribution and the kinetics of the administered radiopharmaceutical (25,26). To do so, we adapted the calculation model to our special conditions to establish the Bad Berka dose protocol, which is practicable in daily clinical routine, and to make dosimetry available for each patient. The dosimetric approach is based on the MIRD scheme, and mean absorbed doses are estimated using the software OLINDA, version 2.0 (27–30). The workflow of the Bad Berka dose protocol is shown in Figure 1.

At least 5 serial planar whole-body scintigraphy studies and 1 SPECT/CT study were acquired per patient. For planar whole-body imaging, we used the following γ-camera settings: MEDISO spirit DH-V dual-head γ-camera (Medical Imaging Systems), medium-energy general-purpose collimator, 15% energy window, peak at 208 keV, and scan speed of 15 cm/min. Whole-body scintigraphy was performed from 0.5 h after injection (immediately after administration of therapeutic activity and before bladder voiding) to 68 h after injection at a total of at least 5 time points. Additionally, posttherapy SPECT/CT images of the kidneys or tumor-involved regions was done at 24, 48, or 72 h after injection using a Symbia T camera system (Siemens) with the following settings: medium-energy low-penetration collimator, peak at 113 keV and 208 keV (15% energy windows and 20% upper and lower scatter window), 128 × 128 matrix, 32 projections with 30 s per step, and body contouring.

Because the patients were not allowed to empty the bladder before the first scan, the total-body counts acquired immediately after the injection were defined to be 100% of the administered activity. By assessing means of regions of interest, which were drawn manually over the source regions, the scintigraphy studies were analyzed using the Hermes system (Hermes Medical Solutions). Regions of interest were always drawn manually by the same physicist, in collaboration with a nuclear medicine physician, who decided which lesions were suitable for dosimetry; preferably, these target lesions had the highest uptake in each organ. The SPECT/CT scans were reconstructed and quantified using the Hermes SUV SPECT software (Hermes Medical Solutions). Mean absorbed doses to organs and tumors were estimated using OLINDA 2.0. Specifically, mean absorbed doses to tumors and to parotid and lacrimal glands were estimated using the unit density sphere module of OLINDA 2.0. A standard volume was used to assess lacrimal glands, according to the study of Bingham et al. (31).

With this dosimetry protocol, the following parameters were assessed: uptake as a fraction of the administered activity, effective half-life (hours), and mean absorbed organ and tumor doses (Gy/GBq). Organs showing tumor involvement were excluded from dosimetric evaluation.

Toxicity Assessment

All patients were clinically monitored during therapy and for at least 2–4 d afterward as inpatients for possible side effects. Vital parameters were recorded during therapy, and a structured questionnaire documented any delayed complication. Laboratory analysis including hematologic status, renal function, and liver function was performed before each PRLT cycle and in follow-up (restaging was performed regularly until death). Treatment-related adverse events were recorded in accordance with the Common Terminology Criteria for Adverse Events, version 5.0, of the National Cancer Institute.

Statistical Analysis

All dosimetric parameters were determined for the whole body and for normal organs (kidneys, parotid glands, and lacrimal glands), as well as for metastases. Results are given as median values. In comparisons of the 2 ^{177}Lu-labeled PSMA ligands, the following parameters were chosen to describe differences between the peptides: uptake at 20 h after injection, effective half-life, and mean absorbed dose. Nonparametric tests for independent samples were used to describe significant differences among ligands. All statistical tests were performed on OriginPro, version 8.1G (OriginLab); P values of less than 0.05 were considered significant.
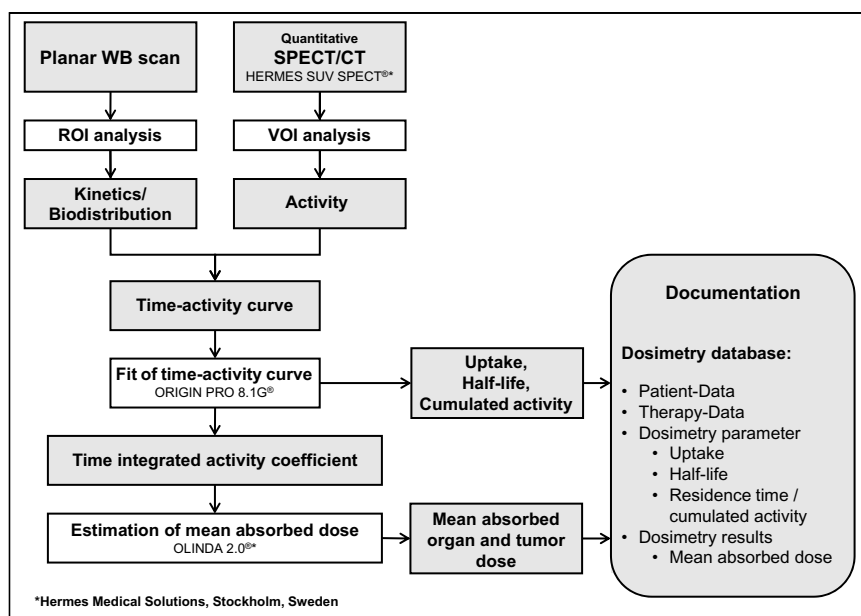
FIGURE 1. Flowchart of Bad Berka dose protocol. ROI = region of interest; VOI = volume of interest.

RESULTS

For both ^{177}Lu-PSMA I&T and ^{177}Lu-PSMA-617, strong physiologic uptake was observed in the lacrimal and salivary glands, kidneys, and small intestine on the posttherapy scans, followed by medium to low uptake in the liver and spleen at all time points. The radiopharmaceutical was excreted predominantly through the kidneys, as visualized by an accumulation in the urinary bladder that was dominant on the early scans 0.5 and 3 h after injection. Excellent uptake and retention of both ^{177}Lu-PSMA I&T and ^{177}Lu-PSMA-617 was noted in metastases and in residual or locally recurrent prostate cancer on posttherapy planar and SPECT/CT images (Fig. 2).

Whole Body

At all time points, retention of ^{177}Lu-PSMA-617 was higher than that of ^{177}Lu-PSMA I&T. The curves demonstrated an initial rapid washout followed by a second slower decline. On that account, the time–activity curves for whole body were fitted to a biexponential function. The half-lives were shorter for ^{177}Lu-PSMA I&T (35 h) than for ^{177}Lu-PSMA-617 (42 h). As a result of calculations from these kinetic parameters, the whole-body mean absorbed dose was higher for ^{177}Lu-PSMA-617 than for ^{177}Lu-PSMA I&T (0.04 vs. 0.03 Gy/GBq, $P < 0.00001$) (Fig. 3).

Kidneys

We analyzed the renal kinetics and kidney dosimetry of the 51 patients treated with ^{177}Lu-PSMA I&T and the 83 patients treated with ^{177}Lu-PSMA-617. Renal uptake was marginally higher for ^{177}Lu-PSMA I&T. For both ligands, uptake declined rapidly between the first scan and 3 h after injection, followed by a slower washout with a longer half-life for ^{177}Lu-PSMA-617. The effective renal half-lives for ^{177}Lu-PSMA-617 and ^{177}Lu-PSMA I&T were 40 and 33 h, respectively ($P = 0.00511$). As compared with ^{177}Lu-PSMA-617, the residence time was longer for ^{177}Lu-PSMA I&T ($P = 0.00138$), with initially higher uptake ($P < 0.00001$),

and the resulting renal dose was slightly but statistically significantly higher for ^{177}Lu-PSMA I&T. Calculated absorbed radiation doses of ^{177}Lu-PSMA-617 and ^{177}Lu-PSMA I&T in the kidneys were 0.8 and 0.9 Gy/GBq, respectively ($P = 0.0015$).

Parotid and Lacrimal Glands

The parotid glands were analyzed in 47 patients treated with ^{177}Lu-PSMA I&T and 80 patients treated with ^{177}Lu-PSMA-617. Both ligands demonstrated a first increase in activity until 3 h after injection before the exponential washout, whereas ^{177}Lu-PSMA-617 showed higher uptake and longer half-lives. The effective half-lives of the parotid glands for ^{177}Lu-PSMA-617 and ^{177}Lu-PSMA I&T were 31 and 23 h, respectively ($P < 0.00001$); yet, the mean absorbed dose of the different ligands was comparable in the parotid glands (0.5 Gy/GBq) ($P = 0.26603$) (Fig. 3).

The lacrimal glands were analyzed in 42 patients treated with ^{177}Lu-PSMA I&T and in 69 patients treated with ^{177}Lu-PSMA-617. Uptake was slightly higher and the half-life longer for ^{177}Lu-PSMA-617. The effective half-lives for ^{177}Lu-PSMA-617 and ^{177}Lu-PSMA I&T were 28 and 25 h, respectively ($P = 0.00269$). The resulting absorbed dose to the lacrimal glands was significantly higher for ^{177}Lu-PSMA-617 than for ^{177}Lu-PSMA I&T (5.1 vs. 3.7 Gy/GBq, $P = 0.000617$). Notably, among all normal organs, the lacrimal glands exhibited the highest absorbed doses— 31 and 22 Gy for ^{177}Lu-PSMA-617 and ^{177}Lu-PSMA I&T, respectively—for an injected activity of 6 GBq.

Tumor Dosimetry

Initial uptake was higher for ^{177}Lu-PSMA I&T than for ^{177}Lu-PSMA-617 (Fig. 4). Fitting of all time–activity curves to monoexponential functions from 20 h after injection led to significantly longer half-lives for ^{177}Lu-PSMA-617. Similar to the results for normal organs, the effective half-life in metastases was longer for ^{177}Lu-PSMA-617 (half-life, 61 h) than for ^{177}Lu-PSMA I&T (half-life, 43 h, $P < 0.00001$). The mean absorbed tumor doses extended over a wide range, whereas the medians of the mean absorbed tumor doses were comparable (^{177}Lu-PSMA-617 vs. ^{177}Lu-PSMA I&T, 5.9 vs. 5.8 Gy/GBq, $P = 0.96257$) (Fig. 5).

Bone and lymph node lesions were considered separately because most of the investigated lesions were bone or lymph node metastases. After administration of the therapeutic activity, the early elimination phase differed between the 2 ligands, demonstrating higher initial uptake and faster washout for ^{177}Lu-PSMA I&T in bone and lymph node lesions (Fig. 4). ^{177}Lu-PSMA-617 had a longer effective half-life than did ^{177}Lu-PSMA I&T in bone metastases (60 vs. 43 h, $P < 0.00001$) and lymph node metastases (55 vs. 42 h, $P = 0.0275$). However, the mean doses absorbed by bone metastases were comparable (^{177}Lu-PSMA-617 vs. ^{177}Lu-PSMA I&T, 6.0 vs. 5.9 Gy/GBq, $P = 0.82564$), as were the doses to lymph node metastases (^{177}Lu-PSMA-617 vs. ^{177}Lu-PSMA I&T, 7.1 vs. 6.9 Gy/GBq, $P = 0.94015$). For both ligands, the mean absorbed tumor dose was higher for lymph
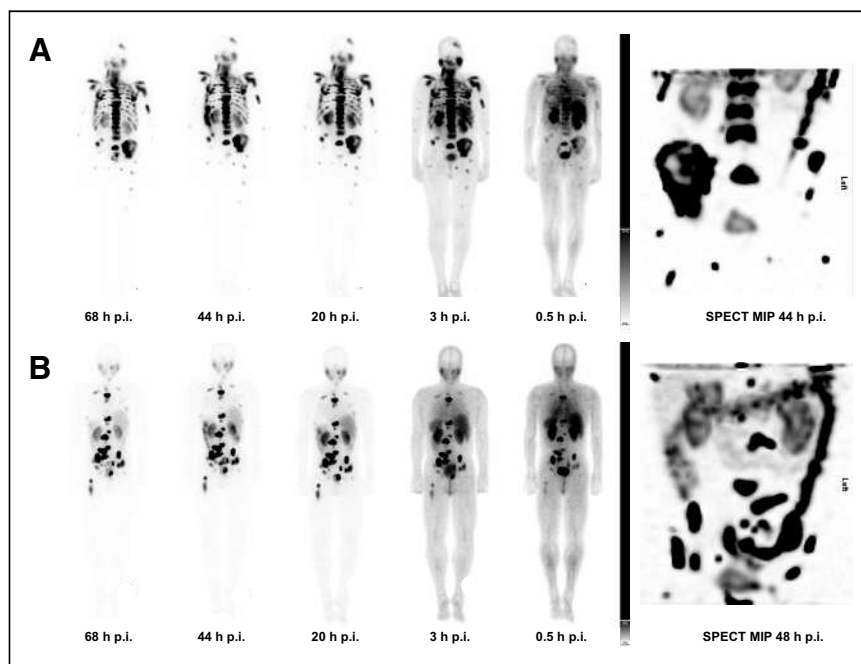
FIGURE 2. PRLT posttherapy scans and SPECT maximum-intensity-projection (MIP) image. (A) Scans after ^{177}Lu-PSMA I&T. (B) Scans after ^{177}Lu-PSMA-617. p.i. = after injection.
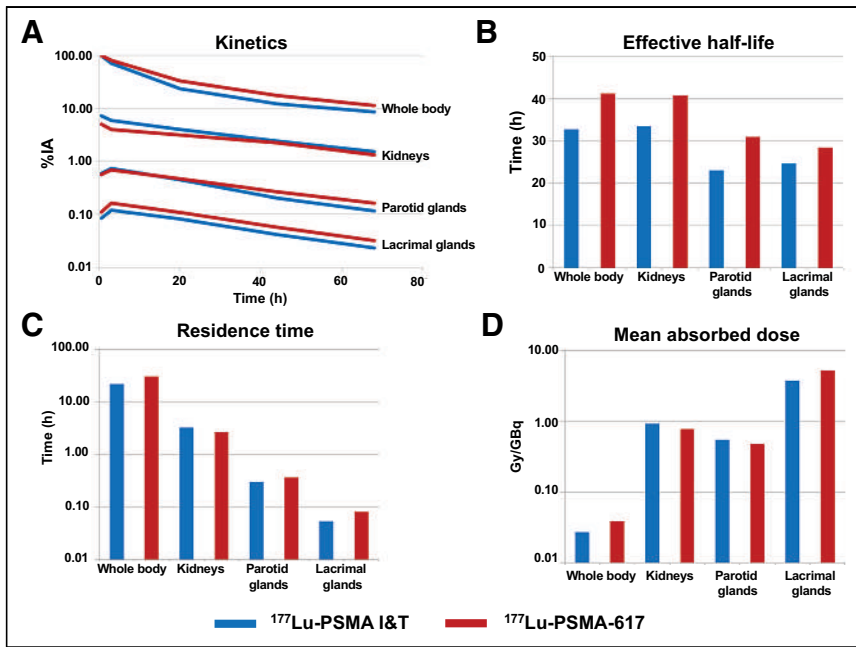
FIGURE 3. Biodistribution and dosimetry results for normal organs in patients treated with different PSMA ligands. (A) Kinetics: median uptakes in percentage administered activity. (B) Median effective half-life in hours. (C) Median residence time in hours. (D) Mean absorbed doses in Gy/GBq.

node lesions than for bone lesions (Fig. 5). The mean tumor-to-kidney absorbed dose ratio was slightly higher for ^{177}Lu-PSMA-617 (7.6) than for ^{177}Lu-PSMA I&T (6.3).

Treatment Toxicity

In no patients receiving either ^{177}Lu-PSMA I&T or ^{177}Lu-PSMA-617 were any serious acute side effects seen, nor were any seen during short-term follow-up (after 2 cycles of PRLT) or long-term follow-up (after 2–6 cycles of PRLT, with follow-up according to the last restaging; observation period, 3.2–48.5 mo; mean ± SD, 17.4 ± 11.9 mo; median, 13.2 mo). No change in blood pressure, heart rate, or body temperature was observed during therapy. The most common adverse effect was mild fatigue, which was observed in 20% of the patients and lasted a few days after therapy, more frequently after the first cycle. Five patients (3.6%) reported mild, reversible xerostomia—2 patients (3.9%) in the ^{177}Lu-PSMA I&T group and 3 (3.4%) in ^{177}Lu-PSMA-617 group—after 2–6 cycles of treatment and in follow-up. Xerophthalmia was not reported by any patients. No other adverse symptoms were noticed during the entire follow-up period.

Hematotoxicity and nephrotoxicity after ^{177}Lu-PSMA I&T and ^{177}Lu-PSMA-617 PRLT are detailed in Tables 2 and 3 and in Figure 6. There was no evidence of renal toxicity after either ^{177}Lu-PSMA I&T or ^{177}Lu-PSMA-617 PRLT, as determined by serum creatinine, creatinine clearance using the Cockcroft–Gault formula, or tubular extraction rate as determined by ^{99m}Tc-mercaptoacetyl-triglycine renal scintigraphy, which was performed before therapy and then every 3 mo during follow-up. No grade 3 or 4 nephrotoxicity, according to the Common Terminology Criteria for Adverse Events, was observed during any treatment cycle or during the longer follow-up. There was a small, statistically significant reduction in hemoglobin, leukocyte counts, and platelet counts after [177]Lu-

PSMA-617 and ^{177}Lu-PSMA I&T (Fig. 6), although the absolute differences were minimal and clinically insignificant. Remarkably, patients with low blood cell counts before therapy did not exhibit a decrease in blood cell counts after either ^{177}Lu-PSMA I&T or ^{177}Lu-PSMA-617 therapy.

DISCUSSION

In this study of a large cohort of mCRPC patients treated at a single center, we used an identical dosimetry protocol when depicting the biodistribution and dosimetric analysis results after either ^{177}Lu-PSMA I&T or ^{177}Lu-PSMA-617 PRLT therapy.

^{177}Lu-PSMA-617 exhibited a higher mean absorbed dose for whole body and lacrimal glands and showed longer half-lives in all normal organs and in tumor lesions, with the highest tumor doses being estimated for lymph node lesions. The initial tumor uptake was higher for ^{177}Lu-PSMA I&T than for ^{177}Lu-PSMA-617. The mean absorbed tumor doses extended over a wide range, whereas the medians of the mean absorbed tumor doses were comparable for both ^{177}Lu-PSMA I&T and ^{177}Lu-PSMA-617.

^{177}Lu-PSMA-617 had an estimated mean absorbed dose of 0.8 Gy/GBq for kidneys, 0.4 Gy/GBq for parotid glands, and 5.1 Gy/GBq for lacrimal glands (median values). Comparable results were reported by Zechmann et al. after they performed dosimetric estimations with ^{131}I-labeled PSMA ligands (32). Kabasakal et al. reported comparable organ doses in 7 patients who had received a pretherapeutic dose of ^{177}Lu-PSMA-617. The dosimetric approach used was based on planar imaging, to which attenuation correction was applied using PET/CT images (11). Delker et al. also evaluated the dosimetry of ^{177}Lu-PSMA-617 in 5 patients using whole-body scans and quantitative SPECT/CT. They estimated a slightly lower renal dose of 0.6 Gy/GBq than the 0.8 Gy/GBq found in the current study. Similarly, 1.4 Gy/GBq was reported for parotid glands, compared with 1.6 Gy/GBq in our study (mean values). Delker et al. reported mean absorbed tumor doses in the range of 1.2–47.5 Gy (14). In the current study, with a much larger patient population, we found a wider range of mean absorbed tumor doses (between 1.0 and 670 Gy per cycle for individual patients). The highest absorbed tumor dose, 670 Gy, was achieved in a lymph node metastasis in an mCRPC patient with lymph node and liver metastases during his second cycle of PRLT with 6.0 GBq of ^{177}Lu-PSMA-617.

The major route of excretion for both ^{177}Lu-labeled PSMA ligands is the kidneys, as noted by the predominant urinary excretion in the bladder. The high uptake in the kidneys may, however, be due to PSMA expression in renal tissue, because substantial uptake of the radiopharmaceutical was noticed, especially on the early ^{177}Lu-PSMA posttherapy images. Blocking of specific PSMA binding in the kidney tissue by 2-(phosphonomethyl)pentanedioic acid has been validated in preclinical studies, but this compound currently has limited availability for clinical use and also blocks tumor uptake (33). There was no evidence of renal toxicity after
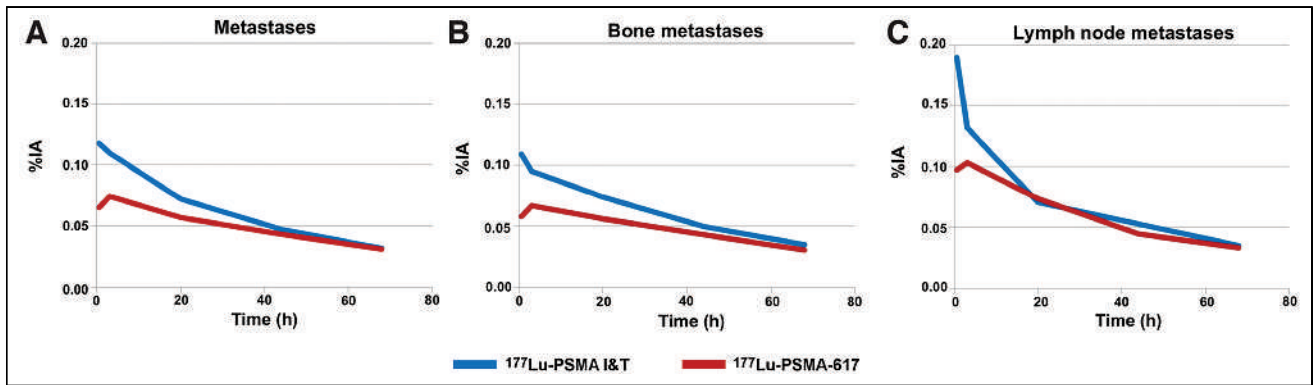
FIGURE 4. Kinetics of metastases and comparative results from 96 metastases (bone, lymph node, liver, lung, and other) of patients treated with ^{177}Lu-PSMA I&T and from 179 tumor lesions (bone, lymph node, liver, lung, and other) of patients treated with ^{177}Lu-PSMA-617. (A) Median kinetics of all types of metastases. (B) Median kinetics of bone metastases. (C) Median kinetics of lymph node metastases. After administration of therapeutic activity, higher initial uptakes and faster washout for ^{177}Lu-PSMA I&T were observed in bone and lymph node lesions. In contrast, curves of ^{177}Lu-PSMA-617 showed initial increase until 3 h after injection. %IA = percentage injected activity.

either ^{177}Lu-PSMA-617 or ^{177}Lu-PSMA I&T PRLT, inasmuch as there was no significant change in serum creatinine, in creatinine clearance as obtained by the Cockcroft–Gault formula, or in tubular extraction rate as determined by ^{99m}Tc-mercaptoacetyltriglycine renal scintigraphy.

According to the presented dosimetry results, we summarized the maximum activity and the number of possible therapy cycles to reach dose limits for both PSMA ligands (Supplemental Table 1; supplemental materials are available at http://jnm.snmjournals.org). Regarding the parotid glands, the maximum number of therapy cycles to reach the dose limit was 16 or 18, assuming an injected activity of 6 GBq of ^{177}Lu-PSMA I&T or ^{177}Lu-PSMA-617, respectively, per cycle. The renal dose, on the other hand, would limit the number of cycles to 4 in the case of ^{177}Lu-PSMA I&T and 5 in the case of ^{177}Lu-PSMA-617, if the 23-Gy rule, as known from external-beam radiotherapy, were used (34). However, the high number of cycles according to the current dose limit derived from external-beam radiotherapy may not reflect the true clinical status of the patients after radionuclide therapy. The absorbed dose to parotid glands in those patients who reported mild, reversible xerostomia in the present study was still under the dose limit. More therapy cycles with an accumulative dose over the absorbed dose limit of 23 Gy were feasible without any relevant side effects to the kidneys.

Therefore, the limit for renal dose from external-beam radiotherapy may not apply to PRLT.

In metastases, despite the increased effective half-life and residence time of ^{177}Lu-PSMA-617, as compared with ^{177}Lu-PSMA I&T, the resulting mean absorbed tumor doses were not significantly different for these 2 ligands. This result is most probably due to the higher initial uptake of ^{177}Lu-PSMA I&T than of ^{177}Lu-PSMA-617. In addition, the nonhomogeneously distributed sample of metastases in both patient cohorts could have had an influence, as the median volume of metastases was lower for patients treated with PSMA I&T (median volume, 3 cm^3) than for those treated with PSMA-617 (median volume, 6 cm^3). When lesions with similar residence times are compared, smaller lesions will get the higher mean absorbed dose.

For the dosimetry results, high interpatient variability was found, especially concerning the mean absorbed doses; this finding was not unexpected since the group of patients was very heterogeneous. In addition, earlier results from a study on peptide receptor radionuclide therapy also demonstrated a high intrapatient variability in patients undergoing therapy with different peptides; even in a large cohort of patients, we found a broad range of results (20,21). This finding implies that the median or mean value of a dosimetric parameter varies among patients. Although the variability may be
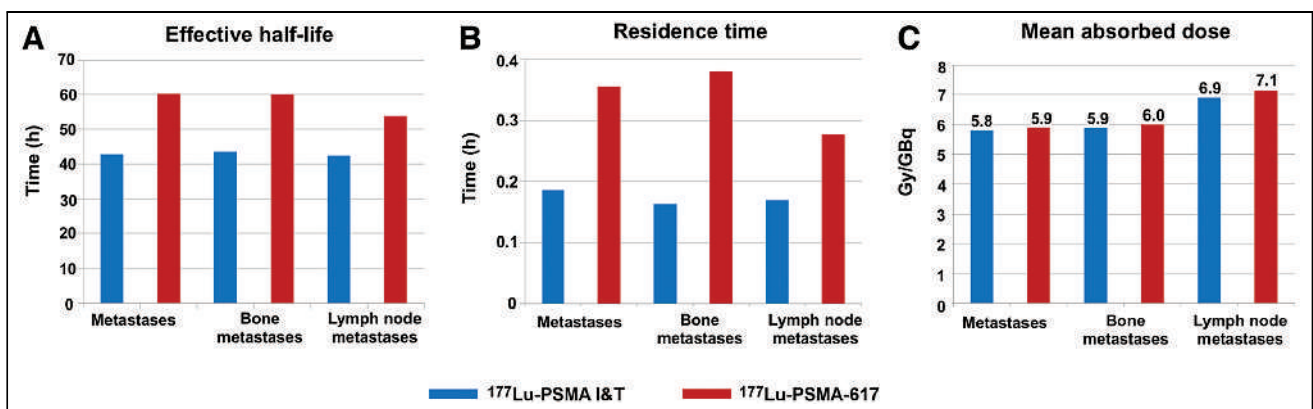
FIGURE 5. Comparative dosimetry results of metastases. (A) Median effective half-life. (B) Median residence time. (C) Mean absorbed dose.

TABLE 2
Hematotoxicity and Nephrotoxicity after ^{177}Lu-PSMA I&T PRLT According to Common Terminology Criteria for Adverse Events, version 5.0 (n = 35)

	Numbers of patients with…											
	Anemia			Leukocytopenia			Thrombocytopenia			Nephrotoxicity		
Grade	Pretherapy	After 2 cycles	Long-term FU	Pretherapy	After 2 cycles	Long-term FU	Pretherapy	After 2 cycles	Long-term FU	Pretherapy	After 2 cycles	Long-term FU
CTC-1	21	30	24	5	3	6	1	2	8	5	5	7
CTC-2	1	2	8	1	1	2	0	1	1	0	0	0
CTC-3	0	0	1	0	0	1	0	0	0	0	0	0
CTC-4	0	0	0	0	0	0	0	0	0	0	0	0
CTC-5	NA	0	0	NA	0	0	NA	0	0	NA	0	0

FU = follow-up; CTC = Common Terminology Criteria grade; NA = not applicable before therapy (grade 5 represents death).

TABLE 3
Hematotoxicity and Nephrotoxicity After ^{177}Lu-PSMA-617 PRLT According to Common Terminology Criteria for Adverse Events, version 5.0 (n = 66)

	Numbers of patients with…											
	Anemia			Leukocytopenia			Thrombocytopenia			Nephrotoxicity		
Grade	Pretherapy	After 2 cycles	Long-term FU	Pretherapy	After 2 cycles	Long-term FU	Pretherapy	After 2 cycles	Long-term FU	Pretherapy	After 2 cycles	Long-term FU
CTC-1	44	45	46	8	12	12	7	12	15	11	12	12
CTC-2	7	14	14	1	3	5	1	2	4	2	1	2
CTC-3	0	0	0	0	1	1	0	0	4	0	0	0
CTC-4	0	0	0	0	0	0	0	0	0	0	0	0
CTC-5	NA	0	0	NA	0	0	NA	0	0	NA	0	0

FU = follow-up; CTC = Common Terminology Criteria grade; NA = not applicable before therapy (grade 5 represents death).
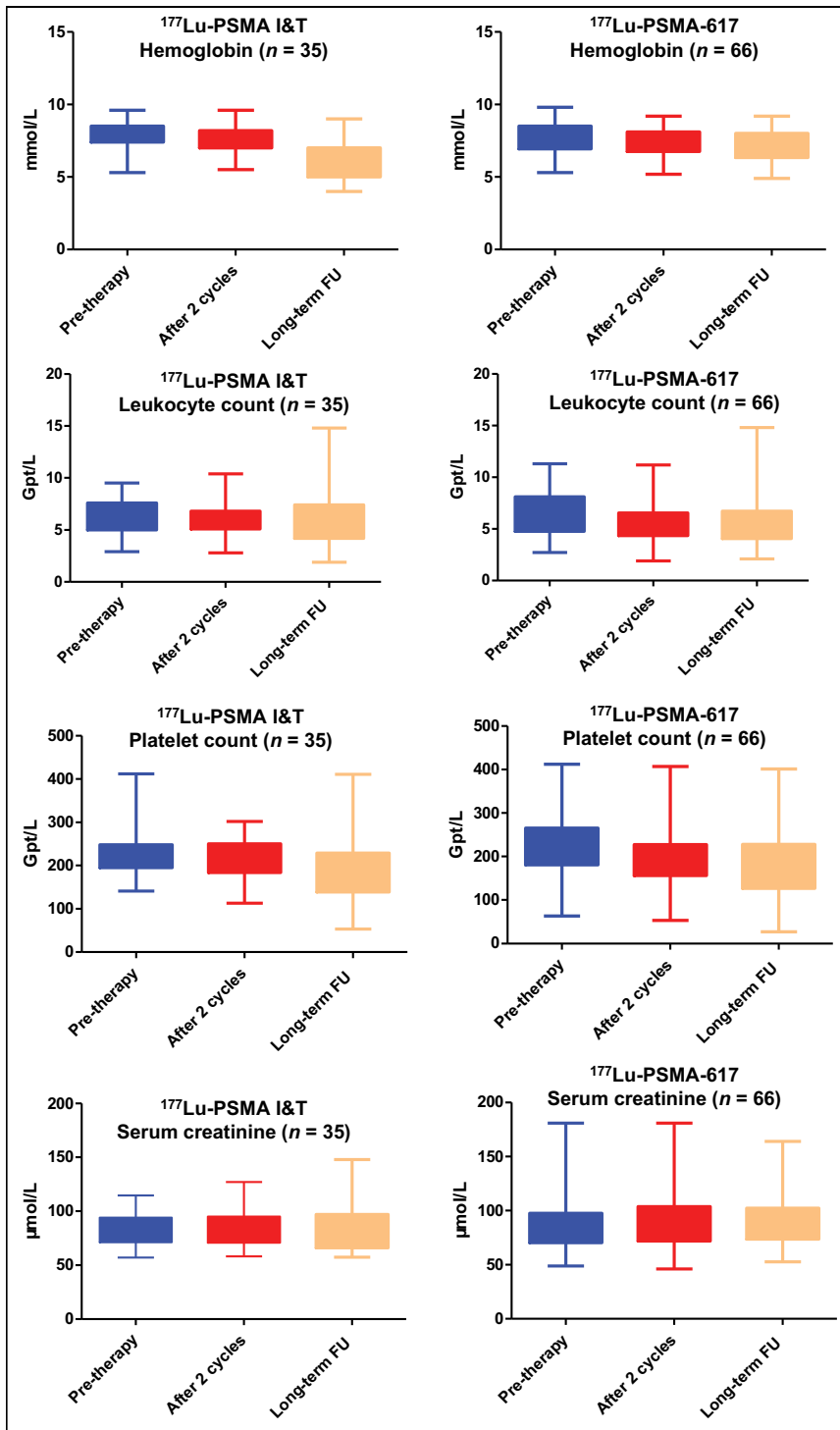
FIGURE 6. Comparison of laboratory parameters (hemoglobin, leukocyte, platelet, and serum creatinine) before therapy, after 2 cycles, and after 2–6 cycles with long-term follow up (FU) (observation period, 3.2–48.5 mo; mean ± SD, 17.4 ± 11.9 mo; median, 13.2 mo) for ^{177}Lu-PSMA I&T and ^{177}Lu-PSMA-617 PRLT.

applied, and the baseline characteristics of the 2 groups were heterogeneous. Additionally, the wide interpatient variability should be addressed in further studies: inasmuch as significant variations were found even in the large cohort of patients, median values of absorbed doses among patients should not be the only criterion for planning PRLT. Besides the described methods for individual dosimetry, interindividual differences should be considered.

CONCLUSION

Both ^{177}Lu-PSMA I&T and ^{177}Lu-PSMA-617 PRLT demonstrated favorable safety in mCRPC patients. The highest absorbed doses among healthy organs were observed for the lacrimal and parotid glands, not, however, resulting in any significant clinical side effects. ^{177}Lu-PSMA-617 showed longer half-lives in all normal organs and in tumor lesions than did ^{177}Lu-PSMA I&T. ^{177}Lu-PSMA I&T exhibited a higher initial tumor uptake than did ^{177}Lu-PSMA-617. The mean absorbed tumor doses were comparable for both ^{177}Lu-PSMA I&T and ^{177}Lu-PSMA-617. The results of this study further demonstrated that estimation of mean absorbed doses to critical organs and tumor lesions is necessary when evaluating the risks of PRLT and, therefore, when describing the clinical benefit to the patient. Individual patient-based dosimetry seems favorable for personalized PRLT.

DISCLOSURE

ACKNOWLEDGMENT

attributed to differences in biologic behavior among the different ligands, it may be also ascribable to widely differing prior therapies.

This study had a few limitations, such as its retrospective design. No strict pretest criteria for selection of patients were

KEY POINTS

QUESTION: Do ^{177}Lu-PSMA I&T and ^{177}Lu-PSMA-617 differ in safety, biodistribution, and dosimetry for PRLT in patients with mCRPC?

PERTINENT FINDINGS: In a large cohort of 138 patients with mCRPC undergoing PRLT under an identical dosimetry protocol, ^{177}Lu-PSMA-617 showed longer half-lives in all normal organs and in tumor lesions; ^{177}Lu-PSMA I&T exhibited a higher initial tumor uptake than did ^{177}Lu-PSMA-617. The mean absorbed tumor doses were comparable for both ^{177}Lu-PSMA I&T and ^{177}Lu-PSMA-617.

IMPLICATIONS FOR PATIENT CARE: The results of this study demonstrate that estimation of mean absorbed doses to critical organs and tumor lesions is necessary when evaluating the risks of PRLT and, therefore, when describing the clinical benefit to the patient.

REFERENCES

1. Sung H, Ferlay J, Siegel RL, et al. Global cancer statistics 2020: GLOBOCAN estimates of incidence and mortality worldwide for 36 cancers in 185 countries. *CA Cancer J Clin.* 2021;71:209–249.

2. Halabi S, Vogelzang NJ, Kornblith AB, et al. Pain predicts overall survival in men with metastatic castration-refractory prostate cancer. *J Clin Oncol.* 2008;26:2544–2549.

3. Hofman MS, Violet J, Hicks RJ, et al. [177Lu]-PSMA-617 radionuclide treatment in patients with metastatic castration-resistant prostate cancer (LuPSMA trial): a single-centre, single-arm, phase 2 study. *Lancet Oncol.* 2018;19:825–833.

4. Violet J, Sandhu S, Iravani A, et al. Long-term follow-up and outcomes of retreatment in an expanded 50-patient single-center phase II prospective trial of ^{177}Lu-PSMA-617 theranostics in metastatic castration-resistant prostate cancer. *J Nucl Med.* 2020;61:857–865.

5. Hofman MS, Emmett L, Sandhu S, et al. [177Lu]Lu-PSMA-617 versus cabazitaxel in patients with metastatic castration-resistant prostate cancer (TheraP): a randomised, open-label, phase 2 trial. *Lancet.* 2021;397:797–804.

6. Kratochwil C, Bruchertseifer F, Giesel FL, et al. [225]Ac-PSMA-617 for PSMA-targeted alpha-radiation therapy of metastatic castration-resistant prostate cancer. *J Nucl Med.* 2016;57:1941–1944.

7. Kratochwil C, Haberkorn U, Giesel FL. [225]Ac-PSMA-617 for therapy of prostate cancer. *Semin Nucl Med.* 2020;50:133–140.

8. Zacherl MJ, Gildehaus FJ, Mittlmeier L, et al. First clinical results for PSMA-targeted α-therapy using [225]Ac-PSMA-I&T in advanced-mCRPC patients. *J Nucl Med.* 2021;62:669–674.

9. Rosar F, Hau F, Bartholoma M, et al. Molecular imaging and biochemical response assessment after a single cycle of [[225]Ac]Ac-PSMA-617/[^{177}Lu]Lu-PSMA-617 tandem therapy in mCRPC patients who have progressed on [^{177}Lu]Lu-PSMA-617 monotherapy. *Theranostics.* 2021;11:4050–4060.

10. van der Doelen MJ, Mehra N, van Oort IM, et al. Clinical outcomes and molecular profiling of advanced metastatic castration-resistant prostate cancer patients treated with [225]Ac-PSMA-617 targeted alpha-radiation therapy. *Urol Oncol.* 2021;39:729.e7–729.e16.

11. Kabasakal L, AbuQbeitah M, Aygun A, et al. Pre-therapeutic dosimetry of normal organs and tissues of ^{177}Lu-PSMA-617 prostate-specific membrane antigen (PSMA) inhibitor in patients with castration-resistant prostate cancer. *Eur J Nucl Med Mol Imaging.* 2015;42:1976–1983.

12. Violet J, Jackson P, Ferdinandus J, et al. Dosimetry of ^{177}Lu-PSMA-617 in metastatic castration-resistant prostate cancer: correlations between pretherapeutic imaging and whole-body tumor dosimetry with treatment outcomes. *J Nucl Med.* 2019;60:517–523.

13. Okamoto S, Thieme A, Allmann J, et al. Radiation dosimetry for ^{177}Lu-PSMA I&T in metastatic castration-resistant prostate cancer: absorbed dose in normal organs and tumor lesions. *J Nucl Med.* 2017;58:445–450.

14. Delker A, Fendler WP, Kratochwil C, et al. Dosimetry for ^{177}Lu-DKFZ-PSMA-617: a new radiopharmaceutical for the treatment of metastatic prostate cancer. *Eur J Nucl Med Mol Imaging.* 2016;43:42–51.

15. Barna S, Haug AR, Hartenbach M, et al. Dose calculations and dose-effect relationships in ^{177}Lu-PSMA I&T radionuclide therapy for metastatic castration-resistant prostate cancer. *Clin Nucl Med.* 2020;45:661–667.

16. Hou X, Brosch J, Uribe C, et al. Feasibility of single-time-point dosimetry for radiopharmaceutical therapies. *J Nucl Med.* 2021;62:1006–1011.

17. Jackson PA, Hofman MS, Hicks RJ, Scalzo M, Violet J. Radiation dosimetry in ^{177}Lu-PSMA-617 therapy using a single posttreatment SPECT/CT scan: a novel methodology to generate time- and tissue-specific dose factors. *J Nucl Med.* 2020;61:1030–1036.

18. Rinscheid A, Kletting P, Eiber M, Beer AJ, Glatting G. Influence of sampling schedules on [^{177}Lu]Lu-PSMA dosimetry. *EJNMMI Phys.* 2020;7:41.

19. Peters SMB, Prive BM, de Bakker M, et al. Intra-therapeutic dosimetry of [^{177}Lu]Lu-PSMA-617 in low-volume hormone-sensitive metastatic prostate cancer patients and correlation with treatment outcome. *Eur J Nucl Med Mol Imaging.* 2022;49:460–469.

20. Wehrmann C, Senftleben S, Zachert C, Muller D, Baum RP. Results of individual patient dosimetry in peptide receptor radionuclide therapy with ^{177}Lu DOTA-TATE and ^{177}Lu DOTA-NOC. *Cancer Biother Radiopharm.* 2007;22:406–416.

21. Schuchardt C, Kulkarni HR, Prasad V, Zachert C, Muller D, Baum RP. The Bad Berka dose protocol: comparative results of dosimetry in peptide receptor radionuclide therapy using ^{177}Lu-DOTATATE, ^{177}Lu-DOTANOC, and ^{177}Lu-DOTA-TOC. *Recent Results Cancer Res.* 2013;194:519–536.

22. "Compassionate use" programmes. Federal Institute for Drugs and Medical Devices website. https://www.bfarm.de/EN/Medicinal-products/Clinical-trials/Compassionate-Use/_node.html. Published 2013. Accessed May 25, 2022.

23. Baum RP, Kulkarni HR, Schuchardt C, et al. ^{177}Lu-labeled prostate-specific membrane antigen radioligand therapy of metastatic castration-resistant prostate cancer: safety and efficacy. *J Nucl Med.* 2016;57:1006–1013.

24. Weineisen M, Schottelius M, Simecek J, et al. [68]Ga- and ^{177}Lu-labeled PSMA I&T: optimization of a PSMA-targeted theranostic concept and first proof-of-concept human studies. *J Nucl Med.* 2015;56:1169–1176.

25. Stabin MG, Siegel JA. Physical models and dose factors for use in internal dose assessment. *Health Phys.* 2003;85:294–310.

26. Sgouros G. Dosimetry of internal emitters. *J Nucl Med.* 2005;46(suppl 1):18S–27S.

27. Siegel JA, Thomas SR, Stubbs JB, et al. MIRD pamphlet no. 16: techniques for quantitative radiopharmaceutical biodistribution data acquisition and analysis for use in human radiation dose estimates. *J Nucl Med.* 1999;40(suppl):37S–61S.

28. Bolch WE, Eckerman KF, Sgouros G, Thomas SR. MIRD pamphlet no. 21: a generalized schema for radiopharmaceutical dosimetry—standardization of nomenclature. *J Nucl Med.* 2009;50:477–484.

29. Stabin MG, Sparks RB, Crowe E. OLINDA/EXM: the second-generation personal computer software for internal dose assessment in nuclear medicine. *J Nucl Med.* 2005;46:1023–1027.

30. Stabin MG, Siegel JA. RADAR dose estimate report: a compendium of radiopharmaceutical dose estimates based on OLINDA/EXM version 2.0. *J Nucl Med.* 2018;59:154–160.

31. Bingham CM, Castro A, Realini T, Nguyen J, Hogg JP, Sivak-Callcott JA. Calculated CT volumes of lacrimal glands in normal Caucasian orbits. *Ophthal Plast Reconstr Surg.* 2013;29:157–159.

32. Zechmann CM, Afshar-Oromieh A, Armor T, et al. Radiation dosimetry and first therapy results with a [124]I/^{131}I-labeled small molecule (MIP-1095) targeting PSMA for prostate cancer therapy. *Eur J Nucl Med Mol Imaging.* 2014;41:1280–1292.

33. Kratochwil C, Giesel FL, Leotta K, et al. PMPA for nephroprotection in PSMA-targeted radionuclide therapy of prostate cancer. *J Nucl Med.* 2015;56:293–298.

34. Emami B, Lyman J, Brown A, et al. Tolerance of normal tissue to therapeutic irradiation. *Int J Radiat Oncol Biol Phys.* 1991;21:109–122.

^{18}F-rhPSMA-7 PET for the Detection of Biochemical Recurrence of Prostate Cancer After Curative-Intent Radiation Therapy: A Bicentric Retrospective Study

Harun Ilhan*[1,2], Markus Kroenke*[3], Alexander Wurzer[4], Marcus Unterrainer[1,5], Matthias Heck[6], Claus Belka[7], Karina Knorr[3], Thomas Langbein[3], Isabel Rauscher[3], Nina-Sophie Schmidt-Hegemann[7], Kilian Schiller[8], Peter Bartenstein[1], Hans-Jürgen Wester[4], and Matthias Eiber[3]

[1]Department of Nuclear Medicine, University Hospital, LMU Munich, Munich, Germany; [2]Die Radiologie, Munich, Germany; [3]Department of Nuclear Medicine, School of Medicine, Technical University of Munich, Munich, Germany; [4]Chair of Pharmaceutical Radiochemistry, Technical University of Munich, Garching, Germany; [5]Department of Radiology, University Hospital, LMU Munich, Munich, Germany; [6]Department of Urology, Technical University of Munich, Munich, Germany; [7]Department of Radiation Oncology, University Hospital, LMU Munich, Munich, Germany; and [8]Department of Radiation Oncology, School of Medicine, Technical University of Munich, Munich, Germany

This bicentric, retrospective analysis investigated the efficacy of PET/CT with a novel theranostic prostate-specific membrane antigen (PSMA)–targeting ligand, ^{18}F-rhPSMA-7, in patients with biochemical recurrence (BCR) of prostate cancer after curative-intent primary radiotherapy. **Methods:** Datasets from patients with BCR of prostate cancer after external-beam radiation therapy or brachytherapy who underwent ^{18}F-rhPSMA-7 PET/CT at either Technical University Munich or Ludwig-Maximilians-University Munich were retrospectively reviewed by experienced nuclear medicine physicians and radiologists at both centers. The median injected activity was 299 MBq (range, 204–420 MBq), and the median uptake time was 77 min (range, 46–120 min). All lesions suggestive of recurrent prostate cancer were noted. Detection rates were correlated with patients' prostate-specific antigen (PSA) level, primary Gleason score, and prior use of androgen-deprivation therapy (ADT). **Results:** Ninety-seven patients were included (65 at Technical University Munich and 32 at Ludwig-Maximilians-University Munich). The median prescan PSA was 4.19 ng/mL (range, 0.1–159 ng/mL). The primary Gleason score was ≤6 in 19 patients, 7 in 25, ≥8 in 33, and unknown in 20. Thirty patients received ADT in the 6 mo preceding PET/CT. ^{18}F-rhPSMA-7 identified lesions in 91 of 97 (94%) patients. Detection rates stratified by PSA were 88% (22/25), 97% (30/31), 90% (19/21), and 100% (20/20) for a PSA of <2, 2–<5, 5–<10, and ≥10 ng/mL, respectively. Detection rates in the subgroup of patients not meeting the Phoenix criteria for BCR were 80% (4/5), 90% (9/10), 100% (4/4), and 83% (5/6) for a PSA of <0.5, 0.5–<1, 1–<1.5, and 1.5–2 ng/mL, respectively. There were no significant differences in detection rates between patients with and without prior ADT (100% vs. 91%, P = 0.173) or patients with a Gleason score of ≤7 and a Gleason score of ≥8 (98% vs. 91%, P = 0.316).^{18}F-rhPSMA-7 revealed local recurrence in 80% (78/97); pelvic lymph node metastases in 38% (37/97); retroperitoneal and supradiaphragmatic lymph node metastases in 9% (9/97) and 4% (4/97), respectively; bone metastases in 27% (26/97); and visceral metastases in 3% (3/97). In the subgroup of patients with a PSA of <2 ng/mL above nadir, local recurrence occurred in 76% (19/25) and pelvic lymph node metastases in 36% (9/25). **Conclusion:** ^{18}F-rhPSMA-7 PET/CT demonstrates high detection rates in prostate cancer patients with BCR after primary radiation therapy, even at low PSA values. Its diagnostic efficacy is comparable to published data for other PSMA ligands.

Key Words: prostate-specific membrane antigen; PSMA; PET imaging; biochemical recurrence; BCR; radiation therapy

Biochemical recurrence (BCR) of prostate cancer with rising prostate-specific antigen (PSA) levels is observed in up to half of patients after radical prostatectomy (RP) or primary radiotherapy with curative intent and represents the first sign of treatment failure (*1*). The definition of BCR, however, depends on the applied primary therapy option. BCR after RP is defined by 2 consecutive PSA rises of >0.2 ng/mL (*2*), whereas BCR after radiotherapy is defined by a PSA rise of ≥2 ng/mL above the nadir (*3*). This PSA threshold defined by the Phoenix criteria was presented in 2006, when detection of prostate cancer recurrence was based on conventional imaging. Highly sensitive molecular imaging methods, such as PET with prostate-specific membrane antigen (PSMA)–targeting ligands, were not yet available.

^{68}Ga-labeled PSMA ligands provide high sensitivity for the detection of BCR, with increasing pooled detection rates of 42%, 58%, 76%, and 95% at rising PSA categories of 0–0.2, >0.2–1, >1–2, and >2 ng/mL (*4*). Thus PSMA PET might also be of high value in patients after primary curative-intent radiotherapy, even those at earlier stages of BCR with low PSA values. Although ^{68}Ga-labeled compounds are currently the most used tracers for PSMA-targeted PET imaging, ^{18}F-labeled PSMA ligands offer advantages regarding half-life and image resolution.

Several ^{18}F-labeled PSMA ligands (e.g., DCFPyL and PSMA-1007) have been introduced and are being evaluated in phase III clinical studies, with DCFPyL being recently approved. The first data indicate similar diagnostic performance, with pooled BCR detection rates of 49%, 73%, 88%, and 92% for PSA categories of 0–0.5, >0.5–1, >1–2, and >2 ng/mL, respectively (*5*). Furthermore, hepatobiliary excretion of ^{18}F-PSMA-1007 reduces tracer accumulation in

the urinary bladder, as might be of particular value in cases of BCR after primary radiotherapy, with local recurrence and pelvic lymph node metastases representing common localizations of prostate cancer recurrence (6,7). Detection rates for BCR are reported mainly in patients after primary RP, and data on the diagnostic efficacy of ^{18}F-labeled PSMA ligands have been presented only within mixed cohorts of RP and radiotherapy patients; therefore, specific information on diagnostic performance in patients with BCR after curative-intent radiotherapy is rare (5).

Recently, radiohybrid PSMA (rhPSMA) ligands have been introduced as novel theranostic PSMA agents enabling radiolabeling with radiometals (e.g., ^{68}Ga and ^{177}Lu) and [18]F (8). Initial data for its lead compound, ^{18}F-rhPSMA-7, state that its diagnostic performance for primary N-staging and localization of BCR after RP is similar to that of other PSMA ligands (9,10). Its urinary excretion is lower than that of ^{68}Ga-PSMA-11 even after an uptake time of up to 2.5 h (11). Here, we present the results of a bicentric, retrospective analysis evaluating the diagnostic efficacy of ^{18}F-rhPSMA-7 PET/CT in patients with BCR after primary curative-intent radiotherapy.

MATERIALS AND METHODS

Patients

Data from prostate cancer patients with BCR after primary radiotherapy with curative intent who underwent PET/CT with ^{18}F-rhPSMA-7 between October 2017 and March 2019 at the Technical University Munich (TUM) or the Ludwig-Maximilians-University Munich (LMU) were retrospectively reviewed. Patients with prior salvage prostatectomy after primary radiotherapy or documented castration-resistant disease were excluded. Finally, 97 patients were included, and their PSA values and clinical information on prior therapies, including prior androgen deprivation therapy (ADT), were noted. The retrospective analysis was approved by the local Ethics Committee at both centers (TUM permit 290/18S; LMU permit 20-178). The requirement to obtain written informed consent was waived.

Synthesis, Administration, and Imaging of ^{18}F-rhPSMA-7

[18]F-rhPSMA-7 was radiolabeled as described previously (8). ^{18}F-rhPSMA-7 was administered in compliance with the German Medicinal Products Act, AMG § 13 2b and the responsible regulatory body (government of Upper Bavaria). The median injected activity was 299 MBq (mean, 306 MBq; range, 204–420 MBq), and the median uptake time was 77 min (mean, 76 min; range, 46–120 min). Patients received a diluted oral contrast medium (300 mg of Telebrix) and 20 mg of furosemide.

[18]F-rhPSMA-7 PET/CT was performed on a Biograph mCT Flow scanner (Siemens Medical Solutions) (73 patients: 65 at TUM and 8 at LMU) and on a Discovery 690 scanner (GE Healthcare) (24 patients at LMU). PET/CT scans were acquired in 3-dimensional mode with an acquisition time of 1.1 mm/s on the Biograph mCT Flow and 2.5 min per bed position on the Discovery 690. PET images were reconstructed using ordered-subset expectation maximization (Biograph mCT Flow: TrueX, 4 iterations, 8 subsets; Discovery 690: VUE point FX, 2 iterations, 26 subsets) followed by a postreconstruction smoothing gaussian filter (5 mm in full width at half maximum). Phantom studies based on the National Electrical Manufacturers Association NU2-2001 standard were conducted at LMU to allow valid pooling of results between Siemens and GE Healthcare scanners. A diagnostic CT scan was performed before the PET scan during the portal venous phase 80 s after intravenous injection of contrast agent.

Image Analysis

All images were interpreted during clinical rounds by a consensus reading by an experienced, board-certified nuclear medicine physician and a board-certified radiologist and centrally reevaluated by an experienced nuclear medicine physician at each site. Any focal tracer accumulation higher than the surrounding background and not associated with physiologic uptake or unspecific tracer uptake due to typical pitfalls (12) was considered suggestive of malignancy. All lesions suspected of representing prostate cancer recurrence were noted. Lesions were categorized as local recurrence (prostate bed), lymph node metastases (further stratified as pelvic, retroperitoneal, or supradiaphragmatic), bone metastases, or other distant metastases (e.g., visceral metastases).

Statistical Analysis

Detection rates of lesions representing prostate cancer recurrence were plotted against baseline PSA values on a per-patient basis and on a localization basis (local recurrence, lymph node metastases, bone metastases, and other metastases). Descriptive analysis was performed by calculating the median, mean, range, and interquartile range. Unpaired 2-sample t tests and Mann–Whitney U tests were used to evaluate differences between single groups. The Fisher exact test was used to evaluate detection rates in patients with and without ADT and in patients with Gleason scores of ≤ 7 and ≥ 8. A P value of less than 0.05 was considered significant. Statistical analyses were performed using SPSS statistics (version 26; IBM).

RESULTS

In total, 97 patients were included in this bicentric retrospective analysis. The median age was 74 y (range, 57–87 y). The PSA value within the 4 wk preceding ^{18}F-rhPSMA-7 PET/CT was documented for every patient; median PSA before PET was 4.19 ng/mL (range, 0.0–159 ng/mL; interquartile range, 1.96–8.6 ng/mL). Twenty-five patients (26%) had a PSA of ≤ 2 ng/mL and did not reach the PSA threshold for BCR defined by the Phoenix criteria; the median PSA in this subgroup was 0.88 ng/mL (range, 0.0–1.96 ng/mL; interquartile range, 0.7–1.46 ng/mL). Thirty patients (31%) had received ADT within 6 mo before PET/CT. Detailed patient characteristics, including primary Gleason score and initial PSA, are provided in Table 1.

Detection Rate of ^{18}F-rhPSMA-7 PET/CT on a Patient Basis

Detection Efficacy. ^{18}F-rhPSMA-7 PET/CT showed pathologic findings suggestive of prostate cancer recurrence in 91 of 97 patients (94%). The mean PSA in patients with at least one localized area suggestive of recurrent prostate cancer was 9.6 ng/mL, compared with 3.1 ng/mL in PET-negative patients ($P = 0.183$). The overall detection efficacy stratified by PSA was 88% (22/25) for a PSA of <2 ng/mL, 97% (30/31) for 2–<5 ng/mL, 90% (19/21) for 5–<10 ng/mL, and 100% (20/20) for ≥ 10 ng/mL (Fig. 1). After further subclassification of patients outside the Phoenix criteria for BCR ($n = 25$), detection rates were 80% (4/5) for a PSA of <0.5 ng/mL, 90% (9/10) for 0.5–<1 ng/mL, 100% (4/4) for 1–<1.5 ng/mL, and 83% (5/6) for 1.5–<2 ng/mL (Fig. 2).

Effect of ADT and Gleason Score. There were no significant differences in detection rates among patients with prior ADT in the 6 mo preceding ^{18}F-rhPSMA-7 PET/CT (100% [30/30]) and those without prior ADT (91% [61/67], $P = 0.173$; Fig. 3A) or patients with a Gleason score of ≤ 7 (98% [42/43]) and those with a Gleason score of ≥ 8 (91% [31/34], $P = 0.316$; Fig. 3B).

Localization of ^{18}F-rhPSMA-7 PET–Positive Lesions

Detailed localization of ^{18}F-rhPSMA-7–avid lesions suggestive of recurrence of prostate cancer is shown in Table 2. A clear trend toward a higher proportion of patients with distant metastases

TABLE 1
Patient Characteristics

Characteristic	Value
Total patients (n)	97
Age at time of ^{18}F-rhPSMA-7 PET/CT (y)	
Median	74
Range	57–87
Previous primary therapy with curative intent (n)	
EBRT (photon therapy)	76
EBRT (proton therapy)	4
Brachytherapy	13
Brachytherapy and photon therapy	4
Gleason score (n)	
≤6	19
7	25
≥8	33
Unknown	20
Initial PSA (ng/mL)	
Median	10.86
Range	0.72–80.77
Interquartile range	7.5–17.6
Unknown (n)	31
PSA before ^{18}F-rhPSMA-7 PET/CT (ng/mL)	
Median	4.19
Range	0.1–159.0
Interquartile range	1.96–8.60
ADT during/within 6 mo before ^{18}F-rhPSMA-7 PET/CT (n)	30
Median time between radiotherapy and ^{18}F-rhPSMA-7 PET/CT (mo)	97

EBRT = external-beam radiation therapy.

FIGURE 2. Detection rate stratified by PSA value in patients with PSA of <2 ng/mL not meeting Phoenix criteria for BCR after radiotherapy (n = 25).

(nonregional lymph node metastases and bone metastases) was noted with rising PSA (Fig. 4). Overall local recurrence was observed in 80% (78/97), pelvic lymph node metastases in 38% (37/97), nonregional lymph nodes in 13% (13/97), bone metastases in 27% (26/97), and visceral metastases in 3% (3/97; 2 patients with penile metastases and 1 patient with lung metastasis).

In the subgroup of patients with PSA values of <2 ng/mL, local recurrence occurred in 76% of patients (19/25) and pelvic lymph node metastases in 36% (9/25). Furthermore, a low number of distant metastases, including bone metastases in 20% (5/25) and visceral metastasis in 4% (1/25), were present; no nonregional retroperitoneal or supradiaphragmatic lymph nodes were detected on ^{18}F-rhPSMA-7 PET/CT.

DISCUSSION

This bicentric, retrospective analysis evaluated the diagnostic efficacy of the novel ^{18}F-labeled PSMA ligand, ^{18}F-rhPSMA-7, for the detection of prostate cancer recurrence in patients after primary radiotherapy with curative intent. Recently, it has been shown that ^{18}F-rhPSMA-7 provides high detection rates for BCR after RP (9). Of 261 patients with a median PSA of 0.91 ng/mL, 211 (81%) showed at least 1 lesion suggestive of prostate cancer

FIGURE 1. Overall detection rate for all patients (n = 97) stratified by PSA value.
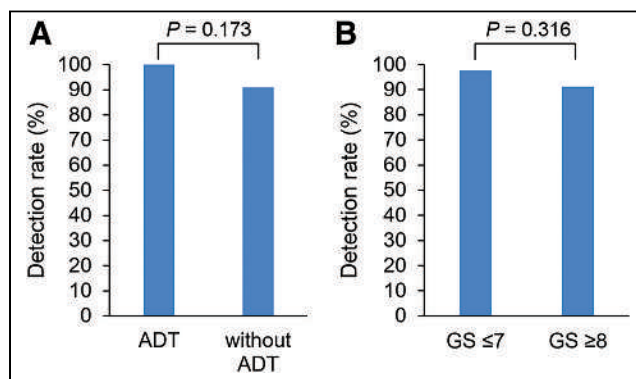
FIGURE 3. Detection rates stratified by prior ADT use within 6 mo preceding ^{18}F-rhPSMA-7 PET/CT (A) and primary Gleason score (B). GS = Gleason score.

| PSA value (ng/mL) | Local recurrence | Pelvic lymph node metastases (N1) | Distant metastases | | | |
			Retroperitoneal lymph nodes (M1a)	Supradiaphragmatic lymph nodes (M1a)	Bone metastases (M1b)	Visceral metastases (M1c)
<2	19/25 (76%)	9/25 (36%)	0/25 (0%)	0/25 (0%)	5/25 (20%)	1/25 (4%)
2–<5	26/31 (84%)	6/31 (19%)	4/31 (13%)	1/31 (3%)	8/31 (26%)	1/31 (3%)
5–<1	16/21 (76%)	12/21 (57%)	1/21 (5%)	1/21 (5%)	3/21 (14%)	0/21 (0%)
≥10	17/20 (85%)	10/20 (50%)	4/20 (20%)	2/20 (10%)	10/20 (50%)	1/20 (5%)
All patients	78/97 (80%)	37/97 (38%)	9/97 (9%)	4/97 (4%)	26/97 (27%)	3/97 (3%)

recurrence. In analogy to previously described data for other [18]F- and ^{68}Ga-labeled PSMA ligands, increasing detection rates were observed at increasing PSA values (9,13–15).

The current analysis focused on patients with BCR after primary curative-intent radiotherapy. A rising PSA after RP and curative-intent radiotherapy is the first sign of primary-therapy failure, and salvage therapies include pelvic lymph node dissection or radiotherapy in cases of pelvic lymph node metastases or systemic therapies, including ADT, and chemotherapy in cases of distant metastases (1). However, detection and localization of prostate cancer recurrence in patients with BCR after curative-intent radiotherapy can be challenging. Considering the availability of different salvage therapy options and the impact of PSMA PET imaging on patient management, early detection of recurrence remains crucial for optimal treatment planning (2,16,17).

BCR rates after primary curative-intent radiotherapy range from 10% to 60% with external-beam radiation therapy or from 7% to 35% with brachytherapy, and up to 44% despite external-beam radiation therapy dose escalation of 78 Gy (18–20). Although the overall pooled diagnostic efficacy of ^{18}F-labeled PSMA ligands for the detection of BCR is 81% (95% CI, 71%–88%), it increases from 49% to 92% at PSA levels of <0.5 and ≥2 ng/mL, respectively (5). However, data are reported mainly after RP, and detailed information on BCR detection rates in patients after primary radiotherapy are available mainly for small subgroups of mixed cohorts (5). Dietlein et al. reported overall BCR detection rates of 79% (19/24) and 92% (56/61) for ^{18}F-DCFPyL PET and ^{68}Ga-PSMA-11 PET, respectively, after primary radiotherapy and 71% (27/38) and 68% (46/68) for ^{18}F-DCFPyL PET and ^{68}Ga-PSMA-11 PET, respectively, after RP (21). Surprisingly, detection rates were PSA-independent in the radiotherapy group, whereas rising PSA levels have been reported to be clearly associated with higher detection rates in patients after RP (13–15). This finding might at least partially be explained by the Phoenix criteria definition of a PSA rise of 2 ng/mL above the nadir. However, with the nadir varying substantially between patients, the absolute PSA value at the time of imaging might be less relevant than in patients with BCR after RP.

Similarly, detection rates also did not correlate positively with PSA in the present study. This finding might be related partly to the high detection efficacy in all subgroups: 88%, 97%, 90%, and 100% for a PSA of <2, 2–<5, 5–<10, and ≥10 ng/mL, respectively. PSA independence was also observed in the subgroup of patients, who did not reach the threshold for BCR defined by the Phoenix criteria (PSA of ≥2 ng/mL above the nadir), with detection rates of 80%, 90%, 100%, and 83% for a PSA of <0.5, 0.5–<1, 1–<1.5, and 1.5–<2 ng/mL, respectively. Similar detection efficacies (including both ^{68}Ga-PSMA-11 and ^{18}F-DCFPyL PET scans) in a subgroup of 63 patients not meeting the Phoenix criteria were most recently reported (22). The authors found no influence of PSA value on PET outcome, and detection rates of 75.0% (12/16), 89.3% (25/28), and 84.2% (16/19) at PSA levels of <1.0, 1.0–1.49, and 1.5–1.99 ng/mL, respectively, above the nadir, were present. However, PSA independence might be a consequence of the relatively small number of patients in each PSA group reported in these cohorts, including the present work (21,22).

Notably, Meredith et al. described increasing detection rates for ^{68}Ga-PSMA-11 in 107 patients after primary radiotherapy; however,
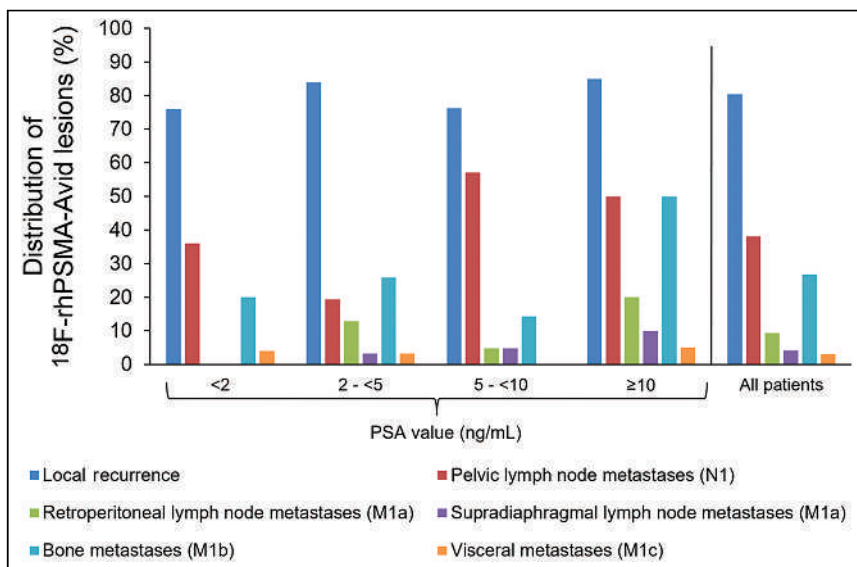
FIGURE 4. Localization of ^{18}F-rhPSMA-7–positive tumor lesions for all patients and stratified by PSA value.

lower detection rates in patients with very low PSA values might also be attributed to the small sample sizes in these groups, with detection rates of 33% at a PSA of 0.01–<0.5 ng/mL in 1 of 3 patients and 71% at a PSA of 0.5–<1 ng/mL in 5 of 7 patients, respectively (23). Recently, Raveenthiran et al. presented data on the diagnostic efficacy of ^{68}Ga-PSMA-11 in 276 patients after primary radiotherapy, representing the largest cohort so far (24). Although 203 patients were above the threshold for BCR defined by the Phoenix criteria, PSA in the remaining 73 patients was <2 ng/mL. They observed a slight trend toward increasing detection rates at rising PSA levels, at 66.7% (8/12) for a PSA of <0.5 ng/mL, 77.8% (14/18) for 0.5–<1 ng/mL, 76.7% (33/43) for 1–<2.0 ng/mL, and 90.6% (184/203) for >2 ng/mL. Likewise, Einspieler et al. presented higher detection rates with rising PSA levels in a cohort of 118 patients with BCR according to the Phoenix criteria, at 81.8% (36/44), 95.3% (41/43), and 96.8% (30/31) for PSA levels of 2–<5, 5–<10, and ≥10 ng/mL, respectively (7).

In summary, the detection efficacy of PSMA ligand PET in patients meeting the Phoenix criteria ranges from 91% to 100% (Table 3) (3,7,23,24). With an overall detection rate of 96%, our data for ^{18}F-rhPSMA-7 PET/CT fit well into this range. Moreover, our data add to the increasing evidence in the literature indicating that PSMA ligand PET imaging might also detect lesions indicative of recurrent disease in patients with PSA levels below the threshold set by the Phoenix criteria for BCR. In the present work, the overall detection rate for ^{18}F-rhPSMA-7 in patients with BCR at PSA levels of <2 ng/mL was 88% (22/25) and highly comparable to the cohorts of Jansen et al. (84% [53/63]) (22), Raveenthiran et al. (75% 55/73]) (24), and Meredith et al. (80% [20/25]) (Table 3) (23). These results strongly indicate that the classic definition of BCR after radiotherapy should be redefined in an era of sensitive PSMA ligand PET imaging. Sonni et al. presented data from a prospective single-center study evaluating the impact of PSMA PET imaging on patient management in different clinical situations (17). According to this trial, patients with BCR after primary radiotherapy who do not meet the Phoenix criteria seem to be those profiting most from the high sensitivity of PSMA PET imaging. In the era of PSMA PET, the definition of BCR according to the Phoenix criteria should be revisited or PSMA PET should be integrated into the definition of recurrence. However, larger patient groups and, preferably, prospective data are required to confirm this hypothesis.

Comparable to previously described data, PSMA PET detection rates for BCR after primary radiotherapy were not clearly influenced by prior ADT therapy or primary Gleason score (7). We found no significant differences in detection rates between patients who received ADT in the 6 mo preceding ^{18}F-rhPSMA-7 PET and patients without prior ADT (100% vs. 91%, P = 0.173). Similar results have been demonstrated using ^{18}F-rhPSMA-7 PET in patients with BCR after RP (detection rate of 81% for both prior ADT and no ADT, P = 0.54) (9). However, the impact of ADT on PSMA PET is still a matter of debate. Despite data indicating reduced PSMA ligand uptake after long-term ADT (25), the need for withdrawal of ADT before PSMA-targeted PET remains controversial, particularly when considering the therapeutic effects of ongoing ADT (26). However, concomitant use of ADT at the time of primary radiotherapy will have an impact on patterns of failure, which might have an impact on lesion detection. Unfortunately, because of the retrospective design of this study, detailed information on concomitant use of ADT during primary radiotherapy was not available for all patients.

Localization of prostate cancer recurrence at early stages of BCR and the impact on treatment planning represent one of the main strengths of PSMA ligand PET. In a recent review, the impact of PSMA ligand PET on therapy planning ranged from 30% to 76% (17,27,28). Up to 40% of patients can be guided away from systemic treatment, and up to 60% of patients can be guided toward application of PSMA-directed local therapy (28). PSA before salvage therapy represents the strongest predictor of survival after salvage RP and salvage radiotherapy (29–31). Most patients in our cohort showed localized disease, with local recurrence in 80% (78/97) and pelvic lymph node metastases in 38% (37/97); however, distant metastases were observed in up to 27% of patients, with bone metastases representing the main site. This analysis lacks details on potential unspecific bone uptake. This potential pitfall has been reported for different PSMA ligands in a large number of case reports, specific analyses, and reviews (12,32–34). Specifically, using ^{18}F-rhPSMA-7, Kroenke et al. (34) reported that 120 areas of focal increased uptake were interpreted as not related to prostate cancer, with the majority (n = 45) being in the ribs.

Likewise, in the study by Raveenthiran et al., local sites of tumor recurrence were most common, but they were seen in only 57% (157/276) of patients, compared with 80% in our cohort (24). This difference might be attributed to the high accumulation of ^{68}Ga-PSMA-11 in the urinary bladder, potentially impairing detection of small local recurrences near the bladder (35). Nonetheless, false-positive findings in the prostate represent a further possible pitfall of PSMA PET imaging, particularly in the postradiotherapy

TABLE 3
Detection Rates in Patients with BCR after Primary Curative-Intent Radiotherapy Stratified by PSA Level

Author	Year	Radiopharmaceutical	n	Detection rate per PSA category	
				<2 ng/mL	≥2 ng/mL
Present study	2021	^{18}F-rhPSMA-7	97	88%	95.8%
Einspieler et al. (7)	2017	^{68}Ga-PSMA-11	118	NR	90.7%
Jansen et al. (22)	2021	^{68}Ga-PSMA-11 and ^{18}F-DCFPyL	63	84.1%	NR
Raveenthiran et al. (24)	2019	^{68}Ga-PSMA-11	276	75.3%	90.6%
Meredith et al. (23)	2016	^{68}Ga-PSMA-11	107	80%	100%

NR = not reported.

setting, as described in a recently published prospective multicenter trial (*36*). We acknowledge that given the lack of histopathologic validation in the present study, this possibility cannot be completely excluded. However, all scans were reevaluated by experienced readers.

Although the small sample size limits meaningful conclusions, the tumor distribution was not influenced by patients' PSA in the present study. However, whereas no nonregional lymph node metastases were observed in patients with PSA levels of <2 ng/mL, bone metastases and even visceral metastases were identified in 20% (5/25) and 4% (1/25), respectively. In the overall cohort, visceral metastases were identified in the lung and in the penile shaft in 2 cases, both representing rare sites of tumor recurrence after BCR (*37,38*). In one patient with a PSA of 0.72 ng/mL, a penile metastasis represented the only finding on ^{18}F-rhPSMA-7 PET. Almost-consistent rates of localized disease and distant metastases indicate that early identification of localized salvage therapy or systemic therapy might be delayed when strictly following Phoenix criteria thresholds in BCR patients after primary radiotherapy. Our findings warrant further investigations using PSMA ligand PET in patients with low PSA not meeting the Phoenix criteria.

This study had several limitations. First, ^{18}F-rhPSMA-7 PET findings were not validated by histology, which represents the reference standard for definition of prostate cancer recurrence. However, biopsy was not feasible for many lesions because of difficulty in localization and their small size. Second, the data were retrospective, and the sample size was relatively small; particularly, only 25 patients were below the threshold of 2 ng/mL defined by the Phoenix criteria. Currently, there are 2 clinical trials investigating the safety and diagnostic efficacy of an ^{18}F-labeled rhPSMA ligand: one on patients with prostate cancer recurrence (SPOTLIGHT trial; NCT04186845) and another on patients with newly diagnosed prostate cancer (LIGHTHOUSE trial; NCT04186819). Furthermore, detailed information on primary radiotherapy was missing because of the retrospective design of this study (e.g., radiation field and dose, concomitant ADT); lack of this information is likely to have an impact on patterns of failure.

CONCLUSION

[18]F-rhPSMA-7 PET/CT demonstrates high detection rates in patients with BCR of prostate cancer after primary radiotherapy. The detection rate was not influenced by Gleason score, prior use of ADT, or PSA levels. Consistent with published data for other PSMA ligands, high detection rates were observed even in patients with PSA levels of <2 ng/mL, indicating that ^{18}F-rhPSMA-7 has the potential to guide salvage therapy even at early stages of BCR after primary radiotherapy.

DISCLOSURE

ACKNOWLEDGMENT

KEY POINTS

QUESTION: What is the detection efficacy of ^{18}F-rhPSMA-7 PET/CT in patients with BCR of prostate cancer after primary curative-intent radiotherapy?

PERTINENT FINDINGS: ^{18}F-rhPSMA-7 PET/CT offers high detection efficacy in patients with BCR of prostate cancer above and below the PSA threshold of 2 ng/mL defined by the Phoenix criteria. Efficacy is highly comparable to data published for ^{68}Ga-PSMA-11.

IMPLICATIONS FOR PATIENT CARE: ^{18}F-rhPSMA-7 has the potential to guide therapy for BCR after failure of primary radiotherapy.

REFERENCES

1. EAU-ESUR-ESTRO-SIOG guidelines on prostate cancer: 2018 update. European Association of Urology website. https://uroweb.org/guidelines/prostate-cancer. Published 2022. Accessed July 21, 2022.
2. Cornford P, Bellmunt J, Bolla M, et al. EAU-ESTRO-SIOG guidelines on prostate cancer. Part II: treatment of relapsing, metastatic, and castration-resistant prostate cancer. *Eur Urol.* 2017;71:630–642.
3. Roach M III, Hanks G, Thames H Jr, et al. Defining biochemical failure following radiotherapy with or without hormonal therapy in men with clinically localized prostate cancer: recommendations of the RTOG-ASTRO Phoenix Consensus Conference. *Int J Radiat Oncol Biol Phys.* 2006;65:965–974.
4. Perera M, Papa N, Christidis D, et al. Sensitivity, specificity, and predictors of positive ^{68}Ga-prostate-specific membrane antigen positron emission tomography in advanced prostate cancer: a systematic review and meta-analysis. *Eur Urol.* 2016; 70:926–937.
5. Treglia G, Annunziata S, Pizzuto DA, Giovanella L, Prior JO, Ceriani L. Detection rate of ^{18}F-Labeled PSMA PET/CT in biochemical recurrent prostate cancer: a systematic review and a meta-analysis. *Cancers (Basel).* 2019;11:710.
6. Giesel FL, Will L, Lawal I, et al. Intraindividual comparison of ^{18}F-PSMA-1007 and ^{18}F-DCFPyL PET/CT in the prospective evaluation of patients with newly diagnosed prostate carcinoma: a pilot study. *J Nucl Med.* 2018;59:1076–1080.
7. Einspieler I, Rauscher I, Duwel C, et al. Detection efficacy of hybrid ^{68}Ga-PSMA ligand PET/CT in prostate cancer patients with biochemical recurrence after primary radiation therapy defined by Phoenix criteria. *J Nucl Med.* 2017; 58:1081–1087.
8. Wurzer A, Di Carlo D, Schmidt A, et al. Radiohybrid ligands: a novel tracer concept exemplified by [18]F- or ^{68}Ga-labeled rhPSMA inhibitors. *J Nucl Med.* 2020;61: 735–742.
9. Eiber M, Kroenke M, Wurzer A, et al. ^{18}F-rhPSMA-7 PET for the detection of biochemical recurrence of prostate cancer after radical prostatectomy. *J Nucl Med.* 2020;61:696–701.
10. Kroenke M, Wurzer A, Schwamborn K, et al. Histologically confirmed diagnostic efficacy of ^{18}F-rhPSMA-7 PET for N-staging of patients with primary high-risk prostate cancer. *J Nucl Med.* 2020;61:710–715.
11. Oh SW, Wurzer A, Teoh EJ, et al. Quantitative and qualitative analyses of biodistribution and PET image quality of a novel radiohybrid PSMA, ^{18}F-rhPSMA-7, in patients with prostate cancer. *J Nucl Med.* 2020;61:702–709.
12. Sheikhbahaei S, Werner RA, Solnes LB, et al. Prostate-specific membrane antigen (PSMA)-targeted PET imaging of prostate cancer: an update on important pitfalls. *Semin Nucl Med.* 2019;49:255–270.
13. Eiber M, Maurer T, Souvatzoglou M, et al. Evaluation of hybrid ^{68}Ga-PSMA ligand PET/CT in 248 patients with biochemical recurrence after radical prostatectomy. *J Nucl Med.* 2015;56:668–674.

14. Giesel FL, Knorr K, Spohn F, et al. Detection efficacy of ^{18}F-PSMA-1007 PET/CT in 251 patients with biochemical recurrence of prostate cancer after radical prostatectomy. *J Nucl Med.* 2019;60:362–368.

15. Mena E, Lindenberg ML, Turkbey IB, et al. ^{18}F-DCFPyL PET/CT imaging in patients with biochemically recurrent prostate cancer after primary local therapy. *J Nucl Med.* 2020;61:881–889.

16. Valle LF, Lehrer EJ, Markovic D, et al. A systematic review and meta-analysis of local salvage therapies after radiotherapy for prostate cancer (MASTER). *Eur Urol.* 2021;80:280–292.

17. Sonni I, Eiber M, Fendler WP, et al. Impact of ^{68}Ga-PSMA-11 PET/CT on staging and management of prostate cancer patients in various clinical settings: a prospective single-center study. *J Nucl Med.* 2020;61:1153–1160.

18. Khuntia D, Reddy CA, Mahadevan A, Klein EA, Kupelian PA. Recurrence-free survival rates after external-beam radiotherapy for patients with clinical T1-T3 prostate carcinoma in the prostate-specific antigen era: what should we expect? *Cancer.* 2004;100:1283–1292.

19. Voulgaris S, Nobes JP, Laing RW, Langley SE. State-of-the-art: prostate LDR brachytherapy. *Prostate Cancer Prostatic Dis.* 2008;11:237–240.

20. Zumsteg ZS, Spratt DE, Romesser PB, et al. The natural history and predictors of outcome following biochemical relapse in the dose escalation era for prostate cancer patients undergoing definitive external beam radiotherapy. *Eur Urol.* 2015;67:1009–1016.

21. Dietlein M, Kobe C, Kuhnert G, et al. Comparison of [^{18}F]DCFPyL and [^{68}Ga]Ga-PSMA-HBED-CC for PSMA-PET imaging in patients with relapsed prostate cancer. *Mol Imaging Biol.* 2015;17:575–584.

22. Jansen BHE, van Leeuwen PJ, Wondergem M, et al. Detection of recurrent prostate cancer using prostate-specific membrane antigen positron emission tomography in patients not meeting the Phoenix criteria for biochemical recurrence after curative radiotherapy. *Eur Urol Oncol.* 2021;4:821–825

23. Meredith G, Wong D, Yaxley J, et al. The use of ^{68}Ga-PSMA PET CT in men with biochemical recurrence after definitive treatment of acinar prostate cancer. *BJU Int.* 2016;118(suppl 3):49–55.

24. Raveenthiran S, Yaxley J, Gianduzzo T, et al. The use of ^{68}Ga-PET/CT PSMA to determine patterns of disease for biochemically recurrent prostate cancer following primary radiotherapy. *Prostate Cancer Prostatic Dis.* 2019;22:385–390.

25. Afshar-Oromieh A, Debus N, Uhrig M, et al. Impact of long-term androgen deprivation therapy on PSMA ligand PET/CT in patients with castration-sensitive prostate cancer. *Eur J Nucl Med Mol Imaging.* 2018;45:2045–2054.

26. Vaz S, Hadaschik B, Gabriel M, Herrmann K, Eiber M, Costa D. Influence of androgen deprivation therapy on PSMA expression and PSMA-ligand PET imaging of prostate cancer patients. *Eur J Nucl Med Mol Imaging.* 2020;47:9–15.

27. Valle L, Shabsovich D, de Meerleer G, et al. Use and impact of positron emission tomography/computed tomography prior to salvage radiation therapy in men with biochemical recurrence after radical prostatectomy: a scoping review. *Eur Urol Oncol.* 2021;4:339–355.

28. Ekmekcioglu Ö, Busstra M, Klass ND, Verzijlbergen F. Bridging the imaging gap: PSMA PET/CT has a high impact on treatment planning in prostate cancer patients with biochemical recurrence—a narrative review of the literature. *J Nucl Med.* 2019;60:1394–1398.

29. Chade DC, Shariat SF, Cronin AM, et al. Salvage radical prostatectomy for radiation-recurrent prostate cancer: a multi-institutional collaboration. *Eur Urol.* 2011;60:205–210.

30. Stish BJ, Pisansky TM, Harmsen WS, et al. Improved metastasis-free and survival outcomes with early salvage radiotherapy in men with detectable prostate-specific antigen after prostatectomy for prostate cancer. *J Clin Oncol.* 2016;34:3864–3871.

31. Siegmann A, Bottke D, Faehndrich J, et al. Salvage radiotherapy after prostatectomy: what is the best time to treat? *Radiother Oncol.* 2012;103:239–243.

32. Rauscher I, Kronke M, Konig M, et al. Matched-pair comparison of ^{68}Ga-PSMA-11 PET/CT and ^{18}F-PSMA-1007 PET/CT: frequency of pitfalls and detection efficacy in biochemical recurrence after radical prostatectomy. *J Nucl Med.* 2020;61:51–57.

33. Grünig H, Maurer A, Thali Y, et al. Focal unspecific bone uptake on [^{18}F]-PSMA-1007 PET: a multicenter retrospective evaluation of the distribution, frequency, and quantitative parameters of a potential pitfall in prostate cancer imaging. *Eur J Nucl Med Mol Imaging.* 2021;48:4483–4494.

34. Kroenke M, Mirzoyan L, Horn T, et al. Matched-pair comparison of ^{68}Ga-PSMA-11 and ^{18}F-rhPSMA-7 PET/CT in patients with primary and biochemical recurrence of prostate cancer: frequency of non-tumor-related uptake and tumor positivity. *J Nucl Med.* 2021;62:1082–1088.

35. Freitag MT, Radtke JP, Afshar-Oromieh A, et al. Local recurrence of prostate cancer after radical prostatectomy is at risk to be missed in ^{68}Ga-PSMA-11-PET of PET/CT and PET/MRI: comparison with mpMRI integrated in simultaneous PET/MRI. *Eur J Nucl Med Mol Imaging.* 2017;44:776–787.

36. Fendler WP, Calais J, Eiber M, et al. False positive PSMA PET for tumor remnants in the irradiated prostate and other interpretation pitfalls in a prospective multi-center trial. *Eur J Nucl Med Mol Imaging.* 2021;48:501–508.

37. Gago JP, Camara G, Dionisio J, Opiniao A. Pulmonary metastasis as sole manifestation of relapse in previously treated localised prostate cancer: three exceptional case reports. *Ecancermedicalscience.* 2016;10:645.

38. Tatkovic A, McBean R, Schoeman J, Wong D. Prostate penile metastasis: Incidence and imaging pattern on ^{68}Ga-PSMA PET/CT. *J Med Imaging Radiat Oncol.* 2020;64:499–504.

Long-Term Outcomes of Transarterial Radioembolization for Large Single Hepatocellular Carcinoma: A Comparison to Resection

Jihye Kim*[1,2], Ju Yeon Kim*[1], Jeong-Hoon Lee[1], Dong Hyun Sinn[2], Moon Haeng Hur[1], Ji Hoon Hong[1], Min Kyung Park[1], Hee Jin Cho[1], Na Ryung Choi[1], Yun Bin Lee[1], Eun Ju Cho[1], Su Jong Yu[1], Yoon Jun Kim[1], Jin Chul Paeng[3], Hyo Cheol Kim[4], Nam-Joon Yi[5], Kwang-Woong Lee[5], Kyung-Suk Suh[5], Dongho Hyun[6], Jong Man Kim[7], and Jung-Hwan Yoon[1]

[1]Department of Internal Medicine and Liver Research Institute, Seoul National University College of Medicine, Seoul, Korea; [2]Department of Internal Medicine, Samsung Medical Center, Sungkyunkwan University School of Medicine, Seoul, Korea; [3]Department of Nuclear Medicine, Seoul National University College of Medicine, Seoul, Korea; [4]Department of Radiology, Seoul National University College of Medicine, Seoul, Korea; [5]Department of Surgery, Seoul National University College of Medicine, Seoul, Korea; [6]Department of Radiology and Center for Imaging Science, Samsung Medical Center, Sungkyunkwan University School of Medicine, Seoul, Korea; and [7]Department of Surgery, Samsung Medical Center, Sungkyunkwan University School of Medicine, Seoul, Korea

The surgical treatment for large hepatocellular carcinoma (HCC) remains controversial because of a high risk of recurrence after resection. This study aimed to compare long-term outcomes of transarterial radioembolization (TARE) with resection for patients with large HCC. **Methods:** This retrospective cohort study included 557 patients who were initially treated with either resection ($n = 500$) or TARE ($n = 57$) for large (≥ 5 cm), single nodular HCC at 2 tertiary centers in Korea. Patients with major portal vein tumor thrombosis or extrahepatic metastasis were excluded. The primary endpoint was overall survival (OS), and secondary endpoints were time to progression (TTP), time to intrahepatic progression (TTIP), and safety. **Results:** The resection group was younger (median, 60 vs. 69 y) and had a smaller tumor size (median, 7.0 vs. 10.0 cm) (all $P < 0.05$). After baseline characteristics were balanced using inverse-probability-of-treatment weighting, the OS (hazard ratio [HR], 0.98; 95% CI, 0.40–2.43; $P = 0.97$), TTP (HR, 1.10; 95% CI, 0.55–2.20; $P = 0.80$), and TTIP (HR, 1.45; 95% CI, 0.72–2.93; $P = 0.30$) of the TARE group was comparable to the resection group. TARE was not an independent risk for OS (adjusted HR, 1.04; 95% CI, 0.42–2.59; $P = 0.93$), TTP (adjusted HR, 0.98; 95% CI, 0.50–1.95; $P = 0.96$), or TTIP (adjusted HR, 1.30; 95% CI, 0.65–2.58; $P = 0.46$). The TARE group had a shorter hospital stay and fewer adverse events than the resection group. **Conclusion:** Compared with surgical resection for large single nodular HCC, TARE showed a comparable OS, TTP, and TTIP and a better safety profile.

Key Words: liver cancer; overall survival; time to progression; safety; initial treatment

Hepatocellular carcinoma (HCC) accounts for most of the liver cancers worldwide and is the leading cause of cancer-related mortality in many countries (1). Despite efforts toward risk factor management, early diagnosis, and therapeutic advances, the disease burden of liver cancer continues to mount (2).

The American Association for the Study of Liver Diseases and the European Association for the Study of the Liver recommend surgical resection as the treatment of choice for adults with single HCC, especially when the size is less than 5 cm (3,4). For those with a large (>5 cm) single HCC, however, controversies exist on the best treatment option. Large tumor size has proven to be related to poor postsurgical outcomes (5,6), high probability of vascular invasion, and poor histologic differentiation (7,8), with the 5-y disease-free survival rate ranging from 20.0% to 41.3% even after curative resection (6,9). Transarterial chemoembolization (TACE) has been investigated as an alternative for large HCC, but a metaanalysis reported the clinical outcome to be worse than that of resection (10).

Transarterial radioembolization (TARE) is a novel procedure that delivers microspheres loaded with the radioactive isotope ^{90}Y to a target lesion; it has emerged as a less invasive treatment option for HCC (11). Previous studies have demonstrated that TARE, compared with TACE, showed a comparable overall survival (OS), a longer time to progression (TTP), and more effective performance in downstaging patients on the liver transplant waiting list (12,13). Furthermore, a recent multicenter study by Salem et al. showed that TARE was effective and safe when used as either a bridging therapy or a stand-alone treatment for a solitary unresectable HCC of less than 8 cm (14). Unlike TACE, which entails risk for delivering suboptimal doses of chemotherapeutic agents to large HCCs due to the possibility of leakage into the systemic circulation (15), TARE has proven to achieve a sufficiently high dose of radiation to large tumors, thereby resulting in a favorable tumor response (16,17). In addition, whereas TACE has a macroembolic effect, which is the main cause of postembolization syndrome, TARE rarely occludes large vessels and consequently results in less risk of postembolization syndrome, fewer adverse events, and a shorter hospital stay (18). Thus, TARE is expected to be more effective and safer for the treatment of large HCCs than is TACE.

This study aimed to compare the long-term outcomes of TARE with those of resection in patients with a large single nodular HCC, with a special interest in whether TARE can be a potential alternative to resection.

MATERIALS AND METHODS

Patients

This was a retrospective cohort study using prospectively established electronic HCC databases from 2 referral centers in Seoul, Korea. This study was approved by the institutional review board of each center (approvals 2101-093-1189 and 2021-05-109-001). The requirement for informed consent was waived.

By screening the HCC cohort databases, we identified consecutive adult (≥18 y) patients who underwent either surgical resection or TARE as an initial treatment for newly diagnosed large (≥5 cm) single nodular HCC (as determined by radiologic assessment) between January 2012 and December 2020. The decision on whether to undergo surgical resection or TARE was made according to each patient's preference after a detailed discussion with a physician. Exclusion criteria were sequential multimodality treatment (e.g., surgical resection after TARE in a prearranged manner), tumor thrombosis involving major portal veins (right/left portal vein or main trunk portal vein tumor thrombosis [PVTT]) (supplemental methods (19,20); supplemental materials are available at http://jnm.snmjournals.org), extrahepatic metastasis, impaired hepatic function (Child–Pugh class B or C), poor performance status graded as a Eastern Cooperative Oncology Group performance status score of 1 or above, and previous other malignancies within 2 y before the initial diagnosis of HCC. Patients with minute satellite lesions around the main nodule or tumor thrombosis involving minor branches of portal vein (second-order branch [Vp2] or distal to second-order branch [Vp1] PVTT) were included (supplemental methods (19,20)).

Liver cirrhosis was diagnosed by radiologic and clinical criteria as follows: platelet count of less than 100,000/mm^3 and a blunted, nodular liver edge accompanied by splenomegaly (>12 cm) or the presence of esophageal or gastric varices, ascites, or hepatic encephalopathy. The albumin–bilirubin grades were calculated using the original formulas (21). The American Society of Anesthesiologists (ASA) physical status classification was documented for each patient. Information on the pretreatment liver imaging tools was also collected. The medical costs for the treatments were obtained from the Health Insurance Review and Assessment Service national patient sample data of the South Korean government (supplemental methods (22–24)).

Procedures

Surgical resection was performed by surgeons with more than 10 y of experience in liver resection. The type and extent of surgery were determined considering tumor size, location, and underlying liver status.

TARE was conducted by interventional radiologists with more than 10 y of experience in vascular intervention. The selection of TheraSphere (Boston Scientific) and SIR-Spheres (Sirtex) microspheres was generally left to the interventional radiologists' personal preference. Microspheres impregnated with the radioisotope ^{90}Y were delivered through the hepatic artery to the tumors with preferential blood flow according to standardized techniques (25,26). As recommended by the manufacturers, the dose calculation was based on the MIRD dosimetry for TheraSphere and partition dosimetry for SIR-Spheres. For TheraSphere, TARE was not applied if the estimated lung dose exceeded 30 Gy by MIRD dosimetry. For SIR-Spheres, TARE was not done if the estimated lung dose was higher than 25 Gy by a partition model. When radiation segmentectomy was feasible, ^{90}Y microspheres were injected at the segmental hepatic artery. If not, lobar treatment was performed. When there was an accessory gastric artery, right gastric artery, or hepatic falciform artery originating from the left hepatic artery, coil embolization was performed before radioembolization. As long as the estimated lung dose was less than the upper limit (30 Gy for TheraSphere and 25 Gy for SIR-Spheres), boosted radioembolization (mean target tissue dose > 150 Gy) was tried (16).

Endpoints and Assessments

The primary endpoint was OS. OS was measured from treatment to death from any cause. Secondary endpoints were TTP and time to intrahepatic progression (TTIP), which were measured from treatment to any tumor progression and from treatment to intrahepatic tumor progression, respectively, according to HCC-specified modified RECIST criteria (27). After initial treatment, tumor progression was monitored every 3 mo from baseline for 24 mo and then every 3–6 mo using either dynamic liver CT or MRI with serum tumor markers (i.e., serum α-fetoprotein and protein induced by vitamin K absence or antagonist II). All imaging scans were reevaluated by 2 radiologists at each center with more than 5 y of experience. In cases of discordance, an additional third independent experienced radiologist reviewed images and consensus was achieved among the 3 radiologists. If the tumor markers rose or the arterially hyperenhancing portion of the treated tumor grew after TARE, we regarded the time point of progression as the date when such changes were first identified on an imaging study. In the measurement of TTP and TTIP, patients were censored at the date of an additional treatment without radiologic evidence of disease progression or at the time of last follow-up, whichever came first. Adverse events according to the Common Terminology Criteria for Adverse Events, version 5.0, were evaluated until 30 d after the initial treatment. Adverse events for which a radiologic or surgical intervention was required, and hospital length of stay for the initial treatment, were assessed. The time interval and modality of follow-up imaging studies were noted.

Statistical Analysis

Patients' baseline characteristics were compared using the χ^2 test or Fisher exact test for categoric variables and the Mann–Whitney U test for continuous variables. To balance the baseline characteristics, inverse-probability-of-treatment weighting (IPTW) was applied (supplemental methods (28–31)).

Using a standard log-rank test, we evaluated the differences in the final outcomes between the groups. We plotted cumulative death rates, cumulative progression rates, and cumulative intrahepatic progression rates by the Kaplan–Meier method. Unadjusted hazard ratios (HRs) were estimated using the Cox proportional-hazards model. Comparative analyses used mainly the IPTW-adjusted population but also the crude population when it came to additional treatment modalities and follow-up imaging modalities. To identify independent predictors of death, tumor progression, and intrahepatic tumor progression, univariable and multivariable logistic regression analyses were performed.

Variables with a P value of less than 0.10 in univariable analysis were used in multivariable analysis. A weighted Cox proportional-hazards model was used to identify independent risk factors for the endpoints. All statistical analyses were performed with SPSS software (version 25.0; SPSS) and the R statistical programming environment (version 4.1.1; R development Core Team [http://www.R-project.org]), with a P value of less than 0.05 indicating statistical significance.

RESULTS

Study Population

A total of 687 patients received either TARE or surgical resection for newly diagnosed large (≥5 cm) single nodular HCC between January 2012 and October 2020. Among them, 130 patients were excluded because of sequential multimodality treatment ($n = 18$), the presence of extrahepatic metastasis ($n = 27$), right/left or main

trunk PVTT ($n = 51$), impaired hepatic function (Child–Pugh class B or C) ($n = 9$), an Eastern Cooperative Oncology Group performance status score of 1 or above ($n = 4$), or a previous history of other malignancies within 2 y before the diagnosis of HCC ($n = 21$). In total, 557 patients (57 for the TARE group, 500 for the resection group) were eligible for the analysis (Fig. 1). The TARE group was older and had poorer baseline physical status (higher proportions of ASA classification 3), larger tumors, and more Vp2 PVTT than the resection group (Table 1). Among the TARE group, 45 patients were treated with TheraSphere, and 12 were treated with SIR-Spheres. The mean total radiation activity administered was higher in TheraSphere cases (median, 4.75 GBq; range, 1.35–11.75 GBq) than in SIR-Spheres cases (median, 3.35 GBq; range, 1.00–4.00 GBq) ($P = 0.001$). The mean target tissue dose of TheraSphere cases was 286.5 ± 177.2 Gy (median, 226.0 Gy; range, 84.0–780.0 Gy), and the mean tumor dose of SIR-Spheres cases was 231.9 ± 84.9 Gy (median, 202.0 Gy; range, 144.4–413.7 Gy). The differences in the baseline characteristics between the TARE group and the resection group were balanced to a statistically insignificant level by means of IPTW, with all listed covariates having a standardized mean difference under 0.25. There were differences in pretreatment liver imaging tools between the TARE group (28.1% patients were assessed only by CT, 71.9% including MRI) and the resection group (0.6% patients were assessed only by CT, 99.4% including MRI) ($P < 0.001$). The imaging interval at which the tumor progression was detected (median, 2.8 vs. 2.9 mo; $P = 0.75$) and imaging modalities (CT, 58.8% vs. 50.4%; MRI, 41.2% vs. 39.3%; $P = 0.87$) were similar between the TARE group and the resection group (Supplemental Table 1).

Overall Survival

During a median follow-up of 38.4 mo, 12 of 57 (21.1%) patients in the TARE group and 102 of 500 (20.4%) patients in the resection group died. The cumulative survival rates at 1, 3, and 5 y were 91.8%, 73.3%, and 66.6%, respectively, in the TARE group and 94.9%, 81.8%, and 74.9%, respectively, in the resection group. OS did not significantly differ between the 2 groups ($P = 0.90$ by log-rank test) (Fig. 2A).

After IPTW, the TARE group still showed comparable OS to the resection group (HR, 0.98; 95% CI, 0.40–2.43; $P = 0.97$) (Fig. 3A). In the multivariable analysis, TARE was not an independent risk factor of death (adjusted HR [aHR], 1.04; 95% CI, 0.42–2.59; $P = 0.93$) after adjustment for ASA classification, liver cirrhosis, albumin–bilirubin grade, presence of satellite nodules, and level of PVTT (Vp2 vs. no or Vp1 PVTT). Albumin–bilirubin grade 2 or above (aHR, 1.98; 95% CI, 1.02–3.83; $P = 0.04$) remained significantly associated with death (Table 2).

Time to Progression

The median TTP was 18.0 mo (interquartile range [IQR], 6.0–34.0 mo) in the TARE group and 41.8 mo (IQR, 8.2 mo–not reached) in the resection group. The cumulative 2-y progression rates were 50.0% in the TARE group and 58.3% in the resection group. The TTP was comparable between the groups ($P = 0.19$) (Fig. 2B).

After using IPTW, there was still no difference in the TTP between the groups (TARE vs. resection: HR, 1.10; 95% CI, 0.55–2.20; $P = 0.80$) (Fig. 3B). In the multivariable regression analysis, TARE over surgery was not an independent risk factor of tumor progression (aHR, 0.98; 95% CI, 0.50–1.95; $P = 0.96$). The presence of satellite nodules (aHR, 1.40; 95% CI, 1.01–1.95; $P = 0.04$) and level of PVTT (Vp2 PVTT vs. no or Vp1 PVTT: aHR, 1.67; 95% CI, 1.16–2.41; $P = 0.006$) remained significantly associated with tumor progression (Supplemental Table 2).

TTIP

During follow-up, intrahepatic tumor progression was observed in 17 of 57 (29.8%) patients in the TARE group and 244 of 500 (48.8%) in the resection group. The median TTIP was 18.0 mo (IQR, 6.0–34.0 mo) in the TARE group and 72.2 mo (IQR, 11.3 mo–not reached) in the resection group. The cumulative 2-y intrahepatic progression rates were 50.0% in the TARE group and 33.4% in the resection group. The TTIP was shorter in the TARE group than in the resection group ($P = 0.01$) (Fig. 2C).

In the IPTW adjusted population, there was no difference in the TTIP between the groups (TARE vs. resection: HR, 1.45; 95% CI, 0.72–2.93; $P = 0.30$) (Fig. 3C). In the multivariable regression analysis, TARE over surgery was not an independent risk factor of intrahepatic tumor progression (aHR, 1.30; 95% CI, 0.65–2.58; $P = 0.46$) after adjustment for level of PVTT (Vp2 PVTT vs. no or Vp1 PVTT: aHR, 1.72; 95% CI, 1.18–2.50; $P = 0.005$) (Supplemental Table 3).

Further Treatment

Patients who experienced disease progression underwent additional treatment with multidisciplinary modalities including additional TARE, TACE, radiofrequency ablation, percutaneous ethanol injection, surgical resection of intrahepatic or extrahepatic lesions, liver transplantation, external-beam radiation therapy, and systemic therapy such as sorafenib (Supplemental Table 4). There
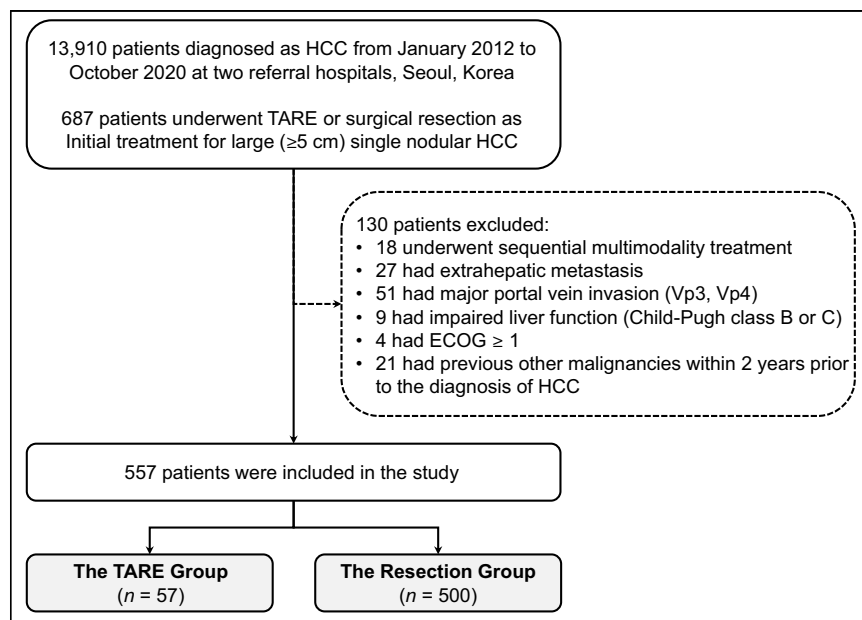
FIGURE 1. Flowchart of study population. ECOG = Eastern Cooperative Oncology Group performance; Vp3 = tumor thrombus in first-order branches of the portal vein; Vp4 = tumor thrombus in the main trunk of the portal vein and/or contralateral portal vein branch to the primarily involved lobe.

TABLE 1
Baseline Characteristics of Study Population

Characteristic	TARE (*n* = 57)	Resection (*n* = 500)	*P*
Age (y)	69.0 (60.0–77.0)	60.0 (52.0–68.0)	< 0.001
Age			< 0.001
< 60 y	13 (22.8%)	246 (49.2%)	
≥ 60 y	44 (77.2%)	254 (50.8%)	
Male sex	50 (87.7%)	417 (83.4%)	0.52
ASA classification			0.047
1 or 2	29 (50.9%)	326 (65.2%)	
3	28 (49.1%)	174 (34.8%)	
Etiology			0.21
Hepatitis B virus	33 (57.9%)	335 (67.0%)	
Hepatitis C virus	3 (5.3%)	31 (6.2%)	
Alcohol	8 (14.0%)	41 (8.2%)	
NASH	0 (0.0%)	15 (3.0%)	
Unknown	13 (22.8%)	78 (15.6%)	
Liver cirrhosis	22 (38.6%)	151 (30.2%)	0.25
ALBI grade			0.30
1	45 (78.9%)	426 (85.2%)	
≥ 2*	12 (21.1%)	74 (14.8%)	
α-fetoprotein (ng/mL)	7.3 (4.3–132.4)	15.4 (4.2–774.4)	0.19
α-fetoprotein			0.09
< 400 ng/mL	47 (82.5%)	355 (71.0%)	
≥ 400 ng/mL	10 (17.5%)	145 (29.0%)	
Tiny satellite nodules	4 (7.0%)	22 (4.4%)	0.33
Tumor size (cm)	10.0 (7.5–11.3)	7.0 (5.5–9.2)	< 0.001
Tumor size			< 0.001
< 8 cm	17 (29.8%)	306 (61.2%)	
≥ 8 cm	40 (70.2%)	194 (38.8%)	
Lobar involvement			0.04
Unilobar	41 (71.9%)	420 (84.0%)	
Bilobar	16 (28.1%)	80 (16.0%)	
Level of PVTT			0.02
Vp0 (absent)	51 (89.5%)	467 (93.4%)	
Vp1	1 (1.8%)	23 (4.6%)	
Vp2	5 (8.8%)	10 (2.0%)	

*One patient in resection group had ALBI grade 3.

NASH = nonalcoholic steatohepatitis; ALBI = albumin–bilirubin; ASA = American Society of Anesthesiologists; Vp0 = absence of tumor thrombus in the portal vein; Vp1 = tumor thrombus in distal to the second order branches of the portal vein, but not of the second order branches; Vp2 = tumor thrombus in second order branches of the portal vein.

Qualitative data are number and percentage; continuous data are median and IQR.

were 26 patients (all 26 were in the TARE group) who received additional treatment to better control the index lesion despite no radiologic evidence of tumor progression. Of the 26 patients, 15 patients experienced disease progression and received further treatment. The TARE group underwent more additional treatments (median, 2.0; IQR, 0.0–3.0) than the resection group (median, 0.0; IQR 0.0–2.0) (*P* = 0.002).

Safety

Overall, adverse events were reported more frequently in the resection group (100%) than in the TARE group (43.9%). All patients in the resection group were graded as having abdominal pain of grade 3 or 4 and routinely received intravenous patient-controlled analgesia using opioids for acute postoperative pain control. Apart from abdominal pain, the resection group more
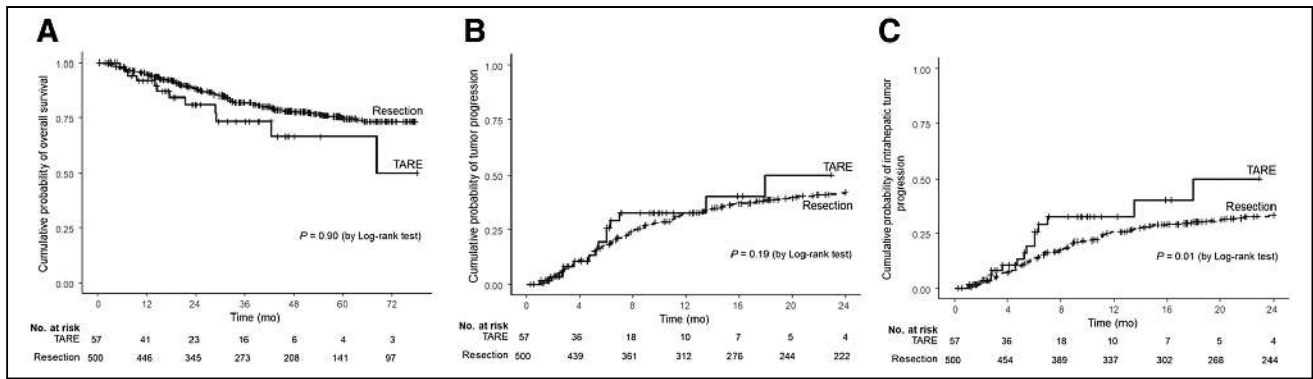
FIGURE 2. Crude analysis: cumulative probability of OS (A), tumor progression (B), and intrahepatic tumor progression (C) according to treatment groups.

frequently reported ascites, fever, aspartate transaminase elevation, alanine transaminase elevation, and bilirubin elevation (Table 3). Most patients in the resection group showed abnormal liver enzyme levels, which returned to baseline levels except in one patient with liver failure. None of the patients in the TARE group and 16 of 484 patients (3.2%) in the resection group experienced adverse events requiring radiologic or surgical intervention ($P = 0.39$). The hospital stay was significantly shorter in the TARE group (median, 3 d; IQR, 3–4 d) than in the resection group (median, 12 d; IQR, 11–16 d) ($P < 0.001$).

Subgroup Analysis of TARE Group

The TheraSphere group ($n = 45$) and the SIR-Spheres group ($n = 12$) showed no significant differences in OS (2-y survival rates, 82.7% vs. 80.0%; $P = 0.4$), TTP (cumulative 2-y progression rates, 51.5% vs. 43.1%; $P = 0.9$), or TTIP (cumulative 2-y intrahepatic progression rates, 51.5% vs. 43.1%; $P = 0.9$). The admission days for the TARE group were similar between both types of ^{90}Y microspheres (median, 3 vs. 3 d; IQR, 3–4 vs. 3–4 d; range, 2–13 vs. 3–6 d, for TheraSphere vs. SIR-Spheres, respectively; $P = 0.99$). Overall adverse events were similar in both groups, whereas mild nausea and vomiting were more frequent in the SIR-Spheres group (nausea, 6.7% vs. 33.3%; $P = 0.03$) (vomiting, 2.2% vs. 33.3%; $P = 0.006$) (Supplemental Table 5).

Cost of Treatment

When we analyzed the cost of initial and additional treatments, the cost of TARE was one of the highest, second only to liver transplantation, among radiologic and surgical treatments for HCC

(Supplemental Table 6). TARE was 2.8-fold more expensive than surgical resection ($22,285 vs. $8,082) in Korea. The TARE group showed a significantly higher overall cost of treatment (mean, $53,541 vs. $16,393; $P < 0.001$) and a higher cost of additional treatment (mean, $596 vs. $292 per patient per month; $P = 0.023$) than the resection group (Supplemental Table 7).

DISCUSSION

When retrospectively compared with resection, TARE showed comparable treatment outcomes in terms of OS, TTP, and TTIP to surgical resection when applied as an initial treatment for a large single nodular HCC in patients with favorable hepatic function and performance status. TARE had benefits over surgical resection when accounting for the length of hospital stay and the incidence of adverse events. However, the TARE group underwent more additional treatments than the resection group.

TARE, when compared with external radiation therapy, can deliver microspheres loaded with a high-energy radioactive particle, ^{90}Y, closer to the target lesion and therefore enables high tumoricidal doses while sparing adjacent liver parenchyma (*32*). Immune activation at the local tumor microenvironment and systemic level is thought to mediate a delayed and sustained clinical response despite the short half-life of ^{90}Y (*33*). Although previous studies have discussed the role of TARE as a downsizing therapy that allows patients with unresectable HCC to consider sequential resection or transplantation (*13,34*), few studies have evaluated the effectiveness of TARE as a curative treatment modality for a single HCC. Our study suggests TARE as a potential alternative to
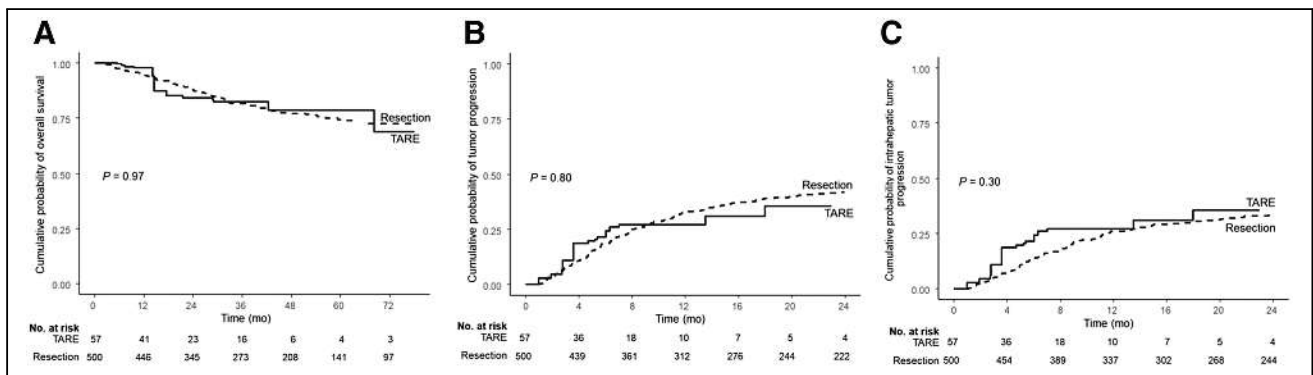
FIGURE 3. After using IPTW: cumulative probability of OS (A), tumor progression (B), and intrahepatic tumor progression (C) according to treatment groups.

TABLE 2
Risk Factor Analysis for OS

Variable	Univariable analysis		Multivariable analysis	
	HR	P	HR	P
Age $\geq$ 60 (vs. < 60)	0.74 (0.38–1.45)	0.38		
Male (vs. female)	1.22 (0.58–2.58)	0.60		
ASA classification 3 (vs. 1 or 2)	2.64 (1.34–5.21)	0.005	1.95 (0.88–4.32)	0.10
Hepatitis B virus–related (vs. the others)	1.23 (0.62–2.43)	0.56		
Liver cirrhosis	2.51 (1.22–5.16)	0.01	1.07 (0.43–2.65)	0.89
Albumin–bilirubin grade $\geq$ 2 (vs. 1)	2.60 (1.23–5.49)	0.01	1.98 (1.02–3.83)	0.04
AFP $\geq$ 400 ng/mL (vs. < 400 ng/mL)	0.80 (0.40–1.60)	0.53		
Satellite nodules	1.47 (0.98–2.20)	0.06	1.29 (0.87–1.90)	0.20
Tumor size $\geq$ 8 cm	1.41 (0.63–3.14)	0.40		
Bilobar involvement	1.51 (0.73–3.12)	0.26		
Vp2 (vs. Vp0 or Vp1)	1.63 (0.94–2.81)	0.08	1.57 (0.86–2.84)	0.14
TARE (vs. resection)	0.98 (0.40–2.43)	0.97	1.04 (0.42–2.59)	0.93

Data are with weighted population, using variables with P value under 0.1 at univariable analysis. Data in parentheses are 95% CI.
AFP = α-fetoprotein; Vp0 = absence of tumor thrombus in the portal vein; Vp1 = tumor thrombus in distal to the second-order branches of the portal vein, but not of the second-order branches; Vp2 = tumor thrombus in second-order branches of the portal vein.

surgical resection in a subgroup of patients with resectable single large HCC. Even though the TARE group was older (median, 69 vs. 60 y), had a higher number of patients with severe systemic disease (ASA 3), and tended to have more advanced disease (i.e., larger tumor size, more bilobar involvement, and more Vp2

PVTT) than the resection group, the clinical outcomes were similar.

The risk of postoperative hepatic decompensation is a major concern in planning surgical resection of HCC, and such concern increases when it comes to a larger tumor, as the remaining liver

TABLE 3
Safety Assessment

Adverse event	TARE (n = 57)		Resection (n = 500)		P	
	Any grade	Grade 3 or 4	Any grade	Grade 3 or 4	Any grade	Grade 3 or 4
Overall incidence	25 (43.9%)	5 (8.8%)	500 (100%)	500 (100%)	< 0.001	< 0.001
Ascites	0	0	37 (7.4%)	5 (1.0%)	0.024	1.00
Fever	3 (5.3%)	0	104 (20.8%)	1 (0.2%)	0.008	1.00
Nausea	7 (12.3%)	0	54 (10.8%)	3 (0.6%)	0.91	1.00
Vomiting	5 (8.8%)	0	33 (6.6%)	1 (0.2%)	0.58	1.00
Abdominal pain	15 (26.3%)	3 (5.3%)	500 (100%)	500 (100%)	< 0.001	< 0.001
Biliary anastomotic leak	0	0	14 (2.8%)	9 (1.8%)	0.38	0.61
Wound complication	0	0	28 (5.6%)	3 (0.6%)	0.10	1.00
Dyspnea	0	0	14 (2.8%)	5 (1.0%)	0.38	1.00
Gastrointestinal hemorrhage	0	0	6 (1.2%)	1 (0.2%)	1.00	1.00
AST elevation	4 (7.0%)	1 (1.8%)	488 (97.6%)	269 (53.8%)	< 0.001	< 0.001
ALT elevation	3 (5.3%)	1 (1.8%)	481 (96.2%)	248 (49.6%)	< 0.001	< 0.001
Bilirubin elevation	2 (3.5%)	1 (1.8%)	350 (70.0%)	37 (7.4%)	< 0.001	0.16
Portal vein thrombosis	0	0	15 (3.0%)	5 (1.0%)	0.39	1.00
Adverse events requiring intervention	0	NA	16 (3.2%)	NA	0.39	NA

Listed are adverse events, as defined by Common Terminology Criteria for Adverse Events (version 5.0). Data are number and percentage.
AST = aspartate aminotransferase; ALT = alanine transaminase; NA = not applicable.

volume is relatively smaller (35,36). In addition, large tumors are associated with a higher incidence of tumor recurrence, and thus remnant liver volume and function are important factors when deciding further treatment (8). TACE, a less invasive modality than surgical resection, has been attempted in treating patients with large HCC. However, a metaanalysis study reported that the outcomes of TACE were even worse than those of surgical resection for patients with solitary large HCC, though the study set aside the risks of postembolization syndrome or aggravation of liver function after repetitive treatment (10). TARE is also advantageous in preserving residual liver volume by inducing hypertrophy of the untreated lobe, which is associated with hypotrophy of the treated hepatic lobe (37–39); this enables more patients to receive further treatment if needed. The fact that no patient in the TARE group had a serious adverse event in our study emphasizes the safety benefits of TARE, which compensate for the high expense of the procedure and costs for sequential treatments.

The percentage of patients having Vp2 PVTT was higher in the TARE group than in the resection group, and Vp2 PVTT over no or Vp1 PVTT was found to be associated with a shorter TTIP in multivariable analysis. This finding could explain the benefit the resection group had over the TARE group in terms of TTIP, evaluated by log-rank testing before applying IPTW. The equivalence in OS despite the difference in TTIP in the crude analysis may be partially attributed to the effects of additional treatment.

In the present study, the TARE group underwent more additional treatments after the initial treatment than did the resection group; however, this difference was due to additional treatment performed because of the difficulty of distinguishing between suspected residual lesion and treatment-related hyperemia, as previously reported (40,41): 26 and 0 patients received additional treatment before definite tumor progression in the TARE group and the resection group, respectively. However, TTP and the number of additional treatments after definite tumor progression did not significantly differ between the 2 treatment groups.

When we further analyzed the cost of treatments, TARE was 2.8-fold more expensive than surgical resection in Korea ($22,285 vs. $8,082). In addition, TARE was associated with more additional treatments and a higher cost of additional treatment than was resection (mean, $596 vs. $292 per patient per month; $P = 0.023$). Thus, the TARE group had a significantly higher overall cost of treatment than the surgical resection group (mean, $53,541 vs. $16,393; $P < 0.001$), and TARE might be less cost-effective than surgical resection for large HCC.

On the other hand, the patients in the TARE group were older and had a worse baseline physical status (i.e., more frequent ASA classification 3) and a higher proportion of unfavorable tumor characteristics than the resection group. The greatest merit of TARE may be that it can be an effective alternative treatment to surgical resection for high-risk patients because of the future liver remnant and overall medical conditions. This possibility is supported by the results of the present study, in which the TARE group had fewer adverse events and possibly a more favorable posttreatment quality of life. However, given the retrospective nature of this study, a future prospective study is warranted to comprehensively investigate quality of life of treated patients.

Additionally, 28.1% of the TARE group were evaluated only by CT before treatment, whereas 99.4% of the resection group underwent liver MRI. This tendency might lead the TARE group to be misclassified as being in an earlier stage because of the difference in sensitivity of detecting nodules between CT and MRI. Despite this disadvantage of the TARE group in comparing the outcomes, the TARE group showed comparable OS, TTP, and TTIP after IPTW in this study.

In the present study, the TARE group showed comparable treatment outcomes and fewer adverse events than the resection group despite worse ASA classification and older age. If the ASA classification or the performance status is poor, TARE, which has a lower risk of side effects than surgery, would be recommended.

Our study had some limitations. First, there can be debate on evaluation of radiologic tumor response to TARE; therapy-induced tumor necrosis or fibrosis is not exactly reflected in tumor size (42), and the combined effects of embolization and radiation-induced lesional and perilesional changes can be more variable than in TACE (43). However, we used strictly predefined criteria for determining the point of disease progression and censoring the patients in measuring TTIP and TTP. Second, this study was retrospective, and there were some notable differences in the baseline profile between the groups. The differences were balanced to some extent by combining IPTW and Cox-proportional hazards regression models (44). Third, because of the operator-dependent nature of surgical resection and TARE, further studies are needed to ensure the generalizability of the results of our study, which was conducted at 2 referral centers with a lot of experience in both treatment modalities. Finally, though a comparison with external charged-particle radiotherapy (such as proton beam therapy) may be helpful in more extensively understanding the potential of selective radiation therapy in treating large single nodular HCCs (45), a practical application of external charged-particle radiotherapy is hampered by the small number of treatment facilities and the high expense of establishing them. Our study focused on TARE, a new modern radiotherapy with relatively high accessibility (46).

CONCLUSION

Our study suggests TARE as a possible alternative to surgical resection in patients with large single nodular HCC, with similar efficacy in terms of OS, TTP, and TTIP. Moreover, the TARE group had significantly shorter hospital stay and a lower tendency to experience serious adverse events requiring intervention than did the resection group. Randomized clinical trials involving larger numbers of patients are needed to assess outcomes in a longer perspective.

DISCLOSURE

KEY POINTS

QUESTION: Is TARE a potential alternative to surgical resection in patients with large single nodular HCC?

PERTINENT FINDINGS: In this retrospective cohort study of newly diagnosed HCC patients with large single nodular tumor, TARE—compared with surgical resection—showed similar OS and TTP and a better safety profile.

IMPLICATIONS FOR PATIENT CARE: TARE can act as a reasonable alternative to surgical resection in a carefully selected group of patients with a large single nodular HCC.

REFERENCES

1. Fitzmaurice C, Abate D, Abbasi N, et al. Global, regional, and national cancer incidence, mortality, years of life lost, years lived with disability, and disability-adjusted life-years for 29 cancer groups, 1990 to 2017: a systematic analysis for the Global Burden of Disease Study. *JAMA Oncol.* 2019;5:1749–1768.

2. El-Serag HB. Epidemiology of viral hepatitis and hepatocellular carcinoma. *Gastroenterology.* 2012;142:1264–1273.e1.

3. Heimbach JK, Kulik LM, Finn RS, et al. AASLD guidelines for the treatment of hepatocellular carcinoma. *Hepatol.* 2018;67:358–380.

4. European Association for the Study of the Liver. EASL Clinical Practice Guidelines: management of hepatocellular carcinoma. *J Hepatol.* 2018;69:182–236.

5. Fuster J, García-Valdecasas JC, Grande L, et al. Hepatocellular carcinoma and cirrhosis: results of surgical treatment in a European series. *Ann Surg.* 1996;223:297–302.

6. Hanazaki K, Kajikawa S, Shimozawa N, et al. Hepatic resection for large hepatocellular carcinoma. *Am J Surg.* 2001;181:347–353.

7. Pawlik TM, Delman KA, Vauthey JN, et al. Tumor size predicts vascular invasion and histologic grade: implications for selection of surgical treatment for hepatocellular carcinoma. *Liver Transpl.* 2005;11:1086–1092.

8. Choi GH, Han DH, Kim DH, et al. Outcome after curative resection for a huge (≥10 cm) hepatocellular carcinoma and prognostic significance of gross tumor classification. *Am J Surg.* 2009;198:693–701.

9. Ramacciato G, Mercantini P, Petrucciani N, et al. Does surgical resection have a role in the treatment of large or multinodular hepatocellular carcinoma? *Am Surg.* 2010;76:1189–1197.

10. Stevens CL, Awad A, Abbas SM, Watters DAK. Systematic review and meta-analysis of hepatic resection versus transarterial chemoembolization for solitary large hepatocellular carcinoma. *HPB (Oxford).* 2017;19:653–658.

11. Sacco R, Mismas V, Marceglia S, et al. Transarterial radioembolization for hepatocellular carcinoma: an update and perspectives. *World J Gastroenterol.* 2015;21:6518–6525.

12. Salem R, Gordon AC, Mouli S, et al. Y90 radioembolization significantly prolongs time to progression compared with chemoembolization in patients with hepatocellular carcinoma. *Gastroenterology.* 2016;151:1155–1163.e2.

13. Lewandowski RJ, Kulik LM, Riaz A, et al. A comparative analysis of transarterial downstaging for hepatocellular carcinoma: chemoembolization versus radioembolization. *Am J Transplant.* 2009;9:1920–1928.

14. Salem R, Johnson GE, Kim E, et al. Yttrium-90 radioembolization for the treatment of solitary, unresectable HCC: the LEGACY study. *Hepatol.* 2021;74:2342–2352.

15. Varela M, Real MI, Burrel M, et al. Chemoembolization of hepatocellular carcinoma with drug eluting beads: efficacy and doxorubicin pharmacokinetics. *J Hepatol.* 2007;46:474–481.

16. Kim HC, Kim YJ, Lee JH, Suh KS, Chung JW. Feasibility of boosted radioembolization for hepatocellular carcinoma larger than 5 cm. *J Vasc Interv Radiol.* 2019;30:1–8.

17. Garin E, Tselikas L, Guiu B, et al. Personalised versus standard dosimetry approach of selective internal radiation therapy in patients with locally advanced hepatocellular carcinoma (DOSISPHERE-01): a randomised, multicentre, open-label phase 2 trial. *Lancet Gastroenterol Hepatol.* 2021;6:17–29.

18. Salem R, Gilbertsen M, Butt Z, et al. Increased quality of life among hepatocellular carcinoma patients treated with radioembolization, compared with chemoembolization. *Clin Gastroenterol Hepatol.* 2013;11:1358–1365.e1.

19. Liver Cancer Study Group of Japan. The general rules for the clinical and pathological study of primary liver cancer. *Jpn J Surg.* 1989;19:98–129.

20. Kudo M, Izumi N, Kubo S, et al. Report of the 20th nationwide follow-up survey of primary liver cancer in Japan. *Hepatol Res.* 2020;50:15–46.

21. Johnson PJ, Berhane S, Kagebayashi C, et al. Assessment of liver function in patients with hepatocellular carcinoma: a new evidence-based approach—the ALBI grade. *J Clin Oncol.* 2015;33:550–558.

22. Peabody JW, Lee SW, Bickel SR. Health for all in the Republic of Korea: one country's experience with implementing universal health care. *Health Policy.* 1995;31:29–42.

23. Kim L, Kim JA, Kim S. A guide for the utilization of Health Insurance Review and Assessment Service national patient samples. *Epidemiol Health.* 2014;36:e2014008.

24. Sherrow C, Attwood K, Zhou K, Mukherjee S, Iyer R, Fountzilas C. Sequencing systemic therapy pathways for advanced hepatocellular carcinoma: a cost effectiveness analysis. *Liver Cancer.* 2020;9:549–562.

25. Gaba RC, Lewandowski RJ, Hickey R, et al. Transcatheter therapy for hepatic malignancy: standardization of terminology and reporting criteria. *J Vasc Interv Radiol.* 2016;27:457–473.

26. Padia SA, Lewandowski RJ, Johnson GE, et al. Radioembolization of hepatic malignancies: background, quality improvement guidelines, and future directions. *J Vasc Interv Radiol.* 2017;28:1–15.

27. Llovet JM, Lencioni R. mRECIST for HCC: performance and novel refinements. *J Hepatol.* 2020;72:288–306.

28. Hernán MA, Brumback B, Robins JM. Marginal structural models to estimate the causal effect of zidovudine on the survival of HIV-positive men. *Epidemiology.* 2000;11:561–570.

29. Lee BK, Lessler J, Stuart EA. Weight trimming and propensity score weighting. *PLoS One.* 2011;6:e18174.

30. Austin PC. The performance of different propensity score methods for estimating marginal hazard ratios. *Stat Med.* 2013;32:2837–2849.

31. Stuart EA. Matching methods for causal inference: a review and a look forward. *Stat Sci.* 2010;25:1–21.

32. Salem R, Thurston KG, Carr BI, Goin JE, Geschwind JF. Yttrium-90 microspheres: radiation therapy for unresectable liver cancer. *J Vasc Interv Radiol.* 2002;13:S223–S229.

33. Chew V, Lee YH, Pan L, et al. Immune activation underlies a sustained clinical response to yttrium-90 radioembolisation in hepatocellular carcinoma. *Gut.* 2019;68:335–346.

34. Iñarrairaegui M, Pardo F, Bilbao JI, et al. Response to radioembolization with yttrium-90 resin microspheres may allow surgical treatment with curative intent and prolonged survival in previously unresectable hepatocellular carcinoma. *Eur J Surg Oncol.* 2012;38:594–601.

35. Bruix J, Castells A, Bosch J, et al. Surgical resection of hepatocellular carcinoma in cirrhotic patients: prognostic value of preoperative portal pressure. *Gastroenterology.* 1996;111:1018–1022.

36. Chen XP, Qiu FZ, Wu ZD, Zhang BX. Chinese experience with hepatectomy for huge hepatocellular carcinoma. *Br J Surg.* 2004;91:322–326.

37. Teo JY, Goh BK. Contra-lateral liver lobe hypertrophy after unilobar Y90 radioembolization: an alternative to portal vein embolization? *World J Gastroenterol.* 2015;21:3170–3173.

38. Garlipp B, de Baere T, Damm R, et al. Left-liver hypertrophy after therapeutic right-liver radioembolization is substantial but less than after portal vein embolization. *Hepatology.* 2014;59:1864–1873.

39. Nebelung H, Wolf T, Bund S, et al. Radioembolization versus portal vein embolization for contralateral liver lobe hypertrophy: effect of cirrhosis. *Abdom Radiol (NY).* 2021;46:4046–4055.

40. Singh P, Anil G. Yttrium-90 radioembolization of liver tumors: what do the images tell us? *Cancer Imaging.* 2014;13:645–657.

41. Bester L, Hobbins PG, Wang SC, Salem R. Imaging characteristics following 90yttrium microsphere treatment for unresectable liver cancer. *J Med Imaging Radiat Oncol.* 2011;55:111–118.

42. Barabasch A, Kraemer NA, Ciritsis A, et al. Diagnostic accuracy of diffusion-weighted magnetic resonance imaging versus positron emission tomography/computed tomography for early response assessment of liver metastases to Y90-radioembolization. *Invest Radiol.* 2015;50:409–415.

43. Spina JC, Hume I, Pelaez A, Peralta O, Quadrelli M, Garcia Monaco R. Expected and unexpected imaging findings after 90Y transarterial radioembolization for liver tumors. *Radiographics.* 2019;39:578–595.

44. Funk MJ, Westreich D, Wiesen C, Stürmer T, Brookhart MA, Davidian M. Doubly robust estimation of causal effects. *Am J Epidemiol.* 2011;173:761–767.

45. Kim TH, Park JW, Kim BH, et al. Does risk-adapted proton beam therapy have a role as a complementary or alternative therapeutic option for hepatocellular carcinoma? *Cancers (Basel).* 2019;11:230.

46. Skinner HD, Hong TS, Krishnan S. Charged-particle therapy for hepatocellular carcinoma. *Semin Radiat Oncol.* 2011;21:278–286.

Combination of Carriers with Complementary Intratumoral Microdistributions of Delivered α-Particles May Realize the Promise for ²²⁵Ac in Large, Solid Tumors

Alaina Howe[1], Omkar Bhatavdekar*[1], Dominick Salerno*[1], Anders Josefsson[2], Jesus Pacheco-Torres[2], Zaver M. Bhujwalla[2], Kathleen L. Gabrielson[3], George Sgouros[2], and Stavroula Sofou[1,4]

[1]Chemical and Biomolecular Engineering, Institute for NanoBioTechnology, Johns Hopkins University, Baltimore, Maryland; [2]Russell H. Morgan Department of Radiology and Radiological Science, Johns Hopkins University, Baltimore, Maryland; [3]Molecular and Comparative Pathobiology, Johns Hopkins University, Baltimore, Maryland; and [4]Sidney Kimmel Comprehensive Cancer Center, Cancer Invasion and Metastasis Program, Department of Oncology, Johns Hopkins University, Baltimore, Maryland

α-particle radiotherapy has already been shown to be impervious to most resistance mechanisms. However, in established (i.e., large, vascularized) soft-tissue lesions, the diffusion-limited penetration depths of radiolabeled antibodies or nanocarriers ($\leq$50–80 μm) combined with the short range of α-particles (4–5 cell diameters) may result in only partial tumor irradiation, potentially limiting treatment efficacy. To address this challenge, we combined carriers with complementary intratumoral microdistributions of the delivered α-particles. We used the α-particle generator ²²⁵Ac, and we combined a tumor-responsive liposome (which, on tumor uptake, releases into the interstitium a highly diffusing form of its radioactive payload [²²⁵Ac-DOTA], potentially penetrating the deeper parts of tumors where antibodies do not reach) with a separately administered, less-penetrating radiolabeled antibody (irradiating the tumor perivascular regions where liposome contents clear too quickly). **Methods:** In a murine model with orthotopic human epidermal growth factor receptor 2–positive BT474 breast cancer xenografts, the biodistributions of each carrier were evaluated, and the control of tumor growth was monitored after administration of the same total radioactivity of ²²⁵Ac delivered by the ²²⁵Ac-DOTA–encapsulating liposomes, by the ²²⁵Ac-DOTA-SCN–labeled trastuzumab, and by both carriers at equally split radioactivities. **Results:** Tumor growth was significantly more inhibited when the same total injected radioactivity was divided between the 2 separate carriers than when delivered by either of the carriers alone. The combined carriers enabled more uniform intratumoral microdistributions of α-particles, at a tumor dose that was lower than the dose delivered by the antibody alone. **Conclusion:** This strategy demonstrates that more uniform microdistributions of the delivered α-particles within established solid tumors improve efficacy even at lower tumor doses. Augmentation of antibody-targeted α-particle therapies with tumor-responsive liposomes may address partial tumor irradiation, improving therapeutic effects.

Key Words: ²²⁵Ac; liposomes; antibodies; tumor microdistributions

Metastatic or recurrent solid cancers present an all too common clinical challenge partly due to development of resistance (*1*). Clinical studies with α-particle emitters have sometimes had exceptional outcomes on patients with metastatic prostate cancer resistant to approved options (*2,3*). The promise of α-particles targeted via antibodies against advanced cancers (not limited to prostate cancer) is currently under investigation in clinical studies. An effective and tolerable α-particle–based treatment against established (i.e., large, vascularized) lesions is critical to successfully handling solid-tumor patients with advanced disease that is resistant to established approaches.

α-particle radiotherapy has already been shown, across a diverse panel of tumor cells, to be impervious to most resistance mechanisms in the absence of transport barriers; the cells most resistant to γ-radiation have been reported to be sensitive to α-particles (*4*). The complexity and level of double-strand DNA damage caused by only a few tracks of α-particles across the cell nucleus overwhelm cellular repair mechanisms mostly independently of the cell oxygenation state and cell cycle (*5*); this inability to repair lethal damage is the reason that α-particle therapy, if optimally delivered, is impervious to resistance. However, the short range of α-particles (40–100 μm), which is ideal for localized irradiation and minimal irradiation of surrounding healthy tissues, also limits penetration within large tumors; the diffusion-limited penetration depths ($\leq$50–80 μm) of established and alternative vectors, such as radiolabeled antibodies or nanocarriers, respectively, combined with the short range of α-particles may result in only partial tumor irradiation (*6*). Importantly, partial tumor irradiation may limit the efficacy of α-particle therapies irrespective of any augmenting bystander effects (*7*).

Tumor-selective delivery strategies for α-particle therapies that aim to spread the intratumoral α-particle distributions over larger regions within solid tumors, and to prolong exposure of cancer cells to delivered radiotherapeutics, may improve efficacy against established tumors. Toward this goal, we evaluated a strategy to deliver the α-particle generator ²²⁵Ac as uniformly as possible throughout established tumors using a human epidermal growth factor receptor 2 (HER2)–positive human breast cancer, chosen as a model tumor for proof of concept. We combined 2 different delivery carriers of ²²⁵Ac, tumor-responsive liposomes and HER2-targeting antibodies, each administered separately. The liposomes were engineered to have 2 key properties for the implementation of our strategy: the

first is to clear slowly from tumors, and the second is—only in the tumor interstitium—to release highly diffusing forms (because of their small size) of the α-particle emitters (^{225}Ac-DOTA), which then may penetrate the deep parts of tumors where antibodies do not reach (6). The antibodies were also labeled with ^{225}Ac, which they deliver mostly closer to the tumor periphery (the perivascular regions), where the liposome-based modality suffers from fast clearance of released therapeutic agents (8).

The tumor-responsive liposomes were designed to exhibit the following properties, all of which were triggered by the slightly acidic pH in the tumor interstitium (extracellular pH [pH$_e$], ∼6.7–6.5) (9): adherence to the tumor's extracellular matrix (resulting in slower liposome clearance from the tumor (8)), low uptake or internalization by cancer cells (8), and release of contents directly into the interstitium as triggered by the tumor acidity (6). The HER2-targeting antibody trastuzumab, which was administered separately from liposomes, was chosen because of its high affinity for the HER2 receptor, reasonable radiolabeling, and well characterized in vivo behavior.

Here, we evaluate our hypothesis that combination of different carriers delivering α-particle radiotherapies to complementary regions of the same solid tumor results in more uniform irradiation over a larger fraction of the solid tumor's volume and, therefore, in greater inhibition of tumor growth than occurs with the same administered radioactivity delivered by each carrier alone.

MATERIALS AND METHODS

Materials

All materials are described in the supplemental section (available at http://jnm.snmjournals.org). ^{225}Ac (actinium chloride) was supplied by the U.S. Department of Energy Isotope Program, managed by the Office of Isotope R&D and Production.

Liposome Formation and Characterization

Tumor-responsive liposomes, composed of 20PC:DPPS:cholesterol:DSPE-polyethylene glycol-diammonium phosphate:DPPE-rhodamine at a 0.61:0.26:0.04:0.09:0.001 molar ratio, were formed using the thin-film hydration method as described in detail in the supplemental section (6). Liposomes were characterized for size and ζ-potential using a Zetasizer NanoZS90 (Malvern).

Radiolabeling of Carriers with ^{225}Ac/^{111}In

DOTA-SCN-trastuzumab (or diethylenetriaminepentaacetic acid [DTPA]-SCN-trastuzumab) was radiolabeled and characterized as described in the supplemental section (6). Liposomes encapsulating DOTA (or DTPA) were loaded with ^{225}Ac (or ^{111}In) using the ionophore A23187 (6).

Cell Culture

BT474 and the trastuzumab-resistant BT474 (BT474_R) were obtained from American Type Culture Collection and grown in treated cell culture flasks at 37°C and 5% CO_2 in Hybri-Care medium (American Type Culture Collection) buffered with sodium bicarbonate supplemented with 10% fetal bovine serum, penicillin (100 U/mL), and streptomycin (100 mg/mL).

Clonogenic Survival

After incubation of cell monolayers for 6 h with varying concentrations of radioactivity, the cells were washed and plated in dishes to grow until formation of colonies, as described in detail in the supplemental section.

TABLE 1
Characterization of Tumor-Responsive Liposomes Loaded with ^{225}Ac-DOTA

Size (nm)	ζ-potential (mV) pH 7.4	ζ-potential (mV) pH 6.5	ζ-potential (mV) pH 6.0	% loading	Specific activity* (MBq/μmol of lipid)	pH	Retention kinetics ($y = y\infty + a \times e^{-bt}$) y∞ (%)	a (%)	b (1/h)	t½ (h)
118 ± 15 (polydispersity index, 0.099 ± 0.051) (n = 15)	−1.5 ± 1.4† (n = 15)	−0.8 ± 1.2‡ (n = 15)	−0.04 ± 1.1‡ (n = 15)	51.1 ± 8.6 (n = 15)	0.5 ± 0.2 (n = 9)	7.4	88.8 ± 0.7	10.9 ± 1.2	1.2 ± 0.3	0.6 ± 0.2
						7.0	84.9 ± 1.3	13.8 ± 1.7	0.5 ± 0.1	1.4 ± 0.1
						6.5	77.8 ± 1.2	21.2 ± 1.5	0.4 ± 0.1	1.7 ± 0.1
						6.0	72.4 ± 0.7	27.8 ± 1.0	0.7 ± 0.1	1.0 ± 0.0

*Starting activity, 1.5–3.7 MBq.
†0.001 < P < 0.01.
‡P < 0.001.
t½ = half-time.

TABLE 2
Characterization of [225]Ac-Labeled HER2-Targeting Trastuzumab

Radiolabeling efficiency (%)	Immunoreactivity (%)	Specific activity* (MBq/mg of antibody)	Radiochemical purity	24-h retention (%)	K_D (nM)	
					BT474	BT474_R
53.8 ± 11.4 (n = 14)	95.9 ± 1.4 (n = 14)	3.4 ± 0.7 (n = 11)	97.8 ± 1.8 (n = 14)	90.6 ± 2.5 (n = 14)	24.6 ± 4.9	10.2 ± 1.7

*Starting activity, 0.4–1.1 MBq
K_D = dissociation constant.

Spheroid Formation and Spatiotemporal Profiles

BT474 cells were seeded on poly-2-hydroxyethyl methacrylate–coated, round-bottomed 96-well plates; were centrifuged; and were allowed to grow to the reported size before initiation of treatment (6). Spheroids were incubated with fluorescently labeled liposomes or antibody for 6 or 24 h, respectively, to scale with their corresponding blood circulation times. As described in the supplemental section (8), at different times spheroids were sampled and sliced, and the equatorial section was imaged using fluorescence microscopy. The spatial profiles (radial concentrations) were evaluated using an in-house eroding code to determine the average fluorescence intensity of each 5-μm concentric ring on the spheroids' sections. The spatial distributions at each time point were integrated (using the trapezoid rule) to evaluate the time-integrated concentration versus radius.

Spheroid Growth and Outgrowth Studies

Spheroids were incubated for 6 h with [225]Ac-DOTA–loaded liposomes (1 mM total lipid) or 24 h with [225]Ac-DOTA-SCN-trastuzumab (10 μg/mL). On completion of incubation, spheroids were transferred to fresh medium and the spheroid volume was monitored until the nontreated spheroids stopped growing (17 d later), at which point spheroids were individually plated on cell culture-treated, flat-bottomed 96-well plates and allowed to grow. The number of live cells per well was reported as percentage outgrowth relative to the numbers of live cells that received no treatment, when the latter reached confluency.

Animal Studies

One million BT474 cells suspended in 100 μL of 50:50 v:v Matrigel (Corning Life Sciences):serum-free Hybri-Care medium were inoculated into the second mammary fat pad of 5- to 6-wk-old NCR-nu/nu female mice (Taconic) at 24 h after subcutaneous implantation of a 17β-estradiol (1.7 mg) + progesterone (10 mg) hormone pellet (Innovative Research of America).

On tumors reaching 50 mm³, mice were randomly assigned to a group. For biodistribution studies, the animals were intravenously administered (352–444 kBq/animal) ^{111}In-DTPA-encapsulating liposomes or ^{111}In-DTPA-SCN-trastuzumab in 0.1 mL, and at different time points the animals were sacrificed and their organs weighed and measured for radioactivity.

In addition to the cold conditions and to no treatment, for treatment studies the mice were administered a single 0.1-mL intravenous injection of 4.625 kBq or 9.25 kBq of [225]Ac-DOTA-SCN-trastuzumab, [225]Ac-DOTA-loaded liposomes, or a combination of the two at a constant total administered radioactivity. The total mass of antibody was kept constant at 15 μg/mouse. Every other day, the mice were weighed and their tumor volumes measured with a digital caliper (resolution, 0.01 mm). Histopathologic analysis of all organs and tumors was performed on hematoxylin- and eosin-stained sections on day 24 after initiation of therapy.

α-Camera Imaging

Tumor-bearing mice were injected intravenously with [225]Ac-DOTA-SCN-trastuzumab, [225]Ac-DOTA-loaded liposomes, or both at 148 kBq of total radioactivity and were sacrificed 24 h later. Tumor and tissues were immediately harvested and sliced. The exposure time for the α-camera was 24 h per sample (10), and the images were analyzed using ImageJ, version 1.49b (National Institutes of Health) after being decay-corrected to the time of sacrifice.
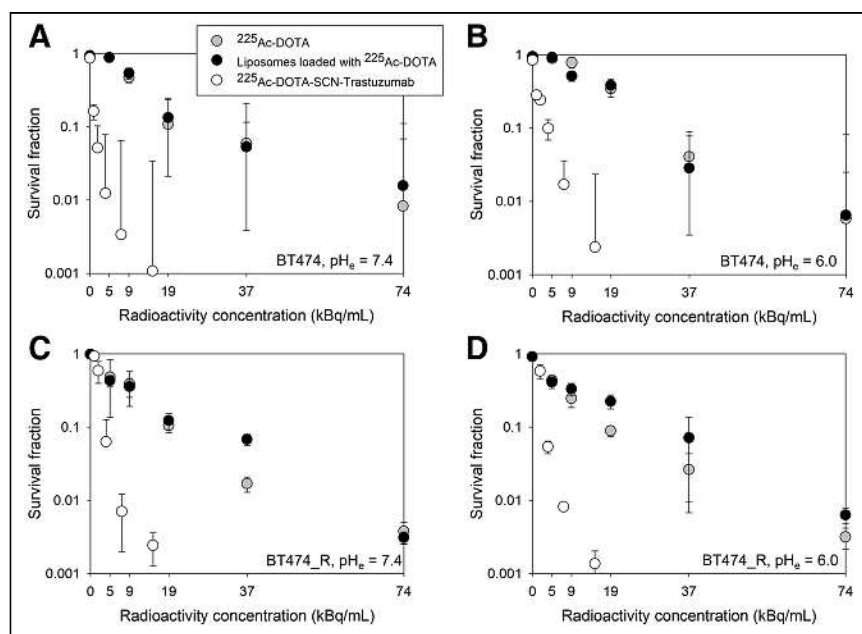
FIGURE 1. Colony survival of trastuzumab-sensitive BT474 (1.50 ± 0.10 × 10⁶ HER2 copies per cell) breast cancer cells after 6 h of incubation at 37°C with free [225]Ac-DOTA, tumor-responsive liposomes loaded with [225]Ac-DOTA, and radiolabeled trastuzumab ([225]Ac-DOTA-SCN-Ab) at extracellular pH of 7.4 (A and C) or 6.0 (B and D), as lowest expected acidic value of tumor interstitial pH_e. Radiolabeled trastuzumab's specific activity was 2.9 MBq/mg at highest radioactivity concentration. Cold conditions of liposomes and antibody are indicated at zero radioactivity concentration. Error bars correspond to SD of repeated measurements (4–6 samples per radioactivity concentration).
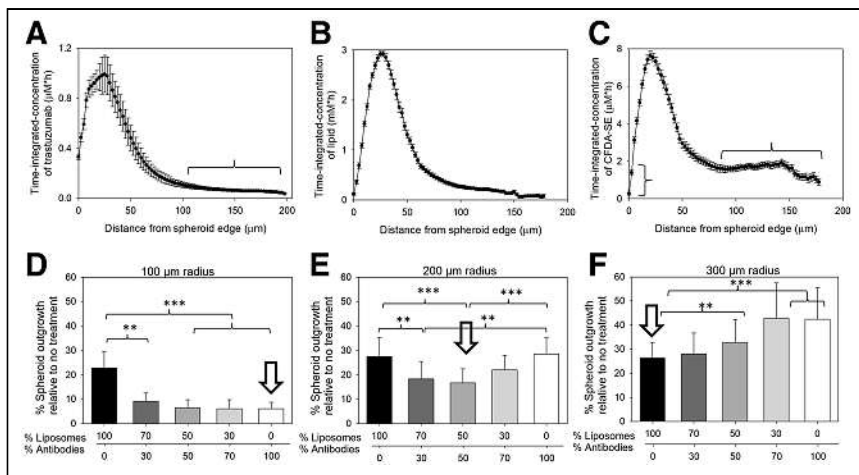
FIGURE 2. (A–C) Time-integrated concentrations in HER2-positive BT474 spheroids ($r = 200$ μm) of fluorescently labeled antibody (AlexaFluor-647-NHS-trastuzumab) used as surrogate of ^{225}Ac-DOTA-SCN-trastuzumab (A; horizontal bracket indicates <10% of peak value at distances beyond 100 μm from edge), lipids (DPPE-rhodamine-labeled liposomes; vertical bracket indicates too-rapid clearance of released fluorophore close to spheroid edge) (B), and carboxyfluorescein diacetate succinimidyl ester (CFDA-SE) fluorophores (used as surrogates of ^{225}Ac-DOTA) (C; horizontal bracket indicates uniform time-integrated values at ∼25% of peak value) delivered by tumor-responsive liposomes. Spatial distributions obtained at different time points (during carrier uptake by and clearance from spheroids) were integrated using trapezoid rule along spheroid radius. Error bars correspond to propagated SD of measurements of 3–6 equatorial spheroid sections per time point. Immunoreactivity of fluorescently labeled antibody was 88.2% ± 2.7%. (D–F) Greatest suppression of extent of outgrowth (used as indirect surrogate of tumor recurrence) by carrier, or combinations of carriers, of ^{225}Ac depends on spheroid size (representing tumor-avascular regions). Outgrowth control was best enabled (indicated by arrow) for small spheroids (radius, 100 μm) by radiolabeled antibodies (^{225}Ac-DOTA-SCN-trastuzumab) (D), for large spheroids (radius, 300 μm) by tumor-responsive liposomes encapsulating ^{225}Ac-DOTA (F), and for medium spheroids (radius, 200 μm) by dividing same total radioactivity between both carriers (E). Total radioactivity concentration was kept constant per spheroid size: 9.25 kBq/mL (D), 13.75 kBq/mL (E), and 18.5 kBq/mL (F). Error bars correspond to SD of repeated measurements (4–5 spheroids per condition, 2 independent preparations). **0.001 < P < 0.01. ***P < 0.001.

MRI for Evaluation of Tumor pH$_e$

Briefly, the animals were injected intraperitoneally with the pH$_e$ probe (±)2-(imidazol-1-yl)succinic acid (ISUCA), and anatomic T2-weighted spin-echo images were acquired using rapid-acquisition relaxation enhancement on a Bruker BioSpec 9.4-T horizontal MRI scanner. pH$_e$ was determined as described in the supplemental section (11).
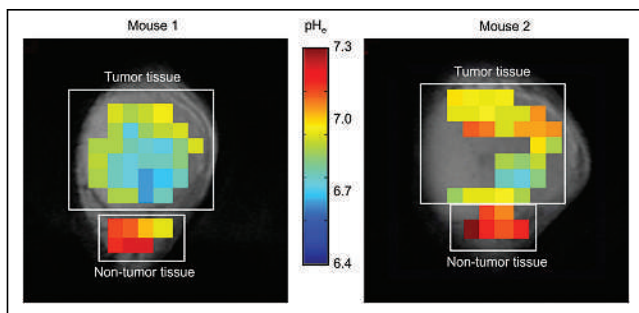
FIGURE 3. Tumor and nontumor pH$_e$ maps of 2 different NCR nu/nu female mice with orthotopic BT474 xenografts that were intraperitoneally administered ISUCA and imaged by spectroscopic MRI. pH$_e$ maps are overlaid with anatomic MR images of tumors. ISUCA chemical shift for each voxel (1 × 1 × 4 mm) of acquired multivoxel spectroscopy grid was transformed into pH value using Henderson–Hasselbalch calibration curve and presented as colored pH$_e$ map.

Dosimetry

Dosimetry was performed following a previously described methodology ($12,13$) using the software package 3D-RD-S (Radiopharmaceutical Imaging and Dosimetry, LLC), based on the biodistributions of ^{111}In-labeled liposomes (Supplemental Tables 1 and 2; Supplemental Fig. 1) or of the radiolabeled antibody (as described previously (14)). ^{111}In has been confirmed as a surrogate of ^{225}Ac biodistribution (Supplemental Fig. 2 (14)). The longest-lived ^{225}Ac daughter, ^{213}Bi, for the non–cell-internalizing liposomes, unlike for the cell-internalizing trastuzumab, was estimated to partly (25%) translocate from the site of the original parent decay (13).

Statistical Analysis

Results are reported as the arithmetic mean of n independent measurements ± SD. Significance in multiple comparisons and pair comparisons was evaluated by 1-way ANOVA and unpaired Student t testing, respectively, with P values of 0.05 considered to be significant.

RESULTS

Carrier Characterization

Table 1 shows the change in the liposomes' apparent ζ-potential toward less negative values with lowering pH; this change was partly attributed to protonation of diammonium phosphate on the adhesion lipid, with an apparent value of 6.8 for negative log of the acid dissociation constant (8). Acidification also resulted in release of encapsulated ^{225}Ac-DOTA from liposomes (Supplemental Fig. 3). The radiolabeled trastuzumab is characterized in Table 2 and Supplemental Figure 4.

Survival Assay on Cell Monolayers

Both cell lines, in monolayers, exhibited the same sensitivity to free ^{225}Ac-DOTA and to ^{225}Ac-DOTA–encapsulating liposomes, independently of pH (Fig. 1; Supplemental Fig. 5), since liposomes were designed to minimally associate with cancer cells (8), as is also the case for free ^{225}Ac-DOTA. Both cell lines exhibited comparable survival responses to ^{225}Ac-DOTA-SCN-trastuzumab, demonstrating lack of resistance to α-particles independently of the reported resistance to trastuzumab for BT474_R. The HER2 expression by the 2 cell lines was comparable (1.5 × 10^6 vs. 0.93 × 10^6 copies per cell, Supplemental Fig. 4).

Spheroids: Spatiotemporal Microdistributions and Response to Delivered ^{225}Ac

The time-integrated microdistributions of trastuzumab in spheroids (Fig. 2A), used as surrogates of tumor-avascular regions, exhibited high accumulation within only the first 60 μm from the spheroid edge, with less than 10% of the peak value at distances beyond 100 μm from the edge. As expected, liposomes did not penetrate the spheroids' longer distances than the antibody (Fig. 2B). Conversely, at distances of 80 μm from the spheroid edge and beyond, the fluorophore (Fig. 2C), which was used as a drug surrogate and was released from the liposomes, exhibited uniform
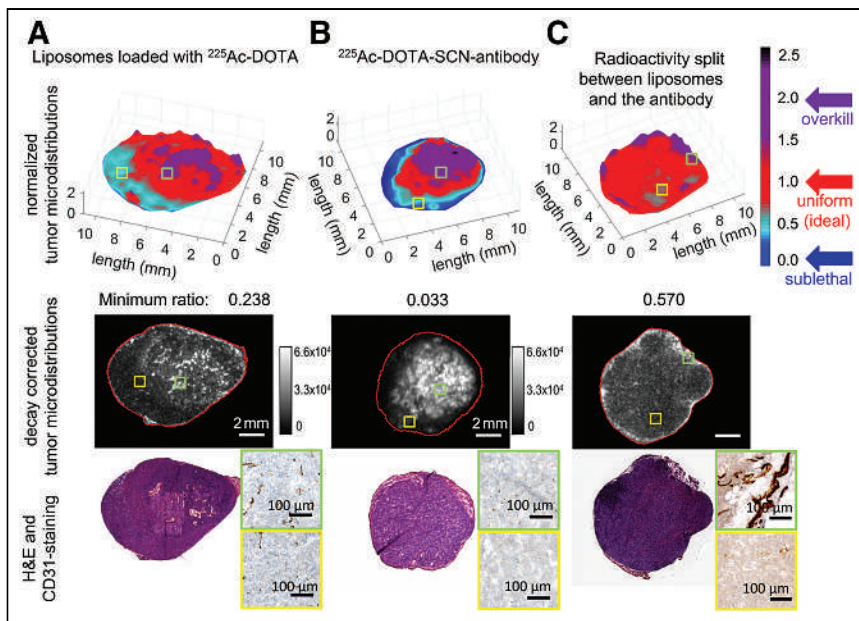
FIGURE 4. Microdistributions of same total radioactivity of ^{225}Ac delivered by tumor-responsive liposomes only (A), radiolabeled trastuzumab only (B), and both liposomes and—separately administered—trastuzumab (C) on tumor sections harvested 24 h after intravenous administration of 148 kBq per animal. High-radioactivity relative levels (ratios > 2, purple) were detected in densely vascularized tumor areas (CD31+, green insets); low-radioactivity relative levels (ratios < 0.6) were detected in sparsely vascularized areas (yellow insets). (Top panel) Map of normalized pixel intensities (where each pixel intensity was divided by average of intensities over entire tumor section) of ^{225}Ac relative to intensities averaged over entire tumor section so as to evaluate range of heterogeneities in ^{225}Ac microdistributions. Regions in red (with ratios around unity) indicate local distributions close to mean radioactivities delivered to tumor. Regions in cyan and dark blue (with normalized pixel intensity ratios well below mean radioactivities delivered to tumor) indicate regions with low or too-low radioactivities relative to tumor mean, expected to result in less cell killing. Regions in purple are where significantly more than tumor-averaged radioactivity is delivered. (Middle and bottom panels) Decay-corrected α-camera images and hematoxylin- and eosin (H&E)-stained and CD31-stained images of sequential 16-μm-thick tumor sections.

time-integrated values at approximately 25% of peak value. However, close to the spheroid edge, the released fluorophore cleared too rapidly from the spheroid. The acidification of the spheroids' interstitial pH (pH$_e$), which triggers the properties of liposome adhesion and content release, ranged from 7.4 close to the spheroid edge to around 6.5 at the spheroid center (Supplemental Fig. 6). The time-integrated microdistributions in Figure 2 reflect the microdosimetry of the delivered ^{225}Ac but not of the radioactive daughters.

After exposure to ^{225}Ac, divided between liposomes and the antibody, the carrier resulting in greatest suppression of spheroid outgrowth depended on the spheroid size at the time of treatment. On small spheroids (100-μm radius), delivery of radioactivity by the targeting antibody (Fig. 2D) was most efficient. The heterogeneous distribution of trastuzumab (high uptake but localized mostly close to the spheroid edge, Fig. 2A) did not impact efficacy because the longest spheroid distance (100-μm radius) was comparable to the range of α-particles in tissue (≤100 μm) (6). On large spheroids (300-μm radius, corresponding to avascular distances almost 3 times longer than the range of α-particles in tissue), delivery of radioactivity by liposomes (that released ^{225}Ac-DOTA into the interstitium) was most efficient; this efficiency was attributed to the deeper penetration (as supported by the fluorescent surrogate in Fig. 2C) of released ^{225}Ac-DOTA toward the spheroid center (6). In spheroids with an intermediate size (200-μm radius), the combination of the 2 carriers resulted in a better cell kill.

Tumor and Tissue pH$_e$ Measurement

The MR images in Figure 3 showed that there was measurable acidity in the tumor interstitium and that the microdistributions of interstitial pH$_e$ tumor maps were not uniform; indeed, they varied across tumors from different animals. Importantly, the pH$_e$ values measured were close to the acidic values that trigger the release and adhesion properties on liposomes.

In Vivo Assessment

In agreement with the profiles of delivered microdistributions of therapeutics in spheroids (Fig. 2), the tumor microdistributions of radioactivity in vivo were more uniform when delivered by both carriers than when delivered by each carrier alone. In particular, the normalized microdistributions of ^{225}Ac in tumor sections were more heterogeneous when the entire radioactivity was delivered by each carrier alone (Figs. 4A and 4B) than when split between the 2 carriers (Fig. 4C). Importantly, in both tumor sections where ^{225}Ac was delivered by only a single carrier, areas with low and too-low delivered radioactivities occupied significant fractions; regions that were too low were well below the mean tumor-delivered values and, therefore, could result in a lower cell kill. In densely vascularized areas (CD31-positive areas) the delivered normalized radioactivity levels were closer to and above unity (levels ranged from ideal to overkill), whereas in sparsely vascularized areas the levels ranged from sublethal (for the antibody) to too low (for liposomes) to least low (for the combination).

In agreement with the extent of uniformity in tumor microdistributions of ^{225}Ac, the volume growth of orthotopic BT474 xenografts was inhibited most when radioactivity was delivered by equally splitting the same total radioactivity (9.25 kBq (6)) between the 2 carriers (4.62 kBq + 4.62 kBq) that were administered simultaneously, as opposed to administering the same total radioactivity (9.25 kBq) by each carrier alone ($P < 0.001$, Fig. 5A).

The dosimetry in Table 3 shows that the equal radioactivity split between the 2 carriers—which resulted in the best tumor inhibition—delivered less dose to the tumor than when the antibody alone was used, underscoring the significance of α-particle microdistributions within the tumors. Individual growth plots for animal tumors are shown in Supplemental Figure 7. The same trend was observed at half the total administered radioactivity (Supplemental Figs. 8 and 9). Table 3 also shows that the carrier combination delivered less dose to the kidneys than did the antibody alone. The delivered dose to the liver by the carrier combination was similar to that delivered by each carrier alone. The error in the calculated dose to the spleen, delivered by the radiolabeled antibody, was large because of poor fitting. For more accurate fitting of the calculated dose to the spleen, sampling at longer time points would be required to capture biologic clearance from the spleen.

Pathologic evaluation of tumors on day 24 demonstrated visibly increased collagen on treatment with ^{225}Ac when delivered by the
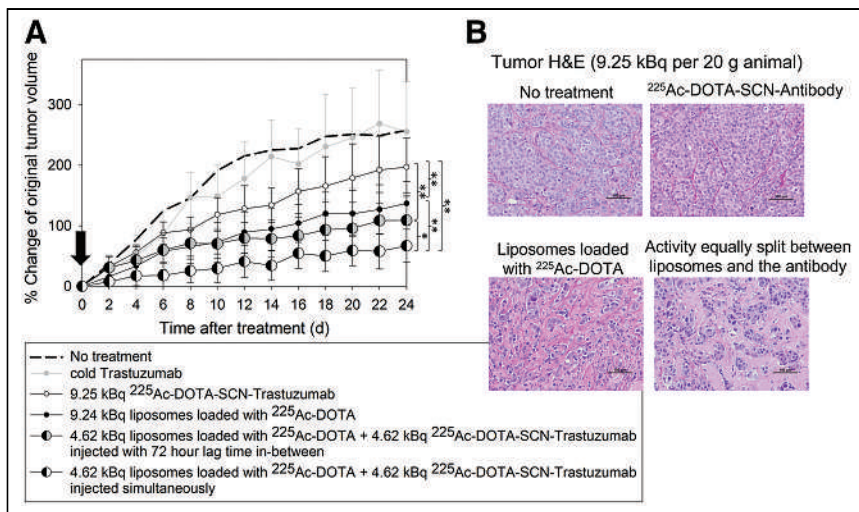
FIGURE 5. (A) Volume progression of HER2-positive BT474 orthotopic xenografts on NCR nu/nu female mice after single intravenous administration (arrow) of 9.25 kBq of ^{225}Ac per 20-g mouse delivered by radiolabeled trastuzumab alone (^{225}Ac-DOTA-SCN-antibody, 2.96 MBq/mg specific radioactivity in injectate); tumor-responsive liposomes loaded with ^{225}Ac-DOTA alone; both carriers at equally split (same total) radioactivity, with radiolabeled antibody being administered 72 h after liposomes (to largely allow for clearance of latter from liver and spleen); and both carriers at equally split (same total) radioactivity injected simultaneously. Data points are mean values of 8–9 animals per group, and error bars are SD. Significance was calculated with 1-way ANOVA ($P < 0.05$). (B) Hematoxylin- and eosin (H&E)-stained tumor sections. Scale bar = 100 μm. *$0.01 < P < 0.05$. **$0.001 < P < 0.01$.

combination of both carriers, compared with either carrier alone (Fig. 5B). Histopathologic analysis showed no noteworthy hepatic, cardiac, or renal toxicities in any construct at the time the animals were killed (Supplemental Fig. 10). Slight inflammation in the diaphragm of the liposome-only treatment group was observed, but otherwise there was no visible lung inflammation. Additionally, increased cell death in and reduced size of the spleen was observed in the liposome-only condition, in agreement with the significant splenic uptake. Long-term renal toxicities (9.5 mo after intravenous injection) of liposomal ^{225}Ac-DOTA at the maximum tolerated dose in tumor-free mice were not detected (13). The animal weight during the study did not decrease below 10% of the starting weight (Supplemental Fig. 11).

Survival was not a meaningful endpoint in this study, because tumor growth was estrogen-dependent; tumor growth rates (as

shown by the nontreated group, Fig. 5A) reached an asymptote after approximately 60 d from estrogen pellet implantation.

DISCUSSION

We hypothesized that improvement in the spatial uniformity of an α-particle emitter within solid tumors may address the challenge of partial irradiation by α-particles and, therefore, improve efficacy even at lower tumor-absorbed doses. Using a simple and clinically implementable approach, we demonstrated that the spatial intratumoral uniformity of ^{225}Ac can be improved by combinations of 2 separate carriers with complementary tumor microdistributions. Our approach optimized payload delivery, delivering a large number of α-particles at the tumor perivascular regions (via the targeting antibody), where the cell number is greatest and where cells are growing most aggressively, and, simultaneously, a high-capacity penetrating payload to the tumor interior (via the tumor-responsive liposomes), where the dormant and resistant cells are most likely to be responsible for treatment failure (15). The same total administered radioactivity was equally divided between the 2 carriers, resulting in synergistic inhibition of tumor growth compared with each carrier alone. It is possible that different radioactivity split ratios between the carriers may result in even better inhibition of tumor growth solely due to more uniform spatiotemporal microdistributions of emitters within tumors.

In contrast to the more homogeneous microdistributions of delivered radioactivity in tumors to improve killing of cancer cells, heterogeneous microdistributions, such as in the liver, could explain the lack of hepatic toxicities on the basis of localized, partial irradiation. Although liver uptake was significant when radioactivity was delivered by liposomes, previous studies at the maximum tolerated dose with liposomes did not reveal any hepatic or splenic toxicities (the main off-target organs) even 9.5 mo after injection (13). At least for the liver, one reason the significant delivered doses do not

TABLE 3
Dosimetry Results

Tissue	Antibody only		Liposomes only		Same total injected radioactivity equally split between antibody and liposomes	
	Absorbed dose (Gy)	SD	Absorbed dose (Gy)	SD	Absorbed dose (Gy)	SD
Kidneys	6.25	0.79	0.17	0.07	3.21	0.79
Liver	2.21	1.21	1.08	0.22	1.64	1.23
Lungs	0.94	0.29	0.22	0.21	0.58	0.36
Spleen	9.51	30.60	1.41	0.54	5.46	30.60
Tumor	6.68	1.55	0.40	0.06	3.54	1.55

Dose is mean and SD, not adjusted by relative biological effectiveness.

cause toxicities might be the localized, patchy patterns of liver irradiation (as opposed to the liver's uniform irradiation by the radiolabeled antibody). Radioactivity delivered to the liver by liposomes was strikingly grainy, suggesting heterogeneous or partial irradiation and possibly a limited cell kill (Supplemental Fig. 12). Liposomes are usually sequestered by Kupffer cells, which reside on the luminal side of the liver sinusoids, possibly limiting irradiation of all hepatocytes. Hepatic toxicity was not observed in the present study, in which 63% of the maximum tolerated dose (6) was administered. Regarding the spleen, we previously showed that at the maximum tolerated dose of ^{225}Ac delivered by liposomes, the initial splenic moderate-to-high hemosiderin deposition in the red pulp and reduced extramedullary hematopoiesis, observed right after administration of radioactivity, subsided and the spleen fully recovered after 9.5 mo in tumor-free mice (13).

Specific to ^{225}Ac are renal toxicities in mice—toxicities that were previously partially connected to escape in the blood of the last radioactive daughter of ^{225}Ac, ^{213}Bi, when ^{225}Ac was delivered by long-circulating carriers, such as antibodies, in addition to antibody renal uptake (14). For the ^{225}Ac-encapsulating liposomes, long-term renal toxicities at the maximum tolerated dose were not observed in mice (13). In human trials using ^{225}Ac-labeled antibodies or small molecules (3,16), renal toxicities have not been reported yet. For liposomes, it would most possibly be the hepatic and splenic uptake that could raise concerns possibly requiring further investigation (17).

To potentially mitigate toxicities in the liver and spleen by decreasing the corresponding delivered dose rates, radiolabeled antibodies were administered 72 h after administration of radiolabeled liposomes. In spheroids, the order and lag time (≤ 72 h) of administering each carrier did not significantly affect inhibition of spheroid outgrowth (Supplemental Fig. 13). In mice, this approach (Fig. 5A) still improved tumor growth inhibition relative to delivering the same total radioactivity by each carrier alone. Alternatively, a strategy that warrants investigation is dose fractionation of the antibody or liposome carriers—a strategy that may provide therapeutic and toxicity advantages. Notably, the presented dosimetry assumed the biologic clearance kinetics of the delivered radionuclides from tissues to be comparable to the half-life of ^{225}Ac. This assumption introduced an uncertainty in the calculated total emitted energies retained by tissues in mice; it is possible that in humans the relative uncertainties are smaller, given that the clearance kinetics of carriers from tissues are known to be slower than in mice.

Two points are key to the clinical relevance and applicability of this approach. The first is the vascular permeability of tumors to the administered liposomes; when human tumors exhibit vascular permeability to liposomes, the extent of liposome uptake by tumors strongly and favorably correlates with tumor response (17). The second is the acidification of the intratumoral pH$_e$, as it relates to triggering the properties of adhesion and release on our liposomes; acidification is common in tumors of patients with breast (and other) cancers (15) and correlates with highly aggressive tumors (9,15,18), with reported values comparable to the values ($6.60 \leq$ pH$_e \leq 6.98$) required to activate our liposomes. Importantly, in our studies, although the intratumoral acidity was highly variant, the strategy of combining the 2 carriers still resulted in better tumor growth inhibition.

Our delivery approach is aimed at the spatial scale of the avascular tumor regions; these regions are bounded and defined by the distances to the nearest blood vessels within the tumors, and their order of magnitude ranges from a few tenths of a micrometer to possibly several hundredths of a micrometer (19). The distances to the nearest blood vessels in tumors are not on the order of magnitude of macroscopic tumor sizes, although they are expected to increase in larger tumors (19). From this perspective, the intratumoral microdistributions of α-particle emitters delivered by our strategy would be driven by the distributions of the distances to the nearest blood vessels within tumors and not directly by the macroscopic size of the tumors themselves (20).

The spheroids studied here demonstrated the different efficacies of each of the 2 delivery carriers as a function of these distances (Figs. 2D–2F). Effective scaling up of this approach to human tumors will depend not only on the lengths of the distances to the nearest blood vessels (which should be within reach by the released highly diffusing forms of the α-particle emitters) but also, importantly, on the extent of uptake and microdistributions of the radioactivity in off-target organs such as the liver. The potential for successful scaling up of this approach to humans will be determined by our ability to optimize the radioactivity microdistributions until they are as uniform as possible within the tumor (for maximum killing efficacy) and as heterogeneous as possible within the off-target normal organs (for minimum toxicities), as we show is the case in mouse liver for radioactivity delivered by liposomes (Supplemental Fig. 12).

CONCLUSION

This study showed that there is potential to expand the impact of α-particle therapies on established solid tumors by choosing combinations of carriers based on the complementarity of the intratumoral microdistributions of the delivered α-particle emitters while maintaining the same administered radioactivities.

DISCLOSURE

KEY POINTS

QUESTION: Can the partial irradiation of solid tumors by α-particles, delivered with traditional radionuclide carriers, be rectified to improve efficacy?

PERTINENT FINDINGS: The partial irradiation of solid tumors by α-particle emitters can be rectified by combining carriers with complementary intratumoral microdistributions of the delivered α-particle emitters.

IMPLICATIONS FOR PATIENT CARE: Combination of separate carriers with complementary intratumoral microdistributions of α-particle emitters (^{225}Ac in this study) could be a general strategy to control solid tumor growth both in preclinical investigations and in the design of personalized α-particle therapies for patients.

REFERENCES

1. Cancer facts and statistics. American Cancer Society website. https://www.cancer.org/research/cancer-facts-statistics.html. Accessed May 4, 2022.

2. Kratochwil C, Bruchertseifer F, Giesel FL, et al. ^{225}Ac-PSMA-617 for PSMA-targeted α-radiation therapy of metastatic castration-resistant prostate cancer. *J Nucl Med.* 2016;57:1941–1944.

3. Kratochwil C, Haberkorn U, Giesel FL. ^{225}Ac-PSMA-617 for therapy of prostate cancer. *Semin Nucl Med.* 2020;50:133–140.

4. Yard BD, Gopal P, Bannik K, Siemeister G, Hagemann UB, Abazeed ME. Cellular and genetic determinants of the sensitivity of cancer to α-particle irradiation. *Cancer Res.* 2019;79:5640–5651.

5. McDevitt MR, Sgouros G, Sofou S. Targeted and nontargeted α-particle therapies. *Annu Rev Biomed Eng.* 2018;20:73–93.

6. Zhu C, Sempkowski M, Holleran T, et al. Alpha-particle radiotherapy: for large solid tumors diffusion trumps targeting. *Biomaterials.* 2017;130:67–75.

7. Wang R, Coderre JA. A bystander effect in alpha-particle irradiations of human prostate tumor cells. *Radiat Res.* 2005;164:711–722.

8. Stras S, Howe A, Prasad A, Salerno D, Bhatavdekar O, Sofou S. Growth of metastatic triple-negative breast cancer is inhibited by deep tumor-penetrating and slow tumor-clearing chemotherapy: the case of tumor-adhering liposomes with interstitial drug release. *Mol Pharm.* 2020;17:118–131.

9. Vaupel P, Kallinowski F, Okunieff P. Blood flow, oxygen and nutrient supply, and metabolic microenvironment of human tumors: a review. *Cancer Res.* 1989;49:6449–6465.

10. Bäck T, Jacobsson L. The alpha-camera: a quantitative digital autoradiography technique using a charge-coupled device for ex vivo high-resolution bioimaging of α-particles. *J Nucl Med.* 2010;51:1616–1623.

11. Pacheco-Torres J, Mukherjee N, Walko M, et al. Image guided drug release from pH-sensitive ion channel-functionalized stealth liposomes into an in vivo glioblastoma model. *Nanomedicine.* 2015;11:1345–1354.

12. Sgouros G, Roeske JC, McDevitt MR, et al; SNM MIRD Committee. MIRD pamphlet no. 22 (abridged): radiobiology and dosimetry of alpha-particle emitters for targeted radionuclide therapy. *J Nucl Med.* 2010;51:311–328.

13. Prasad A, Nair R, Bhatavdekar O, et al. Transport-driven engineering of liposomes for delivery of α-particle radiotherapy to solid tumors: effect on inhibition of tumor progression and onset delay of spontaneous metastases. *Eur J Nucl Med Mol Imaging.* 2021;48:4246–4258.

14. Song H, Hobbs RF, Vajravelu R, et al. Radioimmunotherapy of breast cancer metastases with alpha-particle emitter ^{225}Ac: comparing efficacy with ^{213}Bi and ^{90}Y. *Cancer Res.* 2009;69:8941–8948.

15. Vaupel P. Tumor microenvironmental physiology and its implications for radiation oncology. *Semin Radiat Oncol.* 2004;14:198–206.

16. Jurcic JG. Targeted alpha-particle therapy for hematologic malignancies. *Semin Nucl Med.* 2020;50:152–161.

17. Lee H, Shields AF, Siegel BA, et al. ^{64}Cu-MM-302 positron emission tomography quantifies variability of enhanced permeability and retention of nanoparticles in relation to treatment response in patients with metastatic breast cancer. *Clin Cancer Res.* 2017;23:4190–4202.

18. Estrella V, Chen T, Lloyd M, et al. Acidity generated by the tumor microenvironment drives local invasion. *Cancer Res.* 2013;73:1524–1535.

19. Lauk S, Zietman A, Skates S, Fabian R, Suit HD. Comparative morphometric study of tumor vasculature in human squamous cell carcinomas and their xenotransplants in athymic nude mice. *Cancer Res.* 1989;49:4557–4561.

20. Baish JW, Stylianopoulos T, Lanning RM, et al. Scaling rules for diffusive drug delivery in tumor and normal tissues. *Proc Natl Acad Sci USA.* 2011; 108:1799–1803.

Absolute Lymphocyte Count After COVID-19 Vaccination Is Associated with Vaccine-Induced Hypermetabolic Lymph Nodes on ^{18}F-FDG PET/CT: A Focus in Breast Cancer Care

Romain-David Seban[1,2], Capucine Richard[1], Camila Nascimento-Leite[1], Jerome Ghidaglia[1], Claire Provost[2,3], Julie Gonin[4], Christophe Le Tourneau[5,6], Emanuela Romano[7,8], Nicolas Deleval[1], and Laurence Champion[1,2]

[1]Department of Nuclear Medicine and Endocrine Oncology, Institut Curie, Saint-Cloud, France; [2]Laboratoire d'Imagerie Translationnelle en Oncologie, InsermU1288, PSL Research University, Institut Curie, Orsay, France; [3]Department of Radio-Pharmacology, Institut Curie, Saint-Cloud, France; [4]Department of Pathology, Institut Curie, Saint-Cloud, France; [5]Department of Drug Development and Innovation (D3i), Institut Curie, Paris, France; [6]INSERM U900 Research team, Paris Saclay University, Saint-Cloud, France; [7]Department of Medical Oncology, Center for Cancer Immunotherapy, Institut Curie, Paris, France; and [8]INSERM U932, PSL Research University, Institut Curie, Paris, France

We aimed to predict the presence of vaccine-induced hypermetabolic lymph nodes (v-HLNs) on ^{18}F-FDG PET/CT after coronavirus disease 2019 (COVID-19) vaccination and determine their association with lymphocyte counts. **Methods:** In this retrospective single-center study, we included consecutive patients who underwent ^{18}F-FDG PET/CT imaging after messenger RNA– or viral vector–based COVID-19 vaccination between early March and late April 2021. Demographics, clinical parameters, and absolute lymphocyte count (ALC) were collected, and their association with the presence of v-HLNs in the draining territory was studied by logistic regression. **Results:** In total, 260 patients were eligible, including 209 (80%) women and 145 (56%) with breast cancer. The median age was 50 y (range, 23–96 y). The messenger RNA vaccine had been given to 233 (90%). Ninety (35%) patients had v-HLNs, with a median SUV$_{max}$ of 3.7 (range, 2.0–26.3), and 74 (44%) displayed lymphopenia, with a median ALC of 1.4×10^9/L (range, $0.3–18.3 \times 10^9$/L). An age of no more than 50 y (odds ratio [OR], 2.2; 95% CI, 1.0–4.5), the absence of lymphopenia (OR, 2.2; 95% CI, 1.1–4.3), and less than a 30-d interval from the last vaccine injection to the ^{18}F-FDG PET/CT (OR, 2.6; 95% CI, 1.3–5.6) were independent factors for v-HLNs on multivariate analysis. In breast cancer patients, the absence of lymphopenia was the only independent factor significantly associated with v-HLNs (OR, 2.9; 95% CI, 1.2–7.4). **Conclusion:** Patients with a normal ALC after COVID-19 vaccination were more likely to have v-HLNs on ^{18}F-FDG PET/CT, both of which might be associated with a stronger immune response to vaccination.

Key Words: ^{18}F-FDG PET/CT; COVID-19 vaccination; absolute lymphocyte count; hypermetabolic lymph nodes; immune response

A billion doses of the currently authorized and recommended messenger RNA (mRNA) (*1,2*) or viral vector vaccine (*3*) against coronavirus disease 2019 (COVID-19) have been administered worldwide. Such vaccination has been shown to promote immunity against the severe acute respiratory syndrome coronavirus 2 (SARS-CoV-2) by inducing strong T- and memory B-cell responses (*4,5*).

Because generation of an immune response increases glucose metabolism in lymphoid organs, which are critical modulators of T- and B-cell immunity (*6,7*), ^{18}F-FDG PET/CT might be used as a potent tool to assess immune response after vaccinations against several infections, including SARS-CoV-2 (*8*), influenza virus (*9*), and human papillomavirus (*10*), as well as against cancer (*11*). Recently, several findings on ^{18}F-FDG PET/CT have been reported in patients vaccinated against COVID-19, most likely related to immune activation in lymphoid organs, hypermetabolic lymph nodes (HLNs) in the drainage territory (*12–19*), or increased glucose metabolism in the spleen (*20–22*).

In patients who received mRNA vaccines for COVID-19, the prevalence of vaccine-induced HLNs (v-HLNs) on ^{18}F-FDG PET/CT was approximately 45% (*12,14,23*). Indeed, v-HLNs were more commonly observed in young and immunocompetent patients (*14*). Additionally, the interval between the last vaccine dose and the number of vaccine doses was also significantly associated with the presence of v-HLNs (*14*). Furthermore, v-HLNs appeared to correlate with an effective humoral response induced by the mRNA vaccination (*13*). However, it remains unclear whether similar results would be obtained after the administration of another type of vaccine (e.g., viral vectors).

Lymphoma patients and breast cancer (BC) patients are considerably more susceptible to v-HLNs than are patients with other types of cancer, as stated by Cohen et al. (*12*). Among BC patients, v-HLNs in the axillary area and beyond can mimic tumor lesions and lead to confounding of imaging results (*16*). Recent publications have emphasized the importance of documenting vaccination history at the time of scanning to avoid false-positive results (*21,24*) and all the attendant negative consequences: unnecessary biopsy/cytology or lymphadenectomy for early-stage BC or unjustified changes in systemic treatment for advanced-stage BC.

In the present study, we specifically aimed to predict the presence of v-HLNs on ^{18}F-FDG PET/CT after COVID-19 vaccination and to investigate their relationships to lymphocyte counts, with a special focus on a subgroup of BC patients.

MATERIALS AND METHODS

Patients

We conducted a retrospective review of 702 consecutive patients who underwent ^{18}F-FDG PET/CT imaging at Institut Curie Hospital, Saint-Cloud, France (the flow chart is provided in Fig. 1). Four hundred forty-two patients were not vaccinated ($n = 437$) or did not want to participate in medical research ($n = 5$) and were excluded. This retrospective data collection complied with the requirements of our Institutional Review Board (DATA210128), which waived the need to obtain informed consent (rule of nonopposition), and the study was conducted according to the Declaration of Helsinki.

Clinicobiologic Data

Clinical data consisted of the patient's age, sex, disease (cancer type if applicable), and current specific treatment (chemotherapy, endocrine therapy, immunotherapy with immune checkpoint inhibitors, or targeted therapy). All patients were asked for the date of their COVID-19 vaccination, the type or brand of vaccine that had been used (mRNA or viral vector), and the injection site for the first and (if applicable) second doses.

We considered a subgroup of patients who theoretically had a weakened immune system, whom we called immunosuppressed, caused by any of the following treatments: chemotherapy within the last 3 mo, rituximab-containing regimens or bone marrow transplantation within the last 6 mo, or current steroid therapy with more than 10 mg/d of prednisone-equivalent. Biologic characteristics, including the absolute lymphocyte count (ALC), were obtained from peripheral blood samples after vaccination (at least 1 dose) and before ^{18}F-FDG PET/CT. For ALC, we used the lower limit of normal for each center. Blood samples were analyzed when performed after vaccination and in the previous 28 d before ^{18}F-FDG PET/CT.

^{18}F-FDG PET/CT Scans

^{18}F-FDG PET/CT was performed in accordance with the applicable European Association of Nuclear Medicine procedure guidelines (25). Patients fasted for at least 6 h before scanning to ensure a blood glucose level of less than 10 mmol/L. Scanning was performed using a Philips Vereos PET/CT device, combining the small lutetium-yttrium oxyorthosilicate scintillator crystal with the silicon photomultiplier block design. PET images were reconstructed with a fully 3-dimensional time-of-flight iterative method (VUE Point FX [an ordered-subsets expectation maximization algorithm; GE Healthcare], a matrix of 288×288, 3 iterations, 5 subsets, and a 2-mm postprocessing filter).

Images were converted to SUV units by normalization using the patient's body weight.

Measurement and Interpretation of ^{18}F-FDG PET/CT Parameters

Four certified nuclear medicine physicians analyzed the ^{18}F-FDG PET/CT images. Measures of SUV_{mean} or SUV_{max} were obtained from HLNs detected in the drainage territory using the PET tumor segmentation tool in Philips IntelliSpace Portal, version 9.0. Readers were masked and did not know the patients' characteristics.

Draining lymph node uptake values were measured on the PET images, assisted by CT data for the anatomic location. As previously published by Thomassen et al. (9), we also recorded contralateral lymph node uptake values, which were used for reference. Similarly, an HLN was defined as having an SUV_{max} ratio of at least 1.5 between the ipsilateral and contralateral reference sites (9,14). The HLN SUV_{max} was defined as the highest SUV_{max} among all HLNs detected in the drainage territory (axillary or supraclavicular for vaccination in the deltoid, inguinal for vaccination in the thigh or buttock). The size of most HLNs was recorded using short-axis diameter on CT images. v-HLNs were characterized using the clinical background: type, stage and site of disease, histologic findings (biopsy or cytology), and other available imaging results (enhanced MRI, CT, or previous ^{18}F-FDG PET/CT). Where there was any uncertainty about HLN etiology (disease-related or vaccine-induced), we categorized the patients into an indeterminate-HLN group.

Statistical Analysis

Continuous and categoric variables are reported as median with range (minimum and maximum) and as frequency and percentage, respectively. Factors associated with v-HLNs were tested by logistic regression analysis using a stepwise Akaike information criterion method for variable selection (26). All reported P values are 2-sided, and P values of less than 0.05 were considered to be significant. Analyses were performed with R software (version 4.0.2).

RESULTS

Whole Cohort

Patient Characteristics. Table 1 summarizes the detailed demographic and clinicobiologic characteristics and PET imaging parameters of the 260 patients. The median age was 50 y (range, 23–96 y), and 80% were women. Two hundred thirty-three patients (90%) received the mRNA vaccine, including 110 (42%) who had 2 doses. The median time between the last vaccination dose and ^{18}F-FDG PET/CT scanning was 14 d (range, 1–51 d) for patients who received only 1 dose and 23 d (range, 1–67 d) for patients who received a second dose. More than half the patients were referred for BC (56%), and 24% were considered immunosuppressed ($n = 62$). Blood sample analysis after vaccination and before PET was available in 170 patients. Among them, median ALC was 1.4×10^9/L (range, 0.3–18.3×10^9/L), and 74 (44%) displayed lymphopenia. Overall, 90 patients (35%) had v-HLNs, with a median SUV_{max} of 3.7 (range, 2.0–26.3).

Association Between v-HLNs on ^{18}F-FDG PET/CT and Clinicobiologic Parameters. An age of no more than 50 y (odds ratio [OR], 2.2; 95% CI, 1.0–4.5), the
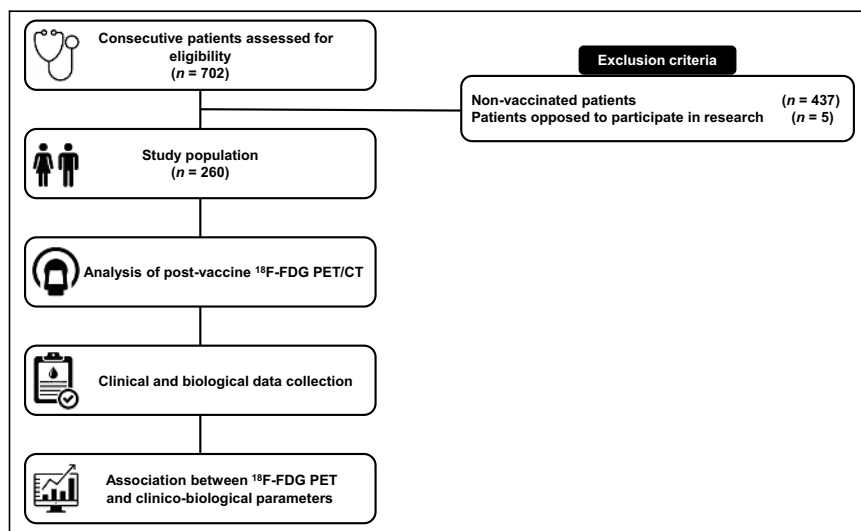
FIGURE 1. Flowchart.

TABLE 1
Patient Characteristics

Characteristic	All patients ($n = 260$)	BC patients ($n = 145$)
Demographics		
Age (y)	50 (23–96)	67 (28–95)
Female	209 (80)	145 (100)
Vaccine		
mRNA vaccine (vs. viral vector vaccine)	233 (90)	128 (88)
2 doses (vs. 1 dose)	110 (42)	61 (42)
Interval between first dose and PET (patients who had 1 dose) (d)	14 (1–51)	13 (1–44)
Interval between second dose and PET (patients who had 2 doses) (d)	23 (1–67)	24 (1–67)
Disease		
BC (early vs. advanced stage)	145 (56)	54 (37) vs. 91 (63)
Hematologic malignancy (lymphoma, leukemia, myeloma)	39 (15)	NA
Thoracic cancer	17 (7)	NA
Digestive cancer	15 (6)	NA
Gynecologic cancer	14 (5)	NA
Head and neck cancer	14 (5)	NA
Other types of cancer (thyroid, sarcoma, melanoma)	11 (4)	NA
Nononcologic indications (inflammatory or infectious diseases)	5 (2)	NA
Treatment		
No specific treatment	106 (41)	47 (32)
Endocrine therapy	28 (11)	24 (16.5)
Chemotherapy	46 (17.5)	25 (17.5)
Targeted therapy	18 (7)	9 (6)
Immune checkpoint inhibitors (single-agent or combined therapies)	8 (3)	0 (0)
Endocrine therapy + targeted therapy	39 (15)	37 (26)
Chemotherapy + targeted therapy	4 (1.5)	3 (2)
Steroids (>10 mg/d of prednisone-equivalent)	12 (5)	5 (3)
Peripheral blood		
Interval between blood analysis and PET (d)	2 (0–28)*	3 (0–28)†
ALC ($\times 10^9$/L)	1.4 (0.3–18.3)*	1.5 (0.4–5.0)†
Lymphopenia	74 (44)*	41 (39)
HLNs on ^{18}F-FDG PET/CT		
Interval‡ (d)	17 (0–67)	19 (0–79)
Etiology		
Vaccine-induced	90 (35)	56 (37)
Tumor-related	14 (5)	6 (4)
Indeterminate	6 (2)	6 (4)
None	150 (58)	77 (53)
HLN SUV$_{max}$	3.7 (2.0–26.3)	3.7 (2.0–26.3)

*$n = 170$ patients.
†$n = 106$ patients.
‡Between last injection and PET.
NA = not applicable.
Qualitative data are number and percentage; continuous data are median and range.
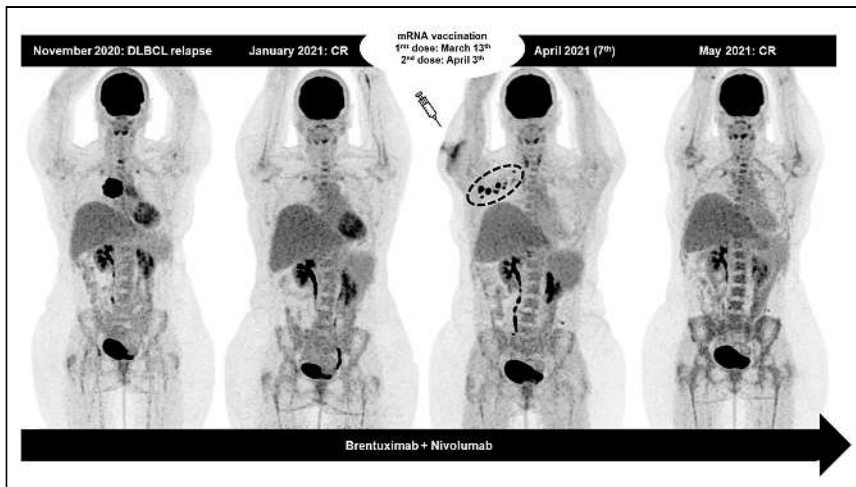
FIGURE 2. Maximum-intensity-projection ^{18}F-FDG PET images of 45-y-old woman with relapsed DLBCL in mediastinum. Patient was treated with brentuximab and nivolumab and experienced complete metabolic response 2 mo after initiation of therapy (January 2021). Although continuing lymphoma therapy, she received 2 mRNA COVID-19 vaccine injections in right deltoid. ^{18}F-FDG PET/CT scan 4 d after last vaccine dose (April 2021) showed several HLNs (encircled). On subsequent ^{18}F-FDG PET/CT scan 1 mo later, HLNs disappeared, strongly suggesting their relation to vaccination. This clinical presentation thus highlights presence of v-HLNs in patient younger than 50 y and with normal ALC at time of ^{18}F-FDG PET/CT, which was performed less than 30 d after last vaccine dose. CR = complete response; DLBCL = diffuse large B-cell lymphoma.

absence of lymphopenia (OR, 2.2; 95% CI, 1.1–4.3), and a less than 30-d interval from the last vaccine injection to the date of ^{18}F-FDG PET/CT (OR, 2.6; 95% CI, 1.3–5.6) were statistically significant factors associated with v-HLNs (Fig. 2) on univariate analysis (Table 2). All parameters remained independent predictors of the v-HLN status on multivariate analysis. Interestingly, for patients displaying lymphopenia after vaccination, we evaluated the dynamic of ALC and found that a low ALC existed before vaccination in most patients (67%, $n = 36$) suggesting that lymphopenia was not related to vaccination. The immunosuppression, the type of vaccine, and the number of doses were not associated with v-HLNs.

BC Cohort

Patient Characteristics. Table 1 summarizes the detailed demographic and clinicobiologic characteristics and PET imaging parameters of the 145 BC patients. All patients were women. About one third had early-stage BC, and the remaining two thirds

TABLE 2
Parameters Associated with v-HLNs in Whole Cohort (260 Patients) on Univariate and Multivariate Logistic Regression Analyses

| | v-HLNs | | | |
| | Univariate | | Multivariate | |
Variable	P	OR	P	OR
Age				
≥50 y	0.02	1 (reference)	0.04	1 (reference)
<50 y		2.4 (1.2–4.9)		2.2 (1.0–4.5)
Immunosuppression				
Yes	0.86	1 (reference)	—	—
No		0.95 (0.5–1.7)		—
Lymphopenia				
Yes		1 (reference)		1 (reference)
No	0.04	1.9 (1.0–3.8)	0.03	2.2 (1.1–4.3)
Unknown	0.38	1.4 (0.7–2.7)	0.37	1.4 (0.7–2.8)
Type of vaccine				
mRNA	0.66	1 (reference)	—	—
Viral vector		1.2 (0.5–2.7)		—
Number of vaccine dose(s)				
1	0.45	1 (reference)	—	—
2		1.2 (0.7–2.0)		—
Interval*				
≥30 d	0.02	1 (reference)	0.01	1 (reference)
<30 d		2.3 (1.2–4.9)		2.6 (1.3–5.6)

*Between last injection and PET.
Data in parentheses are 95% CIs.

TABLE 3
Parameters Associated with v-HLNs in BC Cohort (145 Patients) on Univariate and Multivariate Logistic Regression Analyses

| | v-HLNs | | | |
| | Univariate | | Multivariate | |
Variable	P	OR	P	OR
Age				
≥50 y	0.17	1 (reference)	—	—
<50 y		1.9 (0.7–4.9)		—
Immunosuppression				
Yes	0.26	1 (reference)	—	—
No		1.2 (0.9–1.9)		—
Lymphopenia				
Yes		1 (reference)		1 (reference)
No	0.04	2.5 (1.1–6.1)	0.02	2.9 (1.2–7.4)
Unknown	0.19	1.9 (0.8–6.7)	0.16	2.0 (0.8–6.9)
Type of vaccine				
mRNA	0.90	1 (reference)	—	—
Viral vector		0.9 (0.3–2.7)		—
Number of vaccine doses				
1	0.55	1 (reference)	—	—
2		0.8 (0.4–1.6)		—
Interval*				
≥30 d	0.12	1 (reference)	0.06	1 (reference)
<30 d		2.0 (0.9–4.8)		2.3 (0.9–6.3)

*Between last injection and PET.
Data in parentheses are 95% CIs.

had advanced-stage BC, treated mainly with endocrine therapy with or without targeted therapy or chemotherapy. Whole blood counts were available for 106 BC patients after vaccination and before PET. Among them, median ALC was 1.5×10^9/L (range, 0.4–5.0×10^9/L), and 41 (39%) displayed lymphopenia. Fifty-six patients (37%) had v-HLNs, with a median SUV_{max} of 3.7.

Association Between v-HLNs on ^{18}F-FDG PET/CT and Clinicobiologic Parameters. Logistic regression analysis summarizing the association between v-HLNs on ^{18}F-FDG PET/CT after COVID-19 vaccination and clinicobiologic parameters is provided in Table 3. The absence of lymphopenia was the only independent factor significantly associated with v-HLNs (OR, 2.9; 95% CI, 1.2–7.4). The patients' age and immune status, the type of vaccine, the number of doses, or the interval from the last vaccine injection to the date of ^{18}F-FDG PET/CT were not significantly associated with v-HLNs in this subgroup of BC patients.

Early-Stage BC Patients with Vaccination Ipsilateral to the Tumor. We identified 7 BC patients who had axillary HLNs ipsilateral to the recently vaccinated arm but also ipsilateral to the known tumor. Their demographic characteristics, vaccination information, ^{18}F-FDG PET/CT parameters, ALC, and histologic data are reported in Table 4. Six of the cases had been histologically documented by fine-needle aspiration cytology ($n = 3$) or sentinel lymph node biopsy ($n = 3$). One patient (14%) was not investigated and began

neoadjuvant endocrine therapy; the planned partial mastectomy with sentinel lymph node biopsy will help determine the cause of HLNs afterward. Although all fine-needle aspiration cytology evidenced signs of malignancy, with tumor cells (43%) (Fig. 3), all sentinel lymph node biopsies revealed benign reactive changes (43%) (Fig. 4).

DISCUSSION

We have shown that patient age (≤50 y), ALC (<lower limit of normal), and timing of last injection dose (<30 d before PET) significantly correlated with v-HLNs on ^{18}F-FDG PET/CT after COVID-19 vaccination in a retrospective cohort of 260 patients. Moreover, among patients with BC, the ALC before ^{18}F-FDG PET/CT remained the most strongly implicated factor associated with v-HLN status. Indeed, BC patients with a normal value of ALC were more likely to have v-HLNs on ^{18}F-FDG PET/CT.

Our results are consistent with previously published data, suggesting that v-HLNs are significantly less common in elderly patients and conversely more frequent in patients who received their last vaccine injection a few days before ^{18}F-FDG PET/CT (14). In addition to providing information on the HLN status, which may help nuclear medicine physicians with image interpretation and oncologists with medical management, these findings also raise the

TABLE 4
Early-Stage BC Cohort with Vaccination Ipsilateral to Tumor

Characteristic	Patient 1	Patient 2	Patient 3	Patient 4	Patient 5	Patient 6	Patient 7
Demographic							
Age (y)	45	52	38	81	48	76	66
Breast tumor	Left	Left	Left	Left	Left	Right	Right
Vaccination							
Injection side (deltoid)	Left	Left	Left	Left	Left	Right	Right
Type	mRNA	mRNA	mRNA	mRNA	Viral vector	Viral vector	mRNA
Number of doses	1	1	1	2	1	1	2
^{18}F-FDG PET/CT imaging							
Interval* (d)	7	3	11	22	32	6	17
HLN location	Left axilla	Left axilla	Left axilla	Left axilla	Left axilla	Right axilla	Right axilla
LN SUV$_{max}$	7.9	2.0	3.2	4.3	3.7	3.4	4.3
LN size (small axis in mm)	11	7	8	6	8	6	12
Number of HLNs	>5	>5	>5	4	2	4	>5
Peripheral blood							
ALC (×10^9/L)	1.92	Unknown	2.35	1.70	0.84	Unknown	2.32
Lymphopenia	No	Unknown	No	No	Yes	Unknown	No
Histology modality	Cytology	Cytology	Sentinel LN	Sentinel LN	Sentinel LN	None	Cytology
Etiology	Tumor	Tumor	Vaccine	Vaccine	Vaccine	Unknown	Tumor

*Between last dose and PET.
LN = lymph nodes.

question of whether the COVID-19 vaccine is triggering a more robust immune response in this population (≤50 y or ALC > lower limit of normal). In the specific setting of hematologic malignancies, Cohen et al. demonstrated that the rate of v-HLNs after mRNA vaccination was significantly higher in patients with positive serology than in those with negative serology (13). This essential result might be the missing link between the presence of v-HLNs and vaccine effectiveness in inducing a strong immune response and, therefore, robust immunity.

Another interesting aspect of our work is that ALC after vaccination and before ^{18}F-FDG PET/CT was an independent factor significantly associated with v-HLNs in the whole cohort of 260 patients—an observation that was further reinforced by our findings in the specific cohort of 145 BC patients. Such important results have been previously demonstrated after vaccination, especially against SARS-CoV-2 (27,28) but also against other viruses (29). Indeed, Achiron et al. showed a correlation between the level of SARS-CoV-2 antibodies on serology and lymphocyte count at 1 mo after the second dose in a cohort of 125 multiple sclerosis patients who were fully vaccinated with BNT162b2 COVID-19 vaccine (27). These results have been confirmed in 427 patients with hematologic malignancies who also received 2 doses of BNT162b2 COVID-19 vaccine, explored by serology (28). In this study, ALC correlated with a higher seropositivity likelihood and antibody titers. This observation is not surprising given the pivotal role of lymphocytes in the immune response, specifically because these are instrumental in the formation of antibodies (30). All these parameters are closely related to the humoral immune response; however, as stated by the authors

of the previously cited studies, the role of lymphocytes in cell-mediated immune response after COVID-19 vaccination remains to be investigated.

On the basis of our findings, there is no evidence to support the conclusion that immunosuppression leads to a lower incidence of v-HLNs. Although we could say that chemotherapy or rituximab-containing regimens are likely to block the serologic response to COVID-19 (13) or influenza A (H1N1) vaccinations (31,32), the relationship between immunodepression and reactive HLNs in the drainage territory remains unclear from the literature. On the one hand, Thomassen et al. showed that immunosuppressive drugs given within 2 wk from vaccination did not affect axillary lymph node uptake in 293 patients who had been vaccinated with at least 1 influenza vaccination in the deltoid region (9). On the other hand, Cohen et al. revealed that lymphoma patients treated during the year before COVID-19 vaccination with rituximab-containing regimens (9%) had significantly lower rates of v-HLNs than did all other lymphoma patients (41%), associated with a strong relationship between v-HLNs and positive serologies (Spearman $\rho = 0.64$ in patients who received the 2 doses of mRNA vaccine) (13). These results are strengthened by a study by Eifer et al. demonstrating a strong inverse association between v-HLNs and immunosuppressive therapies (OR, 0.37; 95% CI, 0.20–0.64; $P < 0.01$) in a large cohort of 377 patients after mRNA-based COVID-19 vaccination (14). However, the determinants that correlated with the high glucose metabolism in the lymph node could be multiple, with, for example, age or lymphocyte count or timing of last injection dose having a higher degree of association. Further analyses are needed to explore

FIGURE 3. In patient with early-stage BC who received vaccine injection ipsilateral to tumor, maximum-intensity-projection ^{18}F-FDG PET image (top) shows HLN in left axilla, axial ^{18}F-FDG PET/CT image (middle) also shows left axillary HLN, and fine-needle aspiration cytology specimen shows tumor cells (May-Grünwald/Giemsa staining, ×20) (bottom).

the specific relationship between v-HLNs, immune status, and the immune response to the COVID-19 vaccine.

In the specific case of early-stage BC patients, it is usually recommended that vaccine be administered in the arm opposite the BC side. However, in rare cases, early-stage BC patients could have bilateral cancers or receive the vaccine injection in the arm ipsilateral to the known tumor, which might falsely influence the PET report. We thus studied patients with axillary HLNs ipsilateral to the recently vaccinated arm but also ipsilateral to the known tumor, and we found signs of malignancy, with tumor cells in half the patients whereas the other half had benign reactive changes. The sample size ($n = 7$) was too small to allow a statistical analysis or to draw any conclusion. Unfortunately, because blood sample analysis was not available for all these patients, we could not determine whether patients with benign reactive changes had significantly higher ALCs than patients with signs of malignancy. Since the date of PET examination could hardly be postponed in cancer patients, predicting the nature of HLNs on ^{18}F-FDG PET/CT has become an area of intensive investigation to avoid unnecessary biopsies or aggressive treatments. As a result, the 3 parameters (age, timing of last injection dose, and ALC) that we identified in the current study may help to guide nuclear medicine physicians in interpreting ^{18}F-FDG PET/CT images and oncologists in choosing whether to perform a biopsy. Further research is required to validate such findings and identify clinical, biologic, and imaging factors associated with the nature of HLNs (benign vs. malignant) ipsilateral to the breast tumor in a larger cohort of patients with early-stage BC.

The strength of our study is the large sample size. The main limitation concerns the retrospective nature and single-center design. We did not include sex in our logistic regression analysis because of a sample-selection bias, explained by the predominance of women, who account for 80%. Indeed, this sex bias in favor of women is due to the nature of our center, which is a referral one for BC treatment. Moreover, only 10% of patients received the viral vector–based COVID-19 vaccine. Consequently, we cannot conclude with sufficient power the specific vaccine-subtype effects on the ^{18}F-FDG PET/CT response to SARS-CoV-2 vaccination.

Studies deciphering metabolic patterns on ^{18}F-FDG PET/CT after vaccination are needed because annual vaccination against SARS-CoV-2 might be needed.

In any case, our work confirms the potential of ^{18}F-FDG PET/CT as a potent tool to assess immune response after COVID-19 vaccination, as can be explained by the fact that immune response increases glucose metabolism in lymphoid organs (e.g., regional lymph nodes), which are critical modulators of immunity (*33*). Now proven to be more than 90% effective against SARS-CoV-2, the mRNA technology will probably modify the therapeutic armamentarium in patients with solid malignant tumors (*34*). However, it remains to be demonstrated that ^{18}F-FDG PET/CT can, in its widest sense, become a relevant imaging tool for in vivo quantification of the immune response in healthy lymphoid tissues after mRNA vaccination (*8*).

CONCLUSION

In this large cohort of 260 patients, we demonstrated that patient ALC was a critical determinant of v-HLNs on ^{18}F-FDG PET/CT after mRNA based- or viral vector–based COVID-19 vaccination, as well as patient age and timing of last injection dose. In BC patients, normal values of ALC after vaccination and before ^{18}F-FDG PET/CT were the best indicator of the v-HLN status. Both of these interrelated elements (age and ALC) might modulate the quality of the immune response after COVID-19 vaccination. Further prospective studies are warranted to investigate whether the metabolism of lymphoid organs on ^{18}F-FDG PET/CT is a crucial effector of the immune response after COVID-19 vaccination.

DISCLOSURE

No potential conflict of interest relevant to this article was reported.
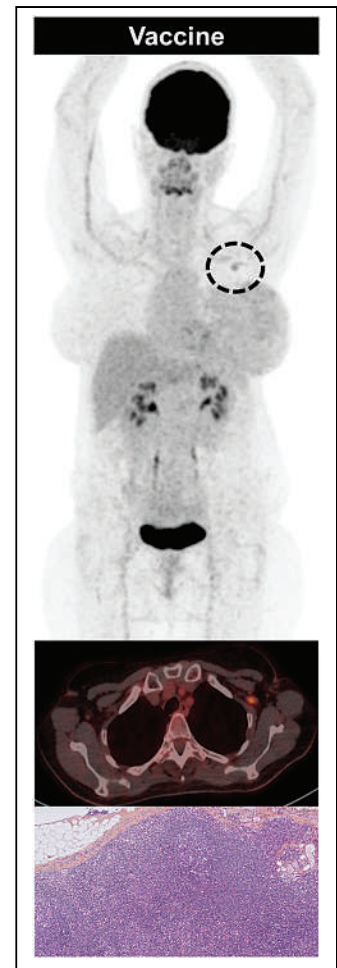

FIGURE 4. In patient with early-stage BC who received vaccine injection ipsilateral to tumor, maximum-intensity-projection ^{18}F-FDG PET image (top) shows HLN in left axilla, axial ^{18}F-FDG PET/CT image (middle) also shows left axillary HLNs, and sentinel lymph node biopsy sample shows benign reactive changes (hematoxylin-eosin-saffron staining, ×5) (bottom).

KEY POINTS

QUESTION: Can we use ALC to predict the presence of v-HLNs in the drainage territory on ^{18}F-FDG PET/CT after COVID-19 vaccination?

PERTINENT FINDINGS: Patient ALC (>lower limit of normal), patient age (≤50 y), and timing of last injection dose (<30 d before PET) significantly correlated with v-HLNs.

IMPLICATIONS FOR PATIENT CARE: Patients displaying a normal ALC after COVID-19 vaccination are more likely to show v-HLNs on ^{18}F-FDG PET/CT and may subsequently have a higher seropositivity likelihood and antibody titers.

REFERENCES

1. Polack FP, Thomas SJ, Kitchin N, et al. Safety and efficacy of the BNT162b2 mRNA Covid-19 vaccine. *N Engl J Med.* 2020;383:2603–2615.
2. Baden LR, El Sahly HM, Essink B, et al. Efficacy and safety of the mRNA-1273 SARS-CoV-2 vaccine. *N Engl J Med.* 2021;384:403–416.
3. Voysey M, Clemens SAC, Madhi SA, et al. Safety and efficacy of the ChAdOx1 nCoV-19 vaccine (AZD1222) against SARS-CoV-2: an interim analysis of four randomised controlled trials in Brazil, South Africa, and the UK. *Lancet.* 2021;397:99–111.
4. Sahin U, Muik A, Derhovanessian E, et al. COVID-19 vaccine BNT162b1 elicits human antibody and TH1 T cell responses. *Nature.* 2020;586:594–599.
5. Laczkó D, Hogan MJ, Toulmin SA, et al. A single immunization with nucleoside-modified mRNA vaccines elicits strong cellular and humoral immune responses against SARS-CoV-2 in mice. *Immunity.* 2020;53:724–732.e7.
6. Matloubian M, Lo CG, Cinamon G, et al. Lymphocyte egress from thymus and peripheral lymphoid organs is dependent on S1P receptor 1. *Nature.* 2004;427:355–360.
7. Bronte V, Pittet MJ. The spleen in local and systemic regulation of immunity. *Immunity.* 2013;39:806–818.
8. Seban R-D, Champion L, Yeh R, Schwartz LH, Dercle L. Assessing immune response upon systemic RNA vaccination on [^{18}F]-FDG PET/CT for COVID-19 vaccine and then for immuno-oncology? *Eur J Nucl Med Mol Imaging.* 2021;48:3351–3352.
9. Thomassen A, Lerberg Nielsen A, Gerke O, Johansen A, Petersen H. Duration of ^{18}F-FDG avidity in lymph nodes after pandemic H1N1v and seasonal influenza vaccination. *Eur J Nucl Med Mol Imaging.* 2011;38:894–898.
10. Coates EE, Costner PJ, Nason MC, et al. Lymph node activation by PET/CT following vaccination with licensed vaccines for human papillomaviruses. *Clin Nucl Med.* 2017;42:329–334.
11. Pektor S, Hilscher L, Walzer KC, et al. In vivo imaging of the immune response upon systemic RNA cancer vaccination by FDG-PET. *EJNMMI Res.* 2018;8:80.
12. Cohen D, Krauthammer SH, Wolf I, Even-Sapir E. Hypermetabolic lymphadenopathy following administration of BNT162b2 mRNA Covid-19 vaccine: incidence assessed by [^{18}F]FDG PET-CT and relevance to study interpretation. *Eur J Nucl Med Mol Imaging.* 2021;48:1854–1863.
13. Cohen D, Hazut Krauthammer S, Cohen YC, et al. Correlation between BNT162b2 mRNA Covid-19 vaccine-associated hypermetabolic lymphadenopathy and humoral immunity in patients with hematologic malignancy. *Eur J Nucl Med Mol Imaging.* 2021;48:3540–3549.
14. Eifer M, Tau N, Alhoubani Y, et al. COVID-19 mRNA vaccination: age and immune status and its association with axillary lymph node PET/CT uptake. *J Nucl Med.* 2022;63:134–139.
15. McIntosh LJ, Rosen MP, Mittal K, et al. Coordination and optimization of FDG PET/CT and COVID-19 vaccination; lessons learned in the early stages of mass vaccination. *Cancer Treat Rev.* 2021;98:102220.
16. Fleury V, Maucherat B, Rusu D, Dumont F, Rousseau C. COVID-19 vaccination may cause FDG uptake beyond axillary area. *Eur J Hybrid Imaging.* 2021;5:11.
17. Skawran S, Gennari AG, Dittli M, et al. [^{18}F]FDG uptake of axillary lymph nodes after COVID-19 vaccination in oncological PET/CT: frequency, intensity, and potential clinical impact. *Eur Radiol.* 2022;32:508–516.
18. Shin M, Hyun CY, Choi YH, Choi JY, Lee K-H, Cho YS. COVID-19 vaccination-associated lymphadenopathy on FDG PET/CT: distinctive features in adenovirus-vectored vaccine. *Clin Nucl Med.* 2021;46:814–819.
19. Avner M, Orevi M, Caplan N, Popovtzer A, Lotem M, Cohen JE. COVID-19 vaccine as a cause for unilateral lymphadenopathy detected by ^{18}F-FDG PET/CT in a patient affected by melanoma. *Eur J Nucl Med Mol Imaging.* 2021;48:2659–2660.
20. Steinberg J, Thomas A, Iravani A. ^{18}F-fluorodeoxyglucose PET/CT findings in a systemic inflammatory response syndrome after COVID-19 vaccine. *Lancet.* 2021;397:e9.
21. Treglia G, Cuzzocrea M, Muoio B, Elzi L. PET findings after COVID-19 vaccination: "keep calm and carry on." *Clin Transl Imaging.* 2021;9:209–214.
22. Seban R-D, Champion L, Deleval N, Richard C, Provost C. Immune response visualized in vivo by [^{18}F]-FDG PET/CT after COVID-19 vaccine. *Diagnostics (Basel).* 2021;11:676.
23. Treglia G, Cuzzocrea M, Giovanella L, Elzi L, Muoio B. Prevalence and significance of hypermetabolic lymph nodes detected by 2-[^{18}F]FDG PET/CT after COVID-19 vaccination: a systematic review and a meta-analysis. *Pharmaceuticals (Basel).* 2021;14:762.
24. Brown AH, Shah S, Groves AM, Wan S, Malhotra A. The challenge of staging breast cancer with PET/CT in the era of COVID vaccination. *Clin Nucl Med.* 2021;46:1006–1010.
25. Boellaard R, Delgado-Bolton R, Oyen WJG, et al. FDG PET/CT: EANM procedure guidelines for tumour imaging—version 2.0. *Eur J Nucl Med Mol Imaging.* 2015;42:328–354.
26. Yamashita T, Yamashita K, Kamimura R. A stepwise AIC method for variable selection in linear regression. *Commun Stat Theory Methods.* 2007;36:2395–2403.
27. Achiron A, Mandel M, Dreyer-Alster S, et al. Humoral immune response to COVID-19 mRNA vaccine in patients with multiple sclerosis treated with high-efficacy disease-modifying therapies. *Ther Adv Neurol Disord.* 2021;14:17562864211012835.
28. Herzog Tzarfati K, Gutwein O, Apel A, et al. BNT162b2 COVID-19 vaccine is significantly less effective in patients with hematologic malignancies. *Am J Hematol.* 2021;96:1195–1203.
29. Mavinkurve-Groothuis AMC, van der Flier M, Stelma F, van Leer-Buter C, Preijers FW, Hoogerbrugge PM. Absolute lymphocyte count predicts the response to new influenza virus H1N1 vaccination in pediatric cancer patients. *Clin Vaccine Immunol.* 2013;20:118–121.
30. Harris TN, Grimm E, Mertens E, Ehrich WE. The role of the lymphocyte in antibody formation. *J Exp Med.* 1945;81:73–83.
31. Yri OE, Torfoss D, Hungnes O, et al. Rituximab blocks protective serologic response to influenza A (H1N1) 2009 vaccination in lymphoma patients during or within 6 months after treatment. *Blood.* 2011;118:6769–6771.
32. Gross PA, Gould AL, Brown AE. Effect of cancer chemotherapy on the immune response to influenza virus vaccine: review of published studies. *Rev Infect Dis.* 1985;7:613–618.
33. Cafri G, Gartner JJ, Zaks T, et al. mRNA vaccine-induced neoantigen-specific T cell immunity in patients with gastrointestinal cancer. *J Clin Invest.* 2020;130:5976–5988.
34. Miao L, Zhang Y, Huang L. mRNA vaccine for cancer immunotherapy. *Mol Cancer.* 2021;20:41.

Comparison of ^{11}C-Pittsburgh Compound B and ^{18}F-Flutemetamol White Matter Binding in PET

Burcu Zeydan[1,2], Christopher G. Schwarz[1], Scott A. Przybelski[3], Timothy G. Lesnick[3], Walter K. Kremers[3], Matthew L. Senjem[1,4], Orhun H. Kantarci[2], Paul H. Min[1], Bradley J. Kemp[1], Clifford R. Jack, Jr.[1], Kejal Kantarci[1], and Val J. Lowe[1]

[1]Department of Radiology, Mayo Clinic, Rochester, Minnesota; [2]Department of Neurology, Mayo Clinic, Rochester, Minnesota; [3]Department of Quantitative Health Sciences, Mayo Clinic, Rochester, Minnesota; and [4]Department of Information Technology, Mayo Clinic, Rochester, Minnesota

PET imaging with β-amyloid ligands is emerging as a molecular imaging technique targeting white matter integrity and demyelination. β-amyloid PET ligands such as ^{11}C-Pittsburgh compound B (^{11}C-PiB) have been considered for quantitative measurement of myelin content changes in multiple sclerosis, but ^{11}C-PiB is not commercially available given its short half-life. A ^{18}F PET ligand such as flutemetamol with a longer half-life may be an alternative, but its ability to differentiate white matter hyperintensities (WMH) from normal-appearing white matter (NAWM) and its relationship with age remains to be investigated. **Methods:** Cognitively unimpaired (CU) older and younger adults ($n = 61$) were recruited from the community responding to a study advertisement for β-amyloid PET. Participants prospectively underwent MRI, ^{11}C-PiB, and ^{18}F-flutemetamol PET scans. MRI fluid-attenuated inversion recovery images were segmented into WMH and NAWM and registered to the T1-weighted MRI. ^{11}C-PiB and ^{18}F-flutemetamol PET images were also registered to the T1-weighted MRI. ^{11}C-PiB and ^{18}F-flutemetamol SUV ratios (SUVrs) from the WMH and NAWM were calculated using cerebellar crus uptake as a reference for both ^{11}C-PiB and ^{18}F-flutemetamol. **Results:** The median age was 38 y (range, 30–48 y) in younger adults and 67 y (range, 61–83 y) in older adults. WMH and NAWM SUVrs were higher with ^{18}F-flutemetamol than with ^{11}C-PiB in both older ($P < 0.001$) and younger ($P < 0.001$) CU adults. ^{11}C-PiB and ^{18}F-flutemetamol SUVrs were higher in older than in younger CU adults in both WMH ($P < 0.001$) and NAWM ($P < 0.001$). ^{11}C-PiB and ^{18}F-flutemetamol SUVrs were higher in NAWM than WMH in both older ($P < 0.001$) and younger ($P < 0.001$) CU adults. There was no apparent difference between ^{11}C-PiB and ^{18}F-flutemetamol SUVrs in differentiating WMH from NAWM in older and in younger adults. **Conclusion:** ^{11}C-PiB and ^{18}F-flutemetamol show a similar topographic pattern of uptake in white matter with a similar association with age in WMH and NAWM. ^{11}C-PiB and ^{18}F-flutemetamol can also effectively distinguish between WMH and NAWM. However, given its longer half-life, commercial availability, and higher binding potential, ^{18}F-flutemetamol can be an alternative to ^{11}C-PiB in molecular imaging studies specifically targeting multiple sclerosis to evaluate white matter integrity.

Key Words: PET; white matter hyperintensity; normal appearing white matter; ^{11}C-Pittsburgh compound B; ^{18}F-flutemetamol

PET imaging with β-amyloid ligands is largely used in the field of dementia clinically, but it is also emerging as a molecular imaging technique targeting various aspects in multiple sclerosis (MS) including demyelination (*1–10*), which correlate well with clinical disability (*6*) and cognition (*7,9*).

Although advanced MRI techniques such as diffusion tensor imaging are widely used in evaluating white matter (WM) integrity, they are not specific measures of myelin. Over the last decade, PET ligands have been used to study myelin kinetics (*1–11*). PET ligands are also being used to understand the underlying mechanisms such as neuroinflammation, neurodegeneration, microglia activation, and myelin kinetics (*11,12*). PET ligands have also been proposed as a potential outcome measure in clinical trials (*11*), which would be especially important for future remyelination trials potentially adding value to MRI alone. Among these ligands, ^{11}C-Pittsburgh compound B (^{11}C-PiB) seems to be a sensitive and reliable imaging marker in measuring WM integrity and potentially myelin integrity both in animal and in human studies (*2,3,5–8*).

[11]C-PiB uptake in the WM correlates with well-established WM integrity imaging markers such as diffusion tensor imaging (*8*) as well as cognitive function (*7–9*). Consistent with that, WM ^{11}C-PiB uptake is lower in white matter hyperintensities (WMH). On the other hand, white matter ^{11}C-PiB uptake increases with aging (*8,13*). This seems rather contradictory as WMH volume also increases with aging, and ^{11}C-PiB uptake is lower in WMH than normal-appearing white matter (NAWM), with uptake in both compartments increasing with aging suggesting that the aging and WMH effects are independently influencing ^{11}C-PiB uptake in the WM. ^{11}C-PiB shows high affinity for WM; however, given its short half-life (20 min), it is not commercially available. To conduct multicenter clinical trials using PET imaging to investigate WM integrity and to make PET imaging more accessible, ^{18}F PET ligands such as ^{18}F-flutemetamol may be a more reliable alternative.

Furthermore, PET ligand uptake in the WM is increasingly being used as a reference region to calculate the SUV ratios (SUVrs) in longitudinal β-amyloid PET studies (*14–18*). Thus, the association between WM ^{11}C-PiB uptake and aging should be carefully considered in serial β-amyloid PET studies and should be investigated further with different PET ligands such as flutemetamol to see if there is a similar variation of WM ^{18}F-flutemetamol uptake.

Both ^{11}C-PiB and ^{18}F-flutemetamol PET ligands have been investigated as potential WM integrity markers in animal and human studies (*11*). Although PET ligands are not identical in their uptake characteristics, their topographic patterns of uptake may

be comparable. In the current study, WM was evaluated in 2 compartments, WMH and NAWM, in cognitively unimpaired (CU) younger and older adults, and the ability of ^{11}C-PiB and ^{18}F-flutemetamol PET ligands to differentiate WMH from NAWM was investigated.

MATERIALS AND METHODS

Study Population

CU older adults with an age range of 61–83 y and younger adults with an age range of 30–48 y were recruited from the community responding to a study advertisement for β-amyloid PET ([13]). Although it is expected to be more significant in older adults, WMH increases with aging across the adult life span including younger adults. Moreover, WMH is clinically relevant in terms of its association with higher blood pressure and higher HbA1C even in younger adults with low WMH ([19]).

To compare WM binding characteristics of 2 ligands (^{11}C-PiB and ^{18}F-flutemetamol), the participants prospectively underwent MRI, ^{11}C-PiB, and ^{18}F-flutemetamol PET scanning. The ^{11}C-PiB and ^{18}F-flutemetamol scans were completed within a median of 4 d. No adverse events were seen from imaging.

Imaging Acquisitions and Analyses

PET imaging was performed using a PET/CT scanner (DRX or DRXT; GE Healthcare) operating in 3-dimensional (3D) mode using ^{11}C-PiB and ^{18}F-flutemetamol tracers. ^{11}C-PiB PET images were acquired in 20 min (in four 5-min dynamic frames), after an injection of ^{11}C-PiB (555 MBq; range, 292–729 MBq) with a 40-min uptake delay. ^{18}F-flutemetamol PET images were also acquired in 20 min, after an injection of ^{18}F-flutemetamol (370 MBq; range, 333–407 MBq) with an 80-min uptake delay ([20]). To create a single static PET image, dynamic frame images were averaged. An iterative reconstruction algorithm was applied with a 5-mm gaussian postprocessing filter, and attenuation, scatter, and random coincidences as well as radioactive decay were corrected ([18]).

An automated imaging processing pipeline was used to analyze PET images ([18]). The cerebellar crus gray matter was used as a reference region to create normalized ^{11}C-PiB and ^{18}F-flutemetamol PET SUVr images, which is a previously established reference region in PET studies that target WM in both CU individuals and patients with MS ([7,8]). For anatomic segmentation and labeling of WMH and NAWM, MRI was performed on 3.0-T scanners (GE Healthcare), which included a T2-weighted fluid-attenuated inversion recovery (FLAIR) sequence and a T1-weighted 3D high-resolution magnetization–prepared rapid acquisition gradient-echo (MPRAGE) sequence ([21]). First, a semiautomated segmentation algorithm on FLAIR-MRI was used to segment WM into WMH and NAWM ([22]). Then, FLAIR images were coregistered to MPRAGE images and MRPAGE images were segmented using SPM12 with the Mayo Clinic Adult Life span Template (https://www.nitrc.org/projects/mcalt/) ([23]). A WM mask was generated using a threshold for SPM12 WM segmentation to include voxels with probability $\geq$ 0.5. To account for T1-hypointense lesions being erroneously called gray matter, voxels segmented as WMH in the coregistered FLAIR images were also included as WM. To exclude voxels severely affected by partial-volume averaging of gray matter and cerebrospinal fluid, the WM mask was eroded by 3 mm. The remaining WM voxels were divided into 2 subclass masks, WMH and NAWM. Finally, the mean value for each of ^{11}C-PiB and ^{18}F-flutemetamol PET SUVrs over all voxels in each of the WMH and NAWM segmentation masks was calculated.

Study Consent

The study protocol was approved by the Mayo Clinic institutional review board. Informed consent was obtained from each participant.

Statistical Analysis

Participants' characteristics were compared among younger and older CU adults using t tests for continuous variables or χ^2 tests for categoric variables. Due to the gap in ages from 48 to 61, all analyses were stratified by younger and older adult age groups. Amyloid imaging SUVrs were compared using paired t tests for pairwise group comparisons. Linear regression models and Pearson correlations were used for testing the association of age with ^{11}C-PiB and ^{18}F-flutemetamol SUVrs in WMH and NAWM. To compare associations of ^{11}C-PiB SUVr with ^{18}F-flutemetamol between WMH and NAWM, we used linear mixed models adjusted for age, across all participants, with 2 values (WMH and NAWM) per participant. The mixed models accounted for within-participant correlations. We used a group variable for WMH/NAWM and tested for an interaction by group. A significant interaction would indicate a difference in slopes for WMH and NAWM. To compare the performance of ^{11}C-PiB and ^{18}F-flutemetamol tracers in groupwise regional differentiation (WMH vs. NAWM), the area under the receiver-operating-characteristic curve (AUROC) generated using a simultaneous 2-stage parameter estimation approach ([24]) was used. Each AUROC had 95% CIs estimated using the bootstrap method. All tests used an α level of 0.05 for significance.

RESULTS

CU older adults ($n = 31$) had a median age of 67 y (range, 61–83 y), and CU younger adults ($n = 30$) had a median age of 38 y (range, 30–48 y). Sex, *APOE ε4* carrier status, and years of education were not different between the groups. As expected, the WMH volume was higher ($P < 0.001$) in older CU (16.74 ± 27.01 cm³) than younger CU adults (2.90 ± 1.65 cm³) (Table 1).

[11]C-PiB SUVr Compared with ^{18}F-Flutemetamol SUVr in WMH and NAWM

WMH SUVrs were higher with ^{18}F-flutemetamol than with ^{11}C-PiB in both younger ($P < 0.001$) and older CU ($P < 0.001$) adults. Similarly, NAWM SUVrs were higher with ^{18}F-flutemetamol than with ^{11}C-PiB in both younger ($P < 0.001$) and older CU ($P < 0.001$) adults.

WM ^{11}C-PiB and ^{18}F-Flutemetamol SUVr in Younger Compared with Older CU Adults

[11]C-PiB SUVr was lower in WMH ($P < 0.001$) in younger than in older CU adults. ^{11}C-PiB SUVr was also lower in NAWM ($P < 0.001$) in younger than in older CU adults. Similarly, ^{18}F-flutemetamol SUVr was lower in the WMH ($P < 0.001$) and NAWM ($P < 0.001$) in younger than in older CU adults (Table 1; Fig. 1). In addition, age correlated with higher WMH ^{11}C-PiB SUVr in younger CU adults ($r = 0.43$; $P = 0.018$) and with higher NAWM ^{11}C-PiB SUVr in older CU adults ($r = 0.38$; $P = 0.037$) (Fig. 2). The slopes of the association between age and ^{11}C-PiB compared with age and ^{18}F-flutemetamol in WMH was not different in older CU adults ($P = 0.16$). The slopes of the association between age and ^{11}C-PiB compared with age and ^{18}F-flutemetamol in WMH was not different in younger CU adults ($P = 0.41$). Similarly, the slopes of association between age and ^{11}C-PiB compared with age and ^{18}F-flutemetamol in NAWM was not different in older CU adults ($P = 0.26$). The slopes of association between age and ^{11}C-PiB compared with age and ^{18}F-flutemetamol in NAWM was not different in younger CU adults ($P = 0.16$) (Fig. 2).

[11]C-PiB and ^{18}F-Flutemetamol SUVr in WMH Compared with ^{11}C-PiB and ^{18}F-Flutemetamol SUVr in NAWM

[11]C-PiB SUVr in WMH was lower than in NAWM in both younger and older CU adults ($P < 0.001$). Similarly, ^{18}F-flutemetamol

TABLE 1
Participants' Demographic and Imaging Characteristics

Demographic	All ($n = 61$)	Younger CU ($n = 30$)	Older CU ($n = 31$)	P
Age (y)	53.7 (15.8)	38.9 (6.0)	68.1 (5.8)	<0.001
Males (n)	23 (38%)	12 (40%)	11 (35%)	0.72
APOE ε4 (n)*	17 (29%)	11 (38%)	6 (21%)	0.15
Education (y)	15.1 (2.0)	15.5 (2.0)	14.7 (2.0)	0.17
WMH volume (cm^3)	9.94 (20.36)	2.90 (1.65)	16.74 (27.01)	<0.001
PiB SUVr WM	1.92 (0.20)	1.81 (0.13)	2.02 (0.20)	<0.001
PiB SUVr WMH	1.75 (0.19)	1.65 (0.13)	1.85 (0.20)	<0.001
PiB SUVr NAWM	1.92 (0.21)	1.81 (0.13)	2.04 (0.20)	<0.001
FMT SUVr WM	2.42 (0.25)	2.29 (0.14)	2.53 (0.28)	<0.001
FMT SUVr WMH	2.14 (0.25)	2.03 (0.15)	2.25 (0.28)	<0.001
FMT SUVr NAWM	2.43 (0.25)	2.29 (0.14)	2.56 (0.27)	<0.001

*3 are missing APOE ε4

Mean with SD in parentheses listed for continuous variables and count with % in parentheses for the categoric variables. P values comparing groups are from a t test or χ-squared test.

FMT = ^{18}F-flutemetamol.

SUVr in WMH was lower than in NAWM ($P < 0.001$) in both younger and older CU adults (Fig. 1). In younger CU adults, the AUROC comparing WMH versus NAWM for ^{11}C-PiB was 0.828 (95% CI, 0.747–0.903) and for ^{18}F-flutemetamol it was 0.902 (95% CI, 0.821–0.982). In older CU adults, the AUROC comparing WMH versus NAWM for ^{11}C-PiB was 0.751 (95% CI, 0.692–0.794) and for ^{18}F-flutemetamol it was 0.787 (95% CI, 0.725–0.845). AUROC analysis suggested no difference between ^{11}C-PiB and ^{18}F-flutemetamol SUVr in differentiating WMH from NAWM in both younger and older adults.

DISCUSSION

β-amyloid PET ligands were originally developed for measuring cortical β-amyloid deposition in Alzheimer disease. However, independent of the presence of cortical β-amyloid deposition, WM uptake is also observed in β-amyloid PET studies (25,26). Recently, β-amyloid PET ligands have been specifically repurposed as potential markers of WM integrity in MS due to an ongoing need for molecular imaging ligands for myelin in MS. None of the existing advanced imaging techniques target myelin specifically. By contrast, β-amyloid PET ligands have showed high affinity to WM with high sensitivity and sensitivity to myelin (1,27). Therefore, β-amyloid PET ligands can successfully differentiate WMH from NAWM (7,8). Moreover, β-amyloid PET ligand uptake decreases in demyelinating lesions and increases in ensuing remyelinated lesions (2,6,28), which generates the possibility of using molecular imaging as a biomarker for potential remyelination therapies. Changes in β-amyloid PET ligand uptake also correlate well with clinical disability scales (6) and cognitive performance (7,9) in patients with MS. Therefore, β-amyloid PET ligand uptake can be a perfect complementary metric to MRI in clinical trials targeting myelin integrity in MS.

Among the β-amyloid PET ligands, ^{11}C-PiB has emerged as a sensitive and reliable imaging marker in measuring WM integrity both in animal and in human studies (2,3,5–8). However, it also has a suboptimal signal-to-noise ratio and a short half-life (T1/2 = 20 min), making it challenging to be widely used and commercially available. ^{18}F-flutemetamol, which is a fluorinated analog of ^{11}C-PiB, has been developed to increase the availability of β-amyloid PET by compensating for the short half-life of ^{11}C-PiB ligand (20).

In the current study, we compared ^{11}C-PiB and ^{18}F-flutemetamol PET ligands in WMH and NAWM in different age groups. We found that WMH and NAWM SUVrs were higher with ^{18}F-flutemetamol than with ^{11}C-PiB in both older and younger CU adults. ^{11}C-PiB and ^{18}F-flutemetamol uptake was higher in older than in younger CU
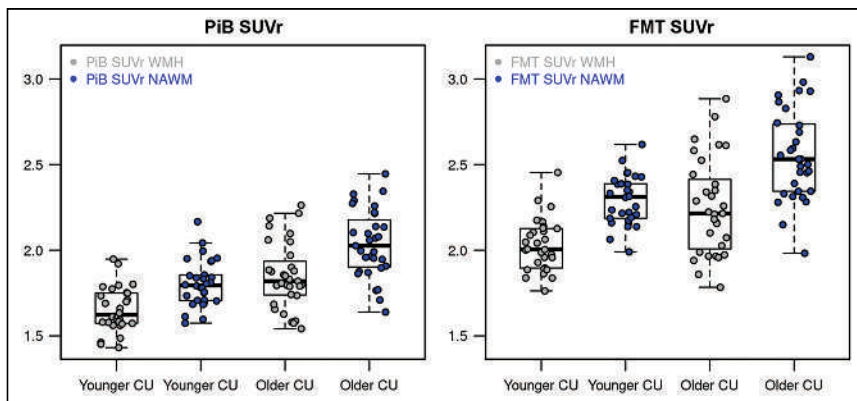
FIGURE 1. ^{11}C-PiB and ^{18}F-flutemetamol SUVr in WMH and NAWM in younger and older CU adults. ^{11}C-PiB SUVr in WMH and NAWM was lower in younger than in older CU adults. ^{11}C-PiB SUVr in WMH was lower than in NAWM in both younger and older CU adults. ^{18}F-flutemetamol SUVr in WMH and NAWM was lower in younger than in older CU adults. ^{18}F-flutemetamol SUVr in WMH was lower than in NAWM in both younger and older CU adults. FMT = ^{18}F-flutemetamol.
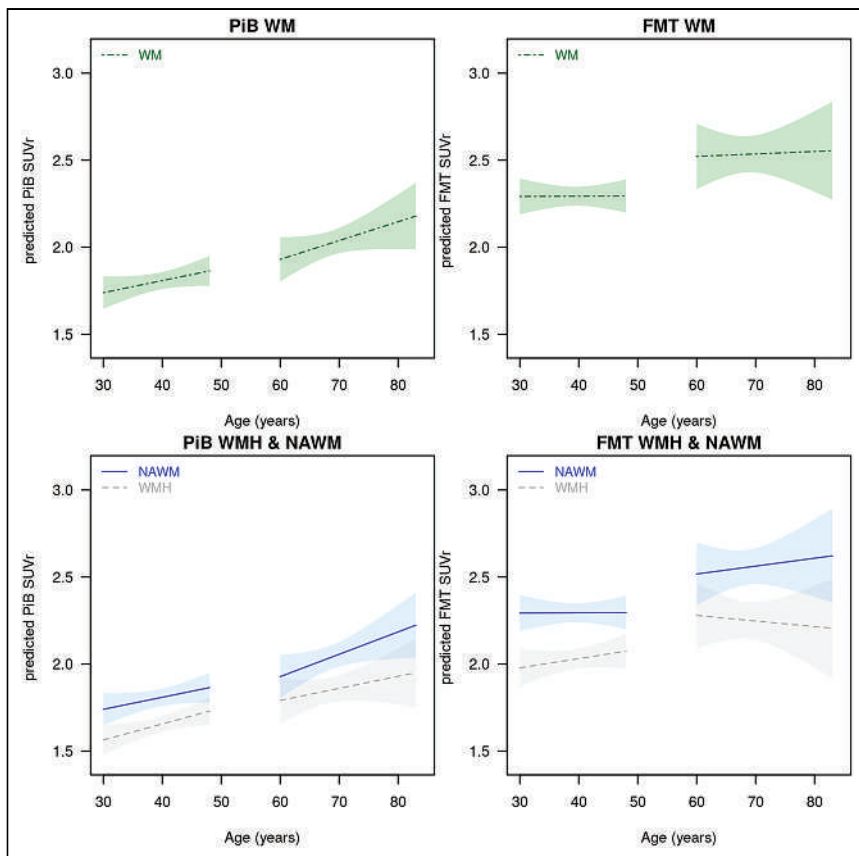
FIGURE 2. Association between age and ^{11}C-PiB and ^{18}F-flutemetamol in WM. (Top) Associations of ^{11}C-PiB and ^{18}F-flutemetamol radioligand uptake with age were compared in WM. (Bottom) Associations of ^{11}C-PiB and ^{18}F-flutemetamol radioligand uptake with age were compared in WMH and NAWM compartments individually. Slopes of association between age and ^{11}C-PiB compared with age and ^{18}F-flutemetamol in WMH were not different in older CU adults. Slopes of association between age and ^{11}C-PiB compared with age and ^{18}F-flutemetamol in WMH were not different in younger CU adults. Slopes of association between age and ^{11}C-PiB compared with age and ^{18}F-flutemetamol in NAWM were not different in older CU adults. Slopes of association between age and ^{11}C-PiB compared with age and ^{18}F-flutemetamol in NAWM were not different in younger CU adults. FMT = ^{18}F-flutemetamol.

adults in both WMH and NAWM. ^{11}C-PiB and ^{18}F-flutemetamol showed a similar topographic pattern of uptake in the WM, with higher uptake in NAWM than WMH in both older and younger CU adults. There was no difference between ^{11}C-PiB and ^{18}F-flutemetamol SUVrs in differentiating WMH from NAWM in both younger and older adults.

[11]C-PiB and ^{18}F-flutemetamol have a similar diagnostic performance for detecting cortical β-amyloid deposition in CU adults and patients with AD (*29,30*). Although, compared with ^{11}C-PiB, a higher ^{18}F-flutemetamol uptake is commonly observed in the WM both visually (*29,30*) and quantitatively (*13,31*). However, less is known about the WMH and NAWM uptake differences between ^{11}C-PiB and ^{18}F-flutemetamol. In the current study, ^{18}F-flutemetamol SUVrs in the WMH and NAWM were higher than ^{11}C-PiB in both older and younger CU adults. Nevertheless, ^{11}C-PiB and ^{18}F-flutemetamol ligands were not superior to one another in differentiating WMH from NAWM in either age group. Similarly, a recent animal study showed a head-to-head comparison of WM binding using [11]C (^{11}C-PiB and ^{11}C-MEDAS) and [18]F (^{18}F-flutemetamol, ^{18}F-florbetaben, ^{18}F-florbetapir) PET ligands in 4 healthy nonhuman primates (baboons) (*31*) to study their ability to distinguish WM from gray matter binding. Consistent with our findings, ^{18}F PET ligands showed higher SUVrs

and higher binding potentials than ^{11}C PET ligands in the WM. It is speculated that several mechanisms may partially contribute to the variability in the amount of WM uptake between different PET ligands such as differences in molar activities, brain penetrance through the blood–brain barrier, and duration to reach a WM–gray matter equilibrium (*31*).

Both ^{11}C-PiB and ^{18}F-flutemetamol ligands showed a similar topographic pattern of uptake in the WM, with higher uptake in NAWM than in WMH. This is in line with previous findings in which ^{11}C-PiB PET imaging was used as a plausible WM integrity marker (*1,3,4,6,7,28*). Both animal and human studies show that ^{11}C-PiB PET may differentiate between myelinated tracts, demyelinated lesions (*2,7*), and remyelinated regions (*3,6*). A recent study demonstrated that lower ^{18}F-florbetapir uptake in WM correlated with large-caliber axon degeneration in Alzheimer disease spectrum, reinforcing previous findings on β-amyloid PET ligand uptake in the WM being myelin-dependent (*32*). The mechanism of β-amyloid tracers' uptake in the WM is not very well understood. However, the β-pleated structure of both the β-amyloid peptide and the myelin basic protein seems to be the common target of β-amyloid PET ligands (*33,34*). Moreover, the β-amyloid PET ligands are lipophilic in nature and this potentially contributes to the higher binding in the WM, which is also high in lipid content (*35*). The mechanism of PET ligand uptake in the WM may partly be also attributed to specific WM kinetics, mainly slower rates of regional clearance of the ligands in the WM (*36*). Alternatively, a dynamic PET acquisition method could be used to compare and explore further WM binding patterns of ^{11}C-PiB and ^{18}F-flutemetamol (*5*). Furthermore, to better understand the differences in topographic uptake patterns of ^{11}C-PiB and ^{18}F-flutemetamol WM, a future study including patients with MS would be of interest.

[11]C-PiB and ^{18}F-flutemetamol ligands also showed a similar pattern of uptake in both WMH and NAWM in association with age. There was higher ^{11}C-PiB and ^{18}F-flutemetamol uptake in older than in younger CU adults in both WMH and in NAWM. The comparison of slopes of association between age and PiB compared with age and ^{18}F-flutemetamol in WMH was not different in older or younger CU adults. Similarly, the comparison of slopes of association between age and ^{11}C-PiB compared with age and ^{18}F-flutemetamol in NAWM was also not different in older or younger CU adults. WM uptake significantly increases with aging (*13,37*). In parallel, WMH and NAWM uptake increase with aging as well (*8,13*). This may be in part due to reduced kinetics (*36,38,39*) and reduced global blood perfusion rate (*40*) in the WM with aging. The increase in PET ligand uptake in the WM with aging is an important factor to consider, because WM is increasingly used as a reference region in longitudinal PET imaging studies. Aging is associated with an increase of WMH volume along with a decrease in myelin integrity, which is expected to result in an overall decrease in PET ligand

uptake in the WM. However, in the current study, higher WMH and NAWM ^{11}C-PiB and ^{18}F-flutemetamol uptake was observed in the older compared with younger adults, in line with previous studies (8,37). This suggests that additional aging-related mechanisms may be influencing WM PET ligand uptake (8,37). Moreover, although ^{11}C-PiB and ^{18}F-flutemetamol show a similar topographic WMH and NAWM uptake in different age groups, there is also a quantitative difference between ^{11}C-PiB and ^{18}F-flutemetamol as ^{18}F-flutemetamol shows a higher uptake in WMH as well as in NAWM compared with ^{11}C-PiB. Therefore, when WM uptake is used as a reference region for the evaluation of cortical uptake in serial PET studies, age, WMH volume and the type of the PET tracer should be carefully considered in these calculations (8).

CONCLUSION

[11]C-PiB can effectively distinguish between WMH and NAWM, but its lower overall binding capacity to WM and to the compartments of WMH and NAWM compared with ^{18}F-flutemetamol may result in a suboptimal signal-to-noise ratio (31). However, a lower signal-to-noise ratio seems to have no impact on the differentiation of WMH and NAWM with ^{11}C-PiB compared with ^{18}F-flutemetamol. With higher binding potentials along with longer half-lives, ^{18}F PET ligands such as ^{18}F-flutemetamol are alternatively positioned to be used in multicenter clinical trials targeting myelin repair as a secondary outcome in demyelinating diseases including MS. Such an outcome measure can potentially provide more myelin-specific information than MR diffusion tensor imaging metrics alone both as a complementary and as a stand-alone metric.

DISCLOSURE

KEY POINTS

QUESTION: Do ^{18}F-flutemetamol and ^{11}C-PiB show a similar topographic pattern of uptake in the WMH and NAWM as there is an ongoing need in MS for molecular imaging of white matter integrity?

PERTINENT FINDINGS: We prospectively investigated ^{11}C-PiB and ^{18}F-flutemetamol uptake in WMH and NAWN in 61 CU adults. WMH and NAWM SUVrs were higher with ^{18}F-flutemetamol than ^{11}C-PiB in both older and in younger CU adults. ^{11}C-PiB and ^{18}F-flutemetamol SUVrs were higher in older than in younger CU adults in both WMH and in NAWM. ^{11}C-PiB and ^{18}F-flutemetamol showed a similar topographic pattern of uptake, with higher SUVr in NAWM than in WMH in both older and younger CU adults. There was no difference between ^{11}C-PiB versus ^{18}F-flutemetamol SUVrs in differentiating WMH from NAWM in both older and younger CU adults.

IMPLICATIONS FOR PATIENT CARE: With a longer half-life and commercial availability, ^{18}F-flutemetamol may be an appealing alternative to ^{11}C-PiB for molecular imaging in demyelinating diseases such as MS to evaluate myelin integrity in clinical trials targeting myelin repair.

REFERENCES

1. Stankoff B, Wang Y, Bottlaender M, et al. Imaging of CNS myelin by positron-emission tomography. *Proc Natl Acad Sci USA.* 2006;103:9304–9309.
2. Stankoff B, Freeman L, Aigrot MS, et al. Imaging central nervous system myelin by positron emission tomography in multiple sclerosis using [methyl-^{11}C]-2-(4'-methylaminophenyl)- 6-hydroxybenzothiazole. *Ann Neurol.* 2011;69:673–680.
3. Faria DP, Copray S, Sijbesma JW, et al. PET imaging of focal demyelination and remyelination in a rat model of multiple sclerosis: comparison of [^{11}C]MeDAS, [^{11}C]CIC and [^{11}C]PIB. *Eur J Nucl Med Mol Imaging.* 2014;41:995–1003.
4. Matías-Guiu JA, Cabrera-Martin MN, Matias-Guiu J, et al. Amyloid PET imaging in multiple sclerosis: an ^{18}F-florbetaben study. *BMC Neurol.* 2015;15:243.
5. Veronese M, Bodini B, Garcia-Lorenzo D, et al. Quantification of [^{11}C]PIB PET for imaging myelin in the human brain: a test-retest reproducibility study in high-resolution research tomography. *J Cereb Blood Flow Metab.* 2015;35:1771-1782.
6. Bodini B, Veronese M, Garcia-Lorenzo D, et al. Dynamic imaging of individual remyelination profiles in multiple sclerosis. *Ann Neurol.* 2016;79:726–738.
7. Zeydan B, Lowe VJ, Schwarz CG, et al. Pittsburgh compound-B PET white matter imaging and cognitive function in late multiple sclerosis. *Mult Scler.* 2018;24:739–749.
8. Zeydan B, Schwarz CG, Lowe VJ, et al. Investigation of white matter PiB uptake as a marker of white matter integrity. *Ann Clin Transl Neurol.* 2019;6:678–688.
9. Pytel V, Matias-Guiu JA, Matias-Guiu J, et al. Amyloid PET findings in multiple sclerosis are associated with cognitive decline at 18 months. *Mult Scler Relat Disord.* 2020;39:101926.
10. Zhang M, Ni Y, Zhou Q, et al. ^{18}F-florbetapir PET/MRI for quantitatively monitoring myelin loss and recovery in patients with multiple sclerosis: a longitudinal study. *EClinicalMedicine.* 2021;37:100982.
11. Bauckneht M, Capitanio S, Raffa S, et al. Molecular imaging of multiple sclerosis: from the clinical demand to novel radiotracers. *EJNMMI Radiopharm Chem.* 2019;4:6.
12. Bodini B, Tonietto M, Airas L, Stankoff B. Positron emission tomography in multiple sclerosis - straight to the target. *Nat Rev Neurol.* 2021;17:663–675.
13. Lowe VJ, Lundt E, Knopman D, et al. Comparison of [^{18}F]flutemetamol and [^{11}C]Pittsburgh compound-B in cognitively normal young, cognitively normal elderly, and Alzheimer's disease dementia individuals. *Neuroimage Clin.* 2017;16:295–302.
14. Brendel M, Hogenauer M, Delker A, et al. Improved longitudinal [^{18}F]-AV45 amyloid PET by white matter reference and VOI-based partial volume effect correction. *Neuroimage.* 2015;108:450–459.
15. Chen K, Roontiva A, Thiyyagura P, et al. Improved power for characterizing longitudinal amyloid-beta PET changes and evaluating amyloid-modifying treatments with a cerebral white matter reference region. *J Nucl Med.* 2015;56:560–566.
16. Landau SM, Fero A, Baker SL, et al. Measurement of longitudinal beta-amyloid change with ^{18}F-florbetapir PET and standardized uptake value ratios. *J Nucl Med.* 2015;56:567–574.
17. Shokouhi S, McKay JW, Baker SL, et al. Reference tissue normalization in longitudinal ^{18}F-florbetapir positron emission tomography of late mild cognitive impairment. *Alzheimers Res Ther.* 2016;8:2.
18. Schwarz CG, Senjem ML, Gunter JL, et al. Optimizing PiB-PET SUVR change-over-time measurement by a large-scale analysis of longitudinal reliability, plausibility, separability, and correlation with MMSE. *Neuroimage.* 2017;144:113–127.
19. Garnier-Crussard A, Bougacha S, Wirth M, et al. White matter hyperintensities across the adult lifespan: relation to age, Abeta load, and cognition. *Alzheimers Res Ther.* 2020;12:127.
20. Nelissen N, Van Laere K, Thurfjell L, et al. Phase 1 study of the Pittsburgh compound B derivative ^{18}F-flutemetamol in healthy volunteers and patients with probable Alzheimer disease. *J Nucl Med.* 2009;50:1251–1259.
21. Lowe VJ, Kemp BJ, Jack CR, Jr., et al. Comparison of ^{18}F-FDG and PiB PET in cognitive impairment. *J Nucl Med.* 2009;50:878-886.
22. Raz L, Jayachandran M, Tosakulwong N, et al. Thrombogenic microvesicles and white matter hyperintensities in postmenopausal women. *Neurology.* 2013;80:911–918.
23. Schwarz CG, Gunter JL, Ward CP, et al. The Mayo Clinic Adult Life Span Template: better quantification across the life span. *Alzheimers Dement.* 2017;13(suppl):P93–P94.
24. Xu H, Qian J, Paynter NP, et al. Estimating the receiver operating characteristic curve in matched case control studies. *Stat Med.* 2019;38:437–451.
25. Vandenberghe R, Van Laere K, Ivanoiu A, et al. ^{18}F-flutemetamol amyloid imaging in Alzheimer disease and mild cognitive impairment: a phase 2 trial. *Ann Neurol.* 2010;68:319–329.
26. Villemagne VL, Mulligan RS, Pejoska S, et al. Comparison of ^{11}C-PiB and ^{18}F-florbetaben for Abeta imaging in ageing and Alzheimer's disease. *Eur J Nucl Med Mol Imaging.* 2012;39:983–989.
27. Wu C, Wang C, Popescu DC, et al. A novel PET marker for in vivo quantification of myelination. *Bioorg Med Chem.* 2010;18:8592–8599.

28. Wu C, Zhu J, Baeslack J, et al. Longitudinal positron emission tomography imaging for monitoring myelin repair in the spinal cord. *Ann Neurol.* 2013;74:688–698.

29. Hatashita S, Yamasaki H, Suzuki Y, Tanaka K, Wakebe D, Hayakawa H. [^{18}C]Flutemetamol amyloid-beta PET imaging compared with [^{11}C]PIB across the spectrum of Alzheimer's disease. *Eur J Nucl Med Mol Imaging.* 2014;41: 290–300.

30. Mountz JM, Laymon CM, Cohen AD, et al. Comparison of qualitative and quantitative imaging characteristics of [^{11}C]PiB and [^{18}F]flutemetamol in normal control and Alzheimer's subjects. *Neuroimage Clin.* 2015;9:592–598.

31. Auvity S, Tonietto M, Caille F, et al. Repurposing radiotracers for myelin imaging: a study comparing ^{18}F-florbetaben, ^{18}F-florbetapir, ^{18}F-flutemetamol,^{11}C-MeDAS, and ^{11}C-PiB. *Eur J Nucl Med Mol Imaging.* 2020;47:490–501.

32. Moscoso A, Silva-Rodriguez J, Aldrey JM, et al. ^{18}F-florbetapir PET as a marker of myelin integrity across the Alzheimer's disease spectrum. *Eur J Nucl Med Mol Imaging.* 2022;49:1242–1253.

33. Klunk WE, Pettegrew JW, Abraham DJ. Quantitative evaluation of Congo red binding to amyloid-like proteins with a beta-pleated sheet conformation. *J Histochem Cytochem.* 1989;37:1273–1281.

34. Ridsdale RA, Beniac DR, Tompkins TA, Moscarello MA, Harauz G. Three-dimensional structure of myelin basic protein. II. Molecular modeling and considerations of predicted structures in multiple sclerosis. *J Biol Chem.* 1997;272:4269–4275.

35. Klunk WE, Engler H, Nordberg A, et al. Imaging brain amyloid in Alzheimer's disease with Pittsburgh Compound-B. *Ann Neurol.* 2004;55:306–319.

36. Fodero-Tavoletti MT, Rowe CC, McLean CA, et al. Characterization of PiB binding to white matter in Alzheimer disease and other dementias. *J Nucl Med.* 2009;50:198-204.

37. Lowe VJ, Lundt ES, Senjem ML, et al. White matter reference region in PET studies of ^{11}C-Pittsburgh Compound B uptake: effects of age and amyloid-beta deposition. *J Nucl Med.* 2018;59:1583–1589.

38. Ichise M, Golan H, Ballinger JR, Vines D, Blackman A, Moldofsky H. Regional differences in technetium-99m-ECD clearance on brain SPECT in healthy subjects. *J Nucl Med.* 1997;38:1253–1260.

39. van Gelderen P, de Zwart JA, Duyn JH. Pittfalls of MRI measurement of white matter perfusion based on arterial spin labeling. *Magn Reson Med.* 2008;59:788–795.

40. Fisher JP, Hartwich D, Seifert T, et al. Cerebral perfusion, oxygenation and metabolism during exercise in young and elderly individuals. *J Physiol (Lond).* 2013; 591:1859–1870.

SV2A PET Imaging Is a Noninvasive Marker for the Detection of Spinal Damage in Experimental Models of Spinal Cord Injury

Daniele Bertoglio[1], Nicolas Halloin[2], Stef De Lombaerde[1,3], Aleksandar Jankovski[4,5], Jeroen Verhaeghe[1], Charles Nicaise*[2], and Steven Staelens*[1]

[1]Molecular Imaging Center Antwerp, University of Antwerp, Antwerp, Belgium; [2]URPhyM–NARILIS, University of Namur, Namur, Belgium; [3]Department of Nuclear Medicine, Antwerp University Hospital, Antwerp, Belgium; [4]Institute of NeuroScience, NEUR Division, Université Catholique de Louvain, Louvain, Belgium; and [5]Department of Neurosurgery, CHU UCL Namur, Yvoir, Belgium

Traumatic spinal cord injury (SCI) is a neurologic condition characterized by long-term motor and sensory neurologic deficits as a consequence of an external physical impact damaging the spinal cord. Anatomic MRI is considered the gold-standard diagnostic tool to obtain structural information for the prognosis of acute SCI; however, it lacks functional objective information to assess SCI progression and recovery. In this study, we explored the use of synaptic vesicle glycoprotein 2A (SV2A) PET imaging to detect spinal cord lesions noninvasively after SCI. **Methods:** Mice ($n = 7$) and rats ($n = 8$) subjected to unilateral moderate cervical (C5) contusion were euthanized 1 wk after SCI for histologic and autoradiographic (^{3}H-labeled (4R)-1-[(3-methylpyridin-4-yl)methyl]-4-(3,4,5-trifluorophenyl)pyrrolidin-2-one [UCB-J]) investigation of SV2A levels. Longitudinal ^{11}C-UCB-J PET/CT imaging was performed in sham ($n = 7$) and SCI rats ($n = 8$) 1 wk and 6 wk after SCI. Animals also underwent an ^{18}F-FDG PET scan during the latter time point. Postmortem tissue SV2A analysis to corroborate in vivo PET findings was performed 6 wk after SCI. **Results:** A significant SV2A loss (ranging from -70.3% to -87.3%; $P < 0.0001$) was measured at the epicenter of the impact in vitro in both mouse and rat contusion SCI models. Longitudinal ^{11}C-UCB-J PET imaging detected SV2A loss in SCI rats ($-49.0\% \pm 8.1\%$ at 1 wk and $-52.0\% \pm 12.9\%$ at 6 wk after SCI), with no change observed in sham rats. In contrast, ^{18}F-FDG PET imaging measured only subtle hypometabolism ($-17.6\% \pm 14.7\%$). Finally, postmortem ^{3}H-UCB-J autoradiography correlated with the in vivo SV2A PET findings ($r = 0.92$, $P < 0.0001$). **Conclusion:** ^{11}C-UCB-J PET/CT imaging is a noninvasive marker for SV2A loss after SCI. Collectively, these findings indicate that SV2A PET may provide an objective measure of SCI and thus represent a valuable tool to evaluate novel therapeutics. Clinical assessment of SCI with SV2A PET imaging is highly recommended.

Key Words: SV2A; ^{11}C-UCB-J; biomarker; contusion SCI; animal model

Spinal cord injury (SCI) is a devastating condition characterized by long-term motor and sensory neurologic deficits as well as a strong impact on the cognitive and social life of patients (1). Traumatic SCI is the consequence of an external physical impact damaging the spinal cord, with the neurologic outcomes being related to the extent of the primary lesion (1,2).

Currently, MRI is considered the gold-standard diagnostic tool to obtain structural information on spinal cord lesions and neighboring tissues during the acute phase of SCI (3–5). Although offering a clear view of the cord edema, hemorrhage, or syrinx formation, routine 1.5-T MRI has been shown to inconsistently correlate with the neurologic findings (6–8). Since MRI-based prognostication, treatment, and rehabilitation planning for spinally injured patients remain a daily clinical challenge (9), there has been increasing interest in developing objective imaging modalities to assess SCI progression and recovery for the noninvasive assessment of emerging therapeutic approaches (4–6).

PET imaging of glucose metabolism using ^{18}F-FDG may represent an imaging modality to monitor metabolic activation and functional neuronal viability at the trauma epicenter. ^{18}F-FDG PET imaging has been performed on both animal models and SCI patients, demonstrating abnormal metabolic activity in animals during the acute phase of experimental SCI or in patients during the active phases of compressive myelopathies (10–15). Although useful, the significance of the ^{18}F-FDG signal remains flawed by its unspecific nature, mixing neuronal metabolism and glial activation (16), and by the lack of correlation with neurologic functions (17).

Recently, novel radioligands based on the antiepileptic drug levetiracetam and targeting the synaptic vesicle glycoprotein 2A (SV2A), a presynaptic protein regulating neurotransmitter release (18), have been developed (19). These ligands, including the selective and high-affinity radioligand ^{11}C-labeled (4R)-1-[(3-methylpyridin-4-yl)methyl]-4-(3,4,5-trifluorophenyl)pyrrolidin-2-one (UCB-J), have emerged as powerful tools to quantify synaptic density in vivo noninvasively (20,21). SV2A PET imaging has already proven a useful tool for assessing synaptic density in various neurodegenerative and neuropsychiatric disorders at clinical and preclinical stages (22–24).

Although SV2A PET imaging has been applied mainly to the brain, SV2A is also present in the gray matter of the spinal cord (25). Furthermore, we recently showed that ^{11}C-UCB-J PET imaging can quantify SV2A density noninvasively in the rodent spinal cord (23). We therefore postulated that SV2A PET imaging could serve as a

biomarker of synaptic loss after SCI. In this study, we explored SV2A levels in experimental models of cervical contusion (26,27), investigated the potential of noninvasive ^{11}C-UCB-J PET imaging to detect spinal damage in rats after SCI, and compared ^{11}C-UCB-J and ^{18}F-FDG PET imaging to verify whether SV2A PET could provide enhanced specificity and sensitivity in detecting spinal injury.

MATERIALS AND METHODS

Animals and Experimental Design

All experiments complied with the European Communities Council Directive (2010/63/EU) and were authorized by the local animal ethic committees (University of Namur [UN19-339] and University of Antwerp [ECD2019-49]). Experiment outcomes were determined at 1 wk after SCI (subacute phase) and 6 wk after SCI (chronic phase), as outlined in Supplemental Figure 1 (supplemental materials are available at http://jnm.snmjournals.org). First, we investigated in vitro both mouse and rat models to assess whether SV2A levels were affected differentially between species. For the longitudinal in vivo study, the rat model was preferred given its favorable body and spinal cord size compared with mice. Nonetheless, investigation in mice is relevant given the abundance of genetic mouse models with relevant spinal cord diseases (23,28).

Adult male C57BL/6J mice (n = 7; body weight, 20–25 g) (internally bred at the University of Namur) and female Sprague–Dawley rats (n = 8; body weight, 225–275 g) (Charles River Laboratories) underwent SCI and were euthanized 1 wk after SCI for histologic and autoradiographic assessment of SV2A. An additional 15 female Sprague–Dawley rats (225–275 g) were subjected either to SCI (n = 8) or laminectomy only (sham, n = 7) and were included in the longitudinal PET study and euthanized at 6 wk after SCI. The animals were group-housed under a 12-h light/dark cycle in a temperature- and humidity-controlled environment with food and water ad libitum.

Contusion SCI

The animals underwent a cervical C5 unilateral right-sided contusion as previously described for mice (26) and rats (27). The animals were anesthetized using a mix of ketamine, 100 mg/kg (ketamine 1000; Ceva), and xylazine, 5 mg/kg (XYL-M 2%; VMD). Briefly, dorsal skin and underlying muscles were cut to access the spine between the spinous processes C2 and T1. The paravertebral muscles overlying C3–C5 were carefully removed. The animals were then subjected to laminectomy at the C5 vertebra before receiving a computer-controlled impact of 51.3 ± 1.7 kdyne for mice and 407 ± 6.1 kdyne for rats (dwell time of 0 s) using an IH Spinal Cord Impactor (Precision Systems and Instrumentation, LLC). The full procedure included unilateral laminectomy on the right side, clamping of the spinous processes of C2 and T2 using toothed Adson forceps to stabilize the whole spinal column, raising of the impactor tip (1.0-mm-diameter impactor for mice and 1.5 mm for rats) 2.5 mm above the dura, and contusion of the right hemicord (bathed in 0.9% sterile saline for rats). Muscles were sutured in layers using silk 2.0 (mice) or 4.0 (rats), and the skin was closed using surgical clippers. The animals received buprenorphine subcutaneously (Vetergesic; Ceva) at a dose of 0.05 mg/kg for analgesia after surgery and again 12 and 24 h after surgery. Saline was subcutaneously administered for rehydration immediately after surgery and 24 h later. One SCI rat did not recover from the surgical procedure and was euthanized. Sham animals underwent the full laminectomy procedure without contusion.

Radiosynthesis

[11]C-UCB-J synthesis was performed on an automated synthesis module (Carbosynthon I; Comecer) as previously described (20,23), with an average molar activity of 52.9 ± 12.4 GBq/μmol. Radiochemical purity was greater than 99% for both ^{11}C-UCB-J and ^{18}F-FDG. ^{3}H-UCB-J (Novandi Chemistry AB) was synthetized with a molar radioactivity of 2,997 MBq/μmol and radiochemical purity of more than 99%.

Small-Animal PET Imaging

Small-animal PET/CT was performed on 2 Siemens Inveon PET/CT scanners (Siemens Preclinical Solutions). The animals were prepared as previously described (29). For the ^{18}F-FDG PET scan, the animals were kept fasting starting the evening before the scan, for an average of 17.7 ± 1.6 h. Glucose strips (OneTouch Ultra 2; LifeScan) were used to measure the glucose concentration (81.2 ± 15.1 mg/dL) in duplicate from blood samples obtained via the tail vein of the rats before radioligand injection. The rats were anesthetized using isoflurane (Forane; Ohio Medical Products) in medical oxygen (induction, 5%; maintenance, 2%–2.5%). The respiration rate and body temperature were monitored and kept constant during the scan. ^{11}C-UCB-J PET images were acquired dynamically (50-min scan), whereas static (20-min) ^{18}F-FDG PET scans were obtained for glucose metabolism after 30 min of radioligand uptake in animals that were awake (29,30). Into a catheterized tail vein over a 30-s interval (1 mL/min) using an automated pump (Pump 11 Elite; Harvard Apparatus), a bolus of ^{11}C-UCB-J (6.7 ± 4.0 MBq) or ^{18}F-FDG (25.1 ± 2.0 MBq) was injected. Data were acquired in list-mode format. After the small-animal PET scan, a 10-min 80 kV/500 μA CT scan was performed for coregistration and attenuation correction.

Image Processing and Analysis

[11]C-UCB-J data were reconstructed into 31 frames of increasing length (12 × 10 s, 3 × 20 s, 3 × 30 s, 3 × 60 s, 3 × 150 s, and 7 × 300 s), whereas a static reconstruction was applied to ^{18}F-FDG data using 8 iterations and 16 subsets of the 3-dimensional ordered-subset expectation maximization algorithm with spatially variant modeling (31) and normalization, dead-time, and CT-based attenuation corrections. Images were reconstructed on a 128 × 128 × 159 grid with 0.776 × 0.776 × 0.796 mm^3 voxels. PET/CT images were processed and analyzed using PMOD software (version 3.6; PMOD Technologies).

To align all brains to a common space and use the same volume of interest to extract the whole-brain activity, brain PET images were rigid-matched to the Schiffer rat ^{18}F-FDG template (32) or the ^{11}C-UCB-J PET template (generated in the same space as the Schiffer one). Cervical spinal cord volumes of interest were manually delineated using the individual coregistered PET/CT images from C3 to C7, with C5 subdivided into right and left segments. Since we anticipated a potential partial-volume effect on the contralateral C5 segment, comparisons were made against the C3 section. The volumes of interest were kept at the same volume across subjects (0.016 cm^3 at each C3–C7 level and 0.008 cm^3 for left and right C5). Across animals, volumes of interest were manually reoriented to follow the profile of the spine. Supplemental Figure 2 shows the CT image of the spine in a representative sham rat with laminectomy.

For ^{11}C-UCB-J analysis, the interval from 25 to 45 min after injection was selected to determine radioligand uptake measured using SUV, calculated as brain activity multiplied by body weight and divided by the injected dose. No difference in cerebral uptake was observed for either ^{11}C-UCB-J (SUV) (Supplemental Fig. 3) or ^{18}F-FDG (SUV corrected for glucose levels) (Supplemental Fig. 4); therefore, spinal uptake was measured as the ratio of regional spinal uptake over whole-brain uptake.

Histologic Analysis

At 1 or 6 wk after injury, the animals were deeply anesthetized with sodium pentobarbital (50 mg/kg, intraperitoneally) and transcardially perfused with ice-cold phosphate-buffered saline (pH 7.4). The spinal

cords were dissected, and a cervical segment containing the contusion injury was snap-frozen in 2-metylbutane at −35°C for 2 min and preserved at −80°C until use. Coronal sections (30 μm thick) were collected on Superfrost Plus slides (Thermo Fischer Scientific) using a cryostat (Leica) and were distributed into a series of 12 slices so that each slide covered rostral, trauma, and caudal sections.

SV2A immunostaining was performed as previously described (23), using the primary antibody anti-SV2A (rabbit IgG; 1:400; catalog number 66724 [Cell Signaling Technologies]) followed by the secondary fluorescent antibody (donkey antirabbit; 1:100; Alexa Fluor 488 [Jackson ImmunoResearch]). Images were acquired at ×10 magnification for quantification with a fluorescence microscope (Olympus) using CellSens software. Images were analyzed using Fiji (version 2.1.0) ImageJ software (National Institutes of Health). SV2A signal intensity was measured in regions of interest (right and left gray matter spinal cord) manually delineated on each section. Adjacent slides were stained with hematoxylin and eosin to visualize tissue morphology.

Autoradiography

In vitro ^{3}H-UCB-J (Novandi Chemistry AB) autoradiography was performed as previously reported (23). Mouse and rat SV2A selectivity in the spinal cord was validated using a blocking solution (1 nM of ^{3}H-UCB-J plus 1 mM of levetiracetam in binding buffer) (Supplemental Fig. 5).

Regional quantification was performed using Fiji (version 2.1.0) ImageJ software. Specific binding of ^{3}H-UCB-J was measured by converting the mean gray values into radioactivity density (Bq/mg), calculated using commercial tritium standards (American Radiolabeled Chemicals). Next, from ^{3}H-UCB-J molar activity on the experimental day, radioactivity density was converted into binding density (pmol/mg) for each region.

Statistical Analysis

In vivo spinal cord PET data, as well as postmortem analyses, were investigated using 2-way ANOVA (experimental group and region as variables). A decrease in spinal PET signal compared with C3 and cerebral binding was assessed using the Mann–Whitney test. Autoradiographic blocking experiments were analyzed using paired t tests. Correlations between in vivo and postmortem SV2A signals were evaluated using a Spearman r test. P values were corrected for multiple comparisons using the Šídák multiple-comparisons test. Statistical analyses were performed with GraphPad Prism (version 9.1) statistical software. Data are represented as mean ± SD. All tests were 2-tailed, and statistical significance was set at a P value of less than 0.05.

RESULTS

SV2A Levels Are Decreased Subacutely in Experimental Models of Contusion SCI

To determine whether SV2A levels are changed after a spinal injury, we performed SV2A histologic and autoradiographic assessment on 2 experimental models of contusion SCI during the subacute phase (Fig. 1A; Supplemental Fig. 6A). In both mouse and rat spinal cord, a significant SV2A loss at the epicenter of impact, but not in rostral sections (C3–C4 level), was observed with SV2A immunostaining (contralateral effect: mouse, $F_{1,24} = 140.4$ [$P < 0.0001$]; rat, $F_{1,28} = 20.2$ [$P < 0.0001$]), which corresponded to an approximately 80% decline compared with rostral sections (mouse, −81.2% ± 8.6% [post hoc $P < 0.0001$]; rat, −78.8% ± 21.1% [post hoc $P < 0.0001$]) (Fig. 1B; Supplemental Fig. 6B). Analogously, ^{3}H-UCB-J binding was significantly affected at the epicenter of the contusion compared with the contralateral side (contralateral effect: mouse, $F_{1,24} = 42.3$ [$P <$
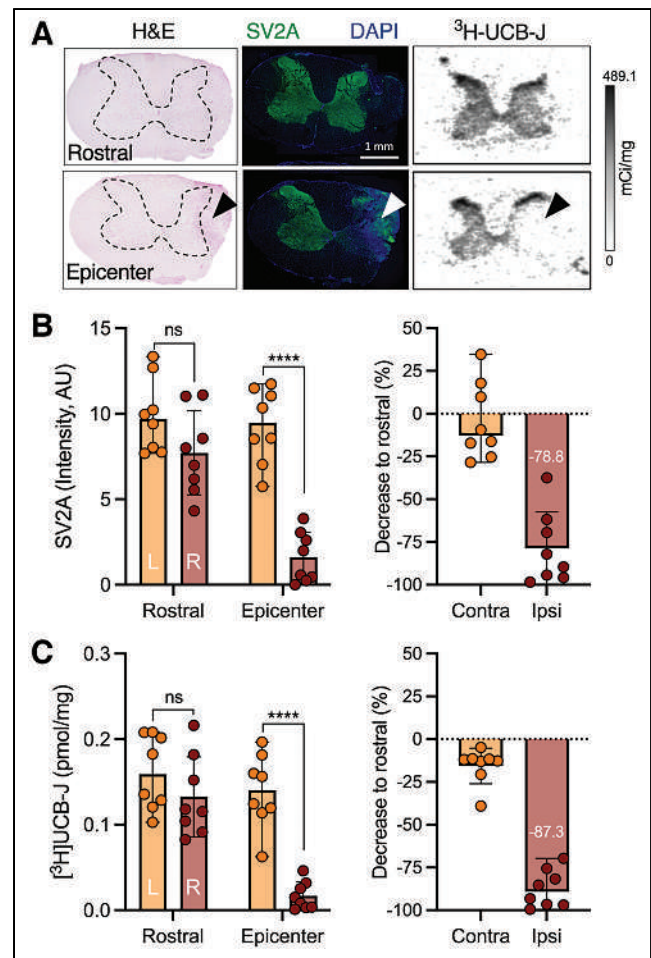
FIGURE 1. SV2A levels are decreased in rat model of contusion SCI. (A) Representative hematoxylin and eosin, SV2A, and ^{3}H-UCB-J images depicting rostral and epicenter spinal cord sections. Arrowheads indicate contusion site at right C5 vertebra; dashed lines outline spinal gray matter. (B and C) SV2A (B) and ^{3}H-UCB-J (C) quantification in spinal cord sections and decrease in C5 section compared with rostral for both contralateral (left) and ipsilateral (right) sides. AU = arbitrary units; H&E = hematoxylin and eosin; ns = not statistically significant. ****$P < 0.0001$.

0.0001]; rat, $F_{1,28} = 24.4$ [$P < 0.0001$]), with a clear decline in relation to rostral sections (mouse, −70.3% ± 11.5% [post hoc $P < 0.0001$]; rat, −87.3% ± 10.9% [post hoc $P < 0.0001$]) (Fig. 1C; Supplemental Fig. 6C). Notably, the SV2A loss was not due to loss of spinal tissue, as depicted by the hematoxylin and eosin staining.

^{11}C-UCB-J PET Detects In Vivo SV2A Loss After SCI

Given the wider diameter of the spinal cord in the rat, the rat model was chosen to investigate ^{11}C-UCB-J PET imaging after SCI. Figure 2 displays representative ^{11}C-UCB-J uptake images in a SCI rat compared with a sham control rat 1 wk after injury. Spinal cord ^{11}C-UCB-J uptake at the contusion site (right C5) was significantly changed compared with sham animals (group effect, $F_{1,54} = 100.2$ [$P < 0.0001$]) (Fig. 3A). ^{11}C-UCB-J uptake was also significantly reduced in surrounding areas (C4, left C5, and C6). Accordingly, SCI animals displayed a ^{11}C-UCB-J binding decline in right C5 compared with C3 (−49.0% ± 8.1%), which significantly differed from sham rats ($P = 0.0043$) (Fig. 3B).
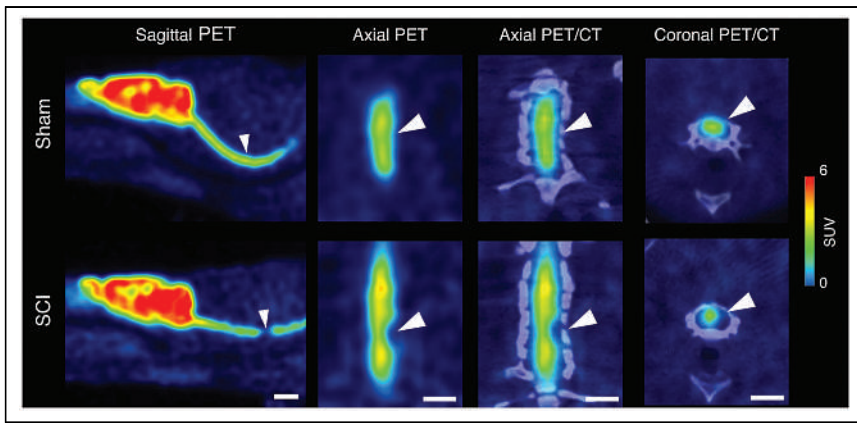
FIGURE 2. Representative ^{11}C-UCB-J PET images are shown of sham and SCI rat 1 wk after trauma. Arrowheads indicate contusion site at C5 vertebra. Interval is 25–45 min after injection. Scale bar = 5 mm.
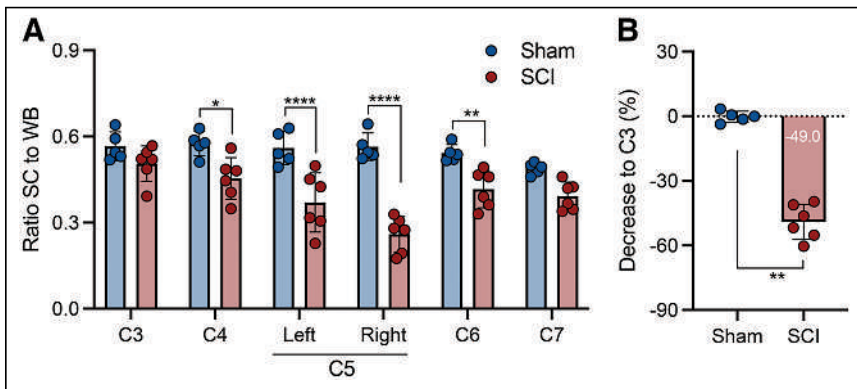
FIGURE 3. ^{11}C-UCB-J PET detects SV2A loss in contusion SCI rat model. (A) Significant reduction in spinal cord ^{11}C-UCB-J uptake around contusion site (right C5), compared with sham animals. (B) Spinal cord ^{11}C-UCB-J uptake at epicenter (right C5) compared with C3 level within each animal. SC = spinal cord; WB = whole brain. *$P < 0.05$. **$P < 0.01$. ****$P < 0.0001$.

^{11}C-UCB-J PET Outperforms ^{18}F-FDG PET for Detection of Chronic SCI

Similarly to 1 wk after injury, the reduction in ^{11}C-UCB-J uptake around the contusion site (right C5) in SCI rats was significant and sustained at 6 wk after injury compared with sham animals (group effect, $F_{1,60} = 190.4$ [$P < 0.0001$]) (Fig. 4A). Hence, SCI animals displayed a ^{11}C-UCB-J binding decline in right C5 compared with C3 ($-52.0\% \pm 12.9\%$), which significantly differed from sham rats ($P = 0.0025$) (Fig. 4B). Interestingly, ^{11}C-UCB-J uptake at the site of chronic trauma in SCI rats was significantly affected until C7 ($P < 0.01$), unlike at 1 wk after SCI ($P > 0.05$), suggesting that the local contusion might induce SV2A loss caudal to the lesion epicenter.

Six weeks after SCI, the animals underwent ^{11}C-UCB-J and ^{18}F-FDG PET to assess whether SV2A PET could provide enhanced sensitivity in detecting spinal injury. ^{18}F-FDG PET could detect hypometabolism at the contusion epicenter (right C5) compared with sham animals (group effect, $F_{1,60} = 70.9$ [$P < 0.0001$]) (Fig. 5A), as well as hypometabolism in surrounding tissue (left C5 and C6). However, the difference compared with C3 was subtle ($-17.6\% \pm 14.7\%$), with no significant change from sham rats ($P = 0.106$) (Fig. 5B).

Postmortem Analysis Corroborates ^{11}C-UCB-J PET Findings

Similar to the analyses at the subacute phase, a significant SV2A loss at the epicenter, but not in rostral (C3 and C4) sections, was observed at the chronic phase with
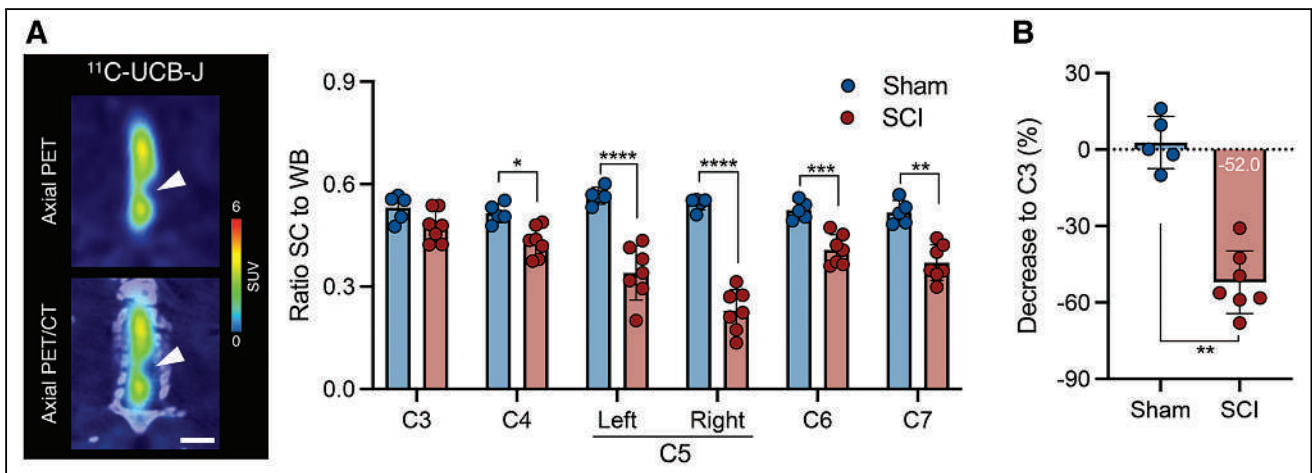
FIGURE 4. ^{11}C-UCB-J reduction is sustained during chronic SCI in contusion rat model. (A) Representative PET image of SCI rat and ^{11}C-UCB-J PET analysis of sham animals and rats with chronic SCI. Interval is 25–45 min after injection. Scale bar = 5 mm. (B) Spinal cord ^{11}C-UCB-J uptake at epicenter compared with C3 level within each animal. SC = spinal cord; WB = whole brain. *$P < 0.05$. **$P < 0.01$. ***$P < 0.001$. ****$P < 0.0001$.

FIGURE 5. ^{18}F-FDG reduction is limited during chronic SCI in contusion rat model. (A) Representative PET image of SCI rat and ^{18}F-FDG PET analysis of sham animals and rats with chronic SCI. Scale bar = 5 mm. (B) Spinal cord ^{18}F-FDG upta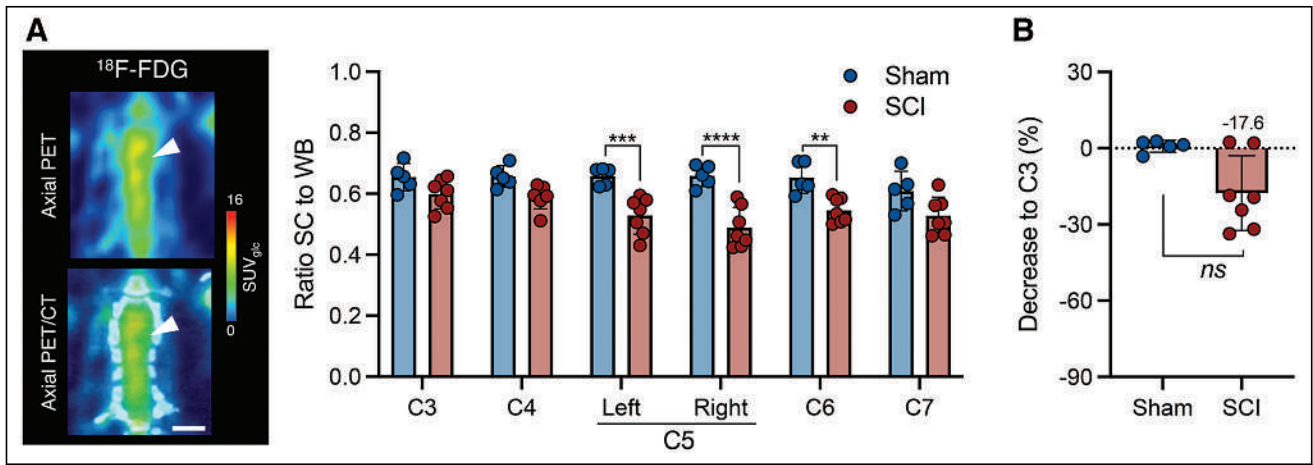ke at epicenter compared with C3 level within each animal. SC = spinal cord; WB = whole brain. **$P < 0.01$. ***$P < 0.001$. ****$P < 0.0001$.

SV2A immunostaining (group effect, $F_{1,22} = 62.0$ [$P < 0.0001$]), corresponding to an 86% ± 17.4% decline compared with rostral sections (Fig. 6A), showing strong consistency with the in vivo ^{11}C-UCB-J PET measurements ($r = 0.86$, $P = 0.0013$; Fig. 6B).

[3]H-UCB-J binding was significantly affected as well (group effect, $F_{1,22} = 31.2$ [$P < 0.0001$]), with a 82.1% ± 22.8% decline compared with rostral sections (Fig. 6C). ^{3}H-UCB-J autoradiography reflected the in vivo ^{11}C-UCB-J PET quantification ($r = 0.92$, $P < 0.0001$; Fig. 6D).

FIGURE 6. Postmortem analyses corroborated sustained SV2A loss measured with ^{11}C-UCB-J PET during chronic SCI. (A) SV2A immunofluorescence quantification. (B) Correlation between rostral and epicenter decrease measured with ^{11}C-UCB-J PET. (C) ^{3}H-UCB-J autoradiography quantification. (D) Correlation between rostral and epicenter decrease measured with ^{11}C-UCB-J PET. ns = not statistically significant. ****$P < 0.0001$.

DISCUSSION

This study showed that SV2A is decreased in mouse and rat experimental models of SCI contusion and that synaptic loss after SCI can be measured noninvasively. Also, the SV2A decrease is sustained over time, and ^{11}C-UCB-J PET imaging provides a 3-fold enhanced sensitivity compared with ^{18}F-FDG PET imaging in assessing spinal damage. Collectively, these findings suggest that SV2A PET imaging could serve as a robust biomarker capable of detecting subtle synaptic loss after SCI.

Validation by histologic and autoradiographic findings confirmed that SV2A is restricted to gray matter (*25*) and that ^{3}H-UCB-J binding was blocked by levetiracetam (*19*). Both experimental models of SCI displayed a comparable unilateral SV2A loss; most importantly, the SV2A decline was not due to a mere tissue loss caused by the initial trauma.

For in vivo PET quantification, we focused on the comparison to the rostral C3 level (which is morphologically unaffected) to avoid the partial-volume effect that is likely present in the uninjured C5 hemicord. We measured a sustained reduction in ^{11}C-UCB-J binding at the SCI epicenter over time, suggesting little-to-no regeneration of synaptic connections and sprouting of spared axons. Notably, a decrease in SV2A was observed in SCI rats over time at the caudal level (C6 and C7). This decrease is a possible result of the deafferentation of the gray matter and consequent caudal synaptic loss, overall reflecting an extension of the secondary lesion, which comprises many processes: apoptosis, demyelination of surviving axons, axonal die-back, and building of a glial scar around the injury site (*1,33,34*).

Previous studies have reported only transient changes in ^{18}F-FDG uptake in rat and canine models (*13,14*). Thus, one objective of the current study was to compare the
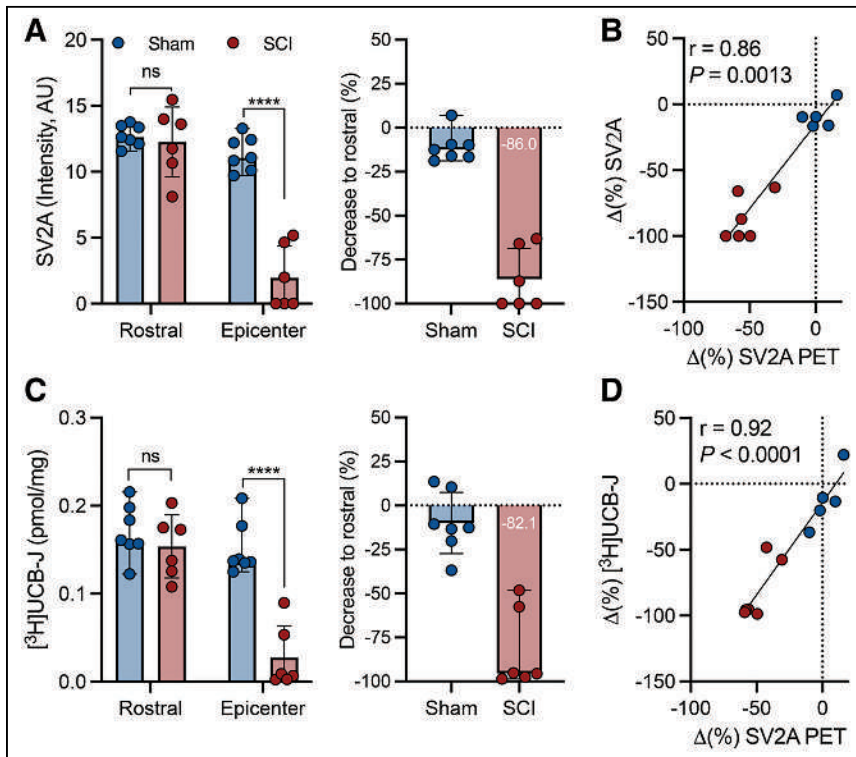
performance of ^{11}C-UCB-J with ^{18}F-FDG in detecting spinal cord damage. Despite the extensive neurodegeneration at the trauma site (1), the observed reduction in glucose uptake was only a fraction (−17.6%) compared with the SV2A loss (−52.0%). This is likely related to the enhanced gliosis driven by microglia/macrophage and astrocyte activation related to primary and secondary injuries. Since glucose uptake is the result of neuronal and glial metabolism (16), the gliosis occurring at the trauma site can largely mask the reduced uptake associated with neurodegeneration. As such, understanding the biologic process driving the ^{18}F-FDG uptake is challenging, especially for the assessment of therapeutics, because of the plethora of processes occurring at the injury site (1,34). In contrast, the precise nature of SV2A as the molecular target of ^{11}C-UCB-J offers a specific measure of synaptic density without being affected by secondary processes. Thus, SV2A PET imaging might provide a powerful tool for the assessment of synaptic loss in traumatic, neurodegenerative, inflammatory, and vascular spinal cord pathologies, as well as for synaptic loss, regeneration (24), and axonal connectivity after gene and cell therapy approaches (35). Future studies investigating the association between spinal SV2A density and degree of motor impairment will be needed to understand whether SV2A loss might represent a biomarker with functional relevance.

Despite being the gold-standard diagnostic tool to obtain structural information on spinal cord lesions during the acute phase of SCI (4), functional assessment based on MRI remains elusive, resulting in inconsistent correlations with the neurologic findings (6–8). Although novel approaches such as diffusion tensor imaging and myelin water transfer can provide added value in terms of axon and myelin integrity (4), their readouts are likely to be affected by evolving edema, hemorrhage, or syrinx formation. SV2A PET imaging can offer an attractive complementary alternative to objectively measure synaptic integrity at the lesion site in preclinical and clinical settings. Although we describe here for the first time (to our knowledge) spinal SV2A changes, SV2A PET imaging has already been performed in several clinical studies of neurologic disorders (22). With a more favorable resolution ratio (spinal cord/scanner resolution) available for human PET imaging, we foresee no limitation for clinical application, as supported by a preliminary report on healthy subjects (36). The high sensitivity of SV2A as compared with ^{18}F-FDG PET and the added value of ^{18}F-FDG PET as compared with MRI (15) suggest that SV2A PET may be of particular interest in the diagnosis and prognosis of cervical spondylotic myelopathy, which is common in the elderly (37).

CONCLUSION

Using ^{11}C-UCB-J PET/CT imaging, we successfully detected SV2A loss in the contusion SCI rat model. The presented findings indicate that synaptic loss after SCI can be quantified noninvasively, SV2A decrease is sustained over time, and ^{11}C-UCB-J PET imaging provides enhanced sensitivity compared with ^{18}F-FDG PET imaging for assessment of spinal damage. Collectively, these findings indicate that SV2A PET may provide an objective measure of SCI and thus be a valuable tool to evaluate novel therapeutics. Clinical assessment of SCI with SV2A PET imaging is highly recommended.

DISCLOSURE

ACKNOWLEDGMENTS

KEY POINTS

QUESTION: Does SV2A represent a biomarker for SCI?

PERTINENT FINDINGS: SV2A levels are significantly reduced in animal models of contusion SCI. Longitudinal ^{11}C-UCB-J PET imaging showed that SV2A loss can be quantified noninvasively, is sustained over time, and outperforms ^{18}F-FDG PET imaging.

IMPLICATIONS FOR PATIENT CARE: SV2A PET imaging offers a novel noninvasive method to quantify SCI, which may provide a promising diagnostic tool for the assessment of functional recovery after SCI therapeutics.

REFERENCES

1. Ahuja CS, Wilson JR, Nori S, et al. Traumatic spinal cord injury. *Nat Rev Dis Primers.* 2017;3:17018.
2. Wilson JR, Hashimoto RE, Dettori JR, Fehlings MG. Spinal cord injury and quality of life: a systematic review of outcome measures. *Evid Based Spine Care J.* 2011;2:37–44.
3. Freund P, Curt A, Friston K, Thompson A. Tracking changes following spinal cord injury: insights from neuroimaging. *Neuroscientist.* 2013;19:116–128.
4. Freund P, Seif M, Weiskopf N, et al. MRI in traumatic spinal cord injury: from clinical assessment to neuroimaging biomarkers. *Lancet Neurol.* 2019;18:1123–1135.
5. Lammertse D, Dungan D, Dreisbach J, et al. Neuroimaging in traumatic spinal cord injury: an evidence-based review for clinical practice and research. *J Spinal Cord Med.* 2007;30:205–214.
6. Ellingson BM, Salamon N, Holly LT. Imaging techniques in spinal cord injury. *World Neurosurg.* 2014;82:1351–1358.
7. Chay W, Kirshblum S. Predicting outcomes after spinal cord injury. *Phys Med Rehabil Clin N Am.* 2020;31:331–343.
8. Sharif S, Jazaib Ali MY. Outcome prediction in spinal cord injury: myth or reality. *World Neurosurg.* 2020;140:574–590.
9. Talbott JF, Huie JR, Ferguson AR, Bresnahan JC, Beattie MS, Dhall SS. MR imaging for assessing injury severity and prognosis in acute traumatic spinal cord injury. *Radiol Clin North Am.* 2019;57:319–339.
10. Flanagan EP, Hunt CH, Lowe V, et al. [^{18}F]-fluorodeoxyglucose-positron emission tomography in patients with active myelopathy. *Mayo Clin Proc.* 2013;88:1204–1212.
11. Floeth FW, Stoffels G, Herdmann J, et al. Prognostic value of ^{18}F-FDG PET in monosegmental stenosis and myelopathy of the cervical spinal cord. *J Nucl Med.* 2011;52:1385–1391.
12. Nandoe Tewarie RD, Yu J, Seidel J, et al. Positron emission tomography for serial imaging of the contused adult rat spinal cord. *Mol Imaging.* 2010;9:108–116.
13. von Leden RE, Selwyn RG, Jaiswal S, Wilson CM, Khayrullina G, Byrnes KR. ^{18}F-FDG-PET imaging of rat spinal cord demonstrates altered glucose uptake acutely after contusion injury. *Neurosci Lett.* 2016;621:126–132.
14. Zhang L, López-Picón FR, Jia Y, et al. Longitudinal [^{18}F]FDG and [^{13}N]NH$_3$ PET/CT imaging of brain and spinal cord in a canine hemisection spinal cord injury model. *Neuroimage Clin.* 2021;31:102692.
15. Eicker SO, Langen KJ, Galldiks N, et al. Clinical value of 2-deoxy-[^{18}F]fluoro-D-glucose positron emission tomography in patients with cervical spondylotic myelopathy. *Neurosurg Focus.* 2013;35:E2.
16. Xiang X, Wind K, Wiedemann T, et al. Microglial activation states drive glucose uptake and FDG-PET alterations in neurodegenerative diseases. *Sci Transl Med.* 2021;13:eabe5640.

17. Byrnes KR, Wilson CM, Brabazon F, et al. FDG-PET imaging in mild traumatic brain injury: a critical review. *Front Neuroenergetics.* 2014;5:13.

18. Bajjalieh SM, Frantz GD, Weimann JM, McConnell SK, Scheller RH. Differential expression of synaptic vesicle protein 2 (SV2) isoforms. *J Neurosci.* 1994;14:5223–5235.

19. Lynch BA, Lambeng N, Nocka K, et al. The synaptic vesicle protein SV2A is the binding site for the antiepileptic drug levetiracetam. *Proc Natl Acad Sci USA.* 2004;101:9861–9866.

20. Bertoglio D, Verhaeghe J, Miranda A, et al. Validation and noninvasive kinetic modeling of [^{11}C]UCB-J PET imaging in mice. *J Cereb Blood Flow Metab.* 2020; 40:1351–1362.

21. Finnema SJ, Nabulsi NB, Eid T, et al. Imaging synaptic density in the living human brain. *Sci Transl Med.* 2016;8:348ra96.

22. Cai Z, Li S, Matuskey D, Nabulsi N, Huang Y. PET imaging of synaptic density: a new tool for investigation of neuropsychiatric diseases. *Neurosci Lett.* 2019;691:44–50.

23. Bertoglio D, Verhaeghe J, Wyffels L, et al. Synaptic vesicle glycoprotein 2A is affected in the CNS of Huntington's disease mice and post-mortem human HD brain. *J Nucl Med.* September 16, 2021 [Epub ahead of print].

24. Toyonaga T, Smith LM, Finnema SJ, et al. In vivo synaptic density imaging with ^{11}C-UCB-J detects treatment effects of saracatinib in a mouse model of Alzheimer disease. *J Nucl Med.* 2019;60:1780–1786.

25. Lambeng N, Gillard M, Vertongen P, Fuks B, Chatelain P. Characterization of [^{3}H]ucb 30889 binding to synaptic vesicle protein 2A in the rat spinal cord. *Eur J Pharmacol.* 2005;520:70–76.

26. Nicaise C, Putatunda R, Hala TJ, et al. Degeneration of phrenic motor neurons induces long-term diaphragm deficits following mid-cervical spinal contusion in mice. *J Neurotrauma.* 2012;29:2748–2760.

27. Nicaise C, Hala TJ, Frank DM, et al. Phrenic motor neuron degeneration compromises phrenic axonal circuitry and diaphragm activity in a unilateral cervical contusion model of spinal cord injury. *Exp Neurol.* 2012;235:539–552.

28. Ross CA, Poirier MA. Protein aggregation and neurodegenerative disease. *Nat Med.* 2004;10(suppl):S10–S17.

29. Bertoglio D, Deleye S, Miranda A, Stroobants S, Staelens S, Verhaeghe J. Estimation of the net influx rate Ki and the cerebral metabolic rate of glucose MRglc using a single static [^{18}F]FDG PET scan in rats. *Neuroimage.* 2021;233: 117961.

30. Deleye S, Verhaeghe J. wyffels L, Dedeurwaerdere S, Stroobants S, Staelens S. Towards a reproducible protocol for repetitive and semi-quantitative rat brain imaging with ^{18}F-FDG: exemplified in a memantine pharmacological challenge. *Neuroimage.* 2014;96:276–287.

31. Miranda A, Bertoglio D, Glorie D, Stroobants S, Staelens S, Verhaeghe J. Validation of a spatially variant resolution model for small animal brain PET studies. *Biomed Phys Eng Express.* 2020;6:045001.

32. Schiffer WK, Mirrione MM, Dewey SL. Optimizing experimental protocols for quantitative behavioral imaging with ^{18}F-FDG in rodents. *J Nucl Med.* 2007;48: 277–287.

33. Alizadeh A, Dyck SM, Karimi-Abdolrezaee S. Traumatic spinal cord injury: an overview of pathophysiology, models and acute injury mechanisms. *Front Neurol.* 2019;10:282.

34. Oyinbo CA. Secondary injury mechanisms in traumatic spinal cord injury: a nugget of this multiply cascade. *Acta Neurobiol Exp (Warsz).* 2011;71:281–299.

35. Assinck P, Duncan GJ, Hilton BJ, Plemel JR, Tetzlaff W. Cell transplantation therapy for spinal cord injury. *Nat Neurosci.* 2017;20:637–647.

36. Rossano S, Bini J, Nabulsi N, Ropchan J, Carson RE. Feasibility of imaging synaptic density in the human spinal cord using 11C-UCB-J PET [abstract]. *J Nucl Med.* 2021;61(suppl 1):112.

37. Kalsi-Ryan S, Karadimas SK, Fehlings MG. Cervical spondylotic myelopathy: the clinical phenomenon and the current pathobiology of an increasingly prevalent and devastating disorder. *Neuroscientist.* 2013;19:409–421.

In Vivo Evaluation of 6 Analogs of ^{11}C-ER176 as Candidate ^{18}F-Labeled Radioligands for 18-kDa Translocator Protein

Jae-Hoon Lee[1,2], Fabrice G. Siméon[1], Jeih-San Liow[1], Cheryl L. Morse[1], Robert L. Gladding[1], Jose A. Montero Santamaria[1], Ioline D. Henter[1], Sami S. Zoghbi[1], Victor W. Pike[1], and Robert B. Innis[1]

[1]Molecular Imaging Branch, National Institute of Mental Health, National Institutes of Health, Bethesda, Maryland; and [2]Department of Nuclear Medicine, Yonsei University College of Medicine, Seoul, South Korea

Because of its excellent ratio of specific to nondisplaceable uptake, the radioligand ^{11}C-ER176 can successfully image 18-kDa translocator protein (TSPO), a biomarker of inflammation, in the human brain and accurately quantify target density in homozygous low-affinity binders. Our laboratory sought to develop an ^{18}F-labeled TSPO PET radioligand based on ER176 with the potential for broader distribution. This study used generic ^{11}C labeling and in vivo performance in the monkey brain to select the most promising among 6 fluorine-containing analogs of ER176 for subsequent labeling with longer-lived ^{18}F. **Methods:** Six fluorine-containing analogs of ER176—3 fluoro and 3 trifluoromethyl isomers—were synthesized and labeled by ^{11}C methylation at the secondary amide group of the respective N-desmethyl precursor. PET imaging of the monkey brain was performed at baseline and after blockade by N-butan-2-yl-1-(2-chlorophenyl)-N-methylisoquinoline-3-carboxamide (PK11195). Uptake was quantified using radiometabolite-corrected arterial input function. The 6 candidate radioligands were ranked for performance on the basis of 2 in vivo criteria: the ratio of specific to nondisplaceable uptake (i.e., nondisplaceable binding potential [BP_{ND}]) and the time stability of total distribution volume (V_T), an indirect measure of lack of radiometabolite accumulation in the brain. **Results:** Total TSPO binding was quantified as V_T corrected for plasma free fraction (V_T/f_P) using Logan graphical analysis for all 6 radioligands. V_T/f_P was generally high at baseline (222 ± 178 mL·cm^{-3}) and decreased by 70%–90% after preblocking with PK11195. BP_{ND} calculated using the Lassen plot was 9.6 ± 3.8; the o-fluoro radioligand exhibited the highest BP_{ND} (12.1), followed by the m-trifluoromethyl (11.7) and m-fluoro (8.1) radioligands. For all 6 radioligands, V_T reached 90% of the terminal 120-min values by 70 min and remained relatively stable thereafter, with excellent identifiability (SEs < 5%), suggesting that no significant radiometabolites accumulated in the brain. **Conclusion:** All 6 radioligands had good BP_{ND} and good time stability of V_T. Among them, the o-fluoro, m-trifluoromethyl, and m-fluoro compounds were the 3 best candidates for development as radioligands with an ^{18}F label.

Key Words: translocator protein; neuroinflammation; PET; specific-to-nondisplaceable uptake; radiometabolites

The mitochondrial protein 18-kDa translocator protein (TSPO) is highly expressed in phagocytic inflammatory cells, including activated microglia and reactive astrocytes in the brain and macrophages in the periphery (1,2). Although numerous PET radioligands have been developed to image TSPO, several limitations have restricted their clinical utility for quantifying inflammation in the brain. Of these radioligands, the first-generation TSPO radioligand ^{11}C-(R)-N-butan-2-yl-1-(2-chlorophenyl)-N-methylisoquinoline-3-carboxamide (PK11195) has been the most extensively studied. ^{11}C-(R)-PK11195 has high affinity for TSPO; however, its utility is limited by a low ratio of specific to nondisplaceable uptake (i.e., nondisplaceable binding potential [BP_{ND}]) in the brain and by the relatively short half-life of ^{11}C (20 min) (3,4). Second-generation radioligands, such as ^{11}C-PBR28, offer a higher in vivo TSPO-specific signal but suffer from sensitivity to the single-nucleotide polymorphism rs6971 (5,6), such that low-affinity binders (LABs) have too little TSPO binding to be accurately measured. This sensitivity to the single-nucleotide polymorphism both complicates the interpretation of results and requires genotyping to exclude LABs before imaging. Consequently, new and more effective radioligands are needed to image TSPO.

Third-generation TSPO radioligands were designed to have adequately high BP_{ND} across all rs6971 genotypes for reliable quantification and to lack the brain radiometabolite accumulation that interferes with the low specific signal in LABs. In this context, ^{11}C-ER176 is arguably the most promising third-generation TSPO radioligand for clinical research (2,7). More specifically, it displays high specific binding (>80%), an adequately high BP_{ND} in LABs, and good time stability of total distribution volume (V_T) across all genotypes (8,9). The whole-brain BP_{ND} of ^{11}C-ER176 for LABs was 1.4 ± 0.8, which is about the same as that for high-affinity binders with ^{11}C-PBR28 (~1.2). For all 3 genotypes, the V_T values of ^{11}C-ER176 stabilized by 60–90 min to within 10% of their final 120-min values, suggesting that no significant amount of radiometabolites accumulated in the brain (8).

In contrast to ^{11}C, ^{18}F has several benefits for clinical PET imaging. Its relatively longer half-life (110 vs. 20 min) allows imaging for a longer period and for broader distribution of the radioligand from a central radiopharmacy, giving ^{18}F-labeled radioligands greater flexibility for widespread use. However, the structure of ER176 does not contain a fluorine atom for labeling with ^{18}F. Thus, as a first step toward developing an ^{18}F-labeled third-generation radioligand, our laboratory synthesized 6 new fluorine-containing analogs of ER176— 3 isomers with a fluoro group and 3 with a trifluoromethyl group at each of 3 positions (ortho, meta, and para) of the pendant aryl ring (Fig. 1) (10). In vitro studies demonstrated that all 6 analogs had high affinity for human TSPO (binding affinity, 1.2 − 7.0 nM) and could
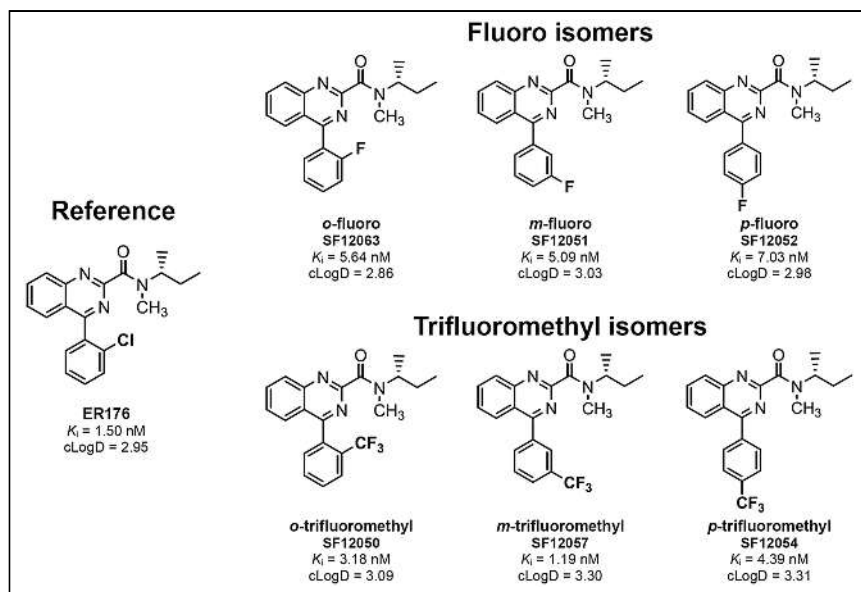
FIGURE 1. Chemical structures of ^{11}C-ER176 and 6 fluorine-containing analogs. K_i = binding affinity.

be successfully labeled with ^{11}C with good yield (66%–81%, decay-corrected) and excellent chemical (>95%) and radiochemical (>99%) purities. Selecting the most promising radioligand among the 6 candidates to label with ^{18}F would significantly reduce the time and cost of future investigations; however, in vitro data alone would not provide sufficient guidance for this decision.

The present study used in vivo performance in the monkey brain to select the most promising of the 6 ^{11}C-labeled analogs of ER176 for subsequent ^{18}F-radiolabeling. The 2 primary performance criteria were BP_{ND} and the stability of V_T over time, which is an indirect measure of lack of radiometabolite accumulation in the brain. Both baseline and preblocked PET scans in the monkey brain were obtained, and brain uptake was quantified as V_T using the radiometabolite-corrected arterial input function.

MATERIALS AND METHODS

Radiochemistry

^{11}C-ER176 was synthesized as previously described (*11*), with a molar activity of 106 ± 65 GBq/μmol ($n = 4$) at the time of injection and radiochemical purity of $97.1\% \pm 4.4\%$.

Six fluorine-containing analogs of ER176 (Fig. 1) were labeled with ^{11}C at the tertiary amide group by ^{11}C-methylation of the respective *N*-desmethyl precursor as previously described (*10*). Briefly, the labeling precursors were synthesized by amidation of 4-oxo-3*H*-quinazoline-2-carboxylic acid followed by palladium-catalyzed coupling with appropriate fluorophenylboronic acids for the fluoro isomers—*o*-fluoro (SF12063), *m*-fluoro (SF12051), and *p*-fluoro (SF12052)—and trifluoromethylphenylboronic acids for the trifluoromethyl isomers—*o*-trifluoromethyl (SF12050), *m*-trifluoromethyl (SF12057), and *p*-trifluoromethyl (SF12054). Six ^{11}C-labeled TSPO radioligands were then obtained by methylation at the secondary amide group of the respective *N*-desmethyl precursors in dimethyl sulfoxide with ^{11}C-methyl iodide. The molar activity was 222 ± 162 GBq/μmol ($n = 18$) for the fluoro radioligands and 111 ± 71 GBq/μmol ($n = 10$) for the trifluoromethyl radioligands at the time of injection (Supplemental Table 1; supplemental materials are available at http://jnm.snmjournals.org). The radiochemical purity of all radioligands was $99.6\% \pm 0.5\%$ ($n = 28$).

Animals

In vivo experiments were performed on 9 healthy male rhesus monkeys (body weight, 12.4 ± 1.3 kg). Anesthesia was maintained with 1%–2% isoflurane and 98% O_2 for the duration of the study. The head was firmly fixed by gauze and tape to the camera bed holder. Body temperature was maintained with air blankets; temperature, oxygen saturation, blood pressure, and end-tidal CO_2 were monitored for the duration of the study. All animal studies were conducted in compliance with the *Guide for the Care and Use of Laboratory Animals* (*12*) and were approved by the National Institute of Mental Health Animal Care and Use Committee.

PET Data Acquisition

The baseline PET scan was acquired for all radioligands (injected activity, 249 ± 78 MBq) using a microPET Focus 220 scanner (Siemens Medical Solutions), with a frame duration ranging from 30 s to 10 min. For the preblocked scans, racemic PK11195 (5 mg/kg) was intravenously administered 5–10 min before the radioligand. All PET scans were acquired for 120 min at baseline and 90 min after preblocking. Concurrent arterial blood sampling was performed in all scans to obtain a radiometabolite-corrected input function for quantification. PET images were reconstructed using a Fourier rebinning algorithm plus 2-dimensional filtered backprojection with attenuation and scatter correction.

Measurement of Parent Radioactivity in Plasma

Fifteen blood samples were drawn from an implanted port in the femoral artery during the PET scan every 15 s for the first 2 min, followed by sampling at 3, 5, 10, 30, 60, 90, and 120 min (varying from 1.0 to 3.0 mL); 14 samples were drawn during the 90-min PET scan. The parent radioligand was separated from radiometabolites as previously described (*13*). Plasma parent and whole-blood activity concentration were fitted with a triexponential function. The plasma free fraction (f_P) was measured by ultrafiltration as previously described (*14*).

Kinetic Analysis

All kinetic analyses were performed using PMOD, version 3.9 (PMOD Technologies Ltd.). V_T was estimated with Logan graphical analysis (LGA) using 90 min of brain time–activity curves and the radiometabolite-corrected arterial input function for both baseline and preblocked studies. Details on the kinetic analysis are provided in the supplemental materials (*15*).

Estimating Ratio of Specific to Nondisplaceable Uptake

BP_{ND} was used to compare the performance of the 6 radioligands; this measure is a ratio of receptor-specific uptake (V_S; $V_T - V_{ND}$) to nondisplaceable uptake (V_{ND}; free plus nonspecific binding) at equilibrium. In our opinion, BP_{ND} is a better binding measure than V_T because BP_{ND} directly quantifies specific binding. BP_{ND} is also more suitable than V_S because it is a signal-to-noise measurement that takes background into consideration. BP_{ND} was calculated as follows (*16*):

$$BP_{ND} = \frac{V_T - V_{ND}}{V_{ND}} = \frac{V_T}{V_{ND}} - 1,$$

where V_T refers to V_T at baseline and V_{ND} was estimated by the Lassen plot.

Because only unbound parent radioligand contributes to specific binding to the receptor, and because f_P was significantly different before and

after preblocking, brain uptake and BP_{ND} were calculated and compared for the 6 radioligands using V_T and V_{ND} corrected for f_P as V_T/f_P and V_{ND}/f_P, respectively.

Time Stability Analysis of V_T

To determine the minimal scan duration needed to reliably measure V_T and to indirectly assess whether radiometabolites enter the brain, time stability was evaluated using 120 min of baseline PET data with a truncated acquisition duration from 30 to 120 min in 10-min increments. The identifiability of V_T was also evaluated as percentage SE at each truncated scan duration.

Ex Vivo Blood Cell Analysis

The utility of radioligand uptake was investigated in blood cells as a surrogate for brain uptake. The radioactivity concentration in ex vivo blood cells was calculated both at baseline and in preblocked studies as follows (17):

$$C_{BC} = C_{PL} + \frac{(C_{WB} - C_{PL})}{\text{hematocrit}}.$$

Here, C_{BC}, C_{PL}, and C_{WB} indicate radioactivity concentrations in the blood cells, plasma, and whole blood, respectively. The distribution volume in blood cells (V_{BC}) was then obtained by dividing the radioactivity concentrations in the blood cells by the radioactivity concentration of the parent radioligand in plasma and then corrected for f_P (V_{BC}/f_P). The correlation between V_{BC}/f_P and whole-brain V_T/f_P and between percentage blockade calculated using V_{BC}/f_P and whole-brain V_T/f_P was assessed using linear regression analysis.

Replication Study and Statistical Analysis

Based on the results of the first scans, replication studies were conducted for selected radioligands in different monkeys to confirm either the radioligands' most favorable properties or aberrant data. When multiple experiments were performed with the same radioligand, quantitative results are presented as mean ± SD. Statistical significance was set at a P value of less than 0.05. All statistical analyses were conducted with Prism, version 5 (GraphPad Software).

RESULTS

Uptake in Monkey Brain

Brain radioactivity at baseline increased rapidly and peaked (SUV_{peak}, 2.7) at about 25 min after injection (Figs. 2A and 2B) except for the p-trifluoromethyl radioligand, which showed very slow uptake that peaked at 75 min. The m-trifluoromethyl radioligand showed the highest SUV_{peak} (3.4), and the m-fluoro radioligand showed the lowest SUV_{peak} (2.6). The brain region with the highest SUV_{peak} was the striatum (3.9), followed by the thalamus (3.2) and cerebellum (3.1); the parietal cortex had the lowest SUV_{peak} (2.4). Peak radioactivity uptake in all regions was followed by a smooth decrease in radioactivity level; for example, radioactivity in the whole brain decreased by 37% at 90 min after injection. In preblocked scans, all 6 radioligands showed a similar brain uptake pattern. Brain radioactivity rapidly increased and reached an SUV_{peak} of 4.1 at 3.5 min after injection, followed by a rapid decline and then a slow washout (Figs. 2C and 2D).

Plasma Concentration of Parent Radioligand

The concentration of parent radioligands in plasma peaked at 1.0–1.3 min after injection at baseline and then rapidly declined, followed by a slow terminal clearance phase. The fitting of plasma parent curves converged by triexponential function in all experiments (Fig. 3). The plasma parent fraction at baseline, expressed as a percentage of total plasma radioactivity, declined rapidly and reached 50% at 25.6 ± 11.6 min for the m-fluoro, p-fluoro, and o-trifluoromethyl radioligands (Supplemental Fig. 1). In contrast, the o-fluoro and m-trifluoromethyl radioligands showed a slower decline, reaching 50% at 50.7 ± 14.5 min after injection, and the p-trifluoromethyl radioligand exhibited an unusually high plasma parent fraction (>90%) during the entire 120 min of the scan. In preblocked scans, the parent radioactivity concentrations in plasma showed a rapid increase, peaking at 1.0–1.5 min, followed by a fast washout and then a slow terminal clearance phase in all radioligands. As in our prior studies (11,18), the peak concentration of parent radioligand in plasma was much higher in the preblocked scans than in the baseline scans, because PK11195 blocks the distribution of radioligand to peripheral organs—such as the lung and kidneys—that have high densities of TSPO. The temporal changes in parent fraction in plasma were similar for all radioligands, characterized by a rapid decline that reached less than 50% by 30 min, with a subsequent gradual decline.

Reversed-phase high-performance liquid chromatography of plasma revealed at least 5 radiometabolites, all of which appeared less lipophilic than the parent radioligand. A lipophilic radiometabolite appeared in plasma from all radioligand experiments, except the baseline study of the p-trifluoromethyl radioligand. Nonetheless, the amount was negligible ($0.07\% \pm 0.08\%$ of total plasma radioactivity across all arterial samples). The f_P was $17.3\% \pm 8.2\%$ at baseline for the
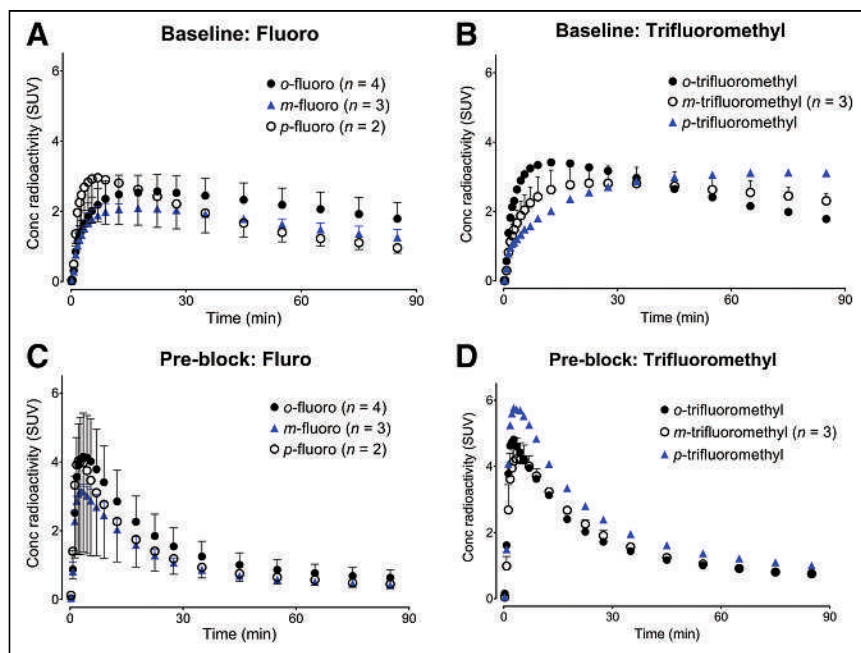

FIGURE 2. Time–activity curves of whole-brain uptake in baseline and preblocked scans for fluoro (A and C) and trifluoromethyl (B and D) radioligands. Points represent SUV_{mean} (±SD). Conc = concentration.
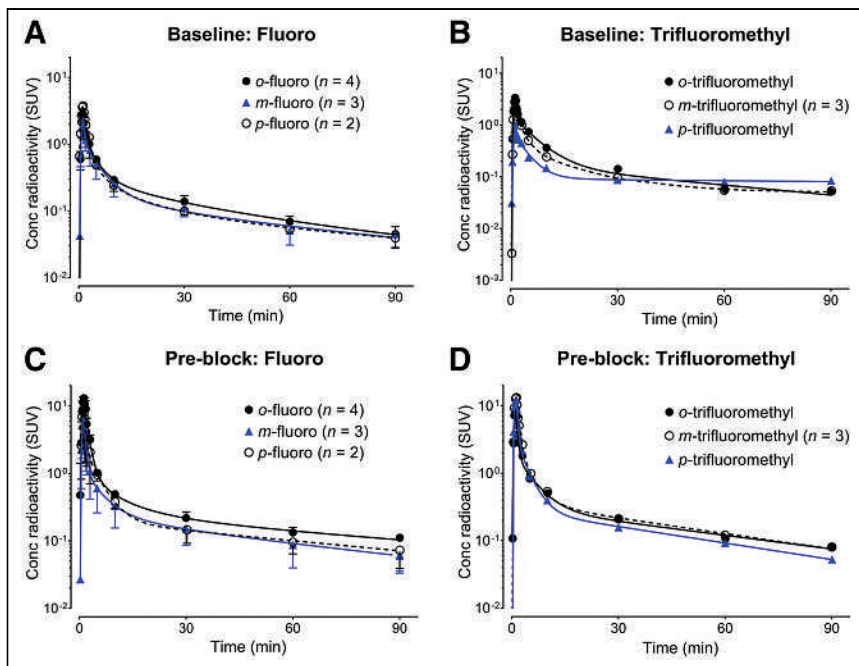
FIGURE 3. Time course of radioactivity concentrations in plasma at baseline and in preblocked scans for fluoro (A and C) and trifluoromethyl (B and D) radioligands. Points represent SUV_{mean} ($\pm$SD). Conc = concentration.

fluoro radioligands, whereas it was significantly higher (22.3% $\pm$ 11.3%) after preblocking ($n = 9$, $P = 0.017$). In contrast, there was no significant difference in f_P at baseline and after preblocking for the trifluoromethyl radioligands; f_P was 10.1% $\pm$ 2.9% at baseline and 10.6% $\pm$ 3.1% at preblock ($n = 5$, $P = 0.423$).

Kinetic Analysis

Brain uptake was well quantified by LGA, which does not require specific compartment configurations. Regional brain uptake was reliably quantified as V_T with excellent identifiability (SE < 10%) in all baseline and preblocked studies. The trifluoromethyl radioligands generally showed higher V_T/f_P (mL$\cdot$cm^{-3}) for baseline and preblocked conditions than the fluoro radioligands (363 vs. 138, respectively, at baseline and 50 vs. 23, respectively, at preblock) (Fig. 4). The *p*-trifluoromethyl radioligand had the highest V_T/f_P (493) at baseline, followed by the *m*-trifluoromethyl (411) and *o*-fluoro (223) radioligands (Table 1). The 3 brain regions with the highest V_T/f_P were the striatum (286), thalamus (283), and frontal cortex (269). The 3 with the lowest V_T/f_P were the cerebellum (208), amygdala (228), and occipital cortex (243). The blockade by PK11195 was 82.5% $\pm$ 7.3% and was similar for all 6 radioligands.

Estimating Ratio of Specific to Nondisplaceable Uptake

The *o*-fluoro radioligand exhibited the highest ratio of specific to nondisplaceable uptake (BP_{ND}, 12.1), followed by the *m*- trifluoromethyl (11.7) and *m*-fluoro (8.1) radioligands (Table 1). The Lassen plot analysis displayed excellent linear correlations ($R^2 > 0.90$) at high receptor occupancies (>87%) in all radioligands (Supplemental Fig. 2). Estimated V_{ND}/f_P (mL$\cdot$cm^{-3})
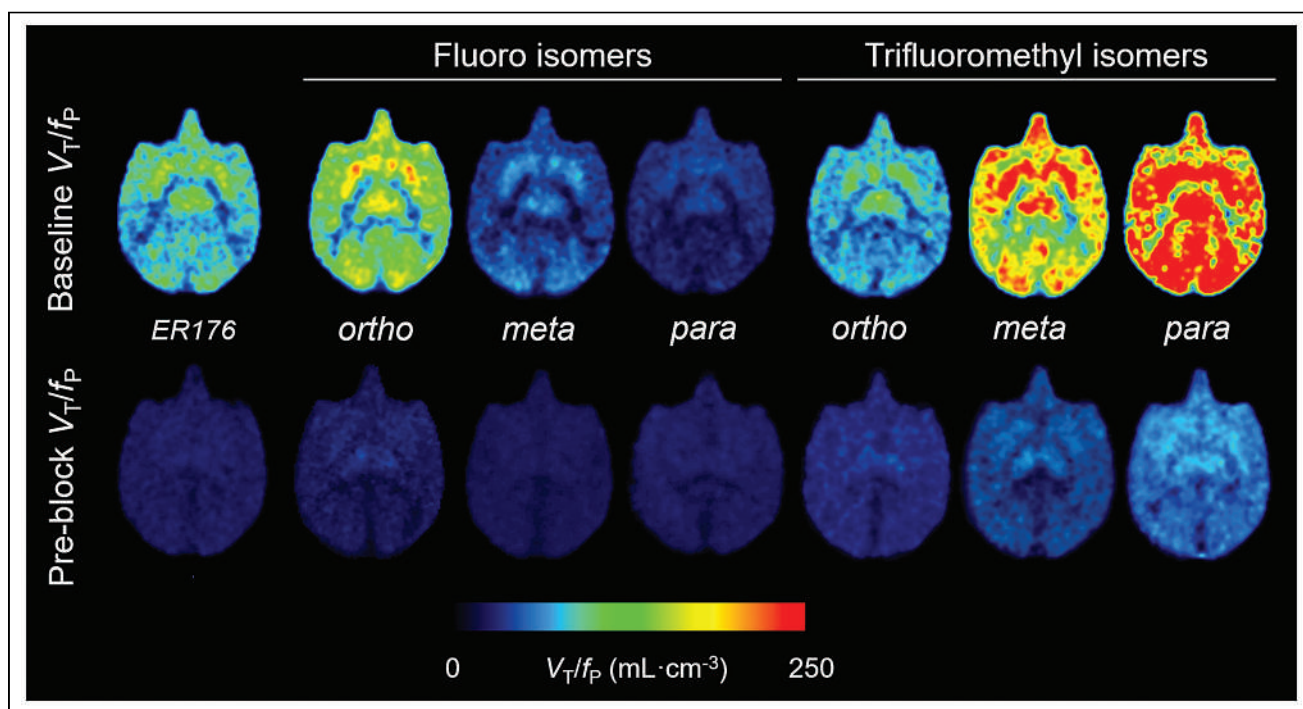

FIGURE 4. Average parametric images of total TSPO binding (V_T/f_P) for ^{11}C-ER176 and 6 analogs in monkey brain at baseline (top row) and preblocked scans (bottom row). Each V_T/f_P image was generated using 0–90 min of PET data obtained via LGA.

Comparison of V_T/f_P, Occupancy, V_{ND}/f_P, and BP_{ND} of Whole Brain Among ^{11}C-ER176 and 6 Fluorine-Containing Analogs

Compound	V_T/f_P (mL·cm^{-3})			Occupancy (%)	V_{ND}/f_P (mL·cm^{-3})	BP_{ND}	Binding affinity ratio*
	Baseline	Preblock	Blockade (%)				
Reference (^{11}C-ER176)	185.8	21.3	88.5	98.6	18.6	8.9	1.3
Fluoro							
o-fluoro	223.8	33.3	85.0	92.9	16.6	12.1	2.8
m-fluoro	92.2	12.7	84.9	95.6	9.8	8.1	2.7
p-fluoro	45.3	13.4	70.3	89.0	7.9	4.8	2.9
Trifluoromethyl							
o-trifluoromethyl	119.7	31.5	73.5	87.1	18.5	5.5	5.5
m-trifluoromethyl	411.0	47.6	86.9	95.0	32.6	11.7	2.0
p-trifluoromethyl	493.0	73.6	84.8	97.7	63.6	6.7	0.8

*Ratio of binding affinity (in nM) in LABs to that in high-affinity binders.
Data are mean.

ranged mainly between 5.0 and 35.0, except for the p-trifluoromethyl radioligand (63.6). V_{ND}/f_P was smallest for the p-fluoro radioligands (7.9), followed by the m-fluoro (9.8) and o-fluoro (16.6) radioligands (Table 1). As shown in Supplemental Table 2, the results were similar to the analysis without f_P correction.

Time Stability of V_T

Whole-brain V_T asymptotically reached terminal values and converged within 10% of terminal values by the 70th minute of a 120-min scan (Figs. 5A and 5B). V_T remained almost stable for the last 50 min, showing an average change of 4.7%, and could be quantified with excellent identifiability (SE < 5%) (Supplemental Fig. 3). The fluoro and trifluoromethyl radioligands took a similar time to achieve a stable V_T (70 min). The relatively stable V_T measurement over the 70–120 min of the scan suggested no significant accumulation of radiometabolites in the brain.

Performance Comparison with ^{11}C-ER176

o-fluoro, m-trifluoromethyl, and m-fluoro radioligands showed a BP_{ND} similar to or higher than that of ^{11}C-ER176 (8.9), whereas the other 3 showed slightly lower values (Table 1). Regarding the time stability of V_T, it took a similar time for the whole-brain

V_T values of ^{11}C-ER176 and its 6 fluorine-containing analogs to reach and remain stable within 10% of their terminal values (90 vs. 70 min) (Fig. 5; Supplemental Fig. 4).

Correlation Between Radioligand Uptake in Blood Cells and Brain

Ex vivo blood cell uptake (V_{BC}/f_P) correlated well with in vivo whole-brain V_T/f_P in both baseline ($R^2 = 0.938$, $P < 0.001$) and preblocked ($R^2 = 0.750$, $P = 0.012$) studies (Supplemental Fig. 5). The percentage blockade of V_{BC}/f_P by PK11195 also correlated significantly with that of whole-brain V_T/f_P ($R^2 = 0.583$, $P = 0.046$).

DISCUSSION

Of the 6 ^{11}C-ER176 analogs developed by our laboratory, the present study found that the o-fluoro, m-trifluoromethyl, and m-fluoro compounds were the most promising. All 3 had a high BP_{ND} (the ratio of specific to nondisplaceable uptake) and a stable V_T measured over time in the monkey brain, consistent with the lack of radiometabolite accumulation. Specifically, the o-fluoro radioligand had the third-highest V_T/f_P at baseline (120 mL·cm^{-3}), 96% of which was specifically bound to TSPO, and the highest BP_{ND} (12.1), making it potentially the most promising of all 6 ^{11}C-ER176 analogs. The m-trifluoromethyl radioligand showed the second-highest V_T/f_P at baseline (411 mL·cm^{-3}), high specific binding to TSPO (96%), and high BP_{ND} (11.7). The m-fluoro radioligand also showed a high V_T/f_P at baseline (92 mL·cm^{-3}), high specific binding to TSPO (95.6%), and a high BP_{ND} (8.1). For these 3 radioligands, V_T reached 90% of terminal 120-min values by 70 min and remained relatively stable thereafter, with excellent identifiability (%SE < 5%), suggesting that no significant radiometabolites accumulated in the brain.

In the present study, LGA was used to quantify and compare brain uptake across
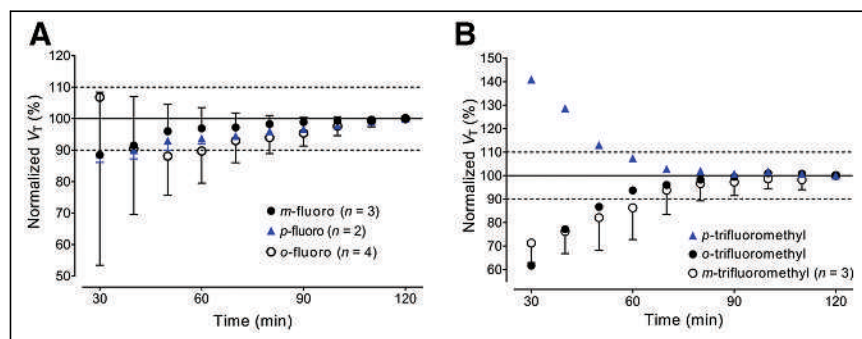

FIGURE 5. Time stability analysis of whole-brain V_T for fluoro (A) and trifluoromethyl (B) radioligands. V_T was calculated via LGA and normalized to terminal V_T at 120 min. Points represent mean normalized V_T (±SD).

all 6 radioligands because neither the 1- nor the 2-tissue-compartment models fitted perfectly for all studies. With LGA, V_T was quantified with excellent identifiability (SE < 10%) in all baseline and preblocked studies. Logan-derived V_{ND}/f_P and BP_{ND} were within acceptable ranges and became less variable within each of the fluoro and trifluoromethyl radioligands. However, LGA tends to underestimate V_T and BP_{ND}, typically by 10%–20% depending on both the noise level and the radioligand concentration (19,20). The degree of underestimation in this study remains uncertain; however, given the same target (TSPO) and similar performance measures, we believe that the underestimation, if any, would have been consistent across all 6 radioligands and would have led to the same finding—that is, that the o-fluoro, m-trifluoromethyl, and m-fluoro analogs were the 3 best candidates.

Evaluation of V_T stability with respect to scan duration allows one to determine the minimum scan time required for obtaining a stable V_T and to indirectly check the possibility that radiometabolites are accumulating in the brain. Acceptable scan durations typically occur when V_T in all regions approaches 10% of a terminal value. If brain-penetrant radiometabolites accumulate in the brain, V_T is expected to increase continuously, making the values unlikely to plateau and stabilize. Whether radiometabolites enter and accumulate in the brain is critical for imaging human TSPO, especially in LABs who have low specific binding. Although some small differences were noted between the radioligands, the present study found that, for all 6 radioligands, whole-brain V_T at baseline reached 10% of the terminal value by 70 min and 5% by 90 min. This similarity in time stability suggests that radiometabolites are unlikely to have interfered with brain uptake.

Interestingly, the present study found that ex vivo blood cells were a useful surrogate for brain tissue. V_{BC} at baseline and under preblocked conditions and the percentage blockade by PK11195 correlated well with those of whole-brain V_T/f_P. The similarity between the 2 organs can be used to evaluate radioligands that specifically bind to receptors expressed in both the brain and blood cells. For example, the blood cell analysis could be used as a quick screening tool for candidate radioligands or a nonimaging supplement to validate imaging results, thus aiding the development of new PET radioligands. However, the utility of ex vivo blood cells should be verified for individual radioligands because the 2 organs differ in their efflux systems and compartmental configurations.

One of the advantages of ^{11}C-ER176 is that it has adequately high TSPO-specific binding for quantification across all *rs6971* genotypes. A previous postmortem analysis of human brain tissue measured the in vitro binding affinities to all *rs6971* genotypes for ER176 and these 6 fluorine-containing analogs (8,10). As summarized in Table 1, the p-trifluoromethyl compound showed the smallest ratio (i.e., binding affinity difference) (0.8) between high-affinity binders and LABs, followed by ER176 (1.3), the m-trifluoromethyl (2.0) compound, the 3 fluoro compounds (2.7–2.9), and the o-trifluoromethyl (5.4) compound. Building on this finding, all 6 analogs investigated here are expected to achieve an adequately high specific signal in LABs, at least higher than PBR28 (55.0) (5), which has been the most widely used of the second-generation TSPO radioligands.

Taken together, these in vitro and in vivo data suggest that the o-fluoro, m-trifluoromethyl, and m-fluoro compounds appear to be the most promising analogs. However, all 6 radioligands performed well and with only small interligand differences (Table 1). For example, the 3 fluoro radioligands exhibited similar BP_{ND}

(4.8–12.1), time stability of V_T (all achieved stable V_T by 70 min), and binding affinity ratios (2.7–2.9), and all these measures were comparable to those of ^{11}C-ER176. Nevertheless, unexpected labeling issues (e.g., unsatisfactory yield, or perhaps only marginally acceptable molar activity for labeling trifluoromethyl groups) for ^{18}F radioligands may also arise in their development, limiting the use of particular radioligands despite solid performance in their ^{11}C-labeled forms. Thus, though the candidate radioligands have now been ranked, priorities for subsequent ^{18}F radiolabeling will also be affected by the time and effort needed for radiochemistry. Moving forward, none of the 6 compounds will be excluded.

The underlying assumption of this study is that ^{18}F-labeled radioligands will perform similarly to their ^{11}C-labeled versions. However, the performance of an ^{11}C-labeled radioligand does not always guarantee success in its ^{18}F-labeled form. ^{18}F labeling at a position different from an ^{11}C position in the molecular structure may change the spectrum of radiometabolites and generate unexpected brain-penetrating radiometabolites. Defluorination may also occur to confound the accurate quantification of receptor-specific brain uptake. Although strategic positioning of an ^{18}F label can reduce the production of these troublesome radiometabolites, the in vivo metabolism of a radioligand (e.g., the sites of metabolic cleavage) is not always predictable and further varies across species (21).

CONCLUSION

The 6 fluorine-containing analogs of ER176 were relatively easily labeled with ^{11}C. PET imaging in the monkey brain showed that all 6 ^{11}C-labeled analogs had a good BP_{ND} and good time stability of V_T. Of the 6 ligands, the o-fluoro, m-trifluoromethyl, and m-fluoro compounds were arguably the 3 best candidates to radiolabel with ^{18}F, a process that is expected to be quite challenging.

DISCLOSURE

ACKNOWLEDGMENTS

KEY POINTS

QUESTION: Which are the most promising fluorine-containing analogs of ^{11}C-ER176 for subsequent ^{18}F radiolabeling?

PERTINENT FINDINGS: This study used generic ^{11}C labeling and in vivo performance in the monkey brain—BP_{ND} and time stability of V_T—to select the most promising analogs among 6 candidates. The o-fluoro, m-trifluoromethyl, and m-fluoro compounds were arguably the 3 best candidates because they showed the 3 highest BP_{ND} values as well as good time stability of V_T.

IMPLICATIONS FOR PATIENT CARE: The development of an ^{18}F-labeled radioligand based on ^{11}C-ER176 would allow greater flexibility and more widespread use of TSPO PET.

REFERENCES

1. Papadopoulos V, Baraldi M, Guilarte TR, et al. Translocator protein (18kDa): new nomenclature for the peripheral-type benzodiazepine receptor based on its structure and molecular function. *Trends Pharmacol Sci.* 2006;27:402–409.

2. Meyer JH, Cervenka S, Kim MJ, Kreisl WC, Henter ID, Innis RB. Neuroinflammation in psychiatric disorders: PET imaging and promising new targets. *Lancet Psychiatry.* 2020;7:1064–1074.

3. Chauveau F, Boutin H, Van Camp N, Dolle F, Tavitian B. Nuclear imaging of neuroinflammation: a comprehensive review of [11C]PK11195 challengers. *Eur J Nucl Med Mol Imaging.* 2008;35:2304–2319.

4. Le Fur G, Perrier ML, Vaucher N, et al. Peripheral benzodiazepine binding sites: effect of PK 11195, 1-(2-chlorophenyl)-N-methyl-N-(1-methylpropyl)-3-isoquinolinecarboxamide. I. In vitro studies. *Life Sci.* 1983;32:1839–1847.

5. Kreisl WC, Jenko KJ, Hines CS, et al. A genetic polymorphism for translocator protein 18 kDa affects both in vitro and in vivo radioligand binding in human brain to this putative biomarker of neuroinflammation. *J Cereb Blood Flow Metab.* 2013;33:53–58.

6. Owen DR, Yeo AJ, Gunn RN, et al. An 18-kDa translocator protein (TSPO) polymorphism explains differences in binding affinity of the PET radioligand PBR28. *J Cereb Blood Flow Metab.* 2012;32:1–5.

7. Kreisl WC, Kim MJ, Coughlin JM, Henter ID, Owen DR, Innis RB. PET imaging of neuroinflammation in neurological disorders. *Lancet Neurol.* 2020;19:940–950.

8. Ikawa M, Lohith TG, Shrestha S, et al. 11C-ER176, a radioligand for 18-kDa translocator protein, has adequate sensitivity to robustly image all three affinity genotypes in human brain. *J Nucl Med.* 2017;58:320–325.

9. Fujita M, Kobayashi M, Ikawa M, et al. Comparison of four 11C-labeled PET ligands to quantify translocator protein 18 kDa (TSPO) in human brain: (R)-PK11195, PBR28, DPA-713, and ER176-based on recent publications that measured specific-to-non-displaceable ratios. *EJNMMI Res.* 2017;7:84.

10. Siméon FG, Lee JH, Morse CL, et al. Synthesis and screening in mice of fluorine-containing PET radioligands for TSPO: discovery of a promising 18F-labeled ligand. *J Med Chem.* 2021;64:16731–16745.

11. Zanotti-Fregonara P, Zhang Y, Jenko KJ, et al. Synthesis and evaluation of translocator 18 kDa protein (TSPO) positron emission tomography (PET) radioligands with low binding sensitivity to human single nucleotide polymorphism rs6971. *ACS Chem Neurosci.* 2014;5:963–971.

12. *Guide for the Care and Use of Laboratory Animals.* 8th ed. National Academy Press; 2011.

13. Zoghbi SS, Shetty HU, Ichise M, et al. PET imaging of the dopamine transporter with 18F-FECNT: a polar radiometabolite confounds brain radioligand measurements. *J Nucl Med.* 2006;47:520–527.

14. Gandelman MS, Baldwin RM, Zoghbi SS, Zea-Ponce Y, Innis RB. Evaluation of ultrafiltration for the free-fraction determination of single photon emission computed tomography (SPECT) radiotracers: beta-CIT, IBF, and iomazenil. *J Pharm Sci.* 1994;83:1014–1019.

15. Yasuno F, Brown AK, Zoghbi SS, et al. The PET radioligand [11C]MePPEP binds reversibly and with high specific signal to cannabinoid CB1 receptors in nonhuman primate brain. *Neuropsychopharmacology.* 2008;33:259–269.

16. Innis RB, Cunningham VJ, Delforge J, et al. Consensus nomenclature for in vivo imaging of reversibly binding radioligands. *J Cereb Blood Flow Metab.* 2007;27:1533–1539.

17. Kanegawa N, Collste K, Forsberg A, et al. In vivo evidence of a functional association between immune cells in blood and brain in healthy human subjects. *Brain Behav Immun.* 2016;54:149–157.

18. Briard E, Zoghbi SS, Imaizumi M, et al. Synthesis and evaluation in monkey of two sensitive 11C-labeled aryloxyanilide ligands for imaging brain peripheral benzodiazepine receptors in vivo. *J Med Chem.* 2008;51:17–30.

19. Logan J, Fowler JS, Volkow ND, Ding YS, Wang GJ, Alexoff DL. A strategy for removing the bias in the graphical analysis method. *J Cereb Blood Flow Metab.* 2001;21:307–320.

20. Slifstein M, Laruelle M. Effects of statistical noise on graphic analysis of PET neuroreceptor studies. *J Nucl Med.* 2000;41:2083–2088.

21. Pike VW. PET radiotracers: crossing the blood-brain barrier and surviving metabolism. *Trends Pharmacol Sci.* 2009;30:431–440.

Optimizing Immuno-PET Imaging of Tumor PD-L1 Expression: Pharmacokinetic, Biodistribution, and Dosimetric Comparisons of [89]Zr-Labeled Anti-PD-L1 Antibody Formats

Alizée Bouleau[1], Hervé Nozach[2], Steven Dubois[2], Dimitri Kereselidze[1], Céline Chevaleyre[1], Cheng-I Wang[3], Michael J. Evans[4], Vincent Lebon[1], Bernard Maillère[2], and Charles Truillet[1]

[1]Paris-Saclay University, CEA, CNRS, INSERM, Multimodal Biomedical Imaging Lab, Orsay, France; [2]Paris-Saclay University, CEA, INRAE, Medicines and Healthcare Technologies Department, SIMoS, Gif-sur-Yvette, France; [3]Singapore Immunology Network, A*STAR, Immunos, Singapore, Singapore; and [4]Department of Radiology and Biomedical Imaging, University of California San Francisco, San Francisco, California

PET imaging of programmed cell death ligand 1 (PD-L1) may help to noninvasively predict and monitor responses to anti–programmed cell death 1/anti-PD-L1 immunotherapies. In this study, we compared the imaging characteristics of 3 radioligands derived from the anti-PD-L1 IgG1 complement 4 (C4). In addition to the IgG C4, we produced a fragment antigen-binding (Fab) C4, as well as a double-mutant IgG C4 (H310A/H435Q) with minimal affinity for the murine neonatal Fc receptor. **Methods:** The pharmacokinetics, biodistribution, and dosimetry of the 3 [89]Zr-labeled C4 ligands were compared by longitudinal PET/CT imaging in nude mice bearing subcutaneous human non–small cell lung cancer xenografts with positive (H1975 model) or negative (A549 model) endogenous PD-L1 expression. **Results:** The C4 radioligands substantially accumulated in PD-L1–positive tumors but not in PD-L1–negative tumors or in blocked PD-L1–positive tumors, confirming their PD-L1–specific tumor targeting. [89]Zr-Fab C4 and [89]Zr-IgG C4 (H310A/H435Q) were rapidly eliminated compared with [89]Zr-IgG C4. Consequently, maximal tumor-to-muscle ratios were obtained earlier, at 4 h after injection for [89]Zr-Fab C4 (ratio, ~6) and 24 h after injection for [89]Zr-IgG C4 (H310A/H435Q) (ratio, ~9), versus 48 h after injection for [89]Zr-IgG C4 (ratio, ~8). Background activity in nontumor tissues was low, except for high kidney retention of [89]Zr-Fab C4 and persistent liver accumulation of [89]Zr-IgG C4 (H310A/H435Q) compared with [89]Zr-IgG C4. Dosimetry estimates suggested that the C4 radioligands would yield organ-absorbed doses tolerable for repeated clinical PET imaging studies. **Conclusion:** This study highlights the potential of designing radioligands with shorter pharmacokinetics for PD-L1 immuno-PET imaging in a preclinical model and encourages further clinical translation of such radioligands.

Key Words: PET; programmed cell death ligand 1; PD-L1; immunotherapy; pharmacokinetics; non–small cell lung cancer; NSCLC

Immunotherapies with monoclonal antibodies targeting the programmed cell death 1 (PD-1)/programmed cell death ligand 1 (PD-L1) immune checkpoint pathway have significantly improved the treatment of non–small cell lung cancer (NSCLC) (1,2). However, despite remarkable results in some NSCLC patients, only a small subset (~10%–20%) actually responded to anti-PD-1/anti-PD-L1 immunotherapies (3). Therefore, reliable predictive biomarkers of response to PD-1/PD-L1 immune checkpoint inhibitors are urgently needed to guide patient stratification and to maximize therapeutic benefit (4).

PD-L1 expression in NSCLC tumors, determined by immunohistochemistry on biopsy material, was associated with higher response rates to anti-PD-1/anti-PD-L1 immunotherapies (5,6). However, immunohistochemistry evaluation of PD-L1 expression suffers from several limitations that might contribute to the discrepancies observed in treatment response (1). Notably, a single biopsy cannot reflect the spatiotemporal heterogeneity of PD-L1 expression within and across the tumor lesions of a patient (4).

PET with radioligands targeting PD-L1 is a promising approach to complement the conventional immunohistochemistry procedure, as it can provide a holistic, noninvasive, quantitative, and real-time assessment of PD-L1 expression (7). Immuno-PET combines the sensitivity of PET with the high specificity and affinity of radiolabeled antibodies or antibody-derived fragments. Clinical studies involving NSCLC patients have shown encouraging results regarding the predictive value of PD-L1 PET imaging for anti-PD-1/anti-PD-L1 immunotherapies (8,9). In addition to supporting patient selection, PD-L1 PET imaging may also assist in treatment monitoring and response evaluation, facilitating personalized immunotherapy.

A wide range of radioligands targeting PD-L1 has been investigated in preclinical and clinical PET imaging studies (7). Many of these studies used the clinically approved monoclonal antibodies atezolizumab or avelumab, radiolabeled with [89]Zr. However, smaller anti-PD-L1 PET radioligands have gained increasing interest. In contrast to full-length antibodies, they can rapidly and deeply diffuse into tumors while being quickly cleared from the blood. As a result, high-contrast images can be obtained within only hours after radioligand administration. Besides size reduction, another strategy for enhancing blood clearance of radiolabeled IgGs relies on altering their binding affinity to the neonatal Fc receptor (FcRn) (10). The FcRn is responsible for the extended plasmatic half-life of IgGs (~21 d), by protecting them from intracellular catabolism through the FcRn-mediated recycling pathway. Introduction of mutations at key amino acid residues in the IgG Fc domain (e.g., I253, H310, and H435) resulted in IgG variants with greatly decreased binding affinity to murine FcRn and significantly faster blood elimination in mice (11–14).

In this comparative study, we investigated 2 different approaches to designing anti-PD-L1 PET radioligands with optimized pharmacokinetic properties. We produced a fragment antigen-binding (Fab) fragment (50 kDa) derived from the antibody complement 4 (C4), a human recombinant IgG1 targeting both human and murine PD-L1. The ^{89}Zr-labeled IgG C4 was previously used for PD-L1 PET imaging in human NSCLC xenograft models and in a patient-derived xenograft model from an NSCLC patient (15). We also engineered a double-mutant IgG C4 (H310A/H435Q) (150 kDa) with minimal affinity for the murine FcRn. The pharmacokinetics, biodistribution, and dosimetry of the ^{89}Zr-labeled IgG C4, IgG C4 (H310A/H435Q), and Fab C4 were evaluated in human NSCLC xenograft models.

MATERIALS AND METHODS

Production of C4 Ligands

The C4 IgG heavy and light chains were cloned into the AbVec2.0-IGHG1 and AbVec1.1-IGLC plasmids, respectively (16). For the Fab C4, the Fc fragment was replaced by a polyhistidine tag. Human HEK293 Freestyle cells (Thermo-Fisher) (2.5×10^6 cells/mL) were transiently cotransfected in 100 mL of Freestyle medium (Thermo-Fisher) by adding 150 µg of each plasmid and 1.8 mL of linear polyethyleneimine (0.5 mg/mL; Polysciences). Cells were incubated for 7 d at 37°C, 120 rpm, and 8% CO_2. The culture supernatant was purified using HiTrap Protein A, Lambda-FabSelect, or HisTrap Excel columns (GE Healthcare) for IgG C4, IgG C4 (H310A/H435Q), and Fab C4, respectively. Size-exclusion chromatography was performed using Sephacryl-S-200 HR columns (Sigma) with phosphate-buffered saline.

Biolayer Interferometry

Binding kinetics of the C4 ligands to human PD-L1 (Sinobiological) were determined by biolayer interferometry using an Octet RED96 instrument (ForteBio). AntihIgG Fc Capture Biosensors (Fortebio) were loaded with the IgG C4 (50 nM) for 60 s. Association of human PD-L1 was measured at different concentrations (1.6–100 nM) for 300 s, before dissociation for 1,000 s in kinetic buffer (phosphate-buffered saline with 0.5% bovine serum albumin and 0.05% polysorbate 20). Streptavidin Biosensors (Fortebio) were loaded with biotinylated human PD-L1 (50 nM) for 60 s. Association of Fab C4 was measured at different concentrations (0.78–6.3 nM) for 200 s, before dissociation for 1,000 s in kinetic buffer. Binding curves were fitted to a global 1:1 binding model.

Radiolabeling

The C4 ligands were conjugated with *p*-isothiocyanatobenzyldesferrioxamine (*p*-NCS-Bz-DFO; Macrocyclics) and radiolabeled with ^{89}Zr (PerkinElmer) according to a previously published protocol (17). A 4-fold molar excess of *p*-NCS-Bz-DFO was added to 1 mL of C4 ligand solution (5 mg/mL), and reaction mixture was incubated for 45 min at 37°C. The DFO-C4 ligand conjugates were purified with a PD-10 column (GE Healthcare) using a gentisic acid solution. The DFO-C4 ligand solution was incubated with ^{89}Zr (111 MBq) for 1 h at 37°C. The ^{89}Zr-DFO-C4 ligand conjugates were purified with a PD-10 column using a gentisic acid solution, before being further concentrated and buffer-exchanged in *N*-(2-hydroxyethyl)piperazine-*N'*-(2-ethanesulfonic acid) with a Vivaspin centrifugal concentrator (Sartorius). Radiochemical purity was assessed by instant thin-layer chromatography and size-exclusion high-performance liquid chromatography.

Cell Culture

The human NSCLC cell lines H1975 and A549 were purchased from the American Type Culture Collection. Cells were cultured in RPMI-1640 medium (Gibco) for H1975 cells or Dulbecco modified Eagle medium (Gibco) for A549 cells, supplemented with 10% fetal bovine serum (Gibco) and 1% antibiotic–antimycotic solution (Gibco), at 37°C in a humidified atmosphere with 5% CO_2.

Cell Binding Assays

Two million H1975 cells were mixed with ^{89}Zr-IgG C4, ^{89}Zr-IgG C4 (H310A/H435Q), or ^{89}Zr-Fab C4 (2 pmol, 148–296 kBq [4–8 µCi]), with or without a ×100 molar excess of nonradiolabeled C4 ligand. The reaction mixture was incubated for 2 h at 37°C. Cell-associated activity was measured with the Wizard^2 γ-counter (PerkinElmer) and expressed as the percentage total activity added per sample.

Immunoblotting

Total proteins (30 µg) from whole-cell lysates were separated by electrophoresis on Mini-PROTEAN TGX gels (Bio-Rad) and transferred to a polyvinylidene fluoride membrane (Merck Millipore). Blots were incubated with the following primary antibodies: rabbit antihuman PD-L1 (1:1,000, clone E1L3N; Cell Signaling) and rabbit antihuman α-tubulin (1:1,000; Cell Signaling). Blots were then incubated with a horseradish peroxidase–conjugated donkey antirabbit secondary antibody (1:10,000; Jackson ImmunoResearch). Proteins were detected using the Clarity Western ECL Substrate (Bio-Rad). Immunoblots were imaged with the FUSION FX imaging system (Vilber).

Animals

Animal experiments were performed according to the European Directive 2010/63/EU and to its transposition into the French law (decree 2013-118). The research project was conducted at the Comissariat à l'Énergie Atomique–Service Hospitalier Frédéric Joliot imaging platform (authorization D91-471-105) and was approved by a local ethics committee (Comité d'Éthique en Expérimentation Animale du Comissariat à l'Énergie Atomique et aux Énergies Alternatives–Direction des Sciences du Vivant, Ile-de-France). Female nude mice (NMRI-FOXN1 nu/nu; Janvier) were housed in individually ventilated cages in a temperature-controlled (22°C) and humidity-controlled (40%) room, with a 12-h light/12-h dark cycle. Animal experiments were performed under anesthesia with isoflurane in oxygen.

Subcutaneous Injections

Anesthetized mice were subcutaneously inoculated in both lower flanks with H1975 or A549 cells ($4–5 \times 10^6$ cells) suspended in phosphate-buffered saline/Matrigel (BD Biosciences) (1:1). Mice were used for PET imaging studies when tumors reached about 8 mm at the largest diameter.

Small-Animal PET/CT Imaging

Mice (10 ± 1 wk, 27.8 ± 1.4 g) were intravenously injected with the ^{89}Zr-labeled C4 ligands (3.7 ± 0.7 MBq, 7.0 ± 3.0 MBq/nmol, 0.6 ± 0.3 nmol). For blocking studies, mice were coinjected with a ×20 molar excess of nonradiolabeled C4 ligands (1.2 nmol). PET emission scans were performed using an Inveon small-animal PET scanner and an Inveon small-animal PET/CT scanner (Siemens). A 60-min dynamic PET scan was performed immediately after radioligand injection. Twenty-minute static PET scans were subsequently acquired at selected times (4 h, 24 h, 48 h, 72 h, and 7 d) after injection. After each PET scan, a transmission scan or a CT scan was obtained for photon attenuation correction. PET images were reconstructed with Inveon Acquisition Workspace software (version 2.1) using the ordinary Poisson ordered-subsets expectation maximization 3-dimensional maximum a posteriori algorithm. Normalization and corrections for dead time, scatter, decay, and attenuation were applied to all PET data. Volumes of interest were defined with PMOD software (version 3.9). Fixed-size spheric volumes of interest (3.5–8 mm^3) were drawn in representative parts of the heart, liver, and kidneys. Mouse whole-body, spleen, and subcutaneous tumors were delineated semiautomatically.

The mean activity concentration (kBq/cm^3) in each volume of interest was divided by the total injected dose (kBq) to obtain the percentage injected dose per volume of tissue (%ID/cm^3).

Immunohistochemistry

Fixed frozen tumor sections (12 μm) were incubated with a rabbit anti-human PD-L1 primary antibody (1:100, clone E1L3N; Cell Signaling). Slides were then incubated with a horseradish peroxidase–conjugated donkey antirabbit secondary antibody (1:500; Jackson ImmunoResearch). Peroxidase activity was detected with 3–3′-diaminobenzidine (BD Pharmingen). Tumor sections were counterstained with Harris hematoxylin (Sigma-Aldrich). Standard hematoxylin and eosin staining was performed on adjacent tumor sections. Images of stained tumor sections were acquired with the Axio Observer 5 microscope (Zeiss).

Flow Cytometry

Single-cell suspensions were incubated with the following fluorescent-labeled antibodies (10 μg/mL): phycoerythrin-conjugated antihuman PD-L1 antibody (clone 29E.2A3; BioLegend) and phycoerythrin-conjugated mouse IgG2b, κ isotype control (clone MPC-11; BioLegend). For viability assessment, cells were incubated with Zombie Green viability dye (1:500; BioLegend). Flow cytometry was performed on an Attune NxT Acoustic Focusing Cytometer (Invitrogen). Data were analyzed with FlowJo (version 10.7).

Blood Pharmacokinetics

Plasma activity concentrations were calculated from image-derived blood-pool activity concentrations. Considering that antibodies are restricted to the plasma, a blood-to-plasma concentration ratio of 0.55 was used. For each C4 radioligand, plasma time–activity curves of individual mice were pooled and fitted to a 2-compartment model with NONMEM software (version 6.2).

Dosimetry

For each C4 radioligand, residence times (kBq·h·kBq^{-1}) in the main source organs (blood pool, liver, kidneys, spleen, and remainder of body) of individual mice were derived from longitudinal PET images and used in IDAC-Dose software (version 2.1) [18] for human dosimetry estimations. Murine dosimetry was also performed (Supplemental Table 1; supplemental materials are available at http://jnm.snmjournals.org) [19].

Statistics

Statistical analyses were performed with GraphPad Prism (version 9.0.1). A 2-tailed Student t test was used for 2-group data comparison.

RESULTS

Production and Characterization of C4 Radioligands

Biolayer interferometry measurements showed that IgG C4, IgG C4 (H310A/H435Q), and Fab C4 displayed high binding affinities for human PD-L1, with nanomolar affinity constants (Supplemental Fig. 1; Supplemental Table 2). The 3 C4 ligands were successfully conjugated to p-NCS-Bz-DFO and subsequently radiolabeled with ^{89}Zr. Radiochemical purity exceeded 95% in all radiosynthesis experiments ($n = 6$) (Supplemental Fig. 2; Supplemental Table 3). Endogenous PD-L1 expression on H1975 and A549 cells was confirmed by immunoblotting and flow cytometry (Fig. 1). H1975 cells exhibited high PD-L1 expression compared with A549 cells, with median fluorescence intensity values of 713 ± 56 and 107 ± 7, respectively. In vitro binding assays showed that binding of the ^{89}Zr-labeled C4 ligands to PD-L1–positive H1975 cells was significantly blocked (>70% reduction) by coincubation with an excess of nonradiolabeled ligands, demonstrating the PD-L1 binding specificity of the C4 radioligands (Fig. 1).

Small-Animal PET/CT Imaging with C4 Radioligands in PD-L1–Positive Human NSCLC Xenograft Model

Female nude mice bearing subcutaneous PD-L1–positive H1975 xenografts were injected with the C4 radioligands (3.7 ± 0.7 MBq, 0.6 ± 0.3 nmol), and longitudinal small-animal PET/CT imaging was performed (Supplemental Figs. 3, 4, 5, and 6; Supplemental Tables 4 and 5).

Various blood pharmacokinetic parameters of the C4 radioligands were estimated (Table 1; Supplemental Fig. 7). The ^{89}Zr-Fab C4 fragment exhibited the fastest blood clearance. The Fc-mutant ^{89}Zr-IgG C4 (H310A/H435Q) was also rapidly cleared from circulation as compared with the wild-type ^{89}Zr-IgG C4, with a ×3.4 superior systemic clearance. Remarkably, the estimated biologic elimination half-lives were similar for ^{89}Zr-IgG C4 and ^{89}Zr-IgG C4 (H310A/H435Q). This finding may be explained by the higher retention of ^{89}Zr-IgG C4 (H310A/H435Q) in the peripheral
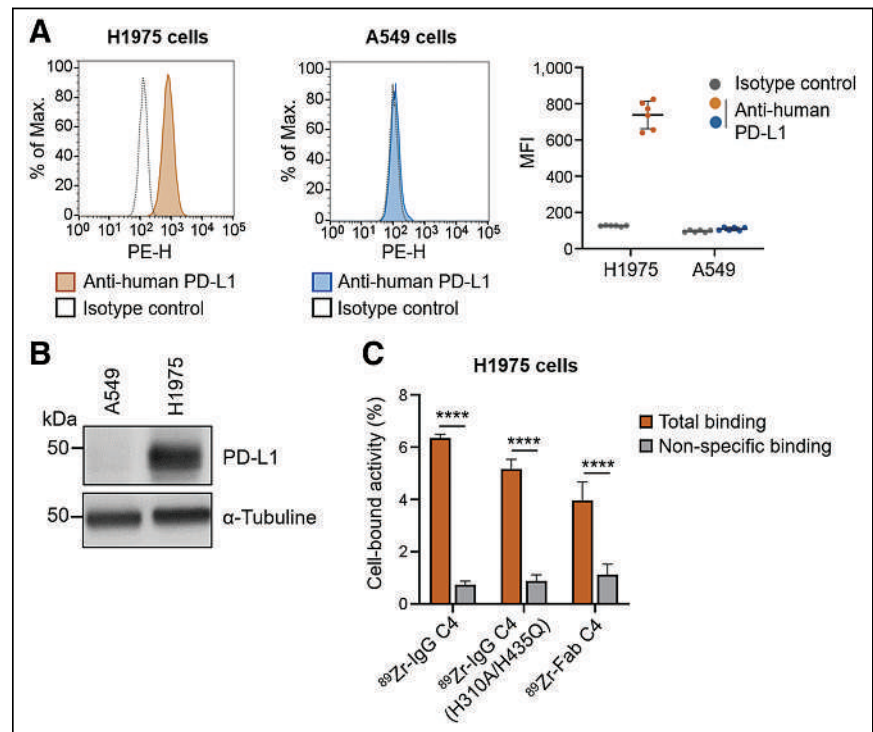

FIGURE 1. Characterization of in vitro PD-L1 expression in human NSCLC cell lines and cell binding assays with C4 radioligands. (A) Representative flow cytometry histograms for cell-surface PD-L1 expression. MFI values are shown on dot plot (6 independent experiments per cell line). (B) Representative immunoblot image showing total PD-L1 expression in whole-cell lysates. (C) Total and nonspecific C4 radioligand binding to PD-L1–positive H1975 cells. Data are mean ± SD, with 6 replicates per condition. Two-tailed paired Student t test was used for data comparison. MFI = median fluorescence intensity; PE-H = phycoerythrin. ****$P < 0.0001$.

TABLE 1
Estimated Blood Pharmacokinetic Parameters

Parameter	^{89}Zr-IgG C4	^{89}Zr-IgG C4 (H310A/H435Q)	^{89}Zr-Fab C4
$t_{1/2\beta}$ (h)	80.25	86.55	1.50
V_c (mL)	2.71	2.41	2.31
CL (mL·h^{-1})	0.047	0.16	2.46
k_{10} (h^{-1})	0.017	0.066	1.06
k_{12} (h^{-1})	0.11	0.08	1.91
k_{21} (h^{-1})	0.12	0.02	1.92
AUC$_{plasma}$ (%ID·h·mL^{-1})	2,137	629	41

$t_{1/2\beta}$ = biologic elimination half-life; V_c = volume of distribution of central compartment; CL = systemic clearance; k_{10} = elimination rate constant from central compartment; k_{12} = distribution rate constant from central to peripheral compartment; k_{21} = distribution rate constant from peripheral to central compartment; AUC$_{plasma}$ = plasmatic exposure.

compartment, as shown by its smaller distribution rate constant from peripheral to central compartment than that of ^{89}Zr-IgG C4.

The 3 C4 radioligands were able to effectively detect PD-L1 expression in H1975 xenografts, but with different tumor uptakes and kinetics (Fig. 2). For ^{89}Zr-IgG C4, optimal PET images were observed at 48 h after injection, with the highest tumor uptake (maximal concentration) being 4.85 $\pm$ 0.61 %ID/cm^3, a maximal tumor-to-muscle ratio of 8.34 $\pm$ 0.63, and a tumor-to-blood ratio of 0.84 $\pm$ 0.35. ^{89}Zr-IgG C4 (H310A/H435Q) tumor accumulation peaked at 24 h after injection, with maximal concentration and maximal tumor-to-muscle ratios similar to those obtained with the ^{89}Zr-IgG C4 (4.60 $\pm$ 0.39 %ID/cm^3 and 9.39 $\pm$ 0.36, respectively) and a tumor-to-blood ratio of 2.20 $\pm$ 1.21. Maximal tumor uptake of ^{89}Zr-Fab C4 was observed even earlier, at 4 h after injection.

However, maximal concentration (1.36 $\pm$ 0.11 %ID/cm^3) and maximal tumor-to-muscle ratio (6.28 $\pm$ 0.24) were substantially lower, even if the tumor-to-blood ratio was still 1.53 $\pm$ 0.85. For the 3 C4 radioligands, H1975 tumor uptake was significantly reduced in mice that received a blocking dose of cold C4 ligand (Fig. 3; Supplemental Table 6), suggesting their PD-L1–specific tumor targeting.

Background activity in most normal tissues was low (Fig. 2). Whereas ^{89}Zr-IgG C4 liver uptake gradually decreased over the imaging time course, ^{89}Zr-IgG C4 (H310A/H435Q) demonstrated high and persistent liver accumulation. The ^{89}Zr-Fab C4 fragment accumulated essentially in the kidneys. This high renal signal retention precluded spleen detection on PET images, and ^{89}Zr-Fab C4 spleen uptake was therefore not quantified.
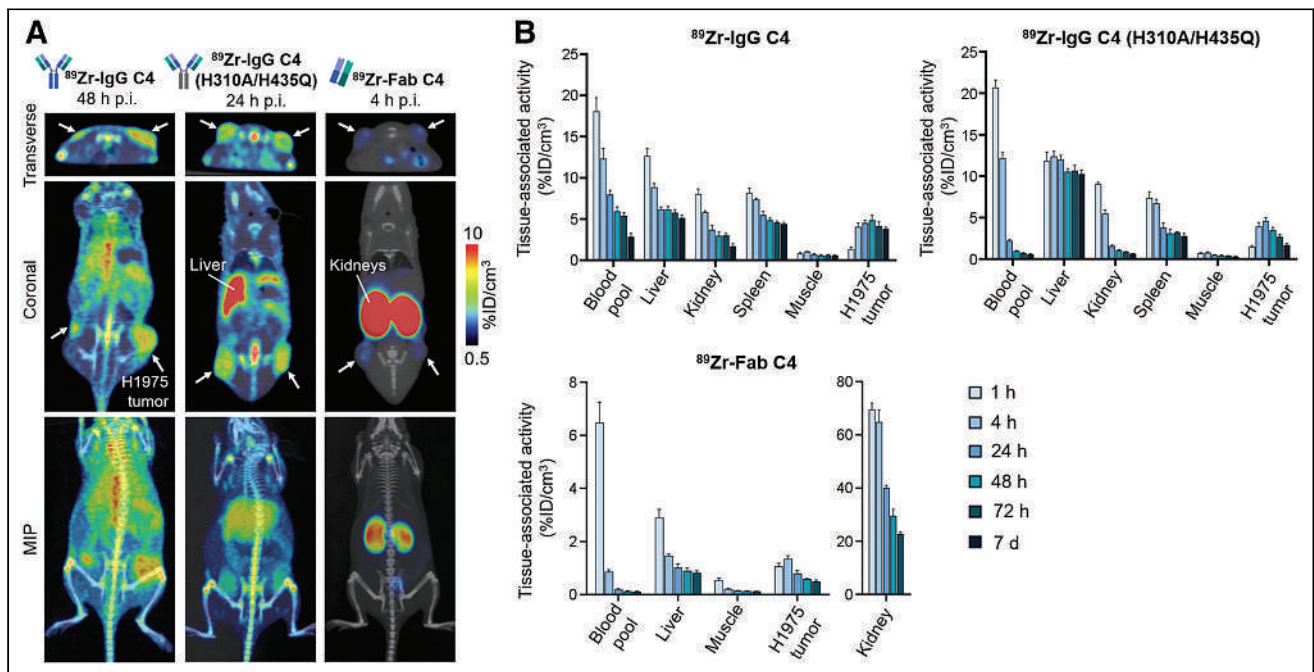

FIGURE 2 Small-animal PET/CT imaging with C4 radioligands in PD-L1–positive human NSCLC xenograft model. (A) Representative small-animal PET/CT image sections and maximum-intensity-projection images of mice bearing PD-L1–positive H1975 xenografts (arrows). (B) Image-derived in vivo biodistribution of C4 radioligands. Data are mean $\pm$ SD, with 6 mice per group. MIP = maximum-intensity projection; p.i. = after injection.
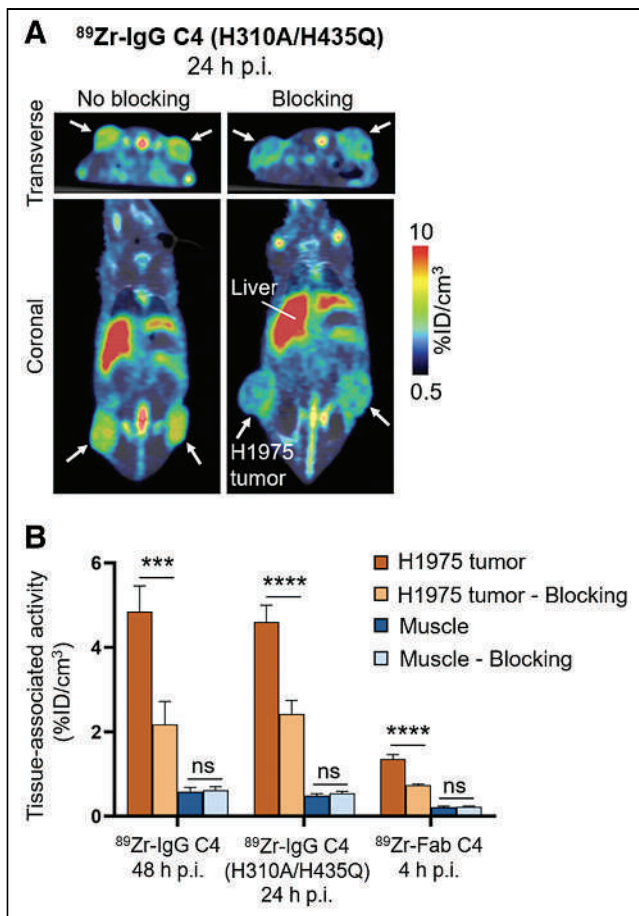
FIGURE 3 PD-L1–specific tumor targeting of C4 radioligands. (A) Representative small-animal PET/CT images of mice bearing PD-L1–positive H1975 xenografts (arrows). (B) Image-derived C4 radioligand uptakes in H1975 tumor and muscle. Data are mean ± SD, with 6 mice per group (no blocking) or 3–4 mice per group (blocking). Two-tailed unpaired Student t test was used for data comparison. ns = not significant. ****$P < 0.0001$.

For each C4 radioligand, human organ-absorbed dose estimates were extrapolated from murine longitudinal biodistribution data. The highest absorbed doses were in the kidneys and adrenals for ^{89}Zr-Fab C4 and in the liver and heart wall for ^{89}Zr-IgG C4 and ^{89}Zr-IgG C4 (H310A/H435Q) (Supplemental Table 7). The estimated effective doses were 0.34 ± 0.03, 0.35 ± 0.02, and 0.26 ± 0.05 mSv/MBq for ^{89}Zr-IgG C4, ^{89}Zr-IgG C4 (H310A/H435Q), and ^{89}Zr-Fab C4, respectively.

Small-Animal PET/CT Imaging with C4 Radioligands in PD-L1–Positive and PD-L1–Negative Human NSCLC Xenograft Models

The ability of ^{89}Zr-IgG C4 to discriminate between various tumor PD-L1 expression levels was previously demonstrated (15). ^{89}Zr-IgG C4 (H310A/H435Q) and ^{89}Zr-Fab C4 effectively accumulated in PD-L1–positive H1975 xenografts but not in PD-L1–negative A549 xenografts (Fig. 4; Supplemental Fig. 8; Supplemental Table 8). For both radioligands, maximal tumor uptake was about 2-fold higher in H1975 tumors than in A549 tumors. PD-L1 immunohistochemistry showed heterogeneous PD-L1 staining in H1975 tumor sections, whereas very little or no PD-L1 staining was detected in A549 tumor sections (Fig. 4). Flow cytometry corroborated the immunohistochemistry results, with PD-L1–associated median fluorescence

intensity values of 223.9 ± 34.7 versus 72.1 ± 2.5 for the H1975 and A549 tumor cells, respectively (Fig. 4; Supplemental Fig. 9). These ex vivo analyses further validated the in vivo PD-L1–specific tumor targeting of ^{89}Zr-IgG C4 (H310A/H435Q) and ^{89}Zr-Fab C4.

DISCUSSION

The 3 C4 radioligand formats exhibited marked differences in kinetics and in vivo biodistribution patterns, but they were all able to detect PD-L1 expression in human NSCLC xenografts. Although rapid elimination of the ^{89}Zr-Fab C4 fragment gave high-contrast images as soon as 4 h after injection, it also resulted in a poor maximal tumor uptake. Nonetheless, this tumor uptake was similar to that obtained in other preclinical studies performing same-day PET imaging with small anti-PD-L1 radioligands, such as the ^{18}F-labeled adnectin BMS-986192 or small-peptide WL12 (20–23). The faster blood clearance of the Fc-mutant ^{89}Zr-IgG C4 also enabled earlier lesion detection than for the wild-type ^{89}Zr-IgG C4. Unlike ^{89}Zr-Fab C4, the decreased background signal was not accompanied by a reduction in tumor uptake, which remained similar to that of ^{89}Zr-IgG C4. In contrast to the monovalent Fab C4, the Fc-mutant IgG C4 retains 2 binding sites, hence maintaining a strong avidity for tumoral PD-L1. Anti-PD-L1 radioligands with low background activity facilitate the detection of low levels of tumoral PD-L1 expression. This is particularly relevant for clinical PD-L1 PET imaging, as patients with only 1% of PD-L1–positive tumor cells can generate higher response rates to anti-PD-1/PD-L1 immunotherapies than patients with PD-L1–negative tumors (6). Moreover, the H310A/H435Q double mutation has a translational interest because IgG1 binding to human FcRn also involves the conserved H310 and H435 residues (10,14).

Liver accumulation of the ^{89}Zr-labeled IgG C4 was consistent with primary clearance of antibodies through the hepatobiliary system. The increased liver retention obtained with the Fc-mutant ^{89}Zr-IgG C4 was also observed in other preclinical studies that altered the interaction of ^{111}In-labeled IgG1s with the murine FcRn (13,24,25). For instance, Yip et al. generated a mutated variant (H310Q) of a humanized IgG1 with greatly decreased binding affinity to murine FcRn. In immunocompetent mice, liver radioactivity uptake of the ^{111}In-IgG1 (H310Q) at 24 h after injection was about twice higher than that of the parental ^{111}In-IgG1 (13). These results suggested that, in the absence of FcRn protection, the liver emerged as a major site of IgG catabolism in mice.

The ^{89}Zr-Fab C4 fragment was small enough to undergo primarily renal clearance (26). The intense signal retention in the kidneys may be due to reabsorption of the radiolabeled Fab C4 fragment by proximal tubular cells after glomerular filtration. Several strategies have been implemented to reduce such renal accumulation of small radioligands, including coinfusion of basic amino acids that compete with the radioligand for tubular reabsorption (27). PET imaging with the ^{89}Zr-Fab C4 fragment may be particularly adapted for detection of PD-L1 expression in tumor lesions within abdominal organs—lesions that would otherwise be obstructed by the liver clearance signal of the ^{89}Zr-IgGs C4. This is especially relevant for PD-L1 immuno-PET imaging in NSCLC patients, as they are often diagnosed at advanced stages with multiple distant metastases already spread. Approximately 17% of NSCLC patients will develop metastasis in the liver (28).

Because we used immunocompromised mice in this study, the impact of endogenous PD-L1 expression in normal tissues (e.g., lymphoid tissues such as the spleen) on biodistribution and tumor
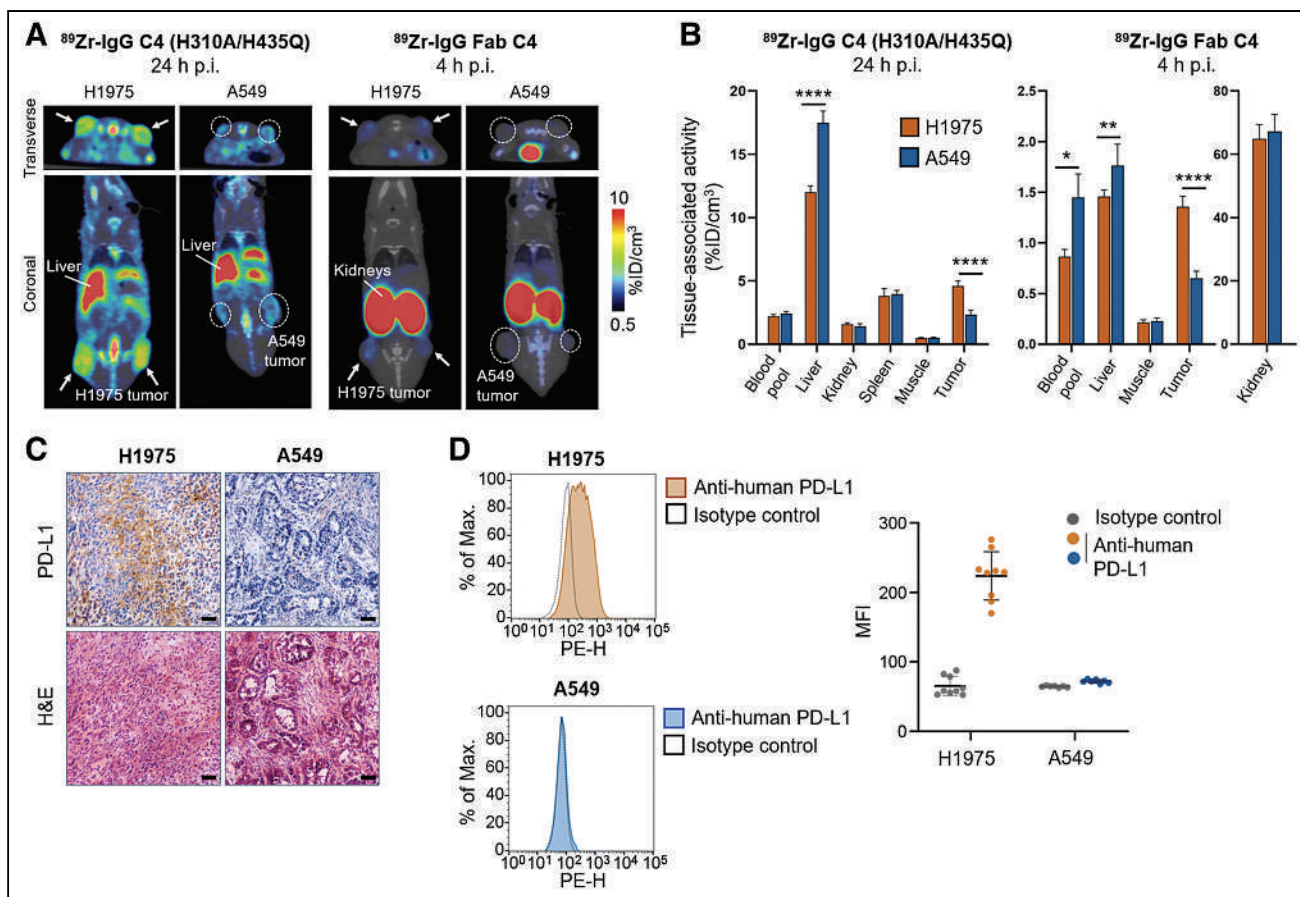
FIGURE 4 Small-animal PET/CT imaging with C4 radioligands in human NSCLC xenograft models with positive or negative PD-L1 expression. (A) Representative small-animal PET/CT images of mice bearing PD-L1–positive H1975 xenografts (arrows) and PD-L1–negative A549 xenografts (dotted circles). (B) Image-derived in vivo biodistribution of C4 radioligands. Data are mean ± SD, with 5–6 mice per group. Two-tailed unpaired Student t test was used for data comparison. (C) Representative images of tumor sections after PD-L1 immunohistochemistry and hematoxylin and eosin staining after imaging. Scale bars = 50 μm. (D) Representative flow cytometry histograms for cell-surface PD-L1 expression on tumor-derived single-cell suspensions. MFI values are shown on dot plot (9 H1975 tumors, 7 A549 tumors). H&E = hematoxylin and eosin; MFI = median fluorescence intensity; PE-H = phycoerythrin; p.i. = after injection. *$P < 0.05$. **$P < 0.01$. ****$P < 0.0001$.

targeting of the C4 radioligands could not be properly evaluated. Thanks to its cross-reactivity with murine PD-L1, the ^{89}Zr-labeled IgG C4 has already been evaluated in a syngeneic mouse model of melanoma (B16-F10) (15). Surprisingly, no notable differences in radioligand uptake within normal tissues were observed between the B16-F10 tumor–bearing immunocompetent mice and the H1975 tumor–bearing immunocompromised mice.

The estimated human effective doses for the 3 C4 radioligands were in the same range as the values obtained in clinical immuno-PET studies using other ^{89}Zr-labeled antibodies. Administration of 37 MBq in patients, as already performed in a clinical study with ^{89}Zr-atezolizumab (8), would result in effective doses of about 13 mSv for the ^{89}Zr-IgG C4 and of about 10 mSv for the ^{89}Zr-Fab C4. By comparison, the effective dose of a ^{18}F-FDG PET scan is about 6–7 mSv (29). The favorable dosimetry of the C4 radioligands may enable repeated PD-L1 immuno-PET imaging, as would be required for treatment response monitoring. Moreover, thanks to its faster pharmacokinetics, the Fab C4 may be radiolabeled with a shorter-lived PET isotope such as ^{18}F, which would minimize the patient radiation burden.

CONCLUSION

The ^{89}Zr-labeled Fab C4 fragment and Fc-mutant IgG C4 enabled specific and efficient detection of PD-L1 expression in a human NSCLC xenograft model at earlier time points than for the parental ^{89}Zr-labeled IgG C4. This study demonstrated the feasibility of designing anti-PD-L1 radioligands with enhanced imaging characteristics for PD-L1 immuno-PET imaging in preclinical models and supports the clinical translation of such engineering approaches.

KEY POINTS

QUESTION: How can immuno-PET imaging of PD-L1 expression be optimized in NSCLC patients?

PERTINENT FINDINGS: A Fab fragment and a double-mutant IgG (H310A/H435Q) with minimal affinity for murine FcRn were derived from the anti-PD-L1 IgG1 C4. The [89]Zr-labeled Fab C4 and IgG C4 (H310A/H435Q) enabled effective detection of PD-L1 expression by PET imaging in a human NSCLC xenograft model, at earlier time points than for the parental [89]Zr-labeled IgG C4.

IMPLICATIONS FOR PATIENT CARE: These results highlight the possibility of designing anti-PD-L1 PET radioligands with optimized pharmacokinetic properties, to better predict and monitor responses to anti-PD-1/anti-PD-L1 immunotherapies with PD-L1 immuno-PET.

REFERENCES

1. Constantinidou A, Alifieris C, Trafalis DT. Targeting programmed cell death-1 (PD-1) and ligand (PD-L1): a new era in cancer active immunotherapy. *Pharmacol Ther.* 2019;194:84–106.

2. Yang C-Y, Yang JC-H, Yang P-C. Precision management of advanced non–small cell lung cancer. *Annu Rev Med.* 2020;71:117–136.

3. Sun C, Mezzadra R, Schumacher TN. Regulation and function of the PD-L1 checkpoint. *Immunity.* 2018;48:434–452.

4. Nishino M, Ramaiya NH, Hatabu H, Hodi FS. Monitoring immune-checkpoint blockade: response evaluation and biomarker development. *Nat Rev Clin Oncol.* 2017;14:655–668.

5. Passiglia F, Bronte G, Bazan V, et al. PD-L1 expression as predictive biomarker in patients with NSCLC: a pooled analysis. *Oncotarget.* 2016;7:19738–19747.

6. Herbst RS, Baas P, Kim D-W, et al. Pembrolizumab versus docetaxel for previously treated, PD-L1-positive, advanced non-small-cell lung cancer (KEYNOTE-010): a randomised controlled trial. *Lancet.* 2016;387:1540–1550.

7. Bouleau A, Lebon V, Truillet C. PET imaging of immune checkpoint proteins in oncology. *Pharmacol Ther.* 2021;222:107786.

8. Bensch F, van der Veen EL, Lub-de Hooge MN, et al. [89]Zr-atezolizumab imaging as a non-invasive approach to assess clinical response to PD-L1 blockade in cancer. *Nat Med.* 2018;24:1852–1858.

9. Niemeijer AN, Leung D, Huisman MC, et al. Whole body PD-1 and PD-L1 positron emission tomography in patients with non-small-cell lung cancer. *Nat Commun.* 2018;9:4664.

10. Pyzik M, Sand KMK, Hubbard JJ, Andersen JT, Sandlie I, Blumberg RS. The neonatal Fc receptor (FcRn): a misnomer? *Front Immunol.* 2019;10:1540.

11. Kim J-K, Firan M, Radu CG, Kim C-H, Ghetie V, Ward ES. Mapping the site on human IgG for binding of the MHC class I-related receptor, FcRn. *Eur J Immunol.* 1999;29:2819–2825.

12. Kenanova V, Olafsen T, Crow DM, et al. Tailoring the pharmacokinetics and positron emission tomography imaging properties of anti–carcinoembryonic antigen single-chain Fv-Fc antibody fragments. *Cancer Res.* 2005;65:622–631.

13. Yip V, Palma E, Tesar DB, et al. Quantitative cumulative biodistribution of antibodies in mice: effect of modulating binding affinity to the neonatal Fc receptor. *MAbs.* 2014;6:689–696.

14. Burvenich IJG, Parakh S, Lee F-T, et al. Molecular imaging of T cell co-regulator factor B7-H3 with [89]Zr-DS-5573a. *Theranostics.* 2018;8:4199–4209.

15. Truillet C, Oh HLJ, Yeo SP, et al. Imaging PD-L1 expression with immunoPET. *Bioconjug Chem.* 2018;29:96–103.

16. Smith K, Garman L, Wrammert J, et al. Rapid generation of fully human monoclonal antibodies specific to a vaccinating antigen. *Nat Protoc.* 2009;4:372–384.

17. Vosjan MJWD, Perk LR, Visser GWM, et al. Conjugation and radiolabeling of monoclonal antibodies with zirconium-89 for PET imaging using the bifunctional chelate p-isothiocyanatobenzyl-desferrioxamine. *Nat Protoc.* 2010;5:739–743.

18. Andersson M, Johansson L, Eckerman K, Mattsson S. IDAC-Dose 2.1, an internal dosimetry program for diagnostic nuclear medicine based on the ICRP adult reference voxel phantoms. *EJNMMI Res.* 2017;7:88.

19. Locatelli M, Miloudi H, Autret G, et al. RODES software for dose assessment of rats and mice contaminated with radionuclides. *J Radiol Prot.* 2017;37:214–229.

20. Wei J, Wang Y, Lee CY, et al. An analysis of isoclonal antibody formats suggests a role for measuring PD-L1 with low molecular weight PET radiotracers. *Mol Imaging Biol.* 2020;22:1553–1561.

21. Donnelly DJ, Smith RA, Morin P, et al. Synthesis and biologic evaluation of a novel ^{18}F-labeled adnectin as a PET radioligand for imaging PD-L1 expression. *J Nucl Med.* 2018;59:529–535.

22. Stutvoet TS, van der Veen EL, Kol A, et al. Molecular imaging of PD-L1 expression and dynamics with the adnectin-based PET tracer ^{18}F-BMS-986192. *J Nucl Med.* 2020;61:1839–1844.

23. Lesniak WG, Mease RC, Chatterjee S, et al. Development of [^{18}F]FPy-WL12 as a PD-L1-Specific PET imaging peptide. *Mol Imaging.* 2019;18:1536012119852189.

24. Jaggi JS, Carrasquillo JA, Seshan SV, et al. Improved tumor imaging and therapy via i.v. IgG–mediated time-sequential modulation of neonatal Fc receptor. *J Clin Invest.* 2007;117:2422–2430.

25. Kenanova V, Olafsen T, Williams LE, et al. Radioiodinated versus radiometal-labeled anti–carcinoembryonic antigen single-chain Fv-Fc antibody fragments: optimal pharmacokinetics for therapy. *Cancer Res.* 2007;67:718–726.

26. Xenaki KT, Oliveira S. van Bergen en Henegouwen PMP. Antibody or antibody fragments: implications for molecular imaging and targeted therapy of solid tumors. *Front Immunol.* 2017;8:1287.

27. Vegt E, de Jong M, Wetzels JFM, et al. Renal toxicity of radiolabeled peptides and antibody fragments: mechanisms, impact on radionuclide therapy, and strategies for prevention. *J Nucl Med.* 2010;51:1049–1058.

28. Zhu T, Bao X, Chen M, et al. Mechanisms and future of non-small cell lung cancer metastasis. *Front Oncol.* 2020;10:585284.

29. Martí-Climent JM, Prieto E, Morán V, et al. Effective dose estimation for oncological and neurological PET/CT procedures. *EJNMMI Res.* 2017;7:37.

Efficient Delay Correction for Total-Body PET Kinetic Modeling Using Pulse Timing Methods

Elizabeth J. Li[1], Benjamin A. Spencer[1], Jeffrey P. Schmall[2], Yasser Abdelhafez[3], Ramsey D. Badawi[1,3], Guobao Wang[3], and Simon R. Cherry[1,3]

[1]Department of Biomedical Engineering, University of California Davis, Davis, California; [2]United Imaging Healthcare America, Inc., Houston, Texas; and [3]Department of Radiology, UC Davis Health, Sacramento, California

Quantitative kinetic modeling requires an input function. A noninvasive image-derived input function (IDIF) can be obtained from dynamic PET images. However, a robust IDIF location (e.g., aorta) may be far from a tissue of interest, particularly in total-body PET, introducing a time delay between the IDIF and the tissue. The standard practice of joint estimation (JE) of delay, along with model fitting, is computationally expensive. To improve the efficiency of delay correction for total-body PET parametric imaging, this study investigated the use of pulse timing methods to estimate and correct for delay. **Methods:** Simulation studies were performed with a range of delay values, frame lengths, and noise levels to test the tolerance of 2 pulse timing methods—leading edge (LE) and constant fraction discrimination and their thresholds. The methods were then applied to data from 21 subjects (14 healthy volunteers, 7 cancer patients) who underwent a 60-min dynamic total-body ^{18}F-FDG PET acquisition. Region-of-interest kinetic analysis was performed and parametric images were generated to compare LE and JE methods of delay correction, as well as no delay correction. **Results:** Simulations demonstrated that a 10% LE threshold resulted in biases and SDs at tolerable levels for all noise levels tested, with 2-s frames. Pooled region-of-interest–based results ($n = 154$) showed strong agreement between LE (10% threshold) and JE methods in estimating delay (Pearson $r = 0.96$, $P < 0.001$) and the kinetic parameters v_b ($r = 0.96$, $P < 0.001$), K_i ($r = 1.00$, $P < 0.001$), and K_1 ($r = 0.97$, $P < 0.001$). When tissues with minimal delay were excluded from pooled analyses, there were reductions in v_b (69.4%) and K_1 (4.8%) when delay correction was not performed. Similar results were obtained for parametric images; additionally, lesion K_i contrast was improved overall with LE and JE delay correction compared with no delay correction and Patlak analysis. **Conclusion:** This study demonstrated the importance of delay correction in total-body PET. LE delay correction can be an efficient surrogate for JE, requiring a fraction of the computational time and allowing for rapid delay correction across more than 10^6 voxels in total-body PET datasets.

Key Words: dynamic PET; input function; delay correction; total-body PET

An input function (IF) is required for fully quantitative PET kinetic modeling and can be derived through arterial blood sampling (*1*). However, arterial blood sampling is invasive and technically challenging and can introduce errors in the measured IF arrival time and bolus shape, which may result in biased kinetic parameter estimates when left uncorrected (*2–4*). An image-derived IF (IDIF) can be sampled from the images directly, reducing errors in arrival time and removing the external dispersion introduced by arterial blood sampling. Still, the delay between the IF peak and arrival time at a tissue or voxel of interest must be considered.

The advent of high-efficiency scanners with a long axial field of view, such as the uEXPLORER (United Imaging) total-body PET system (*5,6*), presents the opportunity for high signal-to-noise total-body kinetic modeling. Short frames with high count statistics are possible for improved estimation of parameters such as delay. Additionally, an IDIF can be derived from the larger vessels, where partial-volume effects are reduced. However, with total-body PET, delay correction becomes more important because the IDIF will be farther from a tissue of interest than a more localized IDIF (e.g., carotid IDIF for gray matter) and incorrect delay estimates may lead to parameter bias (*2–4*). Because different tissues will also have their own unique delay values, delay correction must be performed for every voxel or regional time–activity curve.

Common methods of delay correction include setting the delay to a predetermined value (*2,7*), adjusting the IF on the basis of an IDIF near the tissue of interest (*2,8*), or jointly estimating the delay during the fitting process (*4,9,10*). However, the widely used joint estimation (JE) method is costly in terms of computation time, especially for voxel-level total-body PET, because it involves nonlinear fitting of kinetic parameters for all possible delay values. Therefore, a much faster method for estimating bolus delay would be beneficial. Applications in which voxel-level parametric imaging is important include the detection and quantification of metastatic lesions, as well as disease processes that result in heterogeneous tracer delivery and uptake within a tissue or organ.

Here, we draw our inspiration from pulse timing methods—including the leading edge (LE) method and the constant fraction discrimination (CFD) method—that are used to efficiently determine the arrival time of electronic pulses from a radiation detector (*11*). In this work, LE and CFD pulse timing methods were applied to time–activity curves rather than electronic pulses. Delay was defined as $t_d - t_0$, which is the difference between the arrival times of the bolus in the region chosen to define the IF (t_0) and of a tissue or voxel time–activity curve determined using one of the pulse timing methods (t_d). Implementation of pulse timing methods would greatly reduce the computational burden of the fitting process for a given kinetic model, since the nonlinear least-squares fitting process can be performed for a single delay value, as determined by these methods. Although these methods are computationally efficient, the choice of parameters (LE trigger threshold, CFD attenuation values)

can impact delay estimation. Therefore, we investigated the use of pulse timing methods for time delay estimation and correction for quantitative total-body kinetic modeling and parametric imaging.

MATERIALS AND METHODS

Simulations

Computer simulations of time–activity curve data were developed to evaluate the bias and SD of delay estimation approaches. A high-temporal-resolution IF (0.1-s sampling) representing a bolus of ^{18}F-FDG was generated on the basis of the triexponential function proposed by Feng et al. (12,13). The IF was shifted by 100 randomly selected delay values between 0 and 50 s. Brain gray matter time–activity curves were simulated on the basis of these delayed IFs and typical kinetic parameters (v_b = 0.05, K_1 = 0.06 mL/min/mL, k_2 = 0.07 min^{-1}, k_3 = 0.07 min^{-1}, and k_4 = 0 min^{-1}) from Huisman et al. (14). For each delay value, 500 noisy realizations were generated using a commonly applied time-changing gaussian noise model (15) with a mean equal to the initial activity in frame m (TAC$_m$) and SD equal to the scaling factor S_c times the unscaled SD, δ_m:

$$\text{TAC}_m \sim \text{gaussian}\left(\overline{\text{TAC}_m}, S_c\delta_m\right), \quad \delta_m = \sqrt{\frac{\overline{\text{TAC}_m} \cdot \exp(\lambda t_m)}{\Delta t_m}},$$

where δ_m is dependent on the radioisotope decay constant λ, frame midpoint t_m, frame length Δt_m, and mean activity $\overline{\text{TAC}_m}$ in frame m. The scale S_c was set to 4 noise levels of 0.03, 0.1, 0.2, and 0.3 to encompass time–activity curves with different statistical quality. To mimic zero-mean noise present in measured time–activity curves before bolus arrival, the activity included in δ_m was modified to have a mean of 0.5% of the maximum activity:

$$\text{TAC}_{\text{early},m} \sim \text{gaussian}(0, S_c\delta_m), \quad \delta_m = \sqrt{\frac{0.005 \cdot \max(\overline{\text{TAC}}) \cdot \exp(\lambda t_m)}{\Delta t_m}}.$$

Time–activity curves were then rebinned to frame lengths of 1, 2, 5, and 10 s and used to assess the impact of framing on delay estimates. Supplemental Figure 1A shows an example time–activity curve with S_c equal to 0.1 (supplemental materials are available at http://jnm.snmjournals.org).

For the LE method (11), a trigger threshold was selected and the time at which the signal amplitude passed that threshold was recorded as the arrival time. LE thresholds were set across a wide range (2.5%–50%) of the peak activity in the first 120 s. A 10% LE threshold is shown in Supplemental Figure 1B. For the CFD method (11), the time–activity curves were shifted in time by 2 s for shorter framing, or by 1 frame for frames longer than 2 s. Attenuated and inverted versions of the time–activity

curve (attenuated to between 2.5% and 50% of the peak activity) were added to the shifted time–activity curve, and the resulting zero-crossing point marked the arrival time (Supplemental Fig. 1C). LE- and CFD-based estimates for each combination of delay value, frame length, noise level, and percentage peak activity were determined. The average bias and SD of the LE and CFD delay estimates were determined by comparing the estimates with the ground truth. On the basis of the results of these simulations, only the LE method was subsequently applied to human data.

Human Data

Institutional Review Board approval and written informed consent were obtained for 14 healthy volunteers (6 male, 8 female; body mass index, 19.4–37.0 kg/m^2; age range, 26–78 y) and 7 male subjects with genitourinary cancer (GUC) (body mass index, 20.1–32.0 kg/m^2; age range, 56–76 y). The subjects were injected with an average dose of 357.8 MBq of ^{18}F-FDG (range, 331.9–391.8 MBq) and underwent 60-min dynamic studies on the uEXPLORER scanner (16). Images were reconstructed with vendor-provided time-of-flight ordered-subsets expectation maximization software (20 subsets, 4 iterations, 150 × 150 × 486 image matrix size, 4-mm isotropic voxels) with corrections for attenuation, scatter, randoms, dead time, and decay (17). No point-spread function modeling was applied. For generating parametric images, image data were smoothed using a composite image prior and the kernel method (18). The following framing protocol was used to generate 66 time points: 30 × 2 s, 12 × 10 s, 6 × 30 s, 12 × 120 s, and 6 × 300 s.

For all human data, an IDIF was derived from a region of interest (ROI) in the left ventricle. Tissue compartment model selection was incorporated to account for tissue spaces where ^{18}F-FDG undergoes minimal metabolism, such as the blood pool. Model selection was performed for a range of tissue ROIs and voxel time–activity curves by fitting a 0-tissue 1-parameter (where v_b was the only nonzero parameter), a 1-tissue 3-parameter, and an irreversible 2-tissue 4-parameter model (k_4 = 0); the model with the lowest Akaike information criterion was chosen. For comparison, parametric Patlak plots (19) were generated with and without using the JE delay estimates from model selection. All results were obtained using a nonlinear least-squares fitting process as described previously (20). Initialization parameters are included in Supplemental Table 1. To assess the impact of delay correction methods, delay was estimated jointly (JE), via the LE method, or not at all (no delay correction). The first 36 dynamic frames, representing the first 120 s of the acquisition, were used to jointly estimate delay before fitting all 66 time points for estimation of the rest of the parameters. For ROI-based analysis, the same LE thresholds used in simulations (between 2.5% and 50% of the peak activity in the first 2 min) were used to determine the IDIF bolus arrival time (t_0) and the arrival time at the tissue (t_d). Both JE and LE estimates of delay ($t_d - t_0$) were estimated in 1-s
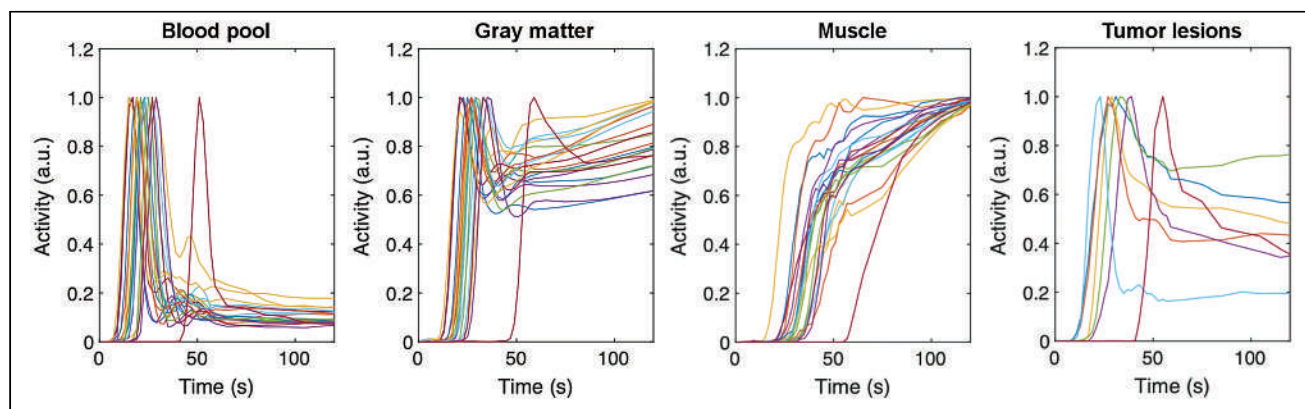

FIGURE 1. Normalized time–activity curves in several healthy-subject and GUC patient tissues. Although injection bolus shape was consistent across pooled human subjects, injection time relative to start of scan, delay in arrival time at individual tissues, and initial lesion uptake differed. Single lesion per GUC patient is shown for ease of visualization. a.u. = arbitrary units.
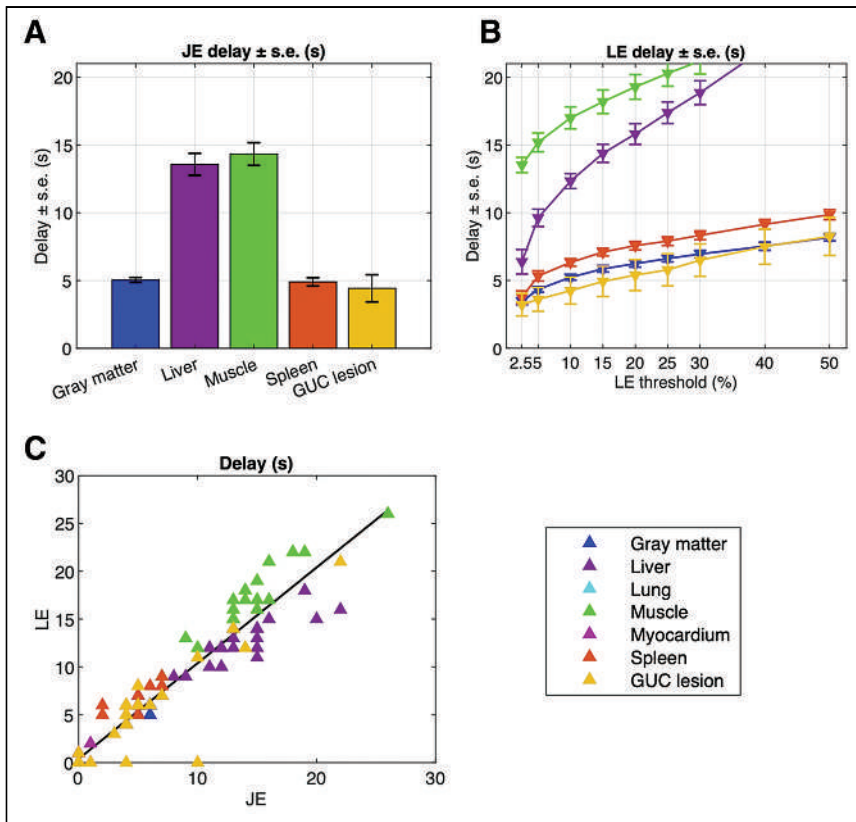
FIGURE 2. (A) Average JE delay estimates with SE. (B) LE estimates at thresholds ranging from 2.5% to 50% for different ROIs. As LE threshold increases, estimates of LE delay exhibit timing walk for tissues with longer rise times such as liver and muscle. On the basis of A and B, threshold of 10% was selected for further kinetic analyses. (C) Agreement between LE method and JE estimates of delay ($r = 0.96$; $P < 0.001$; slope, 1.00) with 10% threshold across all regions.

steps and were constrained to be between 0 and 50 s. The conventional JE method was considered ground truth, such that the optimal LE threshold could be determined across a variety of ROIs. After determining the optimal LE threshold, a single LE threshold was used for kinetic modeling, and the quality of ROI-based and parametric image–derived parameter estimates was assessed using Pearson r.

ROIs were identified in 6 tissue types (gray matter, liver, lungs, muscle, myocardium, and spleen) and in the left ventricle blood pool. An additional 28 GUC lesions were delineated on the basis of a threshold of 41% of SUV_{max}, as recommended by Boellaard et al. (21). All ROIs were manually corrected for subject motion. ROIs were delineated using PMOD (PMOD Technologies).

To highlight a variety of tissue types for prototyping of the method, parametric maps of delay and other kinetic parameters (v_b, K_1, K_i) were generated with both JE and LE methods using the entire image volumes of 1 representative healthy subject and 1 GUC subject. The tissue ROIs were used to generate tissue-specific voxel-wise parameter estimates from the parametric images (Supplemental Fig. 2). A vascular ROI was also included to assess the impact of delay within the blood pool in the parametric images.

RESULTS

Simulations

Delay estimates were determined for different framing schemes and noise levels (e.g.,

TABLE 1
Estimated Kinetic Parameters Obtained from Pooled Regions

Parameter	JE	LE	r^*, JE vs. LE	No delay correction	r^*, JE vs. no delay correction
All regions ($n = 154$)					
v_b	0.070 (0.079)	0.076 (0.080)	0.96	0.050 (0.078)	0.86
K_1	0.553 (0.629)	0.529 (0.584)	0.97	0.541 (0.622)	0.89
K_i	0.012 (0.017)	0.012 (0.017)	1.00	0.012 (0.017)	1.00
Delay	5.981 (6.073)	6.377 (6.331)	0.96	0 (0)	NA
k_2	1.213 (1.292)	1.171 (1.277)	0.94	1.205 (1.348)	0.85
k_3	0.039 (0.069)	0.037 (0.057)	0.97	0.040 (0.063)	0.96
Regions[†] with positive delay ($n = 112$)					
v_b	0.036 (0.056)	0.044 (0.061)	0.91	0.011 (0.036)	0.57
K_1	0.600 (0.677)	0.569 (0.618)	0.98	0.571 (0.656)	0.88
K_i	0.011 (0.014)	0.011 (0.014)	1.00	0.011 (0.015)	0.99
Delay	8.205 (5.701)	8.732 (5.888)	0.94	0 (0)	NA
k_2	1.133 (1.230)	1.084 (1.188)	0.95	1.085 (1.233)	0.79
k_3	0.035 (0.064)	0.032 (0.046)	0.96	0.036 (0.057)	0.94

[*]$P < 0.001$.
[†]Excludes lung and myocardium.
NA = not available.
Data are mean followed by SD in parentheses.

TABLE 2
Estimated Kinetic Parameters for Healthy Subjects ($n = 14$) and GUC Patients ($n = 7$)

Parameter	JE	LE	r^*
Gray matter			
v_b	0.030 (0.006)	0.030 (0.006)	0.98
K_1	0.107 (0.017)	0.107 (0.018)	1.00
K_i	0.031 (0.007)	0.031 (0.007)	1.00
Delay	5.048 (0.805)	5.238 (0.944)	0.77
k_2	0.165 (0.027)	0.163 (0.029)	0.95
k_3	0.067 (0.012)	0.066 (0.013)	0.99
Liver			
v_b	0.001 (0.003)	0.001 (0.005)	NS
K_1	0.660 (0.286)	0.636 (0.291)	0.98
K_i	0.002 (0.002)	0.002 (0.001)	0.81
Delay	13.571 (3.723)	12.333 (2.536)	0.87
k_2	0.765 (0.374)	0.737 (0.381)	0.98
k_3	0.002 (0.002)	0.002 (0.002)	0.84
Lung			
v_b	0.128 (0.039)	0.128 (0.039)	1.00
K_1	0.023 (0.012)	0.023 (0.012)	1.00
K_i	0.000 (0.000)	0.000 (0.000)	1.00
Delay	0.000 (0.000)	0.000 (0.000)	NA
k_2	0.205 (0.090)	0.205 (0.090)	1.00
k_3	0.001 (0.004)	0.001 (0.004)	1.00
Muscle			
v_b	2.3E-4 (4.7E−4)	0.001 (0.001)	0.69
K_1	0.026 (0.012)	0.026 (0.012)	1.00
K_i	0.002 (0.000)	0.002 (0.000)	1.00
Delay	14.333 (3.812)	17.000 (3.715)	0.94
k_2	0.249 (0.142)	0.249 (0.136)	1.00
k_3	0.016 (0.006)	0.016 (0.006)	1.00
Myocardium			
v_b	0.190 (0.063)	0.192 (0.068)	0.98
K_1	0.832 (0.307)	0.820 (0.356)	0.81
K_i	0.029 (0.024)	0.028 (0.024)	1.00
Delay	0.095 (0.301)	0.190 (0.512)	NS
k_2	2.651 (1.044)	2.597 (1.215)	0.78
k_3	0.099 (0.088)	0.098 (0.088)	1.00
Spleen			
v_b	0.044 (0.025)	0.083 (0.029)	NS
K_1	1.593 (0.556)	1.458 (0.467)	0.99
K_i	0.003 (0.001)	0.003 (0.001)	0.99
Delay	4.905 (1.411)	6.333 (1.278)	0.71
k_2	2.867 (0.980)	2.709 (0.882)	1.00
k_3	0.006 (0.003)	0.006 (0.003)	0.99
GUC lesions ($n = 28$)			
v_b	0.089 (0.086)	0.089 (0.092)	0.93
K_1	0.609 (0.614)	0.605 (0.573)	0.92
K_i	0.017 (0.016)	0.018 (0.016)	0.99
Delay	4.429 (5.295)	4.250 (5.254)	0.90
k_2	1.496 (1.213)	1.443 (1.272)	0.79
k_3	0.071 (0.114)	0.062 (0.074)	0.97

*$P < 0.001$.
NA = not available; NS = not significant.
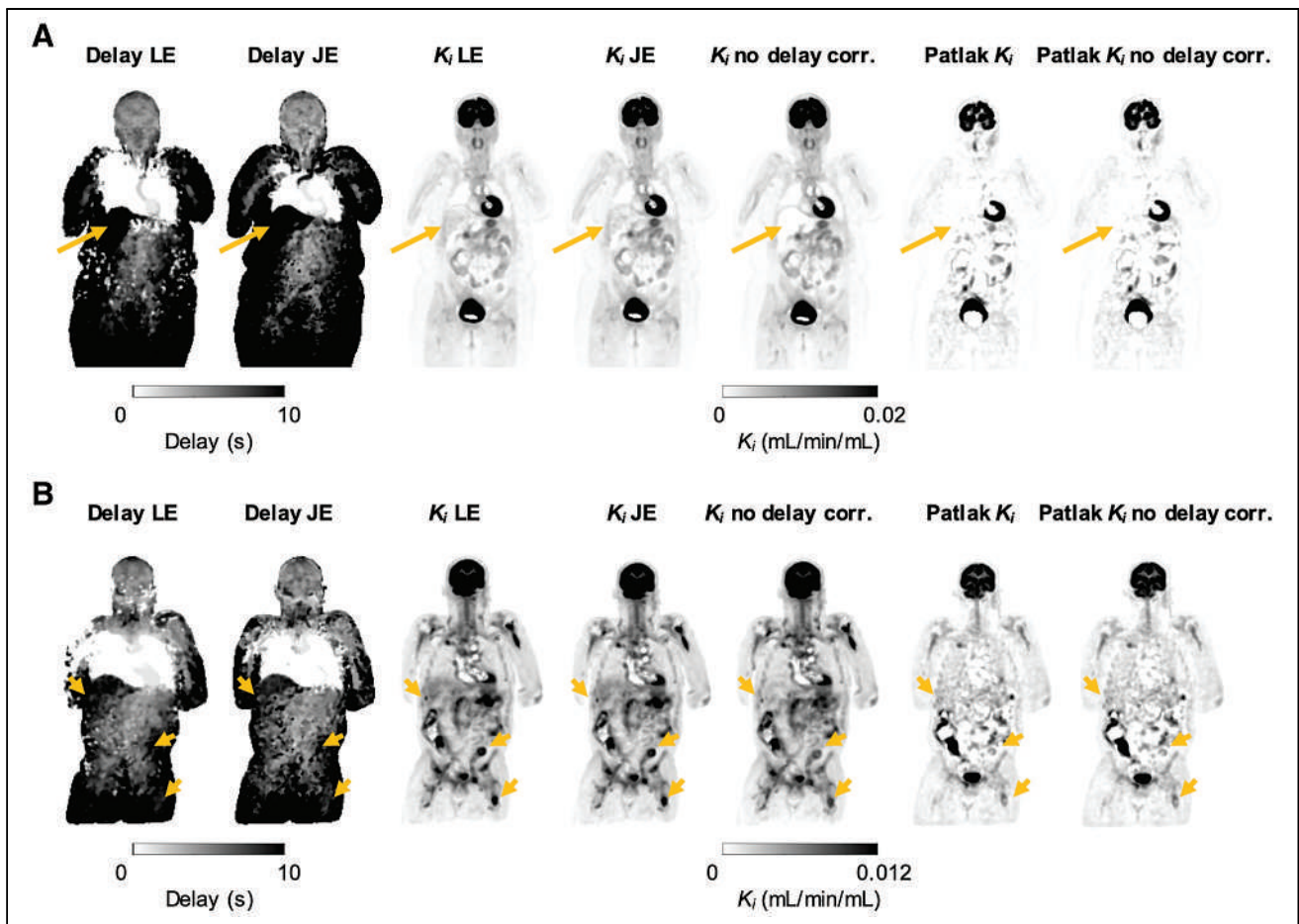Data are mean followed by SD in parentheses.

FIGURE 3. Maximum-intensity-projection parametric images of delay and K_i for representative healthy subject (A) and GUC patient (B). Images were generated using 4 coronal slices (1.6 cm thick). Ten percent LE threshold-derived delay maps showed some differences from JE delay maps, particularly near injection site, but were broadly in agreement across rest of body. Compartment modeling–based K_i maps were similar with JE and LE methods of delay correction, and both methods resulted in improved liver signal (A, arrows) and lesion contrast (B, arrows) compared with Patlak results or compared with no delay correction.

Supplemental Fig. 1). From the wide range of LE thresholds and CFD attenuation fractions tested, LE results indicated that higher noise levels resulted in only marginal increases in bias and SD, particularly with 2-s frames and an LE threshold of less than 15%, whereas CFD bias and SD increased with higher noise levels for attenuation fractions of 15% or less (Supplemental Table 2). With 2-s frames, there was less than a 1-s bias in delay for all LE thresholds of 10% or greater, and a 30% LE threshold led to the lowest bias in delay (0.11–0.18 s, Supplemental Table 2, bold). As frame length increased from 2 to 10 s, the effect of frame length dominated the bias, particularly at higher LE thresholds and higher CFD attenuation fractions. This effect was mitigated for LE results by increasing the LE threshold to 25% or greater, which reduced bias to less than 5 s for all noise levels. With a 30% LE threshold, absolute biases for 10-s frames were between 3.80 and 3.96 s for all noise levels tested. The CFD method was not investigated further because of its poorer performance on noisy simulated data and reliance on a user-chosen time shift, traditionally based on waveform rise time (*11*). The LE method does not rely directly on the rise time, making it the more practical method for total-body PET human subject data. Supplemental Table 3 expands on the LE results, showing data for additional frame lengths. The impact of frame length dominated the bias estimates for large (5- and 10-s)

frames; the bias estimates were within 0.5 s of each other across the different noise levels at the same LE threshold.

Although an LE threshold of 25% was the most insensitive to noise level, and a threshold of 30% resulted in the lowest biases and SD for 2-s frames, the simulations focused solely on a gray matter time–activity curve with an ideal bolus injection. Therefore, to assess the performance of the LE method on different tissue types with varying kinetics and the effect of timing walk on LE estimates in slowly rising time–activity curves (e.g., liver), a variety of LE thresholds was tested in human ROI-based analyses.

Human ROI-Based Analysis

Tissue-specific time–activity curves were consistent across organ type among subjects (Fig. 1; Supplemental Fig. 3). The subset of the 28 lesion time–activity curves shown in Figure 1 demonstrates the heterogeneity of tracer arrival time and metabolism. Since there were no noticeable differences between healthy-subject and GUC-patient time–activity curves, ROI-based parameter estimates were pooled across the 14 healthy subjects and 7 GUC patients. Average JE and LE delay estimates, with their standard errors (Figs. 2A and 2B), demonstrated the impact of slower time–activity curve rise times on the LE estimates of liver and muscle,
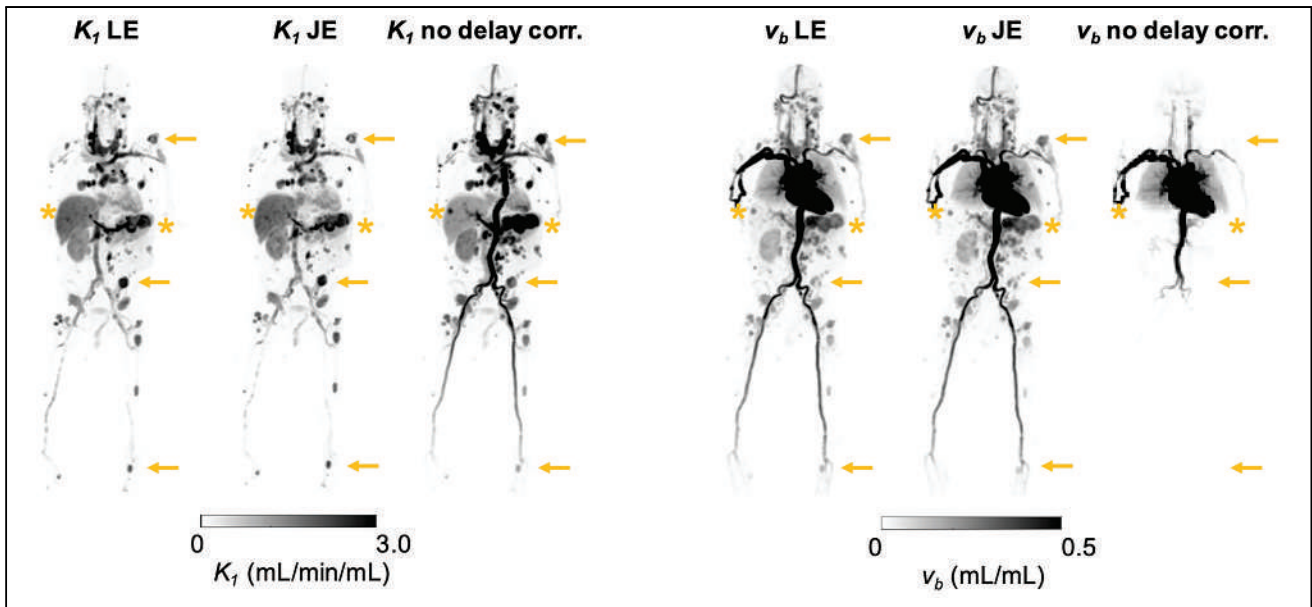
FIGURE 4. Maximum-intensity projections of K_1 and v_b parametric maps for representative GUC patient. Overall, LE-derived parametric images were similar to JE-based images. Without delay correction, K_1 was increased whereas v_b was underestimated in much of abdomen and lower body compared with JE-based v_b. Multiple GUC lesions (arrows) demonstrated increased K_1 and v_b when delay correction was applied, whereas vessels in legs and some lesions in upper abdomen and liver (asterisks) showed reduction in K_1 and increase in v_b.

as compared with gray matter, spleen, and GUC lesions, all of which demonstrated a sharp rising edge (Supplemental Fig. 3). On the basis of the simulation results and the timing walk, or overestimation of the delay that occurs for more slowly rising time–activity curves as LE thresholds are increased (Fig. 2B), an LE threshold of 10% was selected for further ROI-based results and implemented for parametric imaging. As shown in Figure 2C, there was good agreement between JE and LE methods in the estimation of delay (Pearson $r = 0.96$; $P < 0.001$; slope, 1.00), with a 10% LE threshold for all ROIs.

The impact of delay correction can be seen in Table 1, which shows parameter estimates obtained with and without delay correction. With LE-based delay estimation, mean parameter estimates agreed with JE results for v_b ($r = 0.96$; $P < 0.001$; slope, 0.98), K_i ($r = 1.00$; $P < 0.001$; slope, 0.99), and K_1 ($r = 0.97$; $P < 0.001$;

slope, 0.91) when all regions were pooled ($n = 154$) (Table 1; Supplemental Fig. 4). When delay correction was not performed, there was little impact on K_i ($r = 1.00$; $P < 0.001$; slope, 1.02); however, v_b ($r = 0.86$; $P < 0.001$; slope, 0.85) and K_1 ($r = 0.89$, $P < 0.001$, slope: 0.89) were poorly estimated in some tissues, including gray matter, spleen, and GUC lesions. When tissues with negative or zero delay (myocardium, lung) were excluded from pooled analyses, K_i remained constant, whereas there was a drop in v_b (69.4%) and K_1 (4.8%) without delay correction (Table 1).

Table 2 shows the mean and SD estimates of the 42 tissue-parameter pairs. LE estimates strongly agreed with JE methods for most tissues; only 5 of 38 statistically significant comparisons had a Pearson r of less than 0.8, though the LE method did not agree with JE results in some liver and spleen ROIs when estimating v_b.
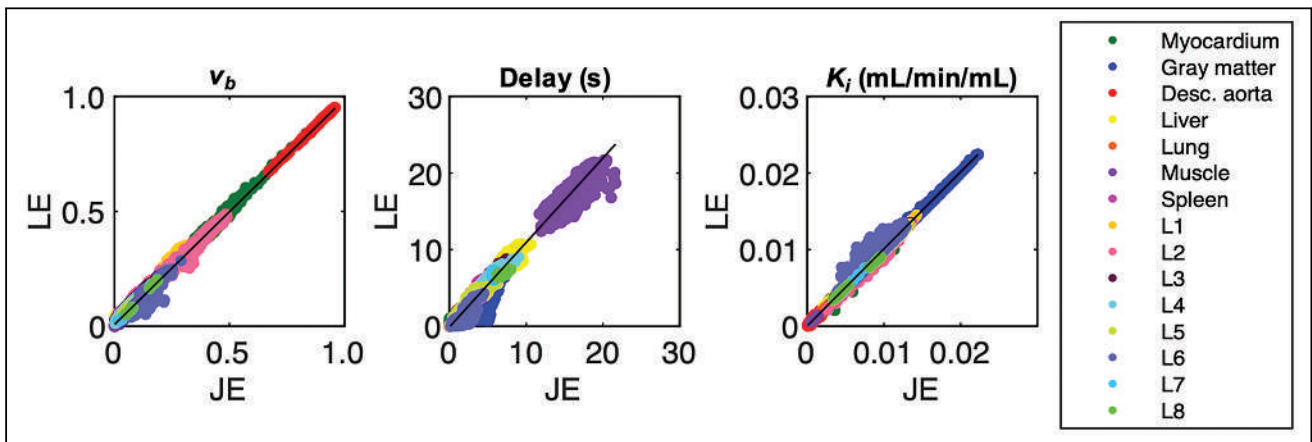

FIGURE 5. Parametric LE vs. JE results for GUC patient were compared across several regions including 8 lesions (L1–L8). Delay was slightly overestimated ($r = 0.99$; $P < 0.001$; slope, 1.10) overall and was underestimated in several tissues, namely in muscle, lesions, and gray matter. LE v_b ($r = 1.00$; $P < 0.001$; slope, 0.98) and K_i ($r = 1.00$; $P < 0.001$; slope, 1.00) estimates demonstrate nearly 1:1 ratios with JE.

Parametric Imaging

Voxelwise LE results were assessed using datasets from 1 representative healthy volunteer and 1 representative GUC subject. Using a high-performance computational node (Xeon Gold 2.6-GHz, 24-core processor; Intel), JE parametric images were produced at an approximate rate of 180 voxels/s, whereas LE parametric images were produced at an approximate rate of 1,200 voxels/s, representing a 6.7-fold increase in computational efficiency. Parametric results agreed with the results of ROI-based methods but were slightly overestimated for both JE ($r = 0.97$; $P < 0.001$; slope, 1.05) and LE ($r = 0.99$; $P < 0.001$; slope, 1.06) (Supplemental Fig. 5). Example delay and K_i maps are shown in Figure 3. LE-derived delay maps showed some artifacts near the injection site compared with JE delay maps, but results were broadly comparable across most tissues. K_i was similar between JE and LE and demonstrated improved K_i contrast in the liver and GUC lesions compared with K_i computed with no delay correction or via Patlak plots (Fig. 3; Supplemental Table 4). GUC-subject maximum-intensity-projection images of K_1 and v_b are shown in Figure 4; delay correction improved visualization of lesions in the thorax, lower torso, and legs. Like the ROI-based results in Tables 1 and 2, voxel-level delay correction resulted in improved estimation of lesion v_b and K_1 (Fig. 4), both of which are sensitive to the early phases of the scan.

Both representative subjects showed some disagreement in LE delay in the muscle and spleen relative to JE delay, though this did not greatly impact K_i or v_b estimates. Scatterplots comparing JE and LE results in a representative healthy subject (Supplemental Fig. 6) demonstrated agreement in the estimation of delay ($r = 0.99$; $P < 0.001$; slope, 1.01). Estimates of v_b ($r = 1.00$; $P < 0.001$; slope, 1.00) and K_i ($r = 1.00$; $P < 0.001$; slope, 0.99) agreed strongly with JE results. Although not shown, K_1 LE estimates also agreed with JE but were underestimated ($r = 0.97$; $P < 0.001$; slope, 0.91).

GUC voxelwise estimates of delay were similarly in disagreement in some muscle, spleen, and lesion voxels, and overall, delay was slightly overestimated ($r = 0.99$; $P < 0.001$; slope, 1.10) (Fig. 5). There was strong agreement for v_b ($r = 1.00$; $P < 0.001$; slope, 0.98) and K_i ($r = 1.00$; $P < 0.001$; slope, 1.00). Although not shown, GUC-subject K_1 estimates were also in agreement ($r = 0.99$; $P < 0.001$; slope, 0.97).

DISCUSSION

Here we have demonstrated, at both the ROI and the voxel levels, the feasibility of using pulse timing methods (LE and CFD) as a surrogate for jointly estimating tracer delay using the first 120 s of data, across a wide range of tissue types present in total-body PET datasets. Noise, in addition to temporal framing, plays an important role in the choice of threshold in the LE method. In simulations, LE with a 10% threshold or greater provided a satisfactory delay bias and SD in short frames at most noise levels, but a 30% threshold resulted in the lowest measured bias and SD at all noise levels. However, the shape of the time–activity curve itself is important and may explain the discrepancies between simulations and acquired time–activity curves in determining the optimal LE threshold for gray matter. Further, tissues with a long rise time, such as the liver, suffer from timing walk, and spillover from the blood pool can cause early triggering. Threshold optimization may be necessary for these tissues. Since the simulation data showed no advantage from using the CFD approach, the simpler LE method was used for human studies.

After assessing regional delay estimates from various LE thresholds, we implemented a 10% threshold for all human analyses. JE and LE methods were in agreement for all estimated kinetic parameters at both the ROI and the voxel levels. v_b and K_1 estimates were sensitive to delay correction, whereas K_i was impacted by delay correction only in the liver and GUC lesions of the parametric images. Improved estimation of v_b and K_1 has implications for perfusion imaging with radiotracers with rapid kinetics (e.g., ^{15}O-water).

The bolus shape is another important consideration; the simulation results indicated that LE methods work well, with a sharp bolus peak for the IF with respect to the frame length such that the timing walk in the tissue and IF curves is as slight as possible. Therefore, these methods are expected to be translatable to other tracers delivered via bolus injection.

Although we implemented model selection in our parametric analyses, special-case tissues (e.g., liver and lung) require additional models that consider dual IFs and dispersion, which were not implemented here but will be a part of our future work. Patient motion is another major challenge with total-body parametric imaging. Short frames capture not only respiratory and cardiac motion but also any gross motion throughout the scan. In practice, application of these methods will likely benefit greatly from incorporation of motion correction in total-body PET (22). Here, we performed simple manual correction of our ROIs and selected image datasets with limited motion for parametric analysis.

Although LE delay correction can be implemented with the Patlak analysis, delay correction has a limited impact on Patlak K_i, indicating that improved lesion contrast seen in this study was a result of implementation of compartment modeling with delay correction.

CONCLUSION

We applied pulse timing methods to dynamic PET images to estimate the arrival time of the radiotracer bolus in ROIs and in every voxel in the body. We demonstrated that pulse timing methods can be an efficient surrogate for JE. Moreover, LE and JE methods of delay correction provided K_i, v_b, and K_1 estimates that were in good agreement and substantially improved parametric results compared with when no delay correction was performed or compared with Patlak analysis. Further, at the voxel level, LE estimates agreed with JE across a variety of tissue types for both healthy and GUC subjects. The results suggest that delay correction should be implemented for total-body PET kinetic modeling using short (<5 s) frames, and implementing the LE method instead of JE will allow for efficient correction of delay.

KEY POINTS

QUESTION: Are pulse timing methods an efficient surrogate for JE of the delay in tracer arrival time for total-body PET kinetic modeling?

PERTINENT FINDINGS: Results from regional and voxelwise studies on 14 healthy volunteers and 7 cancer patients showed strong agreement between LE and JE methods in estimating delay and the kinetic parameters v_b, K_i, and K_1. Improved regional estimates, as well as increased parametric image contrast of v_b and K_1 were observed when delay correction was performed.

IMPLICATIONS FOR PATIENT CARE: This study demonstrated the importance of delay correction in total-body PET kinetic modeling and that LE delay correction can be a computationally efficient surrogate for JE, making the methods more translatable for patient studies.

REFERENCES

1. Lammertsma AA. Essentials of quantitative imaging with PET. In: Volterrani D, Erba PA, Carrió, I, Strauss HW, Mariani G, eds. *Nuclear Medicine Textbook.* Springer; 2019:219–233.

2. Iida H, Kanno I, Miura S, Murakami M, Takahashi K, Uemura K. Error analysis of a quantitative cerebral blood flow measurement using $H_2^{15}O$ autoradiography and positron emission tomography, with respect to the dispersion of the input function. *J Cereb Blood Flow Metab.* 1986;6:536–545.

3. Islam MM, Tsujikawa T, Mori T, Kiyono Y, Okazawa H. Pixel-by-pixel precise delay correction for measurement of cerebral hemodynamic parameters in $H_2^{15}O$ PET study. *Ann Nucl Med.* 2017;31:283–294.

4. Feng T, Zhao Y, Shi H, et al. Total-body quantitative parametric imaging of early kinetics of ^{18}F-FDG. *J Nucl Med.* 2021;62:738–744.

5. Cherry SR, Badawi RD, Karp JS, Moses WW, Price P, Jones T. Total-body imaging: transforming the role of positron emission tomography. *Sci Transl Med.* 2017; 9:eaaf6169.

6. Zhang X, Cherry SR, Xie Z, Shi H, Badawi RD, Qi J. Subsecond total-body imaging using ultrasensitive positron emission tomography. *Proc Natl Acad Sci USA.* 2020;117:2265–2267.

7. Iida H, Law I, Pakkenberg B, et al. Quantitation of regional cerebral blood flow corrected for partial volume effect using O-15 water and PET: I. Theory, error analysis, and stereologic comparison. *J Cereb Blood Flow Metab.* 2000; 20:1237–1251.

8. Iida H, Kanno I, Takahashi A, et al. Measurement of absolute myocardial blood flow with $H_2^{15}O$ and dynamic positron-emission tomography: strategy for quantification in relation to the partial-volume effect. *Circulation.* 1988;78:104–115.

9. Meyer E. Simultaneous correction for tracer arrival delay and dispersion in CBF measurements by the $H_2^{15}O$ autoradiographic method and dynamic PET. *J Nucl Med.* 1989;30:1069–1078.

10. Lammertsma AA, Cunningham VJ, Deiber MP, et al. Combination of dynamic and integral methods for generating reproducible functional CBF images. *J Cereb Blood Flow Metab.* 1990;10:675–686.

11. Knoll GF. *Radiation Detection and Measurement.* John Wiley and Sons, Inc.; 2005:659–662.

12. Feng D, Huang SC, Wang X. Models for computer simulation studies of input functions for tracer kinetic modeling with positron emission tomography. *Int J Biomed Comput.* 1993;32:95–110.

13. Feng D, Wong KP, Wu C-M, Siu WC. A technique for extracting physiological parameters and the required input function simultaneously from PET image measurements: theory and simulation study. *IEEE Trans Inf Technol Biomed.* 1997;1: 243–254.

14. Huisman MC, van Golen LW, Hoetjes NJ, et al. Cerebral blood flow and glucose metabolism in healthy volunteers measured using a high-resolution PET scanner. *EJNMMI Res.* 2012;2:63.

15. Wu Y, Carson RE. Noise reduction in the simplified reference tissue model for neuroreceptor functional imaging. *J Cereb Blood Flow Metab.* 2002;22: 1440–1452.

16. Spencer BA, Berg E, Schmall JP, et al. Performance evaluation of the uEXPLORER total-body PET/CT scanner based on NEMA NU 2-2018 with additional tests to characterize PET scanners with a long axial field of view. *J Nucl Med.* 2021;62:861–870.

17. Leung EK, Berg E, Omidvari N, et al. Quantitative accuracy in total-body imaging using the uEXPLORER PET/CT scanner. *Phys Med Biol.* 2021;66:10.1088/1361-6560/ac287c.

18. Wang G, Qi J. PET image reconstruction using kernel method. *IEEE Trans Med Imaging.* 2015;34:61–71.

19. Patlak CS, Blasberg RG, Fenstermacher JD. Graphical evaluation of blood-to-brain transfer constants from multiple-time uptake data. *J Cereb Blood Flow Metab.* 1983;3:1–7.

20. Wang G, Qi J. Generalized algorithms for direct reconstruction of parametric images from dynamic PET data. *IEEE Trans Med Imaging.* 2009;28:1717–1726.

21. Boellaard R, Delgado-Bolton R, Oyen WJG, et al. FDG PET/CT: EANM procedure guidelines for tumour imaging—version 2.0. *Eur J Nucl Med Mol Imaging.* 2015;42:328–354.

22. Wang Y, Li E, Cherry SR, Wang G. Total-body PET kinetic modeling and potential opportunities using deep learning. *PET Clin.* 2021;16:613–625.

Total-Body PET Multiparametric Imaging of Cancer Using a Voxelwise Strategy of Compartmental Modeling

Guobao Wang[1], Lorenzo Nardo[1], Mamta Parikh[2], Yasser G. Abdelhafez[1], Elizabeth Li[3], Benjamin A. Spencer[1,3], Jinyi Qi[3], Terry Jones[1], Simon R. Cherry[1,3], and Ramsey D. Badawi[1,3]

[1]Department of Radiology, University of California Davis Medical Center, Sacramento, California; [2]UC Davis Comprehensive Cancer Center, Sacramento, California; and [3]Department of Biomedical Engineering, University of California at Davis, Davis, California

Quantitative dynamic PET with compartmental modeling has the potential to enable multiparametric imaging and more accurate quantification than static PET imaging. Conventional methods for parametric imaging commonly use a single kinetic model for all image voxels and neglect the heterogeneity of physiologic models, which can work well for single-organ parametric imaging but may significantly compromise total-body parametric imaging on a scanner with a long axial field of view. In this paper, we evaluate the necessity of voxelwise compartmental modeling strategies, including time delay correction (TDC) and model selection, for total-body multiparametric imaging. **Methods:** Ten subjects (5 patients with metastatic cancer and 5 healthy volunteers) were scanned on a total-body PET/CT system after injection of 370 MBq of ^{18}F-FDG. Dynamic data were acquired for 60 min. Total-body parametric imaging was performed using 2 approaches. One was the conventional method that uses a single irreversible 2-tissue-compartment model with and without TDC. The second approach selects the best kinetic model from 3 candidate models for individual voxels. The differences between the 2 approaches were evaluated for parametric imaging of microkinetic parameters and the ^{18}F-FDG net influx rate, K_i. **Results:** TDC had a nonnegligible effect on kinetic quantification of various organs and lesions. The effect was larger in lesions with a higher blood volume. Parametric imaging of K_i with the standard 2-tissue-compartment model introduced vascular-region artifacts, which were overcome by the voxelwise model selection strategy. **Conclusion:** The time delay and appropriate kinetic model vary in different organs and lesions. Modeling of the time delay of the blood input function and model selection improved total-body multiparametric imaging.

Key Words: image processing; PET; radiotracer tissue kinetics; compartmental modeling; parametric imaging; total-body dynamic PET

PET allows for dynamic scanning to monitor the spatiotemporal distribution of a radiotracer in the living body. With tracer kinetic modeling (e.g., compartmental models or graphical methods (*1*)), dynamic PET allows quantification of kinetic parameters in regions of interest (ROIs) and voxelwise (i.e., parametric imaging) (*2,3*). PET parametric imaging has the potential to improve tumor contrast, derive meaningful biologic measures of tracer transport and binding, and enable quantitative assessment of tumor response to cancer treatment as compared with SUV (*4*). As the axial length of conventional PET scanners commonly ranges from 15 to 30 cm, clinical studies using dynamic PET have typically been limited to a restricted axial field of view that can cover only single organs or specific tumor locations. Whole-body implementation of parametric imaging has been pursued using conventional PET scanners but is limited mainly to the simplified Patlak graphical method (*5–7*), which is computationally efficient but does not explore the full potential of kinetic modeling for multiparametric imaging.

The advent of PET scanners with an extended long axial field of view, such as the uEXPLORER (United Imaging) (*8–10*), the PennPET Explorer (*11,12*), and the Quadra (Siemens) (*13*), is providing a paradigm shift in dynamic imaging. The longest of these has an axial field of view of 194 cm, providing not just unprecedented photon detection sensitivity but also simultaneous dynamic imaging and parametric imaging of the entire body (*9,14*). Image-derived input function (IDIF) can also be obtained from the left ventricle or the aorta. Metastatic lesions that are widely separated can now be imaged at the same time with total-body PET. The objective of this work was to conduct a pilot clinical study to test the feasibility of multiparametric imaging with compartmental modeling in total-body dynamic PET.

A typical approach to PET parametric imaging is to apply a single model to all voxels in the image (*6,14,15*). This approach can be appropriate for conventional single-organ parametric imaging but becomes insufficient for total-body parametric imaging in which organ- and tissue-appropriate models are required. In this work, we evaluated a voxelwise compartmental modeling strategy for total-body PET multiparametric imaging.

MATERIALS AND METHODS

Total-Body Dynamic PET/CT Image Acquisition

Ten subjects, including 5 patients with metastatic genitourinary cancer and 5 healthy volunteers, were recruited into this study at the University of California (UC) Davis Medical Center. Prior Ethics Committee and Institution Review Board approval and written informed consent were obtained. Patients were enrolled and scanned before the initialization of targeted therapy or immunotherapy. All subjects fasted for at least 6 h before the study.

PET/CT imaging was performed on the uEXPLORER total-body system at the UC Davis EXPLORER Molecular Imaging Center. Each subject had a total-body CT scan from head to toe with arms down, followed by a 60-min dynamic PET scan using an injection of approximately 370 MBq (10 mCi) of ^{18}F-FDG. List-mode data were acquired and binned into 29 frames: 6 × 10 s, 2 × 30 s, 6 × 60 s, 5 × 120 s, 4 × 180 s, and 6 × 300 s. Each frame was reconstructed into an image
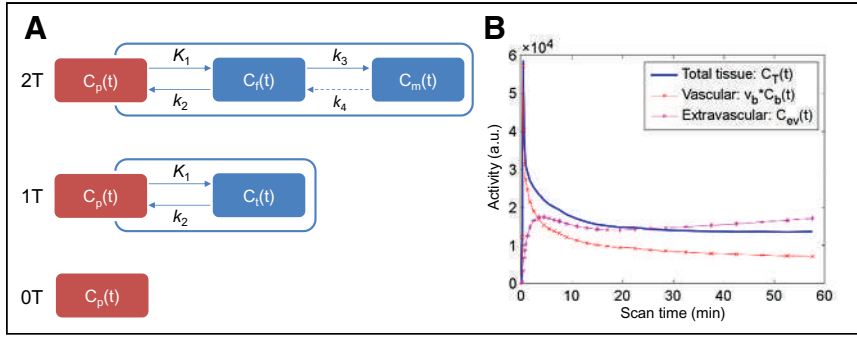
FIGURE 1. Compartmental modeling of ^{18}F-FDG. (A) 2T model and reduced 1T and 0T models. (B) Graph of time courses of ^{18}F-FDG in vascular and extravascular spaces that constitute total tissue time–activity curve. a.u. = arbitrary units.

of size $150 \times 50 \times 486$ with $4 \times 4 \times 4$ mm voxels using the vendor implementation of the time-of-flight ordered-subset expectation maximization algorithm with 4 iterations and 20 subsets. Standard corrections, including normalization, attenuation correction, dead-time correction, decay correction, random correction, and scatter correction, were all applied (*10*).

Compartmental Modeling and Parametric Imaging

Lesion Selection and ROI Placement. For each scan, ROIs were placed in various organs and on suspected lesions to extract regional time–activity curves. Up to 5 target lesions (maximum, 2 per organ) were identified per scan. The lesion ROIs were defined using 41% of the SUV$_{max}$ (at 60 min after injection) in each lesion (*16*). An additional ROI was placed in the ascending aorta using both early-frame and late-frame images as guidance to extract an IDIF, which is denoted by $C_{IDIF}(t)$. Lesion were delineated using AMIDE software (*17*).

Compartmental Models. The commonly used irreversible 2-tissue-compartment (2T) model (Fig. 1A) (*1*) was used to model the dynamic ^{18}F-FDG PET data. The corresponding ordinary differential equation of this 2T model is …

$$\frac{d}{dt}\begin{bmatrix} C_f(t) \\ C_m(t) \end{bmatrix} = \begin{bmatrix} -(k_2+k_3) & 0 \\ k_3 & 0 \end{bmatrix}\begin{bmatrix} C_f(t) \\ C_m(t) \end{bmatrix} + \begin{bmatrix} K_1 \\ 0 \end{bmatrix}C_p(t), \quad \text{(Eq. 1)}$$

where $C_p(t)$ is the ^{18}F-FDG concentration in the plasma, $C_f(t)$ is the concentration of free ^{18}F-FDG and $C_m(t)$ is the concentration of metabolized tracer in the tissue space at time t. The constant K_1 is the rate of ^{18}F-FDG delivery from the plasma to the tissue space in units of mL/min/cm^3 (*18*); k_2 (min^{-1}) is the rate constant of tracer exiting the tissue space; k_3 (min^{-1}) is the rate constant of ^{18}F-FDG being phosphorylated. This irreversible model assumes that the dephosphorylation process is negligible (i.e., $k_4=0$). The total concentration of ^{18}F-FDG in the extravascular space is …

$$C_{ev}(t) = C_f(t) + C_m(t) = H(t; \kappa) \otimes C_p(t), \quad \text{(Eq. 2)}$$

where $\kappa = [K_1, k_2, k_3]^T$ and $H(t; \kappa)$ is the impulse response function defined by …

$$H(t; \kappa) = \frac{K_1 k_3}{k_2+k_3} + \frac{K_1 k_2}{k_2+k_3}e^{-(k_2+k_3)t}. \quad \text{(Eq. 3)}$$

The macro parameters K_i (net influx rate) and V_0 (initial volume of distribution) can be calculated by (*5,19*) …

$$K_i = \frac{K_1 k_3}{k_2+k_3}, \quad V_0 = \frac{K_1 k_2}{(k_2+k_3)^2}. \quad \text{(Eq. 4)}$$

The total radioactivity that can be measured by PET is modeled as the sum of the time courses of ^{18}F-FDG in the vascular and

extravascular spaces (Fig. 1B):

$$C_T(t) = (1-v_b)C_{ev}(t) + v_b C_b(t), \quad \text{(Eq. 5)}$$

where v_b (mL/mL) is the fractional blood volume and $C_b(t)$ represents the whole blood.

Modeling of Voxelwise Time Delay in IDIF. A time delay exists between where the IDIF is extracted and the arrival of the radiotracer in the tissue of interest. Within the limited axial field of view of conventional PET scanners, the time delay effect has been commonly neglected because of the short distance between an IDIF and tissue ROIs, especially if the temporal resolution is low (e.g., 20–40 s per frame). Accounting for the time delay has conventionally been considered necessary only for fast kinetics when relatively high temporal sampling is used (*20,21*). A recent example was shown by Feng et al. (*22*) for fast total-body imaging of early ^{18}F-FDG kinetics. In our work, whereas the dynamic scan used a standard temporal resolution (10 s/frame), we noted the long distance between the ascending aorta and distant lesions, as well as potentially high vascular contributions in some lesions. Hence, the time delay effect is explicitly modeled in the blood input to each voxel by …

$$C_T(t) = (1-v_b)H(t; \kappa) \otimes C_p(t-t_d) + v_b C_b(t-t_d), \quad \text{(Eq. 6)}$$

with the time delay parameter t_d to be jointly estimated with other kinetic parameters though the time–activity curve fitting of a voxel. We postulate that time delay correction (TDC) has a higher impact on kinetic quantification if the fractional blood volume, v_b, is larger in the tissue, because the increased fraction of the vascular time course in turn influences the estimate of the extravascular time course, $C_{ev}(t)$, as projected from Figure 1B.

Fitting Optimization and Setting. A measured time–activity curve, $\check{C}_T(t)$, is fitted with the model time–activity curve, $C_T(t)$, using a nonlinear least-square formulation:

$$\hat{\theta} = \arg\min_{\theta} RSS(\theta), \quad RSS(\theta) = \sum_{m=1}^{M} w_m[\check{C}_T(t_m) - C_T(t_m)]^2, \quad \text{(Eq. 7)}$$

where $RSS(\theta)$ denotes the residual sum of squares of the curve fitting. θ is the unknown parameter set. For the irreversible 2T model, $\theta = [v_b, K_1, k_2, k_3, t_d]^T$. t_m is the midpoint of the mth frame in a total of M frames, and w_m is the weight for frame m. Given our interest in both K_i and K_1, a uniform weight was used as suggested by prior studies (*23–25*) (also demonstrated in Supplemental Fig. 1; supplemental materials are available at http://jnm.snmjournals.org).

The classic Levenberg–Marquardt algorithm with 50 iterations was used to solve the optimization problem in a similar way to our other work (*26*) and was implemented using C/C++ programming.

TABLE 1
Models Used for Dynamic ^{18}F-FDG PET Kinetic Modeling

Model order	Unknown parameters (n)	Kinetic parameters to be estimated
2T	5	v_b, K_1, k_2, k_3, t_d
1T	4	v_b, K_1, k_2, t_d
0T	2	v_b, t_d

TABLE 2
Subject Characteristics

Subject	Age (y)	Sex	BMI (kg/m^2)	Blood glucose level (mg/dL)	Fasting (h)	Disease	Initial therapy
1	78	M	24.4	101	11	Healthy	NA
2	26	M	33.8	77	6	Healthy	NA
3	50	M	27.2	94	12	Healthy	NA
4	51	F	24.2	93	12	Healthy	NA
5	62	M	29.5	92	12	Healthy	NA
6	65	M	32.0	154	12	CC RCC grade 2	Partial nephrectomy
7	62	M	26.3	84	8	CC RCC grade 4	Radical nephrectomy
8	65	M	25.3	65	20	CC RCC grade 3	Radical nephrectomy
9	76	M	20.1	128	10	CC RCC grade 2	Radical nephrectomy
10	70	M	24.3	131	11	High-grade TCC	Radical cystectomy

BMI = body mass index; NA = not applicable; CC RCC = clear cell renal cell carcinoma; TCC = transitional cell carcinoma.
All cancer patients had stage IV disease. Fuhrman grade was used.

The initial values of κ and v_b were set to $[0.01, 0.01, 0.01]^T$ and 0.01, respectively. The lower bound was zero and the upper bound was $[5.0, 5.0, 1.0]^T$ and 1.0, respectively. The time delay, t_d, was jointly estimated by a grid search with the lower and upper bounds set to -10 and 50 s, respectively.

Voxelwise Model Selection. Conventionally for simplicity, parametric imaging uses a single kinetic model (e.g., the irreversible 2T model) for all voxels. In total-body parametric imaging, a wide physiologic heterogeneity may exist within the field of view. In addition to the 2T model, we also considered the 1-tissue-compartment (1T) model and zero-tissue-compartment (0T) model (Fig. 1A; Table 1). The 0T model is more suitable for those voxels containing only blood. The 1T model is equivalent to the 2T model with $k_3 = 0$, implying that the phosphorylation process can be neglected when k_3 is small and the data are noisy. The 0T model is a special case of the 1T model with $K_1 = 0$. The best model was chosen for each voxel j from a set of candidate models (0T, 1T, and 2T in Table 1) according to the minimum Akaike information criterion (AIC),

$$l_j = \text{argmin}_l \ \text{AIC}_j(l), \qquad \text{(Eq. 8)}$$

where $\text{AIC}_j(l)$ denotes the AIC of model order l ($l = 0, 1, 2$) for fitting the time–activity curve at voxel j. The AIC with correction for a small number of frames is calculated by (27)…

$$\text{AIC} = M\ln(RSS/M) + 2n \qquad \text{(Eq. 9)}$$
$$+ 2n(n+1)/(M-n-1),$$

where RSS is calculated using Equation 7 for a specific model and n denotes the total number of unknown parameters in the model. A lower AIC value indicates a better model (27).

Parametric Imaging with Kernel Smoothing. Voxelwise implementation of compartmental modeling leads to the generation of parametric images of tracer kinetics, which usually suffer from high noise in voxels. The kernel method (28) was applied here as postreconstruction smoothing to reduce noise in the dynamic images, a process that is also equivalent to nonlocal means smoothing (28). Fundamentally, it rests on deriving, for each patient dataset, a kernel matrix built from 4 consecutive composite frames of 5, 15, 20, and 20 min, respectively. For each voxel, k-nearest neighbors with k
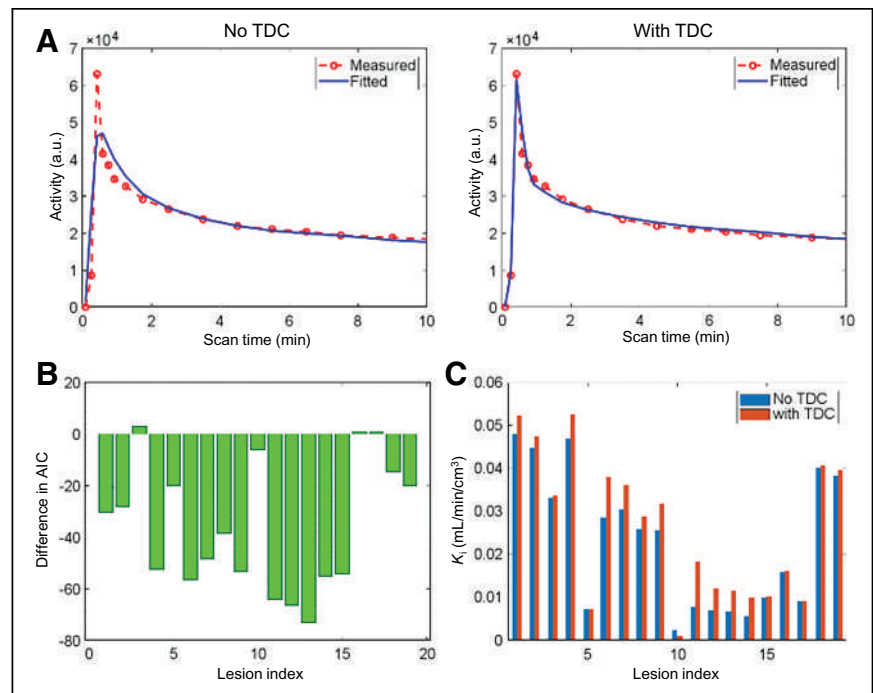

FIGURE 2. Graphs of time delay and its impact on lesion time–activity curve fitting and kinetic quantification. (A) Fitting of liver lesion time–activity curve with no TDC and with time delay jointly estimated. (B) AIC difference between 2T models with and without TDC for time–activity curve fitting in 19 lesions. (C) Comparison of K_i values for individual lesions. a.u. = arbitrary units.

TABLE 3
Mean and SD of Lesion Kinetic Parameters Estimated by 2T Model With and Without TDC

Parameter	Without TDC	With TDC	P of paired t test	P of paired signed-rank test
t_d (s)	0	7 ± 5	0.0001	0.0008
v_b (mL/cm^3)	0.027 ± 0.053	0.232 ± 0.181	0.0002	0.0002
K_1 (mL/min/cm^3)	0.974 ± 0.814	0.331 ± 0.383	0.0017	0.0002
K_i (mL/min/cm^3)	0.023 ± 0.016	0.026 ± 0.017	0.0003	0.0005
V_0 (mL/cm^3)	0.420 ± 0.267	0.380 ± 0.221	0.0161	0.0123

Paired t test and Wilcoxon signed-rank test were both used for calculating P value.

(number of nearest neighbors) = 50 was constructed in a cubic 9 × 9 × 9 voxel space. More details of the method have been previously published (28). The same kernel matrix was also applied to the parametric images for further noise suppression.

Statistical Analysis

Statistical data were analyzed mainly for demonstrating the impact of TDC and model selection. To evaluate the effect of TDC, linear regression analysis and a group comparison were performed for different kinetic parameters of lesions using the paired Student t test and Wilcoxon signed-rank test. A P value of less than 0.05 was considered statistically significant. For assessing the impact of model selection, artifacts in the K_i parametric images were identified visually in blood regions. AIC was calculated to indicate a potential overfitting of the blood time–activity curves.

RESULTS

Patient Characteristics and Image Data

Table 2 lists the characteristics of the study subjects. All dynamic scans of the 5 healthy subjects and 5 cancer patients were successful. Nineteen lesions were identified on the SUV images of the cancer patients. Supplemental Figure 2 shows the dynamic ^{18}F-FDG PET images and regional time–activity curves for 2 patients with cancer. The 2 patients shared a similar time–activity curve shape for the brain and liver, but the time–activity curves of the lesions were very different.

Effect of Time Delay Correction (TDC)

Figure 2 shows the results of applying TDC by joint estimation to fit lesion time–activity curves using the 2T model. The TDC resulted in an improvement in fitting the lesion time–activity curve, particularly in the early phase where the peak is. The improved fit is further evidenced by a statistical quality evaluation using AIC in the lesions (Fig. 2B). A lower AIC was achieved by the TDC in most lesions. The individual lesion K_i values by the 2 approaches are

shown in Figure 2C. Generally, K_i became higher after TDC. The percentage change in K_i and K_1 was further plotted against the fractional blood volume v_b in Supplemental Figure 3. As v_b increased, the difference in the 2 approaches became larger for both K_i and K_1.

Table 3 summarizes the kinetic results estimated by the 2 approaches (i.e., with and without TDC) in all lesions. The time delay was 7 ± 5 s (range, −2 to 18 s), which is significantly different from zero as indicated by the small P value of the statistical tests.
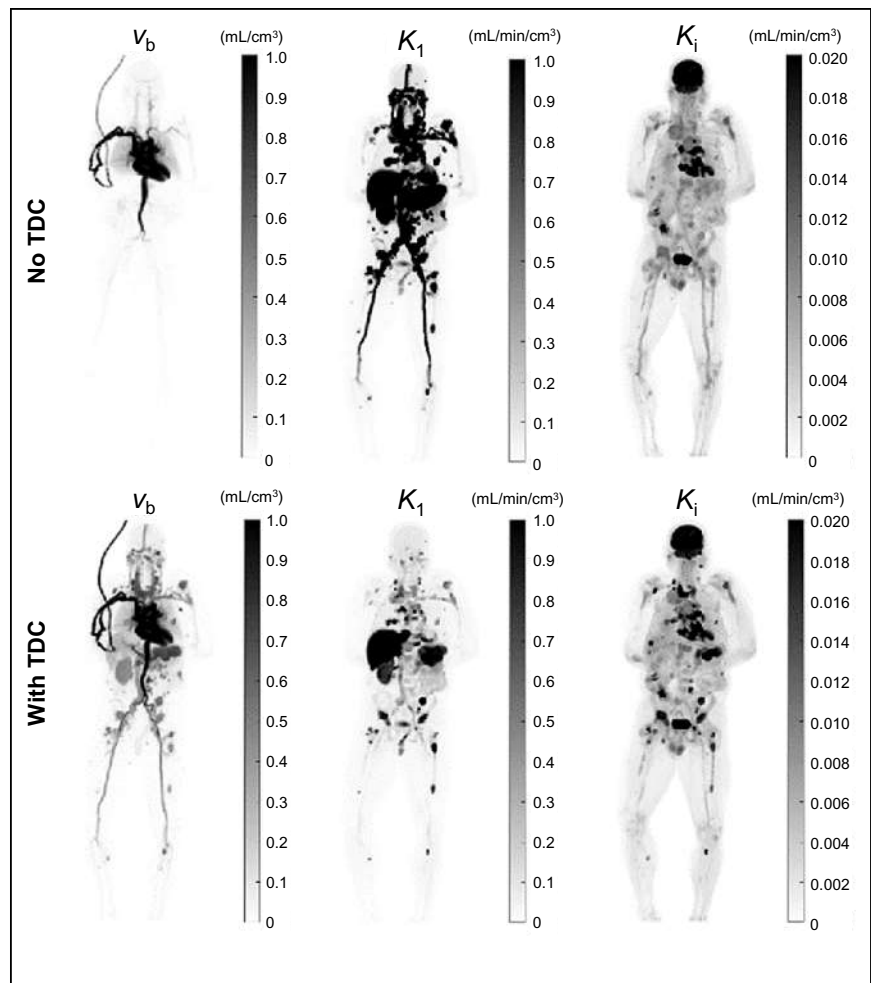
FIGURE 3. Demonstration of parametric imaging using 2T model with and without TDC for cancer patient. Shown are maximum-intensity-projection maps for v_b, K_1, and K_i.
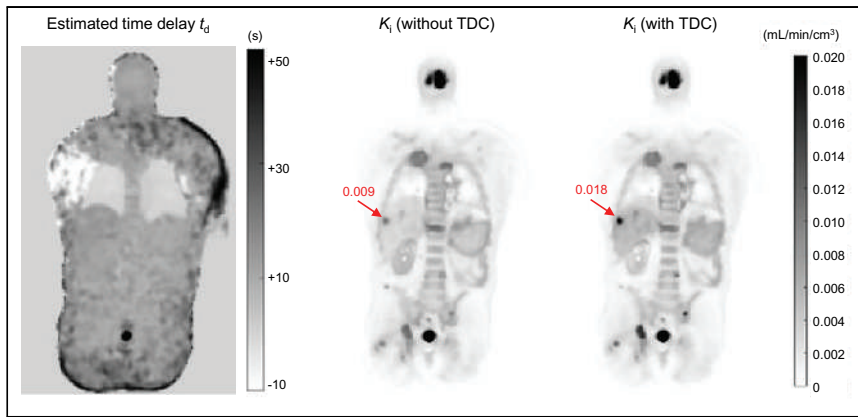
FIGURE 4. Coronal plane of estimated time delay t_d map and K_i parametric images with and without TDC for cancer patient. Arrows point to liver lesion.

TDC led to a much higher v_b and appreciably lower K_1 estimates ($P < 0.002$). Although the mean and SD of K_i in the pooled analysis had only a small difference between the 2 approaches, the paired statistical tests show TDC had a statistically significant effect ($P \leq 0.0005$) on K_i estimation, as reflected by the pairwise changes shown in Figure 2C and Supplemental Figure 3. The impact on V_0 was also statistically significant ($P < 0.02$).

Examples of parametric images of different kinetic parameters are shown in Fig. 3 for 1 cancer patient. Without TDC, the v_b image did not show all the vasculature, especially in the legs, where the time delay was large. The K_1 image became clearer after the TDC because the vasculature disappeared in this image. Fig. 4 further shows the estimated time delay map and K_i images. Lesions were less visible with low K_i values if no TDC was implemented; most lesions were enhanced, with a higher value after TDC.

Effect of Voxelwise Model Selection

Figure 5A shows the map of the model order (0T, 1T, and 2T) selected for individual voxels for a cancer patient scan. Most body parts, such as soft tissues, followed the 2T model, whereas the lungs and skin favored the 1T model according to AIC. Vascular regions (e.g., the heart chambers and arteries) followed the 0T model. All lesions followed the 2T model. The parametric image of K_i generated using a single 2T model (Fig. 5B) contains a suggestive hot spot of a high K_i value. It disappeared after applying voxelwise model selection. Figure 5C demonstrates that both the 2T and the 0T models fitted the time–activity curve well but that the resulting K_i values were very different (0.018 vs. 0.0 mL/min/cm^3). The AICs of different fits by the 0T, 1T, and 2T models are compared in Figure 5D. It indicates that the 0T model was best for fitting the blood time–activity curve, whereas the 2T model overfitted the time–activity curve and resulted in a falsely high value of K_i.

Figure 6 compares the conventional single 2T model (with TDC) with the proposed method (with model selection and TDC) for parametric imaging of K_i at the level of the heart in all 10 subjects. The conventional method resulted in artificially high K_i values in some voxels containing primarily blood. The myocardium was also difficult to visualize in each patient scan. In comparison, the proposed method largely removed those artifacts, and appropriate model selection led to clear visualization of the myocardium in all subjects.

Demonstration of Multiparametric Images

With the improved voxelwise modeling strategy, we show parametric images for a range of kinetic parameters, including v_b, K_1, K_i, and V_0, for 1 cancer patient in Figure 7 and for 1 healthy subject in Supplemental Figure 4. The SUV images at 60 min after injection are also included. Although the K_i and SUV images share similar information in most patients, the v_b, K_1, and V_0 images demonstrate very different spatial patterns in the body, thus providing information complementary to that provided by SUV. Supplemental Figure 5 demonstrates that parametric images can potentially be more useful than SUV for liver tumor imaging and brain tumor imaging.

DISCUSSION

In this paper, we have evaluated a voxelwise strategy for total-body ^{18}F-FDG PET parametric imaging using compartmental modeling. TDC through joint estimation during time–activity curve fitting was found to be significant (Fig. 2) and had a high impact on quantification and parametric imaging of v_b and K_1 (Table 3; Fig. 3). The impact on K_i was of lesser extent when v_b was small but became higher as v_b increased (Fig. 4; Supplemental Figure 3). Dispersion correction was not explicitly included in this study, but the incorporation of v_b may partly account for the
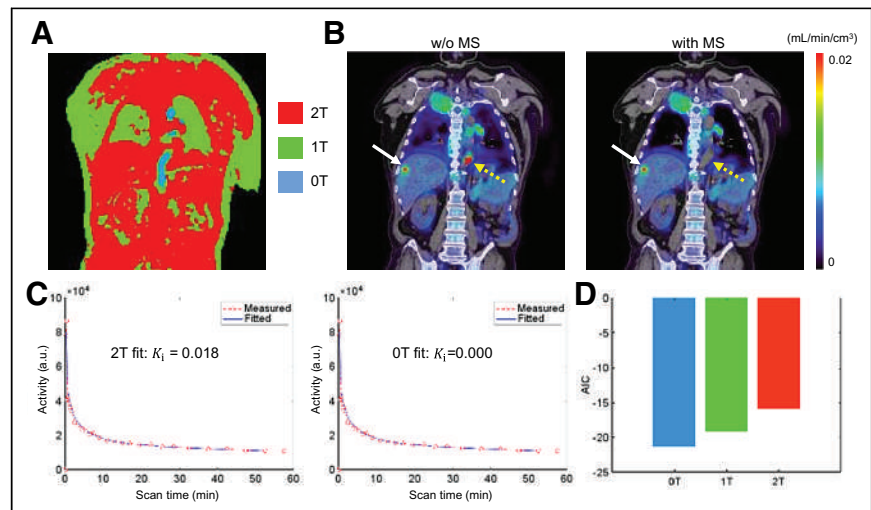

FIGURE 5. Evaluation of impact of model selection (MS). (A) Distribution map of different kinetic models (0T, 1T, and 2T). (B) Parametric image of K_i (overlaid on CT images) by 2T model with and without (w/o) voxelwise MS. Solid arrows point to potential lesions, and dashed arrows point to blood voxels in descending aorta. (C) Blood time–activity curve fitted with 2T and 0T models. (D) AIC values of 3 models (0T, 1T, and 2T). a.u. = arbitrary units.
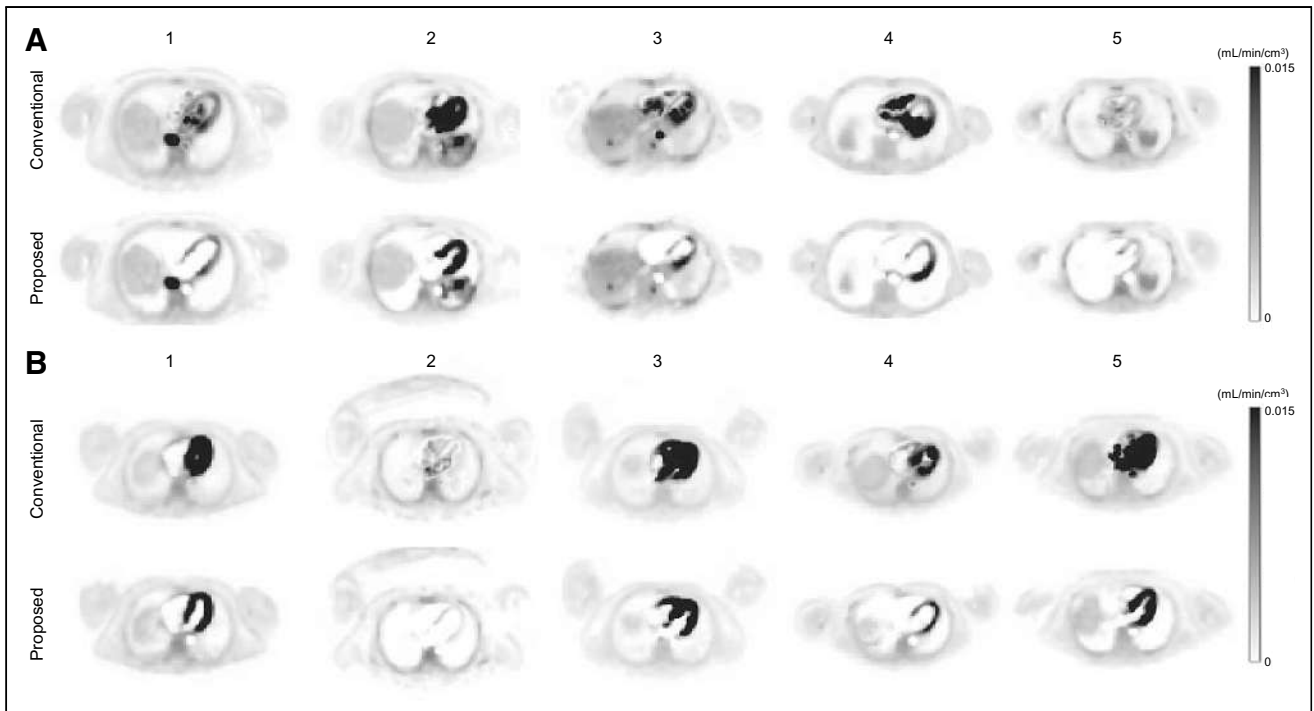
FIGURE 6. Comparison of ^{18}F-FDG K_i parametric images generated by conventional 2T model (with TDC) and proposed approach that includes model selection and TDC in 5 patients with cancer (A) and 5 healthy subjects (B).

potential dispersion effect (*29*). The v_b values of lesions estimated in this study were relatively high (0.23 ± 0.18 mL/cm^3), as likely reflects that most patients had clear cell renal cell carcinoma, which tends to be highly vascular (*30*). It is also perhaps because v_b is more like a method parameter than being quantitative, given that it also accounts for the dispersion effect.

Our study also found that the standard 2T model led to artificially high values in the K_i image in those voxels containing primarily blood. This effect was caused by overfitting of the time–activity curves that better follow the 0T model or 1T model, as indicated by the AIC comparison (Fig. 5). We addressed this problem by applying voxelwise model selection using AIC. The method led to clear

visualization of the myocardium, whereas the standard model did not (Fig. 6). The AIC-based model selection is driven by a statistical fit quality evaluation and cannot be overinterpreted physiologically. For example, the choice of 1T over 2T does not indicate the nonexistence of phosphorylation but suggests that k_3 can be neglected when the data are noisy. As an alternative to AIC, other approaches are also possible by applying sparsity constraints to kinetic parameters or using sparse spectral analysis (*31*). In addition, factor analysis (*32*) and mixture models (*33*) could also be advantageous to explore in total-body parametric imaging (*34*).

As the first step for demonstrating a workable modeling strategy, we considered only the irreversible 2T model. This model is
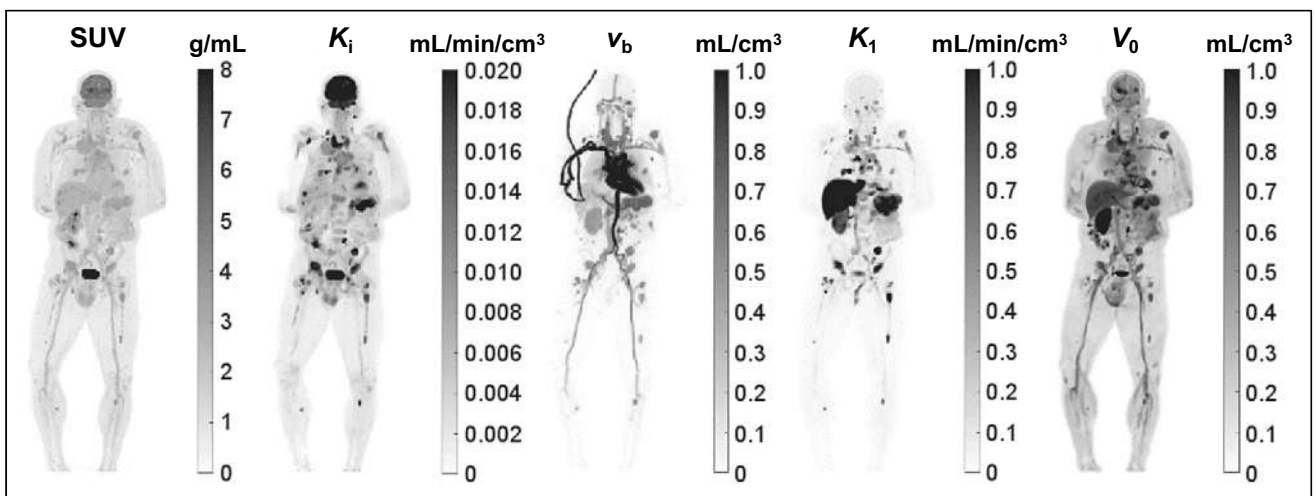
FIGURE 7. Comparison of standard SUV image with parametric images of ^{18}F-FDG influx rate K_i, fractional blood volume v_b, ^{18}F-FDG delivery rate K_1, and volume of distribution V_0 images of cancer patient. Shown are maximum-intensity-projection maps.

appropriate when the dephosphorylation process is negligible during the 1-h dynamic scan time. However, the reversible 2T model (with $k_4 > 0$) can be more appropriate for kinetic quantification of organs such as the liver (35) and myocardium (36). The liver and lungs also receive dual blood supplies and require modeling of their dual-blood input function for accurate kinetic quantification. These aspects were not addressed in this study. Motion correction may also further improve the quantification performance. Implementation of these more complex models in total-body parametric imaging is a part of our ongoing effort.

The focus of this paper was mainly on the methodologic implementation for multiparametric imaging using compartmental modeling. Because of the page limit, the benefits of parametric images have not been directly compared with the SUV images (other than Supplemental Fig. 5) and with the parametric images determined from the linear Patlak plot (5,14,37). In general, multiparametric imaging with compartmental modeling not only generates K_i and V_0 but can also provide other microkinetic parameters, including v_b and K_1 (Fig. 7), that go beyond what the Patlak method can offer. Exploring the potential benefits of these multiparametric images will be reported in future work.

This study had several other limitations. The temporal sampling rate for early dynamic scanning was relatively limited (10 s/frame) but was a reasonable choice based on our preliminary study as shown in Supplemental Figure 6. Within this context, the time delay t_d is mainly a method parameter that is coarsely estimated. Optimal sampling (trade-off between temporal resolution and voxel noise level) and the effect on kinetic quantification remain to be further investigated. In addition, the number of studied subjects was relatively small, and the study did not have a reference or outcome measure to evaluate the impact of kinetic quantification. The studied cancer type was also limited to genitourinary cancer. It will be worth evaluating the proposed kinetic modeling strategies in other cancers. Future studies will take these aspects into account.

CONCLUSION

We successfully conducted total-body PET multiparametric imaging using compartmental modeling for the dynamic ^{18}F-FDG PET data acquired on the uEXPLORER system in both healthy subjects and cancer patients. TDC led to improved lesion time–activity curve fitting, physiologically more consistent vasculature in the v_b image, and a generally higher K_i in lesions, especially when v_b was large. Voxelwise model selection reduced artifacts in the K_i parametric images and led to clearer visualization of the myocardium. Both the modeling of time delay of the blood input function and model selection are necessary for accurate total-body multiparametric imaging.

DISCLOSURE

KEY POINTS

QUESTION: Is it feasible to perform multiparametric imaging with compartmental modeling in total-body dynamic PET of cancer?

PERTINENT FINDINGS: Voxelwise modeling of the time delay of the blood input function and model selection are necessary for accurate total-body multiparametric imaging.

IMPLICATIONS FOR PATIENT CARE: Total-body dynamic PET can enable single-tracer multiparametric imaging, which may be further explored to improve tumor detection and treatment response assessment.

REFERENCES

1. Morris ED, Endres CJ, Schmidt KC, Christian BT, Muzic RF, Fisher RE. Kinetic modeling in positron emission tomography. In: Wermick MN, JN A, eds. *Emission Tomography: The Fundamentals of PET and SPECT*. Elsevier Inc.; 2004:499–540.
2. Gallezot JD, Lu YH, Naganawa M, Carson RE. Parametric imaging with PET and SPECT. *IEEE Trans Radiat Plasma Med Sci*. 2020;4:1–23.
3. Wang G, Rahmim A, Gunn RN. PET parametric imaging: past, present, and future. *IEEE Trans Radiat Plasma Med Sci*. 2020;4:663–675.
4. Dimitrakopoulou-Strauss A, Pan LY, Sachpekidis C. Kinetic modeling and parametric imaging with dynamic PET for oncological applications: general considerations, current clinical applications, and future perspectives. *Eur J Nucl Med Mol Imaging*. 2021;48:21–39.
5. Rahmim A, Lodge MA, Karakatsanis NA, et al. Dynamic whole-body PET imaging: principles, potentials and applications. *Eur J Nucl Med Mol Imaging*. 2019;46:501–518.
6. Karakatsanis NA, Lodge MA, Tahari AK, Zhou Y, Wahl RL, Rahmim A. Dynamic whole body PET parametric imaging: I. Concept, acquisition protocol optimization and clinical application. *Phys Med Biol*. 2013;58:7391–7418.
7. Hu JC, Panin V, Smith AM, et al. Design and implementation of automated clinical whole body parametric PET with continuous bed motion. *IEEE Trans Radiat Plasma Med Sci*. 2020;4:696–707.
8. Cherry SR, Jones T, Karp JS, Qi J, Moses WW, Badawi RD. Total-body PET: maximizing sensitivity to create new opportunities for clinical research and patient care. *J Nucl Med*. 2018;59:3–12.
9. Badawi RD, Shi H, Hu P, et al. First human imaging studies with the EXPLORER total-body PET scanner. *J Nucl Med*. 2019;60:299–303.
10. Spencer BA, Berg E, Schmall JP, et al. Performance evaluation of the uEXPLORER total-body PET/CT scanner based on NEMA NU 2-2018 with additional tests to characterize PET Scanners with a long axial field of view. *J Nucl Med*. 2021;62:861–870.
11. Pantel AR, Viswanath V, Daube-Witherspoon ME, et al. PennPET Explorer: human imaging on a whole-body imager. *J Nucl Med*. 2020;61:144–151.
12. Karp JS, Schmall J, Geagan M, et al. Imaging performance of the PennPET Explorer scanner [abstract]. *J Nucl Med*. 2018(suppl 1);59:222.
13. Alberts I, Hunermund JN, Prenosil G, et al. Clinical performance of long axial field of view PET/CT: a head-to-head intra-individual comparison of the Biograph Vision Quadra with the Biograph Vision PET/CT. *Eur J Nucl Med Mol Imaging*. 2021;48:2395–2404.
14. Zhang X, Xie ZH, Berg E, et al. Total-body dynamic reconstruction and parametric imaging on the uEXPLORER. *J Nucl Med*. 2020;61:285–291.
15. Gunn RN, Lammertsma AA, Hume SP, Cunningham VJ. Parametric imaging of ligand-receptor binding in PET using a simplified reference region model. *Neuroimage*. 1997;6:279–287.
16. Boellaard R, Delgado-Bolton R, Oyen WJG, et al. FDG PET/CT: EANM procedure guidelines for tumour imaging—version 2.0. *Eur J Nucl Med Mol Imaging*. 2015;42:328–354.
17. Loening AM, Gambhir SS. AMIDE: a free software tool for multimodality medical image analysis. *Mol Imaging*. 2003;2:131–137.

18. Innis RB, Cunningham VJ, Delforge J, et al. Consensus nomenclature for in vivo imaging of reversibly binding radioligands. *J Cereb Blood Flow Metab.* 2007;27:1533–1539.

19. Gunn RN, Gunn SR, Cunningham VJ. Positron emission tomography compartmental models. *J Cereb Blood Flow Metab.* 2001;21:635–652.

20. Iida H, Higano S, Tomura N, et al. Evaluation of regional difference of tracer appearance time in cerebral tissues using O-15 water and dynamic positron emission tomography. *J Cereb Blood Flow Metab.* 1988;8:285–288.

21. Lammertsma AA, Cunningham VJ, Deiber MP, et al. Combination of dynamic and integral methods for generating reproducible functional CBF images. *J Cereb Blood Flow Metab.* 1990;10:675–686.

22. Feng T, Zhao Y, Shi H, Li H, et al. Total-body quantitative parametric imaging of early kinetics of ^{18}F-FDG. *J Nucl Med.* 2021;62:738–744.

23. Thiele F, Buchert R. Evaluation of non-uniform weighting in non-linear regression for pharmacokinetic neuroreceptor modelling. *Nucl Med Commun.* 2008;29:179–188.

24. Winterdahl M, Munk OL, Sorensen M, Mortensen FV, Keiding S. Hepatic blood perfusion measured by 3-minute dynamic F-18-FDG PET in pigs. *J Nucl Med.* 2011;52:1119–1124.

25. Yaqub M, Boellaard R, Kropholler MA, Lammertsma AA. Optimization algorithms and weighting factors for analysis of dynamic PET studies. *Phys Med Biol.* 2006;51:4217–4232.

26. Wang G, Qi J. An optimization transfer algorithm for nonlinear parametric image reconstruction from dynamic PET data. *IEEE Trans Med Imaging.* 2012;31:1977–1988.

27. Burnham KP, Anderson DR. Multimodel inference: understanding AIC and BIC in model selection. *Sociol Methods Res.* 2004;33:261–304.

28. Wang G, Qi J. PET image reconstruction using kernel method. *IEEE Trans Med Imaging.* 2015;34:61–71.

29. Mourik JEM, van Velden FHP, Lubberink M, et al. Image derived input functions for dynamic High Resolution Research Tomograph PET brain studies. *Neuroimage.* 2008;43:676–686.

30. Chen Y, Zhang J, Dai JR, Feng XL, Lu HZ, Zhou CW. Angiogenesis of renal cell carcinoma: perfusion CT findings. *Abdom Imaging.* 2010;35:622–628.

31. Gunn RN, Gunn SR, Turkheimer FE, Aston JAD, Cunningham TJ. Positron emission tomography compartmental models: a basis pursuit strategy for kinetic modeling. *J Cereb Blood Flow Metab.* 2002;22:1425–1439.

32. Wu HM, Hoh CK, Buxton DB, et al. Quantification of myocardial blood flow using dynamic nitrogen-13-ammonia PET studies and factor analysis of dynamic structures. *J Nucl Med.* 1995;36:2087–2093.

33. O'Sullivan F. Imaging radiotracer model parameters in PET: a mixture analysis approach. *IEEE Trans Med Imaging.* 1993;12:399–412.

34. Viswanath V, Chitalia R, Pantel AR, Karp JS, Mankoff DA. Analysis of four-dimensional data for total body PET imaging. *PET Clin.* 2021;16:55–64.

35. Wang G, Corwin MT, Olson KA, Badawi RD, Sarkar S. Dynamic PET of human liver inflammation: impact of kinetic modeling with optimization-derived dual-blood input function. *Phys Med Biol.* 2018;63:155004.

36. Zuo Y, Badawi RD, Foster CC, Smith T, Lopez JE, Wang G. Multiparametric cardiac ^{18}F-FDG PET in humans: kinetic model selection and identifiability analysis. *IEEE Trans Radiat Plasma Med Sci.* 2020;4:759–767.

37. Dias AH, Pedersen MF, Danielsen H, Munk OL, Gormsen LC. Clinical feasibility and impact of fully automated multiparametric PET imaging using direct Patlak reconstruction: evaluation of 103 dynamic whole-body ^{18}F-FDG PET/CT scans. *Eur J Nucl Med Mol Imaging.* 2021;48:837–850.

Posterior Cingulate Involvement Does Not Argue Against LATE

TO THE EDITOR: Accurate antemortem diagnosis of neurodegenerative dementia is vital for appropriate counseling and enrollment of patients in disease-modifying clinical trials. Although the advent of biomarker imaging such as amyloid and tau PET has drastically improved our antemortem ability to diagnose Alzheimer disease (AD) pathology, the recognition of specific patterns of glucose metabolism on ^{18}F-FDG PET is crucial for the diagnosis of degenerative conditions without disease-specific neuroimaging biomarkers, such as dementia with Lewy bodies or limbic-predominant age-related TAR DNA binding protein 43 (TDP-43) encephalopathy (LATE). Because of the significant clinical overlap between LATE and typical AD, ^{18}F-FDG PET serves as a valuable diagnostic tool for the workup of amnestic dementia (1).

In a recent issue of *The Journal of Nuclear Medicine* (2), Rieger and Silverman aimed to highlight ^{18}F-FDG PET neuroimaging findings differentiating LATE from other neurodegenerative dementias with a case example. They reported a patient with multidomain amnestic cognitive dysfunction with ^{18}F-FDG PET imaging showing moderately severe anterior temporal and parietotemporal hypometabolism with preservation of the posterior cingulate cortex (PCC) and occipital cortex. They argued that sparing of the PCC in their patient would be inconsistent with AD whereas the absence of occipital hypometabolism would argue against dementia with Lewy bodies, both of which may support LATE as an etiology for the patient's amnestic cognitive impairment. Although sparing of the PCC compared with the precuneus or cuneus (cingulate island sign) and involvement of the occipital lobe is indeed the classic pattern for dementia with Lewy bodies, we disagree that sparing of the PCC in this case is supportive of LATE and inconsistent with AD (3).

Recent data suggest that medial temporal, posterior cingulate, and frontal supraorbital hypometabolism are predictors of LATE whereas prominent inferior temporal involvement may be predictive of AD (4). Antemortem studies of amnestic dementia patients have demonstrated medial temporal and PCC hypometabolism to be more prominent in amyloid-negative (5) and tau-negative patients (6), whereas tau-positive (i.e., AD) patients showed more lateral and inferior temporal involvement, as well as parietal involvement. This pattern was corroborated by autopsy data showing patients with LATE and hippocampal sclerosis who had prominent medial temporal and PCC hypometabolism (6). On the basis of these data, an elevated ratio of inferior-to-medial temporal lobe metabolism was proposed as an ^{18}F-FDG PET marker of LATE, as the authors correctly pointed out. This pattern was subsequently confirmed by an independent group of investigators in the Alzheimer's Disease Neuroimaging Initiative (7).

The relevance of PCC involvement or sparing in predicting the underlying pathology is more nuanced. Although not all studies have supported PCC hypometabolism as predictive of LATE (4), some autopsy-confirmed cases of LATE had marked, focal hypometabolism of the PCC (inverse cingulate island sign) (6). We provide 3 examples of amyloid- and tau-negative amnestic dementia cases with clear PCC involvement in Figure 1. Molecular pathology data have shown lower mitochondrial DNA copy numbers in the PCC—a finding that was explained by the presence of TDP-43 pathology but not tau, further supporting the link between LATE and PCC hypometabolism (8). PCC hypometabolism has also been tied to hippocampal atrophy in cognitively normal individuals and those with MCI, whereas it was attributed to local atrophy in AD dementia (9). PCC hypometabolism likely reflects the presence of limbic, and more specifically medial temporal, neurodegeneration, which would explain why the PCC is involved in LATE and typical AD but is relatively spared in dementia with Lewy bodies and some hippocampal-sparing AD phenotypes (10). As such, the preservation of PCC metabolism in the absence of medial temporal hypometabolism in the authors' case is entirely expected and should not be taken as evidence for LATE or against some forms of AD, especially in light of the inferior temporal and parietal hypometabolism.

Although we await TDP-43–specific tracers for an antemortem diagnosis of LATE, ^{18}F-FDG PET in conjunction with structural brain imaging remains our most useful neuroimaging tool in individuals presenting with amnestic cognitive impairment. Clinicians and radiologists should pay specific attention to the medial temporal lobe and PCC in older patients with amnestic dementia. Specifically, greater medial than inferior temporal lobe hypometabolism is highly suggestive of the presence of LATE. Finally, PCC metabolism may be affected by multiple processes, highlighting the importance of integrating the clinical phenotype with all available neuroimaging data to obtain the most accurate diagnosis.
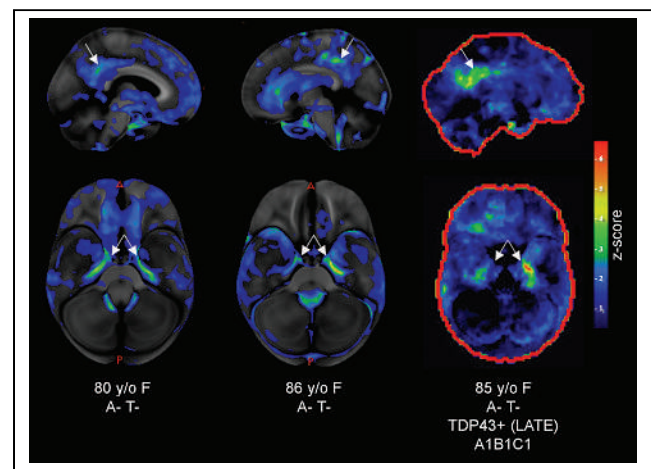

FIGURE 1. Amyloid- and tau-negative amnestic dementia patients with PCC involvement. Shown are 3-dimensional stereotactic surface projection z score images generated with CortexID (GE Healthcare) indicating hypometabolism in patients compared with age- and sex-matched controls. All 3 patients were from our recent paper on ^{18}F-FDG PET in tau-negative amnestic dementia (6). All 3 patients had PCC hypometabolism (top row, arrows), as well as prominent medial temporal hypometabolism (bottom row, arrows). Third patient (right column) has since come to autopsy and had low-stage Alzheimer disease (A1B1C1) according to criteria of National Institute on Aging–Alzheimer's Association, as well as hippocampal sclerosis with TDP-43 (LATE). A = amyloid; T = tau.

REFERENCES

1. Botha H, Mantyh WG, Graff-Radford J, et al. Tau-negative amnestic dementia masquerading as Alzheimer disease dementia. *Neurology.* 2018;90:e940–e946.
2. Rieger AC, Silverman D. Is it too soon to know when it's LATE? *J Nucl Med.* 2022; 63:180–182.
3. Lim SM, Katsifis A, Villemagne VL, et al. The ^18F-FDG PET cingulate island sign and comparison to ^123I-beta-CIT SPECT for diagnosis of dementia with Lewy bodies. *J Nucl Med.* 2009;50:1638–1645.
4. Buciuc M, Botha H, Murray ME, et al. Utility of FDG-PET in diagnosis of Alzheimer-related TDP-43 proteinopathy. *Neurology.* 2020;95:e23–e34.
5. Chételat G, Ossenkoppele R, Villemagne VL, et al. Atrophy, hypometabolism and clinical trajectories in patients with amyloid-negative Alzheimer's disease. *Brain.* 2016;139:2528–2539.
6. Botha H, Mantyh WG, Murray ME, et al. FDG-PET in tau-negative amnestic dementia resembles that of autopsy-proven hippocampal sclerosis. *Brain.* 2018;141:1201–1217.
7. Grothe M, Lang C, Kwangsik N, et al. A topographic imaging biomarker of TDP43 pathology in amnestic dementia based on autopsy derived FDG-PET patterns [abstract]. *Alzheimers Dement.* 2019;15:61–62.
8. Klein HU, Trumpff C, Yang HS, et al. Characterization of mitochondrial DNA quantity and quality in the human aged and Alzheimer's disease brain. *Mol Neurodegen.* 2021;16:75.
9. Teipel S, Grothe MJ; Alzheimer's Disease Neuroimaging Initiative. Does posterior cingulate hypometabolism result from disconnection or local pathology across preclinical and clinical stages of Alzheimer's disease? *Eur J Nucl Med Mol Imaging.* 2016;43:526–536.
10. Whitwell JL, Graff-Radford J, Singh TD, et al. ^18F-FDG PET in posterior cortical atrophy and dementia with Lewy bodies. *J Nucl Med.* 2017;58:632–638.

Stuart J. McCarter
David T. Jones
Clifford R. Jack Jr.
Val Lowe
Hugo Botha*
*Mayo Clinic
Rochester, Minnesota
E-mail: botha.hugo@mayo.edu

Reply: Posterior Cingulate Involvement Does Not Argue Against LATE—And Who Said It Does?

REPLY: In response to our recent article evaluating the potential promise and current limitations of neuroimaging methods in contributing to the premortem diagnosis of limbic-predominant age-related TAR DNA-binding protein 43 (TDP-43) encephalopathy (LATE) (*1*), the letter by McCarter et al. not only mischaracterizes the content of our article but also, perhaps more surprisingly, mischaracterizes that of its authors' own prior publications. For example, the letter states, "Recent data suggest that medial temporal, posterior cingulate, and frontal supraorbital hypometabolism are predictors of LATE whereas prominent inferior temporal involvement may be predictive of AD [Alzheimer disease] (*4*)." Their reference 4 (our article's reference 6) cited here corresponds to a 2020 *Neurology* article, of which 4 of the 5 authors of the present letter served as coauthors. Neither the word *posterior* nor the word *cingulate* occurs once in that entire article. This is understandable given that, in its direct comparison of TDP-43–positive versus TDP-43–negative cases, whereas relative hypometabolism of medial temporal and frontal supraorbital regions was seen in the TDP-43–positive group, not a single voxel of hypometabolism in the posterior cingulate cortex was identified, even at the statistical criterion (quite loose for this kind of analysis) of $P < 0.001$ uncorrected for multiple comparisons (Fig. 2 in that article). Their own article thus fails to support the authors' claim in their letter.

Their letter further states, "Antemortem studies of amnestic dementia cases have demonstrated medial temporal and PCC [posterior cingulate cortical] hypometabolism to be more prominent in amyloid-negative (*5*) and tau-negative patients (*6*)," again citing themselves (their reference 6, our reference 11) referencing a 2018 *Brain* article by Botha et al. for which again 4 of the 5 authors of their present letter were coauthors (including one who served as first author and another who served as senior author). In fact, among their autopsy-proven diagnoses, a total of 2 were tau-negative, and both were documented to have hippocampal sclerosis (a feature that not only is unnecessary for LATE to be diagnosed but also was present in only 22% of TDP-43–positive cases in their own larger autopsy series published in the abovementioned *Neurology* article), and even including their non–autopsy-proven cases, a total of only 4 were amyloid-negative and tau-negative. Moreover, all 8 of the TDP-43–positive cases identified on autopsy were confounded by the concomitant presence of hippocampal sclerosis (perhaps reflecting the selection bias imposed by the inclusion criteria). The importance of this confound is made all the more clear by a recent article by Gauthreaux et al. (*2*). This article examined 408 autopsied participants having LATE or hippocampal sclerosis in a multicenter national neuropathology dataset and reported that LATE with hippocampal sclerosis is neuropathologically distinct from LATE without hippocampal sclerosis (beyond the presence of the sclerosis itself), with the former group not only demonstrating a wider distribution of TDP-43 in the cortex but also harboring more cerebrovascular pathologies. Thus, the prior work of the letter authors had literally no bearing on the pattern of hypometabolism seen in LATE per se, but only on the pattern seen in patients with hippocampal sclerosis, about whom they (properly) had previously confined their comments.

The other source (their reference 5) that the authors cite in their letter as supporting their thesis is an excellent 2016 article by Chetelat et al., which, however, had nothing to do with either LATE or TDP-43. Then, combining all of these references together, their letter asserts, "On the basis of these data, an elevated ratio of inferior-to-medial temporal lobe metabolism was proposed as an ^18F-FDG PET marker of LATE, as the authors [that is, Rieger and Silverman (2022)] correctly pointed out"—this time mischaracterizing *our* article. What we pointed out was only that, in their 2020 *Neurology* article tellingly entitled "Utility of FDG PET in Diagnosis of Alzheimer-Related TDP-43 Proteinopathy," the marker distinguished patients who had what was

denoted as an "AD spectrum pathologic diagnosis" with TDP-43 from those who had autopsy-confirmed AD spectrum diagnoses without TDP-43—that is, 2 different variants of the AD spectrum diagnosis—and thus casts no light on the population of LATE subjects who lack coexistent AD spectrum pathology, since none was included in their study. It is of course entirely unsurprising that 2 separate diseases characterized by processes capable of occurring independently, and both attacking medial temporal structures preferentially, would lead to worse medial temporal hypometabolism for the same degree of inferior temporal hypometabolism associated with AD, in those instances when both diseases concomitantly occur (and, for that matter, when LATE occurs concomitantly with hippocampal sclerosis).

Next, the letter's cited reference 7, by Grothe et al. (3), is actually an abstract published in a supplement and representing a conference poster. It is therefore more difficult to fully assess the significance of this study to the present discussion, but in any event the study included only 4 TDP-43–positive cases without hippocampal sclerosis. Moreover, even granting that limitation, it is evident from visual inspection of the poster online that the "TDP-43–typical" pattern displayed there demonstrated substantially less extensive posterior cingulate and precuneus hypometabolism than the "AD-typical pattern."

The figure and accompanying remainder of the letter by McCarter et al. is devoted primarily to showing 3 cases of LATE that are less relevant than anecdotal cases might otherwise be. All 3 cases are confounded by the concomitant presence of hippocampal sclerosis, again demonstrating the authors' lack of an evidentiary basis for their comments about posterior cingulate hypometabolism in LATE (other than when LATE and hippocampal sclerosis are both present). After these cases is a passing mention of 3 more articles (their references 8–10), the first having no direct relationship to imaging and the others having nothing to do with TDP-43 or LATE.

Finally, the entirety of the objection of the letter by McCarter et al. is directed at a single phrase (constituting one-fifth of a sentence of our 2-page article) regarding when LATE may be suspected, namely "… a pattern of diminished regional cerebral metabolism that is posterior-predominant but nevertheless differs from AD in lacking as marked a defect of posterior cingulate" activity, in cases when occipital metabolism is also relatively preserved (thus making Lewy body–based or posterior cortical atrophy–based causes of dementia less likely). For context, this phrase occurred in the paragraph immediately after our paragraph stating, "A definitive diagnosis of LATE will likely not be possible in the premortem setting, however, without neuroimaging that specifically includes assessment of limbic structures with a clinically available tracer for TDP-43 that is sensitive and specific" and immediately after a sentence indicating that this is in reference to scans of patients with "an AD-like clinical picture in older adults." As we point out in our article, the TDP-43 proteinopathy of LATE often coexists with other processes such as amyloidopathy, tauopathy, and hippocampal sclerosis, and it also occurs in the absence of those additional processes. We obviously then would not suggest that the presence of posterior cingulate hypometabolism would exclude the presence of LATE, given that the presence of LATE does not exclude the presence of other pathologies that affect posterior cingulate metabolic activity. Rather, we suggest that when other clinical and metabolic features we described are present in the absence of hypometabolism of both the posterior cingulate and the occipital cortex, then those are "bases for suspecting this neurodegenerative process." Their letter thereby commits a basic logical fallacy—that is, confusing an if–then statement (if no posterior cingulate or occipital hypometabolism, then LATE) with its inverse (if posterior cingulate or occipital hypometabolism, then not LATE)—which is to say, we agree with the title of their letter, but it has nothing to do with our published article.

REFERENCES

1. Rieger AC, Silverman DHS. Is it too soon to know when it's LATE? *J Nucl Med.* 2022; 63:180–182.
2. Gauthreaux KM, Teylan MA, Katsumata Y, et al. Limbic-predominant age-related TDP-43 encephalopathy: medical and pathologic factors associated with comorbid hippocampal sclerosis. *Neurology.* 2022;98:e1422–e1433.
3. Grothe MJ, Lang C, Nho K, et al. A topographic imaging biomarker of TDP43 pathology in amnestic dementia based on autopsy-derived FDG-PET patterns [abstract]. *Alzheimer Dement.* 2019;15(suppl):7 P61–P62.

Angela C. Rieger
Daniel H.S. Silverman*
*UCLA David Geffen School of Medicine
Los Angeles, California
E-mail: dsilver@ucla.edu

MY SNMMI

Renew Your Membership and Update Your Member Profile

Your **"My SNMMI"** dashboard is an easy way to navigate the many member benefits available to you. Take 5 minutes when you renew your membership to customize your member experience through SNMMI profile options.

- Access the SNMMI Member Directory to begin expanding your professional network
- Manage your credit history, see your transcript, and access the SNMMI Learning Center
- Manage your email and publication preferences to ensure you get the latest news from SNMMI
- Review and update new demographic questions and professional certifications
- Choose your journal preferences for both JNM and JNMT online or print issues
- Stay up-to-date by updating your email and mailing address as needed

www.snmmi.org/MySNMMI
We encourage you to bookmark this page for future use

SNMMI | Value Initiative
SOCIETY OF NUCLEAR MEDICINE & MOLECULAR IMAGING

NUCLEAR MEDICINE & MOLECULAR IMAGING WEEK

OCT 2-8 2022

Grab your 2022 Gear and Show Your Support for the Profession!

T-Shirts

Ladies' & Men's Sport-Wick® Stretch Contrast Full-Zip Jacket

Hand Sanitizers

Lunch Bag
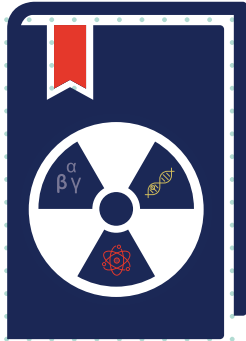
Vacuum Bottle

Silicone Phone Holder/Lanyards

Pen

Poster

SNMMI Value Initiative
SOCIETY OF NUCLEAR MEDICINE & MOLECULAR IMAGING

WWW.SNMMI.ORG/NMW

NOW AVAILABLE

80 Hour Radionuclide Authorized User
TRAINING COURSE

The Society of Nuclear Medicine and Molecular Imaging (SNMMI) and American Society of Nuclear Cardiology (ASNC) are excited to announce the launch of a new online course designed to provide nuclear medicine physicians with the knowledge needed to establish a culture of safety and quality in their practice.

The **ASNC/SNMMI 80 Hour Radionuclide Authorized User Training Course** features lectures on radiation protection and safe radioisotope handling, physics and instrumentation, radiochemistry and radiopharmaceuticals, radiation biology, and nuclear medicine mathematics and statistics, and will fulfill the 80 hours of classroom training that the U.S. Nuclear Regulatory Commission (NRC) and Agreement States require for physicians to become authorized users of radioisotopes for imaging and localization studies.

LEARN MORE: www.snmmi.org/80HourCourse

Explore SNMMI's Online Career Center!

Explore the benefits of the SNMMI Career Center by logging in or creating a new account today.

careercenter.snmmi.org

SNMMI | Value Initiative

SOCIETY OF NUCLEAR MEDICINE & MOLECULAR IMAGING

Streamlined. Simple. Accurate.

CRC® Dose Calibrator Family

Combine the speed and accuracy you need to measure and prepare doses with the performance and reliability that you've come to expect in one of the industry's finest packages.

CRC® - PC Smart Chamber
Network Ready with Remote Connectivity
The Most Advanced in Dose Calibration.

CRC®-55tPET Dose Calibrator (Touch Screen)
Speed and accuracy to measure
and prepare doses.

Driving Innovation... Together

Two leading brands of nuclear medicine products and technology, the
Capintec™ and **Biodex™** teams have joined forces under Mirion Medical.

CAPINTEC
A MIRION MEDICAL COMPANY

Visit capintec.com to learn
how we can support your
unique requirements.